UNIVERSITÉ PARIS-SUD

ÉCOLE DOCTORALE: RAYONNEMENT ET ENVIRONNEMENT

Laboratoire: Institut de Physique Nucléaire d'Orsay

DISCIPLINE: PHYSIQUE NUCLÉAIRE

THÈSE DE DOCTORAT

soutenue le 26/09/2013

par

Nicholas A. N. HIRLINGER SAYLOR

A MEASUREMENT OF UNPOLARIZED CROSS SECTIONS AND POLARIZED CROSS SECTION DIFFERENCES OF DEEPLY VIRTUAL COMPTON SCATTERING ON THE PROTON AT JEFFERSON LABORATORY USING CLAS (e1-dvcs2)

Directeur de thèse:	Michel GUIDAL
Co-directeur de thèse:	Paul STOLER

Composition du jury:

Président du jury:	Bruno ESPAGNON
Rapporteurs:	Valery KUBAROVSKY
	Eric VOUTIER
Examinateurs:	Joel GIEDT
	James NAPOLITANO

TABLE OF CONTENTS

LIST OF TABLES 4

LIST OF FIGURES 5

ACKNOWLEDGEMENTS 29

ABSTRACT 32

RÉSUMÉ 33

1. INTRODUCTION 1

2. MOTIVATION AND THEORY 2

2.1 Electron Scattering - A Historical Background 2

2.1.1 Electron-Nucleon Elastic Scattering 3

2.1.2 Deep Inelastic Scattering (DIS) 5

2.1.3 Bjorken Scaling 6

2.1.4 Light Cone Coordinates 9

2.2 Generalized Parton Distributions 10

2.2.1 Accessing GPDs - Deeply Virtual Compton Scattering 10

2.2.2 Properties of GPDs 16

2.3 The Interference of DVCS and Bethe-Heitler 17

2.3.1 Properties of the BH Cross Section 19

2.4 Available Data, Existing Publications and Parallel Analyses 20

2.5 Beyond Experiment - Models for GPDs 20

2.5.1 Double Distributions 20

2.5.2 D-term 21

2.5.3 VGG Model 21

3. EXPERIMENTAL METHODS 23

3.1 Thomas Jefferson National Accelerator Facility (TJNAF) / Jefferson Laboratory (JLab) 23

3.2 Continuous Electron Beam Accelerator Facility (CEBAF) 23

3.3 CEBAF Large Acceptance Spectrometer (CLAS) 24

3.3.1 Torus Electromagnets and Drift Chambers (DC) 25

3.3.2 Forward Electromagnetic Calorimeters (EC) 26

3.3.3 Large-Angle Electromagnetic Calorimeters (LAC) 27

3.3.4 Time of Flight Scintillators (TOF/SC) 27

3.3.5 Cherenkov Counters (CC) 28

3.3.6 Inner Calorimeter (IC) 29

3.3.7 Solenoid 30

4. DATA ANALYSIS 31

4.1 DVCS Analysis . . . 31
4.1.1 DVCS Cross Section - A Road Map . . . 31
4.1.2 Kinematical Domain and Binning - Bin by Bin Analysis . . . 32
4.2 Particle Identification . . . 34
4.2.1 Electron Identification . . . 35
4.2.2 Proton Identification . . . 53
4.2.3 Photon Identification - EC . . . 65
4.2.4 Photon Identification - IC . . . 72
4.2.5 Neutral Pion π^0 Identification . . . 72
4.2.6 Summary of Cuts . . . 73
4.3 Acceptance . . . 77
4.3.1 Definition of the Acceptance of CLAS . . . 77
4.3.2 DVCS Generator . . . 78
4.3.3 GEANT3 Simulations (GSIM) . . . 78
4.3.4 GSIM Post-Processing (GPP) . . . 79
4.3.5 Background Merging . . . 80
4.3.6 Particle Identification . . . 81
4.3.7 Comparison to Data . . . 82
4.3.8 Final Results for the Acceptance of CLAS . . . 86
4.4 Momentum and Angle Corrections . . . 87
4.4.1 Energy Loss Corrections . . . 87
4.4.2 Empirical Kinematical Corrections for Charged Particles . . . 96
4.4.3 Corrections to Photon Energies in Data . . . 116
4.5 DVCS Event Selection . . . 121
4.5.1 Exclusivity Cuts . . . 121
4.6 Bin Volume Determination . . . 131
4.6.1 A Monte Carlo Method for Determining Bin Volumes . . . 131
4.7 Integrated Luminosity . . . 133
4.7.1 Good Run List . . . 133
4.7.2 Integrated Luminosity . . . 136
4.8 Pion Subtraction . . . 142
4.8.1 A Method for Estimating the Pion Contamination . . . 142
4.8.2 Computing $N_{\pi^0}^{\gamma\gamma}$ from Data . . . 143
4.8.3 Computing $\frac{A_{\pi^0}^{\gamma}}{A_{\pi^0}^{\gamma\gamma}} = \frac{N_{\pi^0,\mathrm{rec}}^{\gamma}}{N_{\pi^0,\mathrm{rec}}^{\gamma\gamma}}$ from Monte Carlo . . . 149
4.8.4 Final Results for the Estimated Pion Contamination $N_{\pi^0}^{\gamma}$ . . . 153
4.9 Radiative Corrections . . . 155
4.9.1 Obtaining the Born Cross Section . . . 155
4.9.2 Final Results for the Radiative Corrections . . . 158

4.10 Elastic Normalization . . . 160
4.10.1 Elastic Cross Section . . . 160
4.11 Estimation of Errors . . . 165
4.11.1 Statistical Errors . . . 165
4.11.2 Systematical Errors . . . 166
5. FINAL RESULTS . . . 168
5.1 DVCS Cross Section - Final Results . . . 168
5.1.1 Unpolarized Cross Section . . . 168
5.1.2 Polarized Cross Section Difference . . . 170
5.1.3 Beam Spin Asymmetry . . . 171
5.2 Comparison with Parallel Analysis of e1-dvcs2, and e1-dvcs1 . . . 173
5.3 Preliminary Interpretation of Final Results . . . 175
5.3.1 Comparison with Existing Models . . . 175
5.3.2 VGG Extraction of Compton Form Factors . . . 176
5.3.3 Extraction of Proton Charge Density . . . 180
6. CONCLUSION . . . 185
7. SYNTHÈSE . . . 187
7.1 Distributions de Partons Généralisées (GPDs) et Diffusion Compton Profondément Virtuelle (DVCS) . . . 187
7.2 Appareillage Expérimental . . . 189
7.3 La Section Efficace de DVCS . . . 191
7.4 Une Interprétation Préliminaire de l'Extraction de la GPD H . . . 195
LITERATURE CITED . . . 203
APPENDICES . . . 207
A. Complete Results for Acceptance . . . 207
B. Complete Results for Bin Volume Corrections . . . 218
C. Complete Results for Pion Subtraction Ratio . . . 229
D. Complete Results for Radiative Corrections . . . 240
E. Comparison with Parallel Analysis of e1-dvcs2, e1-dvcs1 - Full List of Plots . . . 251
F. Complete Results for GPD Models . . . 317

LIST OF TABLES

Table 2.1 A table of DVCS variables, their Sudakov decompositions, and their values in the Bjorken limit where $Q^2 >> m_N, -t$. 13
Table 4.1 The boundaries of each of the bins according to their four dimensions. . . 34
Table 4.2 A table of cuts used in the identification of electrons. 73
Table 4.3 A table of cuts used in the identification of protons. 74
Table 4.4 A table of cuts used in the identification of EC photons. 75
Table 4.5 A table of cuts used in the identification of IC photons. 76
Table 4.6 A table containing all of the parameters for equation 130 and 131, the ionization corrections for electrons and protons respectively. 94
Table 4.7 The table of parameters corresponding to equation 142, the equation which gives the kinematic corrections to the polar angle θ_e for the electrons. . . 101
Table 4.8 The table of parameters corresponding to equation 148, the equation which gives the kinematic corrections to the momentum, p_e, for the electrons. . 104
Table 4.9 The table of parameters corresponding to equation 158, the equation which gives the kinematic corrections to the momentum for positive pions and protons. 111
Table 4.10 The table of parameters corresponding to equation 165, the equation which gives the energy correction to the energy of photons in the EC. 118
Table 4.11 The "stretch" factors for $p_{X,\perp}$ and $\theta_{X,\gamma}$. 122
Table 4.12 A table of cuts corresponding to the variables $p_{X,\perp}$ and $\theta_{X,\gamma}$ for IC and EC, and data and Monte Carlo. 125
Table 4.13 A table of cuts corresponding to the variable E_X for IC and EC, and data and Monte Carlo. 126
Table 4.14 A table of cuts in data corresponding to the case where both π^0 photons are detected in the IC. 144
Table 4.15 A table of cuts in data corresponding to the case where both π^0 photons are detected in the EC. 145
Table 4.16 A table of cuts in Monte Carlo corresponding to the case where both π^0 photons are detected in the IC. 149
Table 4.17 A table of cuts in Monte Carlo corresponding to the case where both π^0 photons are detected in the EC. 150
Table 4.18 A table of the measured and predicted sources of systemically error. The first four quantities are estimated from e1-dvcs1. The last two systematic errors of ϵ and $\mathcal{L}_{\text{int}}$ are calculated from e1-dvcs2, and have already been presented earlier in this thesis. For the moment, we take our systematic to be about 18 %. 167

LIST OF FIGURES

Figure 2.1 A Feynman diagram of elastic $e - \mu$ scattering. 3
Figure 2.2 A Feynman diagram of elastic $e - p$ scattering. 5
Figure 2.3 A Feynman diagram of inelastic $e + p \rightarrow e + X$ scattering. 6
Figure 2.4 Log-log F_2 measurements from H1+ZEUS, BCDMS, E665, NMC, and SLAC as a function of Q^2, and x_B. This plot is courtesy of reference[8], with data from[9–13] 8
Figure 2.5 The handbag diagrams of DVCS, including the uncrossed and crossed diagrams. 10
Figure 2.6 The handbag diagram of DVMP, including quark GPDs on top and gluon GPDs on bottom. 11
Figure 2.7 The unfactorized DVCS diagram. 12
Figure 2.8 The region where $x < -\xi$ and $x > \xi$ is called the DGLAP region, corresponding to the QCD evolution equations in Q^2 for the PDFs we introduced earlier in this section. This physically corresponds to a quark, or an antiquark, being emitting, and then later reabsorbed into the nucleon. The region where $-\xi < x < \xi$ is called the ERBL region, corresponding to the QCD evolution equations in Q^2 for the Distribution Amplitudes, and physically corresponds to a quark-antiquark pair being emitted or reabsorbed into the nucleon. Illustration is courtesy of the Diehl review article.[18] . . 14
Figure 2.9 The two possible leading order BH diagrams. 17
Figure 3.1 An aerial view of JLab.[38] 23
Figure 3.2 A schematic of CEBAF.[39] 24
Figure 3.3 A sliced and labeled cartoon of CLAS.[39] 25
Figure 3.4 A cross section of CLAS on the x-y plane, and on the x-z plane.[40] 26
Figure 3.5 A sector of the EC, showing the different layers and planes peeled away.[41] 27
Figure 3.6 A sector of the TOF.[43] 28
Figure 3.7 A sector of the CC.[44] 28
Figure 3.8 A single section of a sector of the CC, showing the configuration of the mirrors.[44] 29
Figure 3.9 A photograph of IC, courtesy of Hyon-Suk Jo. 30
Figure 3.10 The solenoid helps direct the Möller electrons in the forward direction in order to prevent them for creating noise in the IC and DC region one. On left, simulation without the use of the solenoid, and on right, with the use of the solenoid. Figure is from reference[20] 30
Figure 4.1 A diagram of DVCS, indicating the leptonic and hadronic planes, and the angle ϕ between them.[18] 31
Figure 4.2 The kinematical domain for e1-dvcs2, after all cuts. On the left, Q^2 versus x_B. The black lines correspond to the bin definitions found in Table 4.1. The red lines correspond to the upper and lower cuts on θ_e, the yellow line corresponds to the cut on Q^2, the green line corresponds to the cut on W, and the blue line corresponds to the cut on p_e. On the right, $-t$ versus x_B. The black lines correspond to the bin definitions found in Table 4.1. The red line corresponds to the minimum t value allowed by kinematics, and the green line corresponds to the minimum x_B allowed due to the cut on p_e. 32
Figure 4.3 Energy deposited in outer stack of EC plotted against energy deposited in the inner stack of EC. The red line represents the cut requiring $E_{inner} > 0.06$ GeV. 36
Figure 4.4 Sampling fraction f_s as a function of momentum, before cut on left, after cut on right. The main features of this plot are the electrons, mostly horizontal on each plot; and the negative pions whose sampling fraction is decreasing with increasing momentum. The purpose of this cut is to separate these pions from the electrons. 37

Figure 4.5 Vertex position of electrons in z-direction for each sector. On the left, before corrections. On the right, after corrections. The red lines represent the final cut. We note that the heights of each sector differ, indicating that each sector has a different level of performance. The periodic behavior, producing regular small spikes, is an artifact of ntuple22 variable compression. . . . 39
Figure 4.6 The number of photoelectrons detected in the CC for electrons. The cut is shown by the vertical line at 25, corresponding to 2.5 photoelectrons. . . 41
Figure 4.7 CC plotted by sector, before fiducial cuts. 43
Figure 4.8 CC plotted by sector, after geometrical cuts. 44
Figure 4.9 CC plotted by sector, after geometrical, efficiency, and dead pmt cuts. . . 44
Figure 4.10 CC efficiencies, $\epsilon_{\mathrm{CC}}(\theta_v, \phi_v)$, plotted by sector, after geometrical, efficiency, and dead pmt cuts. This plot determines the cuts placed in Figure 4.9, with everything below 80% removed. 45
Figure 4.11 Occupancy of CC PMTs, per sector, per PMT, as a function of run number. The top third of each sector, partitioned by black lines, represents the left side PMTs. The bottom third represents the right side PMTs. The middle third represents a simultaneous signal in both left and right PMTs. The PMT which is removed from the analysis is number 47 in sector 1, which can be seen in the upper left panel. 45
Figure 4.12 On the left, the intersection position of the electron candidate track on the plane which contains the back face of the IC. On the right, the same plot after fiducial cuts. One can see the octagonal shadow, as well as the shape of the IC cradle structure on the bottom. 46
Figure 4.13 A drawing of the region 1 DC configuration, not to scale. 48
Figure 4.14 Track position in region 1 drift chamber for electrons, plotted in coordinates y and s_e, before cuts. 49
Figure 4.15 Track position in region 1 drift chamber for electrons, plotted in coordinates y and s_e, after IC shadow fiducial cut. 49
Figure 4.16 Track position in region 1 drift chamber for electrons, plotted in coordinates y and s_e, after IC shadow fiducial cut, and DC fiducial cut. 50
Figure 4.17 In the first row, from left to right, u, v, and w distributions for all sectors for electrons. The vertical red lines represent the cuts on the three variables. The black distributions are before all cuts, and the red distributions are after cuts on u, v, w, dead strips, and IC shadow cut. On the bottom row is the front face of the EC, in x and y, from left to right: before cuts; after cuts on u, v, w, and dead strips; and after cuts on u, v, w, dead strips, and IC shadow cut. 51
Figure 4.18 SC hit position for electrons, as determined by region 3 drift chambers before CC fiducial cuts, plotted in coordinates y and x. 52
Figure 4.19 SC hit position for electrons, as determined by region 3 drift chambers, plotted in coordinates y and x, after CC fiducial cuts. 52
Figure 4.20 Occupancy of SC paddles as a function of run number. Each panel represents a sector. The y-axis represents paddle number. Each occupancy is normalized to the average number of hits over all sectors for that particular paddle number. In other words, for sector i, the value on the z-axis corresponds to the quantity $N_{i,\mathrm{normalized}} = \frac{N_{i,\mathrm{unnormalized}}}{\sum_{i=1}^{6} N_{i,\mathrm{unnormalized}}}$. 53
Figure 4.21 On the left, a plot of $\Delta\beta$ as a function of momentum p. The red lines represent the restriction that $|\Delta\beta| < 0.05$. On the right, β versus p of the particles selected by the cut applied on the left. Here, the protons are selected based on the requirement that the two different measurements of β are in agreement. 54
Figure 4.22 Vertex position of protons in z-direction. On the left, before corrections. On the right, after corrections. The red lines represent the final cut. . . . 55

Figure 4.23 On the x-axis, the difference of electron and proton vertex position in the z direction. On the y-axis, momentum. The red lines correspond to the momentum dependent cuts at 3σ. 56
Figure 4.24 On the x-axis, vertex position in z direction for electrons. On the y-axis, vertex position in z direction for protons, before the cut described in Figure 4.23. 56
Figure 4.25 On the x-axis, vertex position in z direction for electrons. On the y-axis, vertex position in z direction for protons, after the cut described in Figure 4.23. 57
Figure 4.26 On the left, the intersection position of the proton candidate track on the plane which contains the back face of the IC. On the right, the same plot after fiducial cuts. 57
Figure 4.27 Track position in region one drift chamber for protons, plotted in coordinates y and s_p, before cuts. 59
Figure 4.28 Track position in region one drift chamber for protons, plotted in coordinates y and s_p, after IC shadow fiducial cut. 59
Figure 4.29 Track position in region one drift chamber for protons, plotted in coordinates y and s_p, after IC shadow fiducial cut, and DC fiducial cut. 60
Figure 4.30 A drawing of the first two panels of the Time of Flight configuration, not to scale. 62
Figure 4.31 SC hit position for electrons, as determined by region 3 drift chambers, plotted in coordinates y and t, before cuts. 62
Figure 4.32 SC hit position for electrons, as determined by region 3 drift chambers, plotted in coordinates y and t, after a geometrical fiducial cut on panels one and two. 63
Figure 4.33 SC hit position for electrons, as determined by region 3 drift chambers, plotted in coordinates y and t, after a geometrical fiducial cut on panels one and two, and a cut on paddle number. 63
Figure 4.34 SC hit position for electrons, as determined by region 3 drift chambers, plotted in coordinates y and t, after a geometrical fiducial cut on panels one and two, a cut on paddle number, and a cut on the coordinates of dead paddles. 64
Figure 4.35 On the left, the raw values of β as a function of p. Entries with values of β less than .95 have their momenta and velocities forced to agree as if they were neutrons. On the right, the reconstructed values of β versus p, allowing for us to accept photons lower than $\beta = .95$. 66
Figure 4.36 βs for photon candidates, with a cut accepting only particles with $\beta > 0.9$. 67
Figure 4.37 In the first row, from left to right, u, v, and w distributions for all sectors for photons. The vertical red lines represent the cuts on the three variables. The black distributions are before all cuts, and the red distributions are after cuts on u, v, w, dead strips, and IC shadow cut. On the bottom row is the front face of the EC, in x and y, from left to right: before cuts; after cuts on u, v, w, and dead strips; and after cuts on u, v, w, dead strips, and IC shadow cut. 68

Figure 4.38 The left column represents the difference between the times as measured by the EC and the SC as a function of run number. The units of the ordinate are in nanoseconds. The right column represents the reconstructed velocity of the photons as a function of run number. The top row represents these values before EC timing calibrations. The bottom row represents these values after EC timing calibrations. We note that there is a very good improvement after the calibration. We make note that on the top row, there are series of points which are all at a fixed value, such as 0.06 for the sigma of the timing difference, and 1.0 and 1.05 for the mean and sigma of the velocity of photons respectively. This exact assignment to these values is a sign that the calibration routine had failed, and that these initial values were entered. 70
Figure 4.39 On the left, the intersection position of the photon candidate track on the plane which contains the back face of the IC. On the right, the same plot after fiducial cuts. 71
Figure 4.40 The IC, on the left, before fiducial cuts, on the right, after fiducial cuts. . 72
Figure 4.41 On each panel, the layer number in DC is plotted against the wire number in the DC. On the top is data. In the center is MC before efficiency corrections. On the bottom is after efficiency corrections. Deep red corresponds to 100% efficiency, while deep blue corresponds to low efficiency. Zero efficiency is represented by white. We note that the inefficiencies seen in data, the top plot, are reproduced in the MC after the corrections, on the bottom plot.[23] 80
Figure 4.42 Q^2 versus x_B for data on left, and Monte Carlo on right, showing a good agreement. 82
Figure 4.43 $-t$ versus x_B for data on left, and Monte Carlo on right, showing a good agreement. 83
Figure 4.44 A comparison of kinematic variables for data on left, and Monte Carlo on right. The top row is Q^2, the second row is x_B, the third row is $-t$, and the bottom row is Φ. We see that the agreement between data and simulation is very good with no extreme deviations visible. 83
Figure 4.45 Momentum versus polar angle for each particle type, data on left, and Monte Carlo on right. On the top row, p_e versus θ_e, on the center row, p_p versus θ_p, and on the bottom row, p_γ versus θ_γ. We notice that there is good agreement between data and simulations, except for energy of the photons in the IC, corresponding to low θ_γ values. There is a concentration of photons at about 4 GeV in data and 4.5 GeV in Monte Carlo. In these plots, this is the only serious discrepancy in simulations, whose cause has yet to be fully understood. 84
Figure 4.46 Angular distributions for each particle type, data on left, and Monte Carlo on right. On the top row, ϕ_e versus θ_e, on the center row, ϕ_p versus θ_p, and on the bottom row, ϕ_γ versus θ_γ. We see that the distributions are well reproduced in the simulations when compared to data. 85
Figure 4.47 The acceptance as a function of ϕ for the fifth bin in x_B and θ_e, where $0.17 < x_B < 0.2$ and $25.5^\circ < \theta_e < 45^\circ$. 86
Figure 4.48 Δp_e for bins in θ_e as measured from the vertex. The black points represent the means of the Gaussian distributions in slices of momentum, and the red points represent one standard deviation from the mean point. The black curve running through the black points represents the best fit according to equation 123. The horizontal green line represents the line $\Delta p_e = 0$. . . . 89
Figure 4.49 $\Delta\theta_e$ for bins in θ_e as measured from the vertex. The black points represent the means of the Gaussian distributions in slices of momentum, and the red points represent one standard deviation from the mean point. The horizontal green line represents the line $\Delta\theta_e = 0$. 90

Figure 4.50 $\Delta\phi_e$ for bins in θ_e as measured from the vertex. The black points represent the means of the Gaussian distributions in slices of momentum, and the red points represent one standard deviation from the mean point. The horizontal green line represents the line $\Delta\phi_e = 0$. 90
Figure 4.51 Δp_p for bins in θ_p as measured from the vertex. The black points represent the means of the Gaussian distributions in slices of momentum, and the red points represent one standard deviation from the mean point. The black curve running through the black points represents the best fit according to equation 124. These curves are in accordance with what we would expect - with large deviations at low angle. This affect at low momentum is due to the momentum dependence of equation 112. The horizontal green line represents the line $\Delta p_p = 0$. 91
Figure 4.52 $\Delta\theta_p$ for bins in θ_p. The black points represent the means of the Gaussian distributions in slices of momentum, and the red points represent one standard deviation from the mean point. The horizontal green line represents the line $\Delta\theta_e = 0$. 91
Figure 4.53 $\Delta\phi_p$ for bins in θ_p. The black points represent the means of the Gaussian distributions in slices of momentum, and the red points represent one standard deviation from the mean point. The horizontal green line represents the line $\Delta\phi_e = 0$. 92
Figure 4.54 α_e and β_e as a function of θ_e, with a polynomial fit. 93
Figure 4.55 α_p, β_p and γ_p as a function of θ_p, with a polynomial fit. 93
Figure 4.56 Δp_{cor} as a function of p for electrons. 95
Figure 4.57 Δp_{cor} as a function of p for protons. 96
Figure 4.58 $\Delta\theta_e$ as a function of $\phi_{\text{DC},e}$, for different bins of $\theta_{\text{DC},e}$. The black points represent the means of the fits of Gaussian peaks to slices in $\phi_{\text{DC},e}$, and the red points represent the standard deviations of the same. The black curves represent the fits in $\phi_{\text{DC},e}$ according to a straight line as seen in equation 139. 100
Figure 4.59 The parameter a_e fit as a function of $\theta_{\text{DC},e}$ sector by sector according to equation 140. 101
Figure 4.60 The parameter b_e fit as a function of $\theta_{\text{DC},e}$ sector by sector according to equation 141. 102
Figure 4.61 δp_e as a function of $\phi_{\text{DC},e}$, for different bins of $\theta_{\text{DC},e}$. The black points represent the means of the fits of Gaussian peaks to slices in $\phi_{\text{DC},e}$, and the red points represent the standard deviations of the same. The black curves represent the fits in $\phi_{\text{DC},e}$ according to a straight line as seen in equation 145. 103
Figure 4.62 The parameter c_e fit as a function of $\theta_{\text{DC},e}$ sector by sector according to equation 146. 104
Figure 4.63 The parameter d_e fit as a function of $\theta_{\text{DC},e}$ sector by sector according to equation 147. 105
Figure 4.64 The left column represents W and the right column represents E_0. The top row is before kinematic corrections on momentum and angle, and the bottom row is after both angle and momentum corrections. We notice almost complete elimination of the slant in $\phi_{\text{DC},e}$. 106
Figure 4.65 The left column represents W and the right column represents E_0. The top row is before kinematic corrections on momentum and angle, and the bottom row is after both angle and momentum corrections. We notice a shift in the average sector value in almost all sectors towards the expected values. 107

Figure 4.66 δp_{π^+} as a function of ϕ_{DC,π^+}, for different bins of $\theta_{\mathrm{DC},\pi^+}$. The black points represent the means of the fits of Gaussian peaks to slices in ϕ_{DC,π^+}, and the red points represent the standard deviations of the same. The black curves represent the fits in ϕ_{DC,π^+} according to a straight line. It is useful to note that the lack of events below $\theta_{\mathrm{DC},\pi^+} = 36^\circ$ due to the fiducial cut we place on positive particles due to the shadow of the IC. Naturally, pions which pass through the IC and are detected by CLAS will have much less energy due to ionization, and will not be useful candidates for this study. For this study, we employ the same exact IC shadow cut to pions as we do to protons. 110
Figure 4.67 The parameter e_{π^+} fit as a function of $\theta_{\mathrm{DC},\pi^+}$ sector by sector according to equation 156. 111
Figure 4.68 The parameter f_{π^+} fit as a function of $\theta_{\mathrm{DC},\pi^+}$ sector by sector according to equation 157. 112
Figure 4.69 δp_{π^+} as a function of ϕ_{DC,π^+}, for different bins of $\theta_{\mathrm{DC},\pi^+}$, before momentum corrections to pions. 113
Figure 4.70 δp_{π^+} as a function of ϕ_{DC,π^+}, for different bins of $\theta_{\mathrm{DC},\pi^+}$, after momentum corrections to pions. 113
Figure 4.71 δM_N as a function of ϕ_{DC,π^+}, for different bins of $\theta_{\mathrm{DC},\pi^+}$, before momentum corrections to pions. 114
Figure 4.72 δM_N as a function of ϕ_{DC,π^+}, for different bins of $\theta_{\mathrm{DC},\pi^+}$, after momentum corrections to pions. 115
Figure 4.73 δM_N as a function of $\theta_{\mathrm{DC},\pi^+}$, before momentum corrections to pions. The black points represent the means in slices of $\theta_{\mathrm{DC},\pi^+}$ and the red points correspond to one standard deviation. 115
Figure 4.74 δM_N as a function of $\theta_{\mathrm{DC},\pi^+}$, after momentum corrections to pions. The black points represent the means in slices of $\theta_{\mathrm{DC},\pi^+}$ and the red points correspond to one standard deviation. Comparing with Figure 4.73, we notice a small, but significant improvement in the mean and sigma. . . . 116
Figure 4.75 For EC studies: we plot on the left column the invariant mass as a function of pion energy; in the middle column the invariant mass as a function of pion polar angle; and on the right column the invariant mass as a function of missing energy of the $e+p+\gamma+\gamma$ system. We plot on the top row results before corrections; on the middle row results after R. de Masi corrections; and on the bottom row results after P. Bosted corrections. 119
Figure 4.76 For IC viewing: on the left, the invariant mass as a function of pion energy, in the middle, the invariant mass as a function of pion polar angle, and on the right, the invariant mass as a function of missing energy of the $e+p+\gamma+\gamma$ system. 119
Figure 4.77 We plot on the top left the means for the mass spectra as a function of pion energy; on the top right the means of the mass spectra as a function of pion polar angle; on the lower right the sigmas for the mass spectra as a function of pion energy; and on the bottom right the sigmas for the mass spectra as a function of pion polar angle. Black points represent results before corrections, red points represent results after R. de Masi corrections, and green points represent results after P. Bosted corrections. We conclude from this graph that the P. Bosted corrections are the best for e1-dvcs2 both in terms of the change in the mean value and the slightly tightened value of sigma. 120

Figure 4.78 For the variable $p_{X,\perp}$, on top, the distributions for data in black, Monte Carlo in red, and stretched Monte Carlo in green. The upper left panel is for the IC and the upper right panel is for the EC. The cuts in black correspond to the IC and EC cuts at 97% of the fit to equation 167. The cut in red corresponds to the scaling of the black cut according to the stretch factor. On the bottom left, the χ^2 value for the comparison between data and stretched Monte Carlo, as a function of "stretching", on left for IC and on right for EC. These plots correspond to events after cuts on all other variables. 123

Figure 4.79 For the variable $\theta_{X,\gamma}$, on top, the distributions for data in black, Monte Carlo in red, and stretched Monte Carlo in green. The upper left panel is for the IC and the upper right panel is for the EC. The cuts in black correspond to the IC and EC cuts at 90% of the fit to equation 167. The cut in red corresponds to the scaling of the black cut according to the stretch factor. On the bottom left, the χ^2 value for the comparison between data and stretched Monte Carlo, as a function of "stretching", on left for IC and on right for EC. These plots correspond to events after cuts on all other variables. 124

Figure 4.80 For the variable E_X, on top, data, on bottom, Monte Carlo. On left is IC, and on right is EC. On the left, the IC distribution is fit to a skewed Gaussian for both data and Monte Carlo. On the right, the EC is fit to a Gaussian for both data and Monte Carlo. The cuts are denoted by the vertical black lines, whose values are written in Table 4.13. These plots correspond to events after cuts on all other variables. 126

Figure 4.81 Exclusivity variables in data for IC. On the top row are the distributions before all cuts. On the bottom are the distributions after all exclusivity cuts except for the cut on the plotted variable. The only exception is Φ, for which all cuts have been applied. The first column represents $p_{X,\perp}$. The second column represents $\theta_{\gamma,X}$. The third column represents E_X. The last column represents Φ. One can see in the missing energy, before cuts, a peak below zero, which corresponds to the elastic channel with an accidental photon of 400 MeV. 127

Figure 4.82 Exclusivity variables in data for EC. On the top row are the distributions before all cuts. On the bottom are the distributions after all exclusivity cuts except for the cut on the plotted variable. The only exception is Φ, for which all cuts have been applied. The first column represents $p_{X,\perp}$. The second column represents $\theta_{\gamma,X}$. The third column represents E_X. The last column represents Φ. One can see in the missing energy, before cuts, a peak below zero, which corresponds to the elastic channel with an accidental photon of 400 MeV. 128

Figure 4.83 Exclusivity variables in Monte Carlo for IC. On the top row are the distributions before all cuts. On the bottom are the distributions after all exclusivity cuts except for the cut on the plotted variable. The only exception is Φ, for which all cuts have been applied. The first column represents $p_{X,\perp}$. The second column represents $\theta_{\gamma,X}$. The third column represents E_X. The last column represents Φ. 129

Figure 4.84 Exclusivity variables in Monte Carlo for EC. On the top row are the distributions before all cuts. On the bottom are the distributions after all exclusivity cuts except for the cut on the plotted variable. The only exception is Φ, for which all cuts have been applied. The first column represents $p_{X,\perp}$. The second column represents $\theta_{\gamma,X}$. The third column represents E_X. The last column represents Φ. 130

Figure 4.85 The bin volume correction $\frac{N_{\text{bin}}}{N_{\text{super}}}$ as a function of Φ for the fifth bin in x_B and θ_e, where $0.17 < x_B < 0.2$ and $25.5^\circ < \theta_e < 45^\circ$. 132

Figure 4.86 The average electron rate for each run. 134
Figure 4.87 The electron rate for each file as a function of run. 135
Figure 4.88 The y-axis projection of Figure 4.87. 135
Figure 4.89 Each panel corresponds to a sector. In each sector is the vertex position of all good electrons for that sector in the empty target run. Each distribution has three peaks. On the far left is the target entry window. On the right is the target exit window. These two are fit to Gaussians, whose means are used to calculate the distance between the two peaks. This difference is the target length. On the very far right, just on the edge of the histogram is the peak corresponding to the foil placed in downstream from the target. This foil insulated the target from heat. 137
Figure 4.90 The abscissa corresponds to sector number, and the ordinate corresponds to the measurement of the target length according to the method of using vertex position. Each of the six measurements corresponds to the values determined from Figure 4.89. The horizontal black line corresponds to the mean value of all six points. The mean and standard deviation are listed in the upper right label. 138
Figure 4.91 The charge asymmetry for e1-dvcs2, as a function of run number. We see that the asymmetry is never more than $\pm$ 0.005, which is sufficiently small for our purposes. 140
Figure 4.92 MM^2_{e+p+X} versus $IM_{\gamma\gamma}$. The upper-left panel corresponds to the IC-IC case. The upper-right panel corresponds to the IC-EC case. The lower-left panel corresponds to the EC-IC case. The lower-right panel corresponds to the EC-EC case. In each of the four panels, a black ellipse is drawn indicating the region where a π^0 should be found. In the cases of the IC-IC and EC-EC topologies, the pions can clearly be seen. In the cases of the mixed topologies IC-EC and EC-IC, there are no pions visible. This is due to the strict fiducial cuts placed on the IC and EC as well as the IC shadow fiducial cuts placed on the EC. These fiducial cuts require the pion to have a restrictively large angle between its two decay photons, causing there to be no detectable pion signal. 145
Figure 4.93 Exclusivity variables in data for IC. On the top row are the distributions before all cuts. On the bottom are the distributions after all exclusivity cuts except for the cut on the plotted variable. The first column represents MM^2_{e+p}. The second column represents $MM^2_{e+\pi^0}$. The third column represents $IM_{\gamma\gamma}$. The last column represents θ_{X,π^0}. 147
Figure 4.94 Exclusivity variables in data for EC. On the top row are the distributions before all cuts. On the bottom are the distributions after all exclusivity cuts except for the cut on the plotted variable. The first column represents MM^2_{e+p}. The second column represents $MM^2_{e+\pi^0}$. The third column represents $IM_{\gamma\gamma}$. The last column represents θ_{X,π^0}. 148
Figure 4.95 Exclusivity variables in Monte Carlo for IC. On the top row are the distributions before all cuts. On the bottom are the distributions after all exclusivity cuts except for the cut on the plotted variable. The first column represents MM^2_{e+p}. The second column represents $MM^2_{e+\pi^0}$. The third column represents $IM_{\gamma\gamma}$. The last column represents θ_{X,π^0}. 151
Figure 4.96 Exclusivity variables in Monte Carlo for EC. On the top row are the distributions before all cuts. On the bottom are the distributions after all exclusivity cuts except for the cut on the plotted variable. The first column represents MM^2_{e+p}. The second column represents $MM^2_{e+\pi^0}$. The third column represents $IM_{\gamma\gamma}$. The last column represents θ_{X,π^0}. 152

Figure 4.97 The neutral pion yields as a function of Φ for the fifth bin in x_B and θ_e, where $0.17 < x_B < 0.2$ and $25.5^\circ < \theta_e < 45^\circ$. The yield for two photons detected in Monte Carlo is green. The yield for one photon detected in Monte Carlo is red. The ratio of these yields is equivalent to the ratio of their acceptances. 153
Figure 4.98 The neutral pion subtraction ratio $R = \frac{N^{\gamma}_{\pi^0}}{N^{e+p+\gamma}}$ as a function of Φ for the fifth bin in x_B and θ_e, where $0.17 < x_B < 0.2$ and $25.5^\circ < \theta_e < 45^\circ$. . . . 154
Figure 4.99 The Born terms for BH and DVCS. Form factors are represented by the black blobs. GPDs are represented by the blue blobs. 155
Figure 4.100 All radiative corrections up to leading order. Form factors are represented by the black blobs. GPDs are represented by the blue blobs. BH or DVCS photons are represented by black photon lines, while real radiative photons are represented by yellow photon lines. 156
Figure 4.101 An example of the post-radiation tail. On the left, for the IC, and on the right for the EC. In both, you can see a radiative tail coming down on the right hand side of the peak. This corresponds to energy lost from a photon radiating from the outgoing electron leg. 157
Figure 4.102 The MM^2_{e+p} distribution in GeV^2 for the IC after all exclusivity cuts, showing the three sigma limit in black, which is taken to be the approximate cutoff, corresponding to a cutoff on the radiated photon energy. The black curve represents the fit to a Gaussian with a second order polynomial background, which is represented by the red line. 158
Figure 4.103 The radiative corrections as a function of Φ for the fifth bin in x_B and θ_e, where $0.17 < x_B < 0.2$ and $25.5^\circ < \theta_e < 45^\circ$. 159
Figure 4.104 The elastic cross section computed from e1-dvcs2 by B. Guegan[23] in black points, and the cross section according to the Brash parameterization[55] displayed as a red line. Each panel corresponds to a sector. This plot is a reproduction of a plot appearing in the thesis manuscript of B. Guegan.[23] 161
Figure 4.105 The ratio of the elastic cross section computed from e1-dvcs2 by B. Guegan[23] to the cross section according to the Brash parameterization.[55] The red line at 1 denoted where a perfect agreement would be. Each panel corresponds to a sector. Each sector is fit to a constant, represented by a horizontal black line, representing the normalization per sector. This plot is a reproduction of a plot appearing in the thesis manuscript of B. Guegan.[23] 162
Figure 4.106 On the left, integrated over all sectors, the elastic cross section computed from e1-dvcs2 by B. Guegan[23] in black points, and the cross section according to the Brash parameterization[55] displayed as a red line. On the right, the ratio of the CLAS cross section to the cross section extracted from Brash.[55] The red line at 1 denotes where a perfect agreement would be. The ratio is fit to a constant, represented by a horizontal black line, representing the overall normalization. This normalization, integrated over all sectors, is the overall correction that is used in the DVCS cross section. This plot is a reproduction of a plot appearing in the thesis manuscript of B. Guegan.[23] 163
Figure 4.107 The abscissa corresponds to sector number, and the ordinate corresponds to the measurement of the elastic renormalization according to the method above. Each of the six measurements corresponds to the values determined from Figure 4.105. The horizontal black line corresponds to the mean value of all six points. The mean and standard deviation are listed in the upper right label. 164
Figure 5.1 The unpolarized cross section as a function of Φ for the fifth bin in x_B and θ_e, where $0.17 < x_B < 0.2$ and $25.5^\circ < \theta_e < 45^\circ$. Each panel corresponds to a bin in $-t$ whose limits are: [0.09, 0.13, 0.18, 0.23, 0.30, 0.39, 0.52, 0.72, 1.10, 2.00] in GeV^2. 169

Figure 5.2 The polarized cross section as a function of Φ for the fifth bin in x_B and θ_e, where $0.17 < x_B < 0.2$ and $25.5° < \theta_e < 45°$. Each panel corresponds to a bin in $-t$ whose limits are: [0.09, 0.13, 0.18, 0.23, 0.30, 0.39, 0.52, 0.72, 1.10, 2.00] in GeV^2. 171
Figure 5.3 The asymmetry as a function of Φ for the fifth bin in x_B and θ_e, where $0.17 < x_B < 0.2$ and $25.5° < \theta_e < 45°$. Each panel corresponds to a bin in $-t$ whose limits are: [0.09, 0.13, 0.18, 0.23, 0.30, 0.39, 0.52, 0.72, 1.10, 2.00] in GeV^2. 172
Figure 5.4 On top, the unpolarized cross section differences as a function of Φ. Black represents this analysis. Green is e1-dvcs2 by B. Guegan. Red is e1-dvcs1 by H.S. Jo. On bottom, the unpolarized cross section ratios. Both are for the fifth bin in x_B and θ_e, where $0.17 < x_B < 0.2$ and $25.5° < \theta_e < 45°$. Each panel corresponds to a bin in $-t$ whose limits are: [0.09, 0.13, 0.18, 0.23, 0.30, 0.39, 0.52, 0.72, 1.10, 2.00] Green is $\frac{e1-dvcs2\ Saylor}{e1-dvcs2\ Guegan}$. Red is $\frac{e1-dvcs2\ Saylor}{e1-dvcs1\ Jo}$. 174
Figure 5.5 The unpolarized cross section as a function of Φ for the fifth bin in x_B and θ_e, where $0.17 < x_B < 0.2$ and $25.5° < \theta_e < 45°$. Each panel corresponds to a bin in $-t$ whose limits are: [0.09, 0.13, 0.18, 0.23, 0.30, 0.39, 0.52, 0.72, 1.10, 2.00] For both, the green curve corresponds to VGG, the light magenta corresponds to KM10, and the dark magenta corresponds to KM10a. . . 176
Figure 5.6 $\mathcal{H}_{\mathrm{Re}}$ as a function of $-t$, for each of the 21 bins in x_B and θ_e. The red points represent the extraction from this analysis, and the black points represent the prediction from VGG. We notice that the agreement of the extraction to predictions is not great. 178
Figure 5.7 $\mathcal{H}_{\mathrm{Im}}$ as a function of $-t$, for each of the 21 bins in x_B and θ_e. The red points represent the extraction from this analysis, and the black points represent the prediction from VGG. We notice that the agreement is good for low values of x_B and θ_e, with worse agreement at higher values. 179
Figure 5.8 The charge density distribution of the proton as a function of impact parameter b. Each panel corresponds to a particular value of x_B. The shape of the distribution is Gaussian, centered around $b = 0$. 182
Figure 5.9 For bins 1 and 2, a three-dimensional view of the charge density distribution of the proton as a function of impact parameter b, for two choices of x_B: 0.12 and 0.155, and two choices of Q^2: 1.135 GeV^2 and 1.305 GeV^2 respectively. 183
Figure 5.10 For bins 3 and 4, a three-dimensional view of the charge density distribution of the proton as a function of impact parameter b, for two choices of x_B: 0.155 and 0.185, and two choices of Q^2: 1.471 GeV^2 and 1.490 GeV^2 respectively. 183
Figure 5.11 For bins 5 and 6, a three-dimensional view of the charge density distribution of the proton as a function of impact parameter b, for two choices of x_B: 0.185 and 0.215, and two choices of Q^2: 1.710 GeV^2 and 1.684 GeV^2 respectively. 184
Figure 5.12 For bins 7 and 9, a three-dimensional view of the charge density distribution of the proton as a function of impact parameter b, for two choices of x_B: 0.215 and 0.245, and two choices of Q^2: 1.964 GeV^2 and 2.187 GeV^2 respectively. 184
Figure 6.1 The kinematic coverage of Hall A, CLAS, HERMES, and the future coverage of COMPASS and CLAS 12. This figure was taken from reference[61]. . . . 186
Figure 7.1 Les diagrammes du “sac à main” du DVCS. 188
Figure 7.2 Les quatre GPDs: H, E, $\tilde{H}$, and $\tilde{E}$. Chacune correspond à des hélicités différentes du proton et du quark. H et E sont les GPDs non polarisées, qui sont indépendantes de l’hélicité du quark. $\tilde{H}$ et $\tilde{E}$ sont les GPDs polarisées, qui sont dépendant de l’hélicité du quark. Pour H et $\tilde{H}$ le spin du proton ne changent pas, mais pour E et $\tilde{E}$, le spin du proton est renversé. 188

Figure 7.3 Les trois diagrammes contribuent à létat final: $e+p+\gamma$. À gauche, le DVCS, au milieu, le BH avec un photon émis par l'électron initial, et à droite, le BH avec un photon émis par l'électron diffusé. La boule bleue correspond aux GPDs, et les boules noires correspondent aux FFs. 189
Figure 7.4 Une illustration de CEBAF avec ses trois salles expérimental.[39] 190
Figure 7.5 Une illustration de CLAS avec ses divers sous-détecteurs.[39] 191
Figure 7.6 La section efficace non polarisée en fonction de Φ pour le cinquième bin en x_B et θ_e, où $0.17 < x_B < 0.2$ et $25.5^\circ < \theta_e < 45^\circ$. Chaque fenêtre correspond à un bin en t avec les limites suivantes: [0.09, 0.13, 0.18, 0.23, 0.30, 0.39, 0.52, 0.72, 1.10, 2.00] en GeV^2. 192
Figure 7.7 La difference des sections efficaces polarisées en fonction de Φ pour le cinquième bin en x_B et θ_e, où $0.17 < x_B < 0.2$ et $25.5^\circ < \theta_e < 45^\circ$. Chaque fenêtre correspond à un bin en t avec les limites suivantes: [0.09, 0.13, 0.18, 0.23, 0.30, 0.39, 0.52, 0.72, 1.10, 2.00] en GeV^2. 193
Figure 7.8 L'asymétrie de spin du faisceau en fonction de Φ pour le cinquième bin en x_B et θ_e, où $0.17 < x_B < 0.2$ et $25.5^\circ < \theta_e < 45^\circ$. Chaque fenêtre correspond à un bin en t avec les limites suivantes: [0.09, 0.13, 0.18, 0.23, 0.30, 0.39, 0.52, 0.72, 1.10, 2.00] en GeV^2. 194
Figure 7.9 $\mathcal{H}_{\text{Re}}$ en fonction de $-t$, pour les 21 bins en x_B et θ_e. Les points rouges représentent l'extraction issue de cette analyse, et les points noirs représentent la prédiction du modèle VGG. 196
Figure 7.10 $\mathcal{H}_{\text{Im}}$ en fonction de $-t$, pour les 21 bins en x_B et θ_e. Les points rouges représentent l'extraction issue de cette analyse, et les courbes noirs représentent l'ajustement issu de cette analyse. 197
Figure 7.11 Les distributions de densité de charge en fonction du paramètre d'impact b. Chaque panneau correspond à une valeur de x_B. Les distribution sont Gaussiennes, centrées autour de $b = 0$. 200
Figure 7.12 Pour les bins 1 et 2, vue tridimensionnelle de la distribution de densité de charge en fonction du paramètre d'impact b, pour les deux valeurs de x_B: 0.12 et 0.155, et les deux valeurs de Q^2: 1.135 GeV^2 et 1.305 GeV^2 respectivement. 201
Figure 7.13 Pour les bins 3 et 4, vue tridimensionnelle de la distribution de densité de charge en fonction du paramètre d'impact b, pour les deux valeurs de x_B: 0.155 et 0.185, et les deux valeurs de Q^2: 1.471 GeV^2 et 1.490 GeV^2 respectivement. 201
Figure 7.14 Pour les bins 5 et 6, vue tridimensionnelle de la distribution de densité de charge en fonction du paramètre d'impact b, pour les deux valeurs de x_B: 0.185 et 0.215, et les deux valeurs de Q^2: 1.710 GeV^2 et 1.684 GeV^2 respectivement. 202
Figure 7.15 Pour les bins 7 et 9, vue tridimensionnelle de la distribution de densité de charge en fonction du paramètre d'impact b, pour les deux valeurs de x_B: 0.215 et 0.245, et les deux valeurs de Q^2: 1.964 GeV^2 et 2.187 GeV^2 respectivement. 202
Figure A.1 The acceptance as a function of ϕ for the first bin in x_B and θ_e, where $0.1 < x_B < 0.14$ and $21^\circ < \theta_e < 45^\circ$. 207
Figure A.2 On top, the acceptance as a function of ϕ for the second bin in x_B and θ_e, where $0.14 < x_B < 0.17$ and $21^\circ < \theta_e < 25.5^\circ$. On bottom, the acceptance as a function of ϕ for the third bin in x_B and θ_e, where $0.14 < x_B < 0.17$ and $25.5^\circ < \theta_e < 45^\circ$. 208
Figure A.3 On top, the acceptance as a function of ϕ for the fourth bin in x_B and θ_e, where $0.17 < x_B < 0.2$ and $21^\circ < \theta_e < 25.5^\circ$. On bottom, the acceptance as a function of ϕ for the fifth bin in x_B and θ_e, where $0.17 < x_B < 0.2$ and $25.5^\circ < \theta_e < 45^\circ$. 209

Figure A.4 On top, the acceptance as a function of ϕ for the sixth bin in x_B and θ_e, where $0.2 < x_B < 0.23$ and $21° < \theta_e < 27°$. On bottom, the acceptance as a function of ϕ for the seventh bin in x_B and θ_e, where $0.2 < x_B < 0.23$ and $27° < \theta_e < 45°$. 210
Figure A.5 On top, the acceptance as a function of ϕ for the eighth bin in x_B and θ_e, where $0.23 < x_B < 0.26$ and $21° < \theta_e < 27°$. On bottom, the acceptance as a function of ϕ for the ninth bin in x_B and θ_e, where $0.23 < x_B < 0.26$ and $27° < \theta_e < 45°$. 211
Figure A.6 On top, the acceptance as a function of ϕ for the tenth bin in x_B and θ_e, where $0.26 < x_B < 0.29$ and $21° < \theta_e < 27°$. On bottom, the acceptance as a function of ϕ for the eleventh bin in x_B and θ_e, where $0.26 < x_B < 0.29$ and $27° < \theta_e < 45°$. 212
Figure A.7 On top, the acceptance as a function of ϕ for the twelfth bin in x_B and θ_e, where $0.29 < x_B < 0.32$ and $21° < \theta_e < 28°$. On bottom, the acceptance as a function of ϕ for the thirteenth bin in x_B and θ_e, where $0.29 < x_B < 0.32$ and $28° < \theta_e < 45°$. 213
Figure A.8 On top, the acceptance as a function of ϕ for the fourteenth bin in x_B and θ_e, where $0.32 < x_B < 0.35$ and $21° < \theta_e < 28°$. On bottom, the acceptance as a function of ϕ for the fifteenth bin in x_B and θ_e, where $0.32 < x_B < 0.35$ and $28° < \theta_e < 45°$. 214
Figure A.9 On top, the acceptance as a function of ϕ for the sixteenth bin in x_B and θ_e, where $0.35 < x_B < 0.38$ and $21° < \theta_e < 28°$. On bottom, the acceptance as a function of ϕ for the seventeenth bin in x_B and θ_e, where $0.35 < x_B < 0.38$ and $28° < \theta_e < 45°$. 215
Figure A.10 On top, the acceptance as a function of ϕ for the eighteenth bin in x_B and θ_e, where $0.38 < x_B < 0.42$ and $21° < \theta_e < 28°$. On bottom, the acceptance as a function of ϕ for the nineteenth bin in x_B and θ_e, where $0.38 < x_B < 0.42$ and $28° < \theta_e < 45°$. 216
Figure A.11 On top, the acceptance as a function of ϕ for the twentieth bin in x_B and θ_e, where $0.42 < x_B < 0.58$ and $21° < \theta_e < 33°$. On bottom, the acceptance as a function of ϕ for the twenty-first bin in x_B and θ_e, where $0.42 < x_B < 0.58$ and $33° < \theta_e < 45°$. 217
Figure B.1 The bin volume correction $\frac{N_{\text{bin}}}{N_{\text{super}}}$ as a function of Φ for the first bin in x_B and θ_e, where $0.1 < x_B < 0.14$ and $21° < \theta_e < 45°$. 218
Figure B.2 On top, the bin volume correction $\frac{N_{\text{bin}}}{N_{\text{super}}}$ as a function of Φ for the second bin in x_B and θ_e, where $0.14 < x_B < 0.17$ and $21° < \theta_e < 25.5°$. On bottom, the bin volume correction $\frac{N_{\text{bin}}}{N_{\text{super}}}$ as a function of Φ for the third bin in x_B and θ_e, where $0.14 < x_B < 0.17$ and $25.5° < \theta_e < 45°$. 219
Figure B.3 On top, the bin volume correction $\frac{N_{\text{bin}}}{N_{\text{super}}}$ as a function of Φ for the fourth bin in x_B and θ_e, where $0.17 < x_B < 0.2$ and $21° < \theta_e < 25.5°$. On bottom, the bin volume correction $\frac{N_{\text{bin}}}{N_{\text{super}}}$ as a function of Φ for the fifth bin in x_B and θ_e, where $0.17 < x_B < 0.2$ and $25.5° < \theta_e < 45°$. 220
Figure B.4 On top, the bin volume correction $\frac{N_{\text{bin}}}{N_{\text{super}}}$ as a function of Φ for the sixth bin in x_B and θ_e, where $0.2 < x_B < 0.23$ and $21° < \theta_e < 27°$. On bottom, the bin volume correction $\frac{N_{\text{bin}}}{N_{\text{super}}}$ as a function of Φ for the seventh bin in x_B and θ_e, where $0.2 < x_B < 0.23$ and $27° < \theta_e < 45°$. 221
Figure B.5 On top, the bin volume correction $\frac{N_{\text{bin}}}{N_{\text{super}}}$ as a function of Φ for the eighth bin in x_B and θ_e, where $0.23 < x_B < 0.26$ and $21° < \theta_e < 27°$. On bottom, the bin volume correction $\frac{N_{\text{bin}}}{N_{\text{super}}}$ as a function of Φ for the ninth bin in x_B and θ_e, where $0.23 < x_B < 0.26$ and $27° < \theta_e < 45°$. 222

Figure B.6 On top, the bin volume correction $\frac{N_{\text{bin}}}{N_{\text{super}}}$ as a function of Φ for the tenth bin in x_B and θ_e, where $0.26 < x_B < 0.29$ and $21° < \theta_e < 27°$. On bottom, the bin volume correction $\frac{N_{\text{bin}}}{N_{\text{super}}}$ as a function of Φ for the eleventh bin in x_B and θ_e, where $0.26 < x_B < 0.29$ and $27° < \theta_e < 45°$. 223
Figure B.7 On top, the bin volume correction $\frac{N_{\text{bin}}}{N_{\text{super}}}$ as a function of Φ for the twelfth bin in x_B and θ_e, where $0.29 < x_B < 0.32$ and $21° < \theta_e < 28°$. On bottom, the bin volume correction $\frac{N_{\text{bin}}}{N_{\text{super}}}$ as a function of Φ for the thirteenth bin in x_B and θ_e, where $0.29 < x_B < 0.32$ and $28° < \theta_e < 45°$. 224
Figure B.8 On top, the bin volume correction $\frac{N_{\text{bin}}}{N_{\text{super}}}$ as a function of Φ for the fourteenth bin in x_B and θ_e, where $0.32 < x_B < 0.35$ and $21° < \theta_e < 28°$. On bottom, the bin volume correction $\frac{N_{\text{bin}}}{N_{\text{super}}}$ as a function of Φ for the fifteenth bin in x_B and θ_e, where $0.32 < x_B < 0.35$ and $28° < \theta_e < 45°$. 225
Figure B.9 On top, the bin volume correction $\frac{N_{\text{bin}}}{N_{\text{super}}}$ as a function of Φ for the sixteenth bin in x_B and θ_e, where $0.35 < x_B < 0.38$ and $21° < \theta_e < 28°$. On bottom, the bin volume correction $\frac{N_{\text{bin}}}{N_{\text{super}}}$ as a function of Φ for the seventeenth bin in x_B and θ_e, where $0.35 < x_B < 0.38$ and $28° < \theta_e < 45°$. 226
Figure B.10 On top, the bin volume correction $\frac{N_{\text{bin}}}{N_{\text{super}}}$ as a function of Φ for the eighteenth bin in x_B and θ_e, where $0.38 < x_B < 0.42$ and $21° < \theta_e < 28°$. On bottom, the bin volume correction $\frac{N_{\text{bin}}}{N_{\text{super}}}$ as a function of Φ for the nineteenth bin in x_B and θ_e, where $0.38 < x_B < 0.42$ and $28° < \theta_e < 45°$. 227
Figure B.11 On top, the bin volume correction $\frac{N_{\text{bin}}}{N_{\text{super}}}$ as a function of Φ for the twentieth bin in x_B and θ_e, where $0.42 < x_B < 0.58$ and $21° < \theta_e < 33°$. On bottom, the bin volume correction $\frac{N_{\text{bin}}}{N_{\text{super}}}$ as a function of Φ for the twenty-first bin in x_B and θ_e, where $0.42 < x_B < 0.58$ and $33° < \theta_e < 45°$. 228
Figure C.1 the neutral pion subtraction ratio $R = \frac{N^{\gamma}_{\pi_0}}{N^{e+p+\gamma}}$ as a function of Φ for the first bin in x_B and θ_e, where $0.1 < x_B < 0.14$ and $21° < \theta_e < 45°$. . . . 229
Figure C.2 On top, the neutral pion subtraction ratio $R = \frac{N^{\gamma}_{\pi_0}}{N^{e+p+\gamma}}$ as a function of Φ for the second bin in x_B and θ_e, where $0.14 < x_B < 0.17$ and $21° < \theta_e < 25.5°$. On bottom, the neutral pion subtraction ratio $R = \frac{N^{\gamma}_{\pi_0}}{N^{e+p+\gamma}}$ as a function of Φ for the third bin in x_B and θ_e, where $0.14 < x_B < 0.17$ and $25.5° < \theta_e < 45°$. 230
Figure C.3 On top, the neutral pion subtraction ratio $R = \frac{N^{\gamma}_{\pi_0}}{N^{e+p+\gamma}}$ as a function of Φ for the fourth bin in x_B and θ_e, where $0.17 < x_B < 0.2$ and $21° < \theta_e < 25.5°$. On bottom, the neutral pion subtraction ratio $R = \frac{N^{\gamma}_{\pi_0}}{N^{e+p+\gamma}}$ as a function of Φ for the fifth bin in x_B and θ_e, where $0.17 < x_B < 0.2$ and $25.5° < \theta_e < 45°$. 231
Figure C.4 On top, the neutral pion subtraction ratio $R = \frac{N^{\gamma}_{\pi_0}}{N^{e+p+\gamma}}$ as a function of Φ for the sixth bin in x_B and θ_e, where $0.2 < x_B < 0.23$ and $21° < \theta_e < 27°$. On bottom, the neutral pion subtraction ratio $R = \frac{N^{\gamma}_{\pi_0}}{N^{e+p+\gamma}}$ as a function of Φ for the seventh bin in x_B and θ_e, where $0.2 < x_B < 0.23$ and $27° < \theta_e < 45°$. 232
Figure C.5 On top, the neutral pion subtraction ratio $R = \frac{N^{\gamma}_{\pi_0}}{N^{e+p+\gamma}}$ as a function of Φ for the eighth bin in x_B and θ_e, where $0.23 < x_B < 0.26$ and $21° < \theta_e < 27°$. On bottom, the neutral pion subtraction ratio $R = \frac{N^{\gamma}_{\pi_0}}{N^{e+p+\gamma}}$ as a function of Φ for the ninth bin in x_B and θ_e, where $0.23 < x_B < 0.26$ and $27° < \theta_e < 45°$. 233
Figure C.6 On top, the neutral pion subtraction ratio $R = \frac{N^{\gamma}_{\pi_0}}{N^{e+p+\gamma}}$ as a function of Φ for the tenth bin in x_B and θ_e, where $0.26 < x_B < 0.29$ and $21° < \theta_e < 27°$. On bottom, the neutral pion subtraction ratio $R = \frac{N^{\gamma}_{\pi_0}}{N^{e+p+\gamma}}$ as a function of Φ for the eleventh bin in x_B and θ_e, where $0.26 < x_B < 0.29$ and $27° < \theta_e < 45°$. 234

Figure C.7 On top, the neutral pion subtraction ratio $R = \frac{N^{\gamma}_{\pi_0}}{N^{e+p+\gamma}}$ as a function of Φ for the twelfth bin in x_B and θ_e, where $0.29 < x_B < 0.32$ and $21^\circ < \theta_e < 28^\circ$. On bottom, the neutral pion subtraction ratio $R = \frac{N^{\gamma}_{\pi_0}}{N^{e+p+\gamma}}$ as a function of Φ for the thirteenth bin in x_B and θ_e, where $0.29 < x_B < 0.32$ and $28^\circ < \theta_e < 45^\circ$. 235

Figure C.8 On top, the neutral pion subtraction ratio $R = \frac{N^{\gamma}_{\pi_0}}{N^{e+p+\gamma}}$ as a function of Φ for the fourteenth bin in x_B and θ_e, where $0.32 < x_B < 0.35$ and $21^\circ < \theta_e < 28^\circ$. On bottom, the neutral pion subtraction ratio $R = \frac{N^{\gamma}_{\pi_0}}{N^{e+p+\gamma}}$ as a function of Φ for the fifteenth bin in x_B and θ_e, where $0.32 < x_B < 0.35$ and $28^\circ < \theta_e < 45^\circ$. 236

Figure C.9 On top, the neutral pion subtraction ratio $R = \frac{N^{\gamma}_{\pi_0}}{N^{e+p+\gamma}}$ as a function of Φ for the sixteenth bin in x_B and θ_e, where $0.35 < x_B < 0.38$ and $21^\circ < \theta_e < 28^\circ$. On bottom, the neutral pion subtraction ratio $R = \frac{N^{\gamma}_{\pi_0}}{N^{e+p+\gamma}}$ as a function of Φ for the seventeenth bin in x_B and θ_e, where $0.35 < x_B < 0.38$ and $28^\circ < \theta_e < 45^\circ$. 237

Figure C.10 On top, the neutral pion subtraction ratio $R = \frac{N^{\gamma}_{\pi_0}}{N^{e+p+\gamma}}$ as a function of Φ for the eighteenth bin in x_B and θ_e, where $0.38 < x_B < 0.42$ and $21^\circ < \theta_e < 28^\circ$. On bottom, the neutral pion subtraction ratio $R = \frac{N^{\gamma}_{\pi_0}}{N^{e+p+\gamma}}$ as a function of Φ for the nineteenth bin in x_B and θ_e, where $0.38 < x_B < 0.42$ and $28^\circ < \theta_e < 45^\circ$. 238

Figure C.11 On top, the neutral pion subtraction ratio $R = \frac{N^{\gamma}_{\pi_0}}{N^{e+p+\gamma}}$ as a function of Φ for the twentieth bin in x_B and θ_e, where $0.42 < x_B < 0.58$ and $21^\circ < \theta_e < 33^\circ$. On bottom, the neutral pion subtraction ratio $R = \frac{N^{\gamma}_{\pi_0}}{N^{e+p+\gamma}}$ as a function of Φ for the twenty-first bin in x_B and θ_e, where $0.42 < x_B < 0.58$ and $33^\circ < \theta_e < 45^\circ$. 239

Figure D.1 The radiative corrections as a function of Φ for the first bin in x_B and θ_e, where $0.1 < x_B < 0.14$ and $21^\circ < \theta_e < 45^\circ$. 240

Figure D.2 On top, the radiative corrections as a function of Φ for the second bin in x_B and θ_e, where $0.14 < x_B < 0.17$ and $21^\circ < \theta_e < 25.5^\circ$. On bottom, the radiative corrections as a function of Φ for the third bin in x_B and θ_e, where $0.14 < x_B < 0.17$ and $25.5^\circ < \theta_e < 45^\circ$. 241

Figure D.3 On top, the radiative corrections as a function of Φ for the fourth bin in x_B and θ_e, where $0.17 < x_B < 0.2$ and $21^\circ < \theta_e < 25.5^\circ$. On bottom, the radiative corrections as a function of Φ for the fifth bin in x_B and θ_e, where $0.17 < x_B < 0.2$ and $25.5^\circ < \theta_e < 45^\circ$. 242

Figure D.4 On top, the radiative corrections as a function of Φ for the sixth bin in x_B and θ_e, where $0.2 < x_B < 0.23$ and $21^\circ < \theta_e < 27^\circ$. On bottom, the radiative corrections as a function of Φ for the seventh bin in x_B and θ_e, where $0.2 < x_B < 0.23$ and $27^\circ < \theta_e < 45^\circ$. 243

Figure D.5 On top, the radiative corrections as a function of Φ for the eighth bin in x_B and θ_e, where $0.23 < x_B < 0.26$ and $21^\circ < \theta_e < 27^\circ$. On bottom, the radiative corrections as a function of Φ for the ninth bin in x_B and θ_e, where $0.23 < x_B < 0.26$ and $27^\circ < \theta_e < 45^\circ$. 244

Figure D.6 On top, the radiative corrections as a function of Φ for the tenth bin in x_B and θ_e, where $0.26 < x_B < 0.29$ and $21^\circ < \theta_e < 27^\circ$. On bottom, the radiative corrections as a function of Φ for the eleventh bin in x_B and θ_e, where $0.26 < x_B < 0.29$ and $27^\circ < \theta_e < 45^\circ$. 245

Figure D.7 On top, the radiative corrections as a function of Φ for the twelfth bin in x_B and θ_e, where $0.29 < x_B < 0.32$ and $21^\circ < \theta_e < 28^\circ$. On bottom, the radiative corrections as a function of Φ for the thirteenth bin in x_B and θ_e, where $0.29 < x_B < 0.32$ and $28^\circ < \theta_e < 45^\circ$. 246

Figure D.8 On top, the radiative corrections as a function of Φ for the fourteenth bin in x_B and θ_e, where $0.32 < x_B < 0.35$ and $21^\circ < \theta_e < 28^\circ$. On bottom, the radiative corrections as a function of Φ for the fifteenth bin in x_B and θ_e, where $0.32 < x_B < 0.35$ and $28^\circ < \theta_e < 45^\circ$. 247
Figure D.9 On top, the radiative corrections as a function of Φ for the sixteenth bin in x_B and θ_e, where $0.35 < x_B < 0.38$ and $21^\circ < \theta_e < 28^\circ$. On bottom, the radiative corrections as a function of Φ for the seventeenth bin in x_B and θ_e, where $0.35 < x_B < 0.38$ and $28^\circ < \theta_e < 45^\circ$. 248
Figure D.10 On top, the radiative corrections as a function of Φ for the eighteenth bin in x_B and θ_e, where $0.38 < x_B < 0.42$ and $21^\circ < \theta_e < 28^\circ$. On bottom, the radiative corrections as a function of Φ for the nineteenth bin in x_B and θ_e, where $0.38 < x_B < 0.42$ and $28^\circ < \theta_e < 45^\circ$. 249
Figure D.11 On top, the radiative corrections as a function of Φ for the twentieth bin in x_B and θ_e, where $0.42 < x_B < 0.58$ and $21^\circ < \theta_e < 33^\circ$. On bottom, the radiative corrections as a function of Φ for the twenty-first bin in x_B and θ_e, where $0.42 < x_B < 0.58$ and $33^\circ < \theta_e < 45^\circ$. 250
Figure E.1 On top, the unpolarized cross section as a function of Φ. Black represents this analysis. Green is e1-dvcs2 by B. Guegan. Red is e1-dvcs1 by H.S. Jo. On bottom, the unpolarized cross section ratios. Both are for the first bin in x_B and θ_e, where $0.1 < x_B < 0.14$ and $21^\circ < \theta_e < 45^\circ$. Each panel corresponds to a bin in $-t$ whose limits are: [0.09, 0.13, 0.18, 0.23, 0.30, 0.39, 0.52, 0.72, 1.10, 2.00] Green is $\frac{e1-dvcs2\ Saylor}{e1-dvcs2\ Guegan}$. Red is $\frac{e1-dvcs2\ Saylor}{e1-dvcs1\ Jo}$. 252
Figure E.2 On top, the unpolarized cross section as a function of Φ. Black represents this analysis. Green is e1-dvcs2 by B. Guegan. Red is e1-dvcs1 by H.S. Jo. On bottom, the unpolarized cross section ratios. Both are for the second bin in x_B and θ_e, where $0.14 < x_B < 0.17$ and $21^\circ < \theta_e < 25.5^\circ$. Each panel corresponds to a bin in $-t$ whose limits are: [0.09, 0.13, 0.18, 0.23, 0.30, 0.39, 0.52, 0.72, 1.10, 2.00] Green is $\frac{e1-dvcs2\ Saylor}{e1-dvcs2\ Guegan}$. Red is $\frac{e1-dvcs2\ Saylor}{e1-dvcs1\ Jo}$. 253
Figure E.3 On top, the unpolarized cross section as a function of Φ. Black represents this analysis. Green is e1-dvcs2 by B. Guegan. Red is e1-dvcs1 by H.S. Jo. On bottom, the unpolarized cross section ratios. Both are for the third bin in x_B and θ_e, where $0.14 < x_B < 0.17$ and $25.5^\circ < \theta_e < 45^\circ$. Each panel corresponds to a bin in $-t$ whose limits are: [0.09, 0.13, 0.18, 0.23, 0.30, 0.39, 0.52, 0.72, 1.10, 2.00] Green is $\frac{e1-dvcs2\ Saylor}{e1-dvcs2\ Guegan}$. Red is $\frac{e1-dvcs2\ Saylor}{e1-dvcs1\ Jo}$. 254
Figure E.4 On top, the unpolarized cross section as a function of Φ. Black represents this analysis. Green is e1-dvcs2 by B. Guegan. Red is e1-dvcs1 by H.S. Jo. On bottom, the unpolarized cross section ratios. Both are for the fourth bin in x_B and θ_e, where $0.17 < x_B < 0.2$ and $21^\circ < \theta_e < 25.5^\circ$. Each panel corresponds to a bin in $-t$ whose limits are: [0.09, 0.13, 0.18, 0.23, 0.30, 0.39, 0.52, 0.72, 1.10, 2.00] Green is $\frac{e1-dvcs2\ Saylor}{e1-dvcs2\ Guegan}$. Red is $\frac{e1-dvcs2\ Saylor}{e1-dvcs1\ Jo}$. 255
Figure E.5 On top, the unpolarized cross section as a function of Φ. Black represents this analysis. Green is e1-dvcs2 by B. Guegan. Red is e1-dvcs1 by H.S. Jo. On bottom, the unpolarized cross section ratios. Both are for the fifth bin in x_B and θ_e, where $0.17 < x_B < 0.2$ and $25.5^\circ < \theta_e < 45^\circ$. Each panel corresponds to a bin in $-t$ whose limits are: [0.09, 0.13, 0.18, 0.23, 0.30, 0.39, 0.52, 0.72, 1.10, 2.00] Green is $\frac{e1-dvcs2\ Saylor}{e1-dvcs2\ Guegan}$. Red is $\frac{e1-dvcs2\ Saylor}{e1-dvcs1\ Jo}$. 256
Figure E.6 On top, the unpolarized cross section as a function of Φ. Black represents this analysis. Green is e1-dvcs2 by B. Guegan. Red is e1-dvcs1 by H.S. Jo. On bottom, the unpolarized cross section ratios. Both are for the sixth bin in x_B and θ_e, where $0.2 < x_B < 0.23$ and $21^\circ < \theta_e < 27^\circ$. Each panel corresponds to a bin in $-t$ whose limits are: [0.09, 0.13, 0.18, 0.23, 0.30, 0.39, 0.52, 0.72, 1.10, 2.00] Green is $\frac{e1-dvcs2\ Saylor}{e1-dvcs2\ Guegan}$. Red is $\frac{e1-dvcs2\ Saylor}{e1-dvcs1\ Jo}$. 257

Figure E.7 On top, the unpolarized cross section as a function of Φ. Black represents this analysis. Green is e1-dvcs2 by B. Guegan. Red is e1-dvcs1 by H.S. Jo. On bottom, the unpolarized cross section ratios. Both are for the seventh bin in x_B and θ_e, where $0.2 < x_B < 0.23$ and $27^\circ < \theta_e < 45^\circ$. Each panel corresponds to a bin in $-t$ whose limits are: [0.09, 0.13, 0.18, 0.23, 0.30, 0.39, 0.52, 0.72, 1.10, 2.00] Green is $\frac{e1-dvcs2\ Saylor}{e1-dvcs2\ Guegan}$. Red is $\frac{e1-dvcs2\ Saylor}{e1-dvcs1\ Jo}$. 258
Figure E.8 On top, the unpolarized cross section as a function of Φ. Black represents this analysis. Green is e1-dvcs2 by B. Guegan. Red is e1-dvcs1 by H.S. Jo. On bottom, the unpolarized cross section ratios. Both are for the eighth bin in x_B and θ_e, where $0.23 < x_B < 0.26$ and $21^\circ < \theta_e < 27^\circ$. Each panel corresponds to a bin in $-t$ whose limits are: [0.09, 0.13, 0.18, 0.23, 0.30, 0.39, 0.52, 0.72, 1.10, 2.00] Green is $\frac{e1-dvcs2\ Saylor}{e1-dvcs2\ Guegan}$. Red is $\frac{e1-dvcs2\ Saylor}{e1-dvcs1\ Jo}$. 259
Figure E.9 On top, the unpolarized cross section as a function of Φ. Black represents this analysis. Green is e1-dvcs2 by B. Guegan. Red is e1-dvcs1 by H.S. Jo. On bottom, the unpolarized cross section ratios. Both are for the ninth bin in x_B and θ_e, where $0.23 < x_B < 0.26$ and $27^\circ < \theta_e < 45^\circ$. Each panel corresponds to a bin in $-t$ whose limits are: [0.09, 0.13, 0.18, 0.23, 0.30, 0.39, 0.52, 0.72, 1.10, 2.00] Green is $\frac{e1-dvcs2\ Saylor}{e1-dvcs2\ Guegan}$. Red is $\frac{e1-dvcs2\ Saylor}{e1-dvcs1\ Jo}$. 260
Figure E.10 On top, the unpolarized cross section as a function of Φ. Black represents this analysis. Green is e1-dvcs2 by B. Guegan. Red is e1-dvcs1 by H.S. Jo. On bottom, the unpolarized cross section ratios. Both are for the tenth bin in x_B and θ_e, where $0.26 < x_B < 0.29$ and $21^\circ < \theta_e < 27^\circ$. Each panel corresponds to a bin in $-t$ whose limits are: [0.09, 0.13, 0.18, 0.23, 0.30, 0.39, 0.52, 0.72, 1.10, 2.00] Green is $\frac{e1-dvcs2\ Saylor}{e1-dvcs2\ Guegan}$. Red is $\frac{e1-dvcs2\ Saylor}{e1-dvcs1\ Jo}$. 261
Figure E.11 On top, the unpolarized cross section as a function of Φ. Black represents this analysis. Green is e1-dvcs2 by B. Guegan. Red is e1-dvcs1 by H.S. Jo. On bottom, the unpolarized cross section ratios. Both are for the eleventh bin in x_B and θ_e, where $0.26 < x_B < 0.29$ and $27^\circ < \theta_e < 45^\circ$. Each panel corresponds to a bin in $-t$ whose limits are: [0.09, 0.13, 0.18, 0.23, 0.30, 0.39, 0.52, 0.72, 1.10, 2.00] Green is $\frac{e1-dvcs2\ Saylor}{e1-dvcs2\ Guegan}$. Red is $\frac{e1-dvcs2\ Saylor}{e1-dvcs1\ Jo}$. 262
Figure E.12 On top, the unpolarized cross section as a function of Φ. Black represents this analysis. Green is e1-dvcs2 by B. Guegan. Red is e1-dvcs1 by H.S. Jo. On bottom, the unpolarized cross section ratios. Both are for the twelfth bin in x_B and θ_e, where $0.29 < x_B < 0.32$ and $21^\circ < \theta_e < 28^\circ$. Each panel corresponds to a bin in $-t$ whose limits are: [0.09, 0.13, 0.18, 0.23, 0.30, 0.39, 0.52, 0.72, 1.10, 2.00] Green is $\frac{e1-dvcs2\ Saylor}{e1-dvcs2\ Guegan}$. Red is $\frac{e1-dvcs2\ Saylor}{e1-dvcs1\ Jo}$. 263
Figure E.13 On top, the unpolarized cross section as a function of Φ. Black represents this analysis. Green is e1-dvcs2 by B. Guegan. Red is e1-dvcs1 by H.S. Jo. On bottom, the unpolarized cross section ratios. Both are for the thirteenth bin in x_B and θ_e, where $0.29 < x_B < 0.32$ and $28^\circ < \theta_e < 45^\circ$. Each panel corresponds to a bin in $-t$ whose limits are: [0.09, 0.13, 0.18, 0.23, 0.30, 0.39, 0.52, 0.72, 1.10, 2.00] Green is $\frac{e1-dvcs2\ Saylor}{e1-dvcs2\ Guegan}$. Red is $\frac{e1-dvcs2\ Saylor}{e1-dvcs1\ Jo}$. 264
Figure E.14 On top, the unpolarized cross section as a function of Φ. Black represents this analysis. Green is e1-dvcs2 by B. Guegan. Red is e1-dvcs1 by H.S. Jo. On bottom, the unpolarized cross section ratios. Both are for the fourteenth bin in x_B and θ_e, where $0.32 < x_B < 0.35$ and $21^\circ < \theta_e < 28^\circ$. Each panel corresponds to a bin in $-t$ whose limits are: [0.09, 0.13, 0.18, 0.23, 0.30, 0.39, 0.52, 0.72, 1.10, 2.00] Green is $\frac{e1-dvcs2\ Saylor}{e1-dvcs2\ Guegan}$. Red is $\frac{e1-dvcs2\ Saylor}{e1-dvcs1\ Jo}$. 265
Figure E.15 On top, the unpolarized cross section as a function of Φ. Black represents this analysis. Green is e1-dvcs2 by B. Guegan. Red is e1-dvcs1 by H.S. Jo. On bottom, the unpolarized cross section ratios. Both are for the fifteenth bin in x_B and θ_e, where $0.32 < x_B < 0.35$ and $28^\circ < \theta_e < 45^\circ$. Each panel corresponds to a bin in $-t$ whose limits are: [0.09, 0.13, 0.18, 0.23, 0.30, 0.39, 0.52, 0.72, 1.10, 2.00] Green is $\frac{e1-dvcs2\ Saylor}{e1-dvcs2\ Guegan}$. Red is $\frac{e1-dvcs2\ Saylor}{e1-dvcs1\ Jo}$. 266

Figure E.16 On top, the unpolarized cross section as a function of Φ. Black represents this analysis. Green is e1-dvcs2 by B. Guegan. Red is e1-dvcs1 by H.S. Jo. On bottom, the unpolarized cross section ratios. Both are for the sixteenth bin in x_B and θ_e, where $0.35 < x_B < 0.38$ and $21^\circ < \theta_e < 28^\circ$. Each panel corresponds to a bin in $-t$ whose limits are: [0.09, 0.13, 0.18, 0.23, 0.30, 0.39, 0.52, 0.72, 1.10, 2.00] Green is $\frac{e1-dvcs2\ Saylor}{e1-dvcs2\ Guegan}$. Red is $\frac{e1-dvcs2\ Saylor}{e1-dvcs1\ Jo}$. 267

Figure E.17 On top, the unpolarized cross section as a function of Φ. Black represents this analysis. Green is e1-dvcs2 by B. Guegan. Red is e1-dvcs1 by H.S. Jo. On bottom, the unpolarized cross section ratios. Both are for the seventeenth bin in x_B and θ_e, where $0.35 < x_B < 0.38$ and $28^\circ < \theta_e < 45^\circ$. Each panel corresponds to a bin in $-t$ whose limits are: [0.09, 0.13, 0.18, 0.23, 0.30, 0.39, 0.52, 0.72, 1.10, 2.00] Green is $\frac{e1-dvcs2\ Saylor}{e1-dvcs2\ Guegan}$. Red is $\frac{e1-dvcs2\ Saylor}{e1-dvcs1\ Jo}$. 268

Figure E.18 On top, the unpolarized cross section as a function of Φ. Black represents this analysis. Green is e1-dvcs2 by B. Guegan. Red is e1-dvcs1 by H.S. Jo. On bottom, the unpolarized cross section ratios. Both are for the eighteenth bin in x_B and θ_e, where $0.38 < x_B < 0.42$ and $21^\circ < \theta_e < 28^\circ$. Each panel corresponds to a bin in $-t$ whose limits are: [0.09, 0.13, 0.18, 0.23, 0.30, 0.39, 0.52, 0.72, 1.10, 2.00] Green is $\frac{e1-dvcs2\ Saylor}{e1-dvcs2\ Guegan}$. Red is $\frac{e1-dvcs2\ Saylor}{e1-dvcs1\ Jo}$. 269

Figure E.19 On top, the unpolarized cross section as a function of Φ. Black represents this analysis. Green is e1-dvcs2 by B. Guegan. Red is e1-dvcs1 by H.S. Jo. On bottom, the unpolarized cross section ratios. Both are for the nineteenth bin in x_B and θ_e, where $0.38 < x_B < 0.42$ and $28^\circ < \theta_e < 45^\circ$. Each panel corresponds to a bin in $-t$ whose limits are: [0.09, 0.13, 0.18, 0.23, 0.30, 0.39, 0.52, 0.72, 1.10, 2.00] Green is $\frac{e1-dvcs2\ Saylor}{e1-dvcs2\ Guegan}$. Red is $\frac{e1-dvcs2\ Saylor}{e1-dvcs1\ Jo}$. 270

Figure E.20 On top, the unpolarized cross section as a function of Φ. Black represents this analysis. Green is e1-dvcs2 by B. Guegan. Red is e1-dvcs1 by H.S. Jo. On bottom, the unpolarized cross section ratios. Both are for the twentieth bin in x_B and θ_e, where $0.42 < x_B < 0.58$ and $21^\circ < \theta_e < 33^\circ$. Each panel corresponds to a bin in $-t$ whose limits are: [0.09, 0.13, 0.18, 0.23, 0.30, 0.39, 0.52, 0.72, 1.10, 2.00] Green is $\frac{e1-dvcs2\ Saylor}{e1-dvcs2\ Guegan}$. Red is $\frac{e1-dvcs2\ Saylor}{e1-dvcs1\ Jo}$. 271

Figure E.21 On top, the unpolarized cross section as a function of Φ. Black represents this analysis. Green is e1-dvcs2 by B. Guegan. Red is e1-dvcs1 by H.S. Jo. On bottom, the unpolarized cross section ratios. Both are for the twenty-first bin in x_B and θ_e, where $0.42 < x_B < 0.58$ and $33^\circ < \theta_e < 45^\circ$. Each panel corresponds to a bin in $-t$ whose limits are: [0.09, 0.13, 0.18, 0.23, 0.30, 0.39, 0.52, 0.72, 1.10, 2.00] Green is $\frac{e1-dvcs2\ Saylor}{e1-dvcs2\ Guegan}$. Red is $\frac{e1-dvcs2\ Saylor}{e1-dvcs1\ Jo}$. 272

Figure E.22 On top, the polarized cross section differences as a function of Φ. Black represents this analysis. Green is e1-dvcs2 by B. Guegan. Red is e1-dvcs1 by H.S. Jo. On bottom, the polarized difference ratios. Both are for the first bin in x_B and θ_e, where $0.1 < x_B < 0.14$ and $21^\circ < \theta_e < 45^\circ$. Each panel corresponds to a bin in $-t$ whose limits are: [0.09, 0.13, 0.18, 0.23, 0.30, 0.39, 0.52, 0.72, 1.10, 2.00] Green is $\frac{e1-dvcs2\ Saylor}{e1-dvcs2\ Guegan}$. Red is $\frac{e1-dvcs2\ Saylor}{e1-dvcs1\ Jo}$. 274

Figure E.23 On top, the polarized cross section differences as a function of Φ. Black represents this analysis. Green is e1-dvcs2 by B. Guegan. Red is e1-dvcs1 by H.S. Jo. On bottom, the polarized difference ratios. Both are for the second bin in x_B and θ_e, where $0.14 < x_B < 0.17$ and $21^\circ < \theta_e < 25.5^\circ$. Each panel corresponds to a bin in $-t$ whose limits are: [0.09, 0.13, 0.18, 0.23, 0.30, 0.39, 0.52, 0.72, 1.10, 2.00] Green is $\frac{e1-dvcs2\ Saylor}{e1-dvcs2\ Guegan}$. Red is $\frac{e1-dvcs2\ Saylor}{e1-dvcs1\ Jo}$. 275

Figure E.24 On top, the polarized cross section differences as a function of Φ. Black represents this analysis. Green is e1-dvcs2 by B. Guegan. Red is e1-dvcs1 by H.S. Jo. On bottom, the polarized difference ratios. Both are for the third bin in x_B and θ_e, where $0.14 < x_B < 0.17$ and $25.5° < \theta_e < 45°$. Each panel corresponds to a bin in $-t$ whose limits are: [0.09, 0.13, 0.18, 0.23, 0.30, 0.39, 0.52, 0.72, 1.10, 2.00] Green is $\frac{e1-dvcs2\ Saylor}{e1-dvcs2\ Guegan}$. Red is $\frac{e1-dvcs2\ Saylor}{e1-dvcs1\ Jo}$. 276

Figure E.25 On top, the polarized cross section differences as a function of Φ. Black represents this analysis. Green is e1-dvcs2 by B. Guegan. Red is e1-dvcs1 by H.S. Jo. On bottom, the polarized difference ratios. Both are for the fourth bin in x_B and θ_e, where $0.17 < x_B < 0.2$ and $21° < \theta_e < 25.5°$. Each panel corresponds to a bin in $-t$ whose limits are: [0.09, 0.13, 0.18, 0.23, 0.30, 0.39, 0.52, 0.72, 1.10, 2.00] Green is $\frac{e1-dvcs2\ Saylor}{e1-dvcs2\ Guegan}$. Red is $\frac{e1-dvcs2\ Saylor}{e1-dvcs1\ Jo}$. 277

Figure E.26 On top, the polarized cross section differences as a function of Φ. Black represents this analysis. Green is e1-dvcs2 by B. Guegan. Red is e1-dvcs1 by H.S. Jo. On bottom, the polarized difference ratios. Both are for the fifth bin in x_B and θ_e, where $0.17 < x_B < 0.2$ and $25.5° < \theta_e < 45°$. Each panel corresponds to a bin in $-t$ whose limits are: [0.09, 0.13, 0.18, 0.23, 0.30, 0.39, 0.52, 0.72, 1.10, 2.00] Green is $\frac{e1-dvcs2\ Saylor}{e1-dvcs2\ Guegan}$. Red is $\frac{e1-dvcs2\ Saylor}{e1-dvcs1\ Jo}$. 278

Figure E.27 On top, the polarized cross section differences as a function of Φ. Black represents this analysis. Green is e1-dvcs2 by B. Guegan. Red is e1-dvcs1 by H.S. Jo. On bottom, the polarized difference ratios. Both are for the sixth bin in x_B and θ_e, where $0.2 < x_B < 0.23$ and $21° < \theta_e < 27°$. Each panel corresponds to a bin in $-t$ whose limits are: [0.09, 0.13, 0.18, 0.23, 0.30, 0.39, 0.52, 0.72, 1.10, 2.00] Green is $\frac{e1-dvcs2\ Saylor}{e1-dvcs2\ Guegan}$. Red is $\frac{e1-dvcs2\ Saylor}{e1-dvcs1\ Jo}$. 279

Figure E.28 On top, the polarized cross section differences as a function of Φ. Black represents this analysis. Green is e1-dvcs2 by B. Guegan. Red is e1-dvcs1 by H.S. Jo. On bottom, the polarized difference ratios. Both are for the seventh bin in x_B and θ_e, where $0.2 < x_B < 0.23$ and $27° < \theta_e < 45°$. Each panel corresponds to a bin in $-t$ whose limits are: [0.09, 0.13, 0.18, 0.23, 0.30, 0.39, 0.52, 0.72, 1.10, 2.00] Green is $\frac{e1-dvcs2\ Saylor}{e1-dvcs2\ Guegan}$. Red is $\frac{e1-dvcs2\ Saylor}{e1-dvcs1\ Jo}$. 280

Figure E.29 On top, the polarized cross section differences as a function of Φ. Black represents this analysis. Green is e1-dvcs2 by B. Guegan. Red is e1-dvcs1 by H.S. Jo. On bottom, the polarized difference ratios. Both are for the eighth bin in x_B and θ_e, where $0.23 < x_B < 0.26$ and $21° < \theta_e < 27°$. Each panel corresponds to a bin in $-t$ whose limits are: [0.09, 0.13, 0.18, 0.23, 0.30, 0.39, 0.52, 0.72, 1.10, 2.00] Green is $\frac{e1-dvcs2\ Saylor}{e1-dvcs2\ Guegan}$. Red is $\frac{e1-dvcs2\ Saylor}{e1-dvcs1\ Jo}$. 281

Figure E.30 On top, the polarized cross section differences as a function of Φ. Black represents this analysis. Green is e1-dvcs2 by B. Guegan. Red is e1-dvcs1 by H.S. Jo. On bottom, the polarized difference ratios. Both are for the ninth bin in x_B and θ_e, where $0.23 < x_B < 0.26$ and $27° < \theta_e < 45°$. Each panel corresponds to a bin in $-t$ whose limits are: [0.09, 0.13, 0.18, 0.23, 0.30, 0.39, 0.52, 0.72, 1.10, 2.00] Green is $\frac{e1-dvcs2\ Saylor}{e1-dvcs2\ Guegan}$. Red is $\frac{e1-dvcs2\ Saylor}{e1-dvcs1\ Jo}$. 282

Figure E.31 On top, the polarized cross section differences as a function of Φ. Black represents this analysis. Green is e1-dvcs2 by B. Guegan. Red is e1-dvcs1 by H.S. Jo. On bottom, the polarized difference ratios. Both are for the tenth bin in x_B and θ_e, where $0.26 < x_B < 0.29$ and $21° < \theta_e < 27°$. Each panel corresponds to a bin in $-t$ whose limits are: [0.09, 0.13, 0.18, 0.23, 0.30, 0.39, 0.52, 0.72, 1.10, 2.00] Green is $\frac{e1-dvcs2\ Saylor}{e1-dvcs2\ Guegan}$. Red is $\frac{e1-dvcs2\ Saylor}{e1-dvcs1\ Jo}$. 283

Figure E.32 On top, the polarized cross section differences as a function of Φ. Black represents this analysis. Green is e1-dvcs2 by B. Guegan. Red is e1-dvcs1 by H.S. Jo. On bottom, the polarized difference ratios. Both are for the eleventh bin in x_B and θ_e, where $0.26 < x_B < 0.29$ and $27° < \theta_e < 45°$. Each panel corresponds to a bin in $-t$ whose limits are: [0.09, 0.13, 0.18, 0.23, 0.30, 0.39, 0.52, 0.72, 1.10, 2.00] Green is $\frac{e1-dvcs2\ Saylor}{e1-dvcs2\ Guegan}$. Red is $\frac{e1-dvcs2\ Saylor}{e1-dvcs1\ Jo}$. 284

Figure E.33 On top, the polarized cross section differences as a function of Φ. Black represents this analysis. Green is e1-dvcs2 by B. Guegan. Red is e1-dvcs1 by H.S. Jo. On bottom, the polarized difference ratios. Both are for the twelfth bin in x_B and θ_e, where $0.29 < x_B < 0.32$ and $21° < \theta_e < 28°$. Each panel corresponds to a bin in $-t$ whose limits are: [0.09, 0.13, 0.18, 0.23, 0.30, 0.39, 0.52, 0.72, 1.10, 2.00] Green is $\frac{e1-dvcs2\ Saylor}{e1-dvcs2\ Guegan}$. Red is $\frac{e1-dvcs2\ Saylor}{e1-dvcs1\ Jo}$. 285

Figure E.34 On top, the polarized cross section differences as a function of Φ. Black represents this analysis. Green is e1-dvcs2 by B. Guegan. Red is e1-dvcs1 by H.S. Jo. On bottom, the polarized difference ratios. Both are for the thirteenth bin in x_B and θ_e, where $0.29 < x_B < 0.32$ and $28° < \theta_e < 45°$. Each panel corresponds to a bin in $-t$ whose limits are: [0.09, 0.13, 0.18, 0.23, 0.30, 0.39, 0.52, 0.72, 1.10, 2.00] Green is $\frac{e1-dvcs2\ Saylor}{e1-dvcs2\ Guegan}$. Red is $\frac{e1-dvcs2\ Saylor}{e1-dvcs1\ Jo}$. 286

Figure E.35 On top, the polarized cross section differences as a function of Φ. Black represents this analysis. Green is e1-dvcs2 by B. Guegan. Red is e1-dvcs1 by H.S. Jo. On bottom, the polarized difference ratios. Both are for the fourteenth bin in x_B and θ_e, where $0.32 < x_B < 0.35$ and $21° < \theta_e < 28°$. Each panel corresponds to a bin in $-t$ whose limits are: [0.09, 0.13, 0.18, 0.23, 0.30, 0.39, 0.52, 0.72, 1.10, 2.00] Green is $\frac{e1-dvcs2\ Saylor}{e1-dvcs2\ Guegan}$. Red is $\frac{e1-dvcs2\ Saylor}{e1-dvcs1\ Jo}$. 287

Figure E.36 On top, the polarized cross section differences as a function of Φ. Black represents this analysis. Green is e1-dvcs2 by B. Guegan. Red is e1-dvcs1 by H.S. Jo. On bottom, the polarized difference ratios. Both are for the fifteenth bin in x_B and θ_e, where $0.32 < x_B < 0.35$ and $28° < \theta_e < 45°$. Each panel corresponds to a bin in $-t$ whose limits are: [0.09, 0.13, 0.18, 0.23, 0.30, 0.39, 0.52, 0.72, 1.10, 2.00] Green is $\frac{e1-dvcs2\ Saylor}{e1-dvcs2\ Guegan}$. Red is $\frac{e1-dvcs2\ Saylor}{e1-dvcs1\ Jo}$. 288

Figure E.37 On top, the polarized cross section differences as a function of Φ. Black represents this analysis. Green is e1-dvcs2 by B. Guegan. Red is e1-dvcs1 by H.S. Jo. On bottom, the polarized difference ratios. Both are for the sixteenth bin in x_B and θ_e, where $0.35 < x_B < 0.38$ and $21° < \theta_e < 28°$. Each panel corresponds to a bin in $-t$ whose limits are: [0.09, 0.13, 0.18, 0.23, 0.30, 0.39, 0.52, 0.72, 1.10, 2.00] Green is $\frac{e1-dvcs2\ Saylor}{e1-dvcs2\ Guegan}$. Red is $\frac{e1-dvcs2\ Saylor}{e1-dvcs1\ Jo}$. 289

Figure E.38 On top, the polarized cross section differences as a function of Φ. Black represents this analysis. Green is e1-dvcs2 by B. Guegan. Red is e1-dvcs1 by H.S. Jo. On bottom, the polarized difference ratios. Both are for the seventeenth bin in x_B and θ_e, where $0.35 < x_B < 0.38$ and $28° < \theta_e < 45°$. Each panel corresponds to a bin in $-t$ whose limits are: [0.09, 0.13, 0.18, 0.23, 0.30, 0.39, 0.52, 0.72, 1.10, 2.00] Green is $\frac{e1-dvcs2\ Saylor}{e1-dvcs2\ Guegan}$. Red is $\frac{e1-dvcs2\ Saylor}{e1-dvcs1\ Jo}$. 290

Figure E.39 On top, the polarized cross section differences as a function of Φ. Black represents this analysis. Green is e1-dvcs2 by B. Guegan. Red is e1-dvcs1 by H.S. Jo. On bottom, the polarized difference ratios. Both are for the eighteenth bin in x_B and θ_e, where $0.38 < x_B < 0.42$ and $21° < \theta_e < 28°$. Each panel corresponds to a bin in $-t$ whose limits are: [0.09, 0.13, 0.18, 0.23, 0.30, 0.39, 0.52, 0.72, 1.10, 2.00] Green is $\frac{e1-dvcs2\ Saylor}{e1-dvcs2\ Guegan}$. Red is $\frac{e1-dvcs2\ Saylor}{e1-dvcs1\ Jo}$. 291

Figure E.40 On top, the polarized cross section differences as a function of Φ. Black represents this analysis. Green is e1-dvcs2 by B. Guegan. Red is e1-dvcs1 by H.S. Jo. On bottom, the polarized difference ratios. Both are for the nineteenth bin in x_B and θ_e, where $0.38 < x_B < 0.42$ and $28° < \theta_e < 45°$. Each panel corresponds to a bin in $-t$ whose limits are: [0.09, 0.13, 0.18, 0.23, 0.30, 0.39, 0.52, 0.72, 1.10, 2.00] Green is $\frac{e1-dvcs2\ Saylor}{e1-dvcs2\ Guegan}$. Red is $\frac{e1-dvcs2\ Saylor}{e1-dvcs1\ Jo}$. 292

Figure E.41 On top, the polarized cross section differences as a function of Φ. Black represents this analysis. Green is e1-dvcs2 by B. Guegan. Red is e1-dvcs1 by H.S. Jo. On bottom, the polarized difference ratios. Both are for the twentieth bin in x_B and θ_e, where $0.42 < x_B < 0.58$ and $21° < \theta_e < 33°$. Each panel corresponds to a bin in $-t$ whose limits are: [0.09, 0.13, 0.18, 0.23, 0.30, 0.39, 0.52, 0.72, 1.10, 2.00] Green is $\frac{e1-dvcs2\ Saylor}{e1-dvcs2\ Guegan}$. Red is $\frac{e1-dvcs2\ Saylor}{e1-dvcs1\ Jo}$. 293

Figure E.42 On top, the polarized cross section differences as a function of Φ. Black represents this analysis. Green is e1-dvcs2 by B. Guegan. Red is e1-dvcs1 by H.S. Jo. On bottom, the polarized difference ratios. Both are for the twenty-first bin in x_B and θ_e, where $0.42 < x_B < 0.58$ and $33° < \theta_e < 45°$. Each panel corresponds to a bin in $-t$ whose limits are: [0.09, 0.13, 0.18, 0.23, 0.30, 0.39, 0.52, 0.72, 1.10, 2.00] Green is $\frac{e1-dvcs2\ Saylor}{e1-dvcs2\ Guegan}$. Red is $\frac{e1-dvcs2\ Saylor}{e1-dvcs1\ Jo}$. 294

Figure E.43 On top, the asymmetry as a function of Φ. Black represents this analysis. Green is e1-dvcs2 by B. Guegan. Red is e1-dvcs1 by H.S. Jo. On bottom, the asymmetry ratios. Both are for the first bin in x_B and θ_e, where $0.1 < x_B < 0.14$ and $21° < \theta_e < 45°$. Each panel corresponds to a bin in $-t$ whose limits are: [0.09, 0.13, 0.18, 0.23, 0.30, 0.39, 0.52, 0.72, 1.10, 2.00] Green is $\frac{e1-dvcs2\ Saylor}{e1-dvcs2\ Guegan}$. Red is $\frac{e1-dvcs2\ Saylor}{e1-dvcs1\ Jo}$. 296

Figure E.44 On top, the asymmetry as a function of Φ. Black represents this analysis. Green is e1-dvcs2 by B. Guegan. Red is e1-dvcs1 by H.S. Jo. On bottom, the asymmetry ratios. Both are for the second bin in x_B and θ_e, where $0.14 < x_B < 0.17$ and $21° < \theta_e < 25.5°$. Each panel corresponds to a bin in $-t$ whose limits are: [0.09, 0.13, 0.18, 0.23, 0.30, 0.39, 0.52, 0.72, 1.10, 2.00] Green is $\frac{e1-dvcs2\ Saylor}{e1-dvcs2\ Guegan}$. Red is $\frac{e1-dvcs2\ Saylor}{e1-dvcs1\ Jo}$. 297

Figure E.45 On top, the asymmetry as a function of Φ. Black represents this analysis. Green is e1-dvcs2 by B. Guegan. Red is e1-dvcs1 by H.S. Jo. On bottom, the asymmetry ratios. Both are for the third bin in x_B and θ_e, where $0.14 < x_B < 0.17$ and $25.5° < \theta_e < 45°$. Each panel corresponds to a bin in $-t$ whose limits are: [0.09, 0.13, 0.18, 0.23, 0.30, 0.39, 0.52, 0.72, 1.10, 2.00] Green is $\frac{e1-dvcs2\ Saylor}{e1-dvcs2\ Guegan}$. Red is $\frac{e1-dvcs2\ Saylor}{e1-dvcs1\ Jo}$. 298

Figure E.46 On top, the asymmetry as a function of Φ. Black represents this analysis. Green is e1-dvcs2 by B. Guegan. Red is e1-dvcs1 by H.S. Jo. On bottom, the asymmetry ratios. Both are for the fourth bin in x_B and θ_e, where $0.17 < x_B < 0.2$ and $21° < \theta_e < 25.5°$. Each panel corresponds to a bin in $-t$ whose limits are: [0.09, 0.13, 0.18, 0.23, 0.30, 0.39, 0.52, 0.72, 1.10, 2.00] Green is $\frac{e1-dvcs2\ Saylor}{e1-dvcs2\ Guegan}$. Red is $\frac{e1-dvcs2\ Saylor}{e1-dvcs1\ Jo}$. 299
Figure E.47 On top, the asymmetry as a function of Φ. Black represents this analysis. Green is e1-dvcs2 by B. Guegan. Red is e1-dvcs1 by H.S. Jo. On bottom, the asymmetry ratios. Both are for the fifth bin in x_B and θ_e, where $0.17 < x_B < 0.2$ and $25.5° < \theta_e < 45°$. Each panel corresponds to a bin in $-t$ whose limits are: [0.09, 0.13, 0.18, 0.23, 0.30, 0.39, 0.52, 0.72, 1.10, 2.00] Green is $\frac{e1-dvcs2\ Saylor}{e1-dvcs2\ Guegan}$. Red is $\frac{e1-dvcs2\ Saylor}{e1-dvcs1\ Jo}$. 300
Figure E.48 On top, the asymmetry as a function of Φ. Black represents this analysis. Green is e1-dvcs2 by B. Guegan. Red is e1-dvcs1 by H.S. Jo. On bottom, the asymmetry ratios. Both are for the sixth bin in x_B and θ_e, where $0.2 < x_B < 0.23$ and $21° < \theta_e < 27°$. Each panel corresponds to a bin in $-t$ whose limits are: [0.09, 0.13, 0.18, 0.23, 0.30, 0.39, 0.52, 0.72, 1.10, 2.00] Green is $\frac{e1-dvcs2\ Saylor}{e1-dvcs2\ Guegan}$. Red is $\frac{e1-dvcs2\ Saylor}{e1-dvcs1\ Jo}$. 301
Figure E.49 On top, the asymmetry as a function of Φ. Black represents this analysis. Green is e1-dvcs2 by B. Guegan. Red is e1-dvcs1 by H.S. Jo. On bottom, the asymmetry ratios. Both are for the seventh bin in x_B and θ_e, where $0.2 < x_B < 0.23$ and $27° < \theta_e < 45°$. Each panel corresponds to a bin in $-t$ whose limits are: [0.09, 0.13, 0.18, 0.23, 0.30, 0.39, 0.52, 0.72, 1.10, 2.00] Green is $\frac{e1-dvcs2\ Saylor}{e1-dvcs2\ Guegan}$. Red is $\frac{e1-dvcs2\ Saylor}{e1-dvcs1\ Jo}$. 302
Figure E.50 On top, the asymmetry as a function of Φ. Black represents this analysis. Green is e1-dvcs2 by B. Guegan. Red is e1-dvcs1 by H.S. Jo. On bottom, the asymmetry ratios. Both are for the eighth bin in x_B and θ_e, where $0.23 < x_B < 0.26$ and $21° < \theta_e < 27°$. Each panel corresponds to a bin in $-t$ whose limits are: [0.09, 0.13, 0.18, 0.23, 0.30, 0.39, 0.52, 0.72, 1.10, 2.00] Green is $\frac{e1-dvcs2\ Saylor}{e1-dvcs2\ Guegan}$. Red is $\frac{e1-dvcs2\ Saylor}{e1-dvcs1\ Jo}$. 303
Figure E.51 On top, the asymmetry as a function of Φ. Black represents this analysis. Green is e1-dvcs2 by B. Guegan. Red is e1-dvcs1 by H.S. Jo. On bottom, the asymmetry ratios. Both are for the ninth bin in x_B and θ_e, where $0.23 < x_B < 0.26$ and $27° < \theta_e < 45°$. Each panel corresponds to a bin in $-t$ whose limits are: [0.09, 0.13, 0.18, 0.23, 0.30, 0.39, 0.52, 0.72, 1.10, 2.00] Green is $\frac{e1-dvcs2\ Saylor}{e1-dvcs2\ Guegan}$. Red is $\frac{e1-dvcs2\ Saylor}{e1-dvcs1\ Jo}$. 304
Figure E.52 On top, the asymmetry as a function of Φ. Black represents this analysis. Green is e1-dvcs2 by B. Guegan. Red is e1-dvcs1 by H.S. Jo. On bottom, the asymmetry ratios. Both are for the tenth bin in x_B and θ_e, where $0.26 < x_B < 0.29$ and $21° < \theta_e < 27°$. Each panel corresponds to a bin in $-t$ whose limits are: [0.09, 0.13, 0.18, 0.23, 0.30, 0.39, 0.52, 0.72, 1.10, 2.00] Green is $\frac{e1-dvcs2\ Saylor}{e1-dvcs2\ Guegan}$. Red is $\frac{e1-dvcs2\ Saylor}{e1-dvcs1\ Jo}$. 305
Figure E.53 On top, the asymmetry as a function of Φ. Black represents this analysis. Green is e1-dvcs2 by B. Guegan. Red is e1-dvcs1 by H.S. Jo. On bottom, the asymmetry ratios. Both are for the eleventh bin in x_B and θ_e, where $0.26 < x_B < 0.29$ and $27° < \theta_e < 45°$. Each panel corresponds to a bin in $-t$ whose limits are: [0.09, 0.13, 0.18, 0.23, 0.30, 0.39, 0.52, 0.72, 1.10, 2.00] Green is $\frac{e1-dvcs2\ Saylor}{e1-dvcs2\ Guegan}$. Red is $\frac{e1-dvcs2\ Saylor}{e1-dvcs1\ Jo}$. 306
Figure E.54 On top, the asymmetry as a function of Φ. Black represents this analysis. Green is e1-dvcs2 by B. Guegan. Red is e1-dvcs1 by H.S. Jo. On bottom, the asymmetry ratios. Both are for the twelfth bin in x_B and θ_e, where $0.29 < x_B < 0.32$ and $21° < \theta_e < 28°$. Each panel corresponds to a bin in $-t$ whose limits are: [0.09, 0.13, 0.18, 0.23, 0.30, 0.39, 0.52, 0.72, 1.10, 2.00] Green is $\frac{e1-dvcs2\ Saylor}{e1-dvcs2\ Guegan}$. Red is $\frac{e1-dvcs2\ Saylor}{e1-dvcs1\ Jo}$. 307

Figure E.55 On top, the asymmetry as a function of Φ. Black represents this analysis. Green is e1-dvcs2 by B. Guegan. Red is e1-dvcs1 by H.S. Jo. On bottom, the asymmetry ratios. Both are for the thirteenth bin in x_B and θ_e, where $0.29 < x_B < 0.32$ and $28° < \theta_e < 45°$. Each panel corresponds to a bin in $-t$ whose limits are: [0.09, 0.13, 0.18, 0.23, 0.30, 0.39, 0.52, 0.72, 1.10, 2.00] Green is $\frac{e1-dvcs2\ Saylor}{e1-dvcs2\ Guegan}$. Red is $\frac{e1-dvcs2\ Saylor}{e1-dvcs1\ Jo}$. 308
Figure E.56 On top, the asymmetry as a function of Φ. Black represents this analysis. Green is e1-dvcs2 by B. Guegan. Red is e1-dvcs1 by H.S. Jo. On bottom, the asymmetry ratios. Both are for the fourteenth bin in x_B and θ_e, where $0.32 < x_B < 0.35$ and $21° < \theta_e < 28°$. Each panel corresponds to a bin in $-t$ whose limits are: [0.09, 0.13, 0.18, 0.23, 0.30, 0.39, 0.52, 0.72, 1.10, 2.00] Green is $\frac{e1-dvcs2\ Saylor}{e1-dvcs2\ Guegan}$. Red is $\frac{e1-dvcs2\ Saylor}{e1-dvcs1\ Jo}$. 309
Figure E.57 On top, the asymmetry as a function of Φ. Black represents this analysis. Green is e1-dvcs2 by B. Guegan. Red is e1-dvcs1 by H.S. Jo. On bottom, the asymmetry ratios. Both are for the fifteenth bin in x_B and θ_e, where $0.32 < x_B < 0.35$ and $28° < \theta_e < 45°$. Each panel corresponds to a bin in $-t$ whose limits are: [0.09, 0.13, 0.18, 0.23, 0.30, 0.39, 0.52, 0.72, 1.10, 2.00] Green is $\frac{e1-dvcs2\ Saylor}{e1-dvcs2\ Guegan}$. Red is $\frac{e1-dvcs2\ Saylor}{e1-dvcs1\ Jo}$. 310
Figure E.58 On top, the asymmetry as a function of Φ. Black represents this analysis. Green is e1-dvcs2 by B. Guegan. Red is e1-dvcs1 by H.S. Jo. On bottom, the asymmetry ratios. Both are for the sixteenth bin in x_B and θ_e, where $0.35 < x_B < 0.38$ and $21° < \theta_e < 28°$. Each panel corresponds to a bin in $-t$ whose limits are: [0.09, 0.13, 0.18, 0.23, 0.30, 0.39, 0.52, 0.72, 1.10, 2.00] Green is $\frac{e1-dvcs2\ Saylor}{e1-dvcs2\ Guegan}$. Red is $\frac{e1-dvcs2\ Saylor}{e1-dvcs1\ Jo}$. 311
Figure E.59 On top, the asymmetry as a function of Φ. Black represents this analysis. Green is e1-dvcs2 by B. Guegan. Red is e1-dvcs1 by H.S. Jo. On bottom, the asymmetry ratios. Both are for the seventeenth bin in x_B and θ_e, where $0.35 < x_B < 0.38$ and $28° < \theta_e < 45°$. Each panel corresponds to a bin in $-t$ whose limits are: [0.09, 0.13, 0.18, 0.23, 0.30, 0.39, 0.52, 0.72, 1.10, 2.00] Green is $\frac{e1-dvcs2\ Saylor}{e1-dvcs2\ Guegan}$. Red is $\frac{e1-dvcs2\ Saylor}{e1-dvcs1\ Jo}$. 312
Figure E.60 On top, the asymmetry as a function of Φ. Black represents this analysis. Green is e1-dvcs2 by B. Guegan. Red is e1-dvcs1 by H.S. Jo. On bottom, the asymmetry ratios. Both are for the eighteenth bin in x_B and θ_e, where $0.38 < x_B < 0.42$ and $21° < \theta_e < 28°$. Each panel corresponds to a bin in $-t$ whose limits are: [0.09, 0.13, 0.18, 0.23, 0.30, 0.39, 0.52, 0.72, 1.10, 2.00] Green is $\frac{e1-dvcs2\ Saylor}{e1-dvcs2\ Guegan}$. Red is $\frac{e1-dvcs2\ Saylor}{e1-dvcs1\ Jo}$. 313
Figure E.61 On top, the asymmetry as a function of Φ. Black represents this analysis. Green is e1-dvcs2 by B. Guegan. Red is e1-dvcs1 by H.S. Jo. On bottom, the asymmetry ratios. Both are for the nineteenth bin in x_B and θ_e, where $0.38 < x_B < 0.42$ and $28° < \theta_e < 45°$. Each panel corresponds to a bin in $-t$ whose limits are: [0.09, 0.13, 0.18, 0.23, 0.30, 0.39, 0.52, 0.72, 1.10, 2.00] Green is $\frac{e1-dvcs2\ Saylor}{e1-dvcs2\ Guegan}$. Red is $\frac{e1-dvcs2\ Saylor}{e1-dvcs1\ Jo}$. 314
Figure E.62 On top, the asymmetry as a function of Φ. Black represents this analysis. Green is e1-dvcs2 by B. Guegan. Red is e1-dvcs1 by H.S. Jo. On bottom, the asymmetry ratios. Both are for the twentieth bin in x_B and θ_e, where $0.42 < x_B < 0.58$ and $21° < \theta_e < 33°$. Each panel corresponds to a bin in $-t$ whose limits are: [0.09, 0.13, 0.18, 0.23, 0.30, 0.39, 0.52, 0.72, 1.10, 2.00] Green is $\frac{e1-dvcs2\ Saylor}{e1-dvcs2\ Guegan}$. Red is $\frac{e1-dvcs2\ Saylor}{e1-dvcs1\ Jo}$. 315
Figure E.63 On top, the asymmetry as a function of Φ. Black represents this analysis. Green is e1-dvcs2 by B. Guegan. Red is e1-dvcs1 by H.S. Jo. On bottom, the asymmetry ratios. Both are for the twenty-first bin in x_B and θ_e, where $0.42 < x_B < 0.58$ and $33° < \theta_e < 45°$. Each panel corresponds to a bin in $-t$ whose limits are: [0.09, 0.13, 0.18, 0.23, 0.30, 0.39, 0.52, 0.72, 1.10, 2.00] Green is $\frac{e1-dvcs2\ Saylor}{e1-dvcs2\ Guegan}$. Red is $\frac{e1-dvcs2\ Saylor}{e1-dvcs1\ Jo}$. 316

Figure F.1 The unpolarized cross section as a function of Φ for the first bin in x_B and θ_e, where $0.1 < x_B < 0.14$ and $21^\circ < \theta_e < 45^\circ$. Each panel corresponds to a bin in $-t$ whose limits are: [0.09, 0.13, 0.18, 0.23, 0.30, 0.39, 0.52, 0.72, 1.10, 2.00] For both, the green curve corresponds to VGG, the light magenta corresponds to KM10, and the dark magenta corresponds to KM10a. . . 317

Figure F.2 On top, the unpolarized cross section as a function of Φ for the second bin in x_B and θ_e, where $0.14 < x_B < 0.17$ and $21^\circ < \theta_e < 25.5^\circ$. On bottom, the unpolarized cross section for the third bin in x_B and θ_e, where $0.14 < x_B < 0.17$ and $25.5^\circ < \theta_e < 45^\circ$. Each panel corresponds to a bin in $-t$ whose limits are: [0.09, 0.13, 0.18, 0.23, 0.30, 0.39, 0.52, 0.72, 1.10, 2.00] For both, the green curve corresponds to VGG, the light magenta corresponds to KM10, and the dark magenta corresponds to KM10a. . . 318

Figure F.3 On top, the unpolarized cross section as a function of Φ for the fourth bin in x_B and θ_e, where $0.17 < x_B < 0.2$ and $21^\circ < \theta_e < 25.5^\circ$. On bottom, the unpolarized cross section for the fifth bin in x_B and θ_e, where $0.17 < x_B < 0.2$ and $25.5^\circ < \theta_e < 45^\circ$. Each panel corresponds to a bin in $-t$ whose limits are: [0.09, 0.13, 0.18, 0.23, 0.30, 0.39, 0.52, 0.72, 1.10, 2.00] For both, the green curve corresponds to VGG, the light magenta corresponds to KM10, and the dark magenta corresponds to KM10a. . . 319

Figure F.4 On top, the unpolarized cross section as a function of Φ for the sixth bin in x_B and θ_e, where $0.2 < x_B < 0.23$ and $21^\circ < \theta_e < 27^\circ$. On bottom, the unpolarized cross section for the seventh bin in x_B and θ_e, where $0.2 < x_B < 0.23$ and $27^\circ < \theta_e < 45^\circ$. Each panel corresponds to a bin in $-t$ whose limits are: [0.09, 0.13, 0.18, 0.23, 0.30, 0.39, 0.52, 0.72, 1.10, 2.00] For both, the green curve corresponds to VGG, the light magenta corresponds to KM10, and the dark magenta corresponds to KM10a. 320

Figure F.5 On top, the unpolarized cross section as a function of Φ for the eighth bin in x_B and θ_e, where $0.23 < x_B < 0.26$ and $21^\circ < \theta_e < 27^\circ$. On bottom, the unpolarized cross section for the ninth bin in x_B and θ_e, where $0.23 < x_B < 0.26$ and $27^\circ < \theta_e < 45^\circ$. Each panel corresponds to a bin in $-t$ whose limits are: [0.09, 0.13, 0.18, 0.23, 0.30, 0.39, 0.52, 0.72, 1.10, 2.00] For both, the green curve corresponds to VGG, the light magenta corresponds to KM10, and the dark magenta corresponds to KM10a. . . 321

Figure F.6 On top, the unpolarized cross section as a function of Φ for the tenth bin in x_B and θ_e, where $0.26 < x_B < 0.29$ and $21^\circ < \theta_e < 27^\circ$. On bottom, the unpolarized cross section for the eleventh bin in x_B and θ_e, where $0.26 < x_B < 0.29$ and $27^\circ < \theta_e < 45^\circ$. Each panel corresponds to a bin in $-t$ whose limits are: [0.09, 0.13, 0.18, 0.23, 0.30, 0.39, 0.52, 0.72, 1.10, 2.00] For both, the green curve corresponds to VGG, the light magenta corresponds to KM10, and the dark magenta corresponds to KM10a. 322

Figure F.7 On top, the unpolarized cross section as a function of Φ for the twelfth bin in x_B and θ_e, where $0.29 < x_B < 0.32$ and $21^\circ < \theta_e < 28^\circ$. On bottom, the unpolarized cross section for the thirteenth bin in x_B and θ_e, where $0.29 < x_B < 0.32$ and $28^\circ < \theta_e < 45^\circ$. Each panel corresponds to a bin in $-t$ whose limits are: [0.09, 0.13, 0.18, 0.23, 0.30, 0.39, 0.52, 0.72, 1.10, 2.00] For both, the green curve corresponds to VGG, the light magenta corresponds to KM10, and the dark magenta corresponds to KM10a. . . 323

Figure F.8 On top, the unpolarized cross section as a function of Φ for the fourteenth bin in x_B and θ_e, where $0.32 < x_B < 0.35$ and $21^\circ < \theta_e < 28^\circ$. On bottom, the unpolarized cross section for the fifteenth bin in x_B and θ_e, where $0.32 < x_B < 0.35$ and $28^\circ < \theta_e < 45^\circ$. Each panel corresponds to a bin in $-t$ whose limits are: [0.09, 0.13, 0.18, 0.23, 0.30, 0.39, 0.52, 0.72, 1.10, 2.00] For both, the green curve corresponds to VGG, the light magenta corresponds to KM10, and the dark magenta corresponds to KM10a. . . 324

Figure F.9 On top, the unpolarized cross section as a function of Φ for the sixteenth bin in x_B and θ_e, where $0.35 < x_B < 0.38$ and $21^\circ < \theta_e < 28^\circ$. On bottom, the unpolarized cross section for the seventeenth bin in x_B and θ_e, where $0.35 < x_B < 0.38$ and $28^\circ < \theta_e < 45^\circ$. Each panel corresponds to a bin in $-t$ whose limits are: [0.09, 0.13, 0.18, 0.23, 0.30, 0.39, 0.52, 0.72, 1.10, 2.00] For both, the green curve corresponds to VGG, the light magenta corresponds to KM10, and the dark magenta corresponds to KM10a. . . 325

Figure F.10 On top, the unpolarized cross section as a function of Φ for the eighteenth bin in x_B and θ_e, where $0.38 < x_B < 0.42$ and $21^\circ < \theta_e < 28^\circ$. On bottom, the unpolarized cross section for the nineteenth bin in x_B and θ_e, where $0.38 < x_B < 0.42$ and $28^\circ < \theta_e < 45^\circ$. Each panel corresponds to a bin in $-t$ whose limits are: [0.09, 0.13, 0.18, 0.23, 0.30, 0.39, 0.52, 0.72, 1.10, 2.00] For both, the green curve corresponds to VGG, the light magenta corresponds to KM10, and the dark magenta corresponds to KM10a. . . 326

Figure F.11 On top, the unpolarized cross section as a function of Φ for the twentieth bin in x_B and θ_e, where $0.42 < x_B < 0.58$ and $21^\circ < \theta_e < 33^\circ$. On bottom, the unpolarized cross section for the twenty-first bin in x_B and θ_e, where $0.42 < x_B < 0.58$ and $33^\circ < \theta_e < 45^\circ$. Each panel corresponds to a bin in $-t$ whose limits are: [0.09, 0.13, 0.18, 0.23, 0.30, 0.39, 0.52, 0.72, 1.10, 2.00] For both, the green curve corresponds to VGG, the light magenta corresponds to KM10, and the dark magenta corresponds to KM10a. . . 327

ACKNOWLEDGEMENTS

I would like to take the opportunity to give my sincerest gratitude to my thesis advisors, Michel and Paul for their unwavering support throughout my years of study.

Michel: I want to thank you for the warm welcome you extended to me, especially on my first visit to Orsay. Your kindness and your expertise make you a very wonderful person to work with. Your way of explaining very difficult things makes those things seem not so intimidating after all. Lastly, I appreciate your patience, especially your willingness to let me practice my not-so-good French with you! Merci mille fois!

Paul: Thank you for being such an understanding advisor. You have been supportive throughout all of my frustrations and trials. I appreciate all our conversations about physics, even when they sometimes digressed to philosophy, and often to politics, and always eventually to a cup of coffee. You have a good attitude, and in my mind you are the "Old Man River" who encourages me to "just keep rolling along."

My next thanks goes out to the Orsay group - the old group which doesn't exist anymore, and the new group! This group is so full of energy and youthfulness. In particular, I would like to thank Silvia for her expertise and her inexhaustible energy, even when juggling nucleons in one hand and sick babies in the other. I would also like to thank Hyon-Suk for his "bushwhacking" in his e1-dvcs1 analysis. His efforts have really paved the way for Baptiste and me, as well as his demand that things be done completely correctly. Finally, I want to thank Baptiste for sharing the burden of the e1-dvcs2 analysis. It has been a real pleasure working with him throughout these past couple of years. Most of all, I would like to thank him for helping me to learn the "real French".

I would like to thank the group at JLab itself. I would like to give thanks to F.X., for being there to answer my persistent stream of questions, having the patience to answer the most simple and complex of inquiries. I would like to give a special thanks to Valery, because in many ways, while Paul was my official thesis advisor at RPI, and Michel was my official thesis advisor at Université Paris-Sud, Valery was often very much like an unofficial thesis advisor while at JLab, investing a significant amount of time to help me in virtually every step of the way. I would also like to thank Volker and Harut for their expert insight into all of my studies. I would also like to thank Alex for being a good office-mate and for helping me finish up that pesky EC-timing project.

I would like to thank my thesis committee for taking the time to read my thesis, for giving valuable advice and edits, and finally for being able to accommodate the very complicated situation involving scheduling both the American and French thesis defenses.

Next, I would like to thank all the members of my fraternity, Epsilon Iota Chapter of Psi Upsilon, at RPI. During my first few years in graduate school (and all of undergraduate studies), which were spent in Troy, NY, these fellows, who are my most steadfast and supportive friends, truly helped anchor me in the most challenging of times, and also reminded me to also enjoy myself. I can't name all of them, but a few names which invoke feelings of gratitude are Elya (Usagi), Nate (Blondie), Jeff (Jeffy-gâteau), Joey, Laura (S.C.), Nicole (Stashy), Cameron (Ronny), Kieran, Ted, Ines (Pinecone), Anton (Peppercorn) and Neill. Among them are a special few culprits who have taught me that almost all of life's problems can be solved over a hand of cards, or game of Mahjong, as long as you aren't in tenpai for an eight of balls.

I would like to give thanks to some old friends, who have been there from the beginning: Mike, Rachel and Tiffy.

I would like to thank the Unitarian Universalist Fellowship of the Peninsula, especially the ChorUUs, for providing a safe and nurturing environment, and a place in which I could keep my musical passions alive.

I would like to take a moment to step back almost a decade, and thank a few people from a little town called Covington, in Washington State, where I went to high school at Kentwood. I had the opportunity to go to a very good high school, with teachers who truly inspired me. I can say, without exaggeration, that some of the teachers I met there seriously influenced my interest in science, and have played a very significant role in where I am today. A very special thanks goes out to Christine Donaldson and Carrie Wattles. Thank you so much for nurturing my curiosity.

Finally, I would like to thank my family. As my parents say, family is everything. Thank you Mariesa, Brian and Shya - you have been the great comic relief during my time living away from the Puget Sound. Every trip back to the Seattle area recharges me with an abundance of laughter that only siblings can provide.

I would like to thank John, my steadfast and loyal spouse, for his support through the good times, as well as the challenging times. His patience and understanding is limitless, and his willingness to take a burden of my shoulders is so wonderfully selfless. Having gone through graduate school himself, I know that he understands the challenge that this undertaking has been. His care and love have been my mighty fortress.

I would like to thank my mother-in-law, Ramona, for being supportive and encouraging me when I was moody and feeling "down in the dumps."

Finally, while deep thanks goes to everyone I have mentioned here, and plenty more thanks goes to those who have gone unsaid, the dedication of this work can only go to my parents, Barry and Cynthia, who have taught me from the very beginning to follow my curiosity, to pursue my passions, to work very hard, and to never give up. Without the foundation they helped me lay, I would never have found myself upon this path. Thank you!

ABSTRACT

This thesis focuses on the Deeply Virtual Compton Scattering (DVCS) reaction $e + p \rightarrow e' + p' + \gamma(DVCS)$. The reaction is measured using the e1-dvcs2 experiment run at Jefferson Laboratory in Hall B using CLAS. The experiment took place from 22 October, 2008 to 23 January, 2009, and experiment run time of 90 days. This analysis focuses on the determination of the DVCS cross section in bins of x_B, Q^2, t and Φ, and makes a comparison with already existing and parallel analyses of DVCS. By factorizing the cross section of the reaction into perturbative and non-perturbative parts, we may relate the cross section of this reaction to Generalized Parton Distributions (GPDs) for the proton, and in doing so, provide better insight as to the distributions of quarks and gluons within it, including spacial distribution and contributions of angular momentum.

RÉSUMÉ

Cette thèse a pour sujet l'étude de la réaction de la Diffusion Compton Profondément Virtuelle (DVCS) sur le proton $e + p \rightarrow e' + p' + \gamma(DVCS)$. Cette réaction est mesurée en analysant l'expérience e1-dvcs2 qui a eu lieu dans le Hall B du Jefferson Laboratory avec CLAS. La prise de données s'est déroulée du 22 octobre 2008 jusqu'au 23 janvier 2009. Cette analyse a pour but la détermination des sections efficaces non polarisées et les différences de sections efficaces polarisées du DVCS, dans divers bins en x_B, Q^2, t et Φ. Cette analyse compare les sections efficaces avec plusieurs mesures existantes du DVCS: une analyse parallèle de e1-dvcs2 et une analyse de e1-dvcs1. En factorisant l'élément de matrice qui correspond au DVCS en deux parties, calculables en QCD perturbative et non perturbative, on peut accéder aux Distributions de Partons Généralisées (GPDs) du proton, et ainsi obtenir une vue en 3D des distributions spatiales et en impulsion des quarks et des gluons dans le proton.

1. INTRODUCTION

This thesis highlights various studies on Deeply Virtual Compton Scattering (DVCS) reaction. In particular, we focus the measurement of its beam polarized cross sections, unpolarized cross sections, and the asymmetries which are computed from the cross section measurements, and the various methods that were implemented to obtain those quantities. The reaction involves an electron incident on a proton, with a final state which consists of the scatted electron, the recoil proton, and an additional photon. The reaction may be written as $e + p \rightarrow e' + p' + \gamma(DVCS)$. It is convenient to write "DVCS" in parentheses after the γ, indicating that this is not an event whose outgoing photon comes from either the incoming or outgoing electron.

A photon which is emitted from one of the electron legs is called a "radiative" event, or a Bethe-Heitler (BH) event: $e + p \rightarrow e' + p' + \gamma(BH)$. Since these two events are experimentally indistinguishable, only a measurement of all $e + p \rightarrow e' + p' + \gamma$ events is possible, including both DVCS and BH. Methods for understanding the role of each process and its contributions to the cross section of $e + p \rightarrow e' + p' + \gamma$ exist. We provide a detailed description of the community's interest in DVCS, outlining the concept of Generalized Parton Distributions (GPDs) and their connection with the DVCS reaction. We explore their roles in helping us solve the so-called Spin Puzzle - the problem of how angular momentum adds up in a nucleon, and their roles in describing the spatial distributions of quarks and gluons that make up nucleons.

The data that is used in this analysis is from e1-dvcs2, which was run at Jefferson Laboratory using its Continuous Electron Beam Accelerator Facility (CEBAF). The experiment is carried out in Hall B, one of four experimental halls, using the CEBAF Large Acceptance Spectrometer (CLAS). It ran from 22 October, 2008 to 23 January, 2009 for a total of 90 days of run time. A feature of the DVCS experiments is the use of the so-called "Inner Calorimeter" (IC) in addition to the standard CLAS. This detector was developed in 2005 and is used to detect more forward going photons which are characteristic of DVCS. In this experiment, an 85% longitudinally polarized beam of electrons was accelerated to 6 GeV and was made to impinge on an unpolarized liquid hydrogen target held at 20K.

2. MOTIVATION AND THEORY

2.1 Electron Scattering - A Historical Background

One of the aims of nuclear physics is to understand nuclear structure, and the laws of nature that give rise to that structure. It is known through experiments carried out by Rutherford et al.[1] that nuclei consist of nucleons: protons and neutrons. Furthermore, in 1968, experiments at Stanford Linear Accelerator Center (SLAC)[2] showed that these nucleons themselves have some structure, which were called partons. This was shown to be in agreement with the theoretical models of Gell-Mann and Zweig, who named these constituent particles quarks.[3]

In discussing our modern understanding of nucleon structure, it is convenient to begin with the simple problem of electron-muon scattering, seen in Figure 2.1. This problem is one of the most easily solved by Quantum Electrodynamics (QED), and represents the scattering of two particles which are believed to be point particles. That is to say, these particles are believed to have no internal structure. To first order in perturbation theory, the matrix element may be calculated from the electron and muon currents:

$$j^{\mu}_{\text{electron}} = -e\overline{u}(k')\gamma^{\mu}u(k)e^{i(k'-k)\cdot x}, \tag{1}$$

$$j^{\nu}_{\text{muon}} = -e\overline{u}(p')\gamma^{\nu}u(p)e^{i(p'-p)\cdot x}, \tag{2}$$

where e is the elementary electric charge, u and $\overline{u}$ are the lepton spinors, γ^{μ} are the so-called gamma matrices, and k, k', p and p' are the four-momenta of the incoming electron, outgoing electron, incoming muon, and outgoing muon, respectively.

The matrix element corresponding to the leading order Feynman diagram seen in Figure 2.1 is then:

$$\mathcal{M} = j^{\mu}_{\text{electron}}\left(\frac{-ig_{\mu\nu}}{q^2+i\epsilon}\right)j^{\nu}_{\text{muon}} = e\overline{u}(k')\gamma^{\mu}u(k)e^{i(k'-k)\cdot x}\left(\frac{-ig_{\mu\nu}}{q^2+i\epsilon}\right)e\overline{u}(p')\gamma^{\nu}u(p)e^{i(p'-p)\cdot x}, \tag{3}$$

where $g_{\mu\nu}$ is the metric tensor and q is the four-momentum of the virtual photon.

Averaging over the spins of the particles and determining the phase space, we calculate the cross section in the lab frame:

$$\left(\frac{\mathrm{d}\sigma}{\mathrm{d}\Omega}\right)_{e^-+\mu^-\to e^-+\mu^-} = \frac{E'}{8\pi m_{\mu}E}\frac{1}{4}\sum_{\text{spins}}|\mathcal{M}|^2 = \frac{\alpha^2}{4E^2\sin^4\frac{\theta}{2}}\frac{E'}{E}\left(\cos^2\frac{\theta}{2} - \frac{q^2}{2m_{\mu}^2}\sin^2\frac{\theta}{2}\right), \tag{4}$$

where α is the fine structure constant, E is the energy of the incident electron, E' is the energy of the outgoing electron, m_μ is the mass of the muon, and θ is the polar scattering angle in the lab frame.

This treatment of scattering point particles transfers naturally to the scattering of particles which have structure. We now look at two processes with which nucleon structure has been studied exclusively: Electron-Nucleon Elastic Scattering, and Deep Inelastic Scattering (DIS).[4,5]

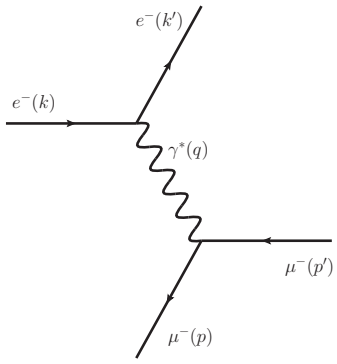

Figure 2.1: A Feynman diagram of elastic $e - \mu$ scattering.

2.1.1 Electron-Nucleon Elastic Scattering

In Electron-Nucleon Elastic Scattering, it is no longer possible to write the nucleon current as if its vertex was a simple QED vertex. Since the vertex involves a more complicated interaction, we express our ignorance of the complex nucleon structure by picturing the vertex as a blob in the Feynman diagram as seen in Figure 2.2 and writing it as Γ^μ mathematically, leaving the nucleon current in the most general form as a Lorentz vector:

$$j^\mu_{\text{nucleon}} = -e\overline{u}(p')\Gamma^\mu u(p)e^{i(p'-p)\cdot x}, \tag{5}$$

where the most general form of Γ^μ is:

$$\Gamma^\mu = F_1(q^2)\gamma^\mu + \frac{\kappa}{2M}F_2(q^2)i\sigma^{\mu\nu}q_\nu + g_A(q^2)\gamma^\mu\gamma_5 + h_A(q^2)q^\mu\gamma_5, \tag{6}$$

where M is the mass of the proton, and γ^μ, $\sigma^{\mu\nu} = \frac{1}{2}[\gamma^\mu, \gamma^\nu]$, $\gamma^\mu\gamma_5$, and $\gamma_5 = i\gamma^0\gamma^1\gamma^2\gamma^3 = \gamma^5$, along with the identity matrix, consist of the entire set of linearly independent 4×4 matrices. These functions, F_1, F_2, g_A, and h_A are known respectively as the Dirac, Pauli, pseudo vector (or axial), and pseudo scalar form factors. One may simplify this expression by realizing this reaction conserves

parity in the case of a photon exchange diagram, where there is no electroweak interaction, in which case the γ_5 terms can be neglected:

$$\Gamma^\mu = F_1(q^2)\gamma^\mu + \frac{\kappa}{2M}F_2(q^2)i\sigma^{\mu\nu}q_\nu. \tag{7}$$

Using the more generalized current, one may reconstruct the cross section in the lab frame:

$$\left(\frac{\mathrm{d}\sigma}{\mathrm{d}\Omega}\right)_{e^-+p^+\to e^-+p^+} = \frac{\alpha^2}{4E^2\sin^4\frac{\theta}{2}}\frac{E'}{E}\left(\left(F_1^2 - \frac{\kappa^2q^2}{4M^2}F_2^2\right)\cos^2\frac{\theta}{2} - \frac{q^2}{2M^2}(F_1+\kappa F_2)^2\sin^2\frac{\theta}{2}\right). \tag{8}$$

Most experimentalists prefer recasting this formula in terms of:

$$G_E \equiv F_1 + \frac{\kappa q^2}{4M^2}F_2, \tag{9}$$

and

$$G_M \equiv F_1 + \kappa F_2, \tag{10}$$

which are known as electric and magnetic Sachs form factors, respectively. This allows one to express the lab frame cross section in a way that has no form factor interference terms:

$$\left(\frac{\mathrm{d}\sigma}{\mathrm{d}\Omega}\right)_{e^-+p^+\to e^-+p^+} = \left(\frac{d\sigma}{d\Omega}\right)_{mott}\frac{E'}{E}\frac{1}{1+\tau}\left(G_E^2 + \frac{\tau}{\epsilon}G_M^2\right), \tag{11}$$

where $\left(\frac{\mathrm{d}\sigma}{\mathrm{d}\Omega}\right)_{mott} = \frac{\alpha^2\cos^2\frac{\theta}{2}}{4E^2\sin^4\frac{\theta}{2}}$, $\tau = \frac{-\kappa q^2}{4M^2}$, and $\epsilon = \frac{1}{1+2(1+\tau)\tan^2\frac{\theta}{2}}$.

If the nucleon had been a point particle, as the electron is believed to be, then this cross section of electron-nucleon elastic scattering should have the same form as the elastic $e-\mu$ scattering. However, the presence of form factors indicates that there is some other structure involved. Specifically, it is interesting because their Fourier transforms have been shown to correspond (non-relativistically) to the charge and current distributions in the Breit frame, in which the nucleon is moving with infinite momentum.[6] This is a suggestion that the form factors are in fact describing a distribution of current and charge within the nucleon, and implies that the nucleon has structure and is not a point particle.[4]

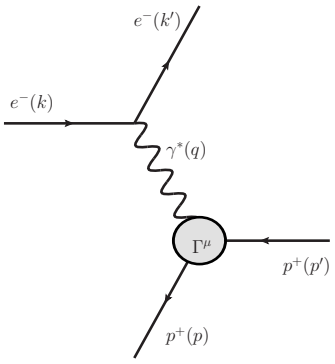

Figure 2.2: A Feynman diagram of elastic $e - p$ scattering.

2.1.2 Deep Inelastic Scattering (DIS)

In the complimentary view of Deep Inelastic Scattering (DIS), it is no longer possible to use a nucleon current. The scattering involves a nucleon which disintegrates into multiple particles, or into an excited state, which thereafter decays into multiple particles, as seen in Figure 2.3. Therefore, a more generalized approach must be made. We write the absolute square of the matrix element $\mathcal{M}$ as

$$|\mathcal{M}|^2 = \frac{L^{\mu\nu}_{\text{electron}}(W_{\text{hadronic}})_{\mu\nu}}{q^2}, \tag{12}$$

where the leptonic part is the product of the lepton current, introduced in equation 1, with its conjugate:

$$L^{\mu\nu}_{\text{electron}}(k,k') = \frac{1}{2}\sum_{e \text{ spins}} j^{\mu}_{\text{electron}}(k,k') j^{\nu *}_{\text{electron}}(k,k') \tag{13}$$

where $L^{\mu\nu}_{\text{electron}}$ is referred to as the lepton tensor, containing the electron current introduced in equation 1.

The hadronic part, however, must be expressed more generally. The most general form it may take is

$$W^{\mu\nu}_{\text{hadronic}}(p,q) = -W_1 g^{\mu\nu} + \frac{W_2}{M^2} p^\mu p^\nu + \frac{W_4}{M^2} q^\mu q^\nu + \frac{W_5}{M^2}(p^\mu q^\nu + q^\mu p^\nu). \tag{14}$$

Not all of these W terms are independent because the requirement that current be conserved at the hadronic vertex implies that $q_\mu W^{\mu\nu} = 0$. The term W_3, missing in this equation, is present

in a similar derivation involving neutrino-proton scattering.[7] This imposes relations between the W terms leading to the final form:

$$W^{\mu\nu}_{\text{hadronic}} = W_1(-g^{\mu\nu} + \frac{q^\mu q^\nu}{q^2}) + \frac{W_2}{M^2}(p^\mu - \frac{p\cdot q}{q^2}q^\mu)(p^\nu - \frac{p\cdot q}{q^2}q^\nu). \tag{15}$$

The cross section may finally be found by the relation

$$\frac{\mathrm{d}^2\sigma}{\mathrm{d}E'\mathrm{d}\Omega} = \frac{\alpha^2}{q^4}\frac{E'}{E}|\mathcal{M}|^2 = \frac{\alpha^2}{q^4}\frac{E'}{E}L^{\mu\nu}_{\text{electron}}(W_{\text{hadronic}})_{\mu\nu} \tag{16}$$

which leads to

$$\frac{\mathrm{d}^2\sigma}{\mathrm{d}E'\mathrm{d}\Omega} = \frac{4\alpha^2 E'^2}{q^4}\left(2W_1(\nu,q^2)\sin^2\frac{\theta}{2} + W_2(\nu,q^2)\cos^2\frac{\theta}{2}\right) \tag{17}$$

where $\nu \equiv \frac{-p\cdot q}{M} = E - E'$.[4]

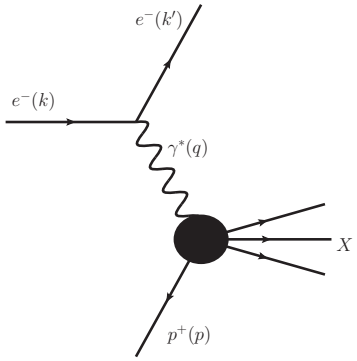

Figure 2.3: A Feynman diagram of inelastic $e + p \to e + X$ scattering.

2.1.3 Bjorken Scaling

Our interest now turns to a interesting feature of inelastic scattering which manifests at high $-q^2 = Q^2$.

In 1968, James Bjorken suggested that in the Deep Inelastic Region (DIS), $Q^2 >> M_N^2$, the structure function might exhibit a scaling feature. He suggested that if there were point particles in the nucleon, at higher Q^2, we should be able to resolve them as separate particles. This would result in the cross section behaving like equation 4. As a result, in this limit we can justify representing the structure functions W as probabilities to strike individual quarks:

$$\lim_{Q^2\to+\infty,\nu/Q^2\text{constant}} MW_1(\nu,Q^2) \equiv f_1(x) = \sum_i e_i^2 \frac{q_i(x)}{2}, \tag{18}$$

$$\lim_{Q^2\to+\infty,\nu/Q^2\text{constant}} \nu W_2(\nu,Q^2) \equiv f_2(x) = \sum_i e_i^2 x q_i(x). \tag{19}$$

We have defined x as the longitudinal momentum fraction of the average nucleon momentum carried by the struck quark of flavor i. We have also defined q_i as the probability density for quarks as a function of this momentum fraction which we refer to as Parton Distribution Functions (PDFs). Lastly, we have defined e_i as the charge corresponding to a quark of flavor i. In the Bjorken limit, this longitudinal momentum fraction becomes equal to Bjorken x, $x_B = \frac{Q^2}{2M\nu} = \frac{Q^2}{2p\cdot q}$.

From equations 18 and 19, it is clear that only one structure function is necessary to describe the system. The identity that is derived from these two equations is called the Callan-Gross relation, and has been experimentally verified for spin $\frac{1}{2}$ particles, implying that these constituent particles are fermions:

$$2xf_1(x) = f_2(x). \tag{20}$$

We can decouple the distributions $q_i(x)$ in terms of their polarization with respect to the nucleon. q_i^+ represents the density of quarks of flavor i with spin aligned parallel to the nucleon, and q_i^- represents the density of quarks of flavor i with spin aligned antiparallel to the nucleon. Additionally we define:

$$q_i = q_i^+ + q_i^-, \tag{21}$$

$$\Delta q_i = q_i^+ - q_i^-, \tag{22}$$

where the former is referred to as the unpolarized PDFs and the latter as the polarized PDFs.

Writing the f's in terms of PDFs casts the inelastic scattering cross-section into a form that is similar to that of elastic electron-nucleon scattering. The fact that the cross section varies only with the dimensionless scaling variable x_B indicates that the photon illuminating a point-like fermion within the nucleon. Data collected from HERA and H1 and ZEUS may be found in Figure 2.4, showing DIS measurements for various choices of x_B.

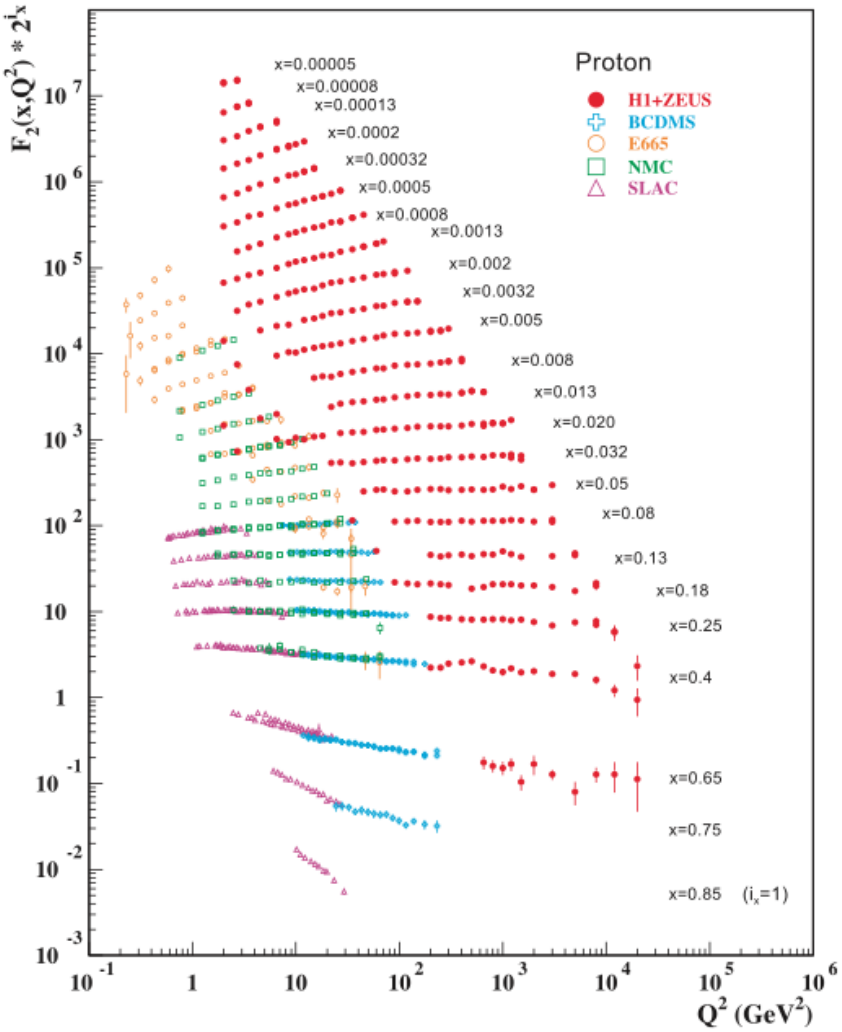

Figure 2.4: Log-log F_2 measurements from H1+ZEUS, BCDMS, E665, NMC, and SLAC as a function of Q^2, and x_B. This plot is courtesy of reference[8], with data from[9–13]

The measurements are consistent with the Bjorken's model, with some deviations. The deviations which appear at higher Q^2 can be explained by the increasing probability of gluon radiation and the production of quark-antiquark pairs. The observation of this scaling was one of the firmest indicators that there was substructure to the nucleon. From this formalism we have a way to describe the structure functions as a sum of probability densities which describe likelihood of each of the quarks being hit and carrying a longitudinal momentum fraction x.[4]

A measurement of $q_i(x)$ allows us to determine the amount of longitudinal momentum carried by the quarks. Taking the first moment in x of each of the PDFs for each flavor of quark, we can determine the fraction of longitudinal momentum carried by them:

$$\sum_i \int_0^1 \mathrm{d}x x \left[q_i(x) + \bar{q}_i(x)\right] = f. \tag{23}$$

This fraction has been computed by the EMC collaboration and it has been shown that $f = 0.465 \pm 0.023$, which implies that only half of the momentum in the longitudinal direction is carried by the quarks.[14]. This is a strong piece of evidence which points towards the existence of other particles beyond the quarks. In fact, the rest of this momentum belongs to the gluons which make up the rest of the nucleon.

2.1.4 Light Cone Coordinates

A convenient coordinate system for theorists is the "light cone" frame. For any four-vector $x^\mu = (x^0, x^1, x^2, x^3)$ in Minkowski space-time coordinates, one has also the equally valid basis:

$$x^+ = \frac{(x^0 + x^3)}{\sqrt{2}}, \tag{24}$$

$$x^- = \frac{(x^0 - x^3)}{\sqrt{2}}, \tag{25}$$

$$x^1, \tag{26}$$

$$x^2, \tag{27}$$

where the x^1 and x^2 are often written as a two-component vector called $\vec{x}_\perp = (x^1, x^2)$. In this basis, we write: $a^\mu = (x^+, \vec{x}^\perp, x^-)$. Dot products of four-vectors are now: $x \cdot y = x^+ y^- + x^- y^+ - \vec{x}_\perp \cdot \vec{y}_\perp$. For further convenience, we define the set of normal four-vectors:

$$n_+^\mu = (1, 0, 0, 1)/\sqrt{2}, \tag{28}$$

$$n_-^\mu = (1, 0, 0, -1)/\sqrt{2}, \tag{29}$$

$$n_\perp^\mu = \frac{1}{\sqrt{2}}(0, 1, 1, 0). \tag{30}$$

We also define Sudakov vectors:

$$p_1^\mu = \frac{P^+}{\sqrt{2}}(1, 0, 0, 1), \tag{31}$$

$$p_2^\mu = \frac{1}{\sqrt{2}P^+}(1, 0, 0, -1), \tag{32}$$

where P^+ is the "+" component of the average four-momentum of the incoming and outgoing nucleon,

$$P^\mu = \frac{p^\mu + p'^\mu}{2}. \tag{33}$$

These Sudakov vectors allow one to decompose any four-vector into their light cone components.

$$a^\mu = a^+ p_1^\mu + a^- p_2^\mu + a_\perp^\mu \tag{34}$$

This notation is appropriate because it is convenient to work in the infinite momentum frame, where the average nucleon four momentum (which we shall call $P = \frac{p+p'}{2}$), and outgoing real photon four momentum lie only in the "plus"-"minus" plane. In mathematical terms, we choose the frame in which $q_\perp = 0$ and $P_\perp = 0$, where the incoming and outgoing protons have infinite momenta.

2.2 Generalized Parton Distributions

2.2.1 Accessing GPDs - Deeply Virtual Compton Scattering

We introduce a new, more generalized parameterization of the structure of the nucleon, called Generalized Parton Distributions (GPDs). These GPDs can be accessed through several deeply virtual exclusive reactions, comprising of Deeply Virtual Compton Scattering (DVCS) as seen in Figure 2.5 and Deeply Virtual Meson Production (DVMP) as seen in Figure 2.6. Each of these reactions consists of a diagram which can be factorized into a perturbative (hard) part, and a non-perturbative (soft) part which contains our new parameterization of quarks and gluons.

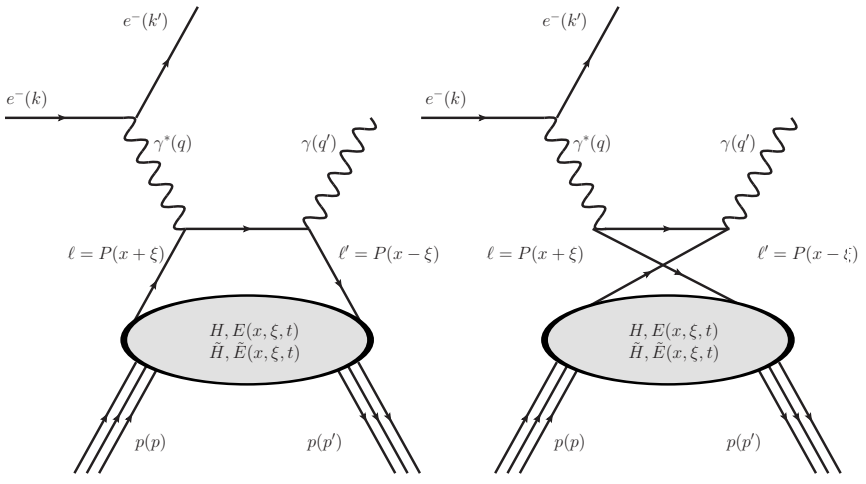

Figure 2.5: The handbag diagrams of DVCS, including the uncrossed and crossed diagrams.

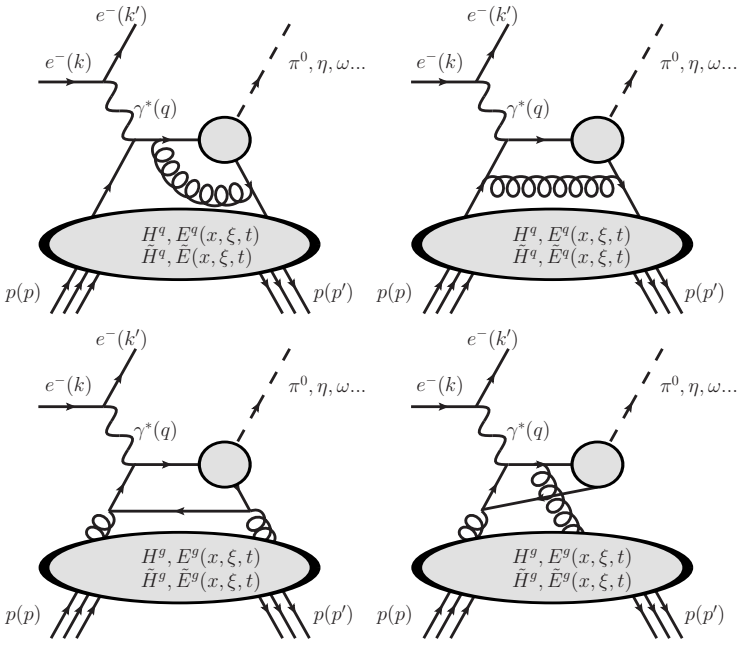

Figure 2.6: The handbag diagram of DVMP, including quark GPDs on top and gluon GPDs on bottom.

This thesis focuses on DVCS on the proton and its relation to quark GPDs. DVCS on the neutron is also not explored in this thesis, but is introduced for completeness since it gives us access to different combinations GPDs than DVCS. Before formally introducing GPDs and their properties, we will study the DVCS reaction. First, we compute the matrix element $\mathcal{M}$ for DVCS using Feynman rules. In order to do that, we have to address the DVCS process in more detail.

About 15 years ago, X. Ji[15], D. Müller[16] and A. Radyushkin[17] showed that in the Bjorken limit, $Q^2 >> 1$ GeV^2, x_B constant, the DVCS diagram can be factorized into two parts. This is best illustrated by Figure 2.5, which is often referred to as the "handbag" diagram. The factorization theorem states that we can treat the process in the leading order and leading twist[1] as if a single quark in the nucleon was struck by the virtual photon, at some point later radiates a real photon, and then rejoins the nucleon; or, in the crossed diagram, as if a quark in the nucleon emits a real photon, then is struck by the virtual photon, after which it is absorbed back into the nucleon. In this view, all of the other quarks are treated only as spectator quarks, with only the one quark interacting with the top half of the diagram. The top half of the diagram, outside of the "blob" is calculable in terms of QED, and is referred to as the hard part of the diagram. The lower half, which consists of the blob is what we will refer to as the soft part of the diagram, which is not exactly

[1]Twist is defined as $n = D - S$ of an operator, where D is the dimension and S is the spin. A diagram is suppressed according to its twist by a factor $\frac{1}{Q^{n-2}}$ for each twist beyond the leading twist $n = 2$.

solvable with current methods. It is the factorization theorem which justifies our ability to consider the Feynman diagram of DVCS in the manner seen in Figure 2.5 compared to the manner in Figure 2.7.

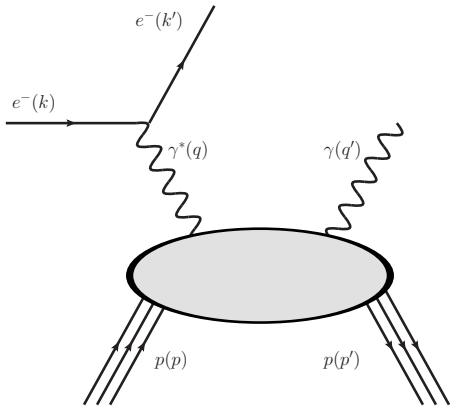

Figure 2.7: The unfactorized DVCS diagram.

Because of this factorization theorem, one may compute the amplitude corresponding to this diagram according to Feynman rules. Before this is done, we are going to move into the infinite momentum frame. In this frame, there are some significant simplifications to the variables in the DVCS amplitude, as one may easily derive, presented in Table 2.1.

Table 2.1: A table of DVCS variables, their Sudakov decompositions, and their values in the Bjorken limit where $Q^2 >> m_N, -t$.

Kinematic Four-Vector	Sudkov Decomposition	Reduction Under Bjorken Limit
P^μ	$p_1^\mu + \frac{\bar{M}^2}{2} p_2^\mu$	p_1^μ
q^μ	$-2\xi' p_1^\mu + \frac{Q^2}{4\xi'} p_2^\mu$	$-2\xi' p_1^\mu + \frac{Q^2}{4\xi'} p_2^\mu$
Δ^μ	$-2\xi p_1^\mu + \xi \bar{M}^2 p_2^\mu + \Delta_\perp^\mu$	$-2\xi p_1^\mu$
q'^μ	$2(\xi - \xi') p_1^\mu + (\frac{Q^2}{4\xi'} - \xi \bar{M}^2) p_2^\mu - \Delta_\perp^\mu$	$\frac{Q^2}{4\xi} p_2$
p^μ	$P^\mu - \frac{\Delta^\mu}{2}$	$(1+\xi) p_1^\mu$
p'^μ	$P^\mu + \frac{\Delta^\mu}{2}$	$(1-\xi) p_1^\mu$
ℓ^μ	$xP^\mu - \frac{\Delta^\mu}{2}$	$(x+\xi) p_1^\mu$
ℓ'^μ	$xP^\mu + \frac{\Delta^\mu}{2}$	$(x-\xi) p_1^\mu$

We have used the abbreviation:

$$\bar{M}^2 = m_N^2 - \frac{\Delta^2}{4}, \tag{35}$$

where $\Delta^\mu = p^\mu - p'^\mu$. We have abbreviated the two parameters ξ and ξ' such that:

$$2\xi = 2\xi' \frac{Q^2 - \Delta^2}{Q^2 + \bar{M}^2 (2\xi')^2} \tag{36}$$

and

$$2\xi = \frac{P \cdot q}{\bar{M}^2} \left[\sqrt{1 + \frac{Q^2 \bar{M}^2}{(P \cdot q)^2}} - 1 \right] \tag{37}$$

where in the Bjorken limit, both ξ and ξ' tend to $\frac{x_B}{2 - x_B}$. These variables are referred to as the "skewness" of the reaction. This skewness helps to define two regions for the loop variable x: ERBL and DGLAP, as seen in Figure 2.8. The region where $x < -\xi$ and $x > \xi$ is called the DGLAP region, corresponding to the QCD evolution equations in Q^2 for the PDFs we introduced earlier in this section. This physically corresponds to a quark, or an antiquark, being emitting, and then later reabsorbed into the nucleon. The region where $-\xi < x < \xi$ is called the ERBL region, corresponding to the QCD evolution equations in Q^2 for the Distribution Amplitudes, and physically corresponds to a quark-antiquark pair being emitted or reabsorbed into the nucleon.

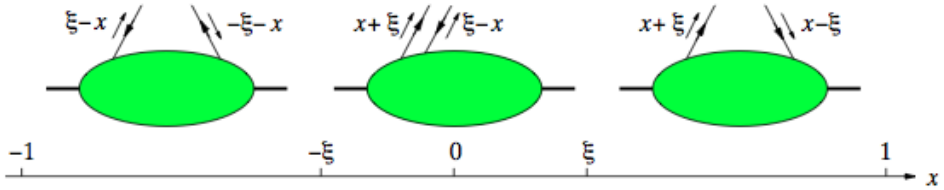

Figure 2.8: The region where $x < -\xi$ and $x > \xi$ is called the DGLAP region, corresponding to the QCD evolution equations in Q^2 for the PDFs we introduced earlier in this section. This physically corresponds to a quark, or an antiquark, being emitting, and then later reabsorbed into the nucleon. The region where $-\xi < x < \xi$ is called the ERBL region, corresponding to the QCD evolution equations in Q^2 for the Distribution Amplitudes, and physically corresponds to a quark-antiquark pair being emitted or reabsorbed into the nucleon. Illustration is courtesy of the Diehl review article.[18]

In this frame, we follow Feynman rules to determine the matrix element $\mathcal{M}$, and parameterize the blob which we have labeled "GPDs" in the most general form possible,

$$\begin{aligned} i\mathcal{M} = -i\sum_q (eQ_q)^2 \epsilon^*_\mu \epsilon_\nu \Big\{ &((n^+)^\mu (n^-)^\nu + (n^+)^\nu (n^-)^\mu - g_\perp^{\mu\nu}) \\ &\int_{-1}^{1} \mathrm{d}x C_1 \frac{1}{2} \left(H^q(x,\xi,t)\bar{u}(p')\gamma^+ u(p) + E^q(x,\xi,t)\bar{u}(p') i\sigma^{+\alpha} \frac{\Delta_\alpha}{2m_N} u(p) \right) \\ +\epsilon^{\mu\nu+-} &\int_{-1}^{1} \mathrm{d}x C_2 \frac{1}{2} \left(\tilde{H}^q(x,\xi,t)\bar{u}(p')\gamma^+\gamma_5 u(p) + \tilde{E}^q(x,\xi,t)\bar{u}(p')\gamma_5 \frac{\Delta^+}{2m_N} u(p) \right) \Big\}, \end{aligned} \tag{38}$$

where

$$C_1 = \left[\frac{1}{x-\xi+i\epsilon} + \frac{1}{x+\xi-i\epsilon} \right], \tag{39}$$

and

$$C_2 = \left[\frac{-1}{x-\xi+i\epsilon} + \frac{1}{x+\xi-i\epsilon} \right]. \tag{40}$$

We have used four functions to parameterize the matrix element: H, E, $\tilde{H}$ and $\tilde{E}$. These are our GPDs, and contain the information about the quarks within the proton. We note that in $\mathcal{M}$, we are integrating over the loop variable x. Using the matrix element $\mathcal{M}$, we can obtain the cross section by the following relation:

$$\frac{\mathrm{d}\sigma}{\mathrm{d}Q^2 \mathrm{d}x_B \mathrm{d}t \mathrm{d}\Phi} = \frac{\frac{1}{(2\pi)^4 32} \frac{x_B y}{Q^4}}{\sqrt{1 + \frac{4M^2 x_B^2}{Q^2}}} |\mathcal{M}|^2, \tag{41}$$

where $y = \frac{E-E'}{E}$, and the four cross section variables are Q^2, the virtuality of the virtual photon, x_B the Bjorken variable, t, the momentum transfer to the proton, squared, and Φ, the angle between the leptonic and hadronic planes.

Because we are only able to access these GPDs appearing in the DVCS cross section after having integrated over x, we define a set of functions which describe the GPDs after they have been x integrated. Note that we are also integrating over the GPDs, as well as the quark propagator which contains an x dependence. We call these functions Compton Form Factors (CFFs).

$$\mathcal{H}(\xi,t) = \int_{-1}^{1} \mathrm{d}x H^q(x,\xi,t) \left[\frac{1}{x-\xi-i\epsilon} + \frac{1}{x+\xi-i\epsilon}\right] \tag{42}$$

$$\mathcal{E}(\xi,t) = \int_{-1}^{1} \mathrm{d}x E^q(x,\xi,t) \left[\frac{1}{x-\xi-i\epsilon} + \frac{1}{x+\xi-i\epsilon}\right] \tag{43}$$

$$\tilde{\mathcal{H}}(\xi,t) = \int_{-1}^{1} \mathrm{d}x \tilde{H}^q(x,\xi,t) \left[\frac{1}{x+\xi-i\epsilon} + \frac{1}{x-\xi-i\epsilon}\right] \tag{44}$$

$$\tilde{\mathcal{E}}(\xi,t) = \int_{-1}^{1} \mathrm{d}x \tilde{E}^q(x,\xi,t) \left[\frac{1}{x+\xi-i\epsilon} + \frac{1}{x-\xi-i\epsilon}\right] \tag{45}$$

As we will see shortly, we have a motivation for decomposing the CFFs into real and imaginary parts. If we assume that the GPDs are analytical on the x-axis from -1 to 1, we are able to decompose them according to the identity:

$$\int_{-1}^{1} \mathrm{d}x \frac{F^q(x,\xi,t)}{x \pm \xi \mp i\epsilon} = \mathcal{P}\int_{-1}^{1} \mathrm{d}x \frac{F^q(x,\xi,t)}{x \pm \xi} \pm i\pi F^q(\mp\xi,\xi,t) \tag{46}$$

where $F^q(x,\xi,t)$ represents any of the GPDs, and $\mathcal{P}$ represents the principal Cauchy value. From this identity, one may obtain expressions for each of the imaginary and real parts of each CFF:

$$\mathcal{H}_{\mathrm{Re}}(\xi,t) = \mathcal{P}\int_{0}^{1} \mathrm{d}x \left[H(x,\xi,t) - H(-x,\xi,t)\right] \left[\frac{1}{x-\xi} + \frac{1}{x+\xi}\right] \tag{47}$$

$$\mathcal{H}_{\mathrm{Im}}(\xi,t) = H(\xi,\xi,t) - H(-\xi,\xi,t) \tag{48}$$

$$\mathcal{E}_{\mathrm{Re}}(\xi,t) = \mathcal{P}\int_{0}^{1} \mathrm{d}x \left[E(x,\xi,t) - E(-x,\xi,t)\right] \left[\frac{1}{x-\xi} + \frac{1}{x+\xi}\right] \tag{49}$$

$$\mathcal{E}_{\mathrm{Im}}(\xi,t) = E(\xi,\xi,t) - E(-\xi,\xi,t) \tag{50}$$

$$\tilde{\mathcal{H}}_{\mathrm{Re}}(\xi,t) = \mathcal{P}\int_{0}^{1} \mathrm{d}x \left[\tilde{H}(x,\xi,t) + \tilde{H}(-x,\xi,t)\right] \left[\frac{1}{x-\xi} - \frac{1}{x+\xi}\right] \tag{51}$$

$$\tilde{\mathcal{H}}_{\mathrm{Im}}(\xi,t) = \tilde{H}(\xi,\xi,t) + \tilde{H}(-\xi,\xi,t) \tag{52}$$

$$\tilde{\mathcal{E}}_{\mathrm{Re}}(\xi,t) = \mathcal{P}\int_{0}^{1} \mathrm{d}x \left[\tilde{E}(x,\xi,t) + \tilde{E}(-x,\xi,t)\right] \left[\frac{1}{x-\xi} - \frac{1}{x+\xi}\right] \tag{53}$$

$$\tilde{\mathcal{E}}_{\mathrm{Im}}(\xi,t) = \tilde{E}(\xi,\xi,t) + \tilde{E}(-\xi,\xi,t) \tag{54}$$

2.2.2 Properties of GPDs

Now that the connection between DVCS and GPDs are established, it is useful to enumerate some of the more interesting and useful properties of GPDs. In particular, it can be shown that the Dirac, Pauli, and axial form factors may be recovered by taking integrals in x.[18]

$$\int_{-1}^{1} \mathrm{d}x H^q(x,\xi,t) = F_1^q(t) \tag{55}$$

$$\int_{-1}^{1} \mathrm{d}x E^q(x,\xi,t) = F_2^q(t) \tag{56}$$

$$\int_{-1}^{1} \mathrm{d}x \tilde{H}^q(x,\xi,t) = g_A^q(t) \tag{57}$$

$$\int_{-1}^{1} \mathrm{d}x \tilde{E}^q(x,\xi,t) = h_A^q(t) \tag{58}$$

It is important to notice that the ξ dependence of GPDs vanishes once integration is performed over x. This is due to the polynomiality of property of GPDs. It can be shown that every moment in x of the GPDs yields a polynomial in ξ.

It was shown by X. Ji[19] that one could link the forward limit of the first moment of the GPDs to the total angular momentum of the quarks:

$$\sum_q \int_{-1}^{1} \mathrm{d}x x(H^q(x,\xi,0) + E^q(x,\xi,0)) = 2J^q. \tag{59}$$

X. Ji was also able to show that the spin of the nucleon could be decomposed in a gauge invariant way into the sum of the quark and gluon angular momenta and written as:

$$\frac{1}{2} = J^g + \sum_q J^q = J^g + \sum_q (S^q + L^q), \tag{60}$$

where the intrinsic angular momentum of the quarks can be expressed as:

$$S^q = \int_{-1}^{1} \mathrm{d}x \frac{\Delta q}{2} = \frac{1}{2}\int_{-1}^{1} \mathrm{d}x (q^+(x) - q^-(x)). \tag{61}$$

This view of angular momentum allows us to access the L^q component of the quark contribution to the total spin of the nucleon once we have measured S^q and the GPDs.

It can also be shown that in the forward limit $(t, \xi \to 0)$ the quark distribution functions are recovered from the GPDs:

$$H(x,0,0) = q(x), \tag{62}$$

$$\tilde{H}(x,0,0) = \Delta q(x), \tag{63}$$

where $q(x)$ is the PDF introduced in equation 21 and $\Delta q(x)$ is the PDF introduced in equation 22.[18]

We have now shown how GPDs reduce to PDFs and FFs. Therefore, the GPDs contain all the information of those "daughter" functions, as well as additional information about the spin contributions of quarks. This may be seen in the following property of the H GPD:

$$q(x,0,b) = \int \frac{\mathrm{d}^2\vec{\Delta}_\perp}{(2\pi)^2} \mathrm{e}^{-i\vec{b}\cdot\vec{\Delta}_\perp} H^q(x,0,-\vec{\Delta}_\perp^2), \tag{64}$$

where q is now the probability density of the quarks as a function of x and $b_\perp$ which are the longitudinal momentum fraction and impact parameter in the infinite momentum frame. The impact parameter is the Fourier conjugate variable of $\vec{\Delta}_\perp (= t^2)$, the perpendicular component of the momentum transfer to the proton.

2.3 The Interference of DVCS and Bethe-Heitler

We are interested in measuring the cross section of DVCS in order to have access to GPDs. However, an attempt to measure the cross section of the reaction $e + p \to e' + p' + \gamma$ will measure all reactions with those incoming and outgoing particles. The two competing processes which dominate this reaction are DVCS and Bethe-Heitler (BH). In DVCS the photon is radiated by a quark in the nucleon, and in BH the photon is radiated by one of the electron legs. There are two possible configurations for BH. The photon may be radiated from the incoming or the outgoing electron. The Feynman diagrams corresponding to these two BH processes may be seen in Figure 2.9.

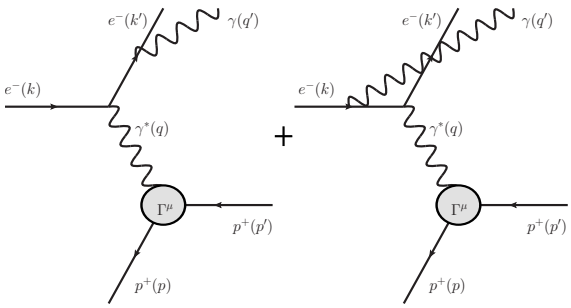

Figure 2.9: The two possible leading order BH diagrams.

Since we measure all $e + p \to e' + p' + \gamma$ events in our cross section in the lab, the matrix element corresponding to such a measurement may be written as:

$$\mathcal{M}_{ep\gamma} = \mathcal{M}_{\text{DVCS}} + \mathcal{M}_{\text{BH}}. \tag{65}$$

It follows that the actual cross section measured in the lab, for any polarization will be:

$$\sigma \propto |\mathcal{M}_{ep\gamma}|^2 = |\mathcal{M}_{\text{DVCS}}|^2 + |\mathcal{M}_{\text{BH}}|^2 + \mathcal{I}, \tag{66}$$

where + and - subscripts correspond to the polarization of the electron beam, and $\mathcal{I}$ is the interference term:

$$\mathcal{I} = \mathcal{M}^*_{\text{DVCS}}\mathcal{M}_{\text{BH}} + \mathcal{M}_{\text{DVCS}}\mathcal{M}^*_{\text{BH}} \tag{67}$$

Each of these terms may be expanded in the variable Φ, with each term corresponding to a particular polarization of the virtual photon[20]:

$$|\mathcal{M}_{DVCS}|^2 = \frac{e^6}{x_B^2 y^2 t(1+\epsilon^2)^2 \mathcal{P}_1(\Phi)\mathcal{P}_2(\Phi)} \left(\sum_{n=0}^{2} c_n^{\text{BH}} \cos(n\Phi) + s_1^{\text{BH}} \sin(\Phi) \right), \tag{68}$$

$$|\mathcal{M}_{BH}|^2 = \frac{e^6}{y^2 Q^2} \sum_{n=0}^{2} \left(c_n^{\text{DVCS}} \cos(n\Phi) + s_n^{\text{DVCS}} \sin(n\Phi) \right), \tag{69}$$

$$\mathcal{I} = \frac{e^6}{x_B y^3 t \mathcal{P}_1(\Phi)\mathcal{P}_2(\Phi)} \sum_{n=0}^{3} \left(c_n^{\text{BH}} \cos(n\Phi) + s_n^{\text{BH}} \sin(n\Phi) \right), \tag{70}$$

where $\epsilon = \frac{2x_B M}{Q^2}$, and $\mathcal{P}_1(\Phi)$ and $\mathcal{P}_2(\Phi)$ correspond to the electron propagator in the Bethe-Heitler diagram. The coefficients for Bethe-Heitler can be expressed completely in terms of kinematical variables and form factors, and can be found in their complete form in reference[20]. The interference terms are defined as:

$$s_1^{\mathcal{I}} = 8K\lambda y(2-y)\text{Im}(\mathcal{C}^{\mathcal{I}}(\mathcal{F})), \tag{71}$$

$$c_0^{\mathcal{I}} = -8(2-y)\text{Re}\left(\frac{(2-y)^2}{1-y} K^2 \mathcal{C}^{\mathcal{I}}(\mathcal{F}) + \frac{t}{Q^2}(1-y)(1-x_B)(\mathcal{C}^{\mathcal{I}} + \Delta\mathcal{C}^{\mathcal{I}}(\mathcal{F}) \right), \tag{72}$$

$$c_1^{\mathcal{I}} = -8K(2-2y+y^2)\text{Re}(\mathcal{C}^{\mathcal{I}}(\mathcal{F})), \tag{73}$$

where λ is the polarization of the electron beam, J and K are complicated functions of the kinematic variables, which can be found in reference[20], and:

$$\mathcal{C}^{\mathcal{I}}(\mathcal{F}) = F_1\mathcal{H} + \frac{x_B}{2-x_B}(F_1+F_2)\tilde{\mathcal{H}} - \frac{t}{4M_p^2}F_2\mathcal{E}, \tag{74}$$

$$\Delta\mathcal{C}^{\mathcal{I}}(\mathcal{F}) = -\frac{x_B}{2-x_B}(F_1+F_2)\left\{\frac{x_B}{2-x_B}(\mathcal{H}+\mathcal{E})+\tilde{\mathcal{H}}\right\}. \tag{75}$$

We note that the only term in twist-two approximation depending on the beam helicity is $s_1^{\mathcal{I}}$. Using this decomposition, we have a way to access the imaginary and real components of the dominant CFF $\mathcal{H}$ by measuring the unpolarized cross sections and polarized cross section differences. In the case of the unpolarized cross section, the amplitude squared of the DVCS matrix element is quite small compared to the Bethe-Heitler contribution. In this case, the BH contribution often dominates, but not so much that we cannot extract the real part of $\mathcal{H}$. In the case of the polarized cross section differences, the pure Bethe-Heitler and DVCS terms cancel out, and only an interference term is present. Since Bethe-Heitler may be written in terms of QED and FFs, which have been extensively studied in experiments, we have a way to understand the contributions due to both Bethe-Heitler and the CFFs.

2.3.1 Properties of the BH Cross Section

One important feature of the BH cross section is its preference to radiate a photon in the direction of the electron that radiated it. We take the case where the photon is radiated from the outgoing electron leg. The propagator may be written as:

$$\frac{i(\not{k}+m)}{(k'+q')^2-m^2+i\epsilon}. \tag{76}$$

Neglecting the mass of the electron and recalling that k' and q' are the outgoing four momenta for the electron and photon respectively, we can multiply out the four vectors:

$$\frac{i\ \not{k}}{2E_\gamma E_{e'}(1-\cos\theta_{\gamma,e'})}, \tag{77}$$

where E_γ and $E_{e'}$ are the energies of the photon and outgoing electron, and $\theta_{\gamma,e'}$ is the angle between the photon and electron. The matrix element, and thus the cross section, blows up when the angle between them approaches zero, in the approximation that the mass of the electron is zero. In reality, since the mass of the electron is non-zero, there is no true singularity. Nonetheless, the matrix element become very large as the photon is radiated nearly in the same direction as the electron. A similar relation exists in the case that the photon is radiated from the incoming electron leg. This spurious singularity in $\theta_{\gamma,e'}$ causes the DVCS cross section to become very large when the cross section variable Φ is close to 0° or 360°. This is due to the fact that when the photon is radiated exactly in the direction of one of the electrons, by definition, the leptonic and hadronic planes are the same plane. In other words, there is a correlation between $\theta_{\gamma,e'}$ and Φ.

2.4 Available Data, Existing Publications and Parallel Analyses

There are several analyses that have already been performed on DVCS experiments. In particular these analyses focused on obtaining beam spin asymmetries, and cross sections. A beam spin asymmetry analysis was performed at CLAS for the data set e1-dvcs1 of Hall B[21], a sister experiment to e1-dvcs2. e1-dvcs1 consists of a 5.75 GeV electron beam on a hydrogen target, whereas e1-dvcs2 consists of a 5.88 GeV electron beam on a hydrogen target with about ten times the statistics. Another completed analysis extracted the DVCS cross section for E00-110 of Hall A of JLab at $Q^2 = 1.5, 1.9$ and 2.3 GeV^2[22]. The CLAS collaboration has also undertaken parallel analyses for e1-dvcs1 to determine the absolute cross sections. A similar analysis has been performed on e1-dvcs2 by B. Guegan; a parallel analysis of the DVCS cross sections of e1-dvcs2 is the aim of this thesis. A comparison of the results of the aforementioned analyses with the results of this thesis will follow in the final section of this thesis, with a particular focus on the parallel analysis by B. Guegan[23]. The benefit of repeating a measurement of DVCS with e1-dvcs2 is the increase in the kinematical regime and statistics as compared to e1-dvcs1, by having 30 extra days of beamtime. The distinctions between the various experiments will be more thoroughly explored in the concluding section of this thesis.

2.5 Beyond Experiment - Models for GPDs

Although an in-depth tour of the different models of GPD parametrization is beyond the scope of this thesis, for completeness, we introduce some basic concepts. A detailed review article by M. Guidal et al.[24] provides a more detailed description of the topic. We present here a brief exposition on double distributions, a method for parameterizing GPDs, with a focus on the Vanderhaeghen-Guichon-Guidal (VGG) model. There exist other methods which are omitted from this thesis, among them being the Goloskokov-Kroll (GK) double distribution method[25–27], Kumerički-Müller (KM)[28], dual parameterization method[29], and the Mellin-Barnes model[28,30].

2.5.1 Double Distributions

The concept of Double Distributions (DDs) in the context of GPDs were originally introduced by A. Radyushkin[31,32] and D. Müller et al.[16]. The basic idea of DDs is to parametrize the GPDs in a way that decorrelates the average nucleon momentum P from the nucleon momentum transfer Δ. This can be done by choosing two parameters α and β such that $x = \alpha + \beta\xi$. In the infinite momentum frame, this allows one to write the struck quark momentum as $\beta P^+ - \frac{1}{2}(1-\alpha)\Delta^+$, instead of $(x+\xi)P^+$. After this change of variables, Δ and P are no longer correlated. In essence,

GPDs are a function of x, ξ and t, and DDs are a reparameterization of GPDs as a function of α, β and t. This can be written explicitly as:

$$GPD^q(x,\xi) = \int_{-1}^{1} d\beta \int_{-1+|\beta|}^{1-|\beta|} d\alpha \delta(x - \beta - \xi\alpha) DD(\alpha,\beta). \tag{78}$$

This form of parameterization is useful because the polynomiality property of the GPDs is automatically satisfied because of the linear relationship between x and ξ.

A possible form for the DD is:

$$DD(\beta,\alpha) = h(\beta,\alpha)q(\beta), \tag{79}$$

$$h(\beta,\alpha) = \frac{\Gamma(2b+2)}{2^{2b+1}\Gamma^2(2b+1)} \frac{\left[(1-|\beta|)^2 - \alpha^2\right]^b}{(1-|\beta|)^{2b+1}}, \tag{80}$$

where b is a free parameter which determines the level at which the DDs are dependent on ξ.

2.5.2 D-term

Equation 80 satisfies the polynomiality requirement of GPDs except that it omits the possibility of a ξ^{n+1} term. In order to remedy this deficiency in the ansatz, we introduce by hand the so-called D-term. This solution was given by C. Weiss and M. Polyakov[33], and can be described as a series involving Gegenbauer polynomials:

$$D\left(\frac{x}{\xi}, t\right) = \frac{1}{3}\left(1 - \frac{x^2}{\xi^2}\right) \sum_{n=0}^{\infty} d_{2n+1}(t) C_{2n+1}^{3/2}\left(\frac{x}{\xi}\right), \tag{81}$$

which is convergent for $\left|\frac{x}{\xi}\right| \leq 1$, and where $C_{2n+1}^{3/2}$ represents the odd Gegenbauer polynomials. This implies that this correction is only present in the ERBL region. The first three values of d have been estimated by using the chiral soliton model:

$$d_1 = -4$$
$$d_3 = -1.2$$
$$d_5 = -0.4$$

2.5.3 VGG Model

The Vanderhaeghen-Guichon-Guidal (VGG) model consists of trying to determine the t-dependence of the DD, inspired by Regge theory.[34–37] We study the H and E GPDs only for the moment, and state that the DDs may be written as:

$$DD_H^q(\alpha,\beta,t) = h(\alpha,\beta)q(\beta)\beta^{-\alpha'(1-\beta)t}, \tag{82}$$

$$DD_E^q(\alpha,\beta,t) = h(\alpha,\beta)q(\beta)(1-\beta)^{\eta_q}\beta^{-\alpha'(1-\beta)t}, \tag{83}$$

where α' and η_q are determined by FF fits. We may finally write the parameterization as:

$$H^q(x,\xi,t) = \int_{-1}^{1} d\beta \int_{-1+|\beta|}^{1-|\beta|} d\alpha\delta(x-\beta-\xi\alpha)DD_H^q + \theta(\xi-|x|)D(\frac{x}{\xi},t) \tag{84}$$

$$E^q(x,\xi,t) = \int_{-1}^{1} d\beta \int_{-1+|\beta|}^{1-|\beta|} d\alpha\delta(x-\beta-\xi\alpha)DD_E^q - \theta(\xi-|x|)D(\frac{x}{\xi},t) \tag{85}$$

We discuss this VGG model in more detail after the section which contains our measurement of the $e+p+\gamma$ cross section. We interpret the comparison of the VGG model to experiment there.

3. EXPERIMENTAL METHODS

3.1 Thomas Jefferson National Accelerator Facility (TJNAF) / Jefferson Laboratory (JLab)

The e1-dvcs2 experiment took place at Jefferson Laboratory. The facility was founded in 1984 in Newport News, VA, USA, and is home to CEBAF and CLAS.

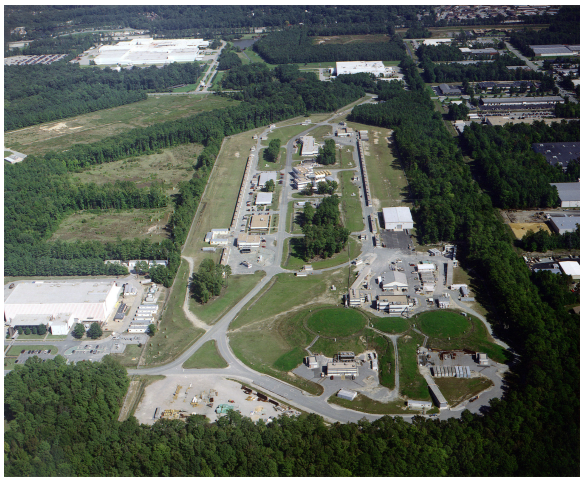

Figure 3.1: An aerial view of JLab.[38]

3.2 Continuous Electron Beam Accelerator Facility (CEBAF)

The CEBAF is an electron accelerator providing electron beams up to energies of 6 GeV. The apparatus consists of two superconducting radio frequency linear accelerators with a length of 1400 m each, and two curved portions which redirect the electron beam from one linac to the other by use of large electromagnets. The electron beam achieves 6 GeV after circulating the track five times, at which point the beam is split, and delivered to one of three experimental halls: Hall A, Hall B, and Hall C. This beam may be polarized with positive or negative helicity, with a polarization of about 85%. There are several upgrades planned for CEBAF. The most notable are the 12GeV upgrade, to be completed in 2015, which will allow a doubling of the beam energy, and the construction of Hall D, a new experimental hall.

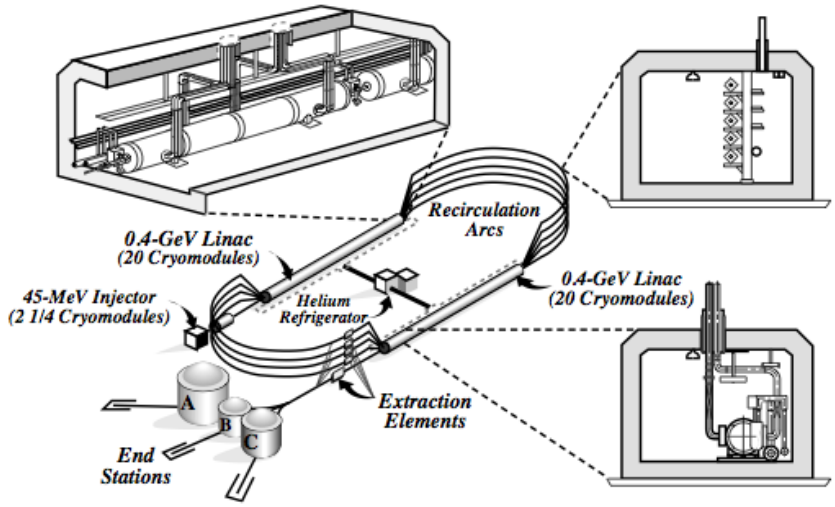

Figure 3.2: A schematic of CEBAF.[39]

3.3 CEBAF Large Acceptance Spectrometer (CLAS)

The CLAS detector[39] is used in most of the Hall B experiments in Jefferson lab. The spectrometer is roughly spherical in shape and spans about 30 feet across. During the course of the e1-dvcs2 experiment, the polarized electron beam was continuously fed into CLAS and impinged on the liquid hydrogen target which was housed inside. The ensuing reactions resulted in various particle production which was then detected by CLAS. It is called a "large acceptance spectrometer" because has around a 2π angular coverage out of 4π. The CLAS detector is comprised of many separate detectors. It is divided into six identical pieces which are referred to as sectors, which each consist of a torus electromagnet, time-of-flight scintillator, electromagnetic calorimeters, Cherenkov counters, and drift chambers. In the e1-dvcs2 experiment there is an added electromagnetic calorimeter in the forward region since the reaction of interest often generates forward going particles which are outside of the usual CLAS acceptance.

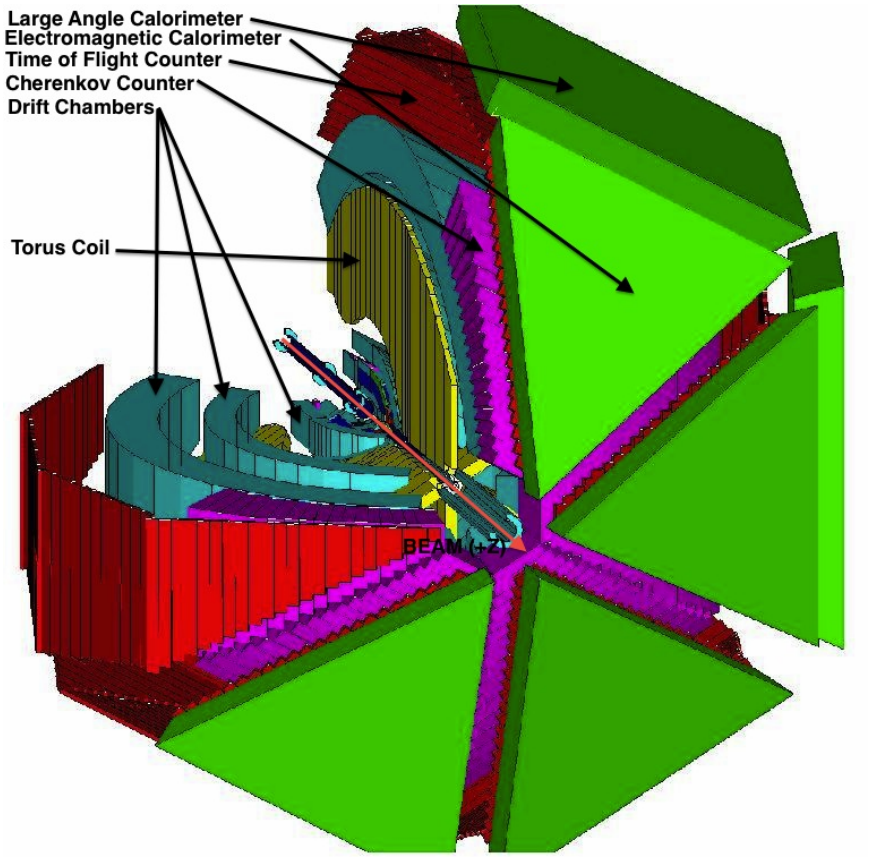

Figure 3.3: A sliced and labeled cartoon of CLAS.[39]

3.3.1 Torus Electromagnets and Drift Chambers (DC)

The inner shell of the CLAS detector is made of six torus magnets, one in each sector, which create a toroidal magnetic field. Each sector also contains three drift chambers (DCs), each placed at different radii. These drift chambers measure the trajectory of the particles that pass through them. Because of the magnetic field provided by the torus magnets, the charged particles will have curved trajectories while the neutral particles will have straight ones. The drift chambers are filled with 90%-10% gas mixture of argon and CO_2. Also inside the chambers are parallel wires which are placed in a hexagonal lattice with a lattice constant on the order of centimeters, varying from region to region. These wires are held at a specific potential. When a charged particle from an event passes through the chamber, some of the gas particles are ionized. These ions drift towards the wires and provide a signal and give a measure of the location of the particle.[39][40] The torus coils block out a region of the detector, so there are "dead" regions in our detector except for the innermost drift chambers which are before the coils.[40]

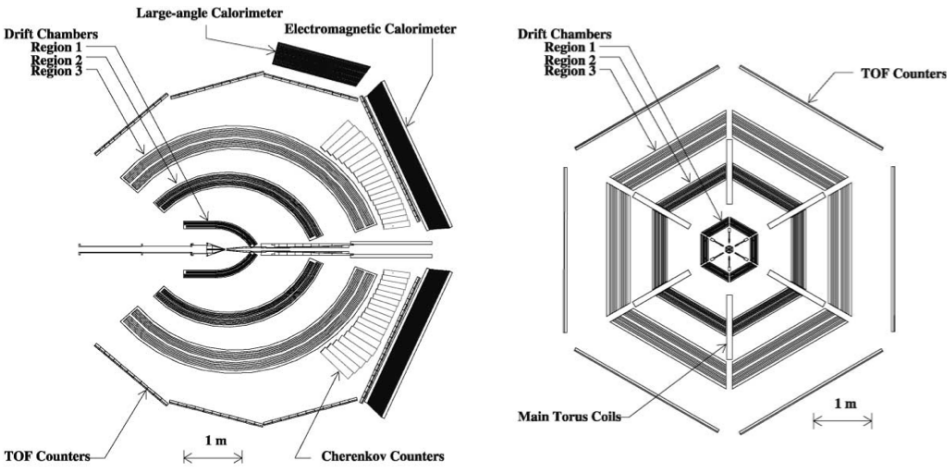

Figure 3.4: A cross section of CLAS on the x-y plane, and on the x-z plane.[40]

3.3.2 Forward Electromagnetic Calorimeters (EC)

The electromagnetic calorimeters (ECs) in the forward direction are used to detect electrons and neutral particles. Electrons and photons which pass into this detector are often stopped, and all or most of their energy is deposited and measured. In particular, when electrons shower they are nearly always completely stopped. The ECs consist of 39 triangular stacked layers each consisting of a lead plate and a plane of 36 scintillator strips which run to photomultiplier tubes (PMTs). This design of alternating lead and scintillator allows for a cascade effect. Each plane of scintillators has it's strips oriented in a direction 60° with respect to the previous plane's strips, which we call 'u', 'v' and 'w' planes. This enables the location of the hit to be determined. Furthermore, the stack is split into two portions which measure the energy deposited in each separately to aid in distinguishing between electrons and hadrons. These two portions are referred to as "inner" and "outer" parts. Electrons and photons deposit most of their energy in the inner portion by showering, and heavier particles such as protons and pions will deposit an almost equal amount of energy in the inner and outer parts of the EC because they are minimum ionizing particles. This detector covers a polar angle range from 8° to 45°.[41]

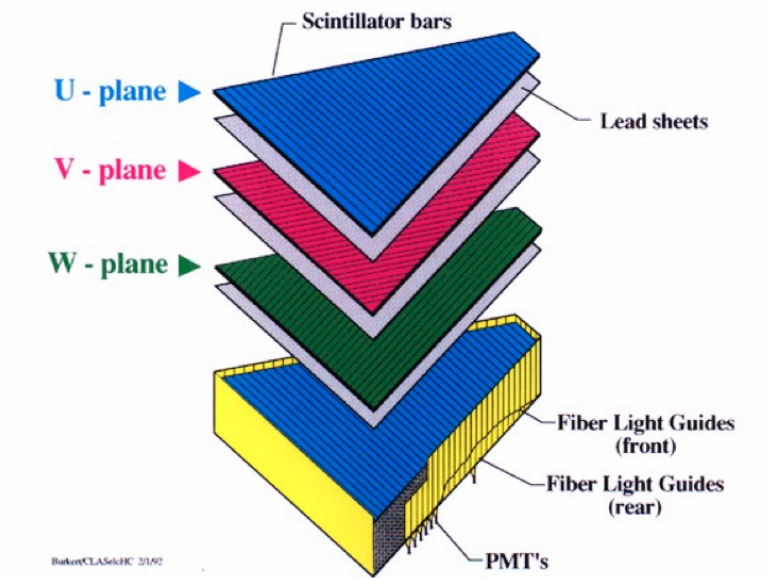

Figure 3.5: A sector of the EC, showing the different layers and planes peeled away.[41]

3.3.3 Large-Angle Electromagnetic Calorimeters (LAC)

The large-angle calorimeter (LAC) is designed similarly to the forward EC except that the polar angle of acceptance runs from 45° to 75°. This detector only spans 120° azimuthally, which corresponds to two sectors. This detector is not used in e1-dvcs2.[42]

3.3.4 Time of Flight Scintillators (TOF/SC)

The time of flight (TOF) detectors, or Scintillator Counters (SC), consist of long plastic scintillators with PMTs at each end. The location of a particle which passes through the scintillator can be determined by the time difference between the light collection by each PMT at each end. The detector also records the time at which the particle passes through it. Since the DC gives a reconstructed track, which gives us the track length and momentum, the measure of the time of flight from the vertex position to the TOF detector can be calculated. This allows the particle's mass also to be calculated. The TOF counters cover a polar angle range from 8° to 142° and is located at a radius greater than that of the drift chambers and Cherenkov counters, but just less than that of the ECs.[43]

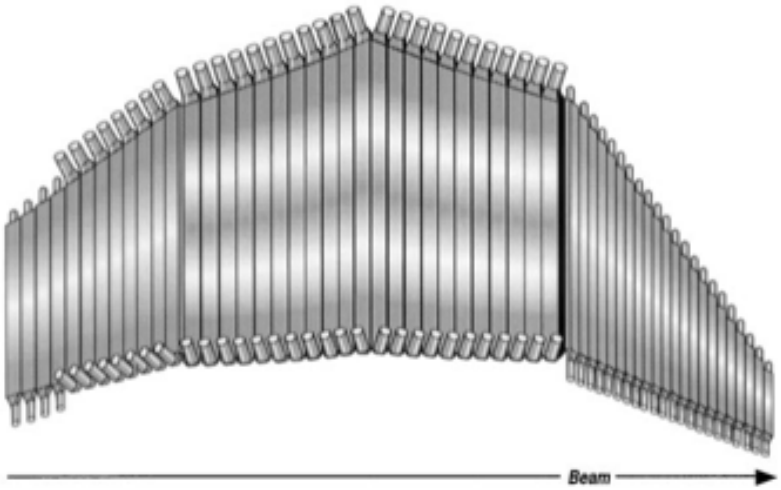

Figure 3.6: A sector of the TOF.[43]

3.3.5 Cherenkov Counters (CC)

The Cherenkov counters (CCs) detect charged particles which pass through it faster than light would pass through it. In particular, it is designed to identify electrons from pions. This separation between electrons and pions is possible up to a threshold energy of 2.2 GeV. The energy threshold for the pions is determined by the amount of energy needed to be moving faster than the Cherenkov velocity of the medium of the detector. The radiator gas used in the CCs is perfluorobutane C_4F_{10} with an index of refraction of n=1.00153. Each sector has about six cubic meters of this gas. The detector makes use of an arrangement of mirrors which reflect the Cherenkov light into PMTs, as can be seen in Figure 3.8. The CCs have a polar acceptance of 8° to 45° and are placed before the TOF counters but after the drift chambers.[44]

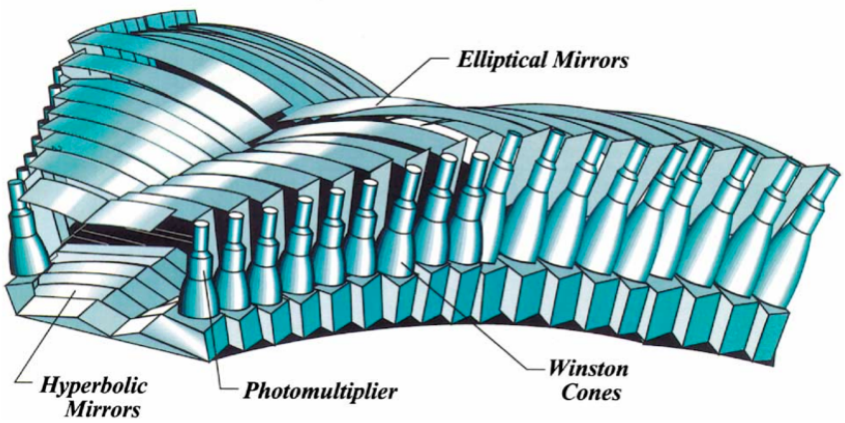

Figure 3.7: A sector of the CC.[44]

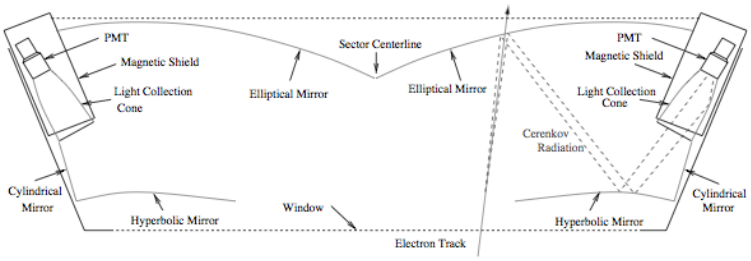

Figure 3.8: A single section of a sector of the CC, showing the configuration of the mirrors.[44]

3.3.6 Inner Calorimeter (IC)

The inner calorimeter is octagonally shaped with 424 $PbWO_4$ crystals of dimension 1.3 cm by 1.3 cm by 16 cm and is placed about 60 cm downstream from the target, with its front face at CLAS center. This detector is designed to accept photons from a polar angle of 4° to 15°. A photograph of the calorimeter may be seen in Figure 3.9.[45]

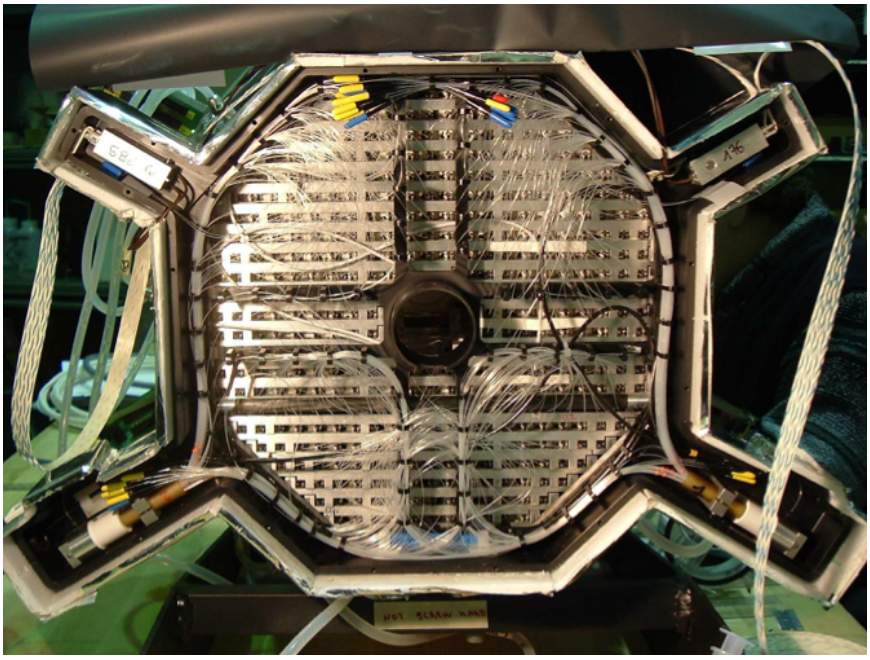

Figure 3.9: A photograph of IC, courtesy of Hyon-Suk Jo.

3.3.7 Solenoid

Because of Möller scattering of electrons, there is a possibility of a lot of noise in the IC and first region drift chambers. In order to combat this scattering, a solenoid was used in e1-dvcs2 in order to focus the scattered Möllers in the forward direction, usually at polar angle of less than 4°. In this way, the noise from possible Möller scattering may be reduced.

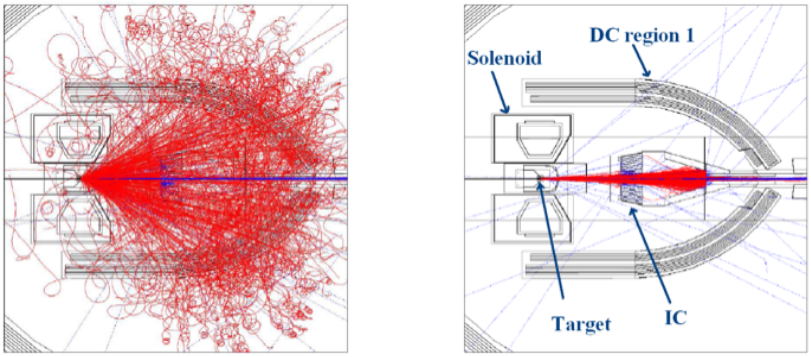

Figure 3.10: The solenoid helps direct the Möller electrons in the forward direction in order to prevent them for creating noise in the IC and DC region one. On left, simulation without the use of the solenoid, and on right, with the use of the solenoid. Figure is from reference[20]

4. DATA ANALYSIS

4.1 DVCS Analysis

4.1.1 DVCS Cross Section - A Road Map

The calculation of the $e + p \rightarrow e' + p' + \gamma$ cross section was done bin per bin, selecting the binning in four kinematic variables. The cross section is written as:

$$\frac{\mathrm{d}^4\sigma_{ep\gamma}}{\mathrm{d}Q^2\mathrm{d}t\mathrm{d}x_B\mathrm{d}\Phi} = \frac{(N_{e+p+\gamma} - N_{e+p+\pi^0(1\gamma)})}{\mathcal{L}_{\mathrm{int}} A \Delta V F_{\mathrm{rad}}}, \tag{86}$$

where $N_{e+p+\gamma}$ is the yield of the experiment, $N_{e+p+\pi^0(1\gamma)}$ is the π^0 subtraction which subtracts out the contamination from $e + p + \pi^0$ events, $\mathcal{L}$ is the integrated luminosity, A is the acceptance, ΔV is the bin volume, and $F_{rad.cor.}$ is the radiative correction. The cross section is a function of four variables: $Q^2 = -q^2$, where q is the four-momentum of the virtual photon exchanged between the electron and the hadronic system; t is the Mandelstam variable representing the momentum transfer to the proton; $x_B = \frac{Q^2}{2p\cdot q}$ is the Bjorken variable and Φ is the angle between the leptonic and hadronic planes, as is most easily seen by Figure 4.1.

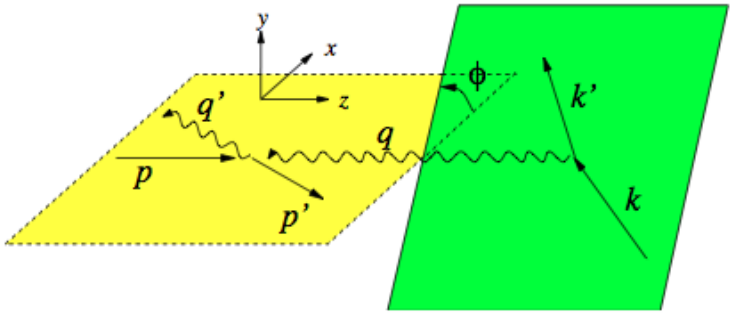

Figure 4.1: A diagram of DVCS, indicating the leptonic and hadronic planes, and the angle ϕ between them.[18]

In order to measure the cross section, we must accomplish the following:

1. Determine a choice of binning in the kinematic variables $\Delta V = \Delta Q^2 \Delta t \Delta x_B \Delta \phi$. (Section 4.1.2)
2. Determine the number of $e + p \to e + p + \gamma$ events that occurred, $N_{e+p+\gamma}$. (Section 4.2)
3. Determine the acceptance A based on simulations. (Section 4.3.)
4. Determine the volumes of each of the bins. (Section 4.6)
5. Make an estimate of the rate of π_0 contamination to the $e+p \to e+p+\gamma$ channel. (Section 4.8)
6. Calculate the integrated luminosity, $\mathcal{L}_{\text{int}}$. (Section 4.7)
7. Determine the effect of the radiative effect due to higher order terms, $F_{rad.cor.}$. (Section 4.9)

4.1.2 Kinematical Domain and Binning - Bin by Bin Analysis

In order to determine our choice of binning, we view the kinematics for both data and Monte Carlo in Figure 4.2. It turns out that the kinematical coverage provided by the experiment is laid out in an inconvenient shape with respect to the Q^2 variable by which we wanted to bin the cross section. Q^2 is a natural choice, because it appears directly in the cross section.

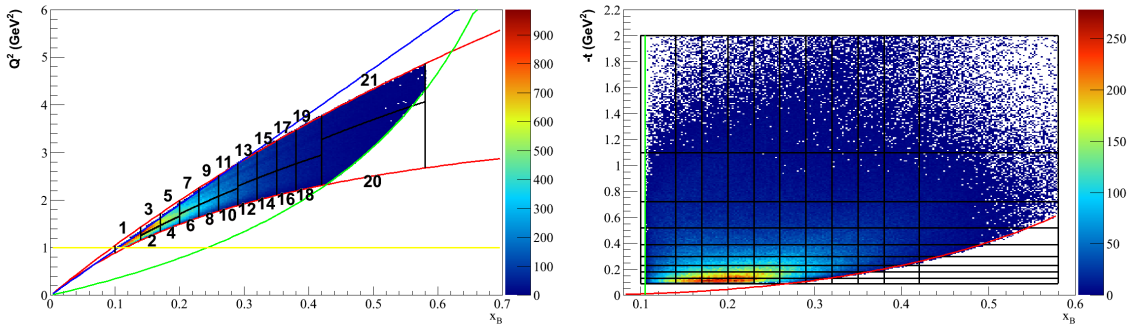

Figure 4.2: The kinematical domain for e1-dvcs2, after all cuts. On the left, Q^2 versus x_B. The black lines correspond to the bin definitions found in Table 4.1. The red lines correspond to the upper and lower cuts on θ_e, the yellow line corresponds to the cut on Q^2, the green line corresponds to the cut on W, and the blue line corresponds to the cut on p_e. On the right, $-t$ versus x_B. The black lines correspond to the bin definitions found in Table 4.1. The red line corresponds to the minimum t value allowed by kinematics, and the green line corresponds to the minimum x_B allowed due to the cut on p_e.

However, our binning must take two things into account. First, the bins must be selected in such a way that there is a reasonable amount of statistics in each bin. Secondly, each bin must be selected in a way which ensures that the bin is completely full. To further explain this second point, let us consider the scattering angle of the electron. In Figure 4.2, the limit of being able to detect

the electron only up to $\theta_e = 45°$ corresponds to an upper limit on the value of Q^2. This limit is a function of x_B and is represented by the upper red line. If a bin is chosen such that it straddles this line, only a fraction of the bin can be expected to be filled. Therefore, the volume of such a bin cannot be expected to represent the true volume which enters into the cross section. The true volume of a bin is the portion of it which is filled by events. Therefore, to avoid the problem (for now) of partially filled bins, we select a binning which covers only our available kinematics. This requires that we exchange the variable Q^2 in favor of a more natural coordinate θ_e which is the scattering angle of the electron. Our choice of binning is laid out in Table 4.1. It is largely conventional, as it is an adoption of the same binning being used by the e1-dvcs analysis. Their reasons for adopting this binning consider that the cross section is rapidly varying, and that it is desirable to have the binning be as fine as statistics will allow without having error bars which are too large. In total, there are 21 bins in θ_e and x_B, 9 bins in $-t$, and 24 bins in Φ. This gives us a total of 4,536 bins. There are some additional constraints that we would like to add to our bin definitions. There are some restrictions on our kinematics, which "cut" into the bins as we have defined them, according to our four cross section variables. For this reason, we must define our bins according to the strictest constraint. An exhaustive list of such cuts may be found on Table 4.1.

- The angular acceptance of electrons runs from 21° to 45°.
- We are interested in restricting our study to be above the resonance region ($W > 2$ GeV), and in the highly virtual ($Q^2 > 1$ GeV^2) region.
- We detect electrons reliably only down to .8 GeV.
- There are some values of $-t$ which are kinematically forbidden. The minimum possible $-t$ can have is t_{min}, which may be found on Table 4.1.
- Because the cross section has a singularity at $\theta_\gamma = 0$, we choose to place a cut at $\theta_\gamma > 4.77°$. The choice of 4.77° allows us to avoid any low angle area which is not covered by the IC. This allows us to avoid relying only on the event generator whose cross sections is varying rapidly in this region.

Table 4.1: The boundaries of each of the bins according to their four dimensions.

21 Bins in x_B and θ_e (degrees)		0.1-0.14 21°-45°	0.14-0.17 21°-25.5°	0.14-0.17 25.5°-45°	0.17-0.2 21°-25.5°	0.17-0.2 25.5°-45°
0.2-0.23 21°-27°	0.2-0.23 27°-45°	0.23-0.26 21°-27°	0.23-0.26 27°-45°	0.26-0.29 21°-27°	0.26-0.29 27°-45°	0.29-0.32 21°-28°
0.29-0.32 28°-45°	0.32-0.35 21°-28°	0.32-0.35 28°-45°	0.35-0.38 21°-28°	0.35-0.38 28°-45°	0.38-0.42 21°-28°	0.38-0.42 28°-45°
0.42-0.58 21°-33°	0.42-0.58 33°-45°					

9 Bins in $-t$ (GeV^2)		0.09-0.13	0.13-0.18	0.18-0.23	0.23-0.3	0.3-0.39
0.39-0.52	0.52-0.72	0.72-1.1	1.1-2.			

24 Bins in Φ (degrees)	every 15°, from 0° to 360°

Additional constraints	$\theta_e > 21°$	$\theta_e < 45°$
$p_e > 0.8$ GeV	$W > 2$ GeV	$Q^2 > 1$ GeV^2
$\theta_\gamma > 4.77°$	$t > t_{min} = \frac{Q^2\{2(1-x_B)(1+\epsilon^2-\sqrt{1+\epsilon^2}\}}{4\epsilon^2+4x_B(1-x_B)}$, where $\epsilon = \frac{4M_p x_B}{Q^2}$	

4.2 Particle Identification

After CLAS and IC have measured and recorded data for the time allotted to the experiment, the responses of the detectors, which correspond to the properties of each of the detected particles, are stored. They are then analyzed with a program on an event by event basis. Variables which are stored for each of the particles include momentum, charge, and position where the particle hit a detector, among other things.

Because of resolution effects within CLAS, it is impossible to determine different types of particles with absolute uncertainty. However, it is possible to separate the different types of particles detected within some degree of uncertainty. This is done by demanding a certain set of criteria on the variables of the particles that are detected. This is achieved by applying cuts on some of the variables. These cuts must be done carefully, because wide cuts will tend to misidentify more particles, and narrow cuts will tend to reject particles which are valid. The correct identification of particles and of the DVCS event are the crux of this work. The criteria that were imposed on each of the particles of interest are enumerated below.

4.2.1 Electron Identification

The particles which satisfy the following criteria are assumed to be electrons for the purpose of this analysis.

Charge:

The charge of the electron candidate must be restricted to be -1. Charge is determined in CLAS by the direction of curvature, or equivalently the radius of curvature, of the particle trajectory, which is determined by reconstruction based on tracks in the DC according to the formula

$$\kappa = \frac{1}{R} = \frac{qB}{\gamma m v} \tag{87}$$

where κ is curvature, R is radius of curvature, q is charge, v is velocity, m is mass, γ is the Lorentz factor, and B is the component of the magnetic field perpendicular to the trajectory of the particle.

In simpler terms, tracks corresponding to negatively charged particles must be in-bending (towards the beam line). The electron must also have good time-based tracking (TBT).

Momentum:

The momentum of the electron candidate must be greater than 0.8 GeV. Given a value for the charge, the momentum is determined by the curvature of the track, which is determined by DC reconstruction.

Energy Deposited in Inner Stack of EC:

It is known that Minimum Ionizing Particles (MIPs) deposit a nearly constant amount of energy into a medium through which it travels as a function of the distance it travels through it. MIPs include protons, charged nuclei, atomic ions, pions and other mesons. Electrons and photons in particular are excluded from this class of particles. A quantitative description of the amount of energy loss per length travelled is given by the Bethe equation,

$$-\frac{\mathrm{d}E}{\mathrm{d}x} = \frac{4\pi\alpha^2}{m_e}\frac{nZ^2}{\beta^2}\left[\ln\left(\frac{2\beta^2}{I(1-\beta^2)}\right) - \beta^2\right], \tag{88}$$

where α is the fine structure constant, n is the electron density of the material that is being passed through, Z is the atomic number of that material, and I is the mean excitation potential.

Unlike the cascade effect which occurs when electrons and photons hit the EC, MIPs will deposit a constant amount of energy per cm, irrespective of their momentum. The inner stack of the EC has a thickness of 183 mm: 150 mm contributed by the BC412 scintillator, and 33 mm by the lead sheet. The outer stack has a thickness of 292.8 mm: 240 mm contributed by the scintillator, and 52.8 mm by the lead. Based on these values, the expected energy deposited inner and outer are .03 and .05 GeV respectively.

As the MIP travels through the material, it slows down, and in doing so the rate of energy loss increases. This effect can be seen by the dominating $\frac{1}{\beta^2}$ term in the Bethe-Bloch equation. As most of the MIPs make it through the inner stack of the EC, the energy deposited in that stack tends to be constant as a function of distance traveled. However, many of the MIPs begin to slow down significantly in the outer stack, contributing to more energy deposited there. This may be seen clearly in Figure 4.3 as a vertical stripe centered around $E_{inner} = 0.03$ GeV, as expected. The cut chosen for this analysis is to accept only particles with $E_{inner} > 0.06$ GeV as electron candidates. This may be seen in Figure 4.3.

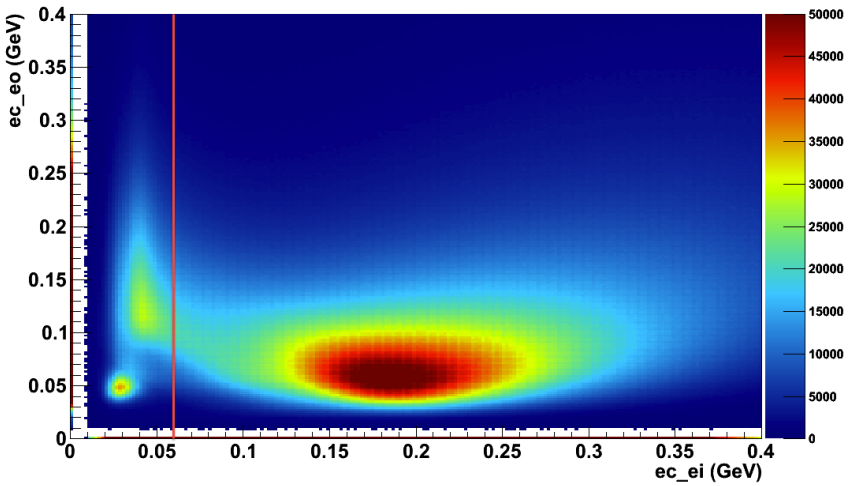

Figure 4.3: Energy deposited in outer stack of EC plotted against energy deposited in the inner stack of EC. The red line represents the cut requiring $E_{inner} > 0.06$ GeV.

Sampling Fraction of EC:

It is expected that electrons will deposit an energy in the EC proportional to their momentum. Therefore a plot of the so-called sampling fraction versus momentum gives a good indication of

which particles may be considered electron candidates. The sampling fraction is defined as

$$f_s = \frac{E_{\text{total}}}{p} \tag{89}$$

where E_{tot} is the total energy deposited in both inner and outer layers of the EC, and p is momentum.

Particles with a total energy proportional to momentum appear as a straight horizontal line on Figure 4.4. In theory, with a perfectly efficient detector, this would be a straight line. Given resolution effects, the line becomes broadened into a distribution. Additionally, the resolution seems to be momentum dependent, worsening at lower momentum. This feature is expected in CLAS. Because of the varying width of this distribution, it is insufficient to take cuts at a constant value of sampling fraction. Our cut must be dependent of momentum. The method used involves taking slices of this plot in momentum, and projecting them onto the y-axis. The resultant histograms are fitted to Gaussians whose means and standard deviations are used in the final cut.

The means for each momentum bin are fitted to:

$$\mu(p) = 0.336948 - 0.0321597p + 0.00433749p^2 - 0.000159799p^3, \tag{90}$$

and the standard deviations for each momentum bin are likewise fitted to:

$$\sigma(p) = 0.00635095 + \frac{0.0621754}{\sqrt{p}}. \tag{91}$$

The final cut requires that a particle have a sampling fraction which lies within the range $(\mu - 2.5\sigma, \mu + 2.5\sigma)$. This cut may be seen in Figure 4.4

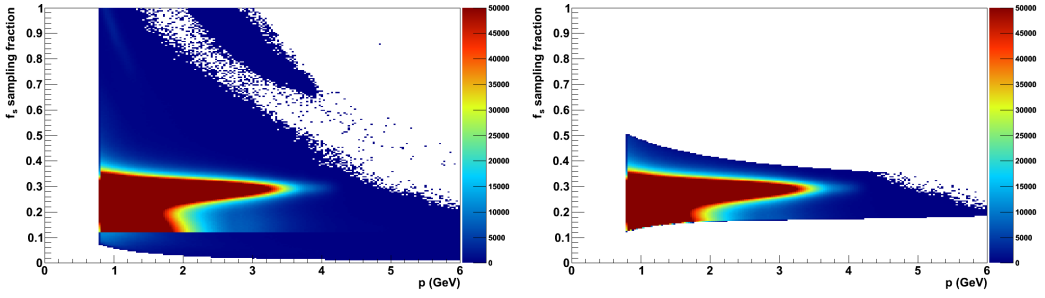

Figure 4.4: Sampling fraction f_s as a function of momentum, before cut on left, after cut on right. The main features of this plot are the electrons, mostly horizontal on each plot; and the negative pions whose sampling fraction is decreasing with increasing momentum. The purpose of this cut is to separate these pions from the electrons.

Vertex Correction and Cut:

The liquid hydrogen target in e1-dvcs2 is located at -57.5 cm with respect to CLAS center, and is about 5 cm in length. The track reconstruction allows us to determine the location along the beam line axis (z) where the electron candidate originated, up to a resolution of tens of microns. There are numerous tracks which originate outside the target according to this reconstruction, and these events should be rejected. It could happen that Möller scattered electrons from the beam line could be the cause of many such events.

However, it turns out that the reconstructed values for the vertex positions are not completely accurate. This may be seen in Figure 4.5. It is necessary to apply a correction to the vertex position variable before placing any cuts or restrictions on it. In order to describe the vertex correction, it is necessary to describe how the uncorrected values are obtained. The determination of the vertex position is accomplished by a process called swimming, which makes use of the sector in which the particle was detected, and the track determined by the DC. The first step is to determine the "special plane" which corresponds with the sector which was hit. There are six sectors and three special planes. The three special planes are: the x-z plane, and the two other orientations of this plane rotated about the z-axis by 60°. Starting from the x-z plane, and going counter-clockwise, the special planes will be labeled plane 1, 2 and 3. Each sector has a corresponding plane. Sector 3 and 5 correspond to plane 1, sector 4 and 6 correspond to plane 2, and sector 5 and 1 correspond to plane 3. An important fact to note is that all three special planes intersect at the z-axis. This reflects the assumption that the electron beam travels along the line $x_0 = 0$ cm, $y_0 = 0$ cm. The uncorrected vertex for each track is determined by identifying the sector in which the particle was detected, and the corresponding special plane. Next, the point at which the particle track crosses this special plane is taken to be the uncorrected vertex position, $(v_{x,0}, v_{y,0}, v_{z,0})$.

However, since the beam position is generally not located at $(x_0, y_0) = (0 \text{ cm}, 0 \text{ cm})$, the assumptions made in determining the vertex position lead to values that are slightly inaccurate. To resolve this discrepancy, one may determine a "corrected" value supposing the special planes intersect at the real beam position. A study carried out by F.X. Girod determined the position of the beam to be at $x_0 = 0.074\text{cm}, y_0 = -0.064\text{cm}$. It turns out that the corrected values $\mathbf{v} = (\mathbf{v_x}, \mathbf{v_y}, \mathbf{v_z})$, may be determined given: the uncorrected vertex position $\mathbf{v_0} = (\mathbf{v_{x,0}}, \mathbf{v_{y,0}}, \mathbf{v_{z,0}})$, the momentum $\mathbf{p} = (\mathbf{p_x}, \mathbf{p_y}, \mathbf{p_z})$, and the beam position $\mathbf{x} = (\mathbf{x_0}, \mathbf{y_0}, \mathbf{z_0})$.

The corrected vertex position is

$\mathbf{v} = \mathbf{v_0} + A\mathbf{v}$, where $A = \frac{S_0 - S_v}{S_p}$, and $S_0 = x_0 \cos\Phi + y_0 \sin\Phi$ $S_v = v_{x,0} \cos\Phi + v_{y,0} \sin\Phi$ $S_p = p_x \cos\Phi + p_y \sin\Phi$ and $\Phi = (\text{Sector Number} - 1) * \frac{2\pi}{6}$.

After correction, the cut is taken to exclude particles which have trajectories that originated too far from the target. The small bump just to the left of -54 cm corresponds to the insulating foil. This must be cut out. The peak of this insulating foil was fitted to a Gaussian, and a cut was applied at three standard deviations to ensure almost complete exclusion of those events. A cut is applied by eye on the left hand side so as to approximate the strictness of the cut applied on the right hand side. The cut applied in this analysis keeps only particles which satisfy -61.25 cm $< v_z < -54.5$ cm. The fact that the plot is not centered around the nominal value of 57.5 cm is notable. While it is easy to obtain a good *relative* measurement in vertex position, it is difficult to get an accurate, *absolute* value of longitudinal position in target given the nature of the vertex position reconstruction. Furthermore, we are are more interested in the relative position of all events.

The distribution of uncorrected and corrected vertex positions may be found in Figure 4.5, as well as the cut that was applied.

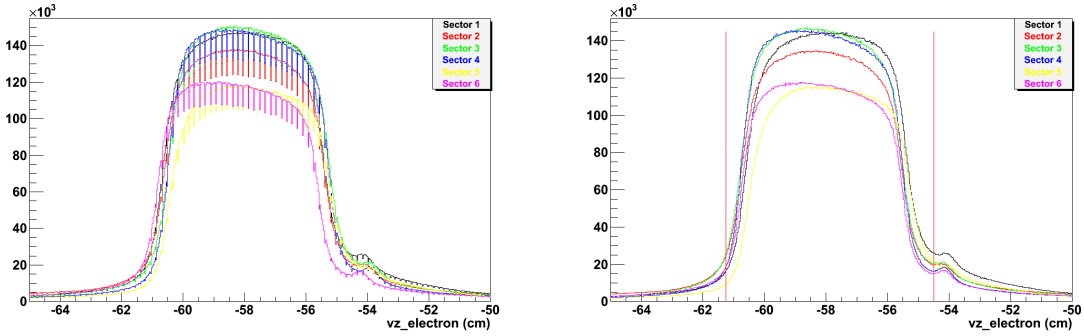

Figure 4.5: Vertex position of electrons in z-direction for each sector. On the left, before corrections. On the right, after corrections. The red lines represent the final cut. We note that the heights of each sector differ, indicating that each sector has a different level of performance. The periodic behavior, producing regular small spikes, is an artifact of ntuple22 variable compression.

Fiducial Cuts:

Each detector, both IC and in CLAS, have regions whose behaviors are understood to a greater or lesser degree. In the center of detectors, the behavior tends to be less distorted and more easily modeled by simulations. However, the edges of detectors are often more unpredictable in their behavior, and are not well understood. For example, a particle which hits near the edge of a calorimeter might create a shower which leaks out the side. This leaked shower will not be collected by the PMT, and will result in a lower detected value for energy. Another example of strange behavior at edges of detectors might involve the reconstruction method of the position of a particle hit. Some detectors operate on a principle of averaging cell positions of a hit cluster while weighing

over energies. This algorithm may result in a lower count of reconstructed hits near detector edges when in fact the number of events might not actually be that low.

Since it is too difficult to accurately model these and other similar strange detector behaviors, it is necessary to determine a fiducial region for each of the detectors, carving out the area where the measured quantities are reliable, and in agreement with simulations. Section 4.3 will have a significant section dedicated to the discussion of Monte Carlo simulations, and their comparison with actual data.

CC Fiducial Cuts, Number of Photoelectrons Detected in CC:

There are several stages to determining the fiducial cuts for the Cherenkov detector. One cut is geometrically based. Another cut is based on the number of photoelectrons (nphe) which are detected by the PMTs in the CC, in order to remove π^+ contamination. Another cut is concerned with efficiency based on this nphe cut. Finally, a study is done to find if there are any dead PMTs in the detector. Once these cuts are done, a map of efficiencies based on the Vlassov coordinates, which we introduce below, must be retained for the cross section level of the analysis.

Cut Based on Number of Photoelectrons in CC: A histogram of the number of photoelectrons detected in the CC PMTs can be seen in Figure 4.6. There are two structures that may be seen. On the left, there is a somewhat Gaussian peak which corresponds to π^+ particles which were just over the threshold energy, and δ-electrons, which are scattered atomic electrons. This is superimposed with another structure, which peaks at the right, but which goes all the way to zero. This second structure has the general shape of a Poisson distribution, and corresponds to electrons in the CC. It is necessary to remove the contamination due to the charged pions. Many studies were done to determine if exclusivity cuts on the $e+p \rightarrow e+p+\gamma$ channel would eliminate this peak. It turns out that because these cuts are ultimately not sufficient to remove the peak, a cut must be done. We opt to take a cut at 2.5 photoelectrons (which corresponds to 25 on the histogram). This ensures nearly a complete removal of the positive pions. However, the cost of this cut is that we have thrown away a significant number of electrons. An analysis must be done to make an estimation of good events which were lost.

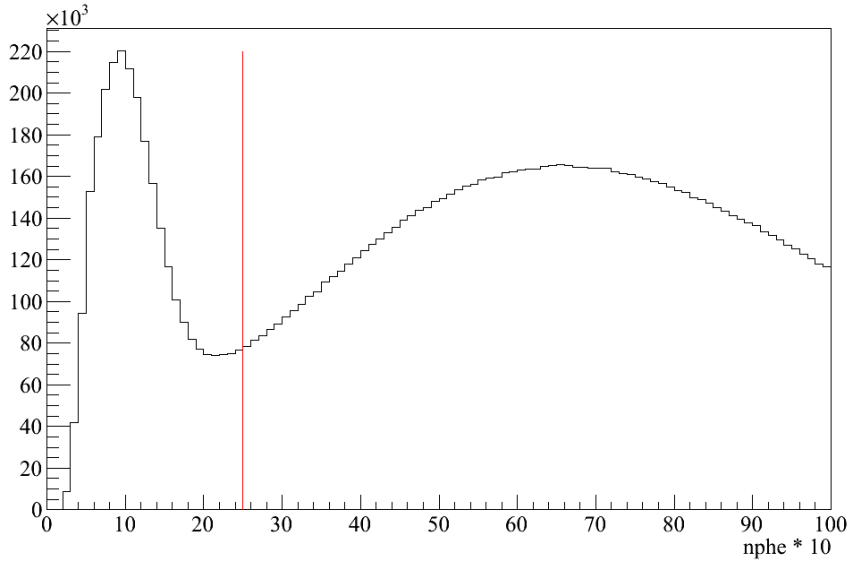

Figure 4.6: The number of photoelectrons detected in the CC for electrons. The cut is shown by the vertical line at 25, corresponding to 2.5 photoelectrons.

Geometrical Based Cut: The most convenient way to study the geometry of CC is to plot the number of hits in so-called Vlassov coordinates. These coordinates are based on two reflections of the light trajectory within the CC and are measured in angles from the CLAS center: θ_v and ϕ_v. A plot showing these coordinates, before the application of any cuts may be seen in Figure 4.7. The cuts that are applied require the particle to have a θ_c and ϕ_c which lie within the functions:

$$\phi_c = -68.975 + 36.996 \ln \theta_v - 1.670\theta_v + 0.011\theta_v^2 \tag{92}$$

$$\theta_c = 43.0 + 0.05|\phi_v| + 0.003|\phi_v^2| \tag{93}$$

The result of this cut may be seen in Figure 4.8.

Efficiency based Cut: The cut at 2.5 photoelectrons which we have imposed in the previous step of the analysis brings up the issue of efficiency. We assert that we can obtain a measure of efficiency as a function of the Vlassov coordinates, by only knowing the average number of photoelectrons detected in the same bin in Vlassov coordinates after the 2.5 photoelectron cut. We begin by making the assumption that the number of photoelectrons due to electron events is well described by a Poisson distribution. This will be reinforced by later analyzing the quality of our fits to this histogram. We begin with the most general form of a Poisson distribution:

$$P(N;\lambda) = \frac{\lambda^N e^{-\lambda}}{N!}, \tag{94}$$

where N is the number of photoelectrons detected in the CC, and λ is the average number of photoelectrons of the distribution, viz.:

$$\langle P(N;\lambda)\rangle = \int_0^\infty dNP(N;\lambda)N = \lambda. \tag{95}$$

The efficiency for a given bin in Vlassov coordinates is then:

$$\epsilon_{\mathrm{CC}} = \frac{\int_{2.5}^\infty dNP(N;\lambda)}{\int_0^\infty dNP(N;\lambda)}. \tag{96}$$

Now, since λ is not known, we must find a way to obtain it using only the average number of photoelectrons in the *cut* distribution. We will call the average of the cut distribution Λ. This is easily obtained by writing the average of the cut distribution explicitly:

$$\Lambda(\lambda) = \frac{\int_{2.5}^\infty dNP(N;\lambda)N}{\int_{2.5}^\infty dNP(N;\lambda)}. \tag{97}$$

It turns out that there is no analytical solution for λ as a function of Λ, $\lambda(\Lambda)$. This is not problematic, because a numerical solution may be determined instead. We write $\lambda(\Lambda)$ anyways, keeping in mind that the value of λ is numerically obtained for a choice of Λ.

Finally, we may write the efficiency as a function of the average number of photoelectrons detected after the 2.5 cut:

$$\epsilon_{\mathrm{CC}}(\Lambda) = \frac{\int_{2.5}^\infty dNP(N;\lambda(\Lambda))}{\int_0^\infty dNP(N;\lambda(\Lambda))}. \tag{98}$$

It is now possible to know the efficiency of the CC as a function of the variables θ_v and ϕ_v. This may be seen in Figure 4.10. The next step is to determine if any parts of the CC will be cut out for having too low of an efficiency. This is reasonable because simulations do not take into account the complex mirror geometry of the CC. In particular, the CC is bisected by a joining of two elliptical mirrors. Because of the lack of perfect continuity at the joining line, there will be a loss of efficiency in this region in the experiment, which is not realistically calculable. A removal of this region by use of a table in θ_v and ϕ_v is easily done, by removing any region with an efficiency less than 80%. The results of this efficiency cut may be seen in Figure 4.9.

Cut on Dead PMTs: There is a PMT in sector 1 which is clearly dead. The top and middle sections of Figure 4.9 shows a slight crescent shaped gap over the region the PMT is responsible for.

A cut is made to carve out that region with the results seen in the bottom third of the same Figure. Another way of identifying this dead PMT is by inspecting the individual PMT occupancies. Figure 4.11 shows the occupancies for each of the detectors as a function of run number. The first eighteen bins from the bottom correspond to PMTs on the left hand side of the CC, the last eighteen correspond to the right side, and the middle eighteen correspond to events which triggered both sides of the CC. It is clear that the dead PMT seen before in sector one corresponds to the one here with low occupancy, the only PMT with less than 30% efficiency.

Based on these two inspections, we can apply cuts to remove this region. The dead areas plotted in Vlassov coordinates were cut out carefully by eye, and all events which triggered the low-occupancy PMT are disregarded.

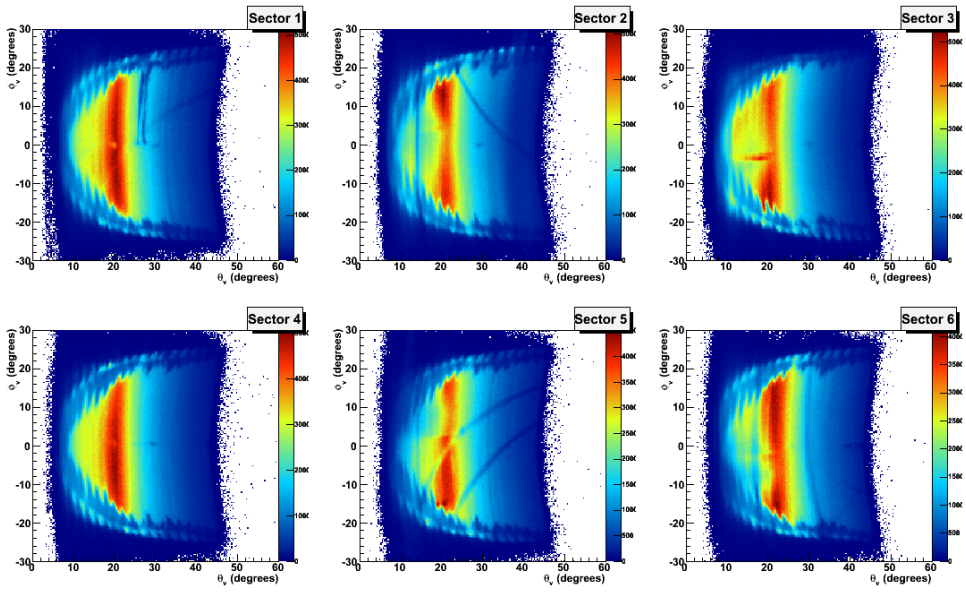

Figure 4.7: CC plotted by sector, before fiducial cuts.

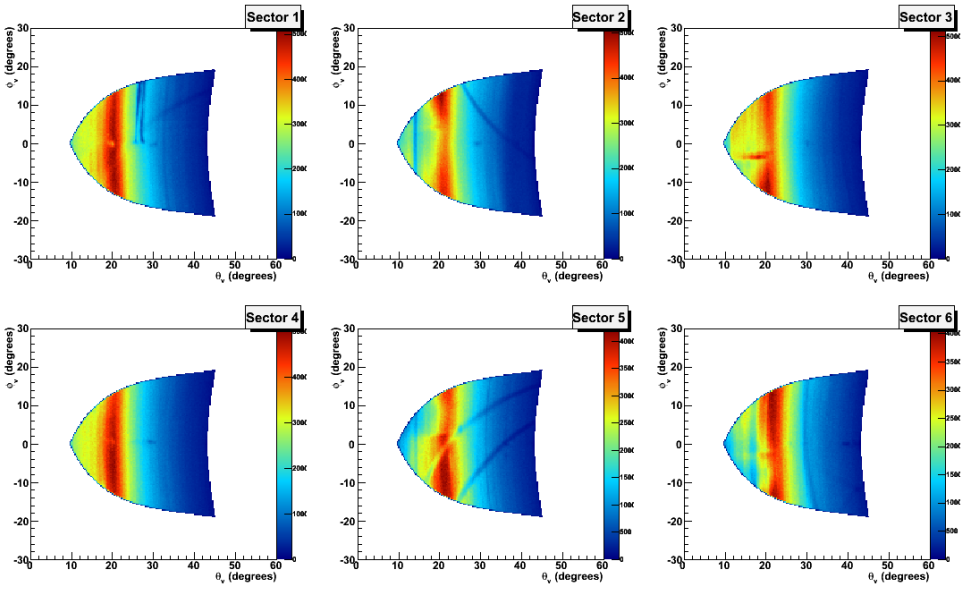

Figure 4.8: CC plotted by sector, after geometrical cuts.

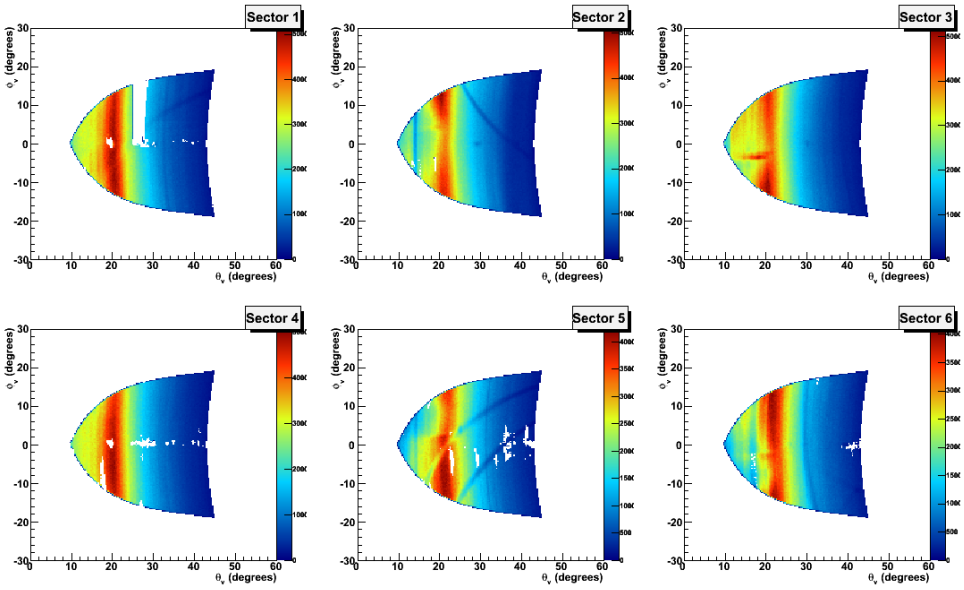

Figure 4.9: CC plotted by sector, after geometrical, efficiency, and dead pmt cuts.

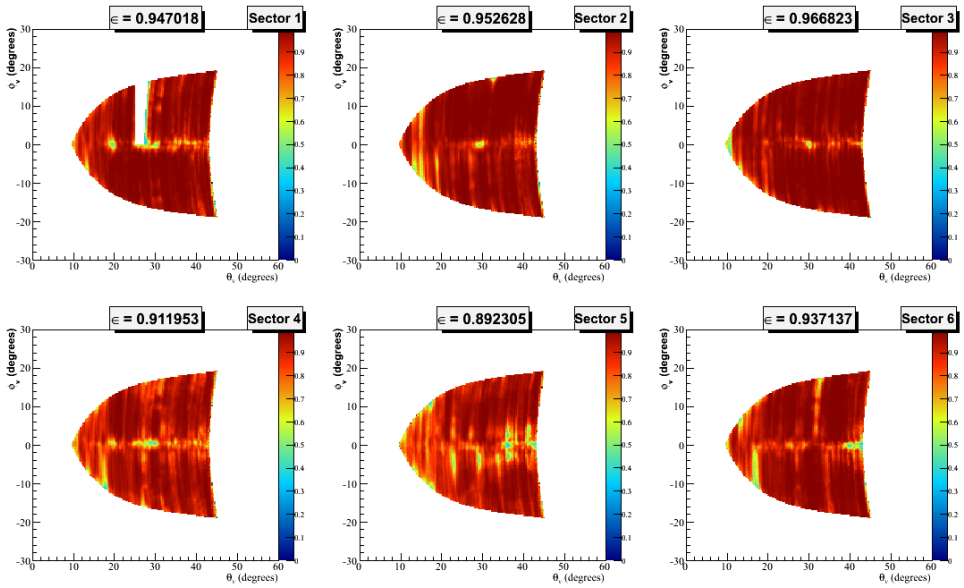

Figure 4.10: CC efficiencies, $\epsilon_{CC}(\theta_v, \phi_v)$, plotted by sector, after geometrical, efficiency, and dead pmt cuts. This plot determines the cuts placed in Figure 4.9, with everything below 80% removed.

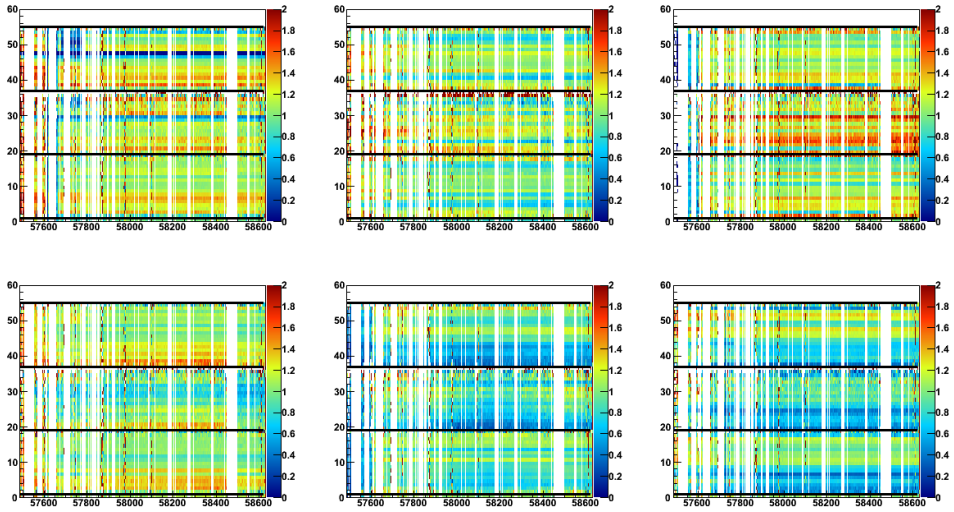

Figure 4.11: Occupancy of CC PMTs, per sector, per PMT, as a function of run number. The top third of each sector, partitioned by black lines, represents the left side PMTs. The bottom third represents the right side PMTs. The middle third represents a simultaneous signal in both left and right PMTs. The PMT which is removed from the analysis is number 47 in sector 1, which can be seen in the upper left panel.

IC Shadow Fiducial Cut:

There is a significant part of IC which lies directly between the target and CLAS. This obstruction should prevent particles from reaching the parts of CLAS with are "behind the shadow" of the IC. However, because of secondary scattering and various other effects, there are many events which are detected behind this shadow. These events cannot be trusted in this analysis and must be removed. The method involves calculating the intersection of the particle trajectory on the plane which contains the back face of the IC. This plane is the x-y plane at $z = 16$ cm, in CLAS coordinates. This can be approximated by making use of the position of the particle when it passed through the region 1 of DC, and assuming that the particle moved in a straight line in the region between the IC and region 1 DC. This is reasonable since the torus magnet lies outside of the DC region 1, and so magnetic field is approximately zero in that region. The electron candidate intersection on this plane can be seen on the plot on the left in Figure 4.12. There is a pronounced shadow, as expected, where the IC should be blocking the particles. We can see the octagonal shadow, as well as the shape of the IC cradle structure on the bottom. The aim of this fiducial cut is to eliminate the events which lie in this shadow. While a few methods have been developed for this cut, we have opted to apply a cut "by eye". The result of this cut can be seen on the plot on the right in Figure 4.12.

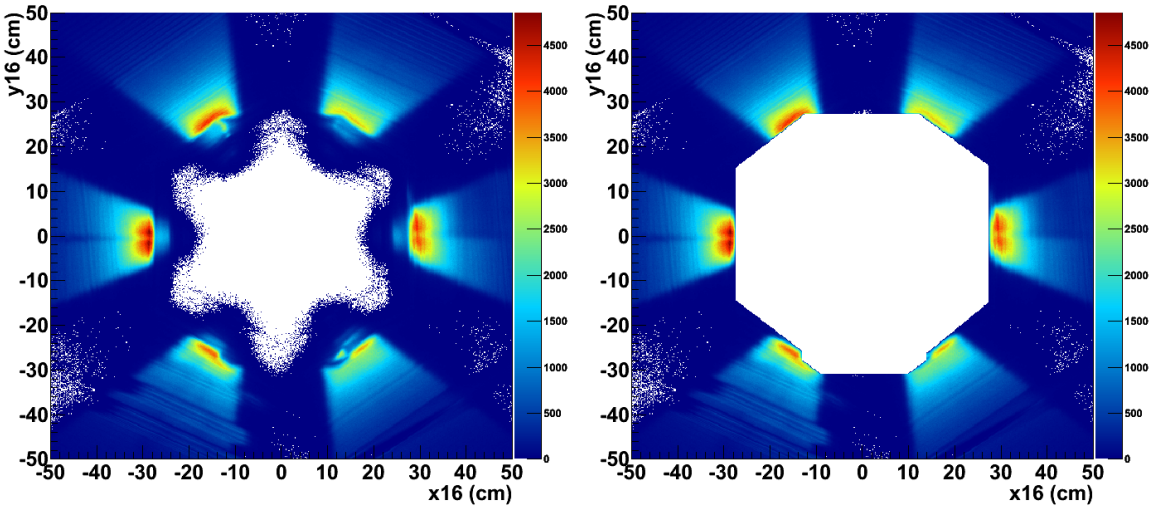

Figure 4.12: On the left, the intersection position of the electron candidate track on the plane which contains the back face of the IC. On the right, the same plot after fiducial cuts. One can see the octagonal shadow, as well as the shape of the IC cradle structure on the bottom.

DC Fiducial Cut:

Events too near the edges of region one DC must be cut. However, because of the curved geometry, a view of the detector in any two combinations of CLAS coordinates will not give a satisfactory representation, or "sharp" view, of the events over its surface. Therefore, a more natural set of coordinates must be developed. This may be done by recognizing that each sector of the region one DC has two distinct sections: a section which is flat, and a section which is curved. This may be seen in Figure 4.13. In this Figure, z runs in the direction of the beam line, x runs in the direction perpendicular to the beam line but contained in the plane bisecting the sector in question, by which y is uniquely defined, coming out of the page. For the curved portion of the detector, where $z > 0$ cm, the ideal choice of coordinates will preserve the y coordinate, but redefine a second variable s which runs along the curved portion of the detector, always in a direction perpendicular to y. The length along this direction is easily obtained by fitting the z-position of the detector as a function of x-position. The fit yields parabolas, which are fitted separately for electrons and protons. These functions $f_{e,p}(z)$ can be used to find the length along the detector by the relation: $s_{e,p} = \int_0^{z'} \sqrt{1 + \frac{d^2 f_{e,p}(z)}{dz^2}} dz$. In the flat portion of the detector, where $z < 0$ cm, it is natural to use the coordinates y and z. Therefore, for the flat portion, we define $s = z$.

Finally, we have:

$$s_{e,p} = \begin{cases} z < 0 : z \\ z > 0 : \int_0^{z'} \sqrt{1 + \frac{d^2 f_{e,p}(z)}{dz^2}} dz \end{cases}$$

Using this unique set of coordinates, we may plot the region one DC, as seen in Figure 4.14, and determine where the cuts are best made. A determination is made by eye, selecting events which satisfy:

$$|y| < 35 \left(-0.5 + \frac{1}{1 + \exp^{0.045(80 - s_e)}} \right)$$

whose effect may be seen in Figure 4.16. It is interesting to notice that the result of the IC shadow fiducial cut for electrons, an intermediary plot between Figure 4.14 and Figure 4.16, significantly cleans up the distribution in the forward region of the sectors. This intermediate plot is shown in Figure 4.15.

One last consideration must be made concerning the region one DC. There are several depletions and displacements which are vertically or semi-vertically situated in the aforementioned plots. The cause of these aberrations have been a source of much speculation and debate. Because of the poor possibility of reproducing these features accurately in simulations, these aberrations must be

carefully carved out. The displacements and depletions are most easily seen in Figure 4.14, but be still be discerned in Figure 4.15. The cuts which exclude events in these regions may be found in Figure 4.16, corresponding to the two vertical cuts in sectors 2 and 4, and the slanted cuts in sector 5 and 6. It is believed generally that the vertical displacements are due to an issue in the axial wires in the region 1 DC and the slanted displacements are due to issues in some stereo wires. A study of these plots in bins of momentum, whose plots are omitted from this thesis for brevity, revealed that these displacements exhibit no momentum dependance, strengthening our belief that the cause of the issue is from region 1 DC. The same exact displacements may also be found in the proton candidates.

A mathematical description of the cuts placed on the variables s_e and y may be expressed as the following equations, where the enclosed events are rejected from the analysis:

$$
\begin{aligned}
&5 \text{ cm} < s_e < 11.5 \text{ cm}, \text{ sector 2} \\
&5.5 \text{ cm} < s_e < 9 \text{ cm}, \text{ sector 4} \\
&9 * (s_e - 15.5) \text{ cm} < y < 9 * (s_e - 22.5) \text{ cm}, \text{ sector 5} \\
&9 * (s_e - 24) \text{ cm} < y < 9 * (s_e - 31) \text{ cm}, \text{ sector 5} \\
&9 * (s_e - 16.5) \text{ cm} < y < 9 * (s_e - 22) \text{ cm}, \text{ sector 6}
\end{aligned}
$$

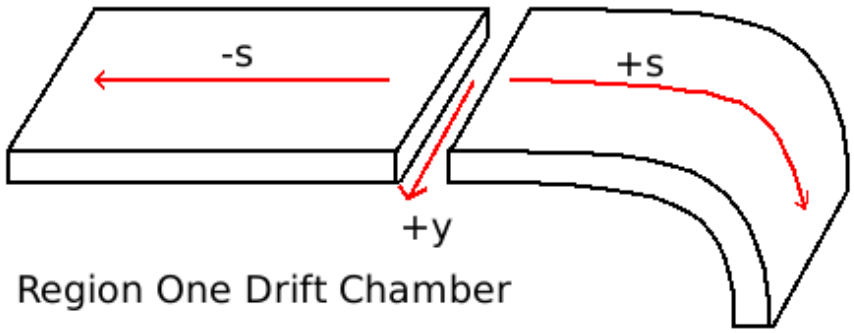

Figure 4.13: A drawing of the region 1 DC configuration, not to scale.

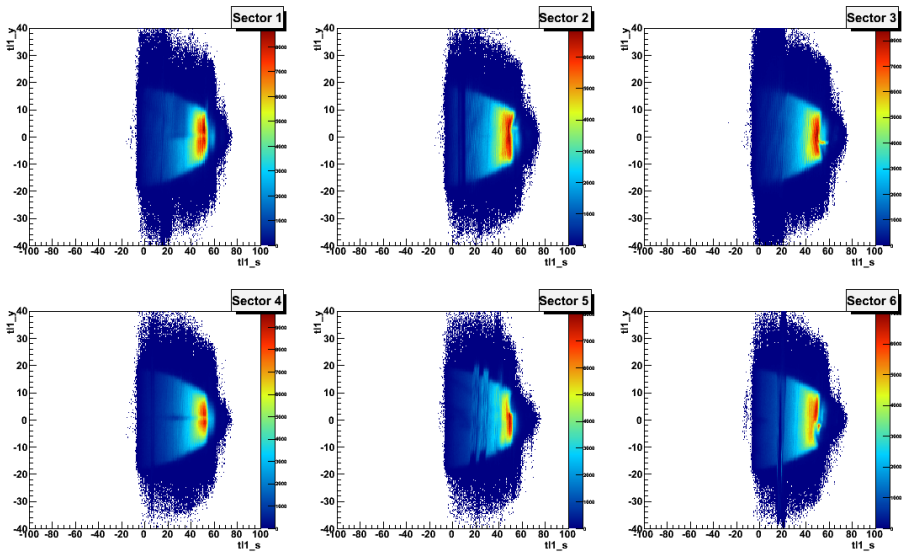

Figure 4.14: Track position in region 1 drift chamber for electrons, plotted in coordinates y and s_e, before cuts.

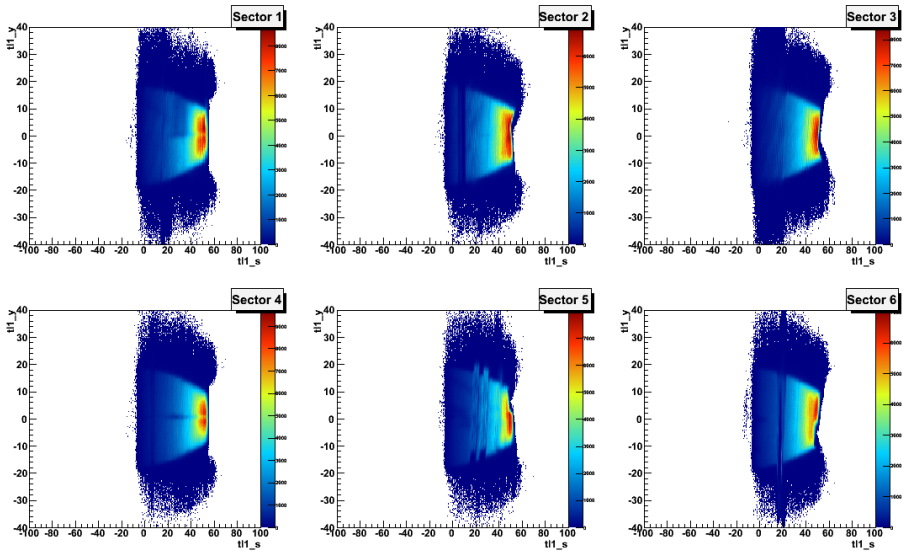

Figure 4.15: Track position in region 1 drift chamber for electrons, plotted in coordinates y and s_e, after IC shadow fiducial cut.

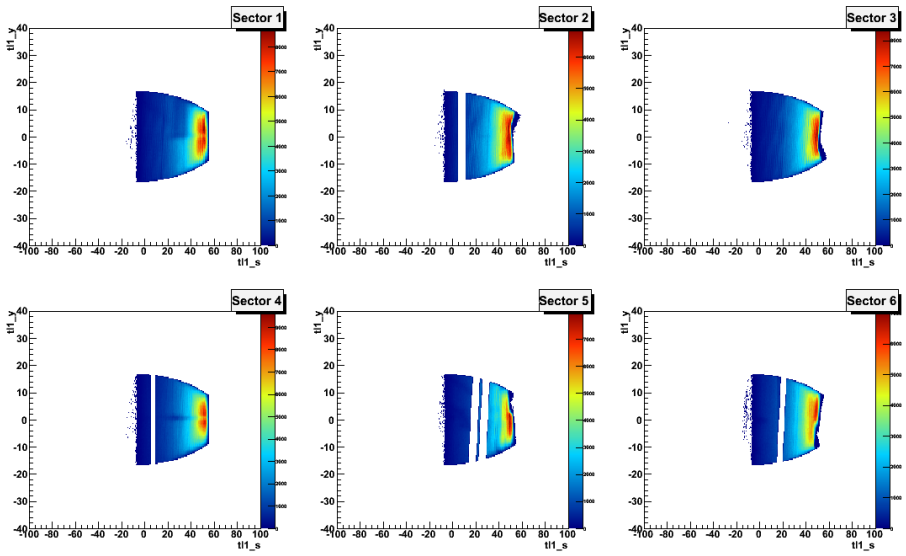

Figure 4.16: Track position in region 1 drift chamber for electrons, plotted in coordinates y and s_e, after IC shadow fiducial cut, and DC fiducial cut.

EC Fiducial Cut:

An event which is detected close to the edge of the EC might not be a trustworthy event. For example, a shower resulting from an electron or photon impinging on the surface of the calorimeter may leak out of the side, even before reaching the outer stack. This may result in an incorrectly measured energy deposit or hit position. To avoid such difficulties, cuts are applied based on the natural geometry of the EC.

The EC is divided into 39 layers, each consisting of a layer of scintillator and lead sheet which alternate 120° every layer. The three orientations are called u, v, and w, and are the natural variables on which our cut is made. u, v, and w may be obtained by a set of transformations on the ntuple22 variables "ech_x," "ech_y," and "ech_z" which represent the rectilinear position of each of the hits on EC with respect to CLAS center. This transformation involves rotations and translations based on the position, and the angles which the EC stacks are tilted, with respect to the beam line. The units of u, v and w are in centimeters.

The values chosen for the cuts in this analysis are:

$u > 40$ cm,

$v < 363$ cm,

$w < 395$ cm.

These cuts correspond to the edges of the detector. Additionally, there are some strips in the EC which underperformed during the experiment. Those must also be cut from the analysis. Viewing u, v, and w separately for each sector allows for one to identify which strips are dead or underperforming, and makes the removal a simple task. These dead strips are easily seen in Figure 4.17, in the lower right corner, which is the front view of the EC in the x, y coordinates.

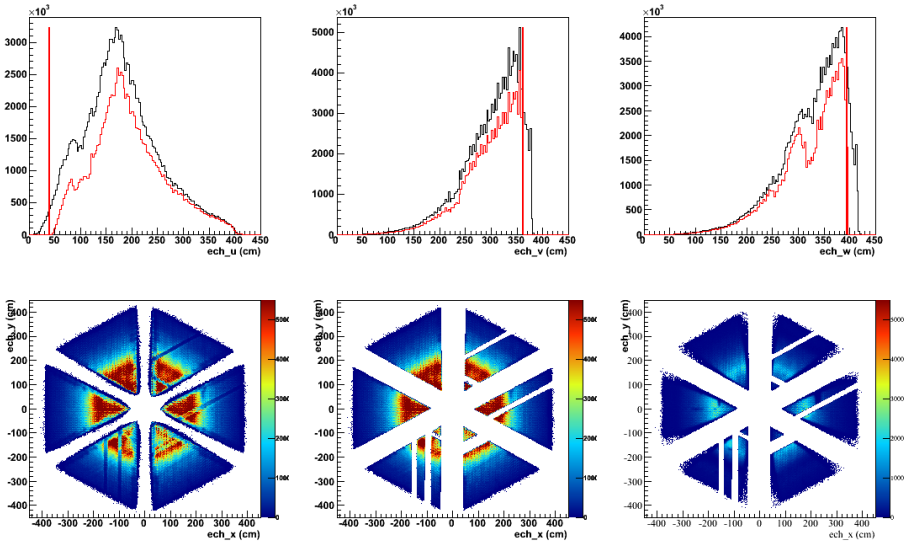

Figure 4.17: In the first row, from left to right, u, v, and w distributions for all sectors for electrons. The vertical red lines represent the cuts on the three variables. The black distributions are before all cuts, and the red distributions are after cuts on u, v, w, dead strips, and IC shadow cut. On the bottom row is the front face of the EC, in x and y, from left to right: before cuts; after cuts on u, v, w, and dead strips; and after cuts on u, v, w, dead strips, and IC shadow cut.

SC Fiducial Cut:

Because the surface area of the SC covers a larger space than the CC, a cut applied on CC will account for the edge of the SC. As seen in Figure 4.18 and Figure 4.19, the cut on the CC was sufficient to clean the edges of SC. However, the detector must still be inspected for dead paddles. A plot of the occupancy of the SC paddles as a function of run number will give a good idea as to the efficiency of the paddles. This may be seen in Figure 4.20. Each panel represents a sector. The y-axis represents paddle number. Each occupancy is normalized to the average number of hits over all sectors for that particular paddle number. In other words, for sector i, the value on the z-axis corresponds to the quantity

$$N_{i,\text{normalized}} = \frac{N_{i,\text{unnormalized}}}{\sum_{i=1}^{6} N_{i,\text{unnormalized}}}.$$

From this Figure, one may see that paddle number two in sector six has too low an efficiency. It turns out that this paddle is the only one which has an efficiency lower than 30%, and is the only one we have chosen to cut out.

One should note that the SC plane is better viewed in its natural coordinates, instead of in x and y shown below. However, since the cuts on CC preclude a need for a careful fiducial study, this is postponed until our analysis of protons in the TOF panels.

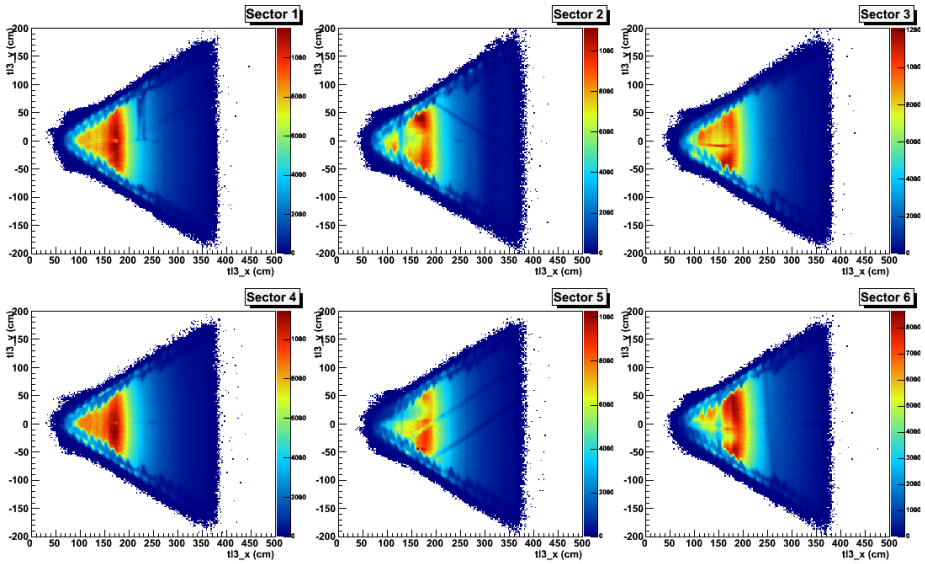

Figure 4.18: SC hit position for electrons, as determined by region 3 drift chambers before CC fiducial cuts, plotted in coordinates y and x.

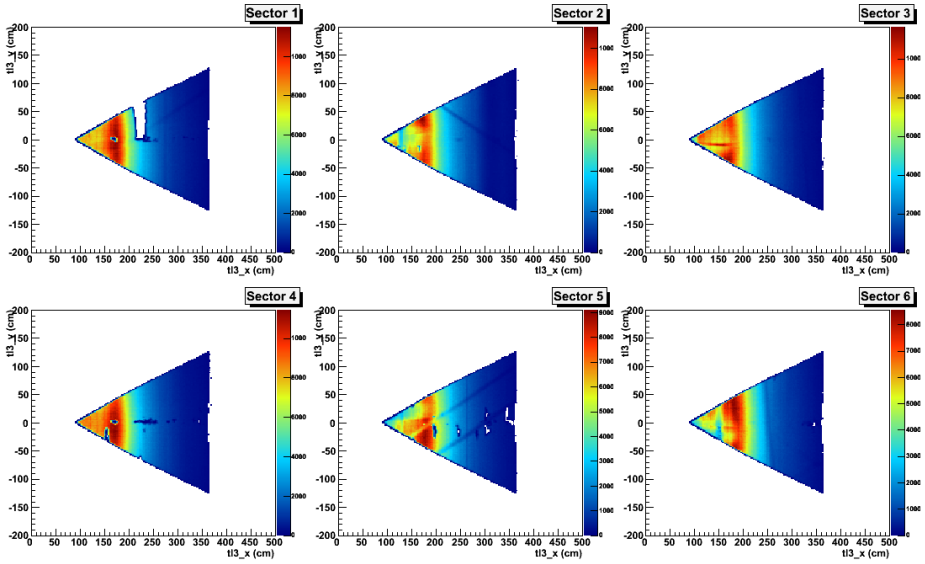

Figure 4.19: SC hit position for electrons, as determined by region 3 drift chambers, plotted in coordinates y and x, after CC fiducial cuts.

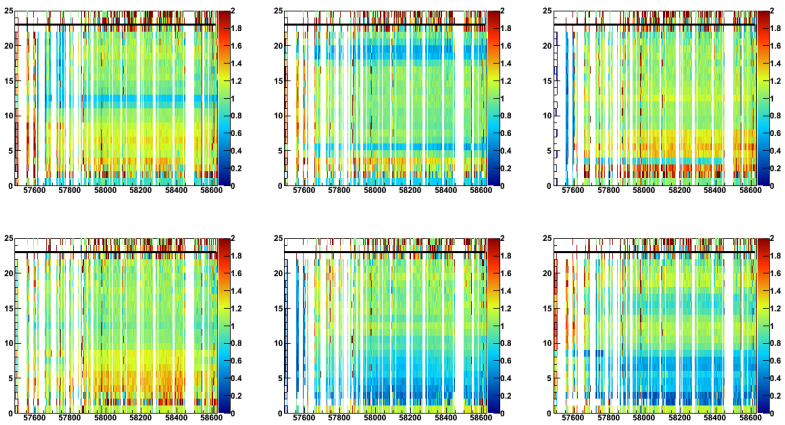

Figure 4.20: Occupancy of SC paddles as a function of run number. Each panel represents a sector. The y-axis represents paddle number. Each occupancy is normalized to the average number of hits over all sectors for that particular paddle number. In other words, for sector i, the value on the z-axis corresponds to the quantity $N_{i,\text{normalized}} = \frac{N_{i,\text{unnormalized}}}{\sum_{i=1}^{6} N_{i,\text{unnormalized}}}$.

4.2.2 Proton Identification

The following describes the criteria for a particle to be considered a proton, in addition to it being in coincidence with an electron.

Charge:

The charge of the proton must be restricted to +1. The method for determining the charge is the same as for the electrons: the curvature of the DC track must be out-bending (away from the beam line), and have good time-based tracking (TBT).

Velocity:

The strongest constraint that is placed on proton candidates compares the velocities of the proton by two different measurements:

$$\beta_{\text{TOF}} = \frac{\ell_{\text{track}}}{t_{\text{TOF}}}, \tag{99}$$

$$\beta_{\text{DC}} = \frac{p}{\sqrt{p^2 + m_p^2}}, \tag{100}$$

where ℓ_{track} is the length of the track as determined by DC, t_{TOF} is the time of flight, p is momentum determined by the curvature of the DC track, and m_p is the mass of the proton. These two quantities

should be equal, within a resolution effect, provided that the particle truly has a mass of m_p. The most convenient variable to look at is therefore the difference of these two velocities.

$$\Delta\beta = \beta_{\mathrm{TOF}} - \beta_{\mathrm{DC}} = \frac{\ell_{\mathrm{track}}}{t_{\mathrm{TOF}}} - \frac{p}{\sqrt{p^2 + m_p^2}}. \tag{101}$$

Since many variables require a momentum dependent cut, we plot this variable as a function of p. A visual inspection is enough to determine that the width of the peak at zero does not significantly broaden at any region, therefore a straight cut may be taken. The cut chosen for this analysis is $|\Delta\beta| < 0.05$. A plot illustrating this cut may be found in Figure 4.21, along with the resultant plot of β versus p corresponding to the same cut.

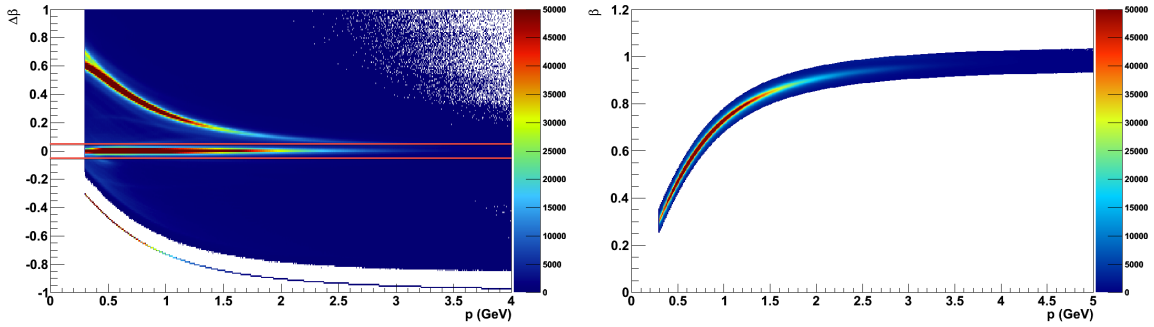

Figure 4.21: On the left, a plot of $\Delta\beta$ as a function of momentum p. The red lines represent the restriction that $|\Delta\beta| < 0.05$. On the right, β versus p of the particles selected by the cut applied on the left. Here, the protons are selected based on the requirement that the two different measurements of β are in agreement.

Vertex Correction and Cut:

The vertex cut that is placed on the proton follows the same procedure outlined for the electrons. First, a vertex correction must be applied, after which a vertex cut is applied such that the selected particles must satisfy: -61.25 cm $< v_z < -54.5$ cm.

The distribution of uncorrected and corrected vertex positions may be found in Figure 4.22, as well as the cut that was applied.

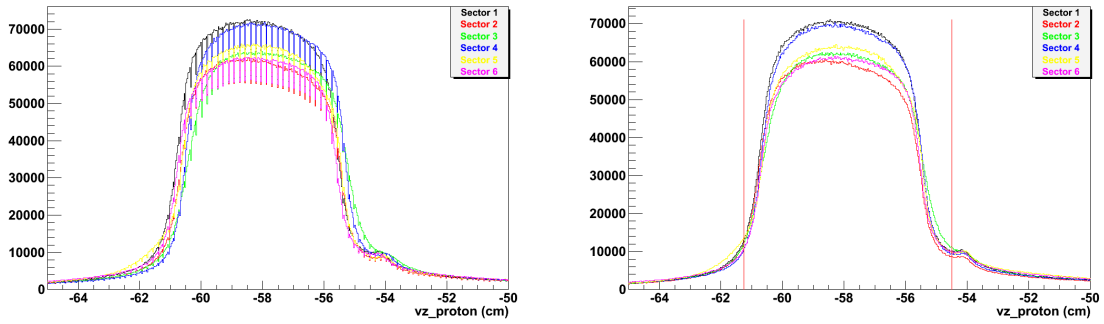

Figure 4.22: Vertex position of protons in z-direction. On the left, before corrections. On the right, after corrections. The red lines represent the final cut.

After separate vertex cuts on the electrons and protons, it is prudent to enforce one last requirement. Not only should all electrons and protons originate from the target. Each event with an electron and proton should have both particles originating from roughly the same location within the target. The most convenient way to verify this is by plotting the electron vertex position against the proton vertex position in the z direction. Another informative plot is one which shows the difference of these two values. It turns out that this distribution has a heavy momentum dependence, so it is more enlightening to see this difference plotted as a function of p. This distribution may be taken in slices of p, projected, and fitted to Gaussians. In this way, a momentum dependent cut may be employed depending on the varying sigma of the cut. The sigmas of the fit were determined to follow the relation $\sigma = 0.3526 + \frac{0.1121}{p-0.1579}$, and the final cut was taken at three times that value:

$$|v_{z,\text{electron}} - v_{z,\text{proton}}| < 3\sigma = 3(0.3526 + \frac{0.1121}{p - 0.1579}). \tag{102}$$

The difference of the electron and proton vertex positions as a function of momentum may be seen in Figure 4.23 with cuts displayed in red. The distributions of vertex positions of electrons versus protons before and after this cut may be seen in Figure 4.24 and Figure 4.25.

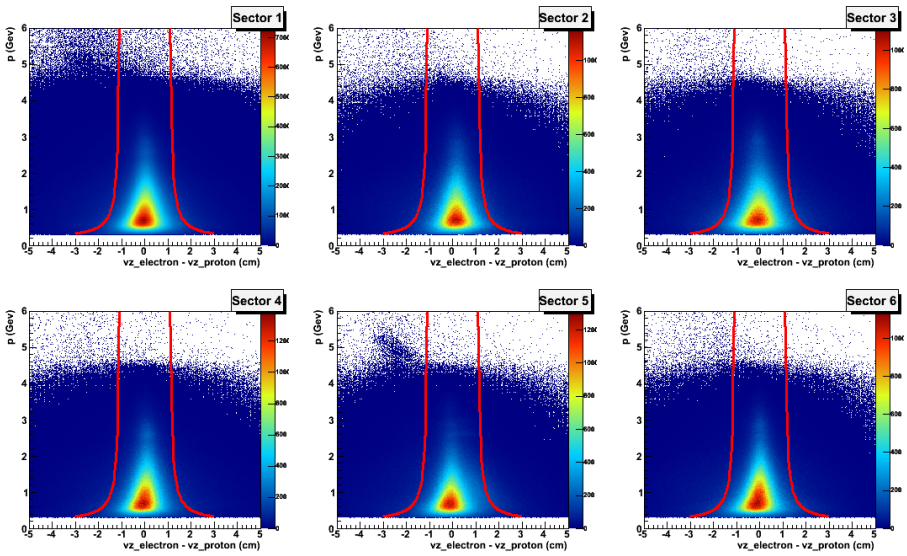

Figure 4.23: On the x-axis, the difference of electron and proton vertex position in the z direction. On the y-axis, momentum. The red lines correspond to the momentum dependent cuts at 3σ.

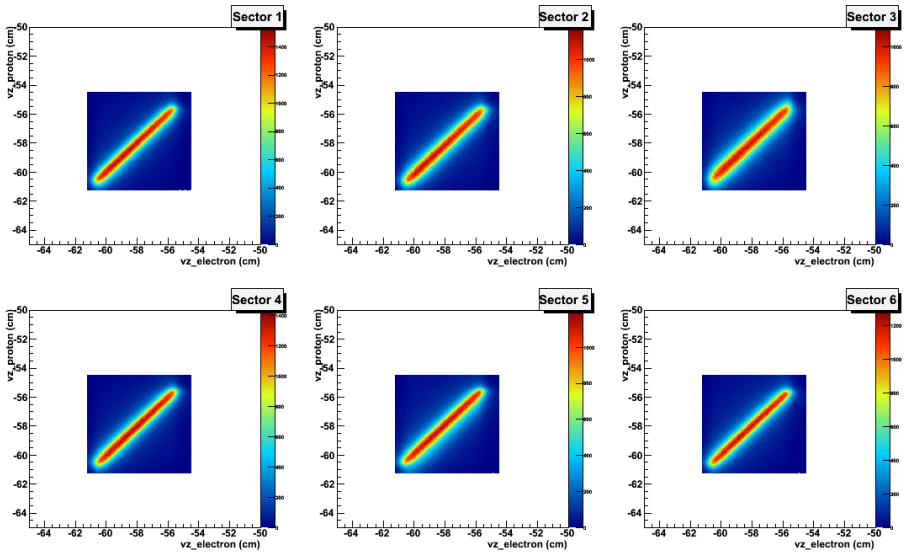

Figure 4.24: On the x-axis, vertex position in z direction for electrons. On the y-axis, vertex position in z direction for protons, before the cut described in Figure 4.23.

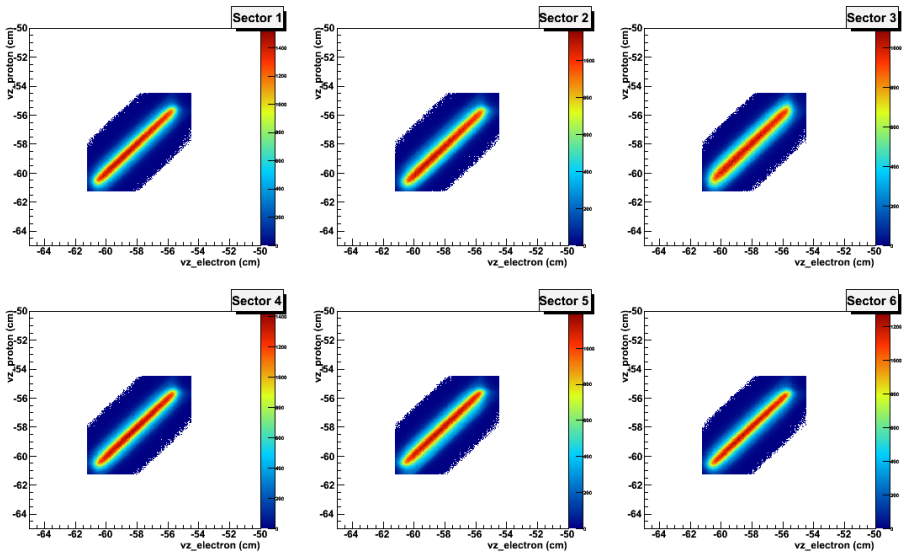

Figure 4.25: On the x-axis, vertex position in z direction for electrons. On the y-axis, vertex position in z direction for protons, after the cut described in Figure 4.23.

IC Shadow Cut:

As discussed previously, the parts of CLAS which are blocked by the IC must have a fiducial cut. The same general concept which was used for the electrons is used for the fiducial cuts for the protons. The shape is slightly modified to accommodate the differing structures appearing in the plot.

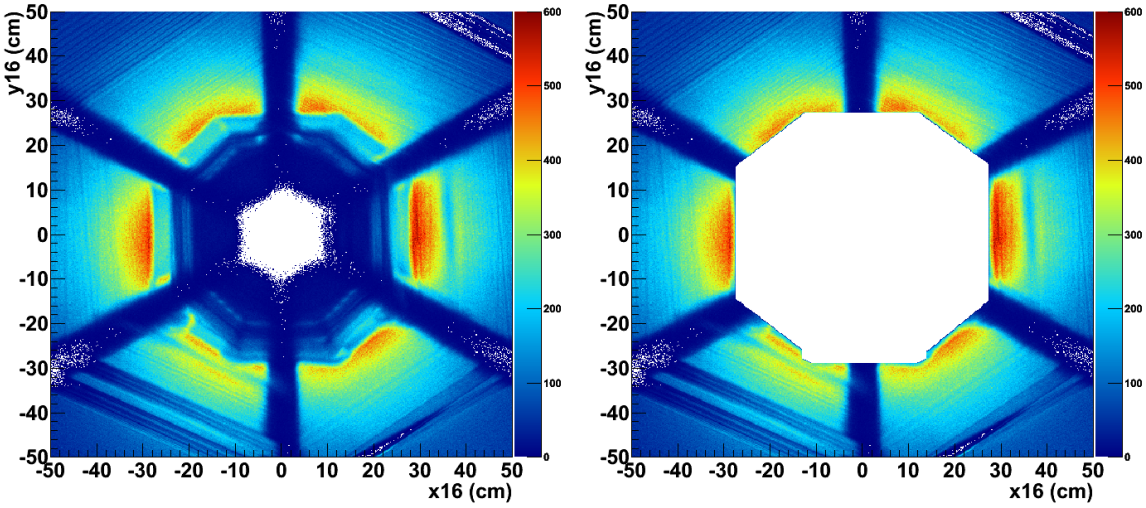

Figure 4.26: On the left, the intersection position of the proton candidate track on the plane which contains the back face of the IC. On the right, the same plot after fiducial cuts.

DC Fiducial Cut:

The special coordinates used for looking at the protons in region 1 of the DC follows the same procedure as for electrons. The parameters for the fits are slightly different, but the principle is the same. This view may be seen in Figure 4.27. The resulting cut is similar to the one for electrons:

$$|y| < 53\left(-0.5 + \frac{1}{1+\exp^{0.045(90-s_p)}}\right)$$

whose effect may be seen in Figure 4.29.

As discussed previously, there are several depletions and displacements which we have little hope of reproducing in simulations. It is prudent to omit events in those regions from the analysis. The displacements are found to be in the exact location as those for electrons, which reinforces our belief that it is a flaw in the region 1 DC or in the processing of its data, and not some other detector which is misbehaving. The effect of this cut may also be found in Figure 4.29.

The mathematical description of the cuts placed on the variables s_p and y are the same as the ones determined for the electrons, listed here again for convenience:

$$5 \text{ cm} < s_p < 11.5 \text{ cm}, \text{ sector 2}$$
$$5.5 \text{ cm} < s_p < 9 \text{ cm}, \text{ sector 4}$$
$$9 * (s_p - 15.5) \text{ cm} < y < 9 * (s_p - 22.5) \text{ cm}, \text{ sector 5}$$
$$9 * (s_p - 24) \text{ cm} < y < 9 * (s_p - 31) \text{ cm}, \text{ sector 5}$$
$$9 * (s_p - 16.5) \text{ cm} < y < 9 * (s_p - 22) \text{ cm}, \text{ sector 6}$$

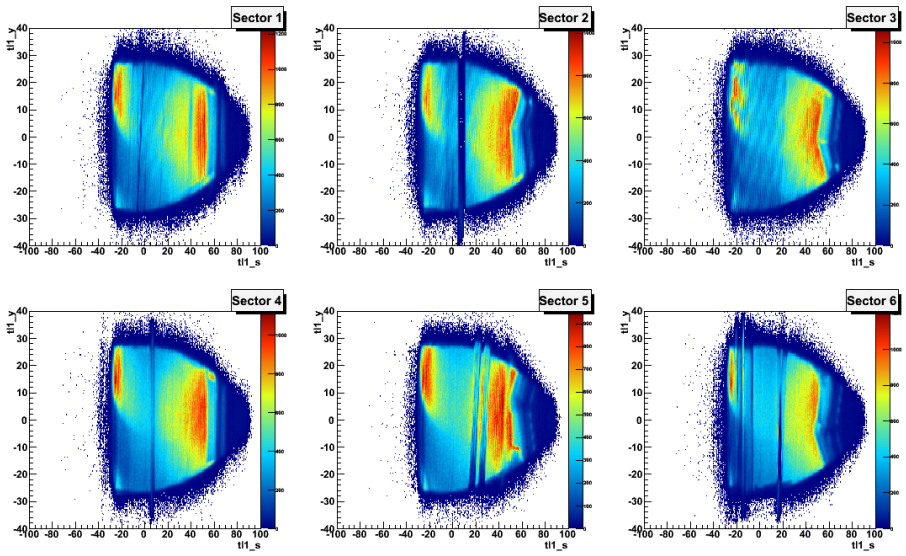

Figure 4.27: Track position in region one drift chamber for protons, plotted in coordinates y and s_p, before cuts.

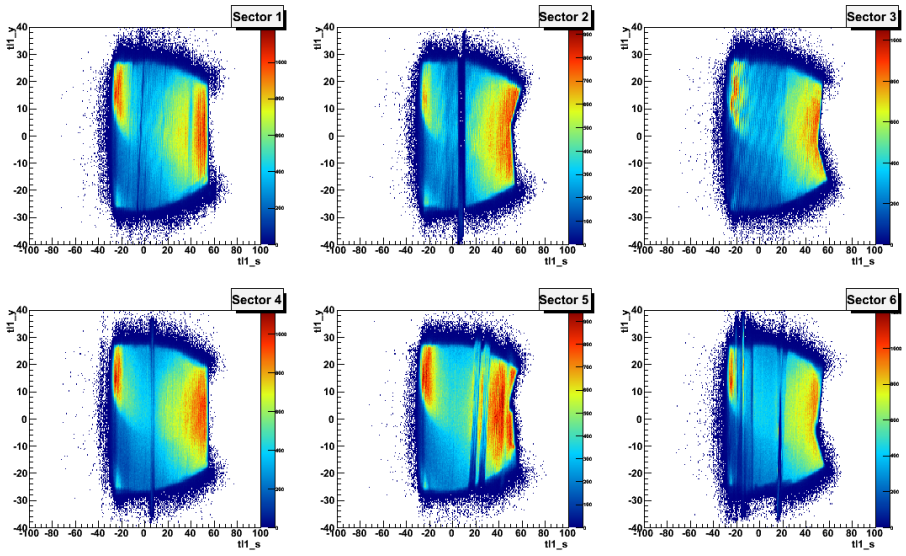

Figure 4.28: Track position in region one drift chamber for protons, plotted in coordinates y and s_p, after IC shadow fiducial cut.

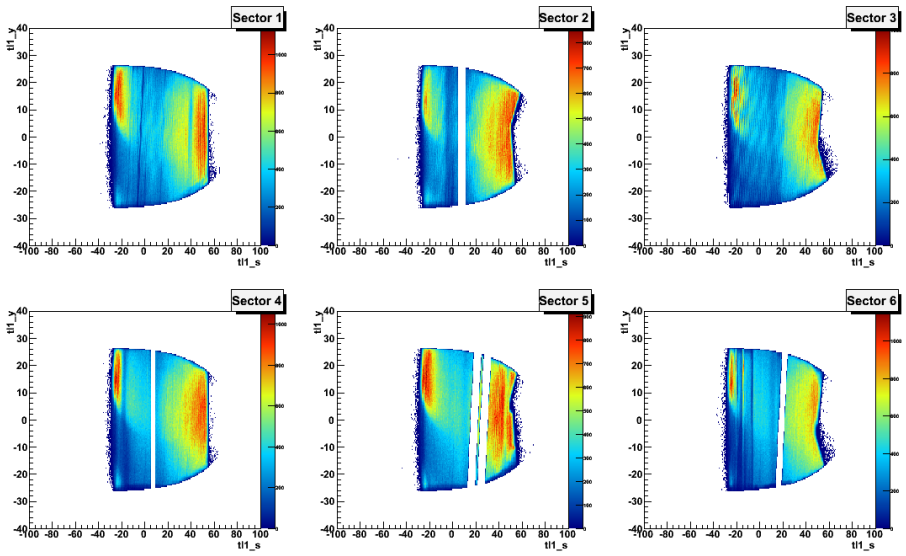

Figure 4.29: Track position in region one drift chamber for protons, plotted in coordinates y and s_p, after IC shadow fiducial cut, and DC fiducial cut.

SC Fiducial Cut:

The geometry of the SC panels is not complicated as seen in Figure 4.30. However, there are four flat panels, and a view in simple CLAS coordinates is not the best view by which one may determine a fiducial cut. Since the analysis we are concerned with only has a significant number of events in the first two panels, those are the only two which will concern us. Figure 4.30 illustrates the geometry of the detector for one sector, for the first two panels only. In the Figure, z runs in the direction of the beam line, x runs in the direction perpendicular to the beam line but contained in the plane bisecting the sector in question, by which y is uniquely defined, coming out of the page. Like the procedure described for region one DC, it is highly desirable to find a coordinate which is natural to the detector. The most convenient way, similar to region one DC is to preserve the y-axis while defining a new variable which we shall call t. t is defined as the distance along the sets of panels, perpendicular to the y-axis, relative to the intersection of panel 1 and 2. That is to say, the point of intersection of SC plane one and plane two has a value of $t = 0$. Everything in the direction of panel one has a coordinate such that $t > 0$. Everything in the direction of panels two and three has a coordinate such that $t < 0$. This parametrization allows for the simultaneous viewing of all three panels in a single plot of t as a function of y, as may be seen in Figure 4.31. Using this plot we may determine where the cuts are best made. A determination is made by eye, selecting events which satisfy the following for each panel separately:

$$panel\ one: \begin{cases} t > -200 \text{ cm} \\ t < 10 \text{ cm} \\ |y| < 0.5(x + 340) \text{ cm} \end{cases}$$

$$panel\ two: \begin{cases} t > 25 \text{ cm} \\ t < 260 \text{ cm} \\ y < +0.1(x + 1750) \text{ cm} \\ y > -0.09(x + 1750) \text{ cm} \end{cases}$$

both of whose effect may be seen in Figure 4.32.

A close inspection of Figure 4.32 reveals that there are several depletions present in each of the sectors. Some of the aberrations are vertical strips. Others have more complicated geometry. Of both categories, there are varying degrees of definiteness in the shapes. The vertical bands correspond to TOF paddles which are either dead for part of the experiment, or are inefficient. Because of the inefficiencies, the number of events in those regions cannot be trusted. Therefore, each paddle corresponding to a depletion must be cut. It was determined that the most inefficient paddles were:

sector 2, paddle 27
sector 2, paddle 34
sector 3, paddle 34
sector 4, paddle 31.

A cut which rejects events based on the paddle number variable was implemented, whose effect may be seen in Figure 4.33. A curious feature of this plot is the lack of sharpness of this cut when viewed in the coordinates t and y. The cause of this blurriness is the symptom of how the variables for TOF position are reconstructed. The position of the hit in TOF is determined by extrapolating the track position in region 3 DC. After this straight line extrapolation, the intersection this line and of the panel plane which contains the fired paddle is taken. It is not necessary that this intersection point be in agreement with the position of the paddle, although it is most often intersecting. Because of the rare cases in which the two are not in agreement, there will be stray events which missed by a cut which is only made based on paddle number. Therefore, a more careful cut will include a geometrical cut on the coordinates of the paddle as well. This is represented by the following equations:

$$85 \text{ cm} < t < 110 \text{ cm}, \text{ sector 2}$$
$$242 \text{ cm} < t < 300 \text{ cm}, \text{ sector 2}$$
$$240 \text{ cm} < t < 300 \text{ cm}, \text{ sector 3}$$
$$176 \text{ cm} < t < 198 \text{ cm}, \text{ sector 4}.$$

whose effect may be seen in Figure 4.34.

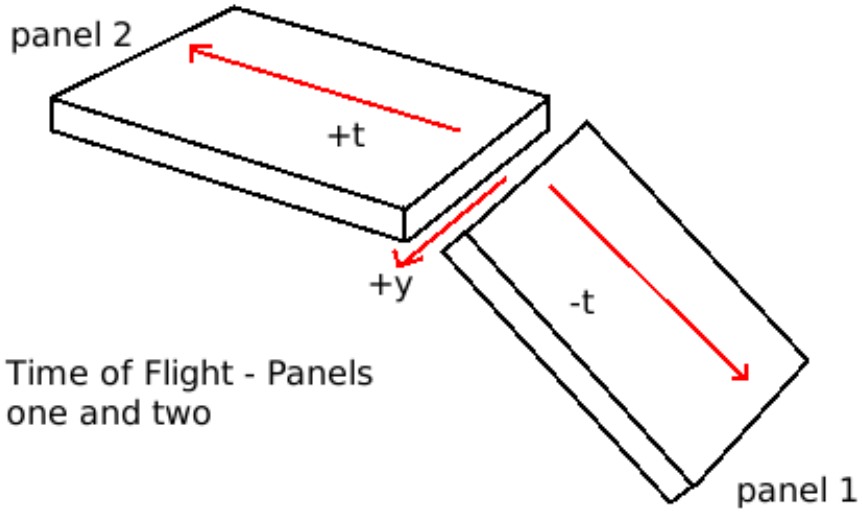

Figure 4.30: A drawing of the first two panels of the Time of Flight configuration, not to scale.

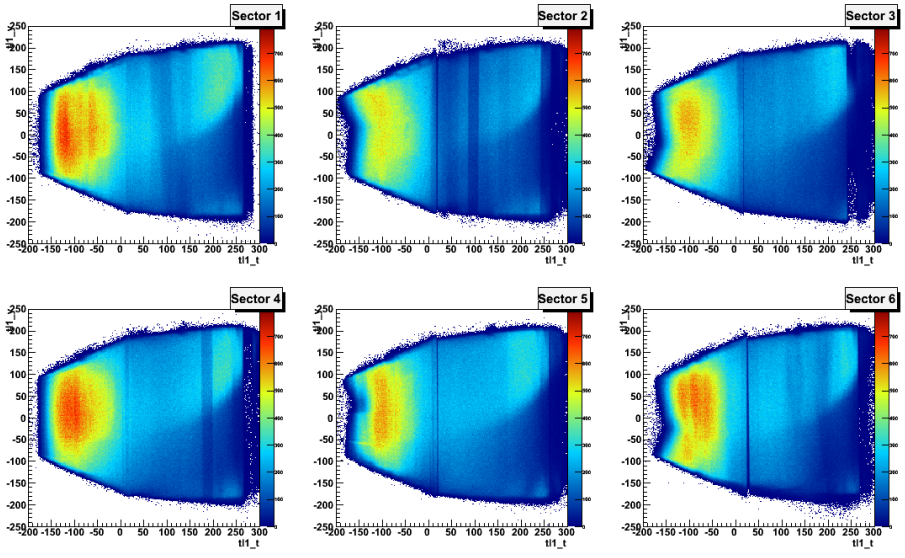

Figure 4.31: SC hit position for electrons, as determined by region 3 drift chambers, plotted in coordinates y and t, before cuts.

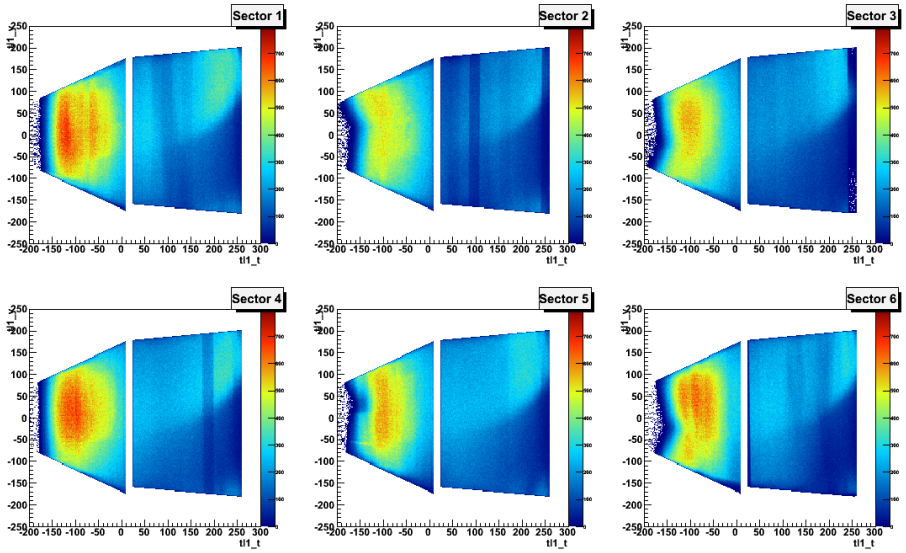

Figure 4.32: SC hit position for electrons, as determined by region 3 drift chambers, plotted in coordinates y and t, after a geometrical fiducial cut on panels one and two.

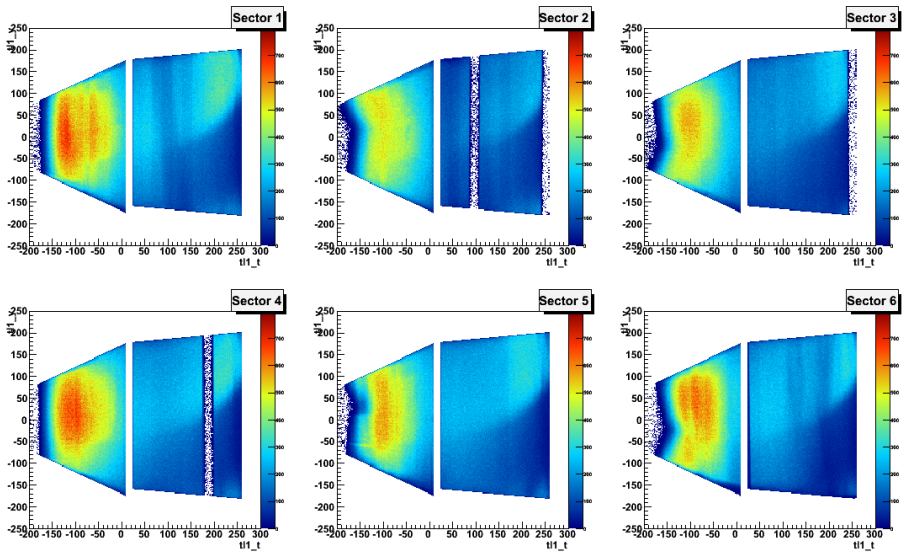

Figure 4.33: SC hit position for electrons, as determined by region 3 drift chambers, plotted in coordinates y and t, after a geometrical fiducial cut on panels one and two, and a cut on paddle number.

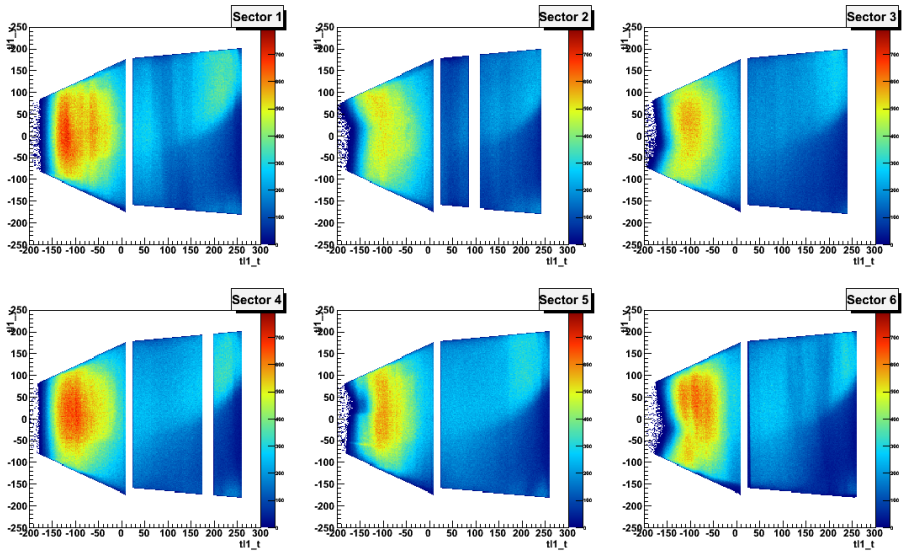

Figure 4.34: SC hit position for electrons, as determined by region 3 drift chambers, plotted in coordinates y and t, after a geometrical fiducial cut on panels one and two, a cut on paddle number, and a cut on the coordinates of dead paddles.

4.2.3 Photon Identification - EC

The following describes the criteria for a particle to be considered a photon, in addition to it being in coincidence with an electron and a proton.

Charge:

The charge of the photon must be restricted to 0. Unlike charged particles, there are no tracks in the DC associated with neutral particles. A neutrally charged particle must therefore not be associated with any DC track, curved or otherwise.

Velocity:

The velocity of the photon is $\beta = 1$. However, because of resolution effects in CLAS, there is some variance in the measured values. For this reason, a range of acceptable β's must be decided upon. Before describing this determination, we must diverge for a moment to describe a peculiar feature of the data reduction program: its requirement for a particle to be identified as a photon is: $\beta > 0.95$. This is much too restrictive for this analysis. To complicate matters, any particle with a $\beta > 0.95$ which becomes categorized as a neutron by this program also has it's variables β and p altered to reflect this. Both β and p variables are forced to exactly obey the relation $\beta = \frac{p}{\sqrt{p^2+m^2}}$. A plot of β as a function of p is shown in Figure 4.35.

The actual β and p must be restored. The real value of β for neutrals is determined by the timing from EC and from the distance of the hit in the EC to the vertex position.

$$\beta_{\rm rec} = \frac{||\mathbf{r}||}{c(t_{\rm EC} - t_{\rm tr})}, \tag{103}$$

given

$$\mathbf{r} = \mathbf{e} - \mathbf{v}, \tag{104}$$

where $t_{\rm EC}$ is the timing in EC from which is subtracted the reference time (trigger time) $t_{\rm tr}$; $\mathbf{e}$ is the vector running from CLAS center to the hit in the EC; and $\mathbf{v}$ is the vector running from CLAS center to the corrected vertex position of the electron which was detected in coincidence.

The reconstruction of p is accomplished by knowing the expected sampling fraction of EC for showering particles. $f_s = \frac{E_{\rm total}}{p} \approx 0.273$. It is useful to note that this sampling fraction is not uniform in momentum p. Simulations for photons show that there is an increase in the average value

of sampling fraction as momentum increases, as well as a decrease in the standard deviation of the distribution. A similar distribution may be seen for electron in both data and simulation.

With both β and p reconstructed, one may view the actual plot of β as a function of momentum. A plot of the reconstructed values of β versus p is shown in Figure 4.35.

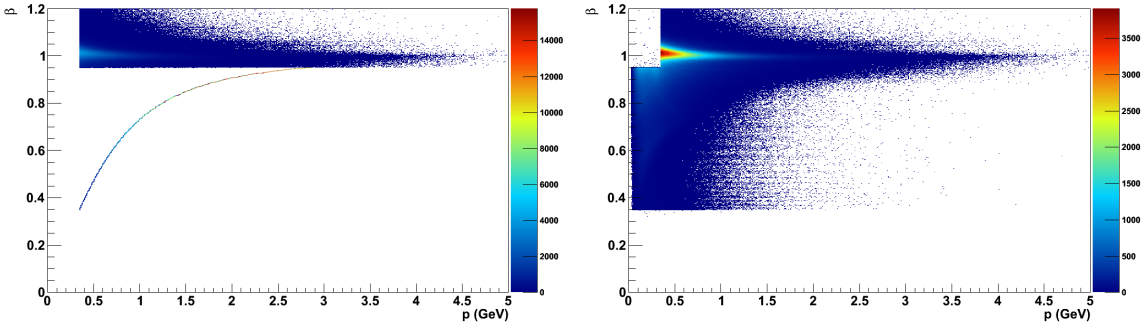

Figure 4.35: On the left, the raw values of β as a function of p. Entries with values of β less than .95 have their momenta and velocities forced to agree as if they were neutrons. On the right, the reconstructed values of β versus p, allowing for us to accept photons lower than $\beta = .95$.

From this restored graph of momentum versus β, a determination of the velocity cut may finally be explored. This is easily accomplished by looking at the velocity distribution of the photon candidates. As expected, one sees a peak at $\beta = 1$, representing a distribution of photons, and a tail trickling down from $\beta = 1$ towards zero, representing the neutrons. A straightforward selection involves fitting this distribution to a Gaussian with a polynomial background. The final cut is taken only on the low (left-hand) side, at a value of $\beta = 0.9$, seen in Figure 4.36. The width of this cut is conservatively loose, and made with the expectation that any neutrons which are accidentally selected will be removed by exclusivity cuts.

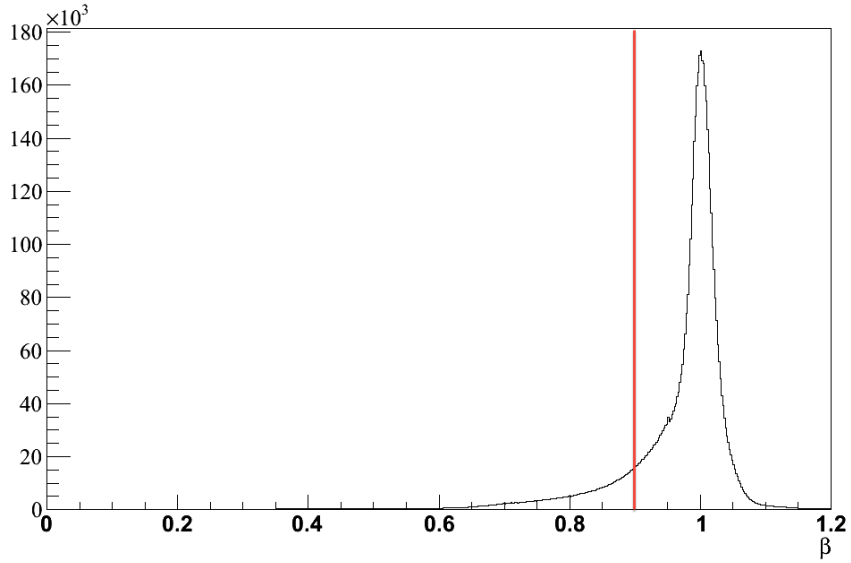

Figure 4.36: βs for photon candidates, with a cut accepting only particles with $\beta > 0.9$.

EC Energy Restriction:

The energy of the photon must be at least 0.35 GeV.

EC Fiducial Cut:

The values chosen for the cuts in this analysis are:

$u > 40$ cm, $v < 363$ cm, and $w < 395$ cm, which are equivalent to the cuts that were made for the electrons. These cuts correspond to the edges of the detector. Additionally, there are some strips in the EC which underperformed during the experiment. As done for the electrons, those must also be cut from the analysis. The same strips are removed as for the electrons. The effects of these cuts may be seen in Figure 4.37.

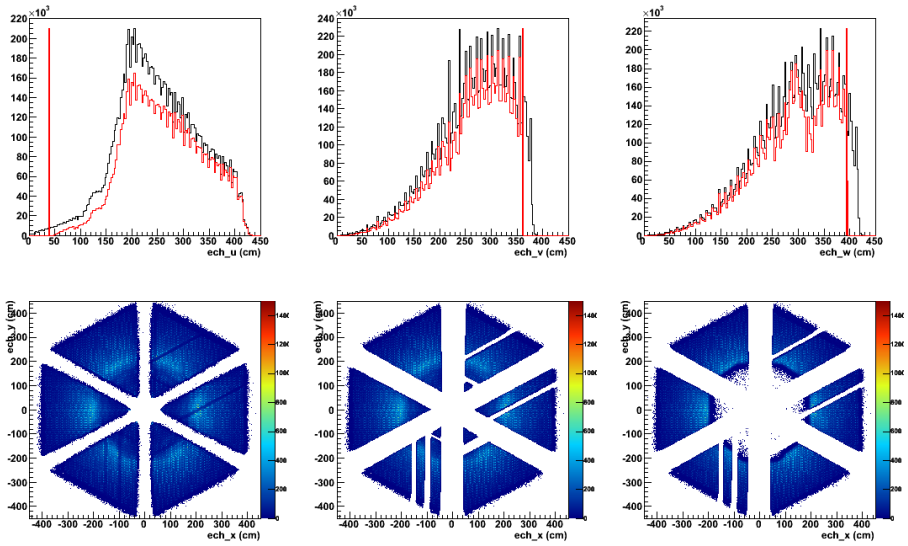

Figure 4.37: In the first row, from left to right, u, v, and w distributions for all sectors for photons. The vertical red lines represent the cuts on the three variables. The black distributions are before all cuts, and the red distributions are after cuts on u, v, w, dead strips, and IC shadow cut. On the bottom row is the front face of the EC, in x and y, from left to right: before cuts; after cuts on u, v, w, and dead strips; and after cuts on u, v, w, dead strips, and IC shadow cut.

EC Timing Calibration

As we have already mentioned, one of the primary techniques for distinguishing photons from neutrons in CLAS is to make a cut on velocity β. Since an accurate determination of β for neutrals was based on a fine timing measurement of particles in the EC, a very careful calibration of this detector was required in order to make a good separation between photons and neutrons.

The method[46] of calibrating EC timing makes the assumption that SC timing is accurate, therefore SC timing calibrations must precede EC timing calibrations. The calibration was achieved by the following method: We define the expected time it takes for a particle to reach the EC as:

$$t_{\text{expected},i} = \frac{L}{c} + \frac{\ell_i}{v}, \tag{105}$$

where L is the distance between the centroid of the hit in the EC and the vertex position, c is the speed of light in vacuum, making the assumption that the particle travels almost completely through vacuum, ℓ_i is the amount of time it takes for the shower in the signal to travel to the PMT in the i-orientation - u, v or w, and v is the speed of propagation in the plastic scintillator, which is known to be 18.1 cm/ns.

We also define the model time, which relates the time for a neutral particle to reach the EC to the ADC values and TDC values:

$$t_{\text{model},i} = a_0 + a_1 \text{TDC}_i + \frac{a_2}{\sqrt{\text{ADC}_i}} + a_3 \ell_i^2 + a_4 \ell_i^3 - T_{\text{vertex}}, \tag{106}$$

where a_0 is a constant time which takes into account cable lengths and the zeroth-order term of the light attenuation term $\exp -\ell_i/\ell_0$, a_1TDC is the TDC constant which also accounts for the first-order term of the light attenuation term, $\frac{a_2}{\sqrt{\text{ADC}_i}}$ is the time-walk correction and ADC term, and $a_3\ell_i^2 + a_4\ell_i^3$ are the second and third order terms from light-attenuation. T_{vertex} serves as the reference time at the vertex.

The calibration program makes use of least-squares method of minimizing the errors of the time difference, namely:

$$\chi_j^2 = \sum_{i=1}^{N_i} \frac{|T_{\text{expected},i} - T_{\text{model},i}|^2}{N_j}. \tag{107}$$

A final note is that this calibration program worked best with the use of photons since they provided the best resolution. The photon selection used in the program is listed below:

- Neutral charge EC hit is detected within the fiducial region.
- No multiple hits in the same sector. This is to prevent difficulties arising in resolution between same-sector hits.
- A minimum of 100 MeV in a hit in order to eliminate accidentals.
- A demand of a hit in the inner stack in order to eliminate neutrons.

The effect of the calibration is displayed in Figure 4.38, before and after EC calibration. The fitness of the timing is judged by looking at the time difference between the EC and the SC. An ideal situation would be complete agreement, with the difference being near zero. We can also look at the velocity of photons, and ensure that their reconstructed velocities are c.[46]

IC Shadow Cut:

As discussed in previously, the parts of CLAS which are blocked by the IC must have a fiducial cut. The same general concept which was used for the electrons and protons is used for the fiducial cuts for the photons. The shape is slightly modified to accommodate the differing structures appearing in the plot.

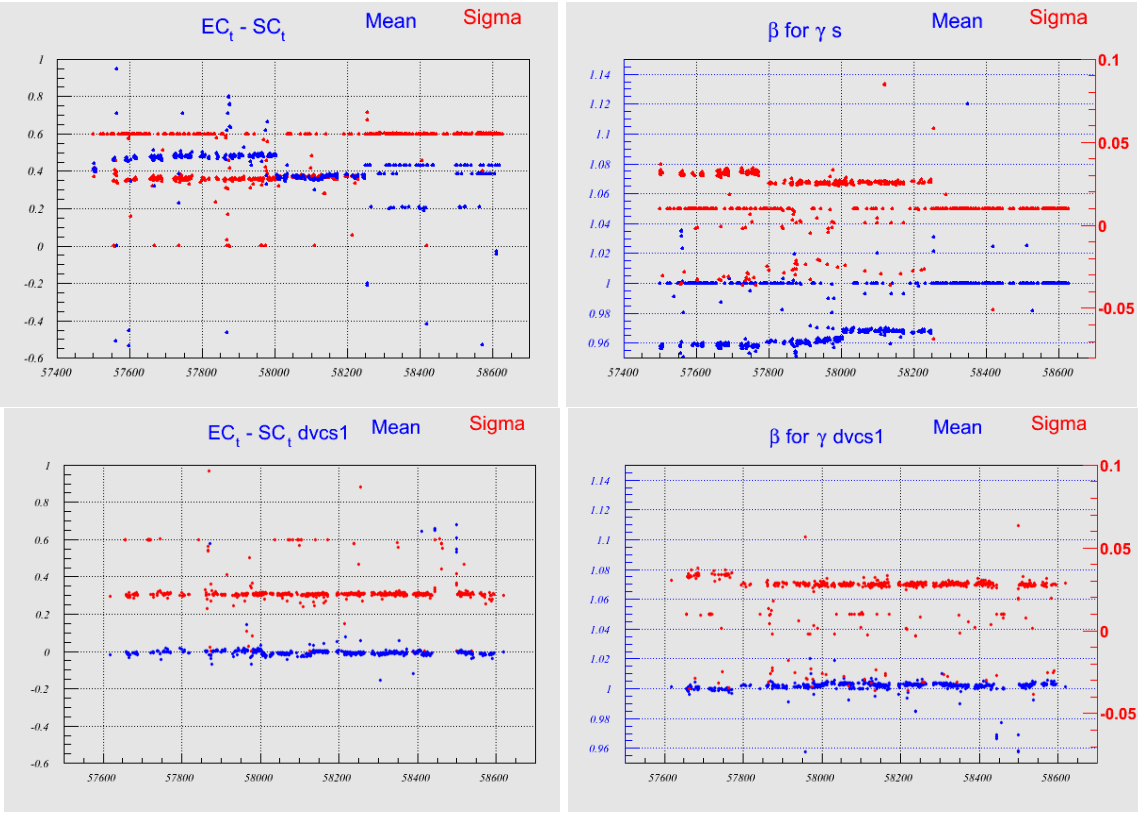

Figure 4.38: The left column represents the difference between the times as measured by the EC and the SC as a function of run number. The units of the ordinate are in nanoseconds. The right column represents the reconstructed velocity of the photons as a function of run number. The top row represents these values before EC timing calibrations. The bottom row represents these values after EC timing calibrations. We note that there is a very good improvement after the calibration. We make note that on the top row, there are series of points which are all at a fixed value, such as 0.06 for the sigma of the timing difference, and 1.0 and 1.05 for the mean and sigma of the velocity of photons respectively. This exact assignment to these values is a sign that the calibration routine had failed, and that these initial values were entered.

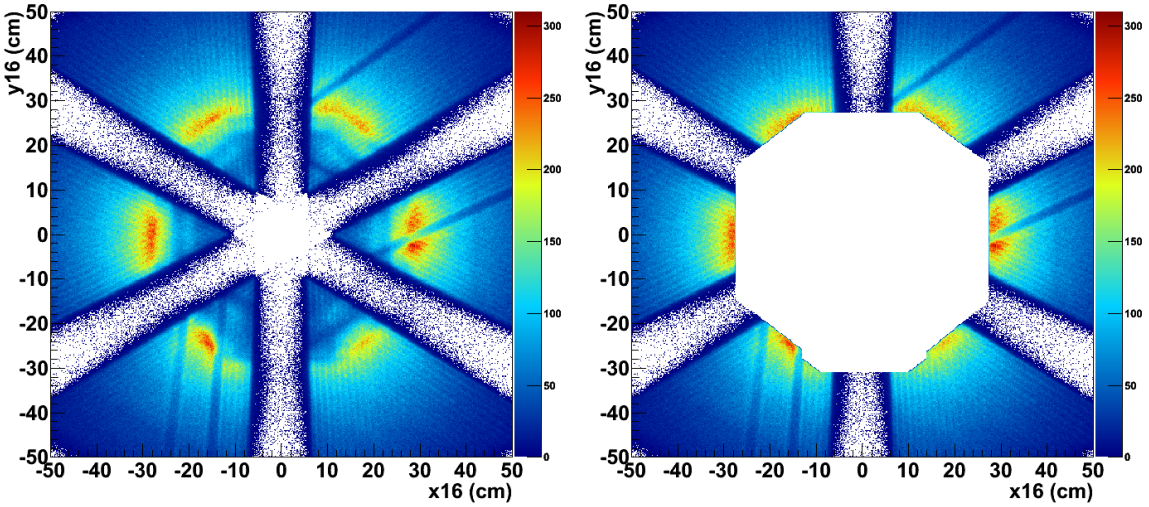

Figure 4.39: On the left, the intersection position of the photon candidate track on the plane which contains the back face of the IC. On the right, the same plot after fiducial cuts.

4.2.4 Photon Identification - IC

IC Fiducial Cut:

The fiducial cut for the photons detected in the IC accomplishes two things. Firstly, it removes particles detected near the edges of the detector. Secondly it removes a single hot crystal near $x = -5.5$ cm, $y = -8$ cm. An additional restriction is made on the polar angle of the photon during the DVCS analysis, but is not included in the initial particle identification.

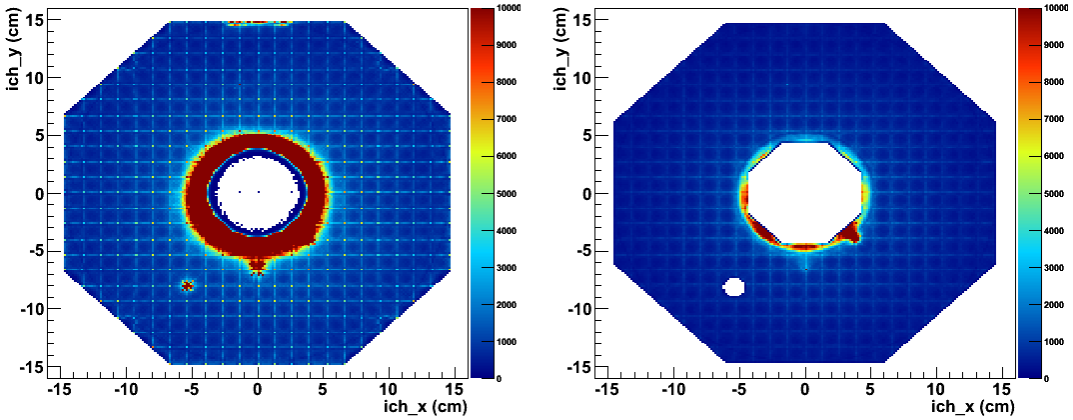

Figure 4.40: The IC, on the left, before fiducial cuts, on the right, after fiducial cuts.

IC Energy Restriction:

The energy of the photon must be at least 0.35 GeV.

4.2.5 Neutral Pion π^0 Identification

The selection process for neutral pions is based on the $\pi^0 \to \gamma + \gamma$ decay mode. This relies on the photon selection described above in both IC and EC. A large portion of this analysis will be focused on the removal of neutral pions whose decay photons may be accidentally selected as a DVCS or BH photon via the channel $e + p \to e + p + \pi^0 \to e + p + \gamma + \gamma$, where either one or both photons have been detected. A detailed description of this selection will be delayed until Section 4.8.

4.2.6 Summary of Cuts

Table 4.2: A table of cuts used in the identification of electrons.

Electron	
Charge	$q = -1$
Momentum	$p > 0.8$ GeV
Energy in Inner Stack of EC	$E_i = 0.06$ GeV
Sampling Fraction of EC	$\mu(p) - 2.5\sigma < f_s < \mu(p) + 2.5\sigma$, where: $\mu(p) = 0.336948 - 0.0321597p$ $+0.00433749p^2 - 0.000159799p^3$ $\sigma(p) = 0.00635095 + \frac{0.0621754}{\sqrt{p}}$
Electron Vertex Cut	-61.25 cm $< V_{z,\text{electron}} < -54.5$ cm
CC Fiducial Cut	For all sectors: $\lvert\phi_v\rvert < -68.975 + 36.996 \ln\theta_v - 1.670\theta_v + 0.011\theta_v^2$ $\theta_v < 43.0 + 0.05\lvert\phi_v\rvert + 0.003\lvert\phi_v^2\rvert$ Excluding in sector 1 events where: $\phi_v > 0$, $\theta_v > 25$ and $\theta_v < 27.5 + 0.027\lvert\phi_v\rvert + 0.002\lvert\phi_v\rvert^2$ Excluding a single dead PMT in sector 1 Excluding $\epsilon_{\text{CC}}(\theta_v, \phi_v) < 80\%$ for each sector
IC Shadow Fiducial Cut	Geometry is complicated. See Figure 4.12.
DC Fiducial Cut	$\lvert y\rvert < 35\left(-0.5 + \frac{1}{1+\exp^{0.045(80-s_e)}}\right)$ cm Excluding: 5 cm $< s_e <$ 11.5 cm, sector 2 5.5 cm $< s_e <$ 9 cm, sector 4 $9(s_e - 15.5)$ cm $< y < 9(s_p - 22.5)$ cm, sector 5 $9(s_e - 24)$ cm $< y < 9(s_p - 31)$ cm, sector 5 $9(s_e - 16.5)$ cm $< y < 9(s_p - 22)$ cm, sector 6
EC Fiducial Cut	$u > 40$ cm, $v < 363$ cm, $w < 395$ cm Removal of dead strips. Geometry is complicated. See Figure 4.17.
SC Fiducial Cut	Geometrical cut accomplished by CC Fiducial Cut Excluding: sector 6, paddle 2

Table 4.3: A table of cuts used in the identification of protons.

Proton	
Charge	$q = +1$
Good Time Based Tracking	
Velocity	$\lvert\Delta\beta\rvert = \lvert\beta_{\text{TOF}} - \beta_{\text{DC}}\rvert = \left\lvert \frac{\ell_{\text{track}}}{t_{\text{TOF}}} - \frac{p}{\sqrt{p^2+m_p^2}} \right\rvert < 0.05$
Proton Vertex Cut	$-61.25 \text{ cm} < V_{z,\text{proton}} < -54.5 \text{ cm}$
Electron-Proton Vertex Cut	$\lvert V_{z,\text{electron}} - V_{z,\text{proton}}\rvert < 3\sigma = 3\left(0.3526 + \frac{0.1121}{p-0.1579}\right)$
IC Shadow Fiducial Cut	Geometry is complicated. See Figure 4.26.
DC Fiducial Cut	$\lvert y\rvert < 53\left(-0.5 + \frac{1}{1+\exp^{0.045(90-s_p)}}\right)$ cm Excluding: $5 \text{ cm} < s_p < 11.5 \text{ cm}$, sector 2 $5.5 \text{ cm} < s_p < 9 \text{ cm}$, sector 4 $9(s_p - 15.5) \text{ cm} < y < 9(s_p - 22.5) \text{ cm}$, sector 5 $9(s_p - 24) \text{ cm} < y < 9(s_p - 31) \text{ cm}$, sector 5 $9(s_p - 16.5) \text{ cm} < y < 9(s_p - 22) \text{ cm}$, sector 6
SC Fiducial Cut	*panel one* : $t > -200$ cm, $t < 10$ cm, $\lvert y\rvert < 0.5(x + 340)$ cm *panel two* : $t > 25$ cm, $t < 260$ cm, $y < +0.1(x + 1750)$ cm, $y > -0.09(x + 1750)$ cm Excluding: sector 2, paddle 27 sector 2, paddle 34 sector 3, paddle 34 sector 4, paddle 31. $85 \text{ cm} < t < 110 \text{ cm}$, sector 2 $242 \text{ cm} < t < 300 \text{ cm}$, sector 2 $240 \text{ cm} < t < 300 \text{ cm}$, sector 3 $176 \text{ cm} < t < 198 \text{ cm}$, sector 4.

Table 4.4: A table of cuts used in the identification of EC photons.

Photon - EC	
EC Energy	$E_\gamma > 0.35$ GeV
Charge	$q = 0$
Velocity	$\beta > 0.9$
EC Fiducial Cut	$u > 40$ cm, $v < 363$ cm, $w < 395$ cm Removal of dead strips. Geometry is complicated. See Figure 4.37.
IC Shadow Fiducial Cut	Geometry is complicated. See Figure 4.39.

Table 4.5: A table of cuts used in the identification of IC photons.

Photon - IC	
IC Energy	$E_\gamma > 0.35$ GeV
IC Fiducial Cut	Geometry is complicated. See Figure 4.40.

4.3 Acceptance

4.3.1 Definition of the Acceptance of CLAS

The CLAS detector only detects a certain percentage of events which occur. A reason for this reduction in events is due to the many gaps in the detector. In particular, the regions behind the torus coils and at large θ are not covered by detectors. The presence of various flaws within CLAS also contributes to a reduction in events detected. There are also detectors with less than desirable efficiencies, or detectors which are malfunctioning or switched off. Because CLAS will only detect a certain fraction of the actual events, we must estimate the fraction of events which are missed by the detector.

Let us define the acceptance A as the fraction of events, for any reaction, which are detected by CLAS. That is to say, if the number of events detected by CLAS is N_{detected}, which we will refer to as the yield, and the number of events which actually occurred is N_{actual}, which we will refer to as the normalized yield, then the acceptance is defined by the relation:

$$A = \frac{N_{\text{detected}}}{N_{\text{actual}}}. \tag{108}$$

The role of the number A in the cross section is to rescale the number of detected events to the expected actual number of events. This formula is valid for any channel. For DVCS, the equation would be:

$$A = \frac{N_{e+p\to e'+p'+\gamma}}{N_{\text{actual}}}. \tag{109}$$

For other channels which we will study, such as $e + p \to e' + p' + \pi^0$ or elastic scattering, one need only replace N_{detected} with the number of events detected of the proper channel.

The quantity A cannot be measured exactly from the actual experiment. We can only determine the acceptance from simulations of the experiment, and from our knowledge of the detector's geometry and properties. The solution can be outlined in three steps. First, an ensemble of events may be generated by simulation over a kinematical region which is similar to the actual experiment. We will call this number: $N_{\text{generated}}$. Second, the response of CLAS to each of these generated events may be simulated. That is to say, we can estimate the number of events which were measured by CLAS according to the simulation. We will call this number: $N_{\text{reconstructed}}$. This is determined by taking the events from the event generator and running them through a program called GSIM which uses GEANT3 to simulate the detector. Third, the ratio between these two is calculated. If the simulation of the experiment is sufficiently close to reality, we can accept this ratio as being

approximately equal to the real acceptance, supplying us with the following relation:

$$A = \frac{N_{\text{detected}}}{N_{\text{actual}}} = \frac{N_{\text{reconstructed}}}{N_{\text{generated}}}. \tag{110}$$

Finally, this acceptance A is generally a function of the cross sections variables. Since this analysis was performed bin per bin in the cross section variables, A must be determined on a bin by bin basis.

4.3.2 DVCS Generator

First, an ensemble of events was generated according to a program written by F. X. Girod. This program was written to take into account both virtual and radiative effects as described in reference.[47] Instead of producing only $e+p \to e'+p'+\gamma$, the program produced $e+p \to e'+p'+\gamma+\gamma'+\gamma''$, where γ represents the DVCS or BH photon; γ' represents the radiated photon coming off of the incoming electron leg, which we will call pre-radiation; and γ'' represents the radiated photon coming off of the outgoing electron leg, which we will call post-radiation. Approximately 40 million events were generated.

4.3.3 GEANT3 Simulations (GSIM)

Now that the simulated events have been generated, it's important to know how the detector will respond to such events, bin per bin. First, a realistic model of CLAS and the IC must be developed. The method for modeling the CLAS detector is to utilize a program called GSIM ((G)EANT (SIM)ulation) which is based on the GEANT3 library developed at CERN.[48] Each of the pieces of the detectors were inserted into the simulation, specifying the geometry, placement, size, and material of each component. It is known, to various degrees, what the behavior of each material is when different particles pass through them. For instance, an electron passing through lead will scatter and produce bremsstrahlung photons, and for thick lead, can be completely stopped. Effects of particles in these materials are simulated to the best of our knowledge, and the response of what we believe our detectors would have read based on this simulation is given in Analog to Digital Converter (ADC) and Time to Digital Converter (TDC) responses. Most of the detectors are understood well enough for our purposes. However, the EC is not perfectly simulated because of the complex showering which occurs within it. To reduce the amount of computing time needed, any electrons or photons below a certain energy threshold are neglected, leading to a slight imperfection in the simulations. In addition, the geometry of the CC is too complicated to represent perfectly in simulations. Therefore, the spectrum of the number of photoelectrons detected in the CC is not

realistically reproduced in simulations. There are also resolution effects which are not taken into account in simulations. In the cases of the SC and DC, the resolution in simulations is too fine in comparison to data. Some of these differences may be taken into account with a program called GSIM Post-Processing (GPP), whereas some effects may not be taken into account.

4.3.4 GSIM Post-Processing (GPP)

There are regions of the DC and SC which have a resolution after GSIM which is finer than the resolution in data. These detectors also have areas which are less efficient than in experiment. In order to reconcile this difference, we processed the GSIM output using a program called GPP, which is able to simulate these efficiencies, and smear out the distributions of these detectors to more accurately represent what appeared in our data. The program makes use of four parameters. Three of the parameters, a, b, and c are used to broaden the resolution of the DC, for each of the three regions. The fourth parameter f is used to broaden the resolution of the SC.[23] The set of parameters which best reproduced the resolutions in data were:

a = 1.2
b = 1.25
c = 1.3
f = 2

The occupancies of the DC were also studied. Wires which had an efficiency of less than 1% in experiment were removed from simulations. For those wires above 1% in efficiency in experiment, the corresponding wires in simulation were modified to have the same efficiency.[23,49]

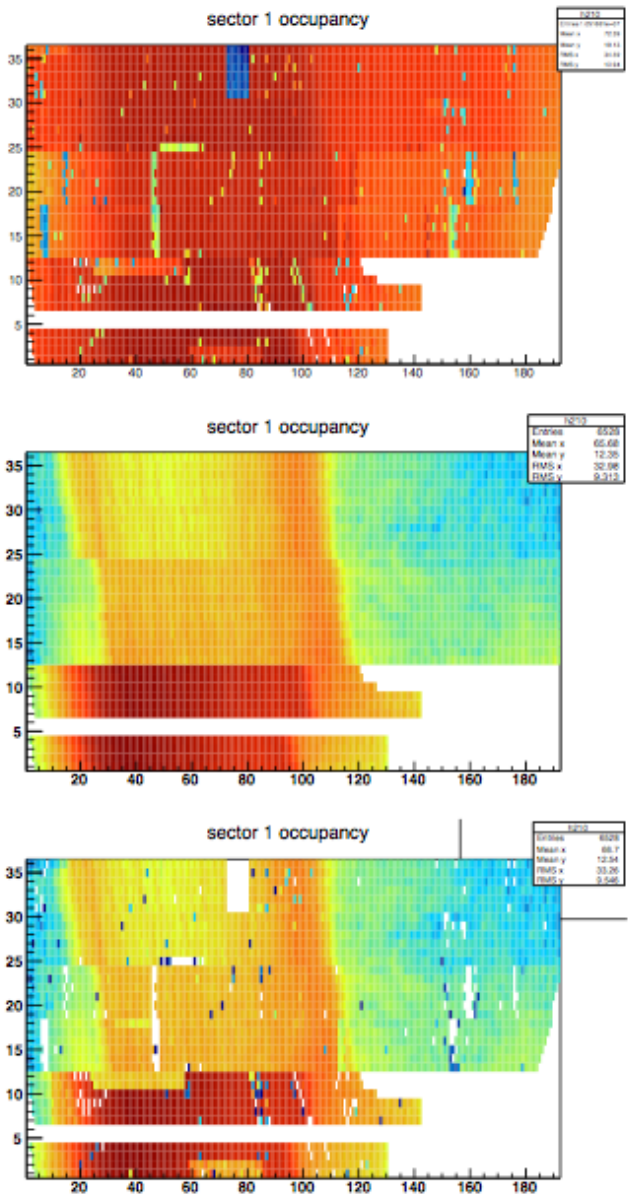

Figure 4.41: On each panel, the layer number in DC is plotted against the wire number in the DC. On the top is data. In the center is MC before efficiency corrections. On the bottom is after efficiency corrections. Deep red corresponds to 100% efficiency, while deep blue corresponds to low efficiency. Zero efficiency is represented by white. We note that the inefficiencies seen in data, the top plot, are reproduced in the MC after the corrections, on the bottom plot.[23]

4.3.5 Background Merging

During the experiment, there is a possibility of Möller scattering, or other accidental events, being detected, such as beam-target interactions, secondary scattering, cosmic rays and other random hits.

Because of these background events, the efficiency of the detectors is reduced in a very non trivial way. It is known that this background is linearly related to the luminosity of the experiment.[23,50] However, this background is not taken into account in GSIM. Therefore, in order to take into account the inefficiency due to this background, we have to make an estimation of the background in data. This can be done by looking at the Faraday cup trigger, which records the state of CLAS at a rate which is proportional to the luminosity of the experiment. Background events are then merged with the generated events in proportion to the background rate which we measure from experiment. Simulations of elastic scattering have been studied by B. Guegan while using this background merging method, and it can be seen that the efficiency is reduced by about 6%.[23]

Efforts to fully understand the background and its contribution to the reduced efficiency of CLAS are ongoing.

4.3.6 Particle Identification

The raw TDC and ADC values of the experiment, or the simulation, are converted into physical values, such as momentum, time-of-flight, and tracks. This is accomplished by the reconstruction software RECSIS. Afterwards, the particle identification is performed for Monte Carlo. It is almost identical to that of the experimental data, with one exception: the number of photoelectrons in the CC for simulations is not accurately calculated. This is due to the fact that the exact geometry of the CC is not very well known, causing the number of photoelectrons in simulation to be unreliable. Therefore, no cut is applied on the number of photoelectrons in simulations.

4.3.7 Comparison to Data

In order to rely on Monte Carlo for our acceptance, it is necessary to have a good agreement between reconstructed events from Monte Carlo, and data. Since we want to estimate the acceptance through Monte Carlo, our estimation is going to be dependent on our ability to accurately reproduce the features of data in Monte Carlo. There are several ways we can check to make sure that the comparison between the two is close enough. Firstly, we can make comparisons between our kinematic variables, Q^2, x_B, t, and Φ. In particular, we can look at Q^2 versus x_B, seen in Figure 4.42, and $-t$ versus x_B, seen in Figure 4.43. We notice a good agreement. We may also look at our event distributions as functions of our kinematic variables, in Figure 4.44. Finally, we can look at the distributions of each of the particles, comparing their momenta and angles. In particular, for each of the three outgoing particles, we plot the momentum versus the polar angle at the vertex in Figure 4.45, and the azimuthal angle at the vertex versus the polar angle at the vertex in Figure 4.46. All of the distributions appear to be accurately reproduced in the Monte Carlo except for the momentum versus polar angle of the photon. One notices that in Figure 4.45, there events are focused around 4 GeV for the data in the IC and focused around 4.5 GeV for the Monte Carlo in the IC.

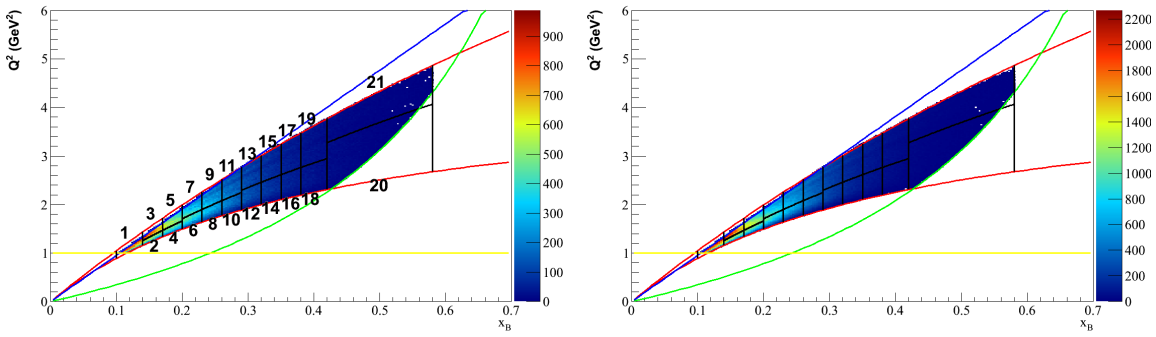

Figure 4.42: Q^2 versus x_B for data on left, and Monte Carlo on right, showing a good agreement.

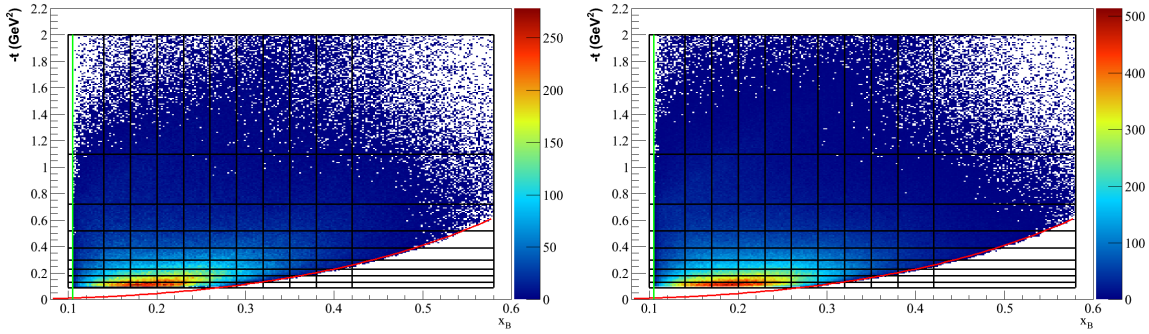

Figure 4.43: $-t$ versus x_B for data on left, and Monte Carlo on right, showing a good agreement.

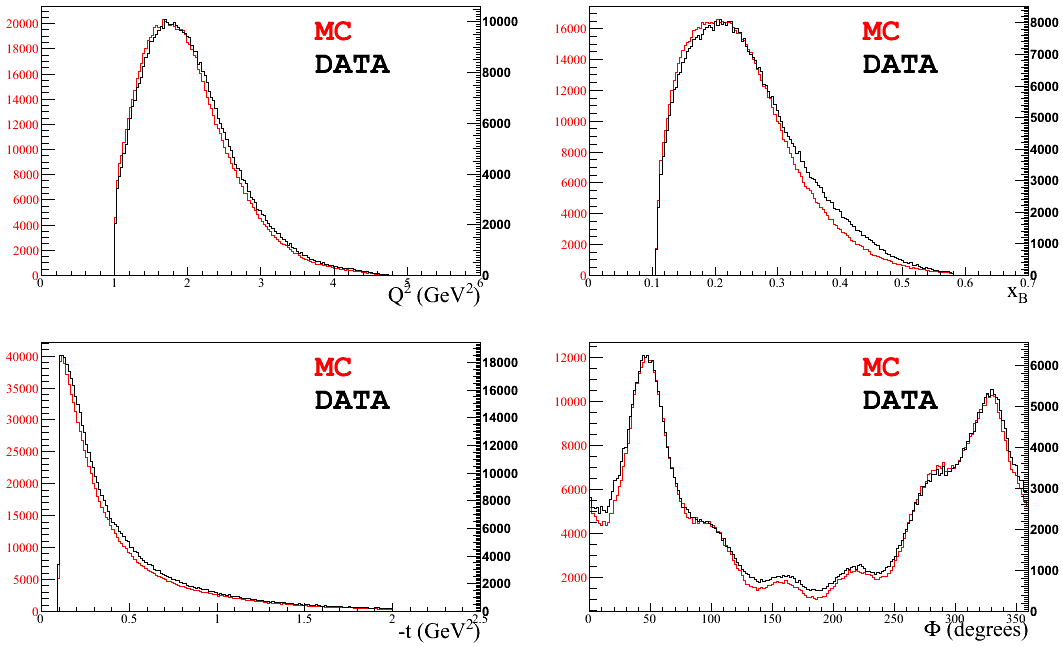

Figure 4.44: A comparison of kinematic variables for data on left, and Monte Carlo on right. The top row is Q^2, the second row is x_B, the third row is $-t$, and the bottom row is Φ. We see that the agreement between data and simulation is very good with no extreme deviations visible.

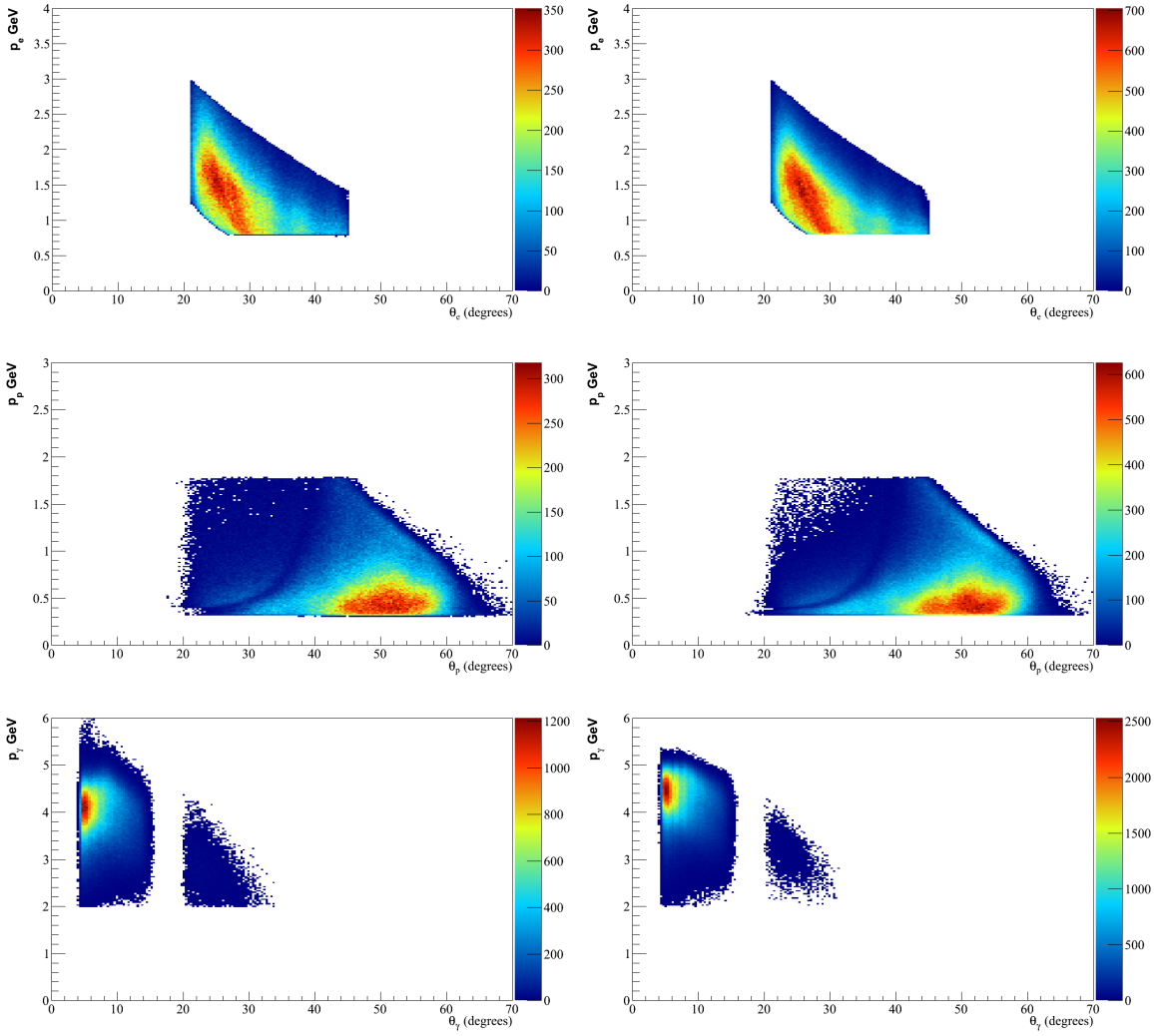

Figure 4.45: Momentum versus polar angle for each particle type, data on left, and Monte Carlo on right. On the top row, p_e versus θ_e, on the center row, p_p versus θ_p, and on the bottom row, p_γ versus θ_γ. We notice that there is good agreement between data and simulations, except for energy of the photons in the IC, corresponding to low θ_γ values. There is a concentration of photons at about 4 GeV in data and 4.5 GeV in Monte Carlo. In these plots, this is the only serious discrepancy in simulations, whose cause has yet to be fully understood.

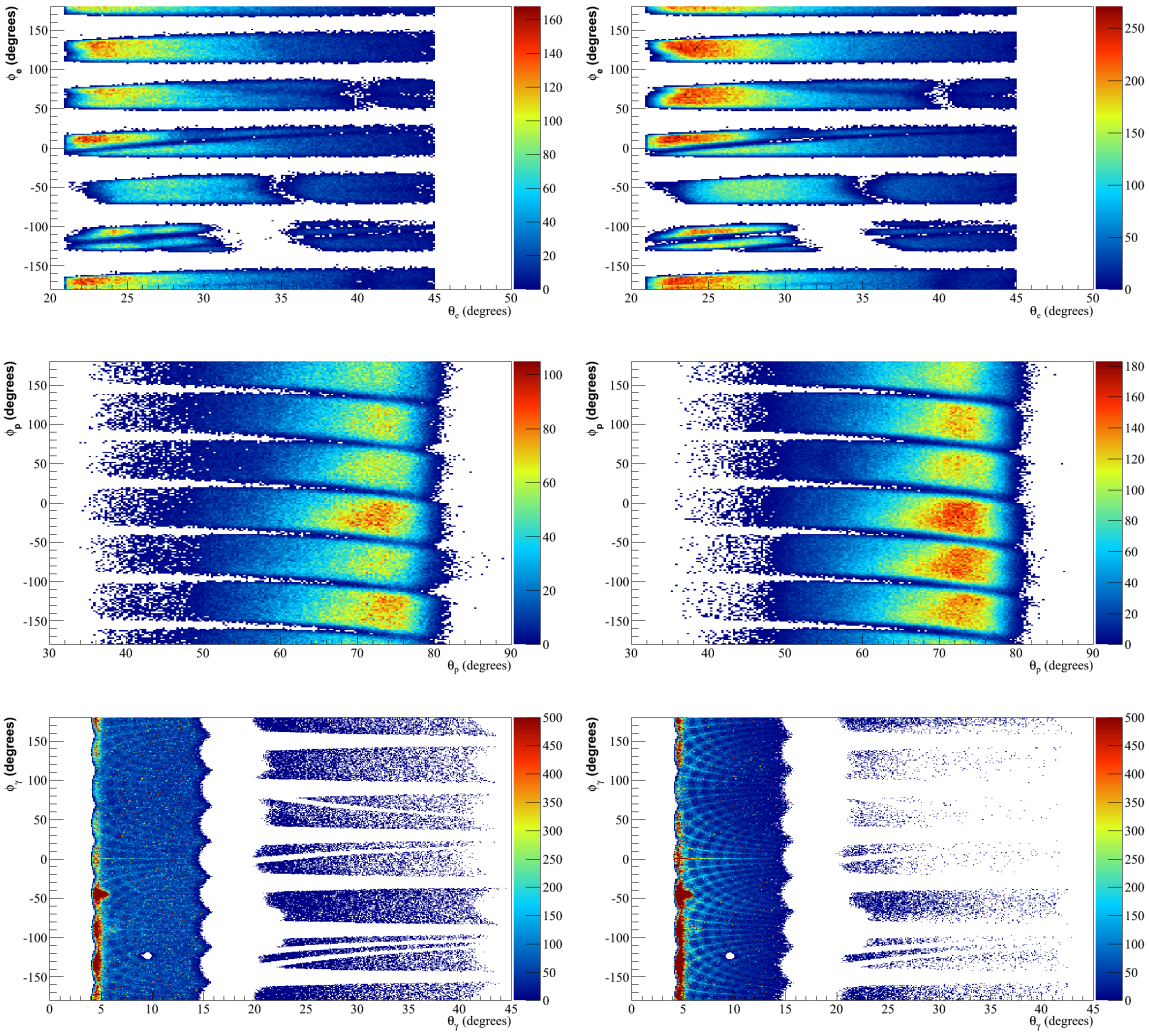

Figure 4.46: Angular distributions for each particle type, data on left, and Monte Carlo on right. On the top row, ϕ_e versus θ_e, on the center row, ϕ_p versus θ_p, and on the bottom row, ϕ_γ versus θ_γ. We see that the distributions are well reproduced in the simulations when compared to data.

4.3.8 Final Results for the Acceptance of CLAS

Using the formula

$$A = \frac{N_{\text{detected}}}{N_{\text{actual}}} = \frac{N_{\text{reconstructed}}}{N_{\text{generated}}}. \tag{111}$$

we are able to calculate the acceptance for each of the bins. Our acceptance is usually from $10-15\%$ in most bins. Each bin also exhibits a periodic shape, with six regions of relatively higher acceptance. This structure is related to the six sector construction of CLAS. An example of the acceptance is presented in Figure 4.47, for the fifth bin in x_B and θ_e. A full list of acceptances may be found in Appendix A.

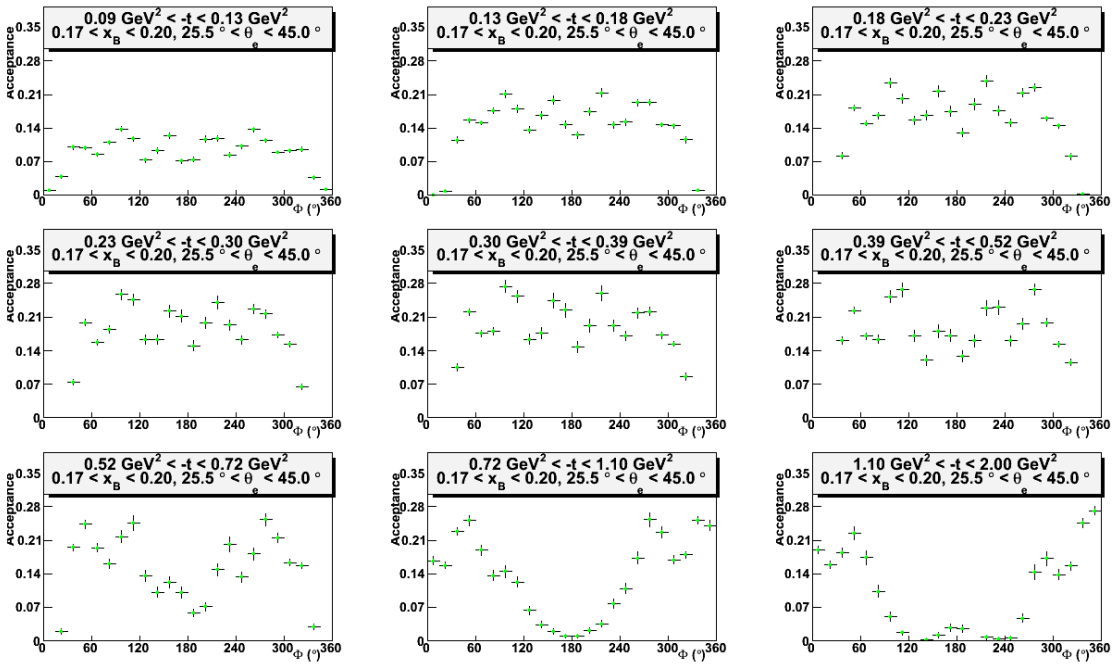

Figure 4.47: The acceptance as a function of ϕ for the fifth bin in x_B and θ_e, where $0.17 < x_B < 0.2$ and $25.5^\circ < \theta_e < 45^\circ$.

4.4 Momentum and Angle Corrections

4.4.1 Energy Loss Corrections

When heavy charged particles pass through matter, they experience a loss of energy due to ionizing of atoms in this matter. This behavior is well understood, and is best described by the relativistic Bethe equation[8]:

$$-\frac{\mathrm{d}E}{\mathrm{d}x} = \frac{4\pi\alpha^2}{m_e}\frac{nz^2}{\beta^2}\left[\ln\left(\frac{2\beta^2}{I(1-\beta^2)}\right) - \beta^2\right], \tag{112}$$

where z is particle charge, and n and I are the electron density and mean excitation potential of the target, respectively.

When electrons, positrons and photons pass through matter, they experience showering effects due to bremsstrahlung, especially when it passes through heavy material such as lead.

We will now focus on the effect of this bremsstrahlung and ionization on electrons and protons detected in CLAS. During our processes, electrons and protons travel through the hydrogen target and the various detectors of CLAS. By the time the particle has reached the last detector of CLAS, energy has been lost due to this ionization, altering the momentum and the angle measured. The reconstruction of the DC track, which determines the momentum and angles will therefore output values which are not the true values at the vertex.

It is therefore desirable to have an effectual method for estimating this energy loss and correcting for it. Since it is impossible to know the amount of energy lost simply from the detector output itself, we must rely on Monte Carlo for this analysis. In simulation, we have generated events with kinematics - momentum and angles at vertex - for particles before entering CLAS. We will call these:

$$p_{\mathrm{gen}}, \theta_{\mathrm{gen}}, \phi_{\mathrm{gen}}. \tag{113}$$

Afterwards, GSIM will simulate the response of CLAS to the particles. The values after considering this detector response will be referred to as:

$$p_{\mathrm{rec}}, \theta_{\mathrm{rec}}, \phi_{\mathrm{rec}}. \tag{114}$$

We then posit that the correction is simply the difference of these two sets of values, which we shall define as:

$$\Delta p = p_{\text{gen}} - p_{\text{rec}}, \tag{115}$$

$$\Delta\theta = \theta_{\text{gen}} - \theta_{\text{rec}}, \tag{116}$$

$$\Delta\phi = \phi_{\text{gen}} - \phi_{\text{rec}}. \tag{117}$$

We suspect that because the geometry of CLAS and the target which the particles encounter will vary as a function of p_{rec} and θ_{rec}, these values must be functions of p_{rec} and θ_{rec}, therefore we choose to write:

$$\Delta p = \Delta p(p_{\text{rec}}, \theta_{\text{rec}}), \tag{118}$$

$$\Delta\theta = \Delta\theta(p_{\text{rec}}, \theta_{\text{rec}}), \tag{119}$$

$$\Delta\phi = \Delta\phi(p_{\text{rec}}, \theta_{\text{rec}}). \tag{120}$$

Next, these functions are analyzed to determine their dependence on p_{rec} and θ_{rec}. Since they are functions of two variables, a two-step method of determining dependence is convenient. We chose to determine the momentum dependence first, then the angular dependence. For this analysis, there are different binnings for electrons and protons in bins of θ_e or θ_p respectively, with the values for electrons and protons respectively being:

$$\theta_e : [20^\circ, 22.5^\circ, 25^\circ, 27.5^\circ, 30^\circ, 32.5^\circ, 35^\circ, 37.5^\circ, 40^\circ, 42.5^\circ, 45^\circ], \tag{121}$$

and

$$\theta_p : [20^\circ, 25^\circ, 30^\circ, 35^\circ, 40^\circ, 45^\circ, 50^\circ, 55^\circ, 60^\circ]. \tag{122}$$

Our analysis, in bins of θ_{rec} are analyzed first as a function of p_{rec}. For $\Delta\theta$ and $\Delta\phi$, the deviations as a function of momentum are significantly smaller than the standard deviations of the fits of the means, so we can abandon these two quantities without much concern. In other words, it seems that any correction we apply would not improve our angular resolution or accuracy. However, the deviations in momentum are significant, so these distributions must be fit. We elect to fit these distributions to the following functions, now writing p_{rec} as p and θ_{rec} as θ from this point forward for the sake of simplicity:

$$\Delta p_e = \alpha_e + \frac{\beta_e}{p_e}, \tag{123}$$

and

$$\Delta p_p = \alpha_p + \frac{\beta_p}{p_p^{\gamma_p}}. \tag{124}$$

Figure 4.48, Figure 4.49, Figure 4.50, Figure 4.51, Figure 4.52 and Figure 4.53 contain plots of the six distributions for electrons and protons and their deviations in momentum and angles. These distributions are fitted with Gaussians, with no background. Also displayed are the means of the fits as black points, and one standard deviation as red points. The black curve running through the black points represents the best fit according to equations 123 and 124. For ease of comparison, a line is drawn at $\Delta p = 0$ or $\Delta\theta = 0$.

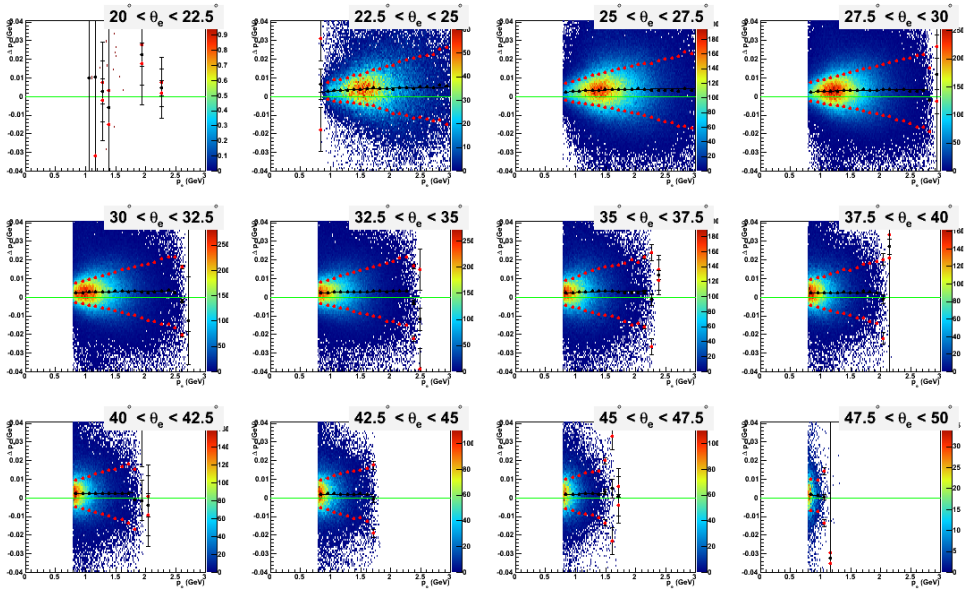

Figure 4.48: Δp_e for bins in θ_e as measured from the vertex. The black points represent the means of the Gaussian distributions in slices of momentum, and the red points represent one standard deviation from the mean point. The black curve running through the black points represents the best fit according to equation 123. The horizontal green line represents the line $\Delta p_e = 0$.

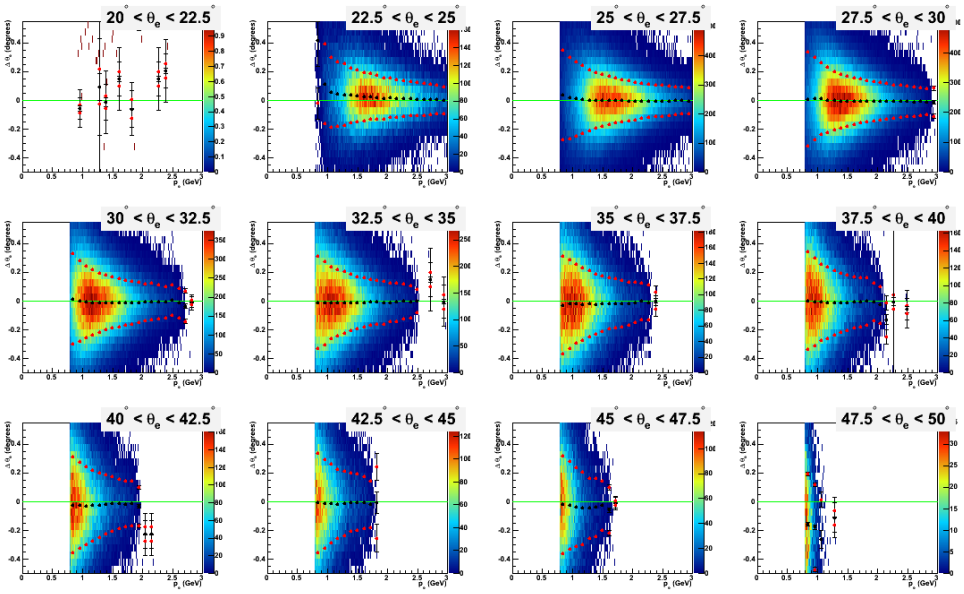

Figure 4.49: $\Delta\theta_e$ for bins in θ_e as measured from the vertex. The black points represent the means of the Gaussian distributions in slices of momentum, and the red points represent one standard deviation from the mean point. The horizontal green line represents the line $\Delta\theta_e = 0$.

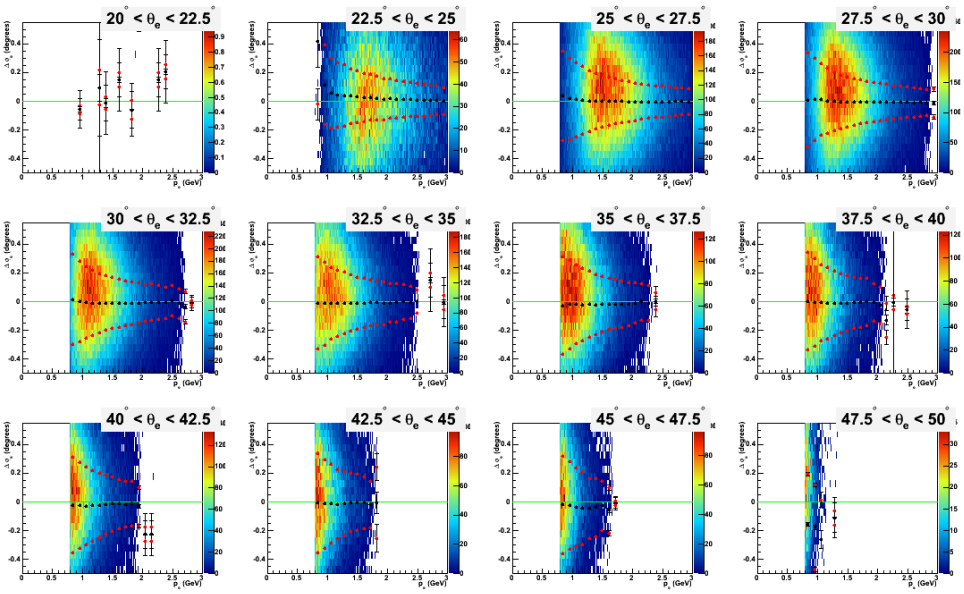

Figure 4.50: $\Delta\phi_e$ for bins in θ_e as measured from the vertex. The black points represent the means of the Gaussian distributions in slices of momentum, and the red points represent one standard deviation from the mean point. The horizontal green line represents the line $\Delta\phi_e = 0$.

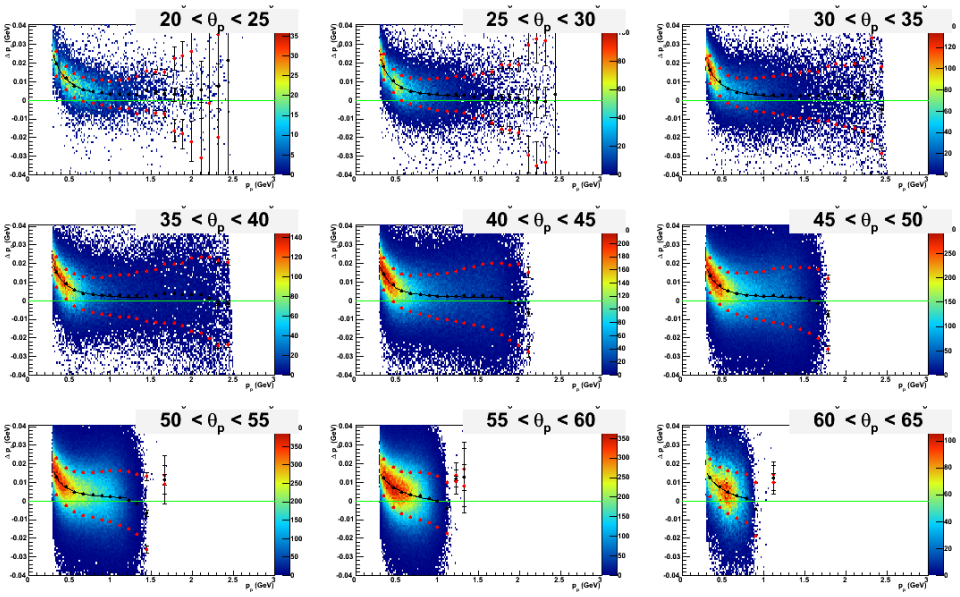

Figure 4.51: Δp_p for bins in θ_p as measured from the vertex. The black points represent the means of the Gaussian distributions in slices of momentum, and the red points represent one standard deviation from the mean point. The black curve running through the black points represents the best fit according to equation 124. These curves are in accordance with what we would expect - with large deviations at low angle. This affect at low momentum is due to the momentum dependence of equation 112. The horizontal green line represents the line $\Delta p_p = 0$.

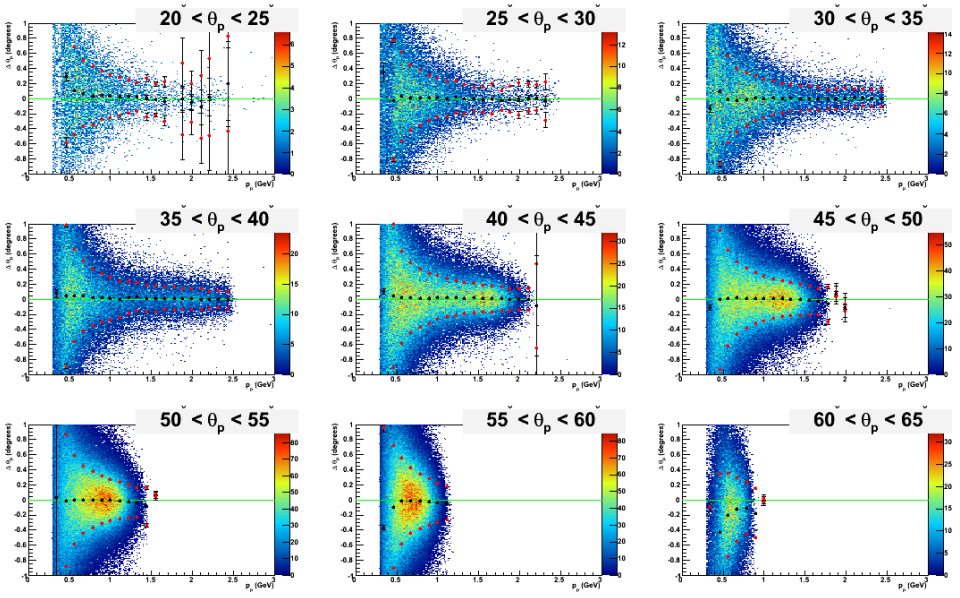

Figure 4.52: $\Delta\theta_p$ for bins in θ_p. The black points represent the means of the Gaussian distributions in slices of momentum, and the red points represent one standard deviation from the mean point. The horizontal green line represents the line $\Delta\theta_e = 0$.

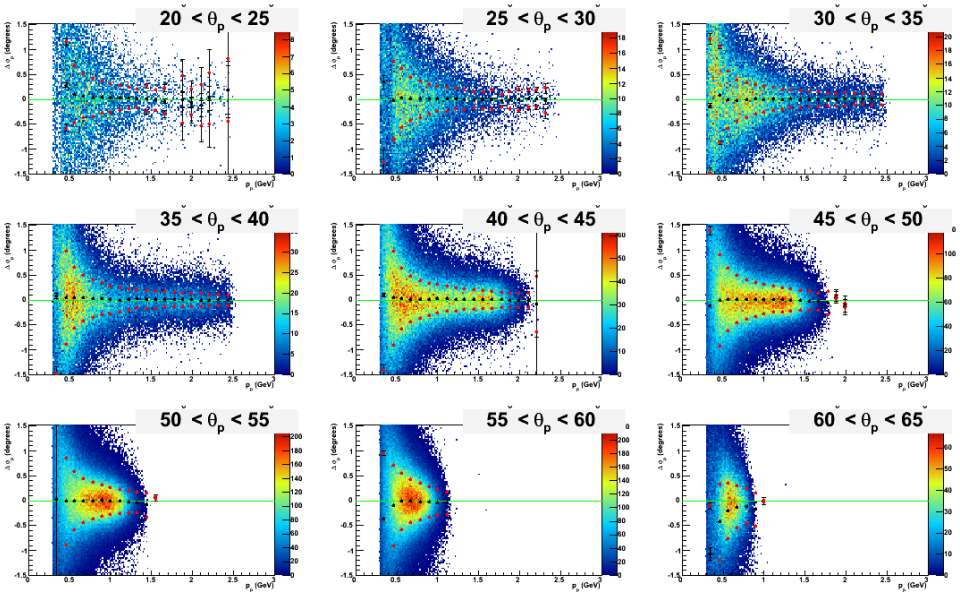

Figure 4.53: $\Delta\phi_p$ for bins in θ_p. The black points represent the means of the Gaussian distributions in slices of momentum, and the red points represent one standard deviation from the mean point. The horizontal green line represents the line $\Delta\phi_e = 0$.

The next step is to determine the θ dependence of these fit parameters α, β and γ. After plotting the parameters as functions of θ, as seen in Figure 4.54 and Figure 4.55, it is determined that the functions which best describe the distributions for these parameters are, for electron and protons respectively:

$$\alpha_e(\theta_e) = \alpha_{e,1} + \frac{\alpha_{e,2}}{\theta_e}, \tag{125}$$

$$\beta_e(\theta_e) = \beta_{e,1} + \frac{\beta_{e,2}}{\theta_e}, \tag{126}$$

and

$$\alpha_p(\theta_p) = \alpha_{p,1} + \alpha_{p,2}\theta_p + \alpha_{p,3}\theta_p^2, \tag{127}$$

$$\beta_p(\theta_p) = \beta_{p,1} + \beta_{p,2}\theta_p + \beta_{p,3}\theta_p^2, \tag{128}$$

$$\gamma_p(\theta_p) = \gamma_{p,1} + \gamma_{p,2}\theta_p + \gamma_{p,3}\theta_p^2. \tag{129}$$

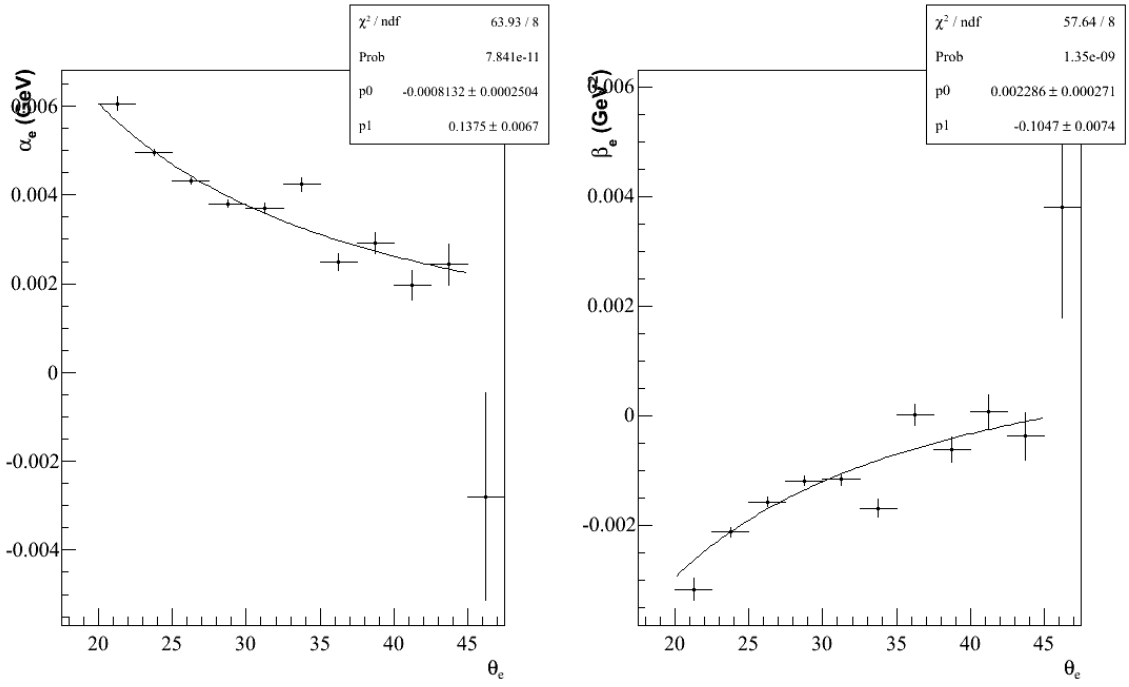

Figure 4.54: α_e and β_e as a function of θ_e, with a polynomial fit.

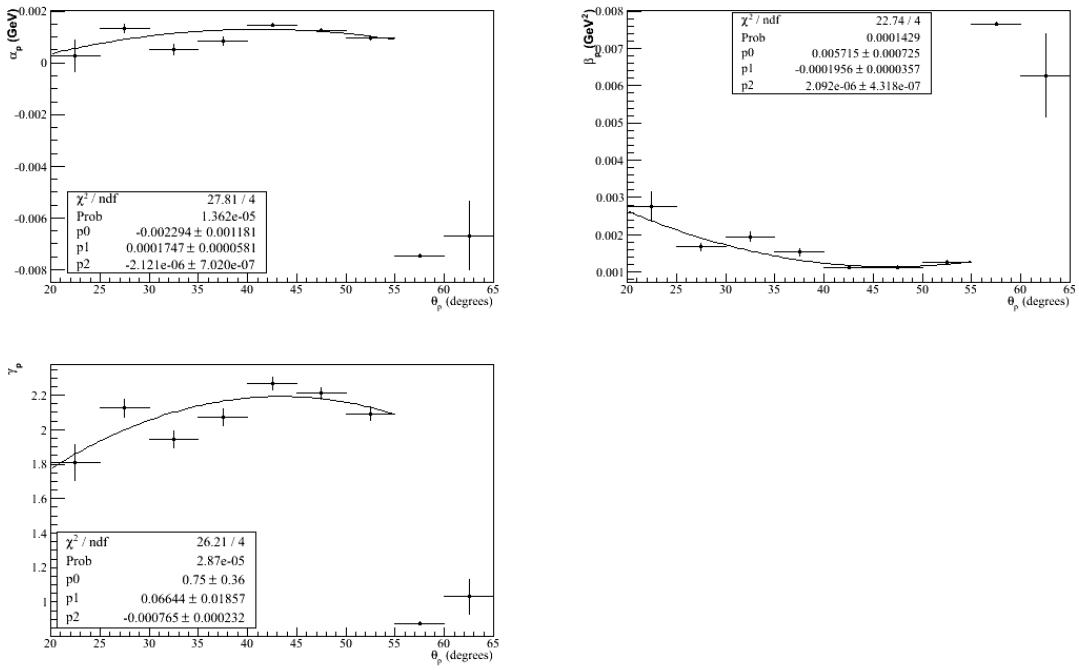

Figure 4.55: α_p, β_p and γ_p as a function of θ_p, with a polynomial fit.

A fit of the means (black points) of Figure 4.54 and Figure 4.55 allow us to determine all of these parameters. Finally, one may write Δp_e and Δp_p with all of the determined parameters:

$$\Delta p_e(p_e, \theta_e) = \left(a_1 + \frac{a_2}{\theta_e}\right) + \frac{\left(a_3 + \frac{a_4}{\theta_e}\right)}{p_e}, \tag{130}$$

$$\begin{aligned} \Delta p_p(p_p, \theta_p) &= (b_1 + b_2\theta_p + b_3\theta_p^2) \\ &+ \left(b_4 + b_5\theta_p + b_6\theta_p^2\right) p_p^{-\left(b_7 + b_8\theta_p + b_9\theta_p^2\right)}. \end{aligned} \tag{131}$$

Table 4.6: A table containing all of the parameters for equation 130 and 131, the ionization corrections for electrons and protons respectively.

Electron Constants	
a_1	-8.13235×10^{-4}
a_2	0.137491
a_3	0.0022856
a_4	-0.104723

Proton Constants	
b_1	-0.00229356
b_2	1.74653×10^{-4}
b_3	-2.12096×10^{-6}
b_4	0.0057151
b_5	-1.9561×10^{-4}
b_6	2.09208×10^{-6}
b_7	0.749952
b_8	0.066442
b_9	-7.65017×10^{-4}

After applying this correction to p_{rec}, one may check its efficacy by plotting the corrected momentum subtracted from p_{gen}. In order for the quality of the correction function to be considered good, this difference should be around zero, within the preferred tolerance. In our case, if the deviations from zero are within the standard deviation of this difference distribution, we can be satisfied with the quality of the correction. In mathematical terms, we may write:

$$p_{\text{cor}} = p_{\text{rec}} + \Delta p(p_{\text{rec}}, \theta_{\text{rec}}), \tag{132}$$

$$\Delta p_{\text{cor}} = p_{\text{gen}} - p_{\text{cor}} = p_{\text{gen}} - p_{\text{rec}} - \Delta p(p_{\text{rec}}, \theta_{\text{rec}}), \tag{133}$$

with the hopes that $\Delta p_{\text{cor}} \approx 0$.

It turns out that the corrections obtained have the desired effect. The correction to the protons is significant, with the correction to the electrons being a little less appreciable due to their large β. The difference may be found in Figure 4.56 and Figure 4.57 for electrons and protons, respectively. One notes that, while the correction renders the distribution fairly close to zero, there are still some deviations from zero, especially at low momentum for protons. However, these deviations are within the standard deviation of the distribution. We conclude that our electron and proton momenta

have been sufficiently corrected. These correction functions, which we have derived from a study on Monte Carlo may be applied to both data and Monte Carlo, with the assumption that our modeling of CLAS is accurate enough to simulate the true amount of ionization energy loss.

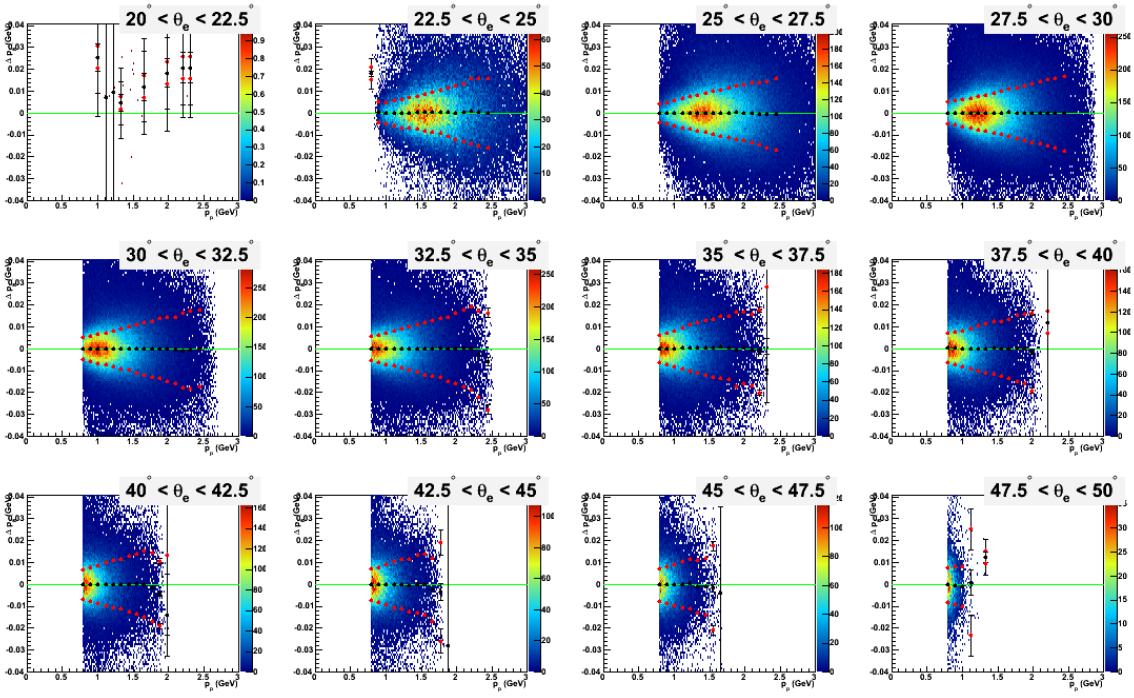

Figure 4.56: $\Delta p_{\rm cor}$ as a function of p for electrons.

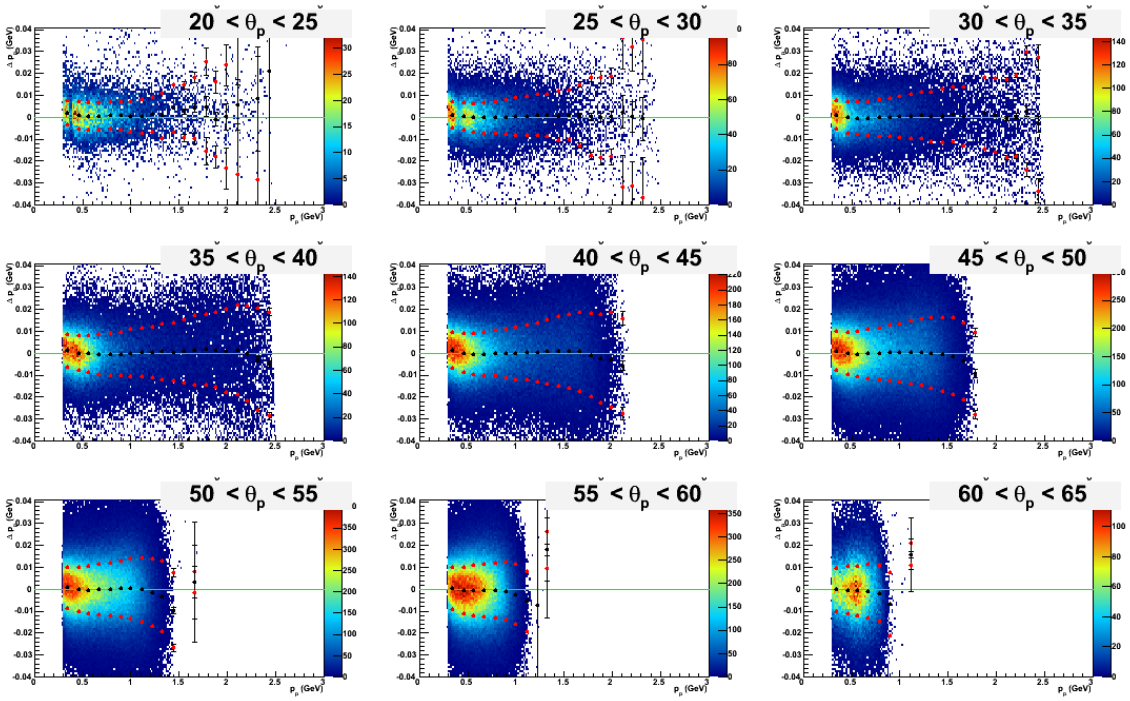

Figure 4.57: Δp_{cor} as a function of p for protons.

4.4.2 Empirical Kinematical Corrections for Charged Particles

In the previous study, we have concerned ourselves with corrections due to ionization loss. However there are other corrections beyond ionization which must be taken into account. We will present the problem by first analyzing our measured W distribution and our reconstructed beam energy E_0 distribution from data, after the application of the ionization loss corrections. In particular, we are going to look at W and our beam energy, E_0, after selecting our elastic channel, and the neutron mass, M_n, after looking at our positive pion electroproduction channel. This provides us a good way to check our understanding of CLAS. If our charged particles are detected correctly, and assigned the proper momenta and angles by our detector, we expect W to be around M_p and for E_0 to be around 5.88 GeV, and for M_n to be around its nominal PDG value. The beam energy was determined by studying elastic scattering. And taking the average reconstructed beam energy according to the equation:

$$E_0 = \frac{M_p}{\tan(\frac{\theta_{e,\text{calc}}}{2})\tan(\theta_{p,\text{calc}})} - M_p \tag{134}$$

In particular, we are interested in learning how these distributions look as a function of θ_{DC} and ϕ_{DC} as measured in the region one coordinates. By analyzing E_0 and W, we can make corrections on electron kinematics. In a similar method, we can look at the reconstructed neutron mass M_n of

the $e + p \rightarrow e + n + \pi^+$ channel to make similar corrections on the pion kinematics, with the intent of using those same corrections on the proton.

The distributions for E_0 and W are displayed in Figure 4.64, and the distributions for M_n are displayed in Figure 4.71, Figure 4.72, Figure 4.73 and Figure 4.74. For each of these three "benchmarks" E_0, W and M_n, we notice two striking features. Firstly, the average values for E_0, W and M_n in each sector do not have the expected value, and each sector varies from the expected value in a sector independent way. Secondly there is also significant deviation with respect to ϕ_{DC} within each sector. There are several suspected reasons why these quantities vary so much from their expected values. Among them include the possibility of the magnetic field map not being well known, the possibility of misalignments of the DC, or even a possible lack of knowledge as to the exact placement of the solenoid near the target. These problems in CLAS will cause the measured momenta and angles of particles to be slightly incorrectly determined. These incorrect values manifest themselves as shifts from the expected values, such as E_0, W or M_n.

We performed the study in the DC coordinates, based on our belief that the DC or the torus is misaligned. In either case, this misalignment can be represented by lack of knowledge of the magnetic field map. Therefore, a study done in the region where the field is the strongest will allow us to analyze our discrepancies with the best resolution. The region where the field is strongest is in region 2 of the DC. However, we do not have information on angles in region 2. Instead, we used region 1 coordinates since they are the closest to region 2. Whatever the cause of these discrepancies in the measured value of E_0, W or M_n, the appearance of these deviations gives us a motivation to make a correction to these momenta and angles. Because the source of the problem is not perfectly understood, one does not have the option of trying to simulate it. Therefore, we must resort to making empirical corrections.[23,51]

Before we begin with our method for correcting these variables, let us set out a list of assumptions, some of which we will justify right away, and some of which we will justify *a posteriori*.

Assumption #1: Any correction function for momenta and angles should approach minimal or no correction at large polar angles $\theta > 35^\circ$.

Assumption #2: θ_p is the most reliable of all of the elastic variables.

Assumption #3: Angular corrections are independent of particle type, as long as they are done in the coordinates of the DC.

Assumption #4: Corrections to particle momentum rely on charge and momentum, not on mass (particle type). In other words, particles of identical charges should have the same momentum corrections.

We justify Assumption #1 by claiming that if these discrepancies in W, E_0 and M_N are truly due to the lack of knowledge about the field map of the torus coils (or equally, the lack of knowledge of the physical placement of the torus coils themselves) then particles with larger angles are, on average, measured with more accuracy because on average the distance from the torus coils to the particle track is larger. This leads us to the belief that the corrections must begin to vanish at larger angles.

We justify Assumption #2 by noting that for elastic scattering, protons are found mostly at larger angles, where on average the distance from the torus coils to the particle track is larger. Using this fact in conjunction with Assumption #1, we are motivated to believe that on average, proton measurements are more reliable. Our preference of θ_p over p_p arises from the fact that resolutions in angle in CLAS are better than resolutions in momentum. This is due to the momentum being measured dependent on the magnetic field map, and the angle being measured independent of the magnetic field map. Finally, this leads us to believe that θ_p is probably the most trustworthy of the four variables: θ_e, θ_p, p_e and p_p.

We justify Assumption #3 by claiming that discrepancies in polar angle at the vertex are mostly due to lack of knowledge of the exact placements of the DC. If this is truly the case, then the correction for polar angles should only rely on the coordinates of the DC, and not the charge of the particle.

We justify Assumption #4 by recalling that $\frac{1}{r} = \kappa = \frac{qB}{p}$. If our lack of knowledge of the value of momentum is due to our lack of knowledge of the magnetic field map, we see that it only depends on the momentum and charge of the particle, and not directly on the mass. Therefore, particles with identical charge will enjoy identical correction in momentum.

Electron Kinematic Corrections Using the Elastic Channel:

For the elastic channel, our empirical measurements consist of p_e, θ_e, p_p and θ_p. If we wish to correct the values of W and E_0, we can easily accomplish this by making corrections to these variables. In order to correct as many variables as possible, we must hold at least one of them constant. We use Assumption #2 to justify selecting θ_p as the variable to hold constant. We begin by attempting to correct W. This can be accomplished by correcting the measured polar angle of the electron. Given a proton polar angle in double-arm elastic scattering, one may calculate the expected electron angle:

$$\theta_{e,\mathrm{calc}} = 2 \arctan \frac{M_p}{(E_0 + M_p) \tan \theta_p}. \tag{135}$$

This, in general, will be different from the measured value $\theta_{e,\text{meas}}$. Our goal is to find a function which brings us from measured polar angle to the corrected polar angle, using the calculated value as our expected value. This function will rely on the angular coordinates of region 1 DC:

$$\theta_{e,\text{corr}} = \theta_{e,\text{meas}} + \Delta\theta_e(\theta_{\text{DC},e}, \phi_{\text{DC},e}) \tag{136}$$

We determine this function by fitting the difference between the measured and expected values, in bins of DC coordinates:

$$\Delta\theta_e = \theta_{e,\text{calc}} - \theta_{e,\text{meas}}. \tag{137}$$

This quantity may be seen in Figure 4.58, with the bins in $\theta_{\text{DC},e}$ being

$$\theta_{\text{DC},e} : [36^\circ, 40^\circ, 42^\circ, 44^\circ, 46^\circ, 48^\circ, 50^\circ, 53^\circ, 56^\circ, 60^\circ, 64^\circ, 70^\circ, 78^\circ]. \tag{138}$$

For each bin in $\theta_{\text{DC},e}$, and for each sector, we analyze $\Delta\theta$ to determine its mean and standard deviations as a function of $\phi_{\text{DC},e}$. We then determine the $\phi_{\text{DC},e}$ dependance of our function by a fit to a first order polynomial, also by sector:

$$\Delta\theta_e = a_e(\theta_{\text{DC},e}) + b_e(\theta_{\text{DC},e})\phi_{\text{DC},e}, \tag{139}$$

where the subscript i represents a bin in θ_{DC}. These fits are represented by the black lines in Figure 4.58.

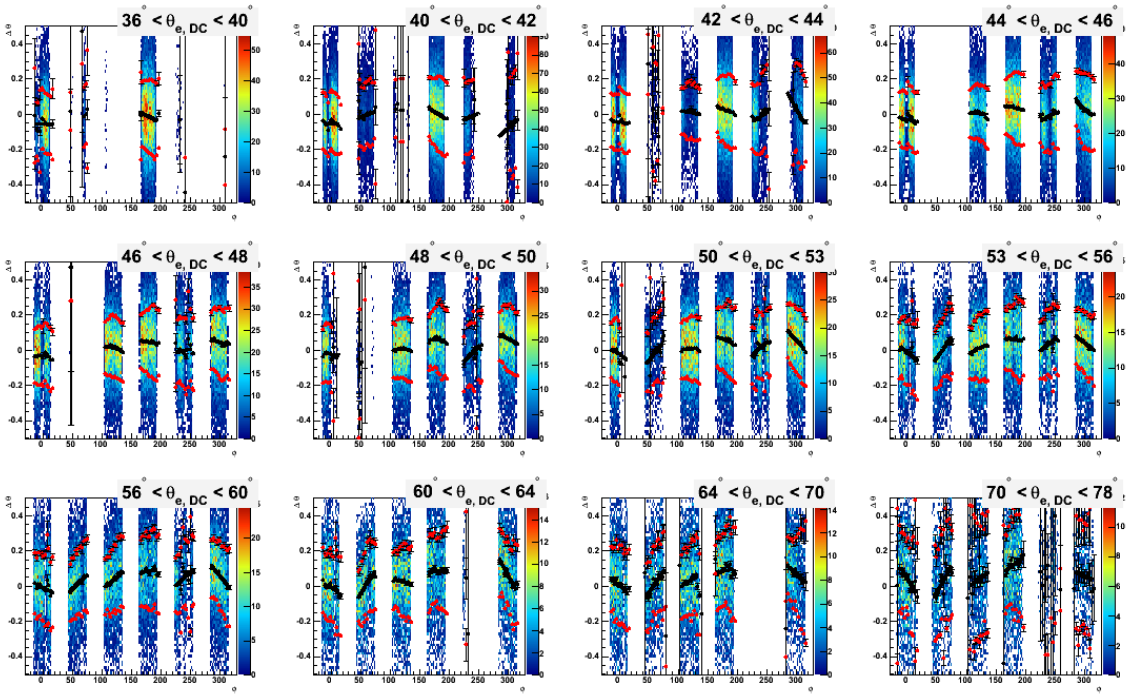

Figure 4.58: $\Delta\theta_e$ as a function of $\phi_{\mathrm{DC},e}$, for different bins of $\theta_{\mathrm{DC},e}$. The black points represent the means of the fits of Gaussian peaks to slices in $\phi_{\mathrm{DC},e}$, and the red points represent the standard deviations of the same. The black curves represent the fits in $\phi_{\mathrm{DC},e}$ according to a straight line as seen in equation 139.

We notice that this figure is riddled with many holes in certain bins in $\theta_{\mathrm{DC},e}$. This is due to the fiducial cuts that we have employed on our electrons and protons. Since we are dealing with elastic scattering, and the angles of electrons and protons are one-to-one in correspondence, the holes which we view in this plot will correspond to both cut electrons and cut protons. In order to extract the $\phi_{\mathrm{DC},e}$ dependance, we fit each parameter as a linear function of $\theta_{\mathrm{DC},e}$:

$$a_e = a_{e,0} + a_{e,1}\theta_{\mathrm{DC},e}, \tag{140}$$

$$b_e = b_{e,0} + b_{e,1}\theta_{\mathrm{DC},e}, \tag{141}$$

whose fits may be seen in Figure 4.59 and Figure 4.60.

We have now determined all 24 parameters corresponding to our θ_e corrections, with our final correction function being:

$$\Delta\theta_e = a_{e,0} + a_{e,1}\theta_{\mathrm{DC},e} + (b_{e,0} + b_{e,1}\theta_{\mathrm{DC},e})\phi_{\mathrm{DC},e}, \tag{142}$$

where the parameters are defined by the following table, by sector.

Table 4.7: The table of parameters corresponding to equation 142, the equation which gives the kinematic corrections to the polar angle θ_e for the electrons.

	$a_{e,0}$	$a_{e,1}$	$b_{e,0}$	$b_{e,1}$
sector 1	-0.146862	0.0024158	0.00421872	-0.000104959
sector 2	-0.039861	0.000822674	-0.00406926	0.000143319
sector 3	-0.0429369	0.00108304	-0.00599707	0.000122858
sector 4	-0.154693	0.00409406	-0.0054311	9.72998e-05
sector 5	-0.186987	0.00398069	-0.00322403	0.000114131
sector 6	-0.0128776	0.00127507	0.00430845	-0.000138372

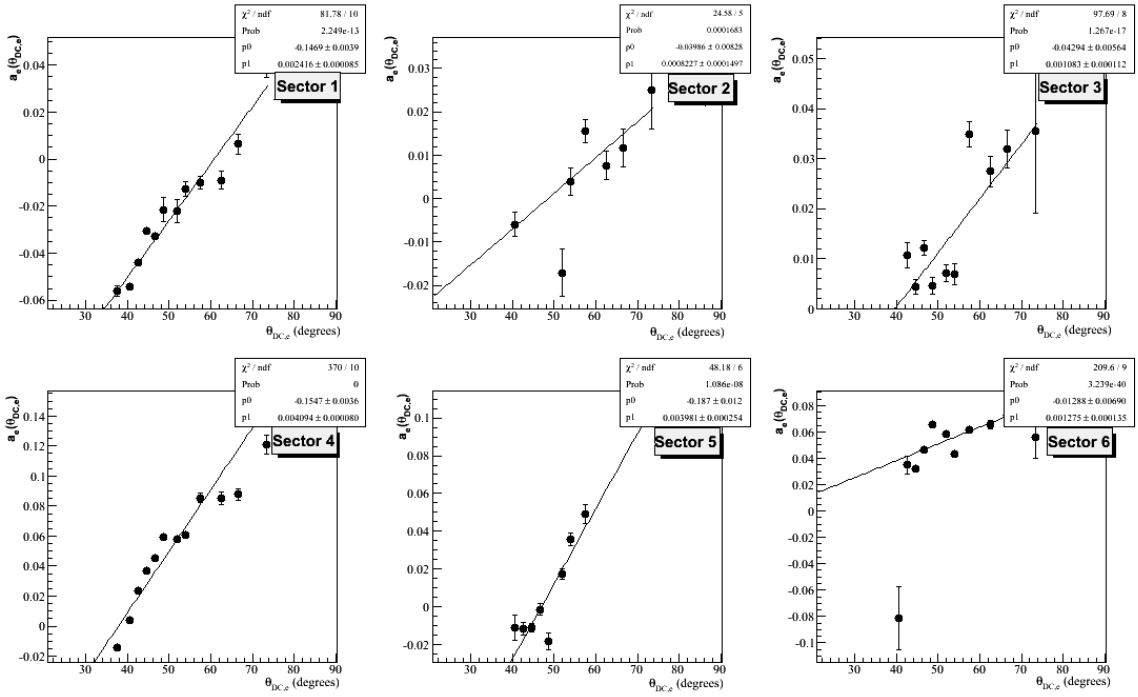

Figure 4.59: The parameter a_e fit as a function of $\theta_{\mathrm{DC},e}$ sector by sector according to equation 140.

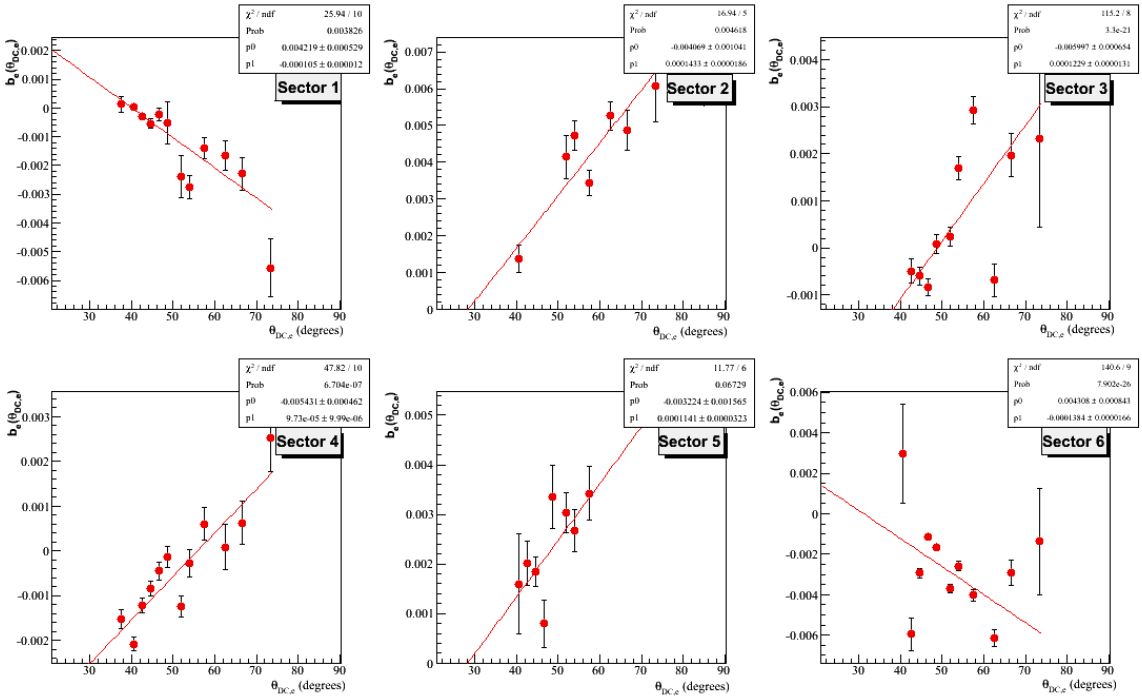

Figure 4.60: The parameter b_e fit as a function of $\theta_{\mathrm{DC},e}$ sector by sector according to equation 141.

Next, we focus our efforts on improving p_e. Now that we have corrected θ_e, we will take it as a trustworthy variable. Like what we have done for the polar angle of the electron, we will compare the measured and calculated momentum for the electron. The calculated value of p_e only relies on θ_e so single arm elastic scattering can be used to avoid losing the events which are lost to protons cut by our DC fiducial region. Unlike the equation for electron angle, an electron momentum calculation does not require the proton angle. We may then rely on the equation:

$$p_{e,\mathrm{calc}} = \frac{E_0}{1 + 2\frac{E_0}{M_p}\sin\frac{\theta_e}{2}^2}. \tag{143}$$

Like the previous method, we compare the measured and calculated values of p_e, except this time for single-arm scattering. In order to ensure that our correction function is approximately independent of momentum, we chose to take the ratio of the momenta instead of the difference. We define:

$$\delta p_e = \frac{p_{e,\mathrm{calc}}}{p_{e,\mathrm{meas}}}. \tag{144}$$

Using the same bins in $\theta_{\mathrm{DC},e}$ as in the previous analysis, we use the same method to extract the correction to p_e as a function of $\theta_{\mathrm{DC},e}$ and $\phi_{\mathrm{DC},e}$. Plotting δp_e as seen in Figure 4.61 we fit each bin in $\theta_{\mathrm{DC},e}$ and each sector with the function:

$$\delta p_e = 1 + c_e(\theta_{\mathrm{DC},e}) + d_e(\theta_{\mathrm{DC},e})\phi_{\mathrm{DC},e}. \tag{145}$$

These fits are represented by the black curves on Figure 4.61.

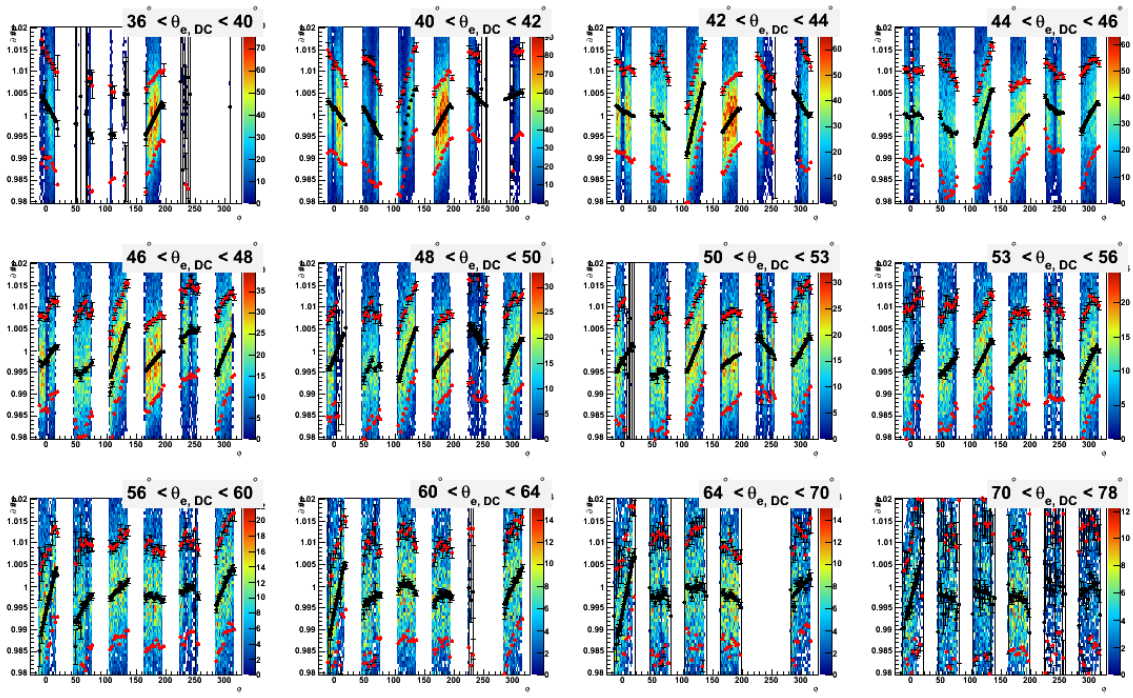

Figure 4.61: δp_e as a function of $\phi_{\mathrm{DC},e}$, for different bins of $\theta_{\mathrm{DC},e}$. The black points represent the means of the fits of Gaussian peaks to slices in $\phi_{\mathrm{DC},e}$, and the red points represent the standard deviations of the same. The black curves represent the fits in $\phi_{\mathrm{DC},e}$ according to a straight line as seen in equation 145.

Next, the parameters of this fit are analyzed in order to determine their $\theta_{\mathrm{DC},e}$ dependance. The functions used for the fit are:

$$c_e = c_{e,0} + c_{e,1}\theta_{\mathrm{DC},e}, \tag{146}$$

$$d_e = d_{e,0} + d_{e,1}\theta_{\mathrm{DC},e}, \tag{147}$$

whose fits may be seen in Figure 4.62 and Figure 4.63. We note that some of these fits may not look impressive. The χ^2 value is quite large, and there are many outliers in the fit. We find that this will be true for all of the following studies. We can justify this "loose" fit procedure in two ways. First, we are interested in empirical corrections which capture leading order deviations from expected values. In this sense, the fits may not be perfect, but at least provide a correction on the order of magnitude which concerns us. Secondly, we can justify the corrections *a posteriori* by viewing the effect they have on our variables W, E_0 and M_N.

We have now determined all 24 parameters corresponding to our p_e corrections, with our final correction function being:

$$\delta p_e = 1 + c_{e,0} + c_{e,1}\theta_{\mathrm{DC},e} + (d_{e,0} + d_{e,1}\theta_{\mathrm{DC},e})\phi_{\mathrm{DC},e}, \tag{148}$$

where the parameters are defined by the following table.

Table 4.8: The table of parameters corresponding to equation 148, the equation which gives the kinematic corrections to the momentum, p_e, for the electrons.

	$c_{e,0}$	$c_{e,1}$	$d_{e,0}$	$d_{e,1}$
sector 1	0.00956388	-0.000213876	-0.00156489	3.53482e-05
sector 2	0.00163266	-8.68628e-05	-0.000609982	1.15357e-05
sector 3	-0.00249147	3.59581e-05	0.00156991	-2.40948e-05
sector 4	0.00155519	-6.81624e-05	0.000647287	-1.03541e-05
sector 5	0.0079693	-0.00013362	-0.000457369	7.85232e-06
sector 6	0.000146967	-9.52163e-06	0.000287862	-6.71992e-07

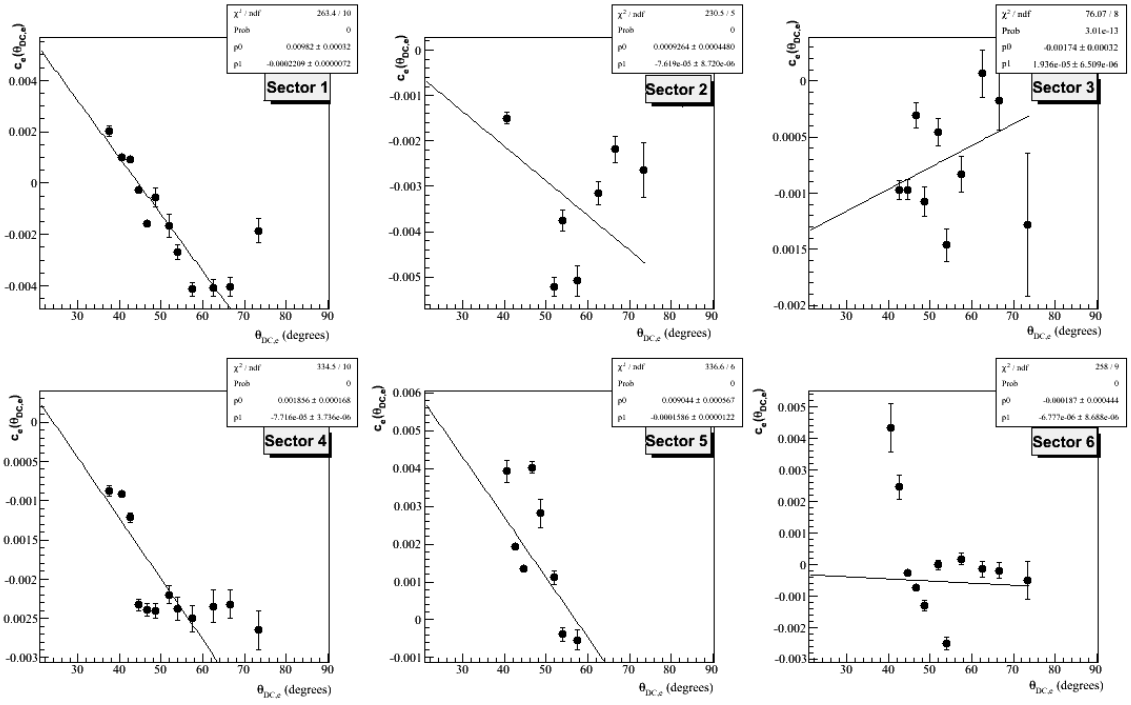

Figure 4.62: The parameter c_e fit as a function of $\theta_{\mathrm{DC},e}$ sector by sector according to equation 146.

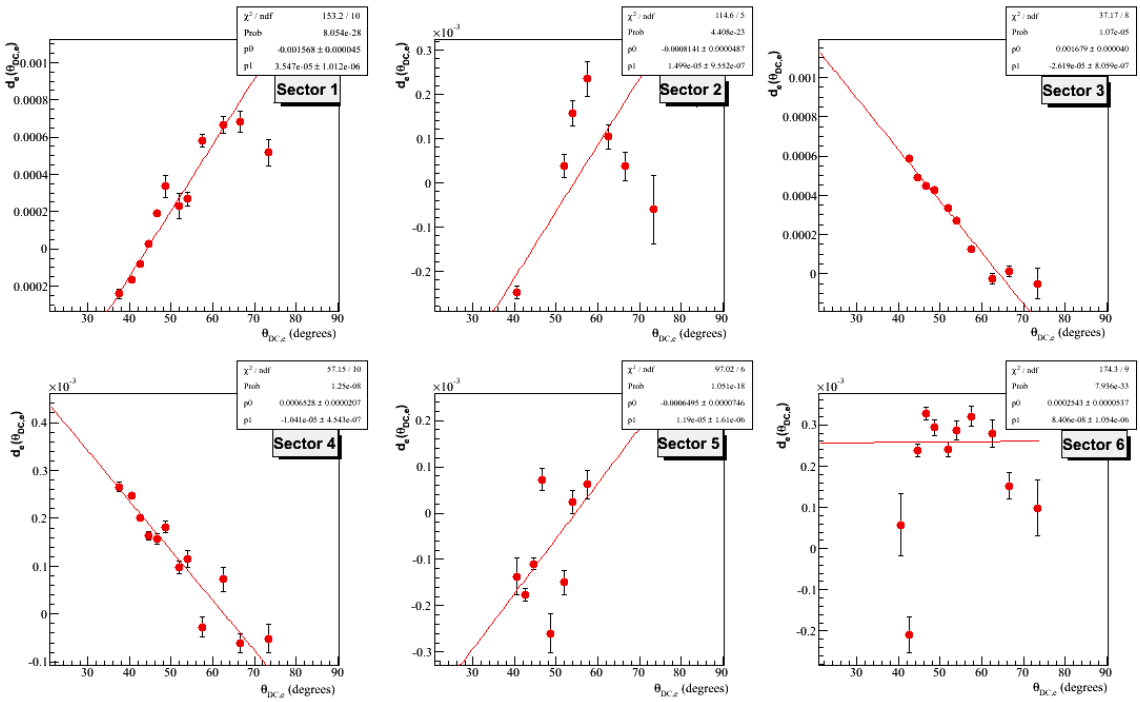

Figure 4.63: The parameter d_e fit as a function of $\theta_{\mathrm{DC},e}$ sector by sector according to equation 147.

Now, the validity of these corrections to both angle and momentum must be verified. For the angle corrections, we can do this by checking the effect of this correction of θ_e on W. Figure 4.64 and Figure 4.65 show the W distribution for each sector, as a function of $\phi_{\mathrm{DC},e}$ and as an average for a sector as a whole respectively. We notice that the average values of W are improved as well as the $\phi_{\mathrm{DC},e}$ dependent slant seen in W before correction. For the momentum corrections, we must check to see if they correct E_0 as originally expected. Figure 4.64 and Figure 4.65 show the E_0 distribution for each sector, as a function of $\phi_{\mathrm{DC},e}$ and as an average for a sector as a whole respectively. We confirm that the average values of E_0 are improved and that the $\phi_{\mathrm{DC},e}$ dependent slant seen in E_0 before correction is somewhat lessened.

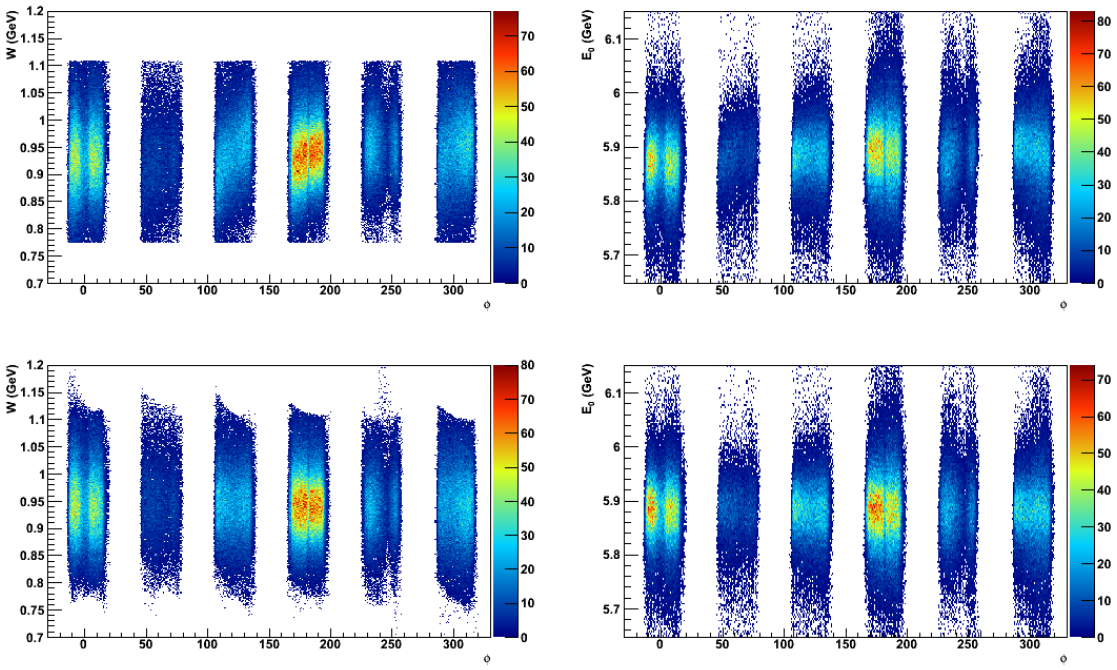

Figure 4.64: The left column represents W and the right column represents E_0. The top row is before kinematic corrections on momentum and angle, and the bottom row is after both angle and momentum corrections. We notice almost complete elimination of the slant in $\phi_{\mathrm{DC},e}$.

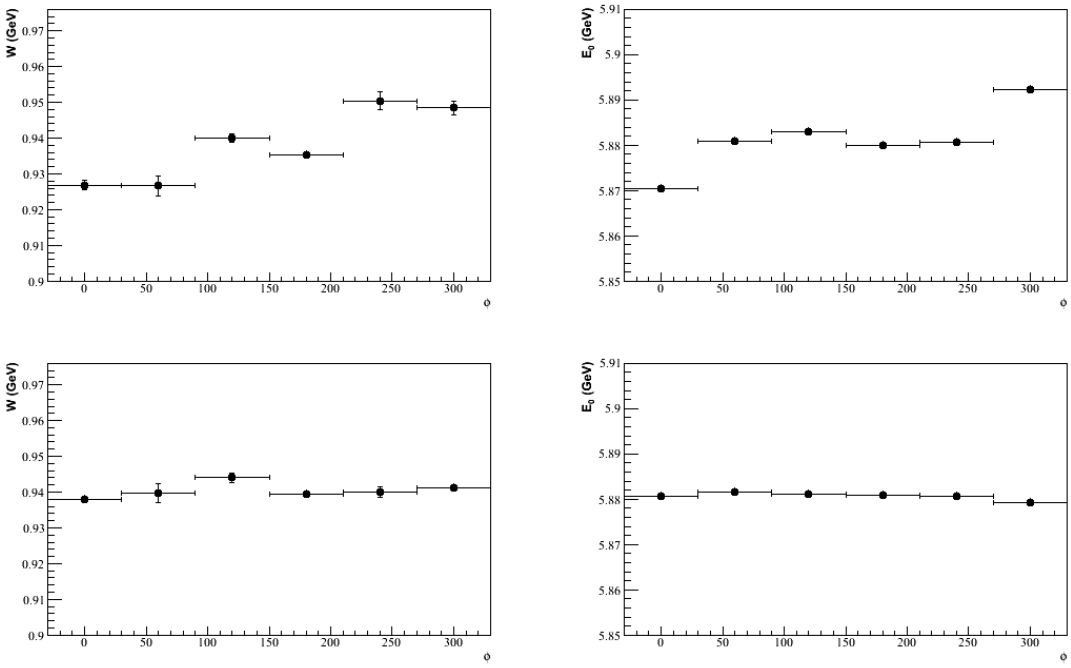

Figure 4.65: The left column represents W and the right column represents E_0. The top row is before kinematic corrections on momentum and angle, and the bottom row is after both angle and momentum corrections. We notice a shift in the average sector value in almost all sectors towards the expected values.

Proton Kinematic Corrections Using the $e + p \rightarrow e + n + \pi^+$ Channel:

Now that the corrections to the electron are completed, we may proceed by correcting the proton quantities. Because of the one-to-one correspondence of electron polar angle to proton polar angle in elastic scattering, proton acceptance is limited to larger angles. This is due to the corresponding electrons at low angles being blocked by the IC. To avoid this restriction, we may look at another channel which has a positive particle to analyze. We opt to use the π^+ electroproduction channel for this purpose, making use of Assumption #4 to apply our corrections to the π^+ on the also positively charged proton. Because the electron angle and momentum are now supposedly trustworthy, the only quantity which is not known is the pion momentum. Consider:

$$p_n^\mu = q^\mu + p_p^\mu - p_{\pi^+}^\mu, \tag{149}$$

where p_n^μ is the outgoing neutron four-vector, q^μ is the virtual photon four-vector, p_p^μ is the incoming proton four-vector, and $p_{\pi^+}^\mu$ is the outgoing pion four-vector. Then, by taking the four-product of each side we have:

$$M_n^2 = M_p^2 + m_{\pi^+}^2 - Q^2 - 2|\vec{p}_{\pi^+}| \left((M_p + \omega)\sqrt{1 + \frac{m_{\pi^+}^2}{|\vec{p}_{\pi^+}|^2}} - \sqrt{Q^2 + \omega^2}\cos\theta_{q,|\vec{p}_{\pi^+}|} \right), \tag{150}$$

where ω is the energy of the virtual photon and $\theta_{q,p_{\pi^+}}$ is the angle between the virtual photon and the pion. At this point, if the pion momentum is the only quantity left uncorrected, the reconstructed mass of the neutron becomes a good way to measure the quality of the pion momentum. We have only to write p_{π^+} explicitly as a function of all the other known variables.

$$p_{\pi^+} = \frac{M^2\sqrt{Q^2+\omega^2}\cos\theta_{q,p_{\pi^+}} - (M_p+\omega)\sqrt{M^4 + 4m_{\pi^+}^2(Q^2+\omega^2)\cos^2\theta_{q,p_{\pi^+}} - 4m_{\pi^+}^2(M_p+\omega)^2}}{2\left[(Q^2+\omega^2)\cos^2\theta_{q,p_{\pi^+}} - (M_p+\omega)^2\right]}, \tag{151}$$

where we have made the convenient substitution:

$$M^2 = M_n^2 - M_p^2 - m_{\pi^+}^2 + Q^2 \tag{152}$$

After the analytical equation $p_{\pi^+}(M_N)$ is obtained, we follow in the footsteps of the electron corrections, and determine

$$\delta p_{\pi^+} = \frac{p_{\pi^+,\text{calc}}}{p_{\pi^+,\text{meas}}} \tag{153}$$

with the intent of finding a correction function for all positive particles which minimizes this difference. As for all our previous kinematical corrections, we prefer to look at δp_{π^+} as a function of DC coordinates, as we stated in the previous section, and it will be done sector by sector. First, we will fit δp_{π^+} as a function of $\phi_{\rm DC}$ in bins of $\theta_{\rm DC}$. For this analysis, we have chosen the bin limits to be:

$$\theta_{\pi^+} : [8^\circ, 28^\circ, 33^\circ, 36^\circ, 40^\circ, 42^\circ, 45^\circ, 49^\circ, 53^\circ, 57^\circ, 61^\circ, 66^\circ, 72^\circ, 79^\circ, 88^\circ, 100^\circ, 120^\circ]. \tag{154}$$

These bins are selected such that each one is filled with approximately the same number of events. This difference, δp_{π^+}, may be seen in Figure 4.66. This difference is fitted to a straight line for each sector and bin in $\theta_{{\rm DC},\pi^+}$ as a function of $\phi_{{\rm DC},\pi^+}$:

$$\delta p_{\pi^+} = 1 + e_{\pi^+}(\theta_{{\rm DC},\pi^+}) + f_{\pi^+}(\theta_{{\rm DC},\pi^+})\phi_{{\rm DC},\pi^+}. \tag{155}$$

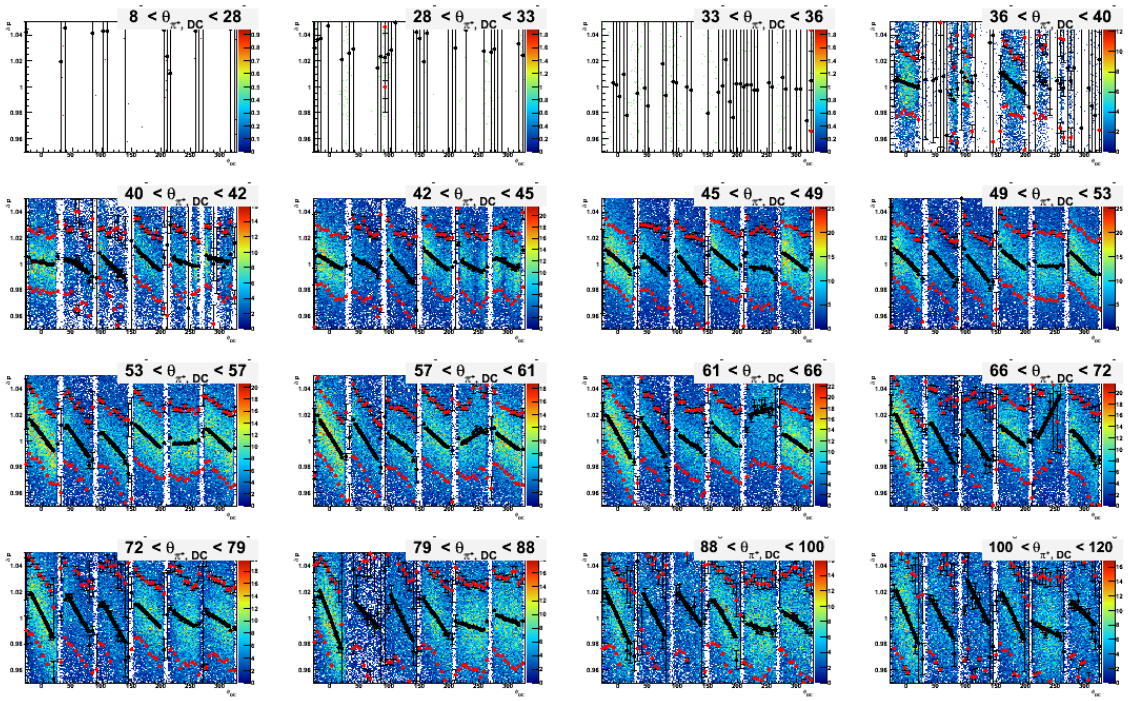

Figure 4.66: δp_{π^+} as a function of ϕ_{DC,π^+}, for different bins of $\theta_{\mathrm{DC},\pi^+}$. The black points represent the means of the fits of Gaussian peaks to slices in ϕ_{DC,π^+}, and the red points represent the standard deviations of the same. The black curves represent the fits in ϕ_{DC,π^+} according to a straight line. It is useful to note that the lack of events below $\theta_{\mathrm{DC},\pi^+} = 36^\circ$ due to the fiducial cut we place on positive particles due to the shadow of the IC. Naturally, pions which pass through the IC and are detected by CLAS will have much less energy due to ionization, and will not be useful candidates for this study. For this study, we employ the same exact IC shadow cut to pions as we do to protons.

Next, e_{π^+} and f_{π^+} are fitted as functions of $\theta_{\mathrm{DC},\pi^+}$ according to the equations

$$e_{\pi^+} = e_{\pi^+,0} + e_{\pi^+,1}\theta_{\mathrm{DC},\pi^+} + e_{\pi^+,2}\theta^2_{\mathrm{DC},\pi^+}, \tag{156}$$

and

$$f_{\pi^+} = f_{\pi^+,0} + f_{\pi^+,1}\theta_{\mathrm{DC},\pi^+} + f_{\pi^+,2}\theta^2_{\mathrm{DC},\pi^+}, \tag{157}$$

whose fits may be seen in Figure 4.67 and Figure 4.68. The parameters according to this analysis are then used in the final master correction function:

$$\begin{aligned} \delta p_{\pi^+} \quad &= 1 + e_{\pi^+,0} + e_{\pi^+,1}\theta_{\mathrm{DC},\pi^+} + e_{\pi^+,2}\theta^2_{\mathrm{DC},\pi^+} \\ &+ \left(f_{\pi^+,0} + f_{\pi^+,1}\theta_{\mathrm{DC},\pi^+} + f_{\pi^+,2}\theta^2_{\mathrm{DC},\pi^+}\right)\phi_{\mathrm{DC},\pi^+}. \end{aligned} \tag{158}$$

These parameters are conveniently provided below in table format:

Table 4.9: The table of parameters corresponding to equation 158, the equation which gives the kinematic corrections to the momentum for positive pions and protons.

	$e_{\pi^+,0}$	$e_{\pi^+,1}$	$e_{\pi^+,2}$
sector 1	-0.00695422	0.000300308	-2.47145e-06
sector 2	-0.00681235	0.00017175	-9.82635e-07
sector 3	-0.00380977	-9.09995e-05	1.85863e-06
sector 4	-0.00194689	0.000175169	-1.62817e-06
sector 5	-0.0141774	0.000464551	-4.12438e-06
sector 6	0.0142706	-0.000422821	2.76701e-06

	$f_{\pi^+,0}$	$f_{\pi^+,1}$	$f_{\pi^+,2}$
sector 1	0.00189944	-6.45155e-05	3.45423e-07
sector 2	0.00147839	-5.57523e-05	3.26713e-07
sector 3	-0.00190681	4.75771e-05	-3.81936e-07
sector 4	-0.00101298	2.35001e-05	-2.16256e-07
sector 5	-0.00124745	3.84751e-05	-2.87222e-07
sector 6	0.00050131	-2.67503e-05	2.0248e-07

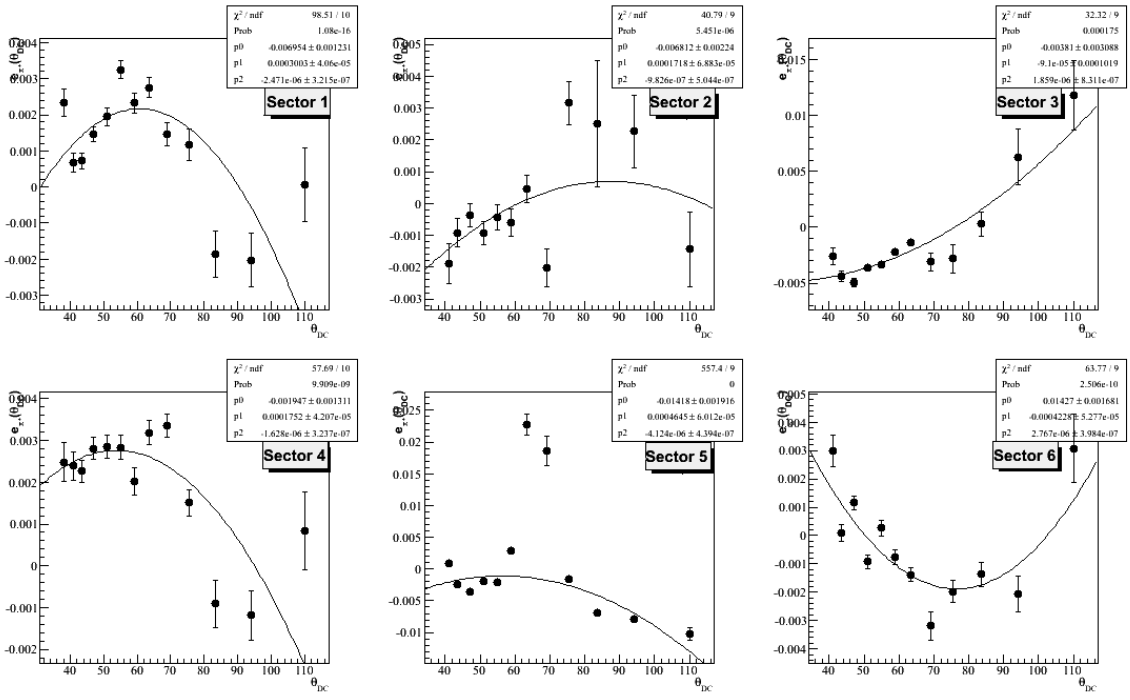

Figure 4.67: The parameter e_{π^+} fit as a function of $\theta_{\mathrm{DC},\pi^+}$ sector by sector according to equation 156.

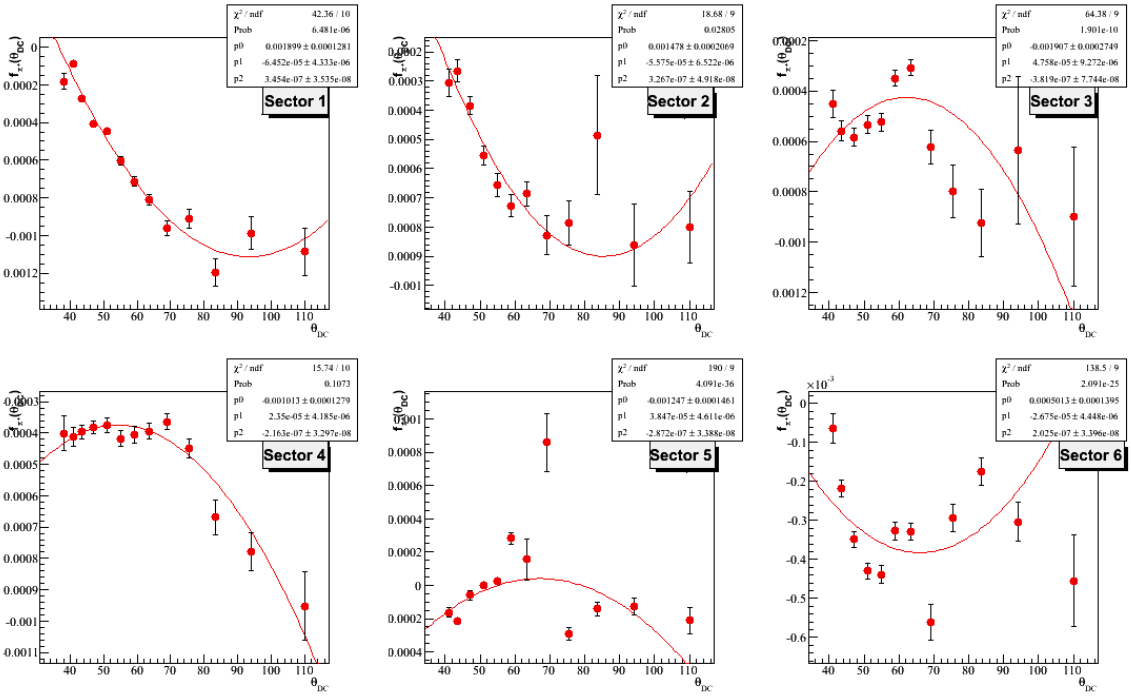

Figure 4.68: The parameter f_{π^+} fit as a function of $\theta_{\mathrm{DC},\pi^+}$ sector by sector according to equation 157.

We finally may find the corrected momentum by the following relation:

$$p_{\pi^+,\mathrm{corr}} = p_{\pi^+,\mathrm{meas}} \delta p_{\pi^+} \tag{159}$$

The histograms measuring the ratio may be seen, corrected $\frac{p_{\pi^+,\mathrm{calc}}}{p_{\pi^+,\mathrm{meas}}}$ and uncorrected $\frac{p_{\pi^+,\mathrm{calc}}}{p_{\pi^+,\mathrm{corr}}}$, in Figure 4.69 and Figure 4.70. We note that the slanted feature of each sector is quite reliably flattened out after the corrections.

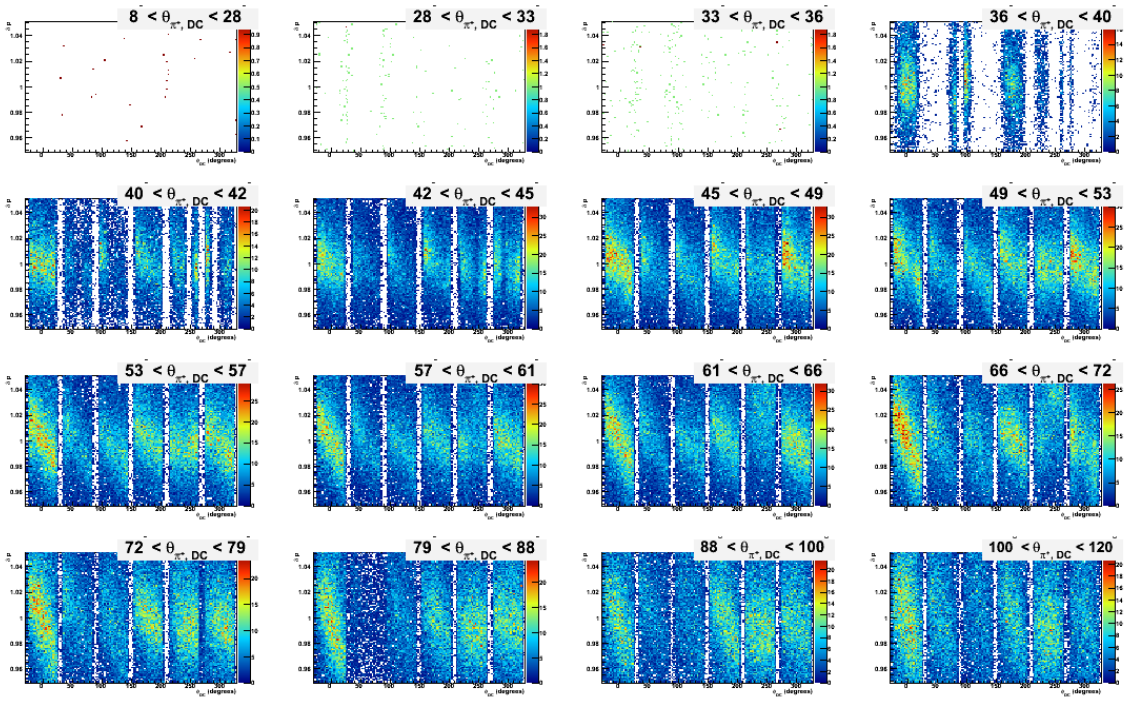

Figure 4.69: δp_{π^+} as a function of ϕ_{DC,π^+}, for different bins of $\theta_{\mathrm{DC},\pi^+}$, before momentum corrections to pions.

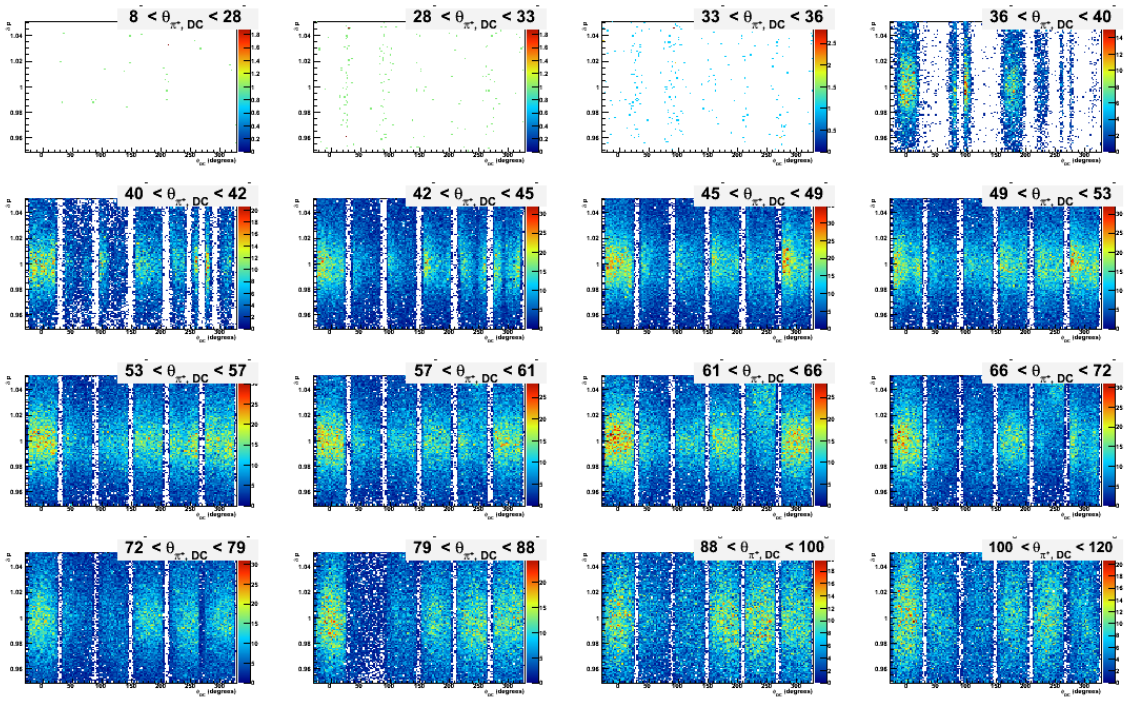

Figure 4.70: δp_{π^+} as a function of ϕ_{DC,π^+}, for different bins of $\theta_{\mathrm{DC},\pi^+}$, after momentum corrections to pions.

Finally, we may view the ratio of the missing mass variable $M_{N,\text{meas}}$ to the nominal mass value M_N to double check the effect of the momentum correction we have just applied, where $M_{N,\text{meas}}$ is calculated according to equation 150, for uncorrected and corrected momenta, as a function of ϕ_{DC,π^+}:

$$\delta M_N = \frac{M_{N,\text{meas}}}{M_N}. \tag{160}$$

These distributions may be seen in Figure 4.71 and Figure 4.72, and they receive a similar effect from the correction, moving from a slanted distribution to a flat one after the momentum correction function is applied. It is also useful to look at the same distributions as a function of θ_{DC,π^+}, as seen in Figure 4.73 and Figure 4.74, before and after corrections. We note that in Figure 4.73 and Figure 4.74, we see several vertical shifts in local areas of θ_{DC,π^+}, especially at $60^\circ - 70^\circ$ in sector 5, but in numerous other places. As we mentioned during our study of fiducial cuts, there are numerous anomalies which occur in the DC. While these are removed for electrons and protons, our π^+ selection is little less delicate and as a result we see the familiar shift reappear. This is of no concern to us, in any case - the correction function at those choices of angles will not affect the analysis because protons in that region have already been rejected. Finally, according to our original assumptions, these corrections may be used for all positive particles.

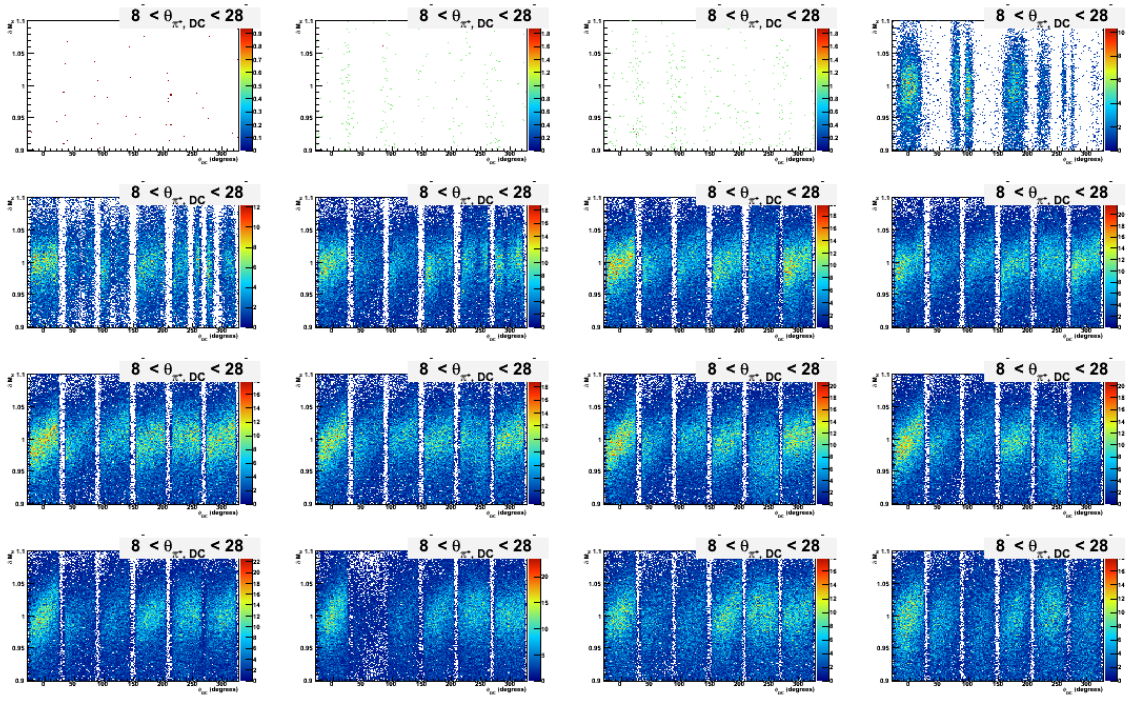

Figure 4.71: δM_N as a function of ϕ_{DC,π^+}, for different bins of θ_{DC,π^+}, before momentum corrections to pions.

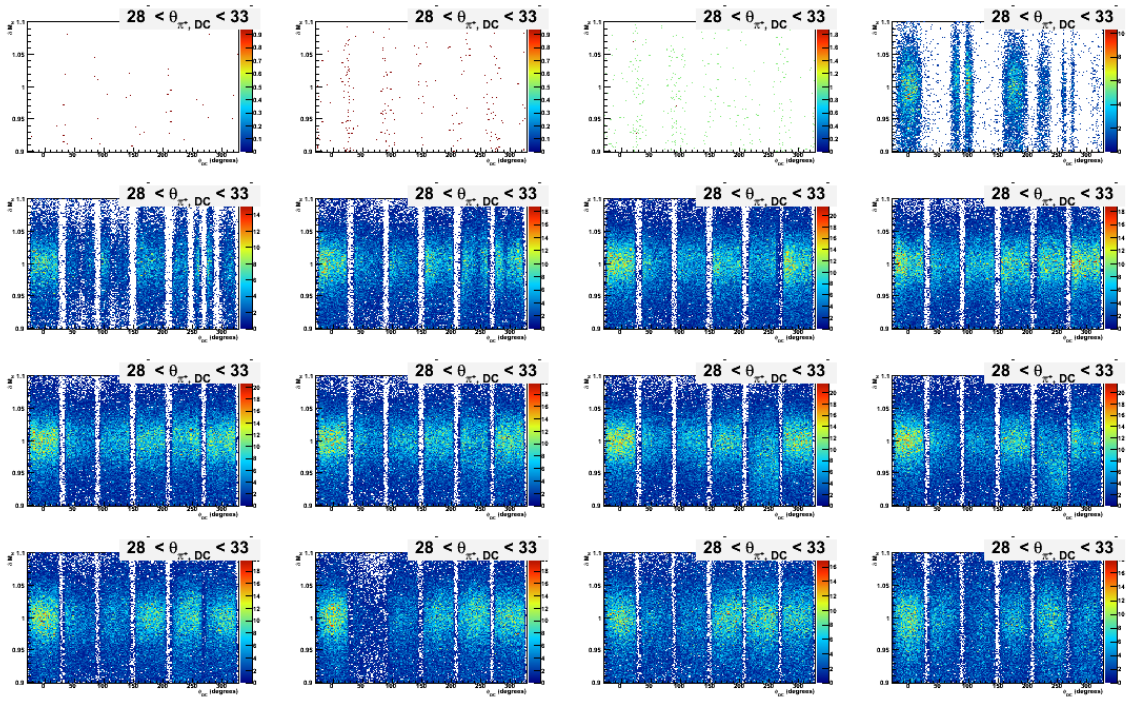

Figure 4.72: δM_N as a function of ϕ_{DC,π^+}, for different bins of $\theta_{\mathrm{DC},\pi^+}$, after momentum corrections to pions.

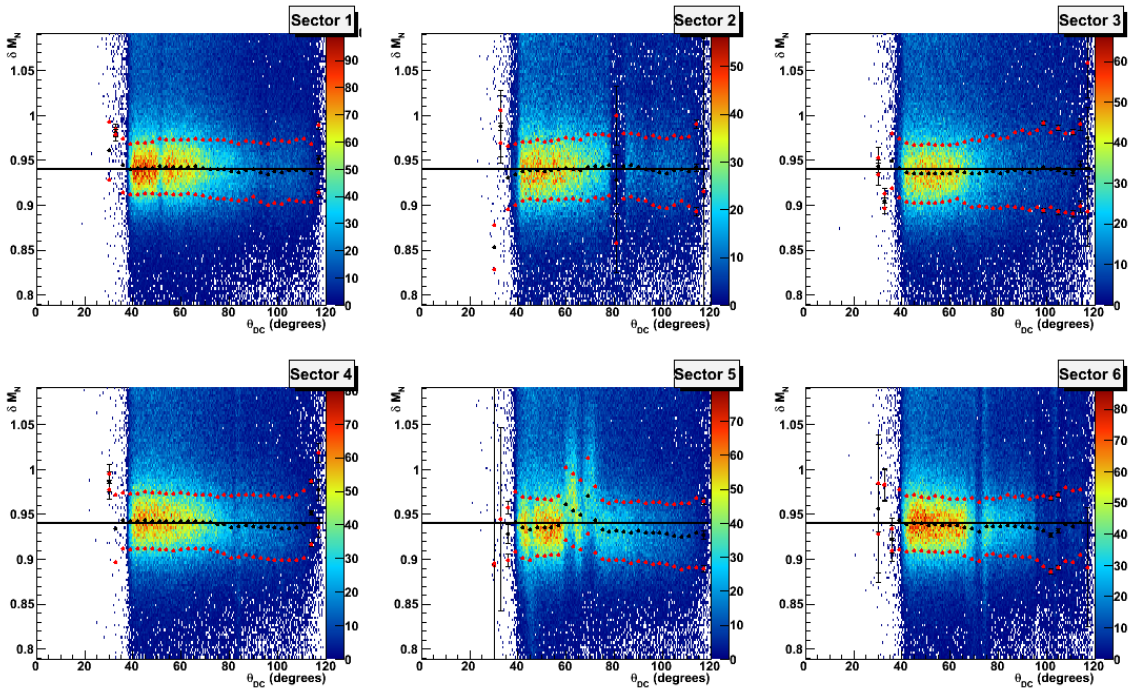

Figure 4.73: δM_N as a function of $\theta_{\mathrm{DC},\pi^+}$, before momentum corrections to pions. The black points represent the means in slices of $\theta_{\mathrm{DC},\pi^+}$ and the red points correspond to one standard deviation.

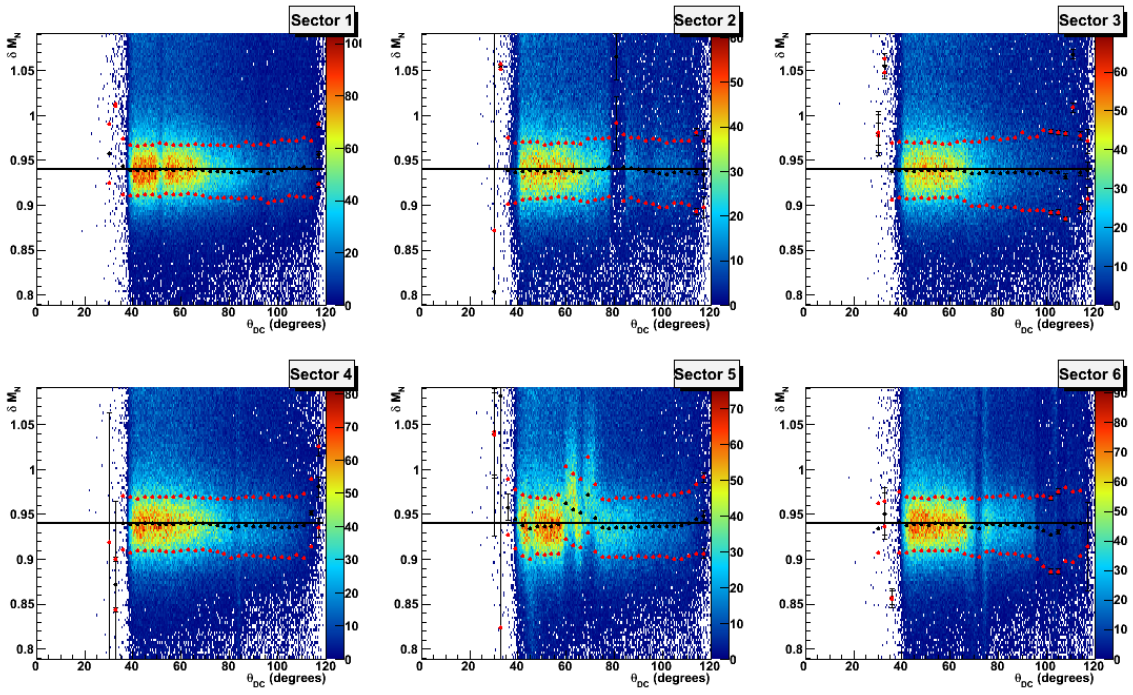

Figure 4.74: δM_N as a function of $\theta_{\mathrm{DC},\pi^+}$, after momentum corrections to pions. The black points represent the means in slices of $\theta_{\mathrm{DC},\pi^+}$ and the red points correspond to one standard deviation. Comparing with Figure 4.73, we notice a small, but significant improvement in the mean and sigma.

Conclusion on Momentum and Angle Corrections:

We conclude with reasonable assurance that the corrections applied for both ionization corrections and kinematic corrections are done correctly based on our use of simulations and our use of E_0, W and M_N as benchmarks. We note in passing that there are some remaining studies that could be of interest, which remain unfinished. In particular, there is belief that a study of kinematical corrections to the photons in both the IC and EC could be fruitful. These corrections may be necessary due to our lack of knowledge concerning the exact hit coordinates on the respective detectors. At the moment, these studies are beyond the scope of this thesis, but could be an interesting point of refinement to the data.

4.4.3 Corrections to Photon Energies in Data

It is important to have a good measurement on the momenta of our photons, not only for our DVCS analysis, but also for our π^0 subtraction analysis. For that reason, we must develop a method for judging the quality of the photon momenta we have measured. For this study, we shall focus on corrections to the EC photons we have measured in our experiment. The method that we elect to

use is the invariant mass of photons pairs from the π^0 decay mode.[52,53]

We begin by looking at every event where at least two photons are detected. For such events, we look at every photon pair combination, and measure their invariant mass. That is to say, if the four-vectors of the two photons in a pair are $p^\mu_{\gamma_1}$ and $p^\mu_{\gamma_2}$, we can find the invariant mass $IM(\gamma_1\gamma_2)$ by the relation:

$$IM^2(\gamma_1\gamma_2) = (p^\mu_{\gamma_1} + p^\mu_{\gamma_2})^2. \tag{161}$$

By analyzing the spectrum of $IM(\gamma_1\gamma_2)$, we can judge the quality of our photon data. There are several studies which have been done to improve photon data by correcting the photon momenta such that the invariant mass peak moves closer to the nominal π^0 mass. Studies have been done by P. Bosted[52] and R. de Masi[53] in experiments eg1-dvcs and e1-dvcs, respectively, and each of these studies have lead to individual corrections to photon energy. For the sake of efficiency, we will make the attempt to recycle one of these studies, applying it to e1-dvcs2, with the hopes that our experiment will receive a similar correction. We safely justify reusing one of these studies in two ways. First, these three experiments are very similar, and each use the EC, with a similar calibration, that is, for each experiment, it is believed that the sampling fraction of the EC is around a value of $f_s = 0.3$. Secondly, we may apply the corrections, and then justify the correction *a posteriori* if we see the pion mass peak has moved in the proper direction. This study will contrast these two methods by P. Bosted and R. de Masi, and determine which, if either, is appropriate for our purposes. The details leading to the exact determination of each correction may be found in the two documents referenced above. We present the corrections as listed in those documents, and refer the reader to those documents for a detailed explanation and justification of the methods.

The "uncorrected" method that is in standard use is to accept a nominal value of $f_s = .273$ as the standard value. That is to say, the total energy that is absorbed in the EC is only 27.3% of the actual photon energy. Mathematically:

$$E_\gamma = \frac{E_{\text{total}}}{.273}, \tag{162}$$

Next we address the R. de Masi method, which takes into account the possibility that this sampling fraction may have a slight dependence on the total energy deposit. Mathematically speaking:

$$E_\gamma = \frac{E_{\text{total}}}{f_s(E_{\text{total}})}, \tag{163}$$

where

$$f_s = 0.273(1.01034 - \frac{0.0272506}{E_{\text{total}}} - \frac{0.00147336}{E_{\text{total}}^2}). \quad (164)$$

Finally, we address the P. Bosted method, which takes into account the possibility of a global offset to the energy deposited, and a sector dependence on the sampling fraction as opposed to a energy deposit dependence. Mathematically:

$$E_\gamma = 0.06GeV + 1.015\frac{E_{\text{total}}}{f_{\text{s,sector}}}, \quad (165)$$

where both energies are measured in GeV, and the sector dependent sampling fraction is determined by the following table.

Table 4.10: The table of parameters corresponding to equation 165, the equation which gives the energy correction to the energy of photons in the EC.

	$f_{\text{s,sector}}$
sector 1	0.307299
sector 2	0.30438
sector 3	0.310337
sector 4	0.312228
sector 5	0.297499
sector 6	0.3021

The effect of these calculations are most easily appreciated by looking not only at the invariant mass peak, but how this invariant mass changes with respect to three different variables: the energy of the pion, the polar angle of the pion, and the missing energy of the $e + p + \gamma + \gamma$ system. The invariant mass may be seen, plotted as a function of each of these variables separately, before and after both corrections in Figure 4.75, for EC only. Since we have a motivation to make sure the IC is calibrated correctly too, we present the same plots for IC only in Figure 4.76. We also note in passing that the invariant mass as measured in the IC, while not corrected in this study, may benefit from similar study in the future. The correction of IC energy is not competed. We list it here as an attractive candidate for future refinements. Finally, for the EC photon pairs, we may look at the means and sigmas of the invariant mass spectra by themselves, comparing the uncorrected and corrected distributions directly in Figure 4.77 both as a function of pion energy and polar angle. We conclude from these plots that the corrections to the mean value of the invariant mass in the EC are best performed by the P. Bosted corrections.

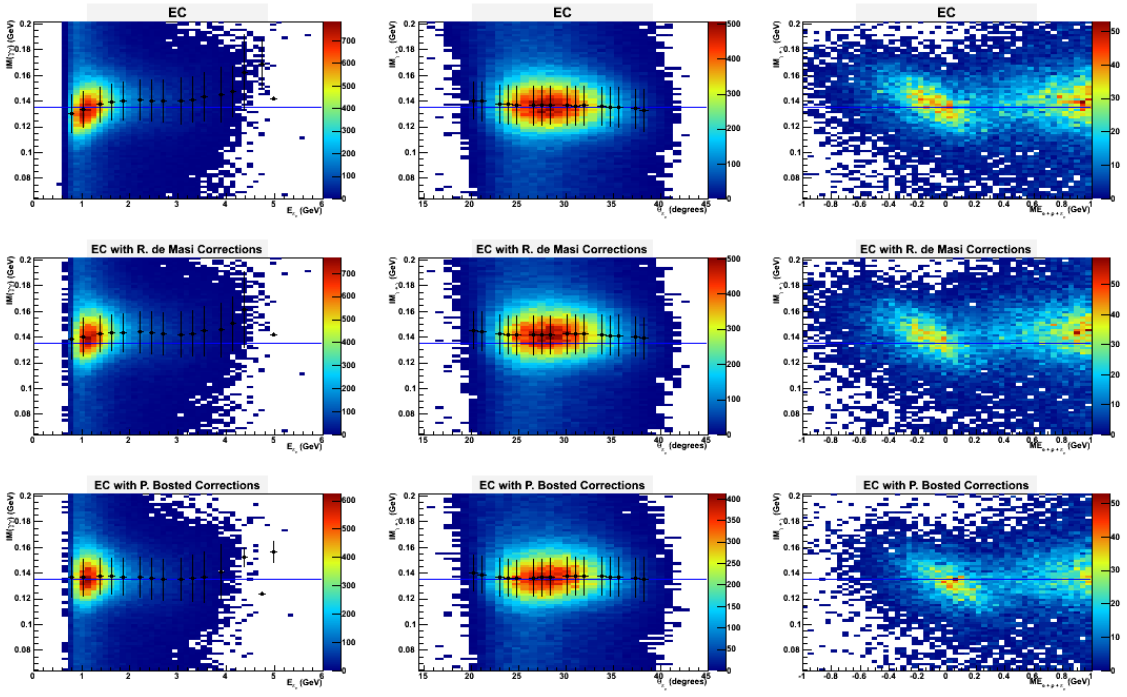

Figure 4.75: For EC studies: we plot on the left column the invariant mass as a function of pion energy; in the middle column the invariant mass as a function of pion polar angle; and on the right column the invariant mass as a function of missing energy of the $e + p + \gamma + \gamma$ system. We plot on the top row results before corrections; on the middle row results after R. de Masi corrections; and on the bottom row results after P. Bosted corrections.

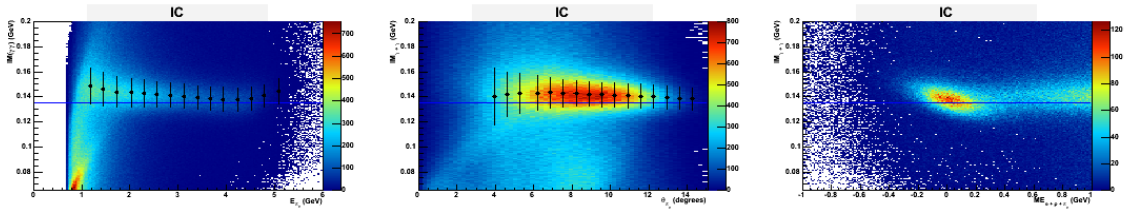

Figure 4.76: For IC viewing: on the left, the invariant mass as a function of pion energy, in the middle, the invariant mass as a function of pion polar angle, and on the right, the invariant mass as a function of missing energy of the $e + p + \gamma + \gamma$ system.

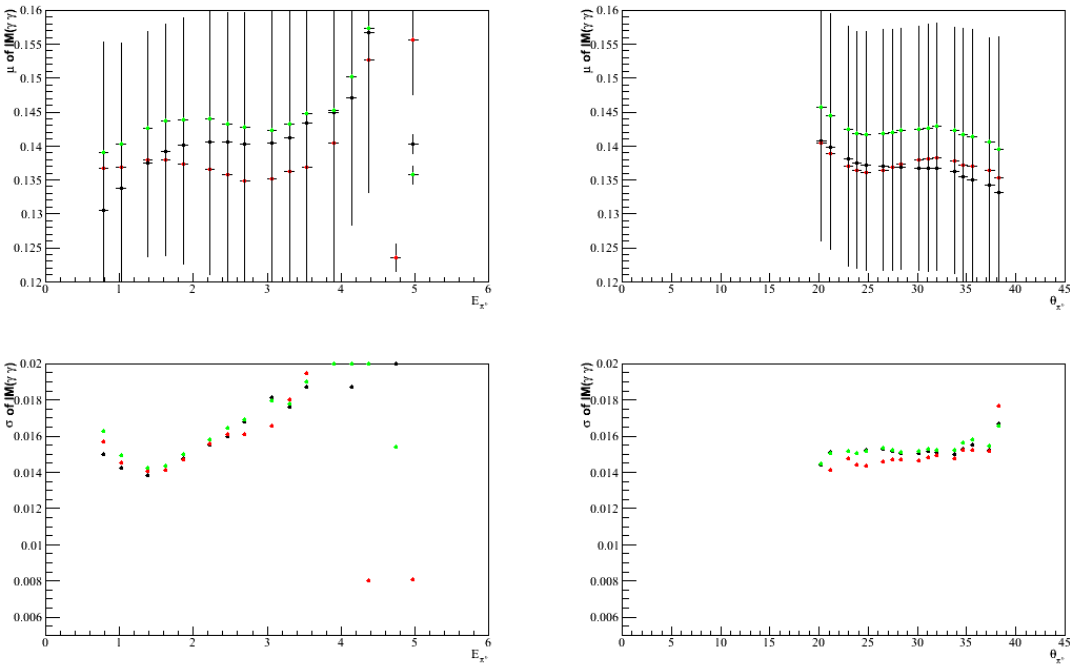

Figure 4.77: We plot on the top left the means for the mass spectra as a function of pion energy; on the top right the means of the mass spectra as a function of pion polar angle; on the lower right the sigmas for the mass spectra as a function of pion energy; and on the bottom right the sigmas for the mass spectra as a function of pion polar angle. Black points represent results before corrections, red points represent results after R. de Masi corrections, and green points represent results after P. Bosted corrections. We conclude from this graph that the P. Bosted corrections are the best for e1-dvcs2 both in terms of the change in the mean value and the slightly tightened value of sigma.

4.5 DVCS Event Selection

After particle identification for both data and Monte Carlo, a selection of the $e + p \rightarrow e' + p' + \gamma$ channel was carried out. For Monte Carlo, it is simple because only $e + p \rightarrow e' + p' + \gamma$ events have been generated. However, in experiment, there is a mixture of many different channels. In order to select DVCS, we began by accepting every event which has one electron, one proton, and at least one photon.

4.5.1 Exclusivity Cuts

To ensure that the events from data are from the channel $e+p \rightarrow e'+p'+\gamma$, we impose conservation laws. We begin by supposing that there was an additional particle X, such that the reaction is $e + p \rightarrow e' + p' + \gamma + X$. For example, if a non-zero value of this mass, momentum, and energy of this "missing particle" are zero, we can be convinced that the event obeys the conservation laws for our channel.

Since there are resolution effects, the conservation laws will not be met exactly, and each variable will have a certain distribution around the expected value. To have guidance on where one should place restrictions on these "missing" quantities, the Monte Carlo distributions may be consulted. These distributions, being only $e + p \rightarrow e' + p' + \gamma$ events, will be an indication as to where the cuts should be placed. This section outlines the list of variables used in such exclusivity cuts, and the methods for determining the cuts on these variables. We choose $p_{X,\perp}$, E_X, $\theta_{X,\gamma}$ and Φ for our exclusivity variables, where each of these variables are: the perpendicular component of missing momentum; the missing energy; the angle between "missing particle" X and the detected photon; and the coplanarity angle. We have chosen these variables because they are not strongly correlated to each other.

There are two challenges that we are met with when trying to examine where to place our cuts on exclusive variables. Firstly, the general shapes of the distributions between Monte Carlo and data are not quite equivalent. While the general shape between the two is similar, there is clear indication that the Monte Carlo at some level is not perfectly reproducing the features in the data. The second challenge is that the exact theoretical shape of each of the variables' distributions is not known, so it is difficult to apply fits. In this analysis, we choose to fit the distribution of the data. We then find a "stretch" factor which correlates data to the uniformly stretched Monte Carlo distributions by looking at the χ^2 comparison between the two distributions after the stretching of the Monte Carlo shape. This χ^2 method involves a comparison test between two variables, with a lower χ^2/ndf indicating a better match between the two histograms. This is useful because the data and Monte Carlo are quite similar in shape, even though their relative widths may not be. A glance

at Figure 4.78 shows, for example, the difference between missing perpendicular momentum for both data and Monte Carlo. We see that the distribution is similar, but that the data is more stretched out than the Monte Carlo. Also demonstrated in this figure is the deformation ("stretching") of the Monte Carlo histogram by a uniform linear scaling in order to reproduce the same shape as in data. For each Monte Carlo distribution, one may find the appropriate "stretch factor" which takes our Monte Carlo to our data. In Figure 4.78, the χ^2/ndf between stretched Monte Carlo and unscaled data can be seen for various choices of stretch factor for $p_{X,\perp}$. We choose the choice of stretch factor which minimizes the difference between the two distributions. In this way, we may feel free to pick a cut for data, according to any criterion we wish, and compute what the corresponding Monte Carlo cut should be, and "capture" the same number of events. Mathematically, given a cut in data, x_{data}, and a stretch factor $f_{\text{sc.}}$, one may compute the corresponding cut to data x_{MC} such that:

$$x_{\text{data}} = f_{\text{sc.}} x_{\text{MC}}. \tag{166}$$

We used this method for both $p_{X,\perp}$ and $\theta_{X,\gamma}$, and the results are displayed in Figure 4.78 and Figure 4.79. Furthermore, since the distributions are different for photon detection in the IC and the EC, the analysis is done separately for both. This method helps us to obtain corresponding cuts even without having a good matching function to fit the distributions. The function that we use to obtain the cut on data is:

$$A \sin(x\sigma) e^{-0.5\left(\frac{55.\tan xk}{\sigma}\right)^2}, \tag{167}$$

where A, k and σ are fit parameters, x is either $p_{X,\perp}$ or $\theta_{X,\gamma}$, and the stretch factors are:

Table 4.11: The "stretch" factors for $p_{X,\perp}$ and $\theta_{X,\gamma}$.

	IC	EC
$f_{sc.}$ - $p_{X,\perp}$	1.6	1.5
$f_{sc.}$ - $\theta_{X,\gamma}$	1.2	2.8

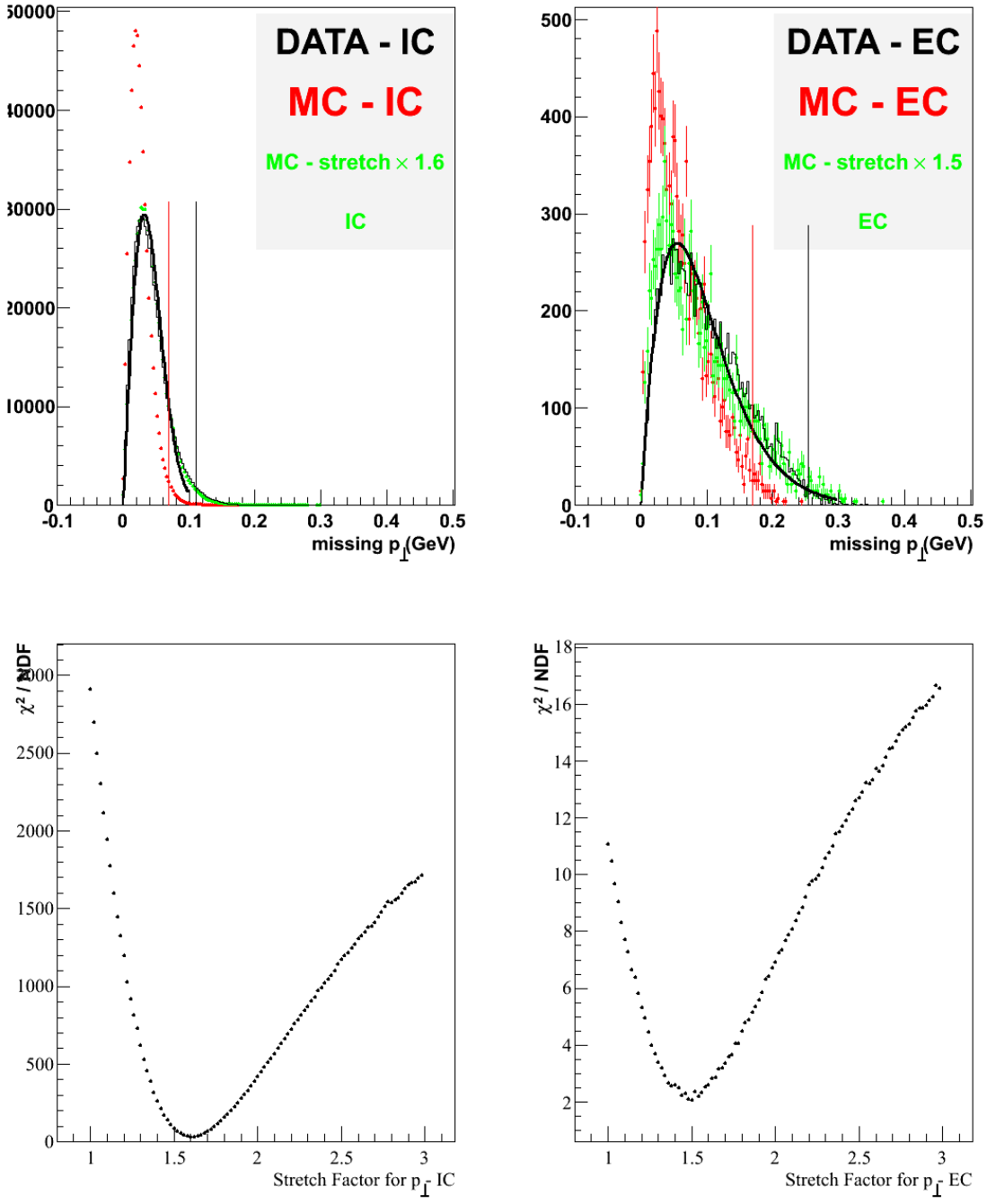

Figure 4.78: For the variable $p_{X,\perp}$, on top, the distributions for data in black, Monte Carlo in red, and stretched Monte Carlo in green. The upper left panel is for the IC and the upper right panel is for the EC. The cuts in black correspond to the IC and EC cuts at 97% of the fit to equation 167. The cut in red corresponds to the scaling of the black cut according to the stretch factor. On the bottom left, the χ^2 value for the comparison between data and stretched Monte Carlo, as a function of "stretching", on left for IC and on right for EC. These plots correspond to events after cuts on all other variables.

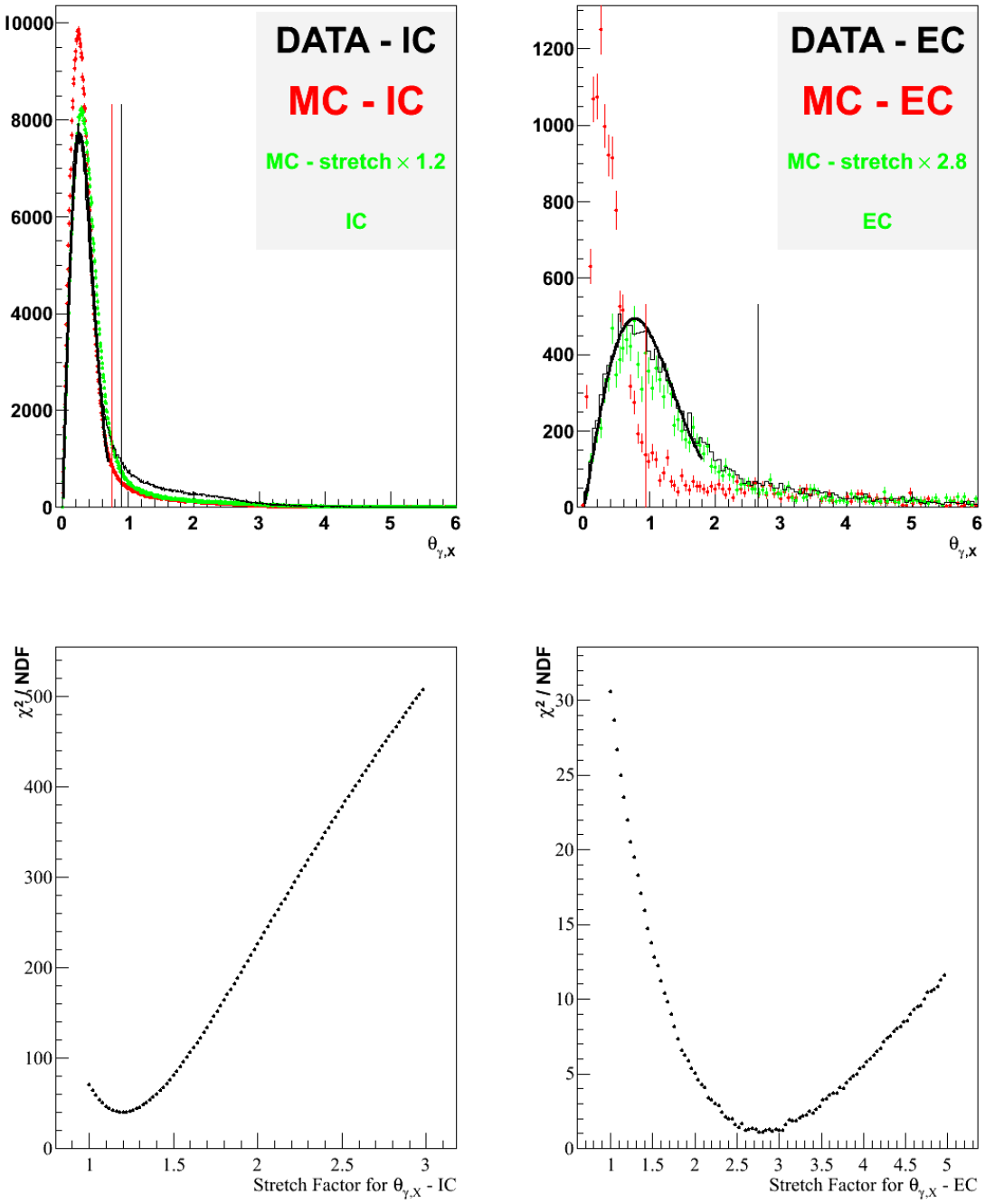

Figure 4.79: For the variable $\theta_{X,\gamma}$, on top, the distributions for data in black, Monte Carlo in red, and stretched Monte Carlo in green. The upper left panel is for the IC and the upper right panel is for the EC. The cuts in black correspond to the IC and EC cuts at 90% of the fit to equation 167. The cut in red corresponds to the scaling of the black cut according to the stretch factor. On the bottom left, the χ^2 value for the comparison between data and stretched Monte Carlo, as a function of "stretching", on left for IC and on right for EC. These plots correspond to events after cuts on all other variables.

In order to determine the cut which will be placed on data, the stretch factor is used to determine where to place the corresponding cut in Monte Carlo. In order to determine the cut for data, we will rely on the stretched Monte Carlo. We decide to take our cut at 97%, as calculated numerically from the stretched Monte Carlo histogram. This will be the value that we use for our cuts on data. The corresponding cuts can be obtained by scaling these values.

Table 4.12: A table of cuts corresponding to the variables $p_{X,\perp}$ and $\theta_{X,\gamma}$ for IC and EC, and data and Monte Carlo.

	IC	EC
$p_{X,\perp}$ data cuts	.1104 GeV	.254 GeV
sig. level	97%	97%
$p_{X,\perp}$ MC cuts	.069 GeV	.169333 GeV
sig. level	97%	97%
$\theta_{X,\gamma}$ data cuts	.894°	2.646°
sig. level	90%	90%
$\theta_{X,\gamma}$ MC cuts	.745°	.945°
sig. level	90%	90%

The method concerning the missing energy of $e+p \to e'+p'+\gamma+X$ is different. The distribution resembles a offset-skewed Gaussian for the IC, and a Gaussian for EC. An skew Gaussian is defined as:

$$f(x) = 2\phi(x)\Phi(\alpha x), \tag{168}$$

where $\phi(x)$ is an ordinary Gaussian, and $\Phi(\alpha x)$ is the cumulative distribution function of $\phi(x)$, where α is the skewness. A offset-skewed Gaussian is then given by:

$$f(x) = 2\phi(x)\Phi(\alpha(x-\beta)), \tag{169}$$

where α is skewness, and β is the offset.

For the IC, we fit to a skewed Gaussian, and reject .2% of events on the left and 2.3% of the events on the right, according to the function of the fit. For the EC, we fit to a standard Gaussian and reject events outside of the 3σ limit. These fits are presented in Figure 4.80.

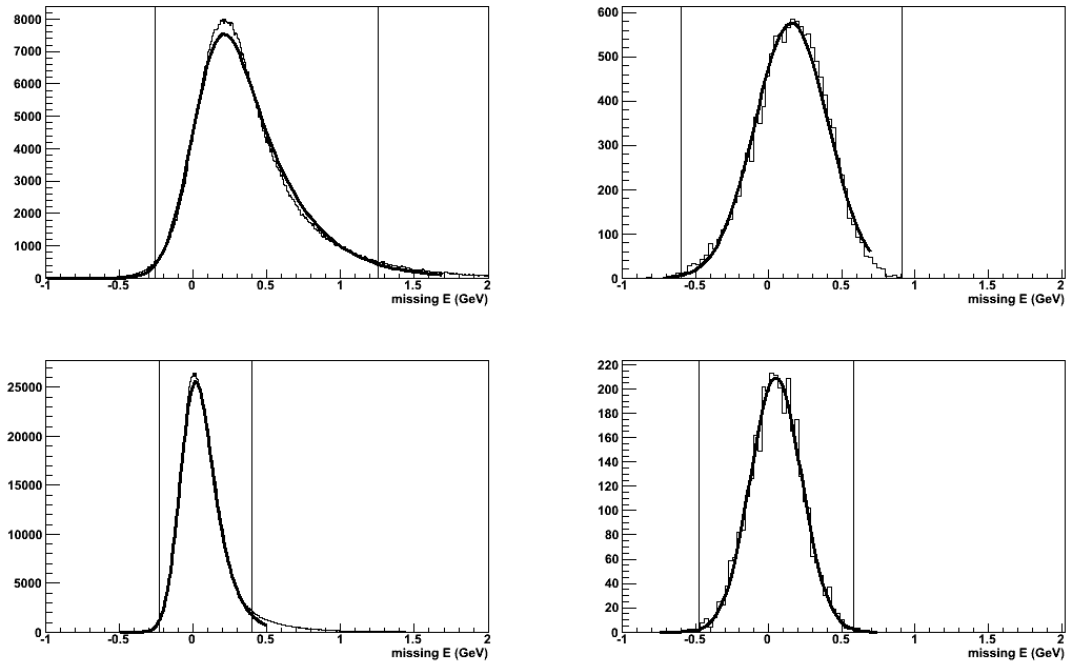

Figure 4.80: For the variable E_X, on top, data, on bottom, Monte Carlo. On left is IC, and on right is EC. On the left, the IC distribution is fit to a skewed Gaussian for both data and Monte Carlo. On the right, the EC is fit to a Gaussian for both data and Monte Carlo. The cuts are denoted by the vertical black lines, whose values are written in Table 4.13. These plots correspond to events after cuts on all other variables.

Table 4.13: A table of cuts corresponding to the variable E_X for IC and EC, and data and Monte Carlo.

	IC	EC
E_X data cuts	$-.259$ GeV $< E_X <$ 1.253 GeV	$-.596876$ GeV $< E_X <$ .907776 GeV
sig. level	97.5% rejecting .2% left and 2.3% right	99.7%
E_X MC cuts	$-.229$ GeV $< E_X. <$ 398 GeV	$-.478361$ GeV $< E_X <$ .577171 GeV
sig. level	97.5% rejecting .2% left and 2.3% right	99.7%

Lastly, we cut on the coplanarity angle Φ at a value of $\pm 5°$. This cut, as we see in Figure 4.81 to Figure 4.84 serves only to clean up pathological events, and does not contribute significantly to the selection of events. A series of plots showing the exclusivity variables before and after cuts can be found in Figure 4.81 to Figure 4.84, for both data and Monte Carlo, as well as for the IC and EC separately.

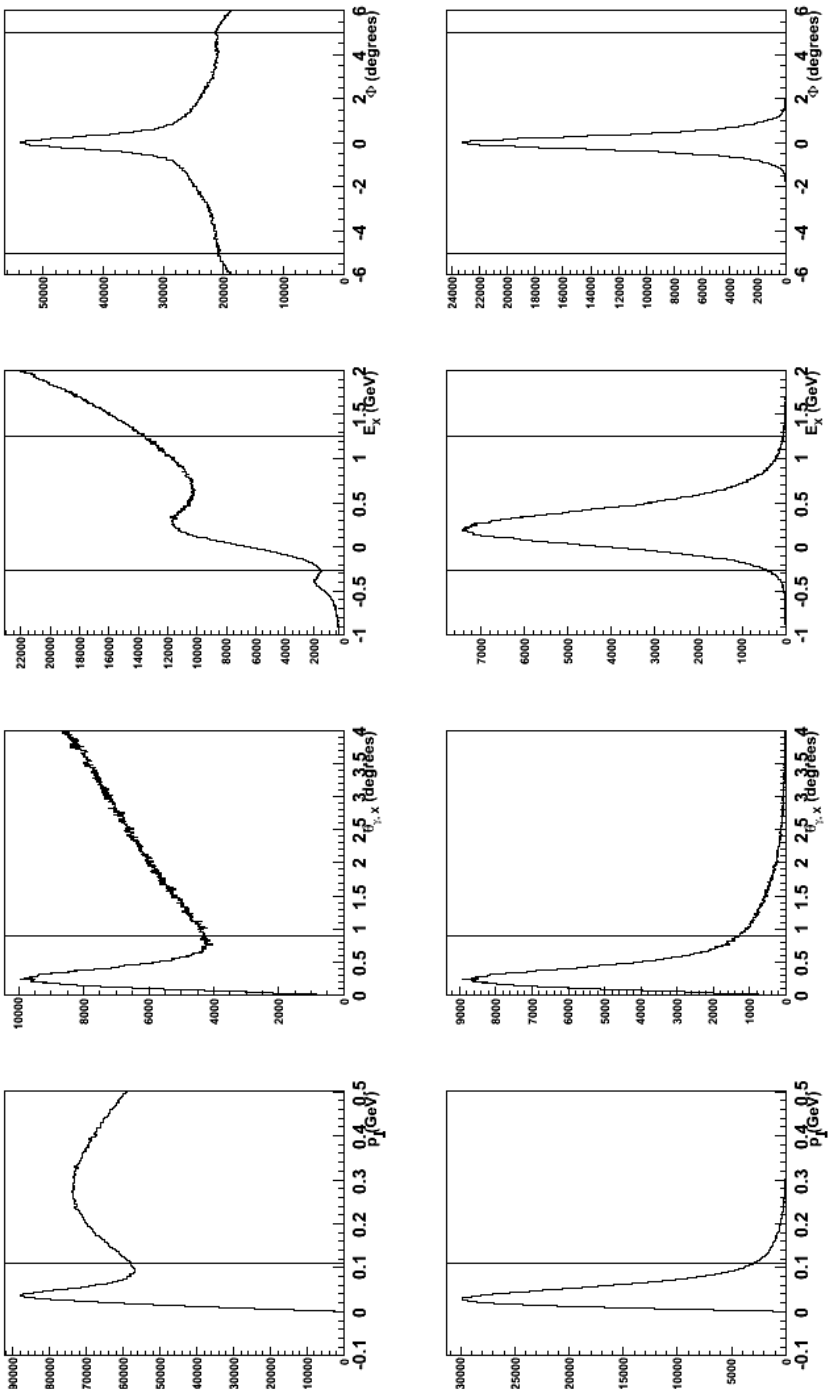

Figure 4.81: Exclusivity variables in data for IC. On the top row are the distributions before all cuts. On the bottom are the distributions after all exclusivity cuts except for the cut on the plotted variable. The only exception is Φ, for which all cuts have been applied. The first column represents $p_{X,\perp}$. The second column represents $\theta_{\gamma,X}$. The third column represents E_X. The last column represents Φ. One can see in the missing energy, before cuts, a peak below zero, which corresponds to the elastic channel with an accidental photon of 400 MeV.

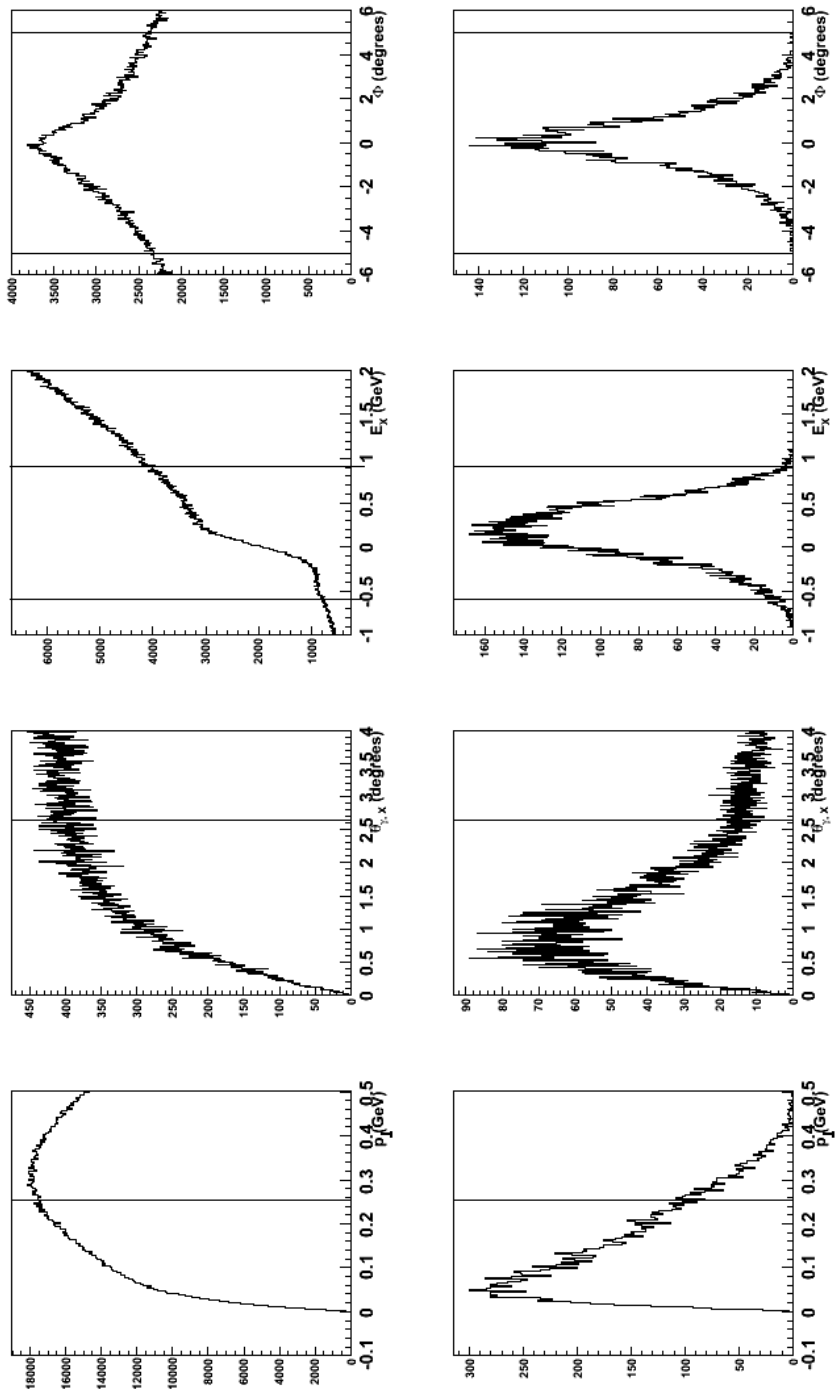

Figure 4.82: Exclusivity variables in data for EC. On the top row are the distributions before all cuts. On the bottom are the distributions after all exclusivity cuts except for the cut on the plotted variable. The only exception is Φ, for which all cuts have been applied. The first column represents $p_{X,\perp}$. The second column represents $\theta_{\gamma,X}$. The third column represents E_X. The last column represents Φ. One can see in the missing energy, before cuts, a peak below zero, which corresponds to the elastic channel with an accidental photon of 400 MeV.

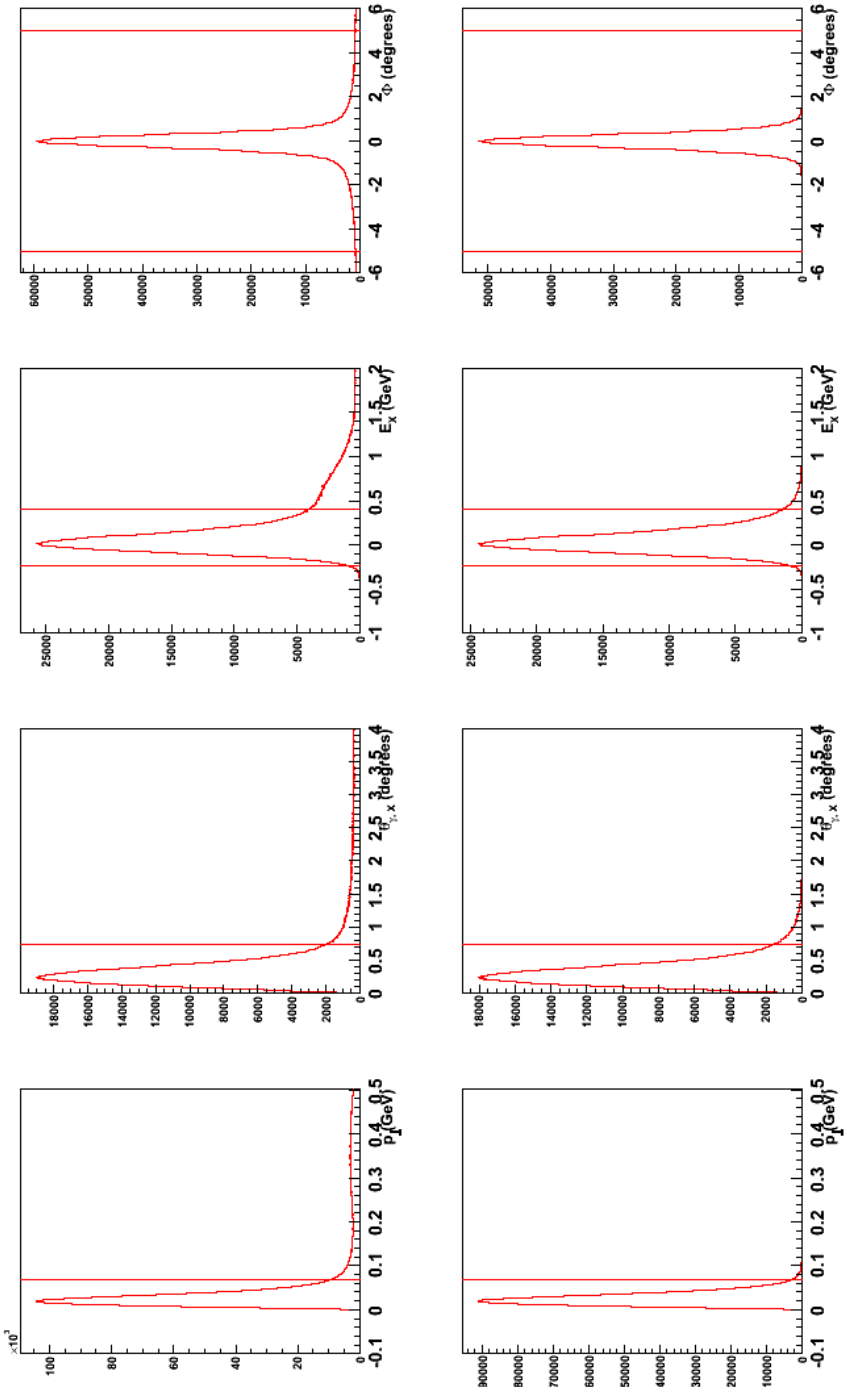

Figure 4.83: Exclusivity variables in Monte Carlo for IC. On the top row are the distributions before all cuts. On the bottom are the distributions after all exclusivity cuts except for the cut on the plotted variable. The only exception is Φ, for which all cuts have been applied. The first column represents $p_{X,\perp}$. The second column represents $\theta_{\gamma,X}$. The third column represents E_X. The last column represents Φ.

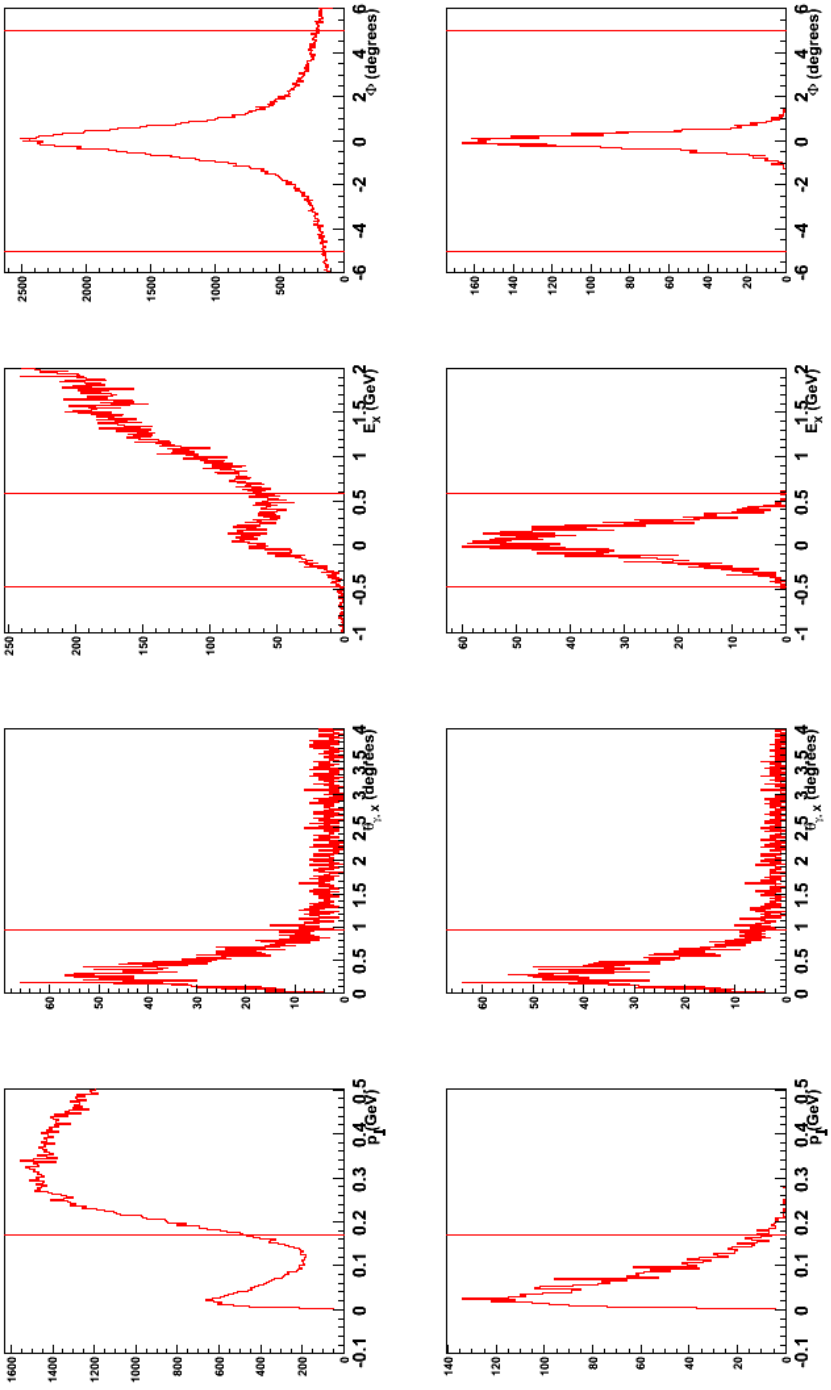

Figure 4.84: Exclusivity variables in Monte Carlo for EC. On the top row are the distributions before all cuts. On the bottom are the distributions after all exclusivity cuts except for the cut on the plotted variable. The only exception is Φ, for which all cuts have been applied. The first column represents $p_{X,\perp}$. The second column represents $\theta_{\gamma,X}$. The third column represents E_X. The last column represents Φ.

4.6 Bin Volume Determination

4.6.1 A Monte Carlo Method for Determining Bin Volumes

One of the ingredients in the cross section calculation is the kinematic volume of each of the bins. We previously wrote this quantity as: $\Delta V = \Delta Q^2 \Delta t \Delta x_B \Delta\Phi$. Since we have determined the bins, we may now proceed to calculate each of those volumes. However, there is one problem: the bins that we have chosen are not completely rectilinear in the variables of the cross section. We have opted to swap the variable Q^2 in our choice of binning, in favor of θ_e. The volume may still be easily calculated by determining the Jacobian:

$$\int_{\mathcal{V}} \mathrm{d}V = \int_{\mathcal{V}} \mathrm{d}Q^2 \mathrm{d}t \mathrm{d}x_B \mathrm{d}\Phi = \int_{\mathcal{V}} \mathcal{J}(\theta_e, t, x_B, \Phi) \mathrm{d}\theta_e \mathrm{d}t \mathrm{d}x_B \mathrm{d}\Phi \tag{170}$$

This can be done analytically for each bin. However, there are some cuts which are placed on our kinematics which still run through some of our bins. One may see five of the following cuts in Figure 4.2. The cut on θ_γ does not show up well on this plot because it only cuts out part of the volume where Φ is close to 0° or 360°, an effect that is independent of the Q^2 and x_B of the aforementioned figure. The $t_{\min}$ cut may be seen in Figure 4.2. These following cuts run through each of the bins in different ways, and, when written as a function of our binning variables, end up being very complicated, rendering an analytical solution for the volume too cumbersome to compute.

1. $\theta_e > 21^\circ$
2. $\theta_e < 45^\circ$
3. $W > 2$ GeV
4. $Q^2 > 1$ GeV^2
5. $p_e > 0.8$ GeV
6. $\theta_\gamma > 4.77^\circ$
7. $-t < t_{\min}$

   where $t_{\min} = \frac{Q^2\{2(1-x_B)(1+\epsilon^2-\sqrt{1+\epsilon^2}\}}{4\epsilon^2+4x_B(1-x_B)}$, and $\epsilon = \frac{4M_p x_B}{Q^2}$.

This cumbersome volume calculation involving Jacobians and extra cuts can be circumvented by employing a Monte Carlo method of integration. To determine the volume of any one bin, we need only to define a new and easily calculated volume V_{super} which completely contains the bin; generate N_{super} several random points within the new volume V_{super}, where N_{super} is "large"; and

determine the ratio of points which lie within the bin and cuts $N_{\rm bin}$ to the total number $N_{\rm super}$. In our case, we take $V_{\rm super}$ to be the smallest bin possible which is rectilinear in x_B, Q^2, $-t$ and Φ, and which contains the bin to be calculated. We may then write the equation for the volume as:

$$\Delta V = V_{\rm super}\frac{N_{\rm bin}}{N_{\rm super}}, \tag{171}$$

with our criterion for "large" being $N_{\rm super} = 1,000,000$. In any Monte Carlo calculation, what is considered large enough for the number of trial events depends on the size of error bars desired. For a binomial distribution as described above, the error is:

$$\Delta V = V_{sup}\frac{\Delta N_{\rm bin}}{N_{\rm super}} = V_{\rm super}\sqrt{N_{\rm bin}\left(1-\frac{N_{\rm bin}}{N_{\rm super}}\right)} \tag{172}$$

We express our final results in terms of the volume correction $\frac{N_{\rm bin}}{N_{\rm super}}$ in Figure 4.85, for the fifth bin in x_B and θ_e. A full list of comparisons for the volume corrections may be found in Appendix B.

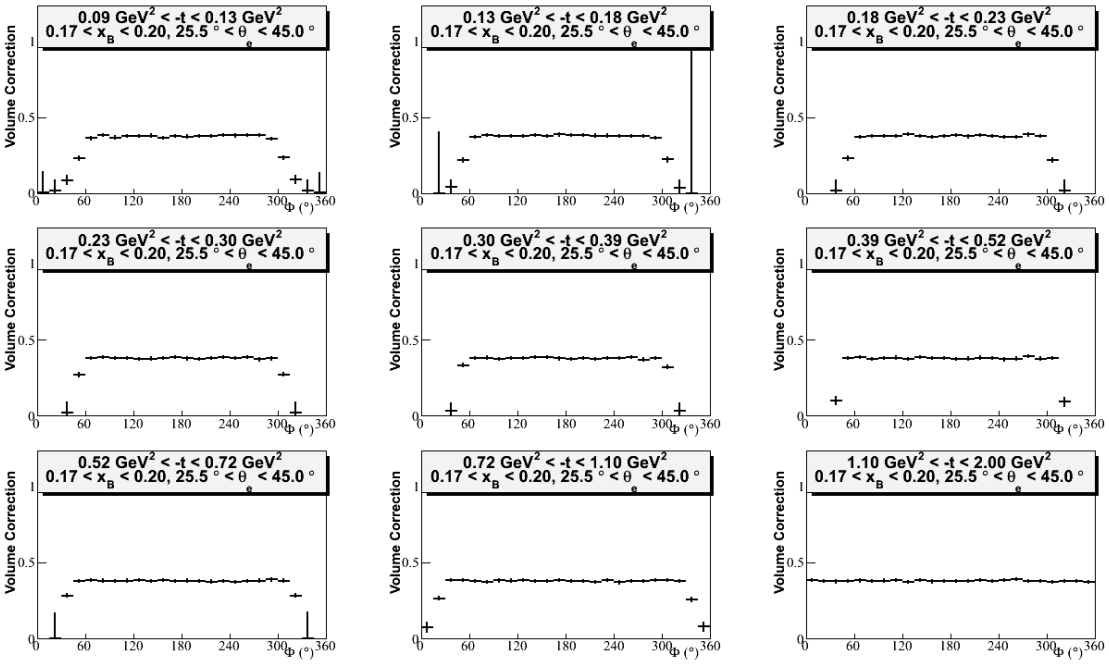

Figure 4.85: The bin volume correction $\frac{N_{\rm bin}}{N_{\rm super}}$ as a function of Φ for the fifth bin in x_B and θ_e, where $0.17 < x_B < 0.2$ and $25.5^\circ < \theta_e < 45^\circ$.

4.7 Integrated Luminosity

[2] During the course of any experiment, the quality of data must be monitored. Data which are incorrectly recorded, or acquired under incorrect conditions, for example, when detectors are malfunctioning, should be rejected. During data acquisition for e1-dvcs2, many runs of data were taken solely for the purpose of calibration or trigger studies, or have a large portion of the detector behaving in an unexpected way. Because of these considerations, a run-by-run analysis for data quality is necessary in order to determine which data should be included in the final analysis of the cross section.

There are several ways of determining the quality of data. For example, the occupancy plots of detectors as a function of run number might reveal which PMTs and paddles were too inefficient for certain runs. A systematic check of each detector will easily reveal which detectors function correctly and incorrectly, and furthermore, which ones are problematic for a few runs, or the entire experiment. Runs with severe problems may be removed from the analysis completely, while runs with problems which last only for a brief period of the run may suffer a removal of only a subset of its files.

e1-dvcs2 consists of 629 runs summing to a total of 3 TB of data. Typically, each run is divided among 100 files. Afterwards, the so-called "ntuple22 skim" is applied to each of the files. This consists of doing a preliminary particle identification, selecting events only with basic requirements for a good electron, and compressing some variables. After this process, each file is reduced to about 17 MB of space. The number of runs remaining is 595, and they are about 0.593 TB worth of data in total. Any file which has corrupted data, or has incorrectly recorded Faraday cup readings is rejected from the good run list. After this is done, a study of the electron rate is made.

4.7.1 Good Run List

Electron Rate:

The most significant effort in determining the good run list is the analysis of the electron rate. The number of electrons detected should be proportional to the luminosity of the electron beam. Therefore, a ratio of the number of electrons detected in CLAS, divided by the luminosity of the beam should remain constant throughout the entire experiment. Any severe deviation from this constant value is a sign that there is a detector failure somewhere, a high number of accidentals, or

[2] As a brief aside, the reason for the insertion of a good run list in this exact moment of the thesis is that it requires some knowledge of particle ID. The same applies for calibration. Chronologically, calibration and a good run list must be done before the final particle ID.

some other malfunction. These files are rejected. This rate, as a function of run number may be found in Figure 4.86. A similar plot, as a function of run number and sector, per file, may be found in Figure 4.87. Each of these seven ratio distributions were projected onto the y-axis and fitted to Gaussians. Each ratio plot was then cut, accepting only files with ratios which fill within a 3.5σ limit of its mean value. These cuts are represented by the black lines. Figure 4.88 represents the projections and fits of Figure 4.87.

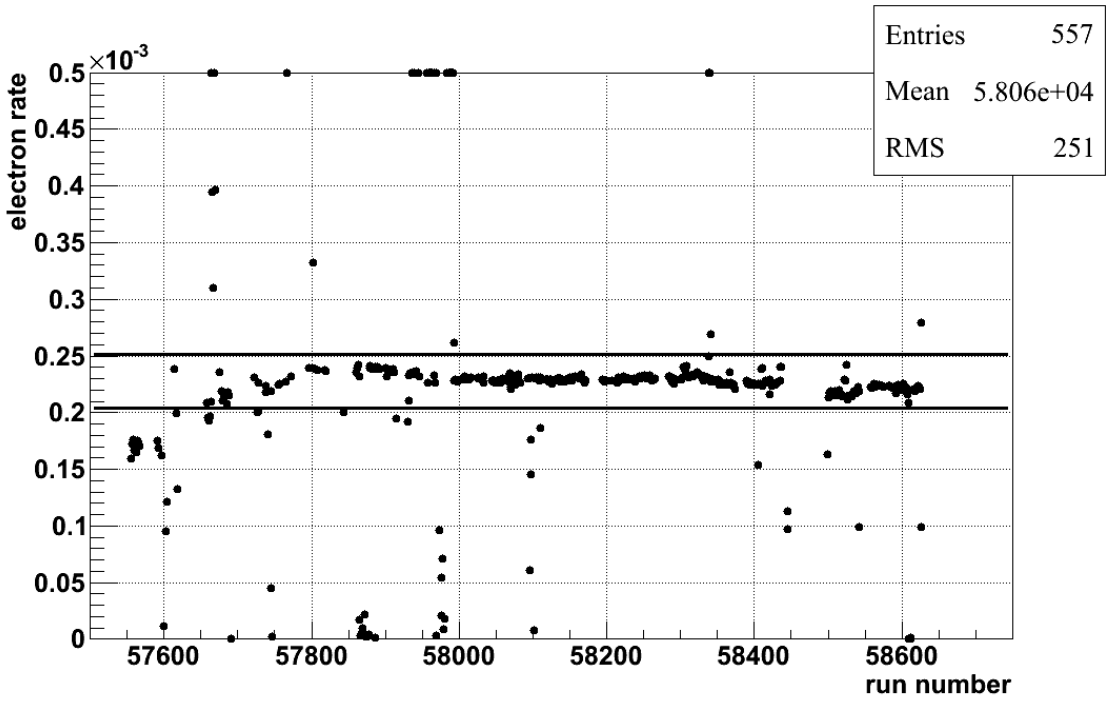

Figure 4.86: The average electron rate for each run.

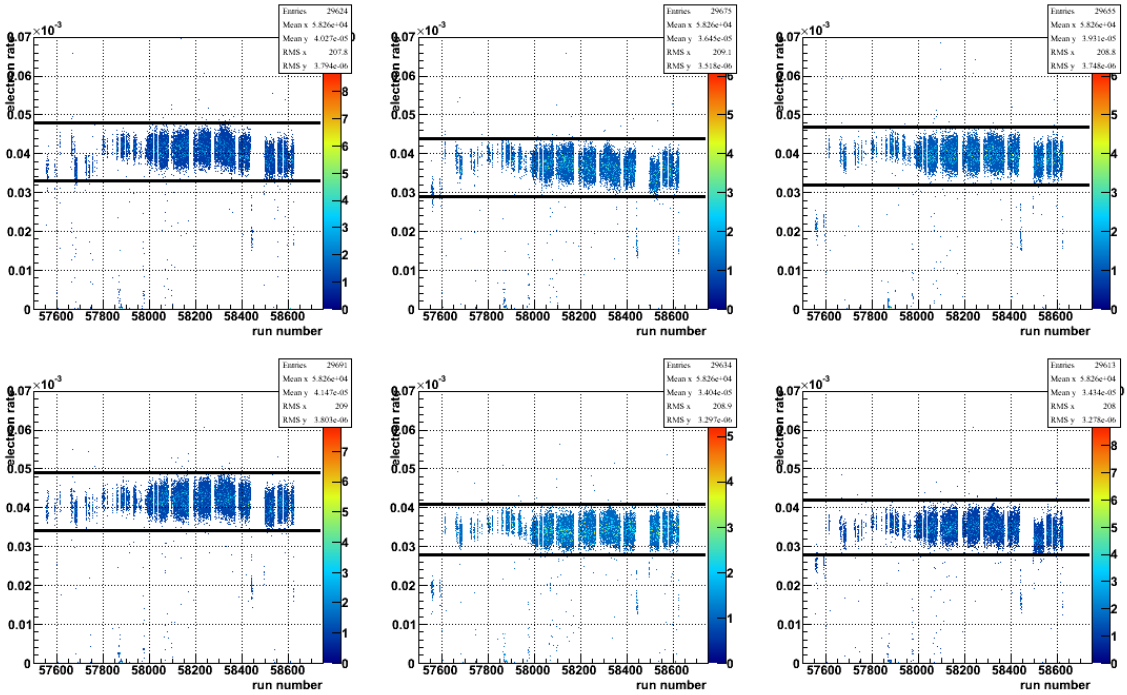

Figure 4.87: The electron rate for each file as a function of run.

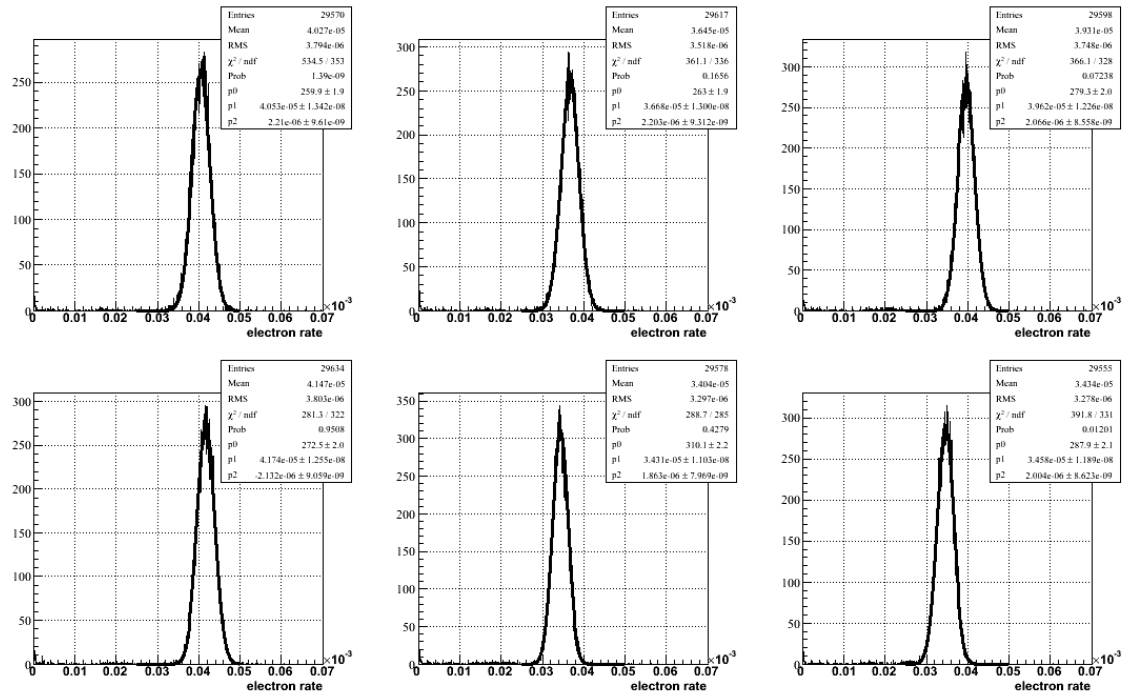

Figure 4.88: The y-axis projection of Figure 4.87.

4.7.2 Integrated Luminosity

After we have determined which runs will be used in the analysis, this is the most convenient time to compute the integrated luminosity $\mathcal{L}_{\text{int}}$. One must, of course, integrate the luminosity only over the runs which are used in the experiment. In order to carry out the calculation we have to review the structure of the target, and also the device which measures the amount of charge deposited by the beam.

Hydrogen Target Properties:

The electron beam is made to impinge on a liquid hydrogen target with the following properties:

- target density, $\rho = 0.071 \frac{\text{g}}{\text{cm}^3}$
- target length, $\ell = 5.048 \pm 0.018$cm
- target molar mass, $M_A = 1.00794 \frac{\text{g}}{\text{mol}}$

There are two ways by which we measure the length of the target. According to measurements taken in the lab at room temperature, the e1-dvcs2 target length was 5.07$\pm$0.01 cm. The uncertainty comes from multiple measurements at different transverse positions. By using the reconstruction of the good electron vertex positions by use of DC information, we are able to measure a length of the target in a second way. By taking an "empty" run, where the target is filled with hydrogen gas instead of liquid hydrogen, we are able to resolve the entry and exit windows of the target. By fitting the peaks of these windows, we are able to determine their mean values. The difference of these values is our target length. In order to have an understanding of our systematics, we have applied the process for each sector, according to the one into which the good electron flew. The actual mean value for target length, $\ell = 5.048 \pm 0.018$ cm, is then the mean of the six sector measurements, and the systematics are determined by the total variance of each of the sectors from this mean value. The fits to the peaks of the entry and exit windows may be seen in Figure 4.89. The target length corresponding to each sector may be found plotted in Figure 4.90. The discrepancy between the two methods could be accounted for by the thermal expansion properties of the target material, Kapton. The lab measurement of 5.07 cm was carried out at room temperature. The vertex measurement of 5.048263 cm was carried out at 19 K.

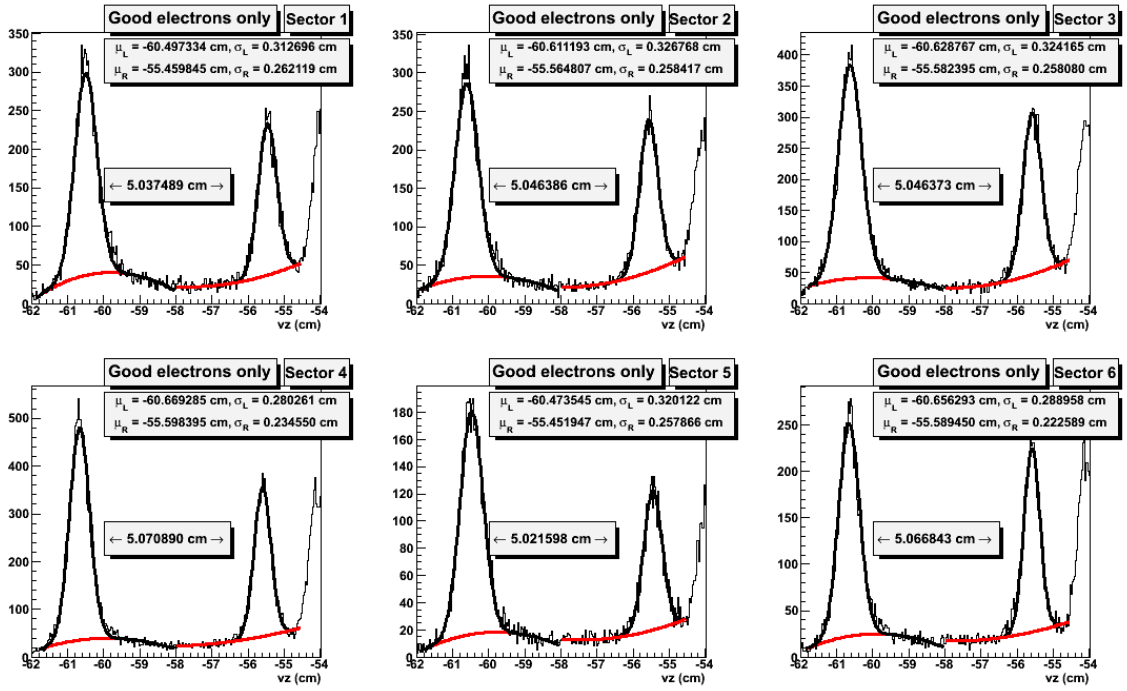

Figure 4.89: Each panel corresponds to a sector. In each sector is the vertex position of all good electrons for that sector in the empty target run. Each distribution has three peaks. On the far left is the target entry window. On the right is the target exit window. These two are fit to Gaussians, whose means are used to calculate the distance between the two peaks. This difference is the target length. On the very far right, just on the edge of the histogram is the peak corresponding to the foil placed in downstream from the target. This foil insulated the target from heat.

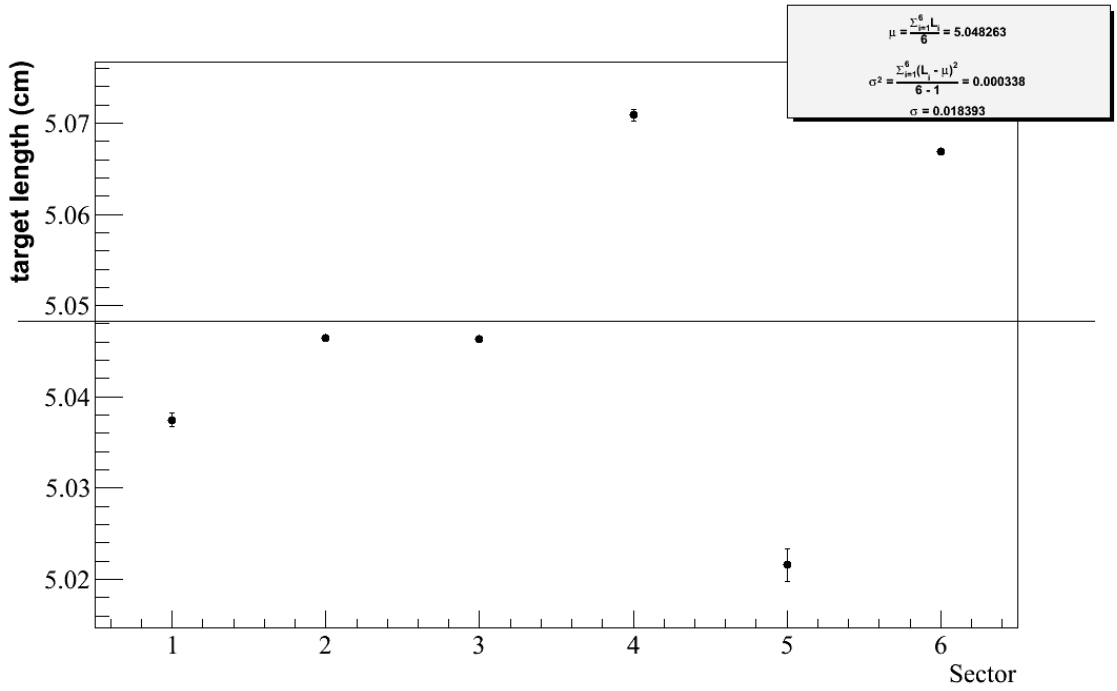

Figure 4.90: The abscissa corresponds to sector number, and the ordinate corresponds to the measurement of the target length according to the method of using vertex position. Each of the six measurements corresponds to the values determined from Figure 4.89. The horizontal black line corresponds to the mean value of all six points. The mean and standard deviation are listed in the upper right label.

Faraday Cup:

The Faraday cup comprises of a lead cylinder weighing 4000kg positioned downstream from the electron beam and the target. The Faraday cup serves the purpose of stopping the electron beam and measuring the deposited charge by use of a capacitor. This capacitor becomes discharged when it accumulates approximately $\frac{1}{9.264\times10^{12}}$C of change. Every discharge is referred to as a "click", and is stored for each electron beam polarization. For the ntuple22 "compressed" formatting, the total number of clicks is stored once for each file for each polarization.

This Faraday cup is continuously measuring the accumulated charge. However, there is some dead-time during the experiment. When CLAS is recording an event, there is a busy signal which temporarily causes us to be blind to other events occurring at that time. This dead-time, which is purely an electronics affect, is completely taken into account by the measurement by the Faraday cup, as it does not continue to measure the accumulated charge during dead-time.

In order to reconstruct the total charge deposited in the cup, one must determine the good run list, or good file list, and sum the total number of clicks for both polarizations. Finally, the clicks must be converted into Coulombs by the relation stated above. The result is then:

$$Q_{\text{int}} = (F^{+}_{\text{int}} + F^{-}_{\text{int}}) \times 9.264 \times 10^{-12}\text{C}, \tag{173}$$

where $F^{+}_{\text{int}} + F^{-}_{\text{int}}$ is the total number of clicks with helicity "+" or "-".

Charge Asymmetry:

As we shall show in Section 5.1, the helicity of the beam of the experiment must be polarized positively half of the time, and negatively half of the time in order for us to extract the polarized cross section differences. In order to demonstrate that this is achieved, we may measure the beam charge asymmetry:

$$\mathcal{A}_q = \frac{q_+ - q_-}{q_+ + q_-}, \tag{174}$$

where q_+ and q_- are the charges deposited in the Faraday cup for positive and negative beam helicities. The measurement is presented in Figure 4.91 as a function of run number, where we see that the asymmetry is never more than $\pm$ 0.005, which is sufficiently small for our purposes.

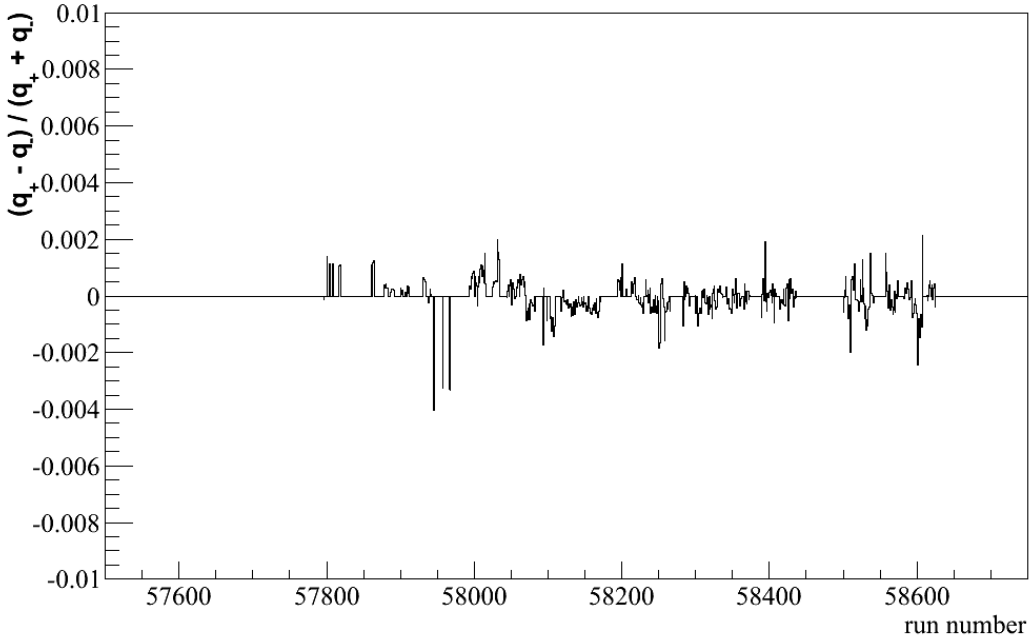

Figure 4.91: The charge asymmetry for e1-dvcs2, as a function of run number. We see that the asymmetry is never more than ± 0.005, which is sufficiently small for our purposes.

Final Calculation of the Integrated Luminosity:

The final calculation for the integrated luminosity uses the results obtained above:

$$\mathcal{L}_{\text{int}} = \frac{\rho \ell N_A Q_{\text{int}}}{M_A e}, \tag{175}$$

where $N_A = 6.022 \times 10^{23} \frac{1}{\text{mol}}$ is Avogadro's number, and $e = 1.60210^{-19}$ C is the elementary charge, with the rest of the terms already having been introduced. For the selected good files of e1-dvcs2, the total number of clicks was:

$$F^+_{\text{int}} + F^-_{\text{int}} = 314911009416 \text{ clicks}. \tag{176}$$

The integrated luminosity is then calculated to be:

$$\mathcal{L}_{\text{int}} = \frac{4.54395 \times 10^{40}}{\text{cm}^2} = \frac{4.54395 \times 10^{7}}{\text{nb}}. \tag{177}$$

The systematic error of the integrated luminosity is currently calculated only from the standard deviation of the measurement of the target length as measured sector by sector:

$$\frac{\sigma}{\mu} = \frac{\sqrt{\frac{1}{6-1}\sum_{i=1}^{6}(L_i - \mu)}}{\mu} = \frac{0.018}{5.048} = 0.33\%, \tag{178}$$

where μ is the target length obtained above, averaged over all six sectors. This small systematic error indicates that we have good certainty in the measurement of our target length.

4.8 Pion Subtraction

4.8.1 A Method for Estimating the Pion Contamination

In Section 4.5, we posited that the exclusivity cuts that were placed on our $e + p + \gamma$ events were not quite sufficient to remove all of the π^0 events. In particular, in Figure 4.81 and Figure 4.82, it was clear that the peaks corresponding to $e + p + \gamma$ events and the $\pi^0 \to \gamma + \gamma$ decay events were too close to be separated by considering that plot. Because of this π^0 background, the DVCS cross section will be overestimated. Therefore, an estimation of this π^0 contamination was made.

With regards to the π^0 decay, there are two cases that we consider. First, the π^0 may decay somewhat "symmetrically," that is, the two photons are both detected, and have comparable energies. We will refer to this instance as $\pi^0 \to \gamma + \gamma$. The second case is where the decay is sufficiently "asymmetric" such that only one photon is detected, and the other is missed by the detector. More specifically, the photon is not detected when its energy is below 150 MeV, this being the threshold of our calorimeters. We will refer to this instance as $\pi^0 \to \gamma + (\gamma)$, with parentheses reminding us that the photon was not detected because of this asymmetry in decay. In this asymmetric case, the missed photon is so weak that the single photon which is detected may be mistaken as coming from an $e + p \to e + p + \gamma$ event when in fact it was truly a $e + p \to e + p + \pi^0 \to e + p + \gamma + (\gamma)$ event.

The actual number of π^0 decays with one photon detected, $N^{\gamma}_{\pi^0}$, cannot be measured directly due to its merging with the $e + p + \gamma$ events. However, the number of π^0 decays with two photons detected, $N^{\gamma\gamma}_{\pi^0}$, can be measured.

In order to estimate the π^0 background, we note that both $N^{\gamma}_{\pi^0}$ and $N^{\gamma\gamma}_{\pi^0}$ can be used separately to determine the π^0 cross section:

$$\frac{\mathrm{d}\sigma_{\pi^0}}{\mathrm{d}\Omega} \propto \frac{N^{\gamma\gamma}_{\pi^0}}{A^{\gamma\gamma}_{\pi^0}}, \tag{179}$$

$$\frac{\mathrm{d}\sigma_{\pi^0}}{\mathrm{d}\Omega} \propto \frac{N^{\gamma}_{\pi^0}}{A^{\gamma}_{\pi^0}}. \tag{180}$$

where $A^{\gamma}_{\pi^0}$ and $A^{\gamma\gamma}_{\pi^0}$ correspond to the acceptances of each, as determined by Monte Carlo. Recall that this is just the ratio of the reconstructed events to generated events. Since both are related to the π^0 cross section, one may write the following equation:

$$N^{\gamma}_{\pi^0} = N^{\gamma\gamma}_{\pi^0} \frac{A^{\gamma}_{\pi^0}}{A^{\gamma\gamma}_{\pi^0}}. \tag{181}$$

Since the acceptances of each are just the ratios of the number of reconstructed particles to the particles generated, and only one generator is used in obtaining both acceptances, the equation can be further reduced:

$$N^{\gamma}_{\pi^0} = N^{\gamma\gamma}_{\pi^0} \frac{N^{\gamma}_{\pi^0,\mathrm{rec}}}{N^{\gamma\gamma}_{\pi^0,\mathrm{rec}}}, \tag{182}$$

where the subscript "rec" corresponds to the reconstructed number of events in the Monte Carlo. From this relation, an estimation of the number of π^0 events with one photon detected may very easily be estimated.

4.8.2 Computing $N^{\gamma\gamma}_{\pi^0}$ from Data

To find the number of pion decays with two photons, we first have to determine our criteria for pion identification. We begin by making the assumption that every π^0 produced decays almost instantly, at the electron vertex position. This is justified by the short lifetime of the π^0, $\tau = 8.4 \pm 0.6 \times 10^{-17}$s. Since the two photon decay $\pi^0 \to \gamma + \gamma$ is the dominant channel, we can then search for every photon pair detected by CLAS. Since we have already identified our photons in Section 4.2, we proceed by retaining every event which has at the very least two photons.

After selecting events with $e + p \to e' + p' + N \times \gamma$, where $N \geq 2$, every photon pair is looped over. Therefore, if there are N photons, there will be $\sum_{i=1}^{N-1} i = \frac{N(N-1)}{2}$ possible combinations. The photons selected will be denoted as γ_1 and γ_2. For ease of reference, we will define a four vector $p_{\pi^0} = p_{\gamma_1} + p_{\gamma_2}$, indicating that the combination is a π^0 candidate. In order to determine if they are truly pions, we must impose some restrictions on certain quantities. First, for each of these combinations, the following quantities are calculated:

- $IM_{\gamma_1+\gamma_2}$, the invariant mass of photon pair of $e + p \to e' + p' + \gamma_1 + \gamma_2$,
- $MM^2_{e'+p'+X}$, the missing mass of the $e + p \to e' + p' + X$ system,
- $MM^2_{e'+X+\pi^0}$, the missing mass of the $e + p \to e' + X + \pi^0$ system,
- $\theta_{\pi^0,X}$ which is the angle between the π^0 in the $e + p \to e' + p' + \pi^0$ system and the X in the $e + p \to e' + p' + X$ system.

These quantities are convenient, because we know which values to expect for a true $e + p \to e' + p' + \pi^0$ channel, viz.:

- $IM_{\gamma_1+\gamma_2} = 0.135$ GeV,
- $MM^2_{e'+p'+X} = 0.0182$ GeV^2,

- $MM^2_{e'+X+\gamma_1+\gamma_2} = 0.880$ GeV^2,
- $\theta_{\pi^0,X} = 0$ rad.

It turns out that the resolution for the IC and EC are different. As a consequence, the distributions of these quantities will look different based on which detector each photon entered. There are four different scenarios which we will consider:

- IC-IC: Both photons were detected in the IC
- IC-EC: One photon was detected in the IC and one photon was detected in the EC, with the photon in the IC being more energetic.
- EC-IC: One photon was detected in the IC and one photon was detected in the EC, with the photon in the EC being more energetic.
- EC-EC: Both photons were detected in the EC

Only two of these "topologies" yield a significant number of events. As seen in Figure 4.92, there is no signal in the mixed topologies. This is due to the opening angle of the pion decay in the lab frame being, in general, too small for one photon to be detected in separate detectors. This is due in turn to the fact that there were strict cuts placed on the IC shadow on the EC, and the IC and EC fiducial cuts themselves. This creates a cut region in which no photons are detected between the IC and EC. The chance of a pion decay resulting with photons detected on opposite sides of this large cut is too low because of the restriction on the opening angle of the pion decay. We then restrict ourselves to the IC-IC and EC-EC cases. Each of the four variables above were plotted for the IC-IC and EC-EC cases. Each of the variables $IM_{\gamma_1+\gamma_2}$, $MM^2_{e'+p'+X}$, $MM^2_{e'+X+\gamma_1+\gamma_2}$, and $\theta_{\pi^0,X}$ were fit to Gaussians with linear backgrounds, and cut at three standard deviations ($\pm 3\sigma$). The results of these fits are displayed in Figure 4.93 and Figure 4.94, with the cuts themselves listed in Table 4.14 and Table 4.15.

Table 4.14: A table of cuts in data corresponding to the case where both π^0 photons are detected in the IC.

IC - IC	μ	3σ
$IM_{\gamma_1+\gamma_2}$	0.13504 GeV	0.02743 GeV
$MM^2_{e'+p'+X}$	0.00413 GeV^2	0.17629 GeV^2
$MM^2_{e'+X+\gamma_1+\gamma_2}$	0.146 GeV^2	1.74 GeV^2
$\theta_{\pi^0,X}$	0°	0.30849°

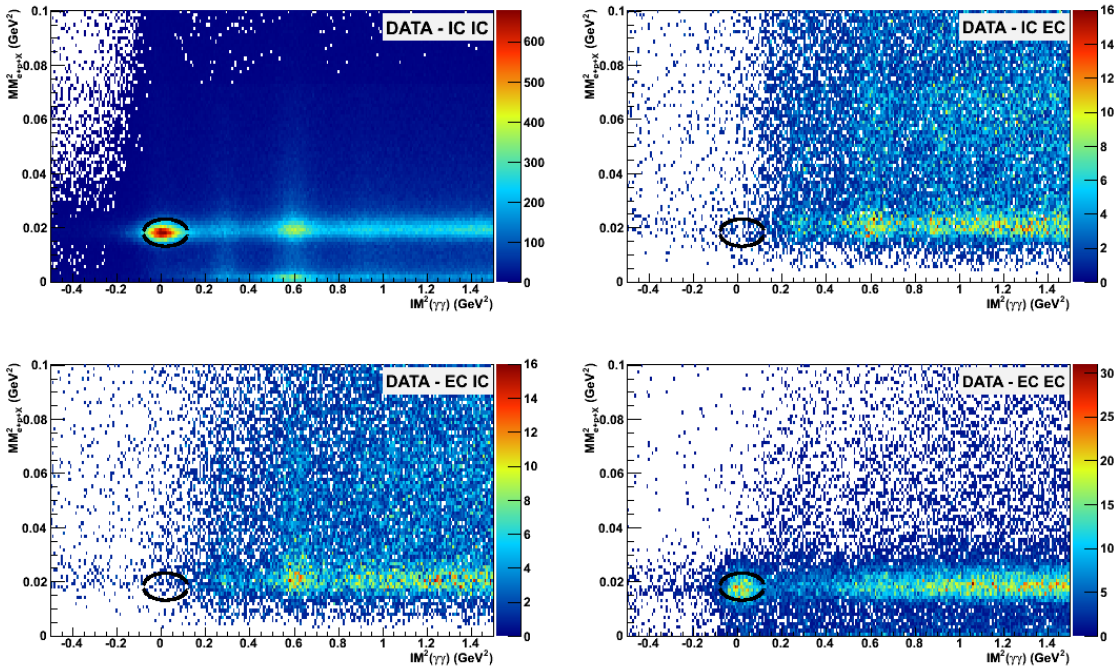

Figure 4.92: MM^2_{e+p+X} versus $IM_{\gamma\gamma}$. The upper-left panel corresponds to the IC-IC case. The upper-right panel corresponds to the IC-EC case. The lower-left panel corresponds to the EC-IC case. The lower-right panel corresponds to the EC-EC case. In each of the four panels, a black ellipse is drawn indicating the region where a π^0 should be found. In the cases of the IC-IC and EC-EC topologies, the pions can clearly be seen. In the cases of the mixed topologies IC-EC and EC-IC, there are no pions visible. This is due to the strict fiducial cuts placed on the IC and EC as well as the IC shadow fiducial cuts placed on the EC. These fiducial cuts require the pion to have a restrictively large angle between its two decay photons, causing there to be no detectable pion signal.

Table 4.15: A table of cuts in data corresponding to the case where both π^0 photons are detected in the EC.

EC - EC	μ	3σ
$IM_{\gamma_1+\gamma_2}$	0.13153 GeV	0.04556 GeV
$MM^2_{e'+p'+X}$	0.01781 GeV^2	0.15456 GeV^2
$MM^2_{e'+X+\gamma_1+\gamma_2}$	0.002 GeV^2	1.866 GeV^2
$\theta_{\pi^0,X}$	0°	0.59733°

After these cuts are applied, an estimate of the background under the peak is made. For most of our cross section bins, there are not enough events to fit every distribution. Therefore, an approximation is made, based on the observation that the background, integrated over all of the bins is approximately linear. If the true signal in the plot of $IM_{\gamma\gamma}$ is a Gaussian sitting on

a linear background, and a cut is taken at 3σ, accepting $N_{\text{signal + background}}$ events, the estimation of the background is obtained by taking all events that lie between 3σ and 6σ, and -3σ and -6σ, $N_{\text{background est.}}$. The total number of events taken is then $N_{signal} = N_{\text{signal + background}} - N_{\text{background est.}}$. This relation is useful because it allows for an estimation of the background without having to fit the distribution of $IM_{\gamma\gamma}$ in every cross section bin.

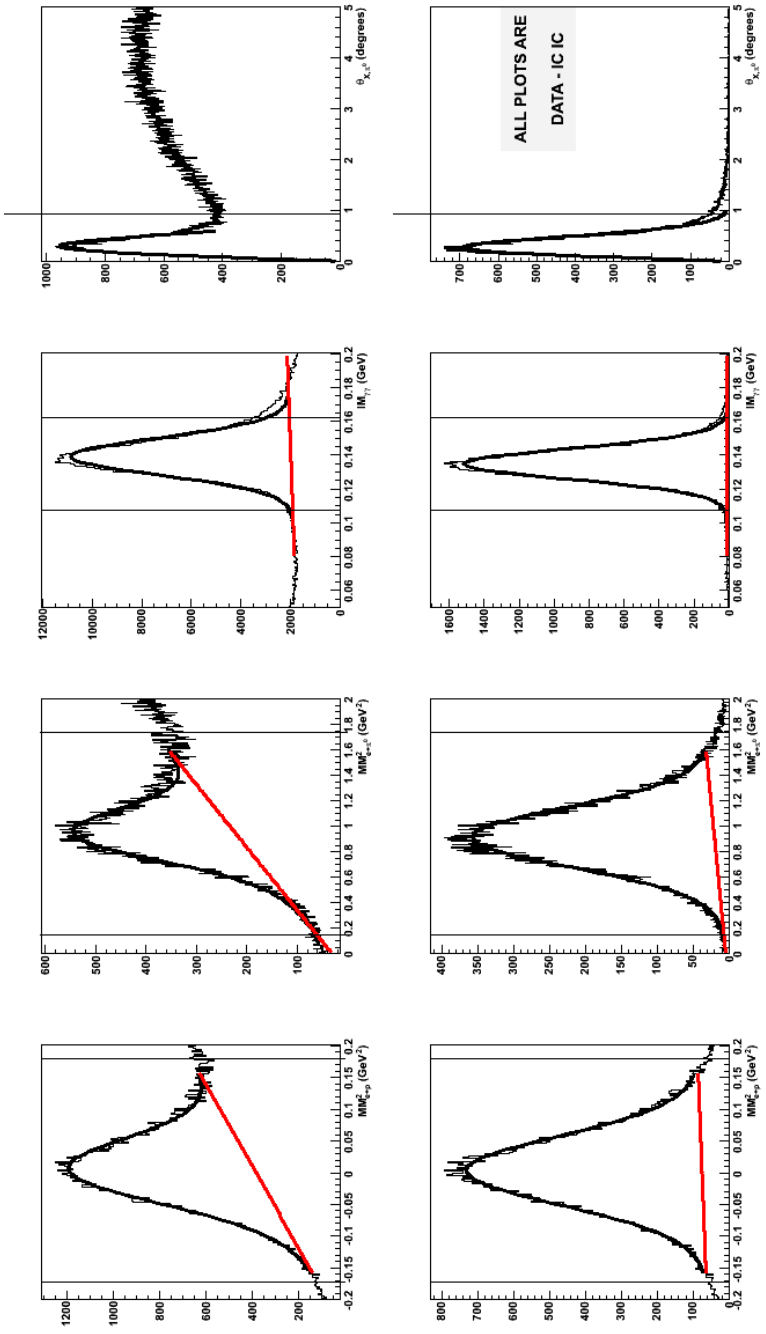

Figure 4.93: Exclusivity variables in data for IC. On the top row are the distributions before all cuts. On the bottom are the distributions after all exclusivity cuts except for the cut on the plotted variable. The first column represents MM^2_{e+p}. The second column represents $MM^2_{e+\pi^0}$. The third column represents $IM_{\gamma\gamma}$. The last column represents θ_{X,π^0}.

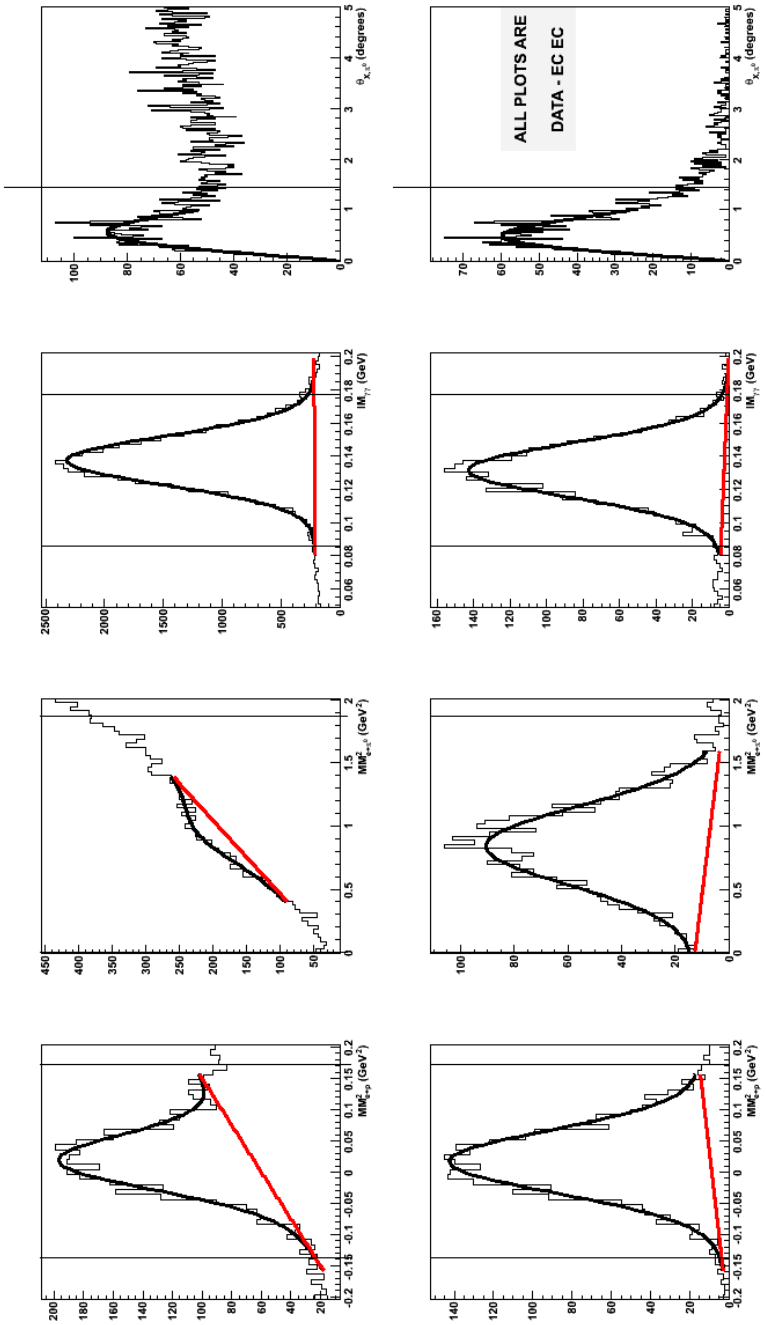

Figure 4.94: Exclusivity variables in data for EC. On the top row are the distributions before all cuts. On the bottom are the distributions after all exclusivity cuts except for the cut on the plotted variable. The first column represents MM^2_{e+p}. The second column represents $MM^2_{e+\pi^0}$. The third column represents $IM_{\gamma\gamma}$. The last column represents θ_{X,π^0}.

4.8.3 Computing $\frac{A^{\gamma}_{\pi^0}}{A^{\gamma\gamma}_{\pi^0}} = \frac{N^{\gamma}_{\pi^0,\mathbf{rec}}}{N^{\gamma\gamma}_{\pi^0,\mathbf{rec}}}$ from Monte Carlo

We now turn our attention to the Monte Carlo simulation for the pion analysis. In the same vein as the DVCS generator, we have a pion generator which simulates $e+p \rightarrow e'+p'+\pi^0$ events. Likewise, this data is fed through GSIM, GPP, and cooked into root files.

Computing $N^{\gamma}_{\pi^0,\mathrm{rec}}$ is a simple matter. The same code that is used for analyzing DVCS in experimental data is used. Because we know that only pions are generated, the code which we previously used for DVCS will now give us a measure of the number of π^0 events in simulation where only one photon was detected and which could be mistaken as DVCS or BH according to our DVCS criteria.

Computing $N^{\gamma\gamma}_{\pi^0,\mathrm{rec}}$ is also straightforward. One must simply take the code which was used to measure the number of π^0 events in which two photons were detected in experimental data, with different cuts appropriate to the distributions of exclusivity variables. In addition, the distributions of the four variables which were listed in Section 4.8.2 have different distributions than that of data. Therefore, a second analysis, following the same method as before, must be made, considering every combination of detectors. The cuts are taken at the 3σ level centered around the means of their fits. The results of these fits may be seen in Figure 4.95 and Figure 4.96, with the cuts themselves listed in Table 4.16 and Table 4.17. The estimation of the background is carried out in the same manner as the previous section, taking the number of events between 3σ and 6σ in the $IM_{\gamma\gamma}$ as the approximate number of background events.

Finally, the yields for one and two photons detected in Monte Carlo are presented in Figure 4.97 for bin 5. The ratio of these yields is equivalent to the ratio of the acceptances.

Table 4.16: A table of cuts in Monte Carlo corresponding to the case where both π^0 photons are detected in the IC.

IC - IC	μ	3σ
$IM_{\gamma_1+\gamma_2}$	0.13611 GeV	.02407 GeV
$MM^2_{e'+p'+X}$	0.02581 GeV^2	0.15077 GeV^2
$MM^2_{e'+X+\gamma_1+\gamma_2}$	0.346 GeV^2	1.324 GeV^2
$\theta_{\pi^0,X}$	0°	0.325867°

Table 4.17: A table of cuts in Monte Carlo corresponding to the case where both π^0 photons are detected in the EC.

EC - EC	μ	3σ
$IM_{\gamma_1+\gamma_2}$	0.13272 GeV	0.03729 GeV
$MM^2_{e'+p'+X}$	0.03154 GeV^2	0.13141 GeV^2
$MM^2_{e'+X+\gamma_1+\gamma_2}$	0.074 GeV^2	1.774 GeV^2
$\theta_{\pi^0,X}$	0°	0.478367°

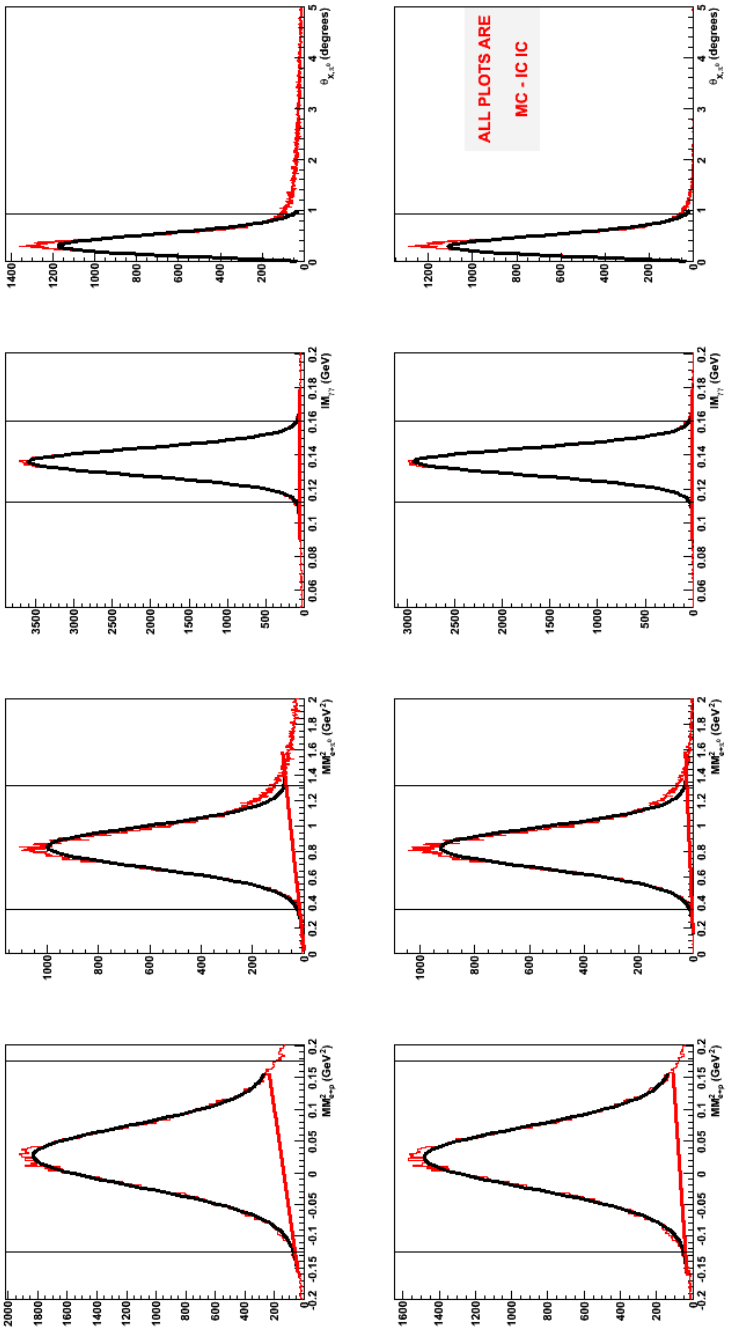

Figure 4.95: Exclusivity variables in Monte Carlo for IC. On the top row are the distributions before all cuts. On the bottom are the distributions after all exclusivity cuts except for the cut on the plotted variable. The first column represents MM^2_{e+p}. The second column represents $MM^2_{e+\pi^0}$. The third column represents $IM_{\gamma\gamma}$. The last column represents θ_{X,π^0}.

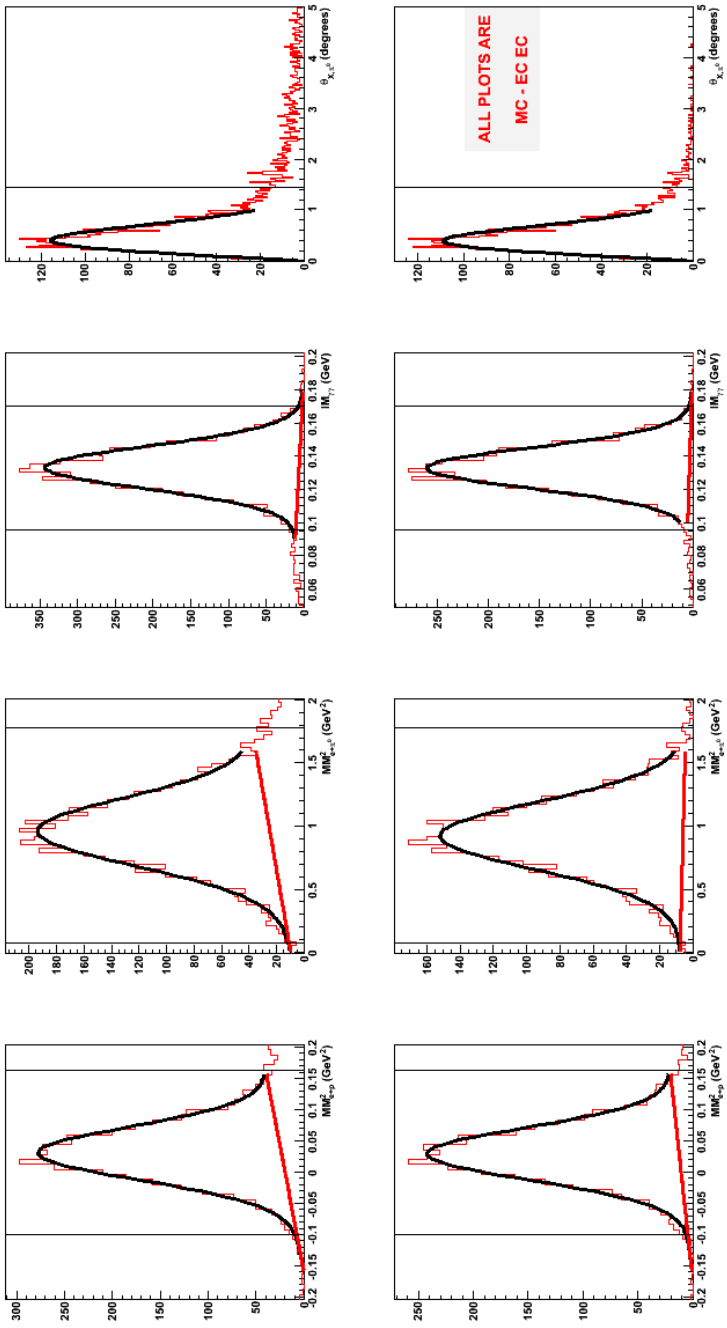

Figure 4.96: Exclusivity variables in Monte Carlo for EC. On the top row are the distributions before all cuts. On the bottom are the distributions after all exclusivity cuts except for the cut on the plotted variable. The first column represents MM^2_{e+p}. The second column represents $MM^2_{e+\pi^0}$. The third column represents $IM_{\gamma\gamma}$. The last column represents θ_{X,π^0}.

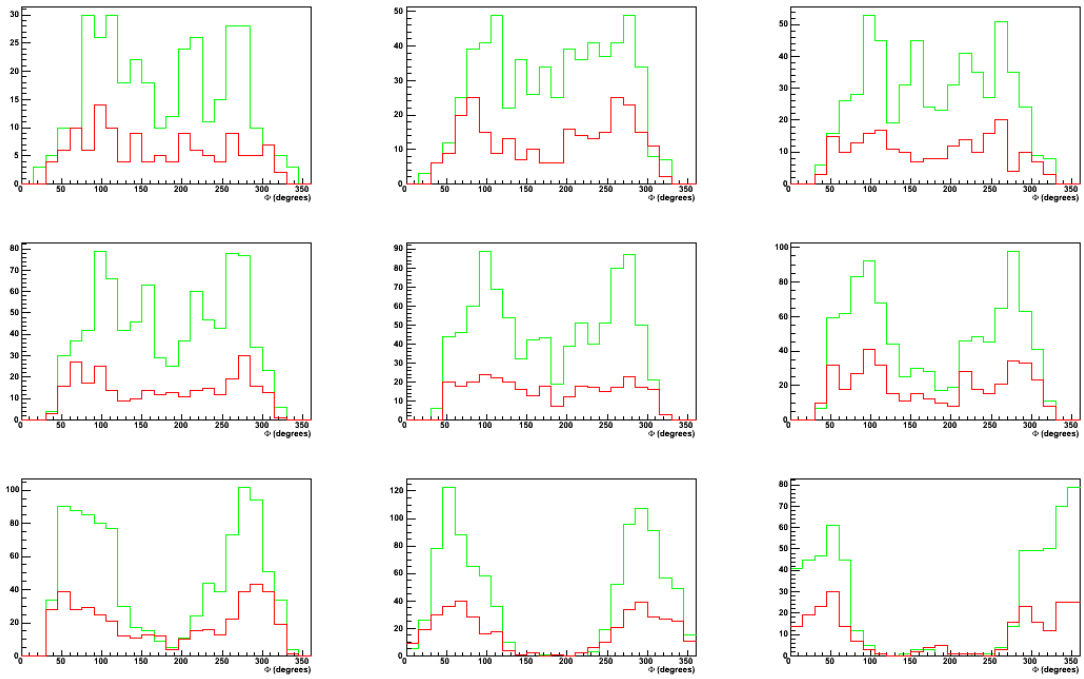

Figure 4.97: The neutral pion yields as a function of Φ for the fifth bin in x_B and θ_e, where $0.17 < x_B < 0.2$ and $25.5^\circ < \theta_e < 45^\circ$. The yield for two photons detected in Monte Carlo is green. The yield for one photon detected in Monte Carlo is red. The ratio of these yields is equivalent to the ratio of their acceptances.

4.8.4 Final Results for the Estimated Pion Contamination $N^{\gamma}_{\pi^0}$

In order to have an estimation of the number of $e + p + \pi^0$ in which only one photon is detected, the following equation is applied,

$$N^{\gamma}_{\pi^0} = N^{\gamma\gamma}_{\pi^0} \frac{N^{\gamma}_{\pi^0,\mathrm{rec}}}{N^{\gamma\gamma}_{\pi^0,\mathrm{rec}}}, \tag{183}$$

substituting the results of the previous two sections, where the number of two photon events are measured, and where the acceptances are calculated. An example of the pion subtraction ratio is presented in Figure 4.98, for the fifth bin in x_B and θ_e. A full list of pion subtraction ratios may be found in Appendix C.

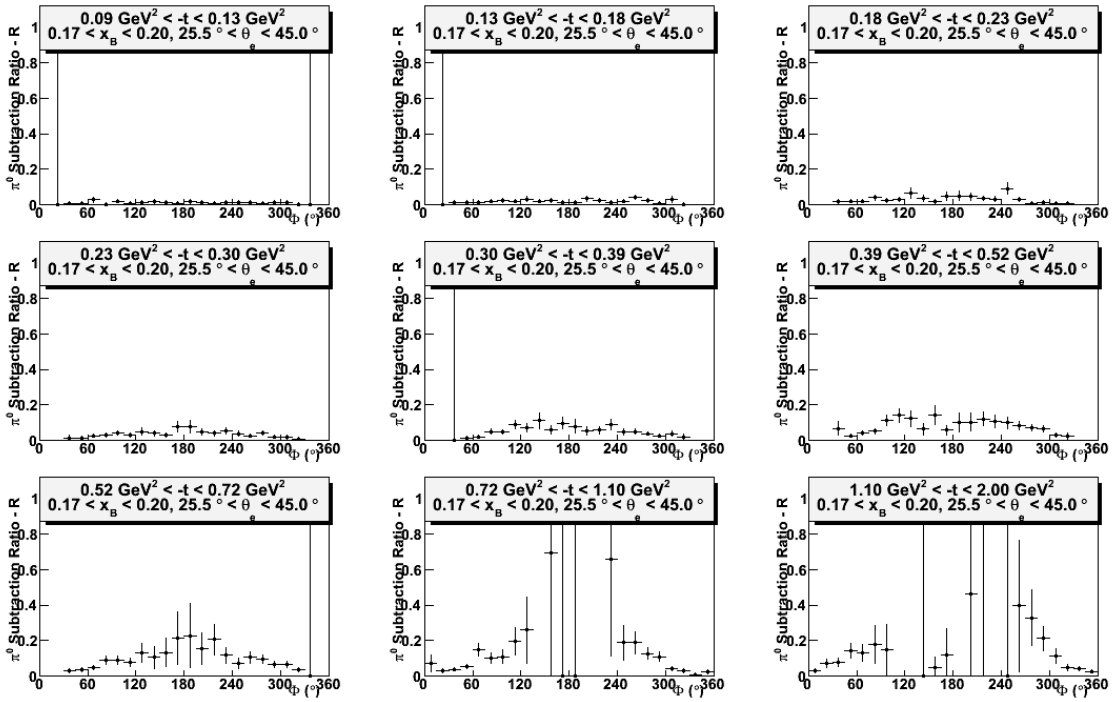

Figure 4.98: The neutral pion subtraction ratio $R = \frac{N^{\gamma}_{\pi 0}}{N^{e+p+\gamma}}$ as a function of Φ for the fifth bin in x_B and θ_e, where $0.17 < x_B < 0.2$ and $25.5^{\circ} < \theta_e < 45^{\circ}$.

4.9 Radiative Corrections

4.9.1 Obtaining the Born Cross Section

The leading order cross section for $e + p \rightarrow e' + p' + \gamma$, corresponding to the Feynman diagrams seen in Figure 4.99, allows us to access GPDs through CFFs. These leading order Feynman diagrams are referred to as the Born terms. The cross section corresponding to these terms is referred to as the Born cross section. The leading order radiative corrections have a significant contribution to the measured cross section. Next-to-leading order radiative corrections also have a noticeable, but not necessarily crucial effect. These corrections are seen especially for higher order diagrams on the electron side of the process, since those corrections are not suppressed by the mass of the proton as in the proton side corrections. Consequently, we concern ourselves with radiative diagrams on the electron side only. Leading order diagrams are drawn in Figure 4.100, consisting of twelve involving the exchange of virtual photons, and eight involving the radiation of a soft photon for both BH and DVCS, to leading order corrections. The next-to-leading order corrections are too numerous to be drawn here. In taking all leading order and next-to-leading order contributions, it is possible to calculate the ratio between the measured cross section, and the Born terms of BH and DVCS. This has been worked out to leading order by M. Vanderhaeghen et al. in the soft photon approximation[47], and without soft photon approximation up to next-to-leading order by I. Akushevich et al.[54]. For this analysis, we take the corrections appearing in reference[54].

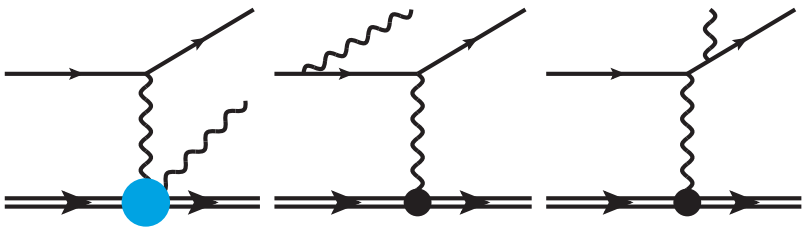

Figure 4.99: The Born terms for BH and DVCS. Form factors are represented by the black blobs. GPDs are represented by the blue blobs.

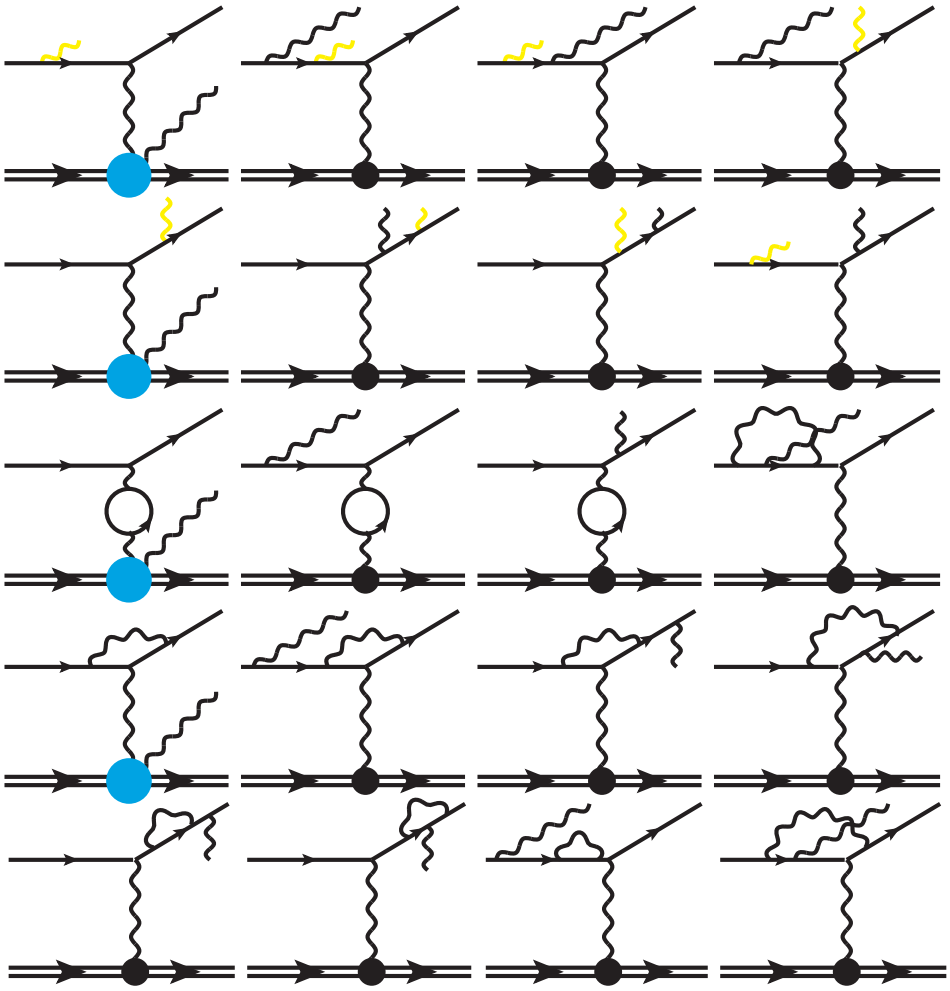

Figure 4.100: All radiative corrections up to leading order. Form factors are represented by the black blobs. GPDs are represented by the blue blobs. BH or DVCS photons are represented by black photon lines, while real radiative photons are represented by yellow photon lines.

The virtual corrections (vacuum and vertex), and real corrections (radiation) affect our measured cross section in two distinct ways. The former interferes coherently, while the later interferes incoherently with the Born terms. The virtual terms consist of diagrams in which there are no extra radiated photons. As a result, there is no missing energy or momentum in the system, aside from resolution effects. As for the real terms, the radiated photon is never detected, but in the experiment is treated as if it was a genuine $e + p + \gamma$ event. Because of this, there will be missing energy and momentum in the system. We distinguish between pre-radiation and post-radiation, the

former being the case where a photon is emitted from the incoming electron leg, and the latter being the case where a photon is emitted from the outgoing electron leg. In the case of post-radiation, the only particle that is affected is the outgoing electron. It has slightly less energy, leading to a greater missing energy, and a greater missing mass. This can be noticed in the missing energy and missing mass spectra as a radiative tail. For example, the missing mass spectra for $e+p+\gamma$ detected is presented in Figure 4.101, before exclusivity cuts. As for the pre-radiation, the entire system is affected. A photon radiated from the incoming electron leg results in an effective change in the beam energy. This is because in the analysis we have assumed that every incoming electron has the same energy - the beam energy. Because of this effective change in beam energy, all of our kinematics will be slightly skewed for these cases.

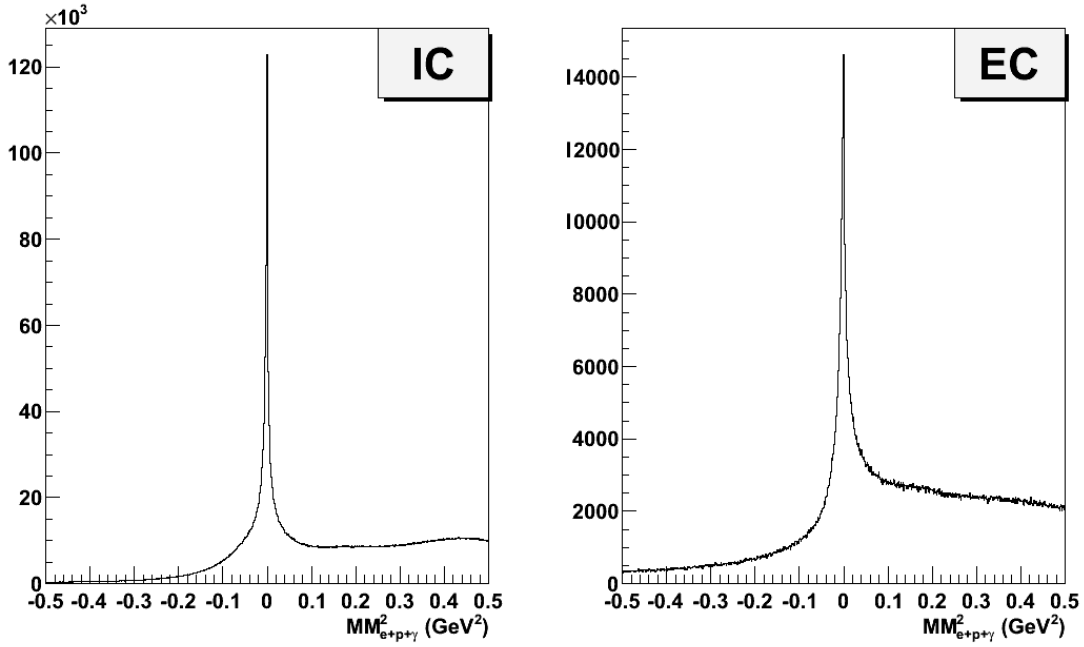

Figure 4.101: An example of the post-radiation tail. On the left, for the IC, and on the right for the EC. In both, you can see a radiative tail coming down on the right hand side of the peak. This corresponds to energy lost from a photon radiating from the outgoing electron leg.

There is one caveat: because of our choices of exclusivity cuts, we are not accepting the entire post-radiative tail. Therefore, when we take into account radiative effects, we should only take into account the radiative events which have survived our cuts. The program that we use takes this into account by introducing a "maximal photon energy" in the center of mass system, which we call ΔE. There is a cutoff to ΔE which corresponds to these cuts. However, the value is not a sharp cutoff. The missing mass spectrum of $e+p$ may be seen in Figure 4.102, after exclusivity cuts, where we have taken our missing mass cutoff to be the three sigma limit of our distribution after all cuts.

According to reference[47], this missing mass cutoff corresponds to a ΔE cutoff of:

$$\Delta E = \frac{MM_{e+p}}{2} = \frac{\sqrt{0.18864 \text{ GeV}^2}}{2} = 0.21716 \text{ GeV}, \tag{184}$$

which is the "maximal photon energy" that we use for an input in our program.

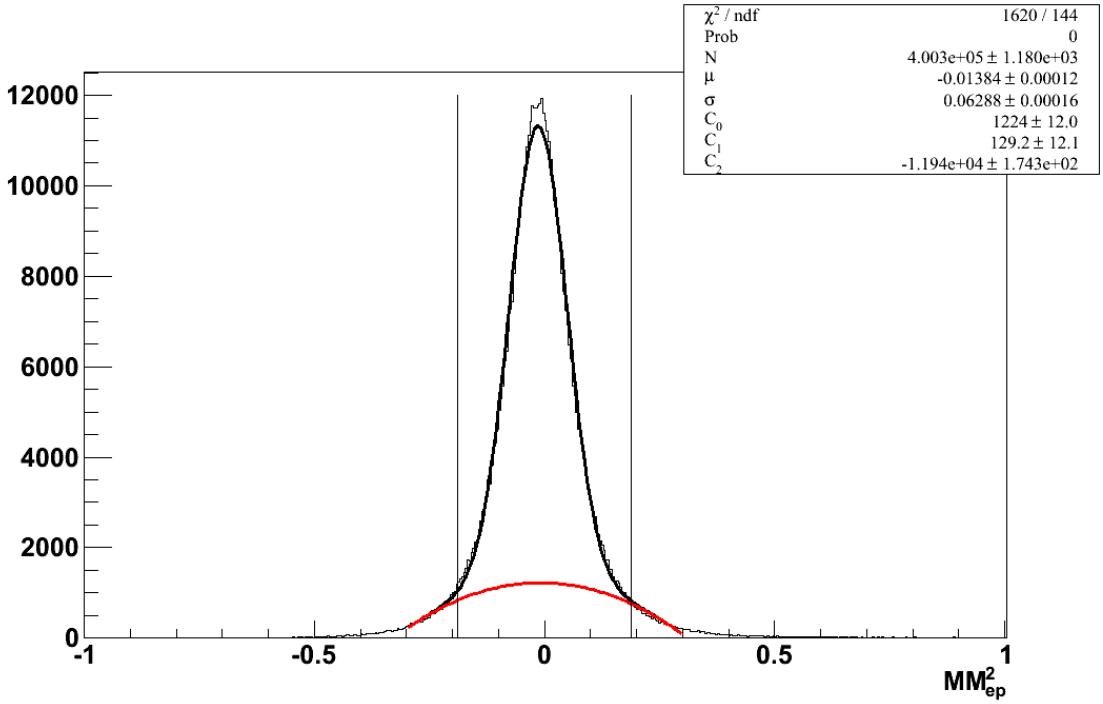

Figure 4.102: The MM^2_{e+p} distribution in GeV^2 for the IC after all exclusivity cuts, showing the three sigma limit in black, which is taken to be the approximate cutoff, corresponding to a cutoff on the radiated photon energy. The black curve represents the fit to a Gaussian with a second order polynomial background, which is represented by the red line.

4.9.2 Final Results for the Radiative Corrections

The corrections, on average, increase the value of the measured cross section by 15%. In general, the correction is larger at $\Phi = 180°$ and is smaller at large and small Φ. We note that the quantity we have obtained is F_{rad}, and that the cross section is modified by being divided by this factor. This means that a value of 1 means there is no correction, and a lower value of F_{rad} means that the cross section is increased. An example of the radiative correction is presented in Figure 4.103, for the fifth bin in x_B and θ_e. A full list of radiative corrections may be found in Appendix D.

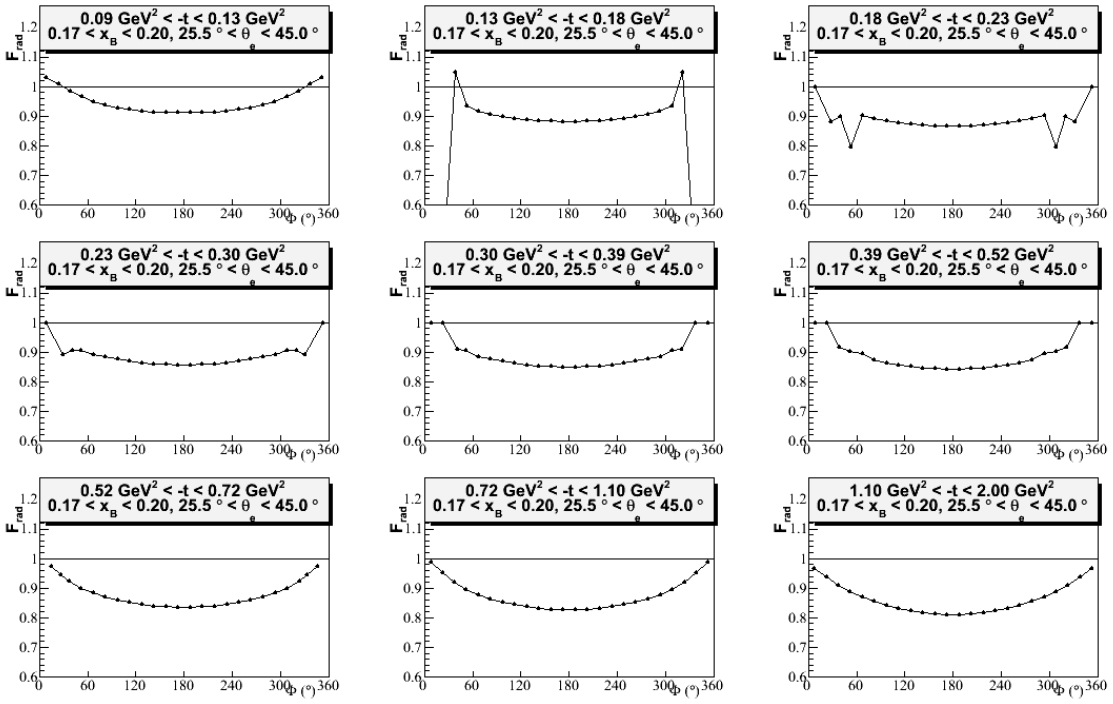

Figure 4.103: The radiative corrections as a function of Φ for the fifth bin in x_B and θ_e, where $0.17 < x_B < 0.2$ and $25.5^\circ < \theta_e < 45^\circ$.

4.10 Elastic Normalization

4.10.1 Elastic Cross Section

One of the challenges that a cross section analysis in CLAS faces is the overall normalization of the final results. In order to judge our understanding of overall normalization, we have made a measurement of the elastic cross section as a function of Q^2, a quantity which has been carefully measured in literature.[23,55] The measurement of the elastic cross section by CLAS was then compared to the cross section according to the parameterization appearing in reference[55]. The elastic cross section may be written as:

$$\frac{\mathrm{d}\sigma}{\mathrm{d}Q^2} = \frac{N_{e+p}}{\mathcal{L}_{\mathrm{int}} A \Delta Q^2}, \tag{185}$$

where $\mathcal{L}_{\mathrm{int}}$ is the same integrated luminosity as that calculated for DVCS; A is the acceptance; N_{e+p} is the number of $e + p \to e + p$ events measured; and ΔQ^2 is the bin volume.

The measurement of the elastic cross section in CLAS as a function of sector is displayed in Figure 4.104, compared to the cross section according to the Brash parameterization.[55] It is easier to compare the difference between the two by plotting the ratio, presented in Figure 4.105. We notice that the overall normalization is different between the two, being lower by $5 - 15\%$ in CLAS. Similarly, the cross section integrated over all sectors is presented in Figure 4.106, comparing the two cross sections, as well as their ratio. The average value for the overall normalization is $\epsilon = .926$. We take the overall normalization for the DVCS cross section to be the same as that for the elastic cross section, integrated over all sectors:

$$\left(\frac{\mathrm{d}\sigma}{\mathrm{d}\Omega}\right)_{\mathrm{renormalized}} = \frac{1}{\epsilon}\left(\frac{\mathrm{d}\sigma}{\mathrm{d}\Omega}\right)_{\mathrm{measured}}. \tag{186}$$

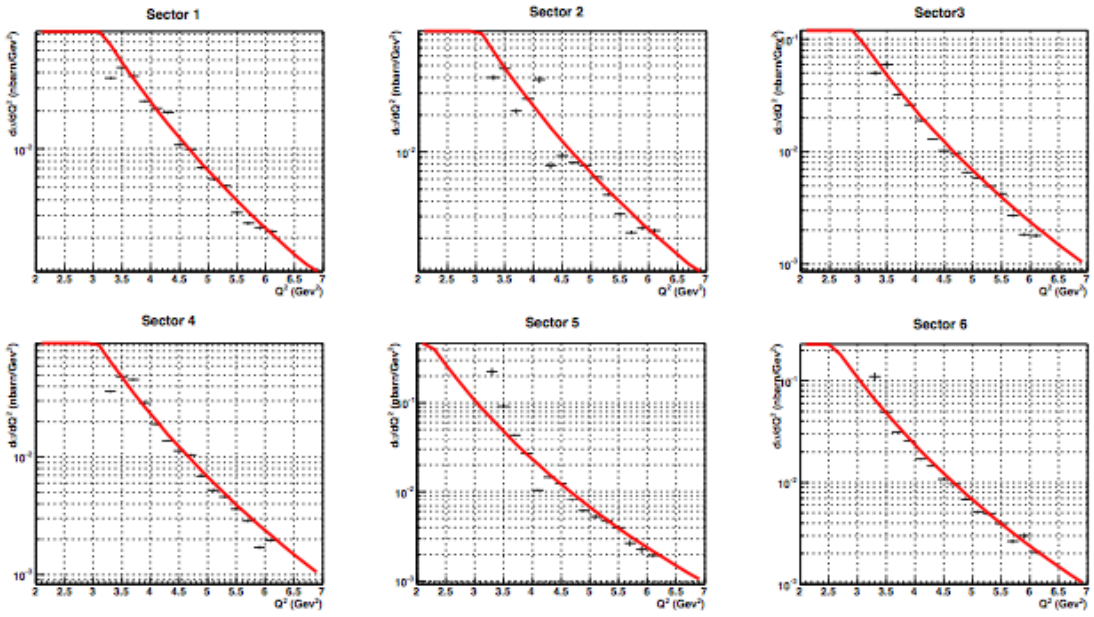

Figure 4.104: The elastic cross section computed from e1-dvcs2 by B. Guegan[23] in black points, and the cross section according to the Brash parameterization[55] displayed as a red line. Each panel corresponds to a sector. This plot is a reproduction of a plot appearing in the thesis manuscript of B. Guegan.[23]

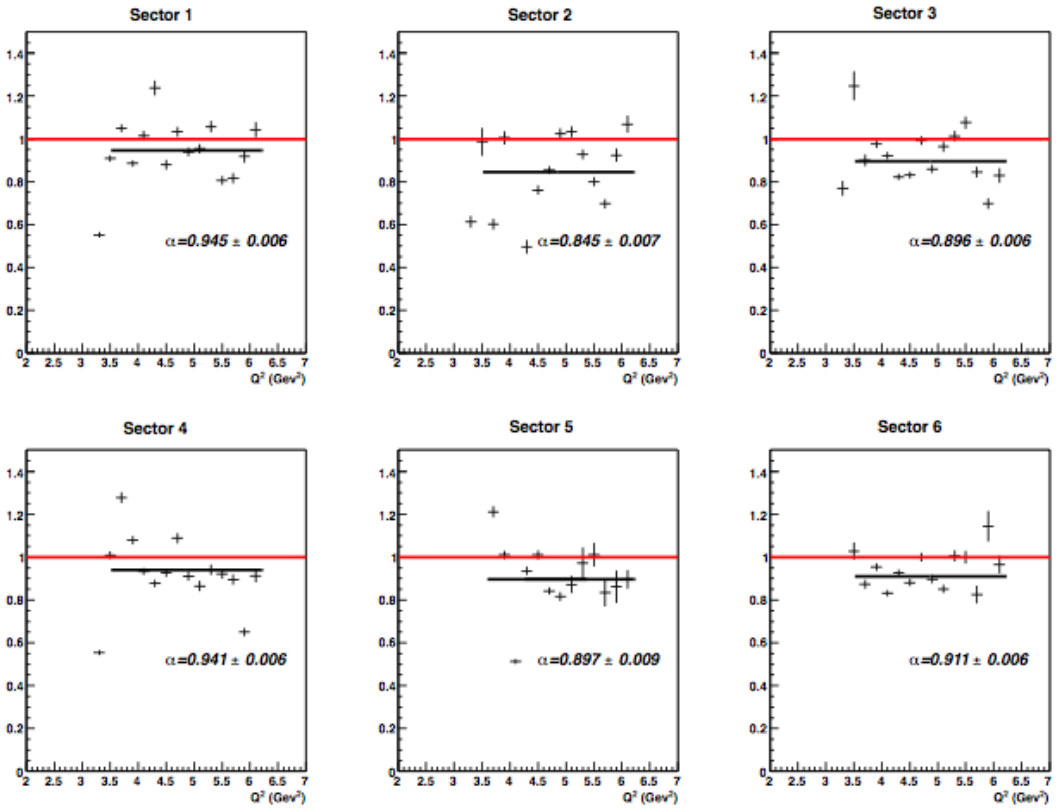

Figure 4.105: The ratio of the elastic cross section computed from e1-dvcs2 by B. Guegan[23] to the cross section according to the Brash parameterization.[55] The red line at 1 denoted where a perfect agreement would be. Each panel corresponds to a sector. Each sector is fit to a constant, represented by a horizontal black line, representing the normalization per sector. This plot is a reproduction of a plot appearing in the thesis manuscript of B. Guegan.[23]

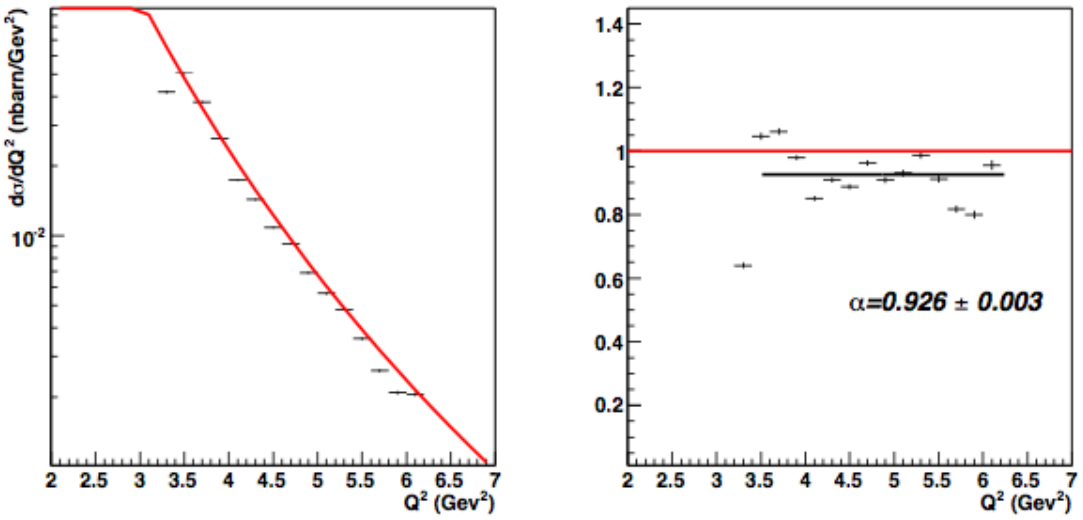

Figure 4.106: On the left, integrated over all sectors, the elastic cross section computed from e1-dvcs2 by B. Guegan[23] in black points, and the cross section according to the Brash parameterization[55] displayed as a red line. On the right, the ratio of the CLAS cross section to the cross section extracted from Brash.[55] The red line at 1 denotes where a perfect agreement would be. The ratio is fit to a constant, represented by a horizontal black line, representing the overall normalization. This normalization, integrated over all sectors, is the overall correction that is used in the DVCS cross section. This plot is a reproduction of a plot appearing in the thesis manuscript of B. Guegan.[23]

The systematic error of the elastic renormalization is currently calculated only from the standard deviation of the measurement of the target length as measured sector by sector:

$$\frac{\sigma}{\mu} = \frac{\sqrt{\frac{1}{6-1}\sum_{i=1}^{6}(\epsilon_i - \mu)}}{\mu} = \frac{0.037}{0.906} = 4.0\%, \tag{187}$$

where μ is the average over all six sectors measured separately.

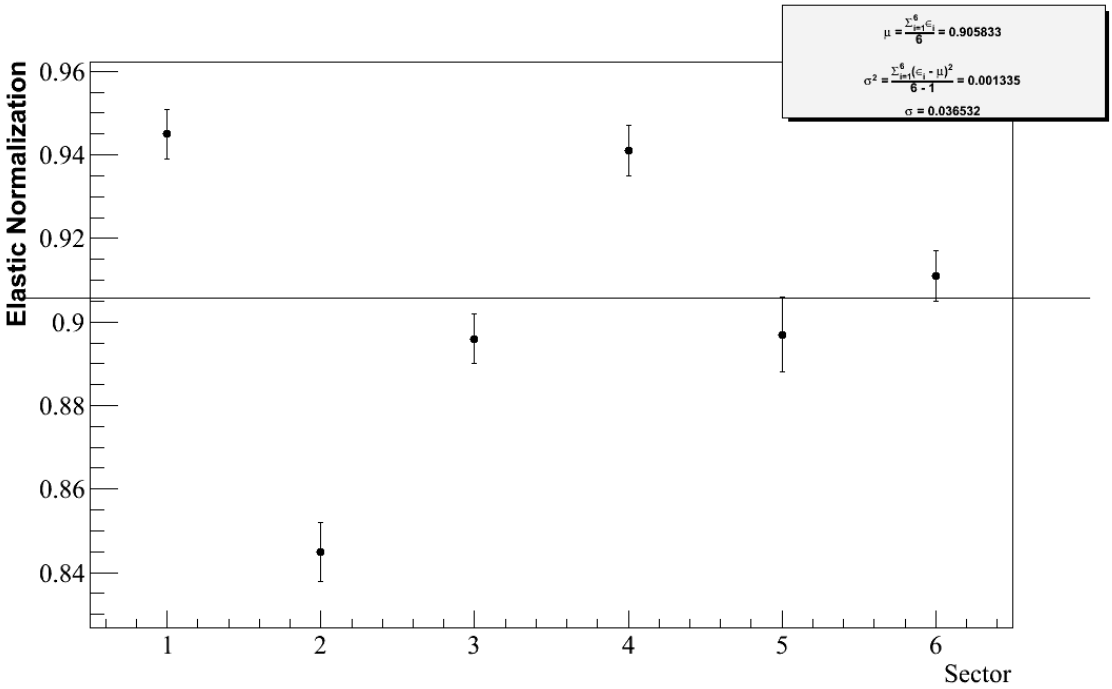

Figure 4.107: The abscissa corresponds to sector number, and the ordinate corresponds to the measurement of the elastic renormalization according to the method above. Each of the six measurements corresponds to the values determined from Figure 4.105. The horizontal black line corresponds to the mean value of all six points. The mean and standard deviation are listed in the upper right label.

4.11 Estimation of Errors

4.11.1 Statistical Errors

The cross section, as mentioned earlier, may be expressed as:

$$\frac{\mathrm{d}^4\sigma_{ep\gamma}}{\mathrm{d}Q^2\mathrm{d}t\mathrm{d}x_B\mathrm{d}\Phi} = \frac{(N_{e+p+\gamma} - N_{e+p+\pi^0(1\gamma)})}{\mathcal{L}_{\mathrm{int}} A \Delta V F_{\mathrm{rad}}}, \tag{188}$$

where $N_{e+p+\gamma}$ is the yield of the experiment, $N_{e+p+\pi^0(1\gamma)}$ is the number of π^0s which subtracts out the contamination from $e+p+\pi^0$ events, $\mathcal{L}$ is the integrated luminosity, A is the acceptance, ΔV is the bin volume, and $F_{rad.cor.}$ is the radiative correction, calculated bin per bin.

In order to know the statistical error of the cross section, the errors of each of the components was calculated, bin by bin.

First, since the yield for $e+p+\gamma$ events, $N_{e+p+\gamma}$, is obtained as a measurement from a counting experiment, its error is simply:

$$\Delta N_{e+p+\gamma} \approx \sqrt{N_{e+p+\gamma}}. \tag{189}$$

Next, the π^0 contamination subtraction, $N_{e+p+\pi^0(1\gamma)}$ is defined as:

$$N_{e+p+\pi^0(1\gamma)} = N^{\gamma\gamma}_{\pi_0} \frac{N^{\gamma}_{\pi_0,\mathrm{rec}}}{N^{\gamma\gamma}_{\pi_0,\mathrm{rec}}}, \tag{190}$$

therefore, its error is calculated to be:

$$\frac{\Delta N_{e+p+\pi^0(1\gamma)}}{N_{e+p+\pi^0(1\gamma)}} = \sqrt{\left(\frac{\Delta N^{\gamma\gamma}_{\pi_0}}{N^{\gamma\gamma}_{\pi_0}}\right)^2 + \left(\frac{\Delta N^{\gamma}_{\pi_0,\mathrm{rec}}}{N^{\gamma}_{\pi_0,\mathrm{rec}}}\right)^2 + \left(\frac{\Delta N^{\gamma\gamma}_{\pi_0,\mathrm{rec}}}{N^{\gamma\gamma}_{\pi_0,\mathrm{rec}}}\right)^2}, \tag{191}$$

where the errors of $N^{\gamma\gamma}_{\pi_0}$, $N^{\gamma}_{\pi_0,\mathrm{rec}}$, and $N^{\gamma\gamma}_{\pi_0}$ are determined as counting experiments:

$$\begin{aligned} \Delta N^{\gamma\gamma}_{\pi_0} &= \sqrt{\Delta N^2_{signal} + \Delta N^2_{background}}, \\ \Delta N^{\gamma}_{\pi_0,\mathrm{rec}} &= \sqrt{N^{\gamma}_{\pi_0,\mathrm{rec}}}, \\ \Delta N^{\gamma\gamma}_{\pi_0,\mathrm{rec}} &= \sqrt{N^{\gamma\gamma}_{\pi_0,\mathrm{rec}}}, \end{aligned} \tag{192}$$

where ΔN_{signal} and $\Delta N_{background}$ are the error on the measurement of the signal of pions and the error on the measurement of the linear background under the pions, both in the case where two photons are detected in data, where

$$\begin{aligned} \Delta N_{signal} &= \sqrt{N_{signal}}, \\ \Delta N_{background} &= \sqrt{N_{background}}. \end{aligned} \tag{193}$$

Next, the acceptance, A, is defined as:

$$A = \frac{N_{rec}}{N_{gen}}, \tag{194}$$

therefore, its error is calculated to be:

$$\frac{\Delta A}{A} = \sqrt{\left(\frac{\Delta N_{rec}}{N_{rec}}\right)^2 + \left(\frac{\Delta N_{gen}}{N_{gen}}\right)^2} \tag{195}$$

Lastly, the error for the $e + p + \gamma$ cross section, $\Delta\sigma_{ep\gamma}$ is calculated to be:

$$\frac{\Delta\sigma_{ep\gamma}}{\sigma_{ep\gamma}} = \sqrt{\left(\frac{\Delta N_{e+p+\gamma}}{N_{e+p+\gamma} - N_{e+p+\pi^0(1\gamma)}}\right)^2 + \left(\frac{\Delta N_{e+p+\pi^0(1\gamma)}}{N_{e+p+\gamma} - N_{e+p+\pi^0(1\gamma)}}\right)^2 + \left(\frac{\Delta A}{A}\right)^2} \tag{196}$$

While the above procedure is approximately correct, the calculation of these errors makes the assumption that there is no covariance between the variables, that is to say we assume there are no correlations. This is not strictly correct, however. For example, $N_{e+p+\pi^0(1\gamma)}$ and $N_{\pi_0}^{\gamma\gamma}$ are both measured in experiment; $N_{\pi_0,\mathrm{rec}}^{\gamma\gamma}$ and $N_{\pi_0,\mathrm{rec}}^{\gamma}$ both come from the same π^0 generator; and N_{gen} and N_{rec} come from the same DVCS generator. Because of this, there is a possibility for correlation between these variables, with a non-zero covariance entering into the errors. This is a potential candidate for further investigation.

4.11.2 Systematical Errors

While a complete study of the systematical errors was not completed, we list in Table 4.18, the few results of the studies which were completed, and also list quantities for which a systemic error study is planned in the near future. For those which are not yet completed, we can realistically estimate the uncertainties to be similar to those found in the sister experiment e1-dvcs1. While these are estimated to be the main sources of systematic error, this list is not necessarily exhaustive. For the moment, we take our systematic to be about 18 % as an estimate.

Table 4.18: A table of the measured and predicted sources of systemically error. The first four quantities are estimated from e1-dvcs1. The last two systematic errors of ϵ and $\mathcal{L}_{\rm int}$ are calculated from e1-dvcs2, and have already been presented earlier in this thesis. For the moment, we take our systematic to be about 18 %.

pion subtraction $N_{e+p+\pi^0(1\gamma)}$, π^0 generator	$\approx 10\%$, estimate from e1-dvcs1
acceptance A, DVCS generator	$\approx 10\%$, estimate from e1-dvcs1
fiducial cuts, exclusivity cuts	$\approx 5\%$, estimate from e1-dvcs1
radiative corrections $F_{\rm rad}$	$\approx 10\%$, estimate from e1-dvcs1
elastic renormalization ϵ, elastic generator	$= 4\%$ see Figure 4.107
integrated luminosity $\mathcal{L}_{\rm int}$ (target length ℓ)	$=0.3\%$ see Figure 4.90

There are several ways we can estimate the systematic errors of the cross section extractions. We outline here a few of the planned studies, and how we plan to achieve them:

- For the pion subtraction, we have a choice of which of a few generators to use. We can attempt to run our analysis with multiple generators, and see how the cross section changes, bin per bin. In this case, we obtain a systematic error for the acceptances of the events where one or two photons are detected, as the cross section should not depend on which generator we select.

- The acceptance for DVCS will have an associated systematic error as described in the case of the pion acceptances. There is a choice of generator, which will affect the systematics.

- The fiducial cuts and exclusivity cuts could affect the systematics. The cross section should be independent of the choice of exclusivity cuts and fiducial cuts. Therefore, if the cross section is changing based on a variation of these cuts, we must assign a systematic error, bin per bin. This is applicable for the case where two photons are detected, in data and Monte Carlo, and also for DVCS in data and Monte Carlo. As for fiducial cuts, the strictness of our geometric cuts on detectors could be varied. If the cross section also varies, we can obtain systematics bin per bin.

- There are a few programs which allow us to calculate the radiative corrections to our cross section. If these programs are equally suitable for addressing the radiative corrections, the value of the cross section should be independent of the choice of the program we select. Therefore, if the cross section varies bin per bin based on our selection of which correction to choose, we have a measure of the systematics associated with this correction.

- The elastic normalization could be further studied using multiple generators in the manner stated above for elastic and DVCS.

5. FINAL RESULTS

5.1 DVCS Cross Section - Final Results

5.1.1 Unpolarized Cross Section

Each element that was needed to extract the cross section has now been obtained. An example of the unpolarized cross section is presented in Figure 5.1, for the fifth bin in x_B and θ_e. A full list of unpolarized cross sections may be found in Appendix E. It is expected that the Bethe-Heitler process dominates at low and high Φ, and DVCS is more dominant in the central Φ range. The unpolarized cross section allows us access to CFFs, and may be written, up to twist-two approximation (leading twist), as:

$$\frac{\mathrm{d}^4\sigma_{\mathrm{unpol}}}{\mathrm{d}Q^2\mathrm{d}t\mathrm{d}x_B\mathrm{d}\Phi} = \frac{\mathrm{d}^4\sigma_{\mathrm{DVCS}}}{\mathrm{d}Q^2\mathrm{d}t\mathrm{d}x_B\mathrm{d}\Phi} + \frac{\mathrm{d}^4\sigma_{\mathrm{BH}}}{\mathrm{d}Q^2\mathrm{d}t\mathrm{d}x_B\mathrm{d}\Phi} + \mathcal{I}, \tag{197}$$

where

$$\begin{aligned}\mathcal{I} = &+ f_1(Q^2,t,x_B,\Phi)\mathrm{Re}(\mathcal{C}^{\mathcal{I}}(\mathcal{F})) \\ &+ \left[f_2(Q^2,t,x_B,\Phi) - f_3(Q^2,t,x_B,\Phi)\cos(\Phi)\right]\mathrm{Re}(\mathcal{C}^{\mathcal{I}}(\mathcal{F}) + \Delta\mathcal{C}^{\mathcal{I}}(\mathcal{F})),\end{aligned} \tag{198}$$

$$\mathcal{C}^{\mathcal{I}}(\mathcal{F}) = F_1\mathcal{H} + \frac{x_B}{2-x_B}(F_1+F_2)\tilde{\mathcal{H}} - \frac{t}{4M_p^2}F_2\mathcal{E}, \tag{199}$$

$$\Delta\mathcal{C}^{\mathcal{I}}(\mathcal{F}) = -\frac{x_B}{2-x_B}(F_1+F_2)\left\{\frac{x_B}{2-x_B}(\mathcal{H}+\mathcal{E}) + \tilde{\mathcal{H}}\right\}, \tag{200}$$

where $\mathcal{F} = \{\mathcal{H},\mathcal{E},\tilde{\mathcal{H}},\tilde{\mathcal{E}}\}$ are the CFFs and F_1 and F_2 are the Dirac and Pauli form factors introduced in Section 2., and the functions f_1, f_2 and f_3 are complicated expressions which depend on the kinematics. A more complete decomposition of the cross section, up to twist-three may be found in reference[56], as well as the expansions of the pure BH and DVCS contributions. We note that in our kinematics, there contribution from the pure DVCS term is quite small. Also, as x_B and t are relatively small, the dominant CFF in this expression is $\mathcal{H}_{\mathrm{Re}}$.

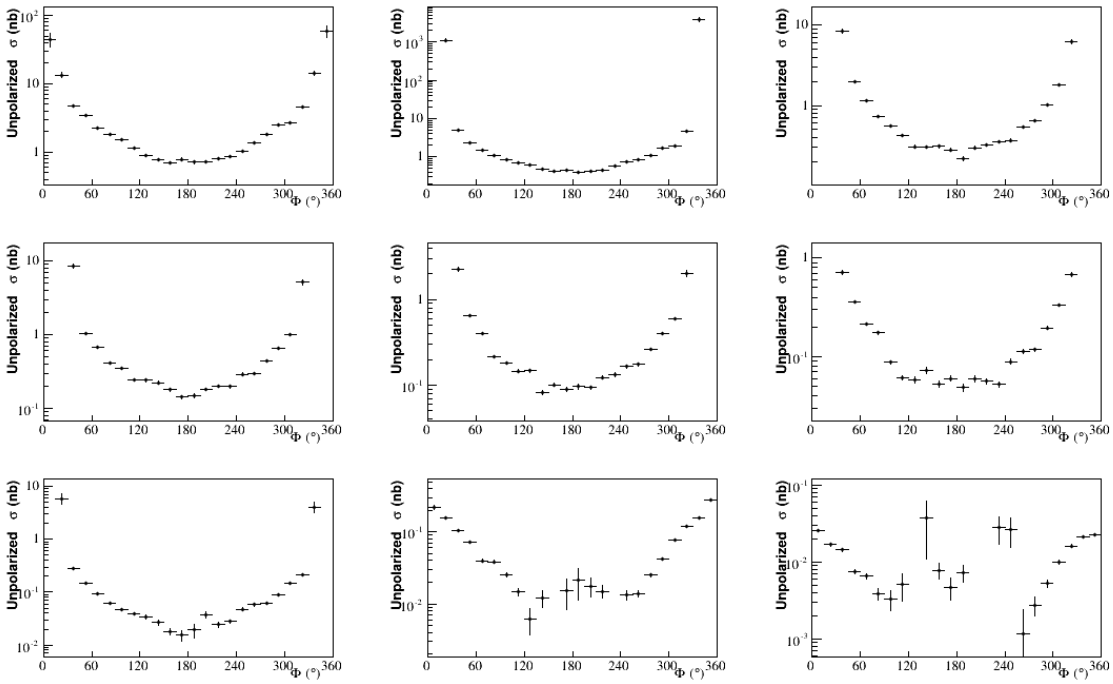

Figure 5.1: The unpolarized cross section as a function of Φ for the fifth bin in x_B and θ_e, where $0.17 < x_B < 0.2$ and $25.5^\circ < \theta_e < 45^\circ$. Each panel corresponds to a bin in $-t$ whose limits are: [0.09, 0.13, 0.18, 0.23, 0.30, 0.39, 0.52, 0.72, 1.10, 2.00] in GeV^2.

5.1.2 Polarized Cross Section Difference

We can also extract the cross section differences. An example of the polarized cross section is presented in Figure 5.2, for the fifth bin in x_B and θ_e. A full list of polarized cross sections may be found in Appendix E. They are determined according to the following formula:

$$\begin{aligned}\frac{\mathrm{d}^4\sigma_{\mathrm{pol}}}{\mathrm{d}Q^2\mathrm{d}t\mathrm{d}x_B\mathrm{d}\Phi} &= \frac{1}{2}\left(\frac{\mathrm{d}^4\sigma_{+,0}}{\mathrm{d}Q^2\mathrm{d}t\mathrm{d}x_B\mathrm{d}\Phi} - \frac{\mathrm{d}^4\sigma_{-,0}}{\mathrm{d}Q^2\mathrm{d}t\mathrm{d}x_B\mathrm{d}\Phi}\right) \\ &= \frac{1}{2P}\left(\frac{N_{+,0}}{\mathcal{L}_{\mathrm{int},+}} - \frac{N_{-,0}}{\mathcal{L}_{\mathrm{int},-}}\right)\frac{1}{A\Delta V F_{\mathrm{rad}}\epsilon},\end{aligned} \tag{201}$$

where the subscripts a and b in $N_{a,b}$ correspond to the polarization of the beam and the target respectively, being either "+" or "−" for the beam, and being "0", unpolarized for the target. P corresponds to the polarization of the e1-dvcs2 experiment. This polarization varies from about 83-87%, and is taken to be at its average value of 85.3%. The experiment was deliberately carried out such that the integrated luminosities of each polarization are approximately equal: $\mathcal{L}_{\mathrm{int},+} \approx \mathcal{L}_{\mathrm{int},-} \approx \mathcal{L}_{\mathrm{int}}/2$. Finally, $N_{+,0}$ and $N_{+,0}$ correspond to the number of events measured after the pion subtraction, viz.:

$$\begin{aligned}N_{+,0} &= N_{+,0}^{e+p+\gamma} - N_{+,0}^{e+p+\pi^0(1\gamma)}, \\ N_{-,0} &= N_{-,0}^{e+p+\gamma} - N_{-,0}^{e+p+\pi^0(1\gamma)}.\end{aligned} \tag{202}$$

The cross section may be expressed in terms of form factors and CFFs. We choose to express it up to twist-two:

$$\frac{\mathrm{d}^4\sigma_{pol}}{\mathrm{d}Q^2\mathrm{d}t\mathrm{d}x_B\mathrm{d}\Phi} = f_4(Q^2,t,x_B,\Phi)\sin(\Phi)\mathrm{Im}(\mathcal{C}^{\mathcal{I}}(\mathcal{F}) + \Delta\mathcal{C}^{\mathcal{I}}(\mathcal{F})). \tag{203}$$

We note that the pure BH and DVCS contributions have vanished in the polarized cross section. This is due to BH not being sensitive to the polarization of the beam, and the fact that pure DVCS is dependent on beam spin at the twist-three approximation, but not at twist-two. Again, due to the relatively small values of x_B and t, the polarized cross sections are mainly sensitive to $\mathcal{H}_{\mathrm{Im}}$.

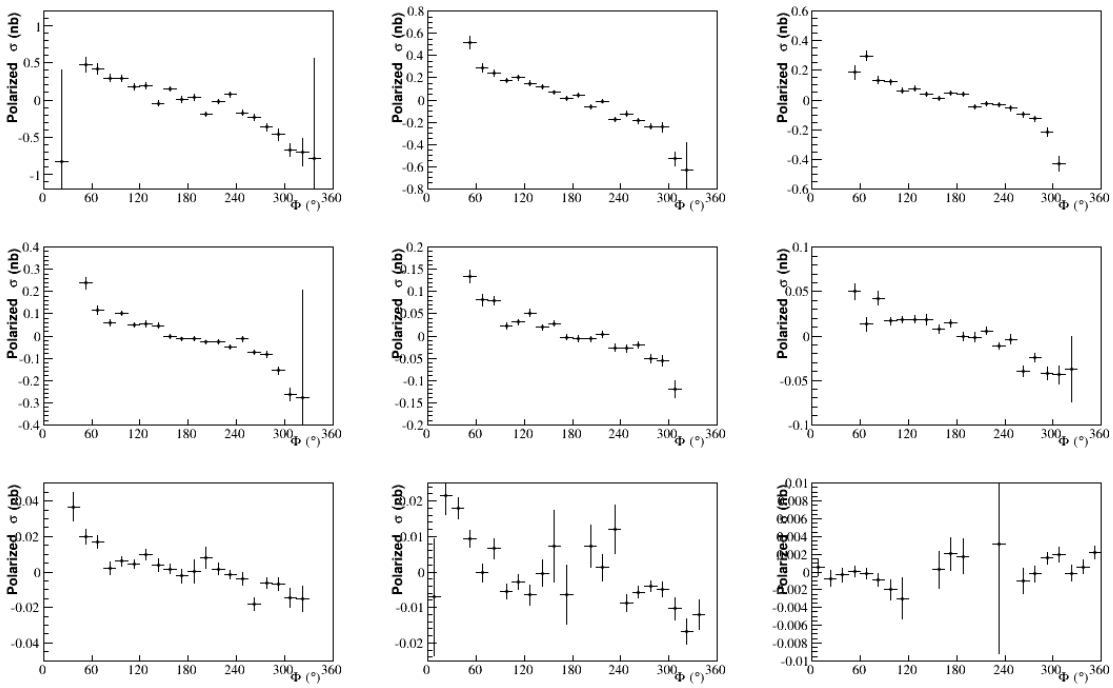

Figure 5.2: The polarized cross section as a function of Φ for the fifth bin in x_B and θ_e, where $0.17 < x_B < 0.2$ and $25.5^\circ < \theta_e < 45^\circ$. Each panel corresponds to a bin in $-t$ whose limits are: [0.09, 0.13, 0.18, 0.23, 0.30, 0.39, 0.52, 0.72, 1.10, 2.00] in GeV^2.

5.1.3 Beam Spin Asymmetry

The last observable that we can extract is the beam spin asymmetry. The asymmetry is defined as the ratio of the unpolarized cross section to the polarized cross section, and is a useful quantity because it allows for a cancellation of the overall normalization. This is a benefit because it cancels out the acceptance, which is a very difficult quantity to know extremely well:

$$\mathcal{A}_{\text{LU}} = \frac{\sigma_{\text{unpol}}}{\sigma_{\text{pol}}} = \frac{1}{P}\left(\frac{N_{+,0} + N_{-,0}}{N_{+,0} - N_{-,0}}\right). \tag{204}$$

Up to a twist-two approximation, the Φ decomposition of the asymmetry may be written as:

$$\mathcal{A}_{\text{LU}} = \frac{\alpha \sin(\Phi)}{\beta + \gamma \cos(\Phi) + \delta \cos(2\Phi)}, \tag{205}$$

where α, β, γ and δ are parameters which can be expressed in terms of the Pauli and Dirac form factors, the CFFs, and kinematical variables. An example of the beam spin asymmetry is presented in Figure 5.3, for the fifth bin in x_B and θ_e. A full list of asymmetries may be found in

Appendix E.

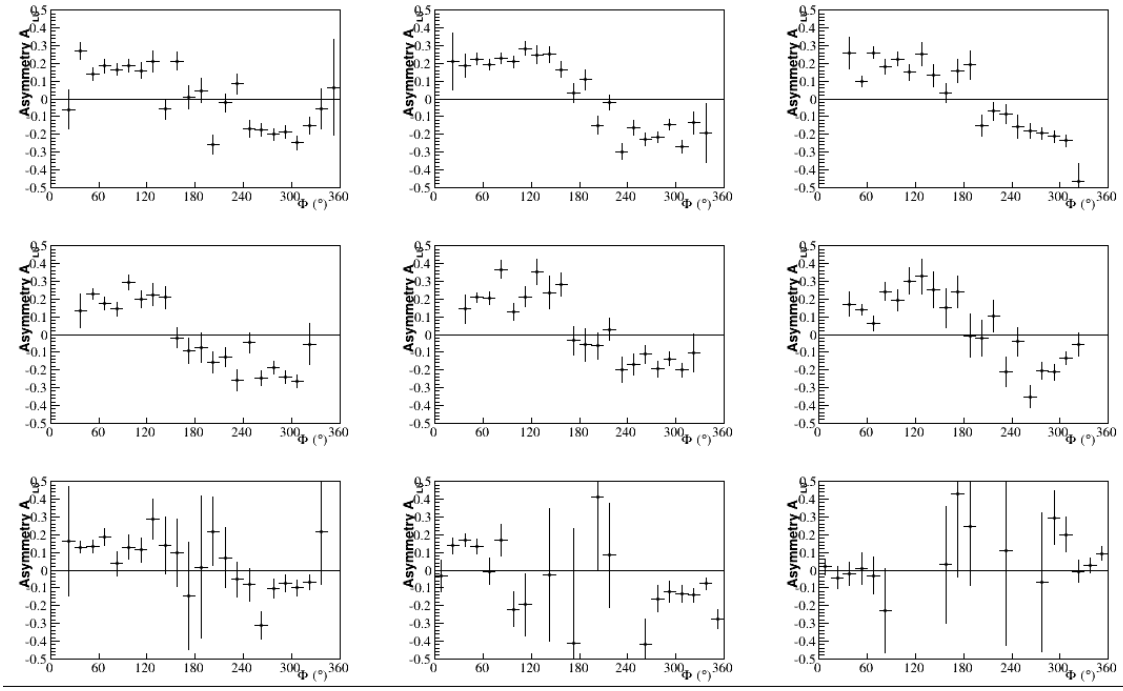

Figure 5.3: The asymmetry as a function of Φ for the fifth bin in x_B and θ_e, where $0.17 < x_B < 0.2$ and $25.5^\circ < \theta_e < 45^\circ$. Each panel corresponds to a bin in $-t$ whose limits are: [0.09, 0.13, 0.18, 0.23, 0.30, 0.39, 0.52, 0.72, 1.10, 2.00] in GeV^2.

5.2 Comparison with Parallel Analysis of e1-dvcs2, and e1-dvcs1

A comparison between the unpolarized cross section of this analysis with parallel analysis of e1-dvcs2 by B. Guegan and an analysis of e1-dvcs1 by H.S. Jo is presented in Figure 5.4, for the fifth bin in x_B and θ_e. A full list of comparisons for the unpolarized cross sections, polarized cross sections, and beam spin asymmetries may be found in Appendix E. For this specific bin, we present this analysis in black, parallel e1-dvcs2 analysis in green, and e1-dvcs1 analysis in red. We also present the ratio of this analysis to these two other analyses, for a better comparison:

$$\begin{aligned} Ratio_{e1-dvcs1} &= \frac{e1-dvcs2\ Saylor}{e1-dvcs1\ Jo}, \\ Ratio_{e1-dvcs1} &= \frac{e1-dvcs2\ Saylor}{e1-dvcs2\ Guegan}. \end{aligned} \tag{206}$$

We find that the comparison yields fair agreement in all bins, with some deviations. The source of these discrepancies is a topic of continued interest. At large Φ, the IC dominates. At Φ around 180°, the EC dominates. One can see that near $\Phi = 180^\circ$ there is a discontinuity in the measured cross section where the IC and EC data meet. The discrepancy between the IC and EC data is a point of ongoing investigation.

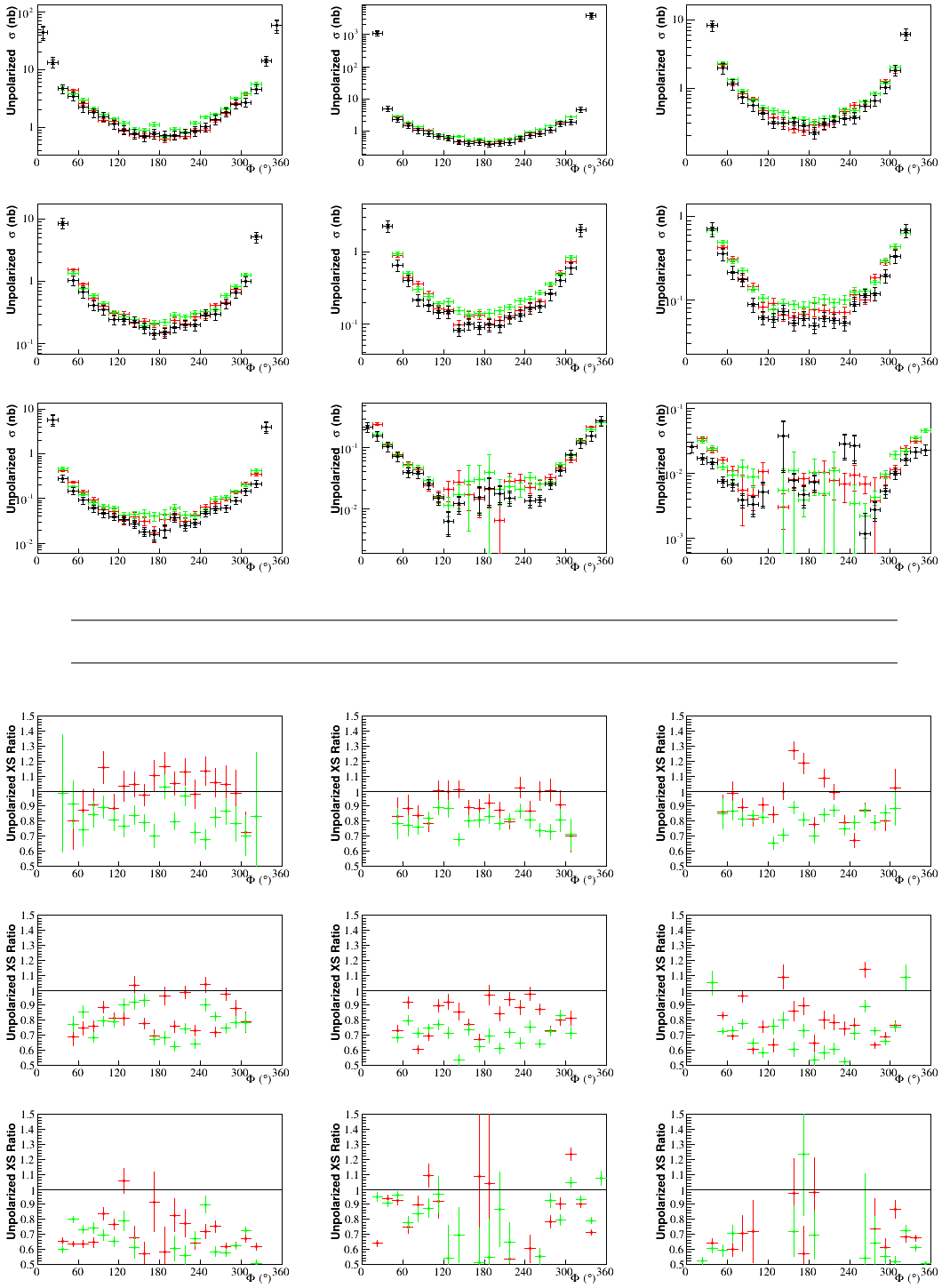

Figure 5.4: On top, the unpolarized cross section differences as a function of Φ. Black represents this analysis. Green is e1-dvcs2 by B. Guegan. Red is e1-dvcs1 by H.S. Jo. On bottom, the unpolarized cross section ratios. Both are for the fifth bin in x_B and θ_e, where $0.17 < x_B < 0.2$ and $25.5^\circ < \theta_e < 45^\circ$. Each panel corresponds to a bin in $-t$ whose limits are: [0.09, 0.13, 0.18, 0.23, 0.30, 0.39, 0.52, 0.72, 1.10, 2.00] Green is $\frac{e1-dvcs2\ Saylor}{e1-dvcs2\ Guegan}$. Red is $\frac{e1-dvcs2\ Saylor}{e1-dvcs1\ Jo}$.

5.3 Preliminary Interpretation of Final Results

5.3.1 Comparison with Existing Models

The focus of this section is centered around the interpretation and comparison of the measured cross section in light of the VGG model. However, we will take the time to briefly compare the predictions of a few other models with our measured cross sections, without going deeply into interpretation. To that end, we give a brief overview of the various other models seen here. A more detailed description of the differences between these models is found in reference[24].

Kumerički-Müller (KM) 10 and 10a:

The KM model is based on the Mellin-Barnes Parameterization, which is based on a partial wave expansion of the GPDs. In this model, each of the four GPDs, H, E, $\tilde{H}$, and $\tilde{E}$, are considered. In KM10, the model uses data from Hall A and CLAS data at JLab, and HERMES to fit its parameters. Whereas in KM10a, $\tilde{H}$ is set to zero and fixes the pion pole. Additionally, data from CLAS and HERMES are used, and Hall A is rejected, as its cross sections are quite difficult to describe. A specific condition of KM is the restriction that t be small, and Q^2 be high.[57] For this reason, one notices that for higher bins in t, and lower bins in Q^2, there are no curves corresponding to KM.

Comparison of the Unpolarized Cross Section with VGG, KM10 and KM10a:

An example of one of these models compared to the cross section of this analysis is presented in Figure 5.5, for the fifth bin in x_B and θ_e. A full list of comparisons may be found in Appendix F. VGG is plotted in green, KM10 is plotted in light magenta, and KM10a is plotted in dark magenta. We note the differences between the models, which tend to agree with each other more for large and small values of Φ, but much less around $\Phi = 180°$.

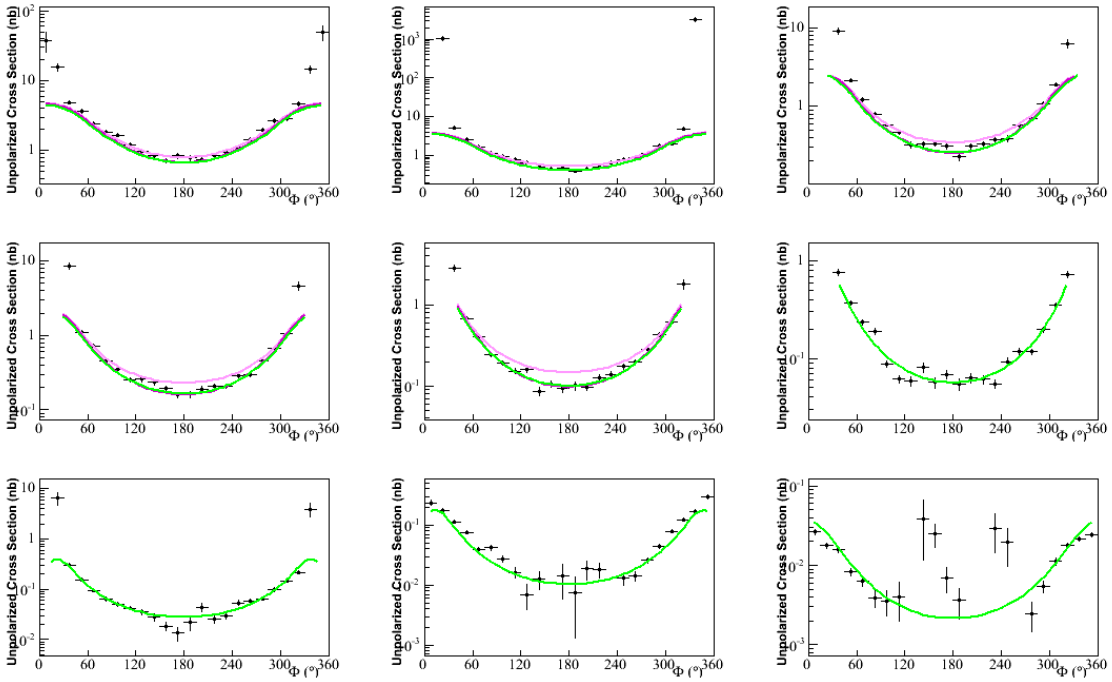

Figure 5.5: The unpolarized cross section as a function of Φ for the fifth bin in x_B and θ_e, where $0.17 < x_B < 0.2$ and $25.5^\circ < \theta_e < 45^\circ$. Each panel corresponds to a bin in $-t$ whose limits are: [0.09, 0.13, 0.18, 0.23, 0.30, 0.39, 0.52, 0.72, 1.10, 2.00] For both, the green curve corresponds to VGG, the light magenta corresponds to KM10, and the dark magenta corresponds to KM10a.

5.3.2 VGG Extraction of Compton Form Factors

In order to extract the CFF which we are sensitive to in this experiment, $\mathcal{H}_{\mathrm{Im}}$, we fit the polarized and unpolarized cross section according to the VGG model. We also extract $\mathcal{H}_{\mathrm{Re}}$, a quantity which we are less sensitive to. The extractions of $\mathcal{H}_{\mathrm{Re}}$ and $\mathcal{H}_{\mathrm{Im}}$ are presented in Figure 5.6 and Figure 5.7, respectively. It is possible to extract the CFF $\mathcal{H}_{\mathrm{Im}}$ as a function of $-t$ for a choice of x_B by fitting each of the distributions to the equation e^{A-Bt}. These fits are presented in Figure 5.7.

For the DVCS reaction, there are eight possible observables which give access to CFFs: the unpolarized cross section σ_{unpol}, the polarized cross section σ_{pol}, and the asymmetries $\mathcal{A}_{\mathrm{C}}$, $\mathcal{A}_{\mathrm{LU}}$, $\mathcal{A}_{\mathrm{UL}}$, $\mathcal{A}_{\mathrm{LL}}$, $\mathcal{A}_{\mathrm{Ux}}$, $\mathcal{A}_{\mathrm{Uy}}$, $\mathcal{A}_{\mathrm{Lx}}$ and $\mathcal{A}_{\mathrm{Ly}}$, where the two subscripts on the asymmetries refer to the polarization of the beam and target respectively, and U means unpolarized, L means longitudinally polarized, and x, y means transversely polarized in the hadronic plane, or perpendicular to the hadronic plane.

In principle, the method for extracting our eight CFFs, involves solving a complicated system of equations using each of these observables, with the CFFs acting as free parameters. It is not a

trivial problem because the equations are non-linear, and for our case, we only have two independent observables measured. However, since our kinematics suppress many of the CFFs, we expect that only $\mathcal{H}_{\mathrm{Re}}$ and $\mathcal{H}_{\mathrm{Im}}$ will have a significant contribution. Additionally, we can apply some realistic constraints on the suppressed CFFs. In this way, our under constrained set of equations can still be solved.

In order to fit these CFFs, we use a model independent method[58,59], in which we vary the CFFs such that the following quantity is minimized:

$$\chi^2 = \sum_{i=1}^{n} \frac{\left(\sigma_{\mathrm{the},i} - \sigma_{\mathrm{exp},i}\right)^2}{\left(\Delta\sigma_{\mathrm{exp},i}\right)^2}, \tag{207}$$

in which i is the bin number; σ is taken to be either the unpolarized or polarized cross section; the subscripts on σ "the" and "pol" refer to either "theoretical" or "experimental" cross sections, and $\Delta\sigma_{\mathrm{exp},i}$ is the error bar associated with the data point. For the moment, since the analysis of systematic errors is incomplete, the extraction only takes into account statistical errors.

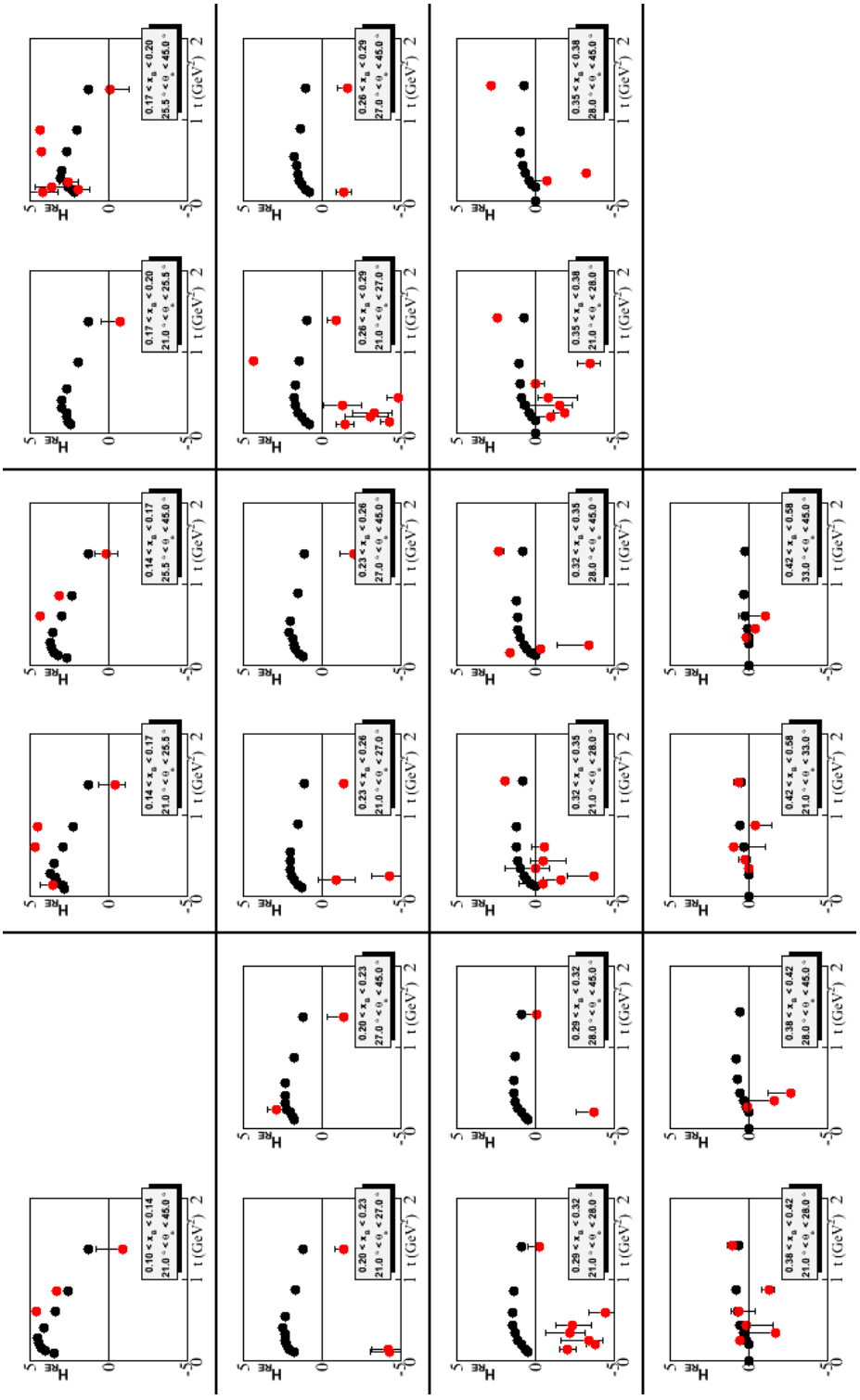

Figure 5.6: $\mathcal{H}_{\mathrm{Re}}$ as a function of $-t$, for each of the 21 bins in x_B and θ_e. The red points represent the extraction from this analysis, and the black points represent the prediction from VGG. We notice that the agreement of the extraction to predictions is not great.

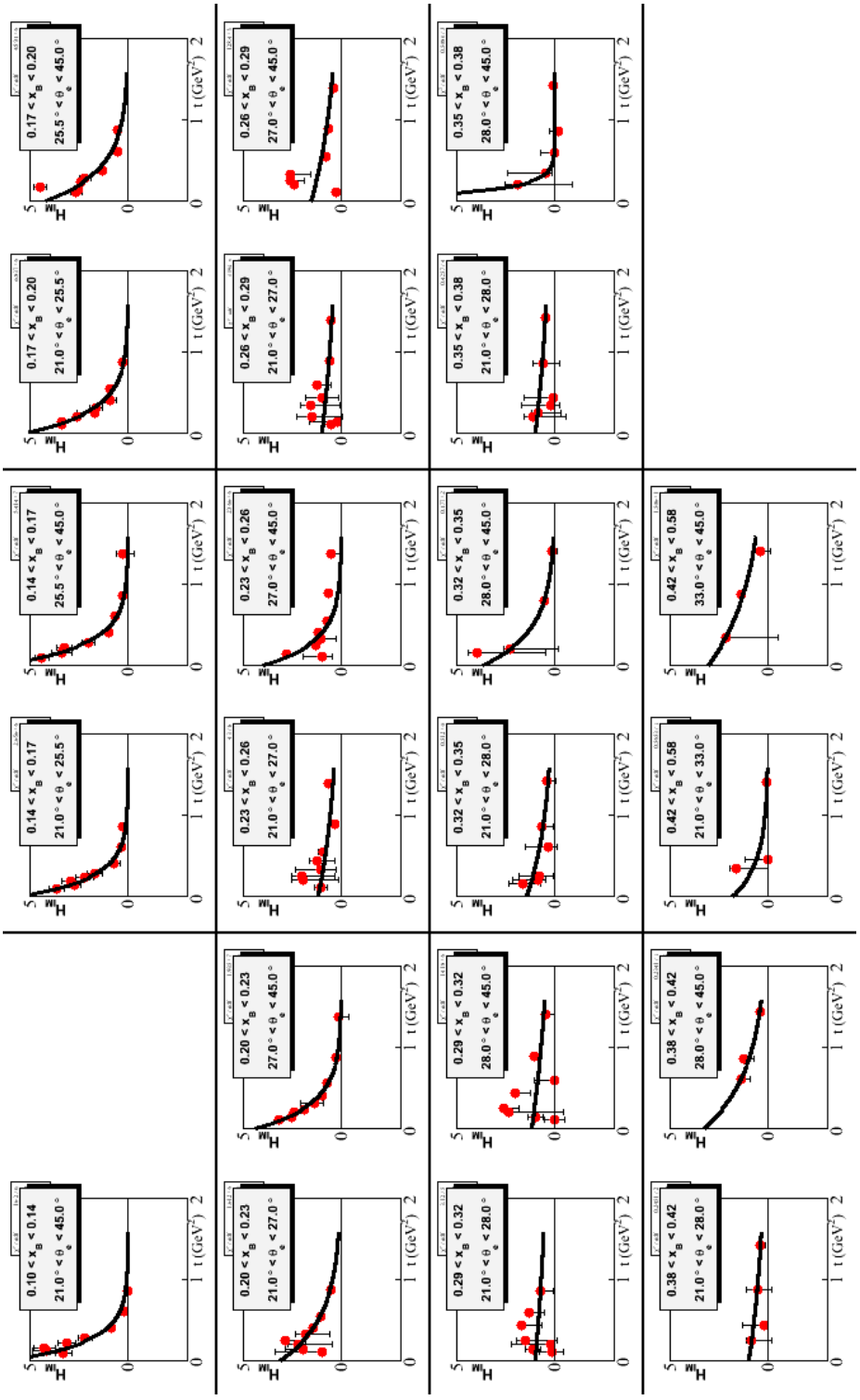

Figure 5.7: $\mathcal{H}_{\mathrm{Im}}$ as a function of $-t$, for each of the 21 bins in x_B and θ_e. The red points represent the extraction from this analysis, and the black points represent the prediction from VGG. We notice that the agreement is good for low values of x_B and θ_e, with worse agreement at higher values.

5.3.3 Extraction of Proton Charge Density

As we discussed on the outset, one of the objectives of measuring the cross sections for DVCS was to make the connection between GPDs and the proton charge density. Here, we outline the procedure to extract the proton charge density, and present our extraction from our measurement.

The proton charge density, as discussed in Section 2., can be extracted from the imaginary part of the GPD $H(x,\xi,t)$, according to the following formula:

$$q(x,0,b) = \int \frac{\mathrm{d}^2\vec{\Delta}_\perp}{(2\pi)^2} \mathrm{e}^{-i\vec{b}\cdot\vec{\Delta}_\perp} H^q(x,0,-\vec{\Delta}_\perp^2), \tag{208}$$

where the charge density is represented by a Fourier transform of the GPD H evaluated at the point $\xi = 0$, exchanging the perpendicular component of the momentum transfer to the proton $\vec{\Delta}_\perp$ for the impact parameter $\vec{b}$. Because of the cylindrical symmetry of the system, the Fourier transform reduces to a Hankel transform,

$$q(x,0,b) = \frac{1}{4\pi}\int_0^\infty \mathrm{d}t J_0(b\sqrt{t}) H(x,0,t), \tag{209}$$

where $J_0(b\Delta_\perp)$ is the zeroth order Bessel function.

In the previous section, we were able to extract the CFF $\mathcal{H}_{\mathrm{Im}}$ at the point (x, $x=\xi$, t). As mentioned in Section 2., equation 48, the imaginary component of $\mathcal{H}$ is defined as:

$$\mathcal{H}_{\mathrm{Im}}(\xi,t) = H(\xi,\xi,t) - H(-\xi,\xi,t). \tag{210}$$

The first term, where $x=\xi$ corresponds to the valence region, and the second term where $x=-\xi$ corresponds to the sea quark region. In JLab kinematics, the second term corresponding to the sea quarks is approximately 20% of the contribution to $\mathcal{H}_{\mathrm{Im}}$ according to the VGG model.[24] We choose to make the approximation that the second term is zero, claiming that we are in the valence region. Therefore, the CFF which we have extracted in the previous section is nearly equivalent to the actual GPD at the point $x=\xi$.

$$\mathcal{H}_{\mathrm{Im}}(\xi,t) \approx H(\xi,\xi,t) \tag{211}$$

However, in order to obtain the charge density, we need to obtain the GPD at the point (ξ, 0, t) instead. This is accomplished by applying a model dependent "deskewing factor", $f_\xi = \frac{H(\xi,0,t)}{H(\xi,\xi,t)}$. This deskewing factor can only be obtained through a model, and in this case has been obtained through VGG. This allows us to express the GPD H as:

$$H(x,0,t) = f_\xi \mathcal{H}_{\rm Im} = f_\xi \mathrm{e}^{A-Bt}. \tag{212}$$

Substituting $H(x,0,t)$ into our Hankel transform, and writing the zeroth order Bessel function as an infinite sum, our charge density may be easily solved analytically:

$$\begin{aligned} q(x,0,b) &= \frac{1}{4\pi}\int_0^\infty \mathrm{d}t \sum_{m=0}^{\infty}\left[\frac{(\frac{-b^2 t}{4})^m}{m!m!}\right] f_\xi \mathrm{e}^{A-Bt} \\ &= \frac{\mathrm{e}^{A-\frac{b^2}{4B}}}{4\pi B} \end{aligned} \tag{213}$$

Figure 5.8, represents the charge density distributions as a function of impact parameter b for each choice of x_B. The distributions are Gaussian in shape, and centralized at the origin, with the charge being even more focused around the origin at higher x_B. Figure 5.9 to Figure 5.12 represent four three-dimensional views as a function of b for various choices of x_B. This three-dimensional view is quite novel, and the interpretation of these distributions is a point of intense focus. A study to compare how models compare to this extraction is also under way.

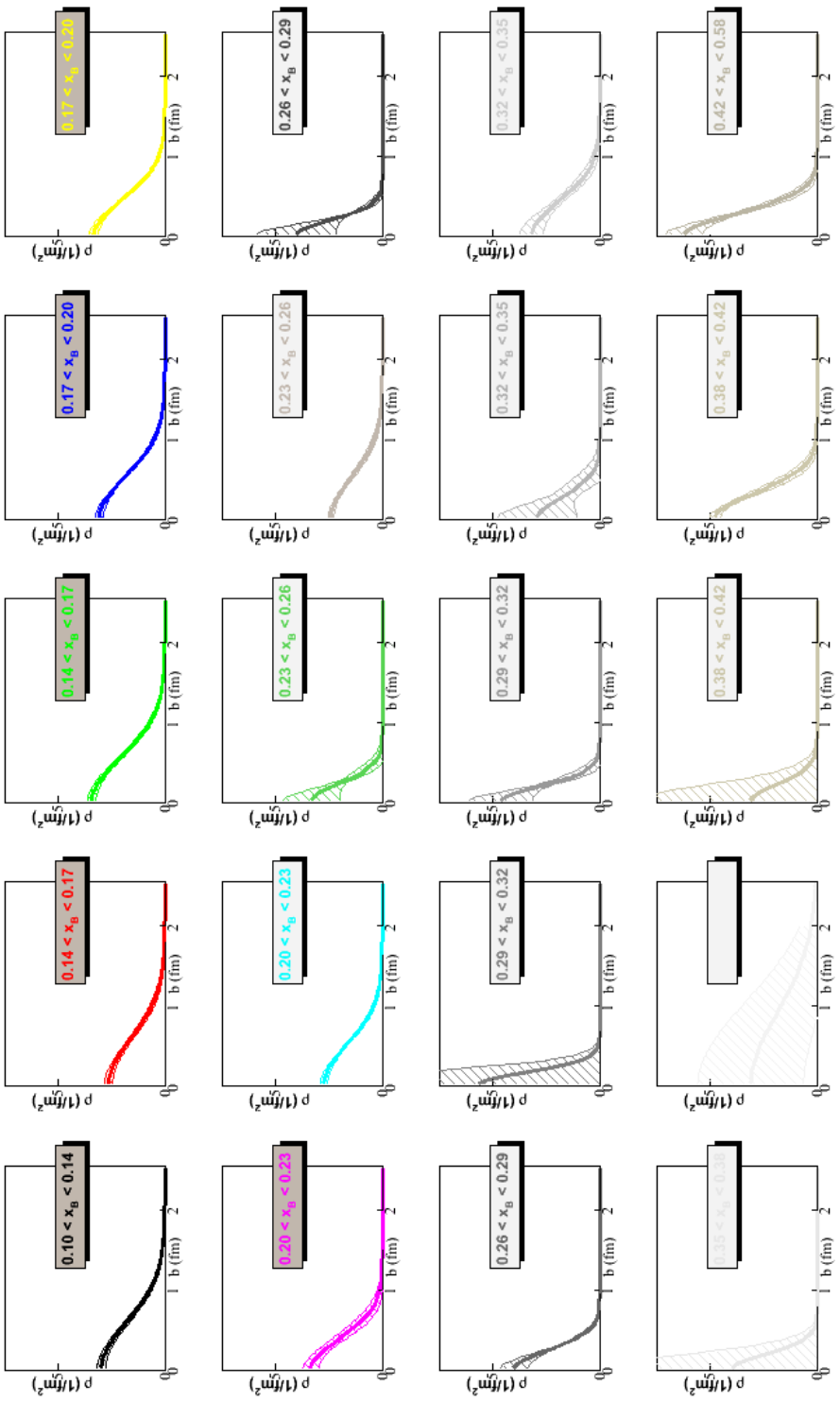

Figure 5.8: The charge density distribution of the proton as a function of impact parameter b. Each panel corresponds to a particular value of x_B. The shape of the distribution is Gaussian, centered around $b = 0$.

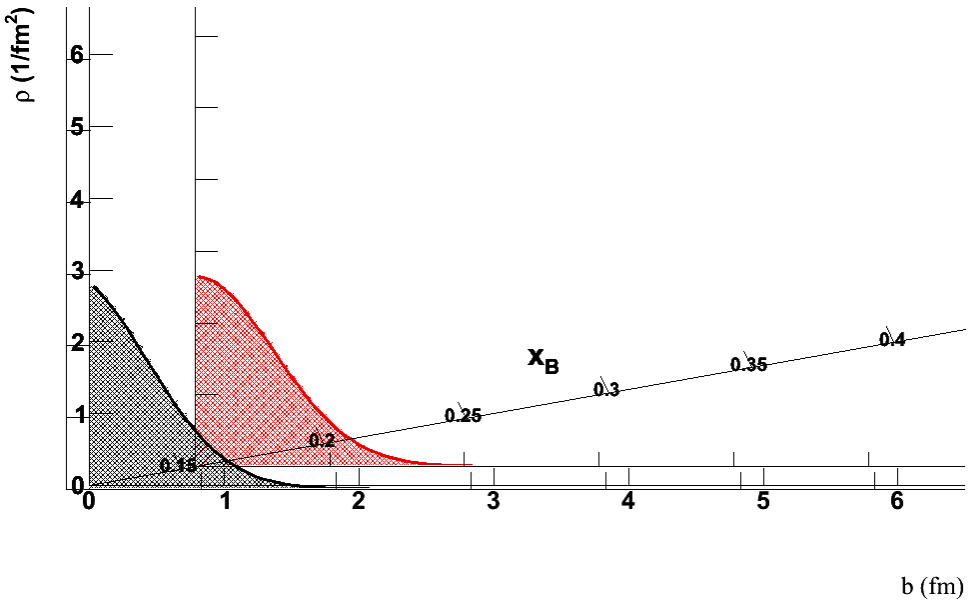

Figure 5.9: For bins 1 and 2, a three-dimensional view of the charge density distribution of the proton as a function of impact parameter b, for two choices of x_B: 0.12 and 0.155, and two choices of Q^2: 1.135 GeV^2 and 1.305 GeV^2 respectively.

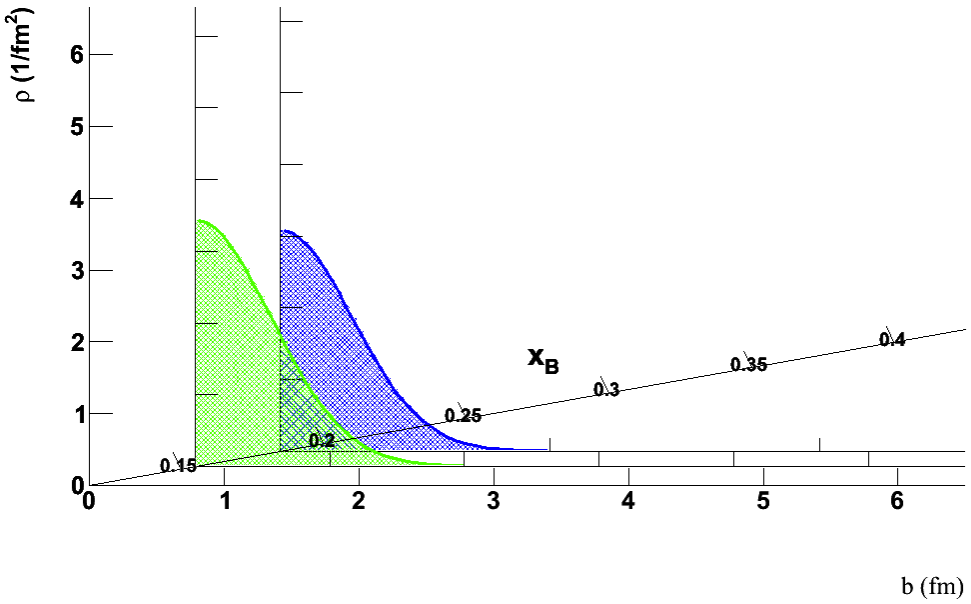

Figure 5.10: For bins 3 and 4, a three-dimensional view of the charge density distribution of the proton as a function of impact parameter b, for two choices of x_B: 0.155 and 0.185, and two choices of Q^2: 1.471 GeV^2 and 1.490 GeV^2 respectively.

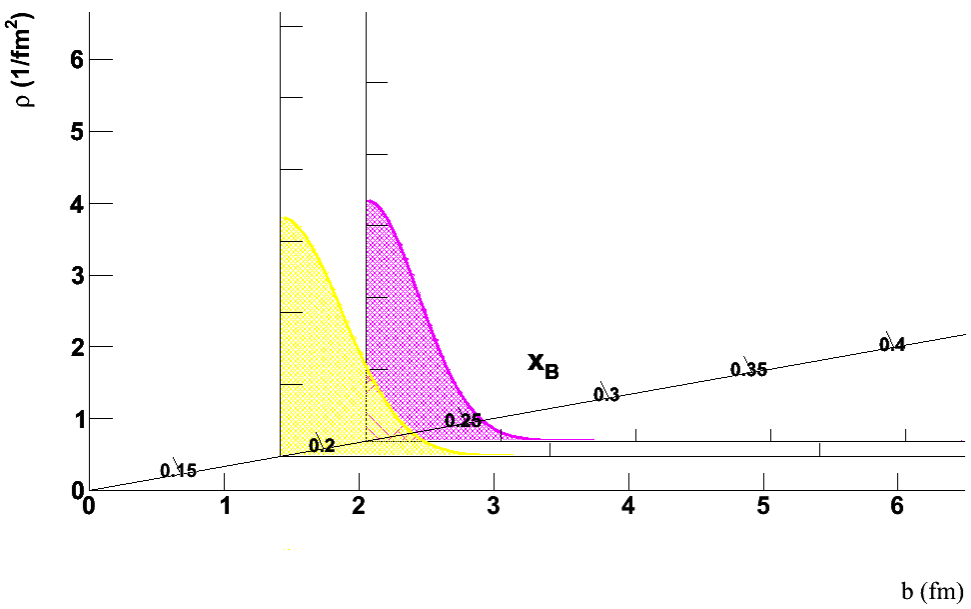

Figure 5.11: For bins 5 and 6, a three-dimensional view of the charge density distribution of the proton as a function of impact parameter b, for two choices of x_B: 0.185 and 0.215, and two choices of Q^2: 1.710 GeV^2 and 1.684 GeV^2 respectively.

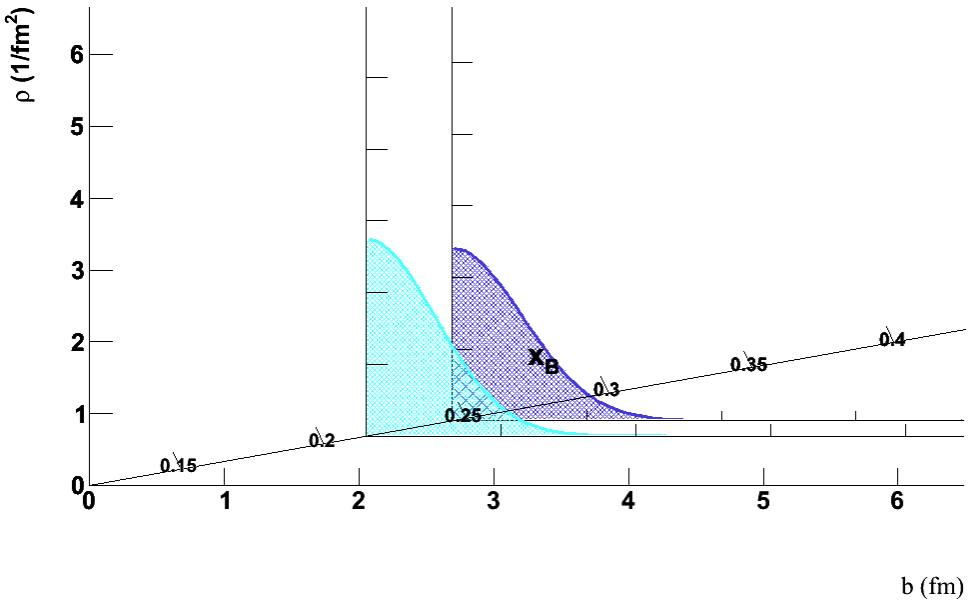

Figure 5.12: For bins 7 and 9, a three-dimensional view of the charge density distribution of the proton as a function of impact parameter b, for two choices of x_B: 0.215 and 0.245, and two choices of Q^2: 1.964 GeV^2 and 2.187 GeV^2 respectively.

6. CONCLUSION

We have measured the polarized and unpolarized cross sections, as well as the beam spin asymmetries of proton DVCS using the CLAS detector at 6 GeV at JLab for e1-dvcs2. With this measurement, we have accessed broad kinematics with many bins, ranging from 1 GeV^2 $< Q^2 <$ 5 GeV^2, 0.1 $< x_B <$ 0.6 and 0.1 GeV^2 $< -t <$ 2 GeV^2. With this measurement, we were able to extract, in a quasi model-independent way, the Compton Form Factor $\mathcal{H}$ in the valence region, giving us access to the GPD H for choices of x_B and $-t$. We were able to extract the proton charge density by taking the Fourier transform of H, giving us a tomographic view of the charge distribution within the proton in terms of x_B and impact parameter b, the conjugate variable of $-t$. Additionally, we were able to compare our cross section results with the predictions of multiple theories, such as VGG, KM10 and KM10a

The DVCS program at CLAS at 6 GeV is part of a larger community interested in the exploration of GPD physics, and the pursuit of a more unified picture of nucleon structure. In particular, Hall A at JLab and HERMES at DESY in the last decade have carried out experiments seeking to access GPDs through DVCS, as well as DVMP at JLab. While CLAS gives access to larger values of x_B, HERMES was carried out at an energy of 27 GeV giving access to the low x_B and high Q^2 region. Experimental data on reactions related to GPDs are still in a somewhat early stage, but the data collected so far seems to indicate that the handbag formalism and factorization approach are validated. With the completion and closure of HERMES and CLAS 6 programs come COMPASS with a 200 GeV muon beam and the upgraded CLAS 12. CLAS 12 seeks to expand our kinematic coverage to higher Q^2 and x_B, whereas COMPASS aims to take measurements in the very low x_B region. The kinematical coverage of these experiments is presented in Figure 6.1. Another candidate for the exploration of GPDs is PANDA at FAIR, which has the ability to measure time-like virtual Compton Scattering ($p + \bar{p} \rightarrow \gamma + \gamma^*$)[60].

A large number of these experiments are focused on hydrogen targets, which allows us to access proton DVCS. While a few experiments have been carried out at JLab with nuclear targets in Hall A with a deuterium target and in Hall B with CLAS with deuterium and helium targets in order to access neutron DVCS (nDVCS), data is quite limited. One of the goals for the near future at CLAS 12 is to give a better access to nDVCS, particularly with the construction of a neutron detector. The measurement of the charge densities for nDVCS and DVCS is necessary in order to have a flavor based separation of the charge distributions within the proton and neutron. This can be accomplished using isospin decomposition. A measurement of nDVCS also gives us access to the GPD E, which along with H appears in Ji's sum rule for the total angular momentum carried by the quarks within the nucleon, allowing for us to access for the very first time the orbital angular

momentum contribution of the quarks to the nucleon.

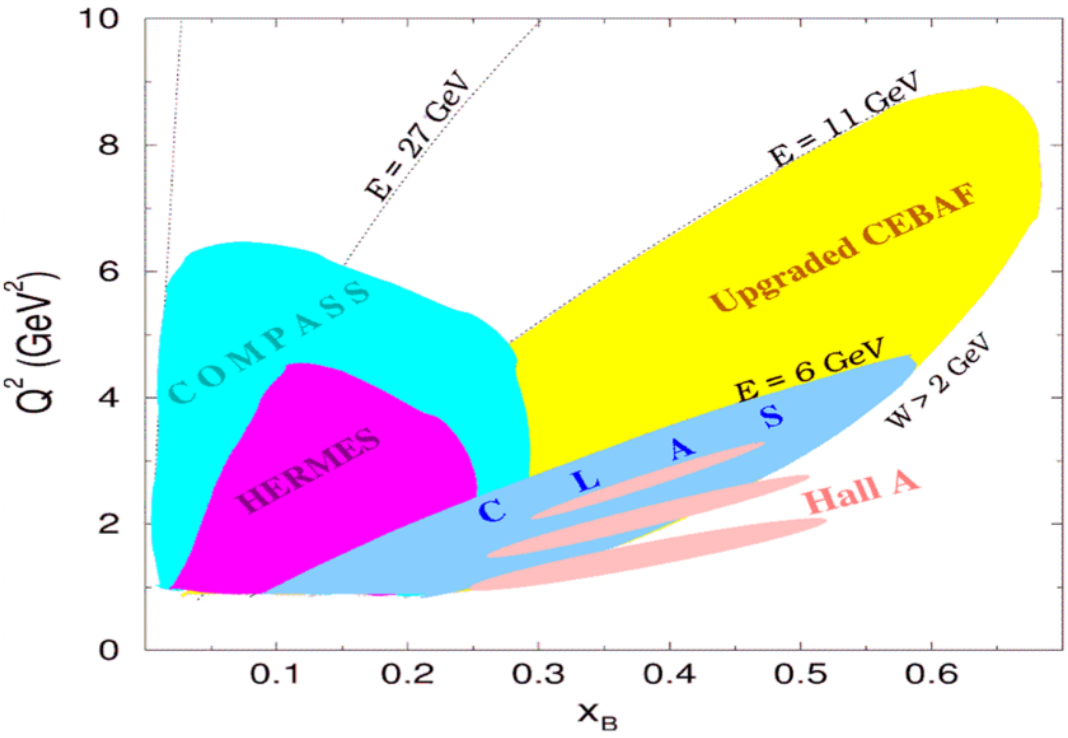

Figure 6.1: The kinematic coverage of Hall A, CLAS, HERMES, and the future coverage of COMPASS and CLAS 12. This figure was taken from reference[61].

7. SYNTHÈSE

7.1 Distributions de Partons Généralisées (GPDs) et Diffusion Compton Profondément Virtuelle (DVCS)

Un des buts de la physique nucléaire est de comprendre la structure des protons et des neutrons. Afin d'explorer leurs structures, on a historiquement étudié la diffusion élastique $e + N \to e + N$ et la diffusion profondément inélastique $e + N \to e + X$ (DIS). En mesurant la diffusion élastique, on obtient les Facteurs de Forme (FFs), et en mesurant la diffusion profondément inélastique, on obtient les distributions de partons (PDFs). Les FFs permettent d'accéder aux distributions spatiales des quarks dans le plan transverse dans le référentiel d'impulsion infinie. Les PDFs permettent d'accéder aux distributions á l'impulsion des quarks dans la direction longitudinale.

Il existe une nouvelle approche, qui a été développée par X. Ji[15], D. Müller[16] et A. Radyushkin[17] il y a environ dix ans, qui permets d'accéder simultanément aux distributions spatiales des quarks dans le plan transverse et aux distributions d'impulsions en direction longitudinale grâce aux Distributions de Partons Généralisées (GPDs). On peut accéder à ces nouvelles distributions en mesurant la réaction de Diffusion Compton Profondément Virtuelle (DVCS), qui se compose dans l'état initial, d'un électron et d'un proton, et dans l'état final, d'un électron diffusé, d'un proton recul, et d'un photon réel qui est émis du quark frappé. Ji, Müller et Radyushkin ont montré qu'est possible de factoriser dans le cadre de la QCD le diagramme du DVCS en deux parties: une partie pertubative (dure) et une partie non-perturbative (molle). Le terme non-perturbatif permet d'accéder aux GPDs.

Cette thèse se concentre sur le DVCS sur le proton. Le diagramme du "sac à main" du DVCS sur le proton est présenté dans Figure 7.1. Dans ce diagramme, k et k' sont les quadri-moments de l'électron incident et de l'électron diffusé, p et p' sont les quadri-moments du proton de la cible, et du proton recul et q' est le quadri-moment du photon réel. q est le quadri-moment du photon virtuel echangé entre l'électron et le parton. $x + \xi$ est la fraction de l'impulsion longitudinale du proton du quark frappé, et -2ξ est la fraction d'impulsion longitudinale qui est transférée au proton de recul. ξ s'appelle la "skewness". t est la variable de Mandelstam classique. Enfin, P est l'impulsion moyenne du proton initial et final: $P = (p + p')/2$. On note que les GPDs sont fonction de x, ξ et t.

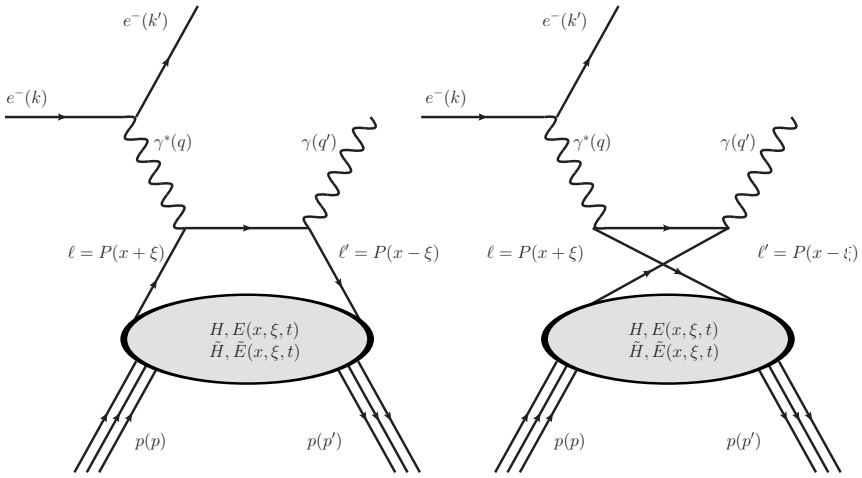

Figure 7.1: Les diagrammes du "sac à main" du DVCS.

Il y a quatre GPDs: H, E, $\tilde{H}$, et $\tilde{E}$. Chacune correspond à des hélicités différentes du proton et du quark comme illustré sur la Figure 7.2. H et E sont les GPDs non polarisés, qui sont indépendantes de l'hélicité du quark frappé. $\tilde{H}$ et $\tilde{E}$ sont les GPDs polarisées, qui sont dépendantes de l'hélicité du quark frappé. Pour H et $\tilde{H}$ le spin du proton ne changent pas, mais pour E et $\tilde{E}$, le spin du proton est renversé. On peut extraire ces GPDs pour le proton ou le neutron. De plus, on peut extraire ces GPDs pour chaque saveur de quark: u, d, s, etc.

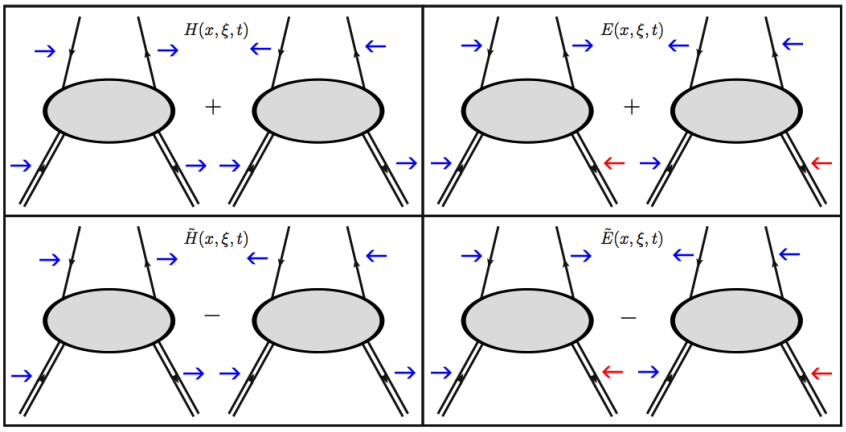

Figure 7.2: Les quatre GPDs: H, E, $\tilde{H}$, and $\tilde{E}$. Chacune correspond à des hélicités différentes du proton et du quark. H et E sont les GPDs non polarisées, qui sont indépendantes de l'hélicité du quark. $\tilde{H}$ et $\tilde{E}$ sont les GPDs polarisées, qui sont dépendant de l'hélicité du quark. Pour H et $\tilde{H}$ le spin du proton ne changent pas, mais pour E et $\tilde{E}$, le spin du proton est renversé.

Dans le laboratoire, on mesure l'état final: un électron, un proton, et un photon. Il y a deux canaux qui contribuent à cet état final: le DVCS et le Bethe-Heitler (BH), illustré sur la Figure 7.3.

La différence entre le DVCS et le BH est que pour le BH le photon réel est émis par l'électron initial ou final, et pas par le quark comme dans le cas du DVCS. Il est impossible de séparer processus.

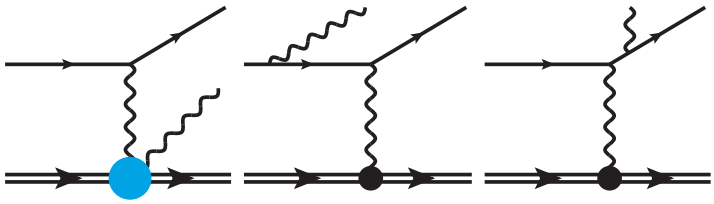

Figure 7.3: Les trois diagrammes contribuent à létat final: $e + p + \gamma$. À gauche, le DVCS, au milieu, le BH avec un photon émis par l'électron initial, et à droite, le BH avec un photon émis par l'électron diffusé. La boule bleue correspond aux GPDs, et les boules noires correspondent aux FFs.

7.2 Appareillage Expérimental

L'expérience a eu lieu à Newport News, en Virginie aux États-Unis, au sein du Jefferson Laboratory, avec un accélérateur d'électrons qui s'appelle Continuous Electron Beam Accelerator Facility (CEBAF). Cet accélérateur est composé de deux accélérateurs linéaires, et de deux arcs, qui sont présentés sur la Figure 7.4. Cet appareillage peut produire un faisceau d'électrons d'environ 6 GeV, avec une polarisation d'environ 85%. Après que les électrons avaient attient 6 GeV, le faisceau est séparé et délivré à une des trois salles expérimentales. Ces trois salles s'appellent Hall A, Hall B, et Hall C. L'expérience qui concerne cette thèse, e1-dvcs2, a eu lieu dans le Hall B.

Elle utilise le détecteur CEBAF Large Acceptance Spectrometer (CLAS). Ce spectromètre est composé de plusieurs sous-détecteurs qui permets identifier les diverses particules, et il est présenté sur la Figure 7.5. Les fonctions des sous-détecteurs et autres composants sont présentées ici:

- Torus: Pour courber les trajectoires des particules chargés.
- Drift Chambers (DC): Trois couches pour mesurer les trajectoire des particules chargées
- Čerenkov Counters (CC): Pour séparer les électrons et les pions
- Scintillator Counters (SC): Pour la mesure du temps.
- Electromagnetic Calorimeters (EC): Pour séparer les électrons et les pions et détecter les photons.
- Inner Calorimeter (IC): Pour identifier les photons.
- Solenoid: Pour réduire le bruit de fond des électrons Møller.

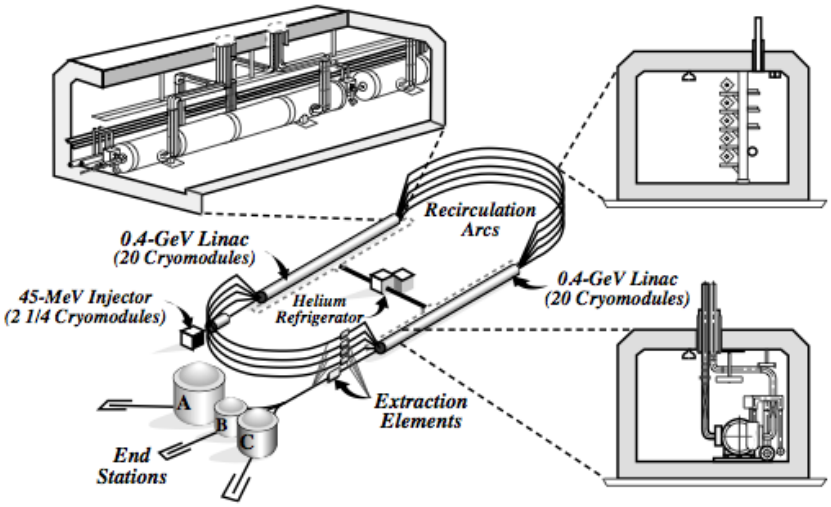

Figure 7.4: Une illustration de CEBAF avec ses trois salles expérimental.[39]

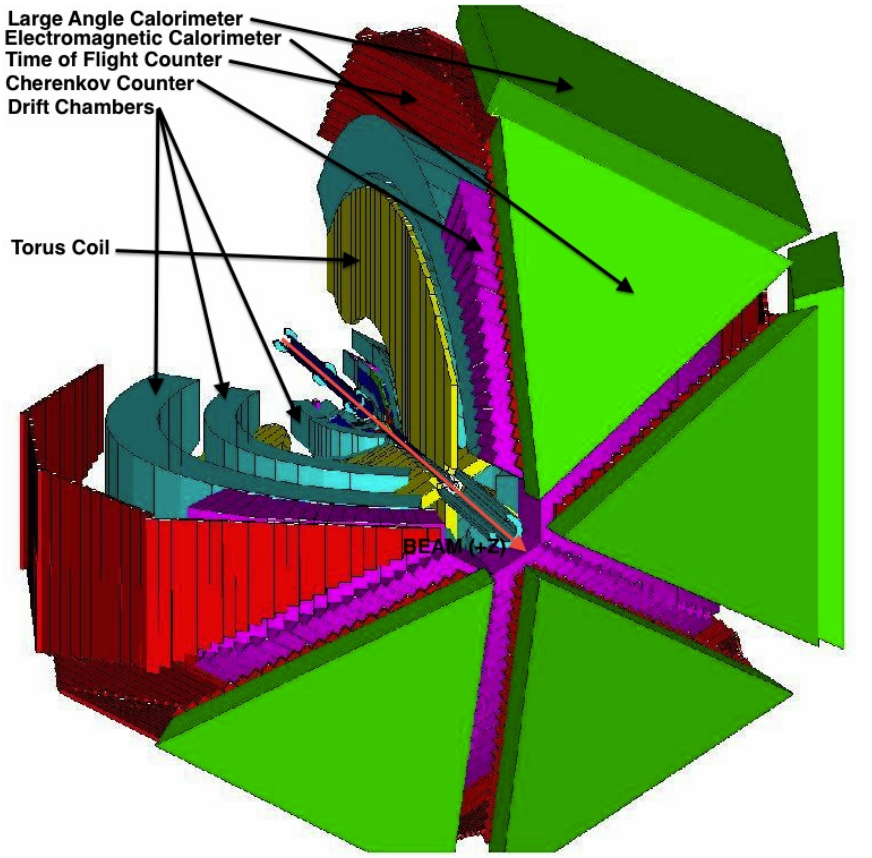

Figure 7.5: Une illustration de CLAS avec ses divers sous-détecteurs.[39]

7.3 La Section Efficace de DVCS

Cette analyse est porte sur la mesure de la section efficace non polarisée du DVCS et la différence des sections efficaces polarisées afin d'accéder aux GPDs. On peut mesurer la section efficace non-polarisée en mesurant ou en calculant chaque terme de l'équation suivante:

$$\frac{\mathrm{d}^4\sigma_{ep\gamma}}{\mathrm{d}Q^2\mathrm{d}t\mathrm{d}x_B\mathrm{d}\Phi} = \frac{N_{e+p+\gamma}}{\mathcal{L}_{\mathrm{int}}A\Delta V F_{\mathrm{rad}}}, \tag{214}$$

où $N_{e+p+\gamma}$ est le nombre d'événements de l'état final $e+p \to e+p+\gamma$, $\mathcal{L}$ est la luminosité integrée, A est l'acceptance, ΔV est le volume de bin, et $F_{rad.cor.}$ est le facteur de corrections radiatives. La section efficace est fonction de quatre variables: $Q^2 = -q^2$, t, x_B, la variable de Bjorken, et Φ qui est l'angle entre le plan hadronique et le plan leptonique. La section efficace non polarisée est sensible au CFF $\mathcal{H}_{Re}$.

L'équation qui correspond à la difference de sections efficaces polarisées est similaire:

$$\begin{aligned}\frac{\mathrm{d}^4\sigma_{\mathrm{pol}}}{\mathrm{d}Q^2\mathrm{d}t\mathrm{d}x_B\mathrm{d}\Phi} &= \frac{1}{2P}\left(\frac{\mathrm{d}^4\sigma_{+,0}}{\mathrm{d}Q^2\mathrm{d}t\mathrm{d}x_B\mathrm{d}\Phi} - \frac{\mathrm{d}^4\sigma_{-,0}}{\mathrm{d}Q^2\mathrm{d}t\mathrm{d}x_B\mathrm{d}\Phi}\right) \\ &= \frac{1}{2P}\left(\frac{N^{e+p+\gamma}_{+,0}}{\mathcal{L}_{\mathrm{int},+}} - \frac{N^{e+p+\gamma}_{-,0}}{\mathcal{L}_{\mathrm{int},-}}\right)\frac{1}{A\Delta V F_{\mathrm{rad}}},\end{aligned} \tag{215}$$

où les deux indices représentent respectivement les hélicités du faisceau et de la cible. "+" représente une hélicité en direction du faisceau, "-" représente une hélicité en direction opposée du faisceau, et "0" représente un état non polarisé. Le faisceau était polarisé la moitié du temps dans l'état "+" et l'autre moitié du temps dans un état "-". Donc, $\mathcal{L}_{\mathrm{int}}/2 = \mathcal{L}_{\mathrm{int},+} = \mathcal{L}_{\mathrm{int},-}$. La différence des sections efficaces polarisées est sensible au CFF $\mathcal{H}_{Im}$

On peut aussi calculer les asymétries de spin du faisceau en utilisant l'équation suivanet:

$$\mathcal{A}_{\mathrm{LU}} = \frac{\sigma_{\mathrm{unpol}}}{\sigma_{\mathrm{pol}}} = \frac{1}{P}\left(\frac{N^{e+p+\gamma}_{+,0} + N^{e+p+\gamma}_{-,0}}{N^{e+p+\gamma}_{+,0} - N^{e+p+\gamma}_{-,0}}\right). \tag{216}$$

Les résultats de l'analyse qui correspondent à ces trois observables sont présentés sur les Figure 7.6, Figure 7.7 et Figure 7.8 pour le cinquième bin en x_B et θ_e. Cet analyse complète comprend 21 bins en Q^2 et x_B, 9 bins en t et 24 bins en Φ.

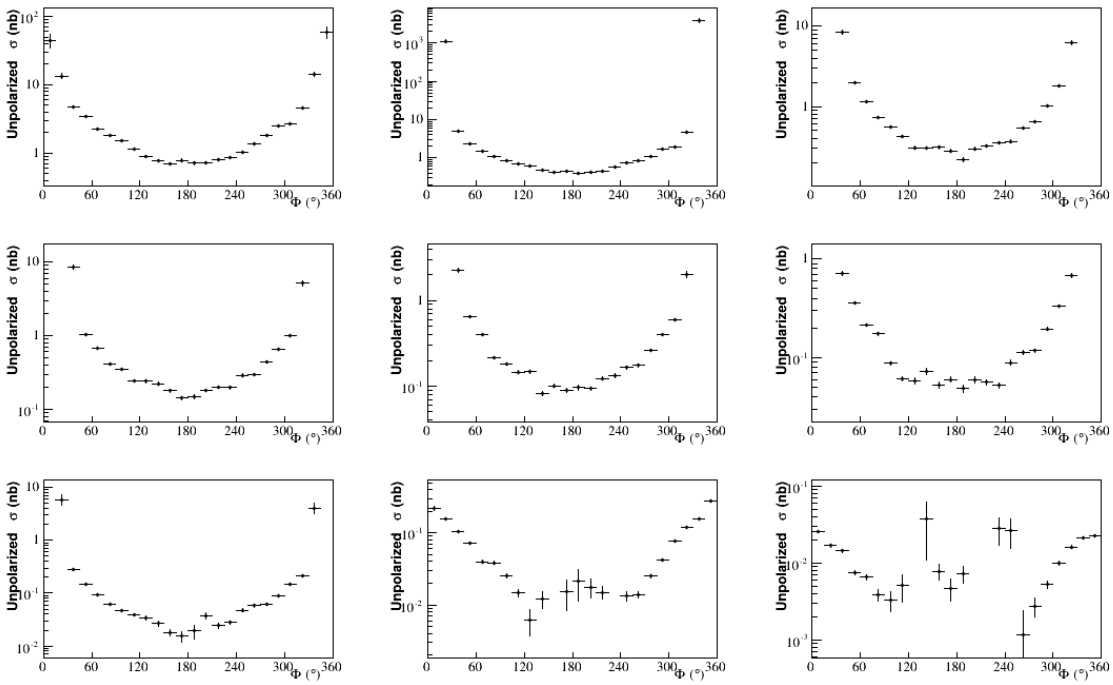

Figure 7.6: La section efficace non polarisée en fonction de Φ pour le cinquième bin en x_B et θ_e, où $0.17 < x_B < 0.2$ et $25.5° < \theta_e < 45°$. Chaque fenêtre correspond à un bin en t avec les limites suivantes: [0.09, 0.13, 0.18, 0.23, 0.30, 0.39, 0.52, 0.72, 1.10, 2.00] en GeV^2.

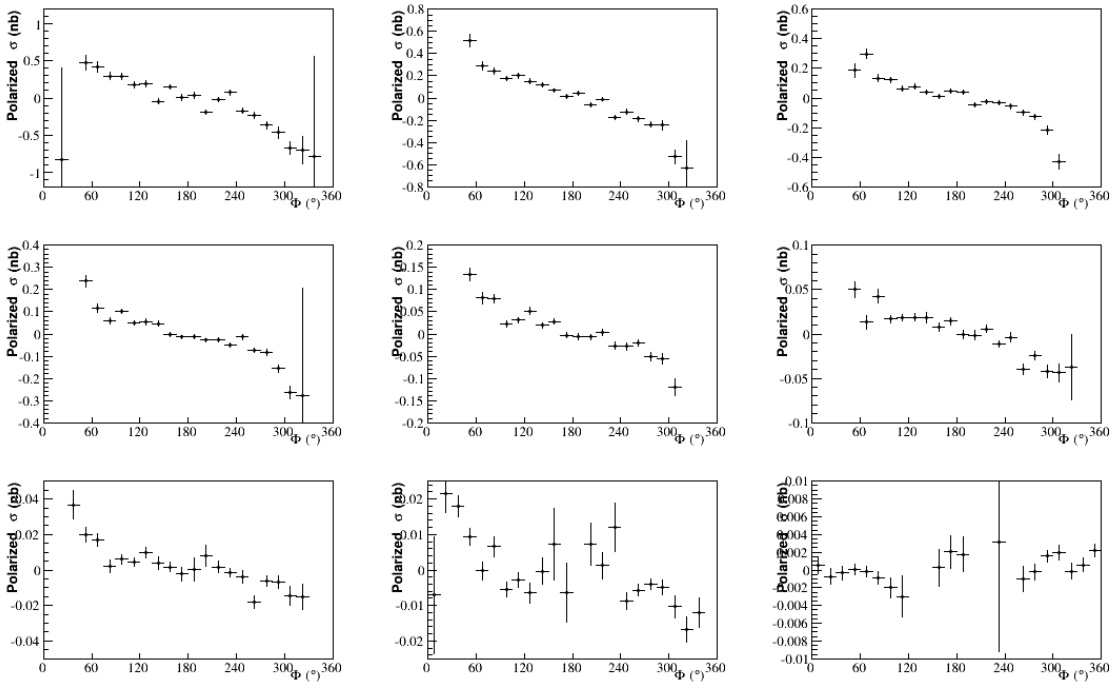

Figure 7.7: La difference des sections efficaces polarisées en fonction de Φ pour le cinquième bin en x_B et θ_e, où $0.17 < x_B < 0.2$ et $25.5^\circ < \theta_e < 45^\circ$. Chaque fenêtre correspond à un bin en t avec les limites suivantes: [0.09, 0.13, 0.18, 0.23, 0.30, 0.39, 0.52, 0.72, 1.10, 2.00] en GeV^2.

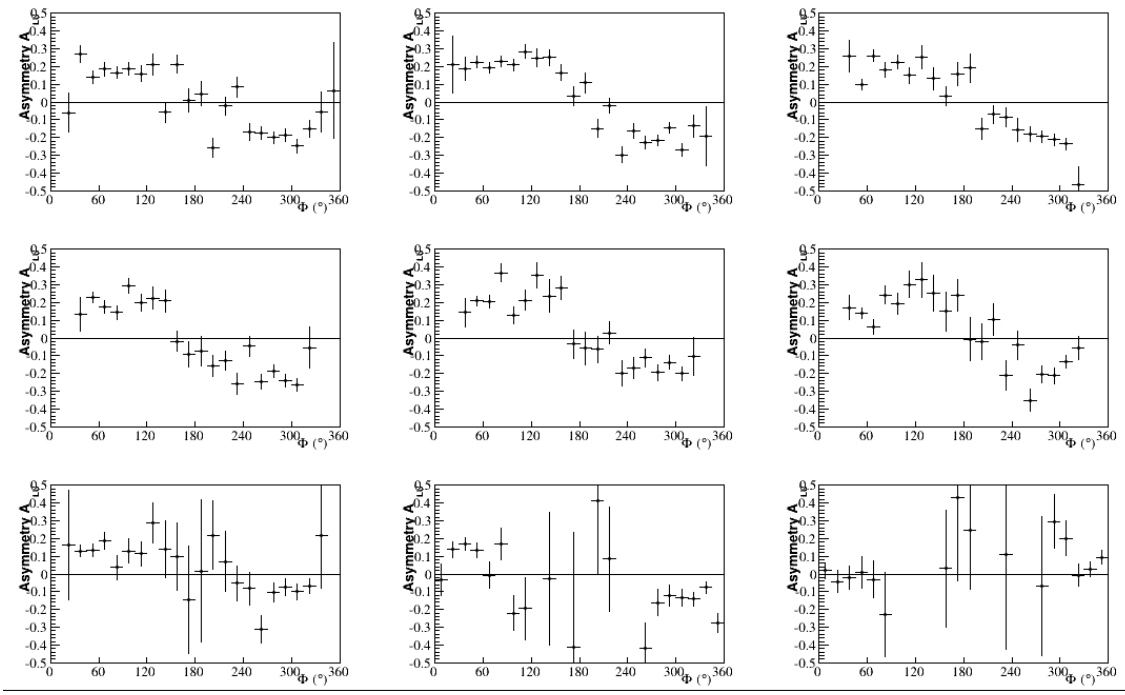

Figure 7.8: L'asymétrie de spin du faisceau en fonction de Φ pour le cinquième bin en x_B et θ_e, où $0.17 < x_B < 0.2$ et $25.5^\circ < \theta_e < 45^\circ$. Chaque fenêtre correspond à un bin en t avec les limites suivantes: [0.09, 0.13, 0.18, 0.23, 0.30, 0.39, 0.52, 0.72, 1.10, 2.00] en GeV^2.

7.4 Une Interprétation Préliminaire de l'Extraction de la GPD H

En utilisant la section efficace non polarisée et la différence des sections efficaces polarisées nous pouvons extraire de façon préliminaire les distributions des quarks du proton. Afin d'extraire le CFF auquel nous sommes sensible avec ces données, $\mathcal{H}_{\mathrm{Im}}$, nous pouvons faire un ajustement des sections efficaces non polarisées et des différences de sections efficaces polarisées. $\mathcal{H}_{\mathrm{Im}}$ représente la taille transverse du proton pour plusieurs tranches d'impulsion longitudinale. Nous pouvons aussi extraire $\mathcal{H}_{\mathrm{Re}}$. Cependant son interprétation n'est pas intuitive. Les extractions de $\mathcal{H}_{\mathrm{Re}}$ et $\mathcal{H}_{\mathrm{Im}}$ sont montrés dans Figure 7.9 et Figure 7.10, respectivement.

Cet ajustement est fait par une méthode qui est quasi-indépendante de modèle[58,59], et qui consiste à minimiser la quantité suivante:

$$\chi^2 = \sum_{i=1}^{n} \frac{\left(\sigma_{\mathrm{the},i} - \sigma_{\mathrm{exp},i}\right)^2}{\left(\Delta\sigma_{\mathrm{exp},i}\right)^2}, \tag{217}$$

où i est le numéro de bin, σ est la section efficace non polarisée ou la difference des sections efficaces polarisées et les indices "the" et "pol" correspondent aux sections efficaces théorétiques ou expérimentales, et $\Delta\sigma_{\mathrm{exp},i}$ est l'erreur.

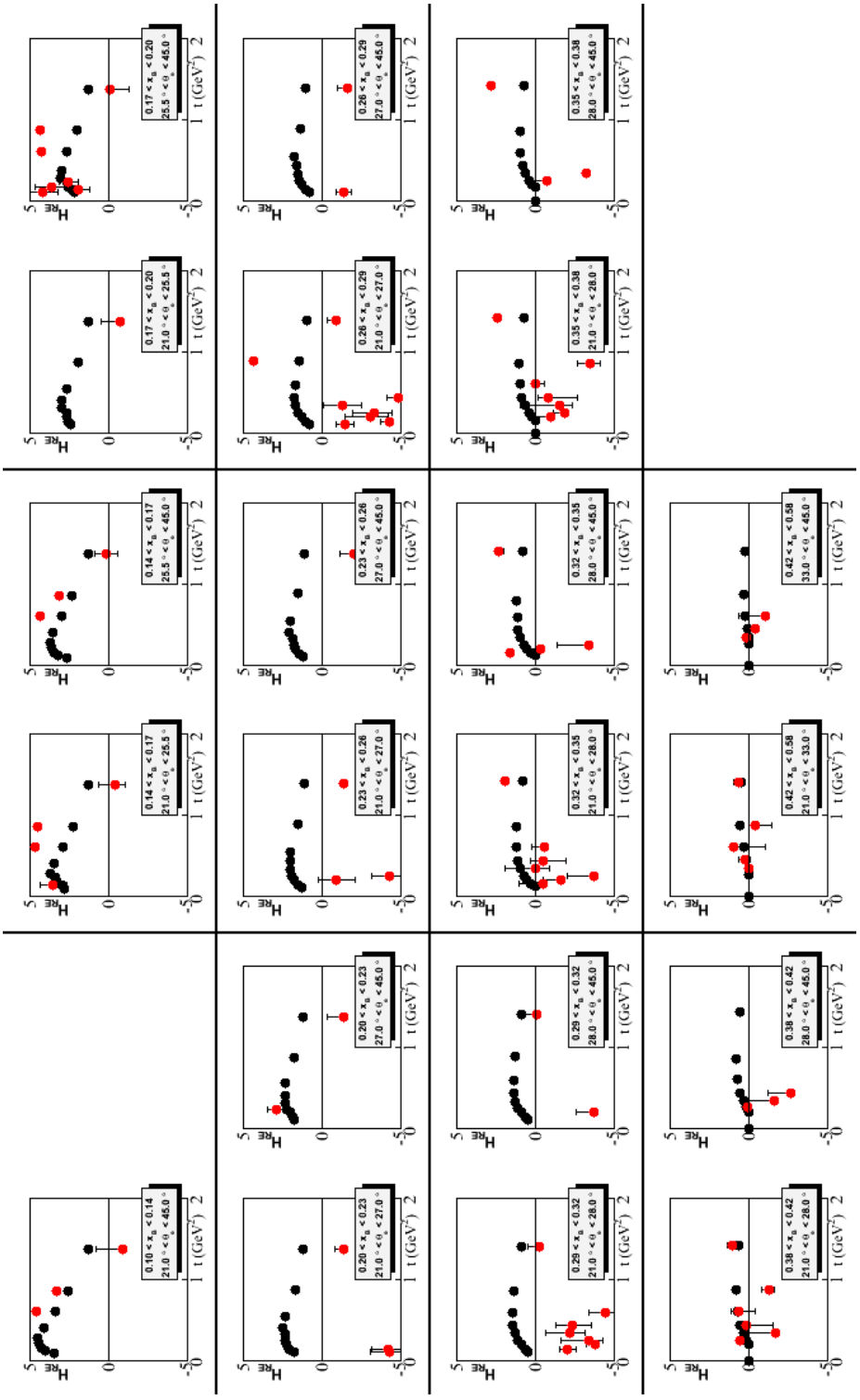

Figure 7.9: $\mathcal{H}_{\mathrm{Re}}$ en fonction de $-t$, pour les 21 bins en x_B et θ_e. Les points rouges représentent l'extraction issue de cette analyse, et les points noirs représentent la prédiction du modèle VGG.

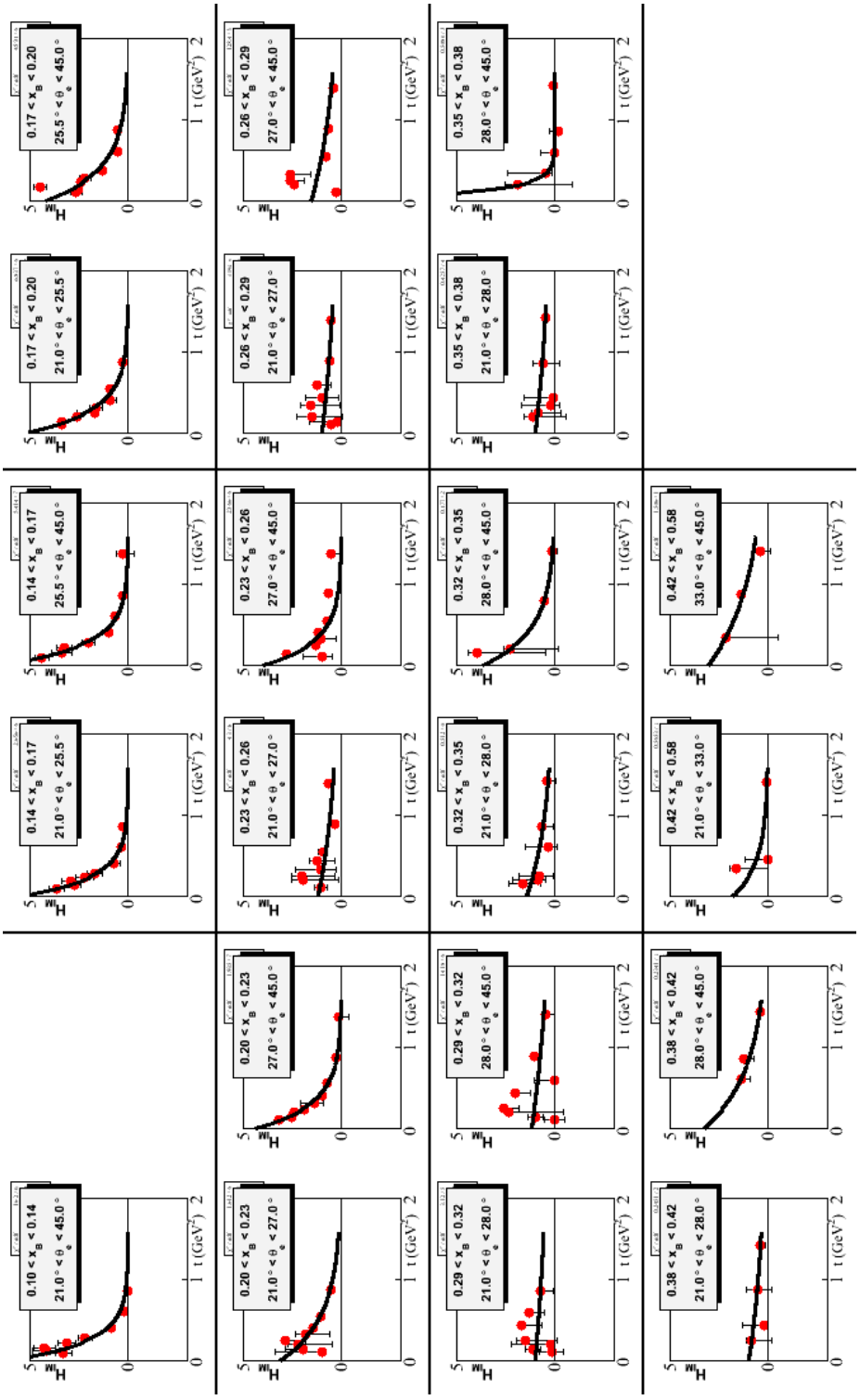

Figure 7.10: $\mathcal{H}_{\mathrm{Im}}$ en fonction de $-t$, pour les 21 bins en x_B et θ_e. Les points rouges représentent l'extraction issue de cette analyse, et les courbes noirs représentent l'ajustement issu de cette analyse.

Alors, la densité de charge du proton peut être extraite à partir de la GPD $H(x,\xi,t)$ selon la formule suivante:

$$q(x,0,b) = \int \frac{\mathrm{d}^2\vec{\Delta}_\perp}{(2\pi)^2} \mathrm{e}^{-i\vec{b}\cdot\vec{\Delta}_\perp} H^q(x,0,-\vec{\Delta}_\perp^2), \tag{218}$$

où la densité de charge est une transformée de Fourier, évaluée au point $\xi = 0$, qui fait correspondre au transfert d'impulsion transverse au proton $\vec{\Delta}_\perp$ le paramètre d'impact $\vec{b}$. Du à la symétrie cylindrique, la transformée de Fourier est en fait une transformée de Hankel:

$$q(x,0,b) = \frac{1}{4\pi} \int_0^\infty \mathrm{d}t J_0(b\sqrt{t}) H(x,0,t), \tag{219}$$

où $J_0(b\Delta_\perp)$ est la fonction de Bessel d'ordre zéro.

$\mathcal{H}$ est défini par:

$$\mathcal{H}_{\mathrm{Im}}(\xi,t) = H(\xi,\xi,t) - H(-\xi,\xi,t). \tag{220}$$

Le premier terme, où $x = \xi$, correspond à la contribution des quarks et le deuxième terme, où $x = -\xi$, correspond à la contribution des antiquarks. Aux cinématiques de JLab, d'après plusieurs modèles, nous pensons que la contribution des antiquarks n'est pas plus que 20%. En considérant que cette contribution est comparativement petite, nous avons extrait une quantité qui est alors proche de la "vraie" GPD H au point $x = \xi$.

$$\mathcal{H}_{\mathrm{Im}}(\xi,t) \approx H(\xi,\xi,t) \tag{221}$$

Cependant, afin d'obtenir la densité de charge, nous devons avoir la GPD H au point (ξ, 0, t) au lieu de (ξ, ξ, t). Ceci est accompli en utilisant un "deskewing factor", $f_\xi = \frac{H(\xi,0,t)}{H(\xi,\xi,t)}$, qui dépend des modèles. Pour cette analyse, nous nous servons du modèle VGG. Nous avons alors:

$$H(x,0,t) = f_\xi \mathcal{H}_{\mathrm{Im}} = f_\xi \mathrm{e}^{A-Bt}. \tag{222}$$

En remplaçant $H(x,0,t)$ dans notre transformée de Hankel par une fonction exponentielle et un "deskewing factor", et en écrivant le fonction de Bessel par une somme infinie, nous pouvons alors trouver une solution analytique:

$$
\begin{aligned}
q(x,0,b) &= \frac{1}{4\pi}\int_0^\infty \mathrm{d}t \sum_{m=0}^{\infty}\left[\frac{(\frac{-b^2 t}{4})^m}{m!m!}\right] f_\xi \mathrm{e}^{A-Bt} \\
&= \frac{\mathrm{e}^{A-\frac{b^2}{4B}}}{4\pi B}
\end{aligned}
\tag{223}
$$

Les distributions de densité de charge obtenues sont présentées sur la Figure 7.11, en fonction de b pour plusieurs tranches en x_B. Les distributions sont Gaussiennes, et centrées autour de l'origine. Figure 7.12 à Figure 7.15 représentent quatre vues tridimensionnel en fonction de b pour plusieurs valeurs de x_B.

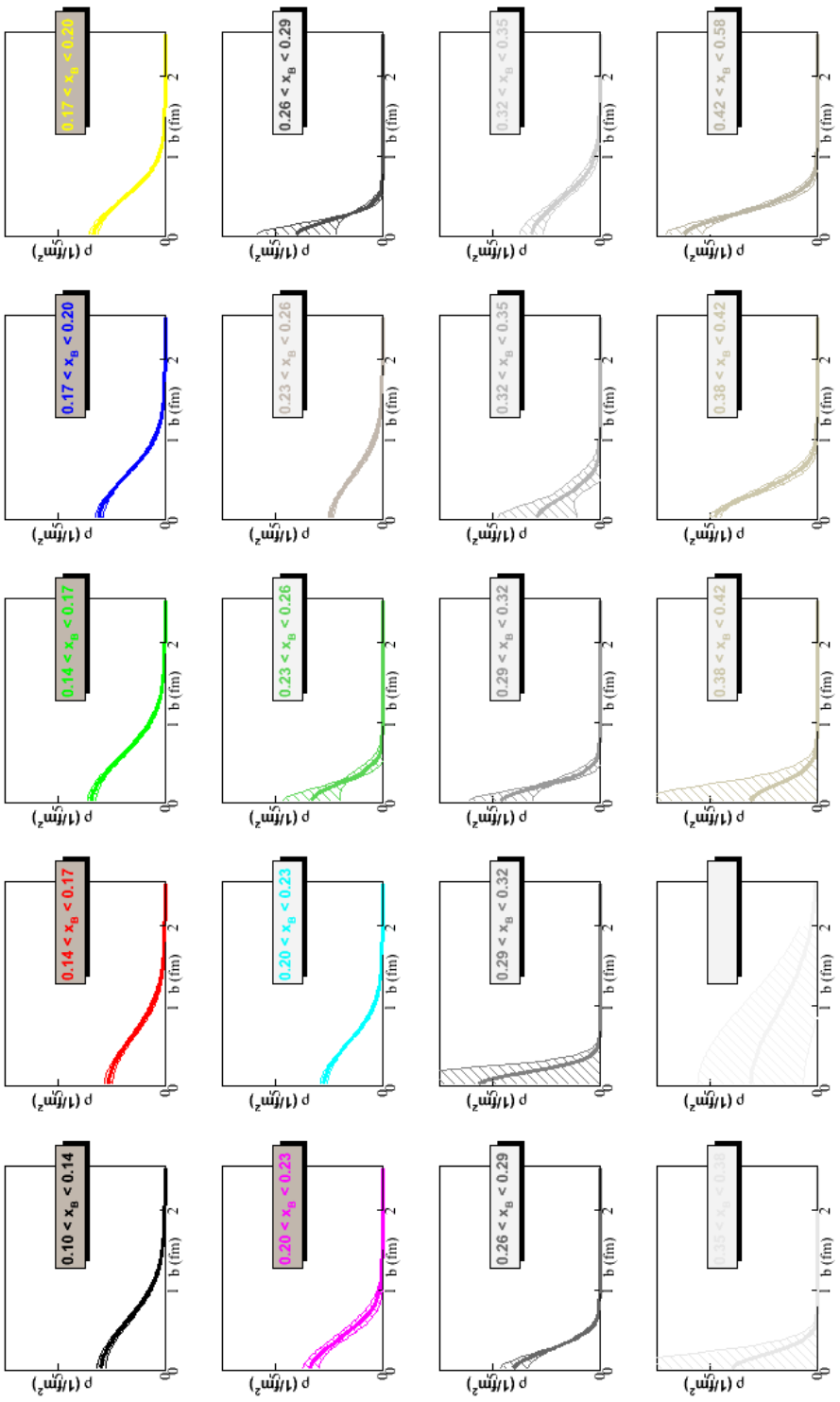

Figure 7.11: Les distributions de densité de charge en fonction du paramètre d'impact b. Chaque panneau correspond à une valeur de x_B. Les distribution sont Gaussiennes, centrées autour de $b = 0$.

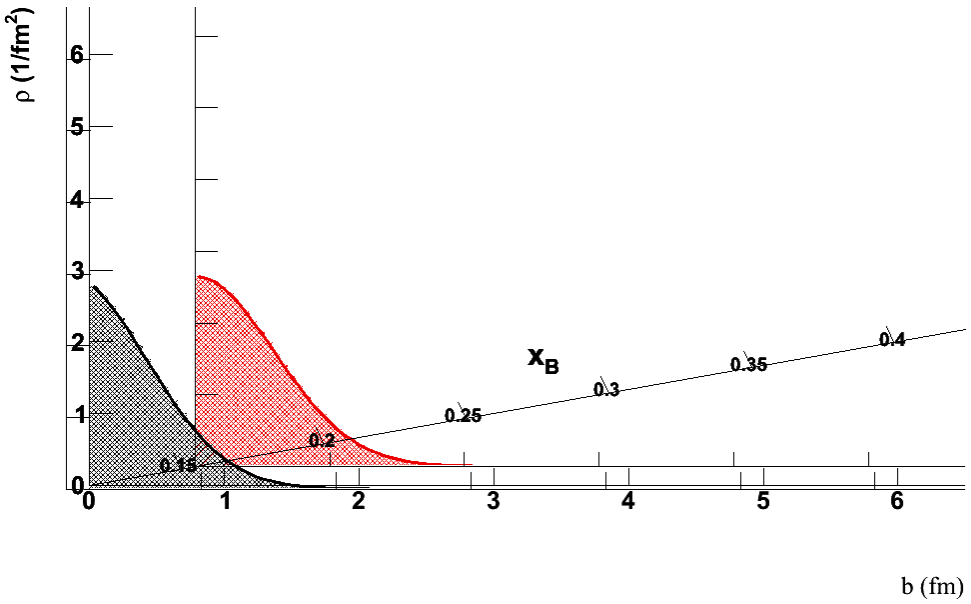

Figure 7.12: Pour les bins 1 et 2, vue tridimensionnelle de la distribution de densité de charge en fonction du paramètre d'impact b, pour les deux valeurs de x_B: 0.12 et 0.155, et les deux valeurs de Q^2: 1.135 GeV^2 et 1.305 GeV^2 respectivement.

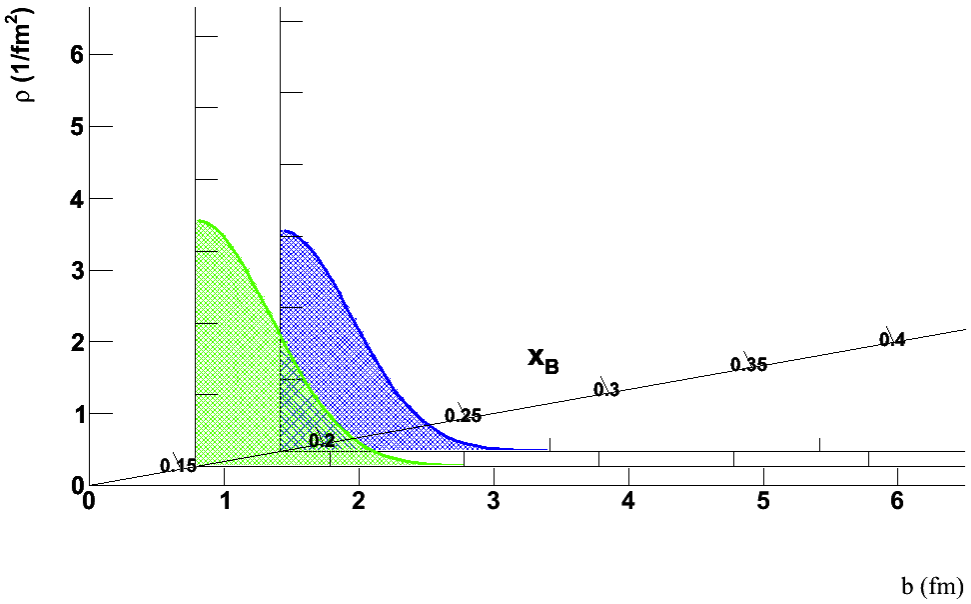

Figure 7.13: Pour les bins 3 et 4, vue tridimensionnelle de la distribution de densité de charge en fonction du paramètre d'impact b, pour les deux valeurs de x_B: 0.155 et 0.185, et les deux valeurs de Q^2: 1.471 GeV^2 et 1.490 GeV^2 respectivement.

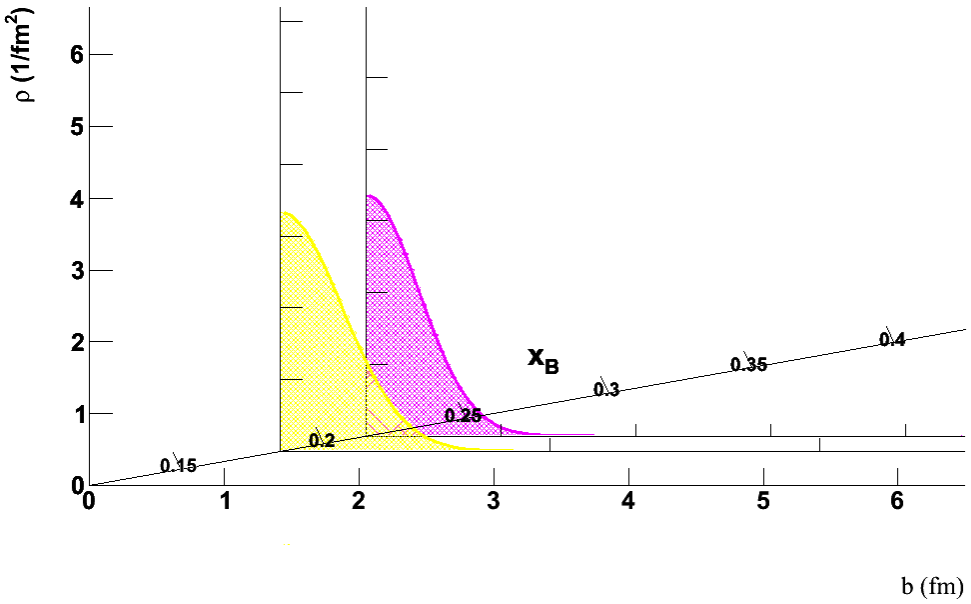

Figure 7.14: Pour les bins 5 et 6, vue tridimensionnelle de la distribution de densité de charge en fonction du paramètre d'impact b, pour les deux valeurs de x_B: 0.185 et 0.215, et les deux valeurs de Q^2: 1.710 GeV^2 et 1.684 GeV^2 respectivement.

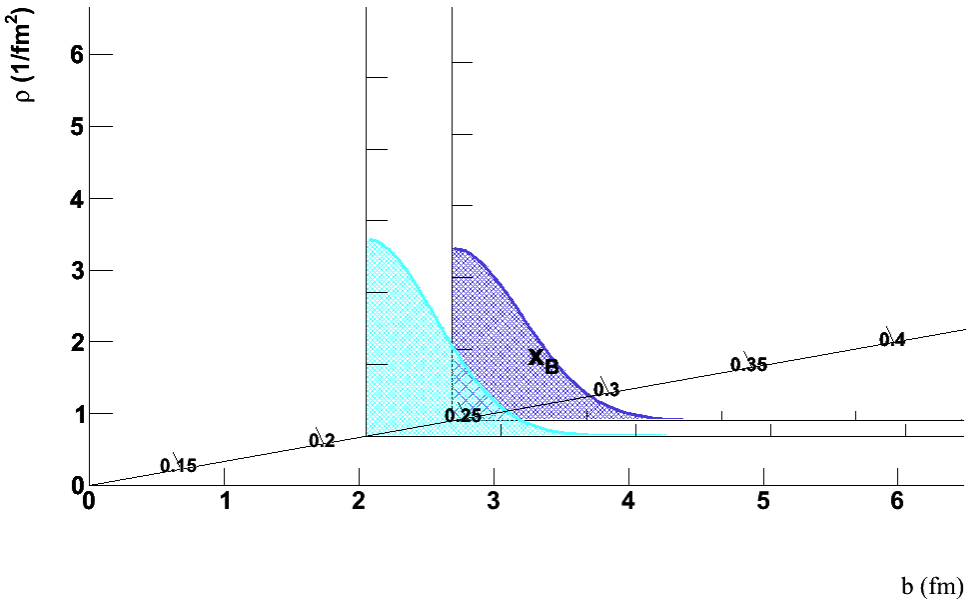

Figure 7.15: Pour les bins 7 et 9, vue tridimensionnelle de la distribution de densité de charge en fonction du paramètre d'impact b, pour les deux valeurs de x_B: 0.215 et 0.245, et les deux valeurs de Q^2: 1.964 GeV^2 et 2.187 GeV^2 respectivement.

LITERATURE CITED

[1]E. Rutherford, "The scattering of alpha and beta particles by matter and the structure of the atom," Philos. Mag. **21**, 669–688 (1911).

[2]E. D. Bloom et al., "High-energy inelastic $e-p$ scattering at 6° and 10°," Phys. Rev. Lett. **23**, 930–934 (1969).

[3]M. Gell-Mann, *The Eightfold Way: A theory of strong interaction symmetry* (Westview Press, Boulder, CO, 1961), pp. 1–37.

[4]F. Halzen and A. D. Martin, *Quarks and leptons: an introductory course in modern physics* (Wiley, Hoboken, NJ, 1984), pp. 172–204.

[5]M. Peskin and D. Schroeder, *An introduction to quantum field theory* (Westview Press, Boulder, CO, 1995), pp. 131–174.

[6]G. A. Miller, "Charge density of the neutron," Phys. Rev. Lett. **99**, 112001 (2007).

[7]D. Griffiths, *Introduction to elementary particles* (Wiley-VCH, Weinheim, Germany, 2008), pp. 275–283.

[8]J. Beringer et al., "Review of particle physics," Phys. Rev. D **86**, 010001 (2012).

[9]F. Aaron et al., "Combined measurement and QCD analysis of the inclusive e+- p scattering cross sections at HERA," J. High Energy Phys. **1001**, 109 (2010).

[10]A. Benvenuti et al., "Test of QCD and a measurement of lambda from scaling violations in the proton structure function F(2) (x, Q**2) at high Q**2," Phys. Lett. **B223**, 490 (1989).

[11]M. Adams et al., "Proton and deuteron structure functions in muon scattering at 470-GeV," Phys. Rev. **D54**, 3006–3056 (1996).

[12]M. Arneodo et al., "Measurement of the proton and deuteron structure functions, F2(p) and F2(d), and of the ratio sigma-L / sigma-T," Nucl. Phys. **B483**, 3–43 (1997).

[13]L. Whitlow et al., "Precise measurements of the proton and deuteron structure functions from a global analysis of the SLAC deep inelastic electron scattering cross-sections," Phys. Lett. **B282**, 475–482 (1992).

[14]T. Sloan, R. Voss, and G. Smadja, "The quark structure of the nucleon from the CERN muon experiments," Phys. Rep. **162**, 45–167 (1988).

[15]X. Ji, "Gauge invariant decomposition of nucleon spin and its spin - off," Phys. Rev. Lett. **78**, 610–613 (1997).

[16]D. Mueller et al., "Wave functions, evolution equations and evolution kernels from light ray operators of QCD," Fortschr. Phys. **42**, 101 (1994).

[17]A. V. Radyushkin, "Scaling limit of deeply virtual Compton scattering," Phys. Lett. **B380**, 417–425 (1996).

[18]M. Diehl, "Generalized parton distributions," Phys. Rep. **388**, 41–277 (2003).

[19]X. Ji, "Deeply virtual Compton scattering," Phys. Rev. **D55**, 7114–7125 (1997).

[20]F. Girod, "Diffusion Compton profondément virtuelle avec le détecteur CLAS pour une étude des distributions de partons généralisées," Ph.D. dissertation, Université Louis Pasteur Strasbourg I, 2006.

[21]F. Girod et al., "Measurement of deeply virtual Compton scattering beam-spin asymmetries," Phys. Rev. Lett. **100**, 162002 (2008).

[22]C. M. Camacho et al., "Scaling tests of the cross-section for deeply virtual Compton scattering," Phys. Rev. Lett. **97**, 262002 (2006).

[23]B. Guegan, "Study of generalized parton distributions and deeply virtual Compton scattering on the nucleon with the CLAS and CLAS12 detectors at the Jefferson Laboratory (Virginia, USA)," Ph.D. dissertation, Rensselaer Polytechnic Institute, 2012.

[24]M. Guidal, H. Moutarde, and M. Vanderhaeghen, "Generalized parton distributions in the valence region from deeply virtual Compton scattering," Rep. Prog. Phys. **76**, 066202 (2013).

[25]S. Goloskokov and P. Kroll, "Vector meson electroproduction at small Bjorken-x and generalized parton distributions," Eur. Phys. J. **C42**, 281–301 (2005).

[26]S. Goloskokov and P. Kroll, "The role of the quark and gluon GPDs in hard vector-meson electroproduction," Eur. Phys. J. **C53**, 367–384 (2008).

[27]S. Goloskokov and P. Kroll, "An attempt to understand exclusive pi+ electroproduction," Eur. Phys. J. **C65**, 137–151 (2010).

[28]K. Kumericki and D. Mueller, "Deeply virtual Compton scattering at small x(B) and the access to the GPD H," Nucl. Phys. **B841**, 1–58 (2010).

[29]V. Braun, G. Korchemsky, and D. Mueller, "The uses of conformal symmetry in QCD," Prog. Part. Nucl. Phys. **51**, 311–398 (2003).

[30]D. Mueller and A. Schafer, "Complex conformal spin partial wave expansion of generalized parton distributions and distribution amplitudes," Nucl. Phys. **B739**, 1–59 (2006).

[31]A. V. Radyushkin, "Symmetries and structure of skewed and double distributions," Phys. Lett. **B449**, 81–88 (1999).

[32]A. V. Radyushkin, "Double distributions and evolution equations," Phys. Rev. **D59**, 014030 (1999).

[33]M. V. Polyakov and C. Weiss, "Skewed and double distributions in pion and nucleon," Phys. Rev. **D60**, 114017 (1999).

[34]M. Guidal et al., "Nucleon form-factors from generalized parton distributions," Phys. Rev. **D72**, 054013 (2005).

[35]M. Vanderhaeghen, P. A. M. Guichon, and M. Guidal, "Deeply virtual electroproduction of photons and mesons on the nucleon: Leading order amplitudes and power corrections," Phys. Rev. **D60**, 094017 (1999).

[36]M. Vanderhaeghen, P. A. M. Guichon, and M. Guidal, "Hard electroproduction of photons and mesons on the nucleon," Phys. Rev. Lett. **80**, 5064–5067 (1998).

[37]K. Goeke, M. V. Polyakov, and M. Vanderhaeghen, "Hard exclusive reactions and the structure of hadrons," Prog. Part. Nucl. Phys. **47**, 401–515 (2001).

[38]J. P. Affairs, *Jlab visitors webpage*, Available: `http://www.jlab.org/visitors/`, Date last accessed: June 2013.

[39]B. Mecking et al., "The CEBAF large acceptance spectrometer (CLAS)," Nucl. Instrum. Meth. **A503**, 513–553 (2003).

[40]M. D. Mestayer et al., "The CLAS drift chamber system," Nucl. Instrum. Meth. **A449**, 81–111 (2000).

[41]M. Amarian et al., "The CLAS forward electromagnetic calorimeter," Nucl. Instrum. Meth. **A460**, 239–265 (2001).

[42]M. Anghinolfi et al., "The CLAS electromagnetic calorimeter at large angles," Nucl. Instrum. Meth. **A537**, 562–570 (2005).

[43]E. S. Smith et al., "The time-of-flight system for CLAS," Nucl. Instrum. Meth. **A432**, 265–298 (1999).

[44]G. Adams et al., "The CLAS Cherenkov detector," Nucl. Instrum. Meth. **A465**, 414–427 (2001).

[45]I. Bedlinskiy et al., "An inner calorimeter for CLAS/DVCS experiments," CLAS-Note (unpublished).

[46]M. Guillo et al., "EC time calibration procedure for photon runs in CLAS," CLAS-Note (unpublished).

[47]M. Vanderhaeghen et al., "QED radiative corrections to virtual Compton scattering," Phys. Rev. **C62**, 025501 (2000).

[48]E. Wolin, *Gsim user's guide version 1.1*, Available: `http://www.jlab.org/Hall-B/document/gsim/userguide.html`, Date last accessed: May 2013.

[49]M. Ungaro and J. Li, "Procedure for drift chamber inefficiencies," CLAS-Note (unpublished).

[50]M. Yurov, *Background*, Available: `https://clasweb.jlab.org/rungroups/e1-dvcs/wiki/index.php/Background`, Date last accessed: May 2013.

[51]K. Park, "Measurement of the polarized structure function using the single pion electroproduction channel in the nuclear resonance region," Ph.D. dissertation, Kyungpook National University, 2006.

[52]P. Bosted, "Photon energy corrections and reduction of backgrounds under $\pi 0$ mass peak," CLAS-Note (unpublished).

[53]R. de Masi et al., "Photon energy corrections in EC (from data)," CLAS-Note (unpublished).

[54]I. Akushevich and A. Ilyichev, "Radiative effects in the processes of exclusive photon electroproduction from polarized protons," Phys. Rev. **D85**, 053008 (2012).

[55]E. J. Brash et al., "New empirical fits to the proton electromagnetic form-factors," Phys. Rev. **C65**, 051001 (2002).

[56]A. V. Belitsky, D. Mueller, and A. Kirchner, "Theory of deeply virtual Compton scattering on the nucleon," Nucl. Phys. **B629**, 323–392 (2002).

[57]D Muller and K. Kumericki, "Deeply virtual compton scattering at small x(Bj)," Mod. Phys. Lett. **A24**, 2838–2847 (2009).

[58]H. Moutarde, "Extraction of the Compton form factor H from recent DVCS measurements at JLab," JLab Report (unpublished).

[59]M. Guidal, "A fitter code for deep virtual Compton scattering and generalized parton distributions," Eur. Phys. J. **A37**, 319–332 (2008).

[60]T. Johansson, "PANDA at FAIR," Acta Phys. Pol. **B5**, 1197–1202 (2012).

[61]M. Garçon, "An introduction to the generalized parton distributions," Eur. Phys. J. **A18**, 389–394 (2002).

A. Complete Results for Acceptance

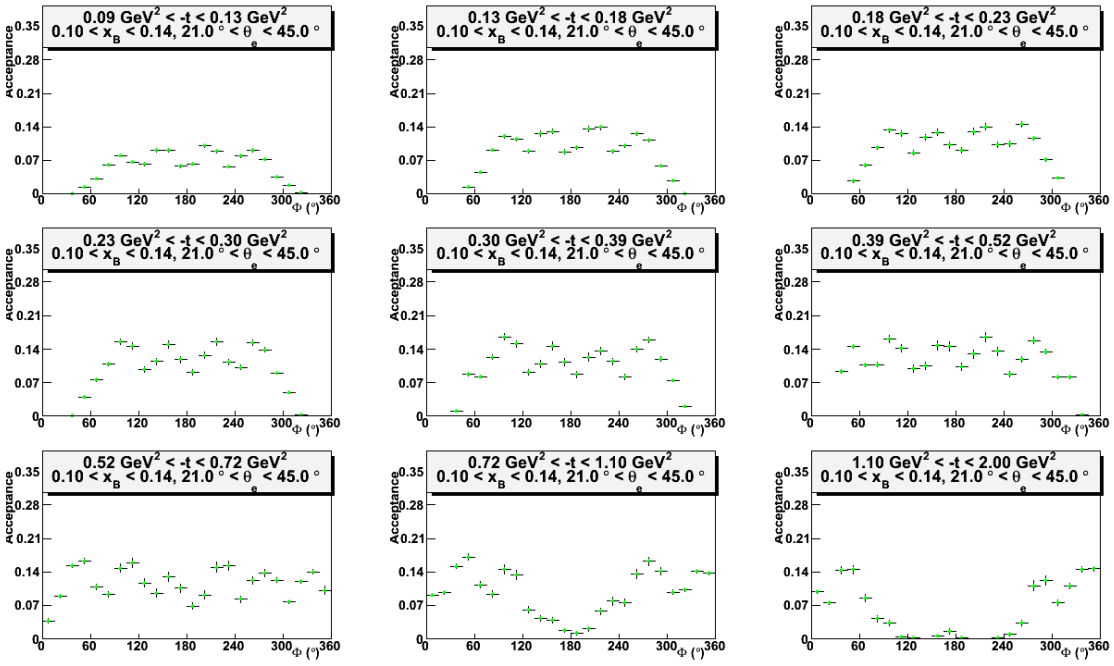

Figure A.1: The acceptance as a function of ϕ for the first bin in x_B and θ_e, where $0.1 < x_B < 0.14$ and $21^\circ < \theta_e < 45^\circ$.

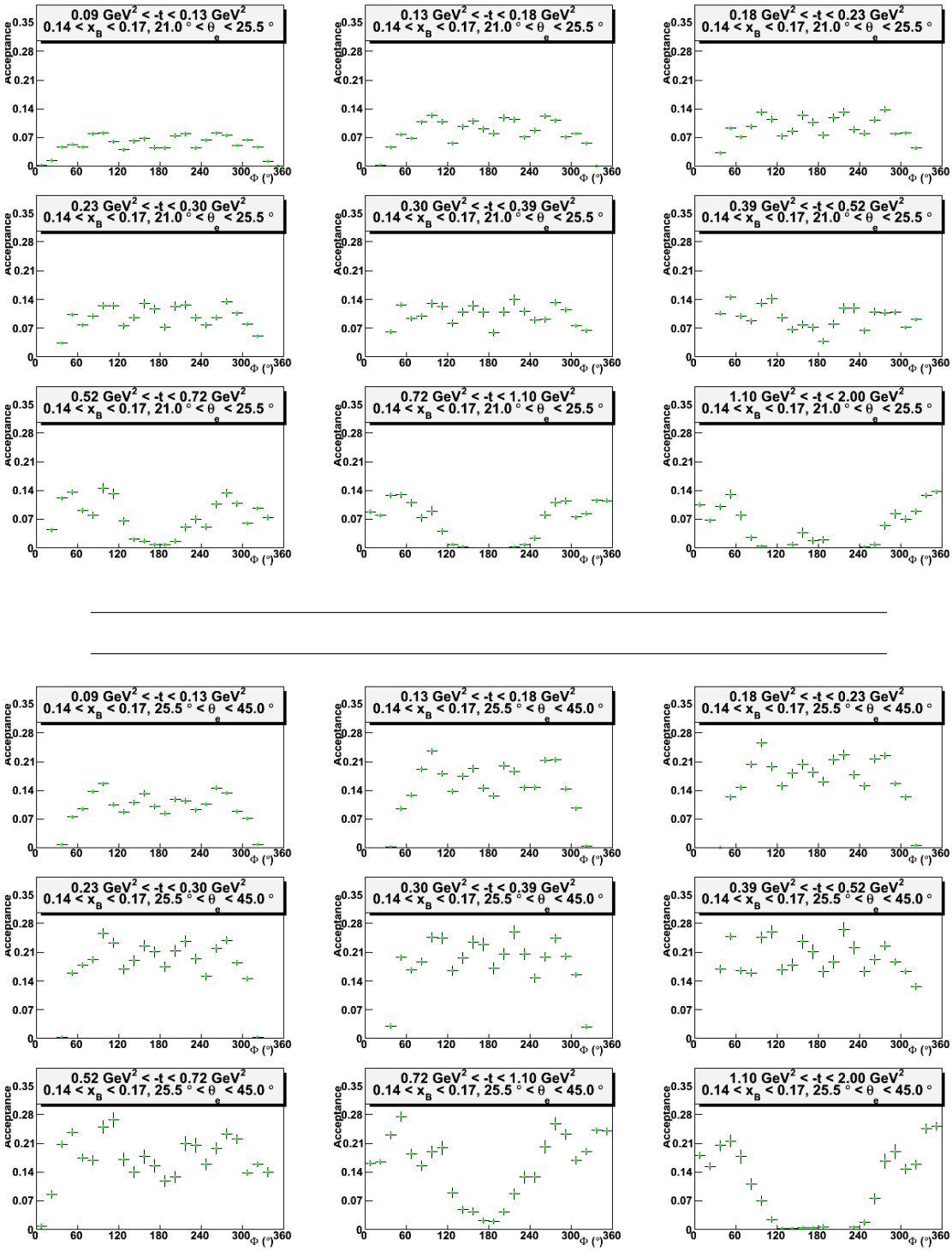

Figure A.2: On top, the acceptance as a function of ϕ for the second bin in x_B and θ_e, where $0.14 < x_B < 0.17$ and $21^\circ < \theta_e < 25.5^\circ$. On bottom, the acceptance as a function of ϕ for the third bin in x_B and θ_e, where $0.14 < x_B < 0.17$ and $25.5^\circ < \theta_e < 45^\circ$.

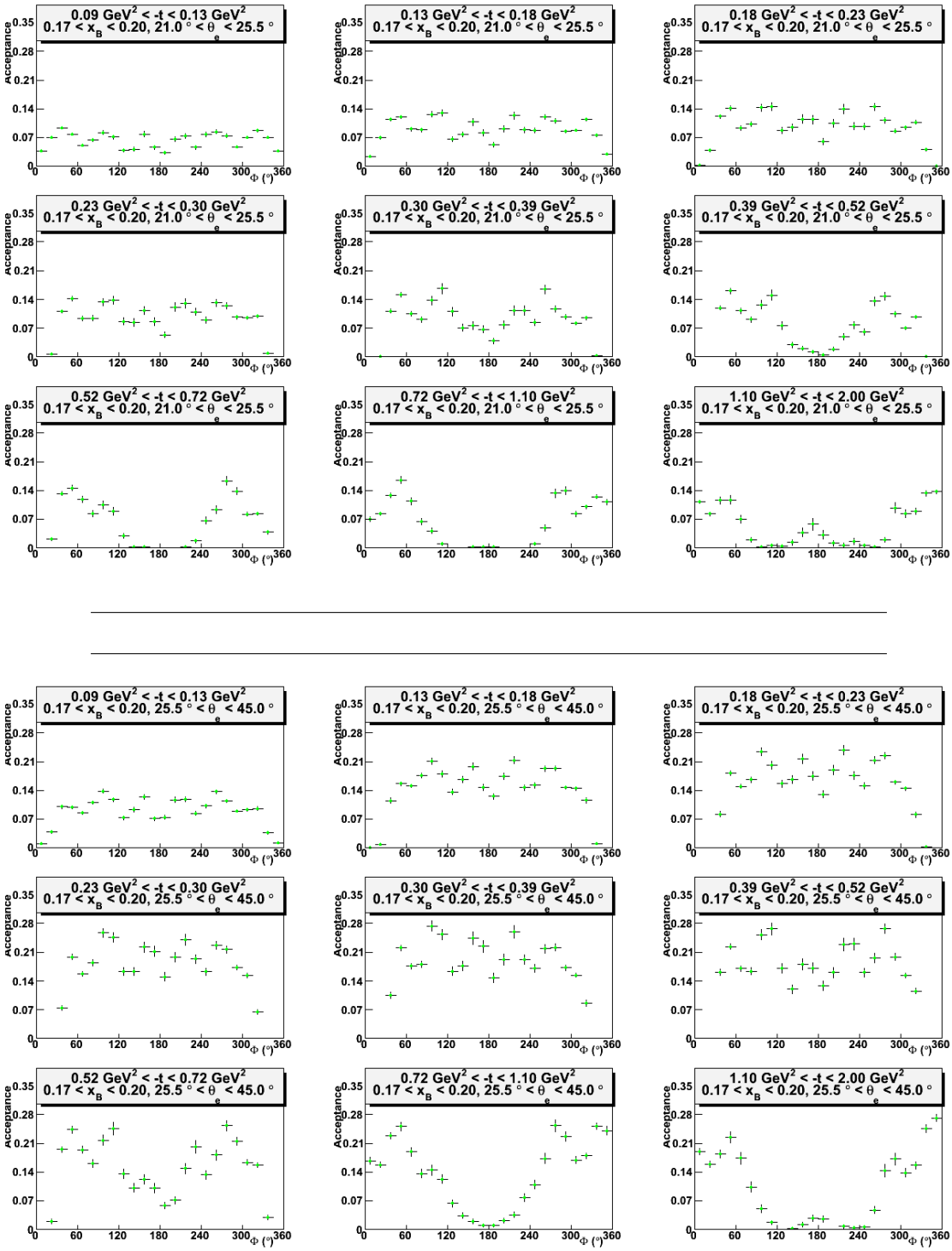

Figure A.3: On top, the acceptance as a function of ϕ for the fourth bin in x_B and θ_e, where $0.17 < x_B < 0.2$ and $21^\circ < \theta_e < 25.5^\circ$. On bottom, the acceptance as a function of ϕ for the fifth bin in x_B and θ_e, where $0.17 < x_B < 0.2$ and $25.5^\circ < \theta_e < 45^\circ$.

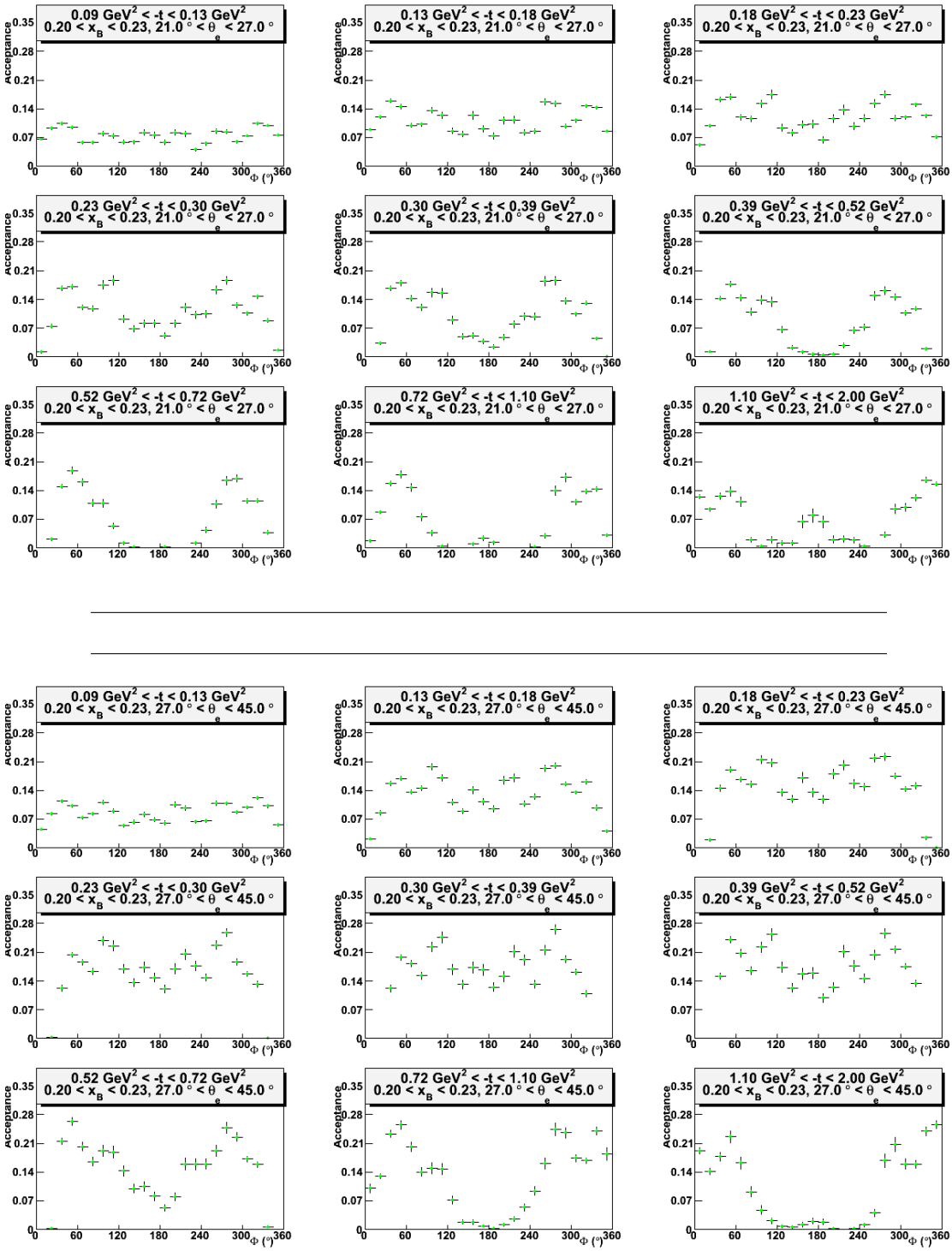

Figure A.4: On top, the acceptance as a function of ϕ for the sixth bin in x_B and θ_e, where $0.2 < x_B < 0.23$ and $21^\circ < \theta_e < 27^\circ$. On bottom, the acceptance as a function of ϕ for the seventh bin in x_B and θ_e, where $0.2 < x_B < 0.23$ and $27^\circ < \theta_e < 45^\circ$.

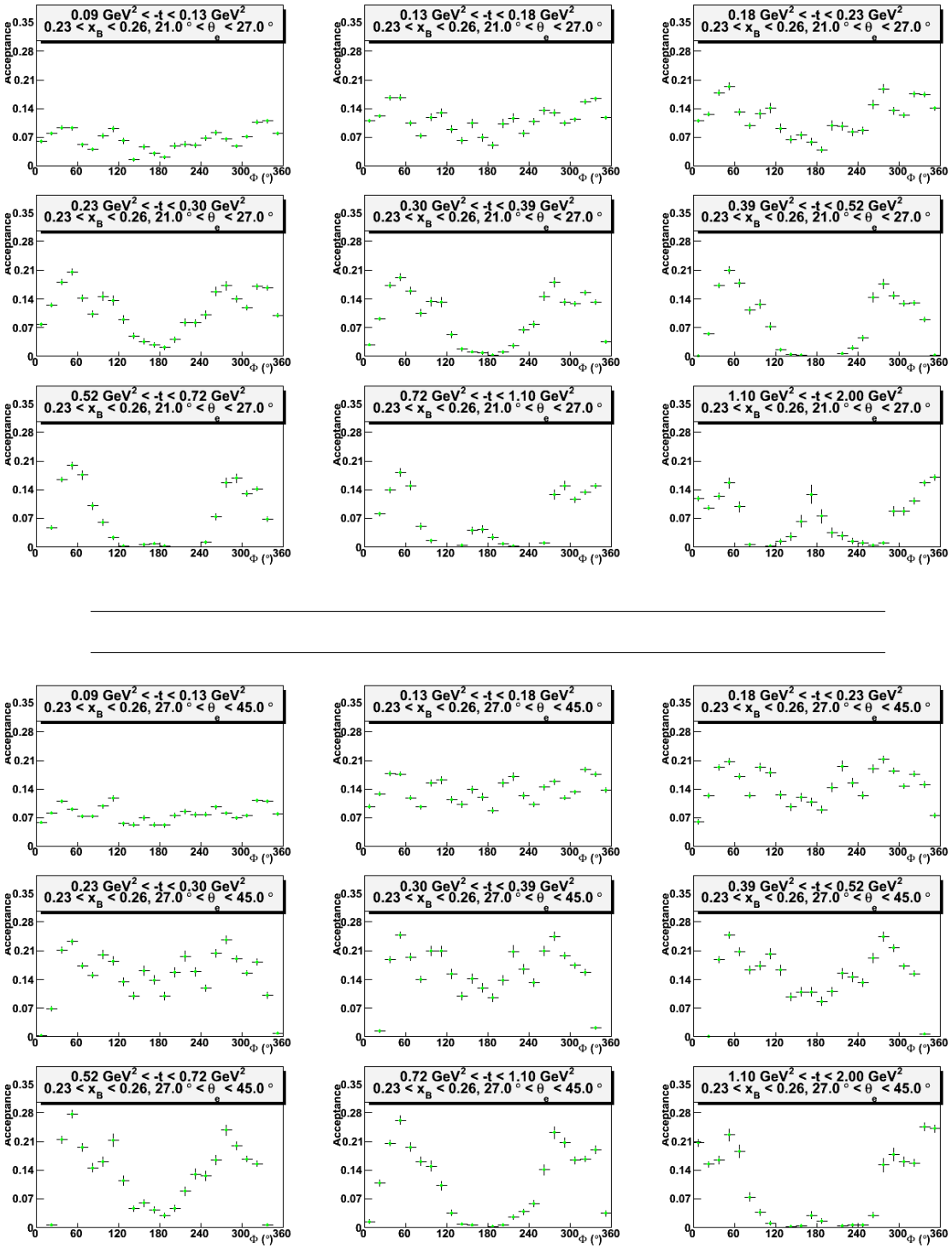

Figure A.5: On top, the acceptance as a function of ϕ for the eighth bin in x_B and θ_e, where $0.23 < x_B < 0.26$ and $21^\circ < \theta_e < 27^\circ$. On bottom, the acceptance as a function of ϕ for the ninth bin in x_B and θ_e, where $0.23 < x_B < 0.26$ and $27^\circ < \theta_e < 45^\circ$.

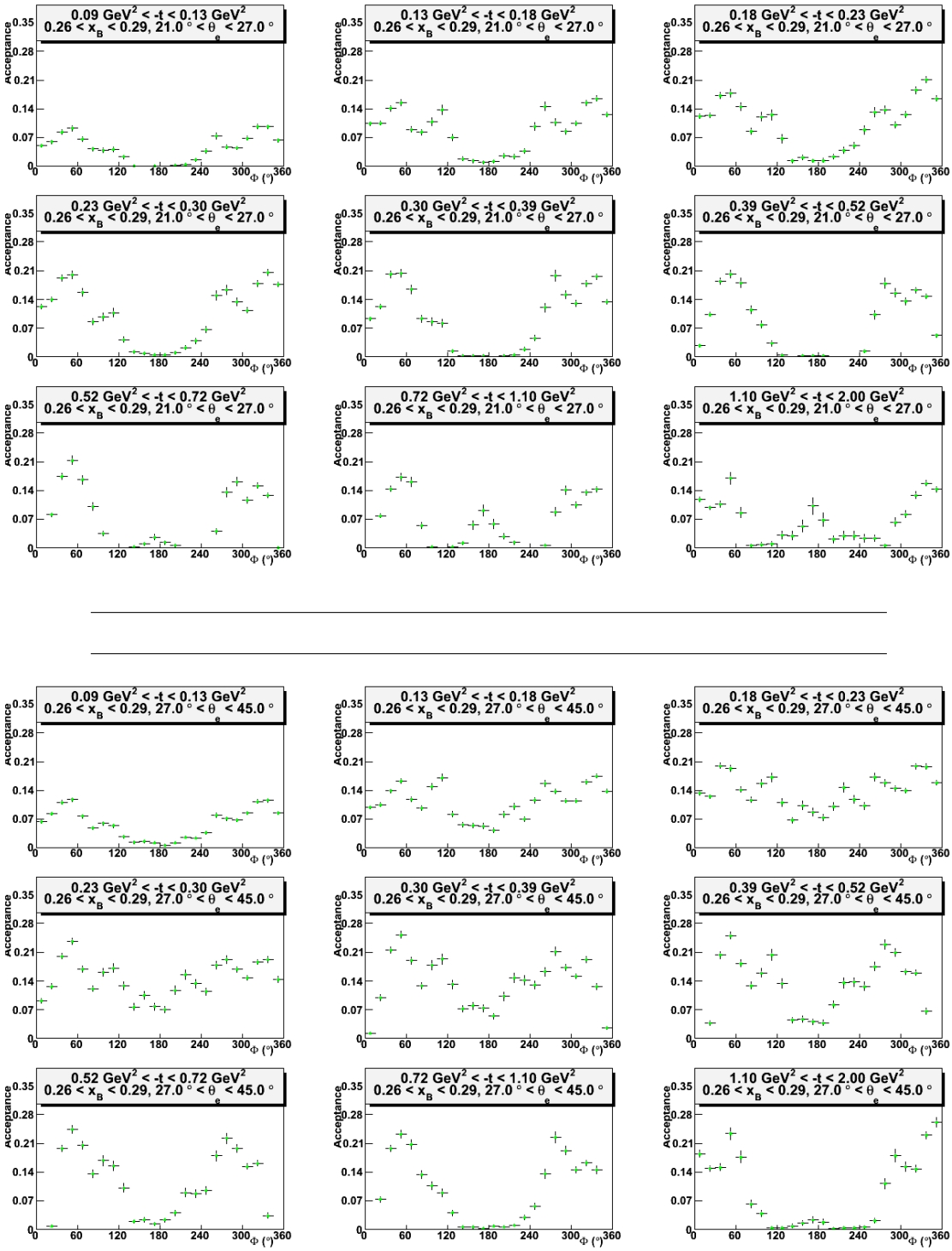

Figure A.6: On top, the acceptance as a function of ϕ for the tenth bin in x_B and θ_e, where $0.26 < x_B < 0.29$ and $21^\circ < \theta_e < 27^\circ$. On bottom, the acceptance as a function of ϕ for the eleventh bin in x_B and θ_e, where $0.26 < x_B < 0.29$ and $27^\circ < \theta_e < 45^\circ$.

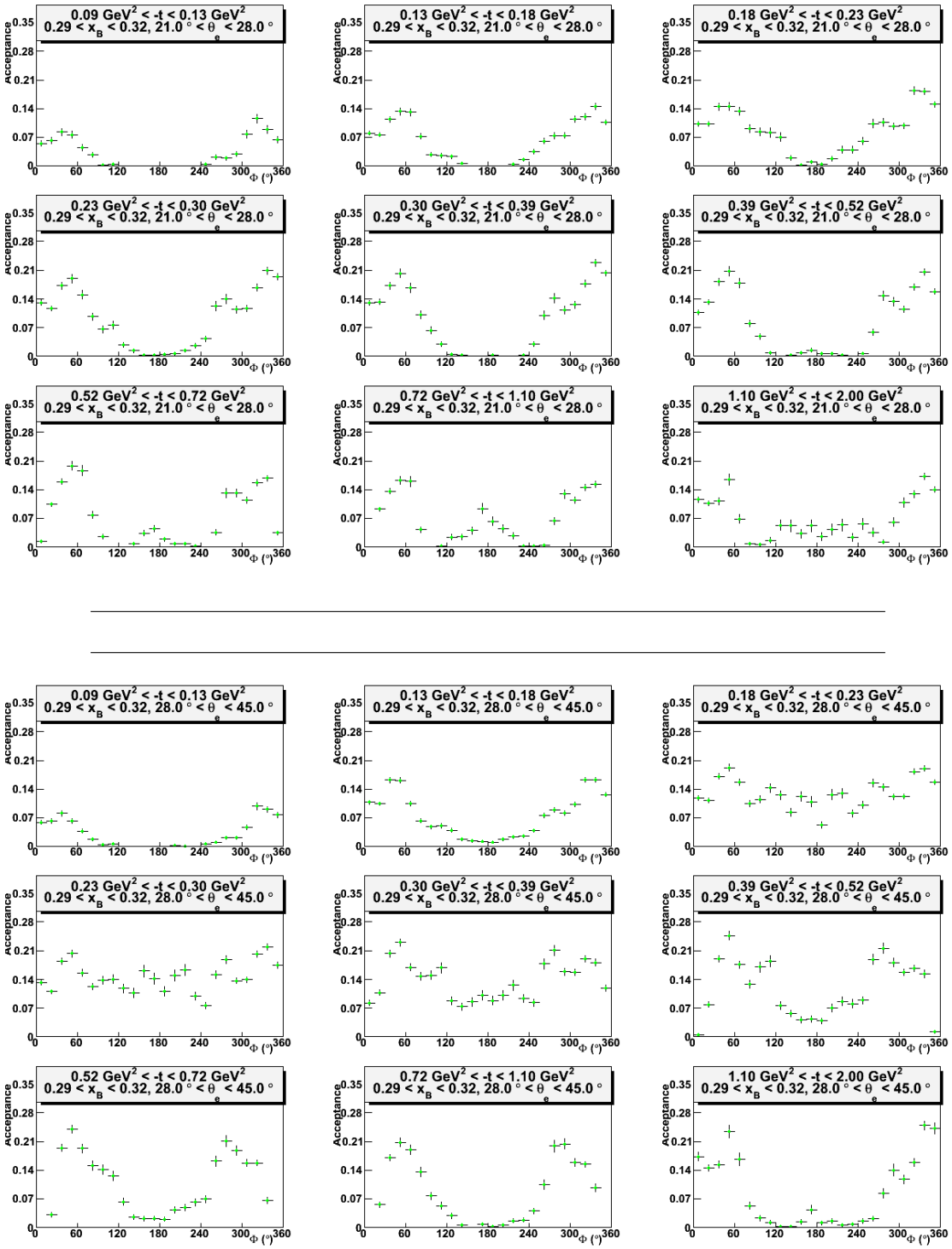

Figure A.7: On top, the acceptance as a function of ϕ for the twelfth bin in x_B and θ_e, where $0.29 < x_B < 0.32$ and $21^\circ < \theta_e < 28^\circ$. On bottom, the acceptance as a function of ϕ for the thirteenth bin in x_B and θ_e, where $0.29 < x_B < 0.32$ and $28^\circ < \theta_e < 45^\circ$.

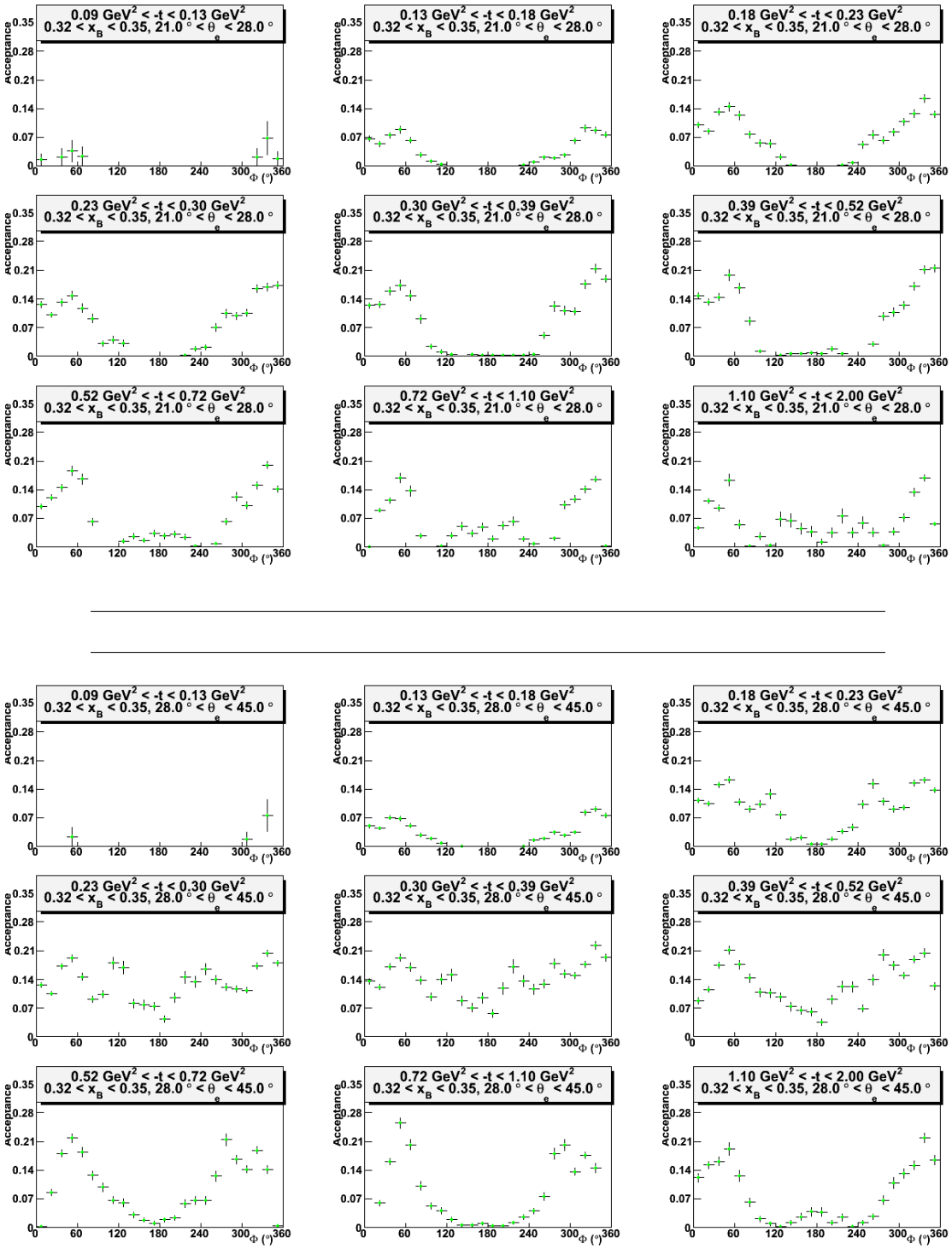

Figure A.8: On top, the acceptance as a function of ϕ for the fourteenth bin in x_B and θ_e, where $0.32 < x_B < 0.35$ and $21^\circ < \theta_e < 28^\circ$. On bottom, the acceptance as a function of ϕ for the fifteenth bin in x_B and θ_e, where $0.32 < x_B < 0.35$ and $28^\circ < \theta_e < 45^\circ$.

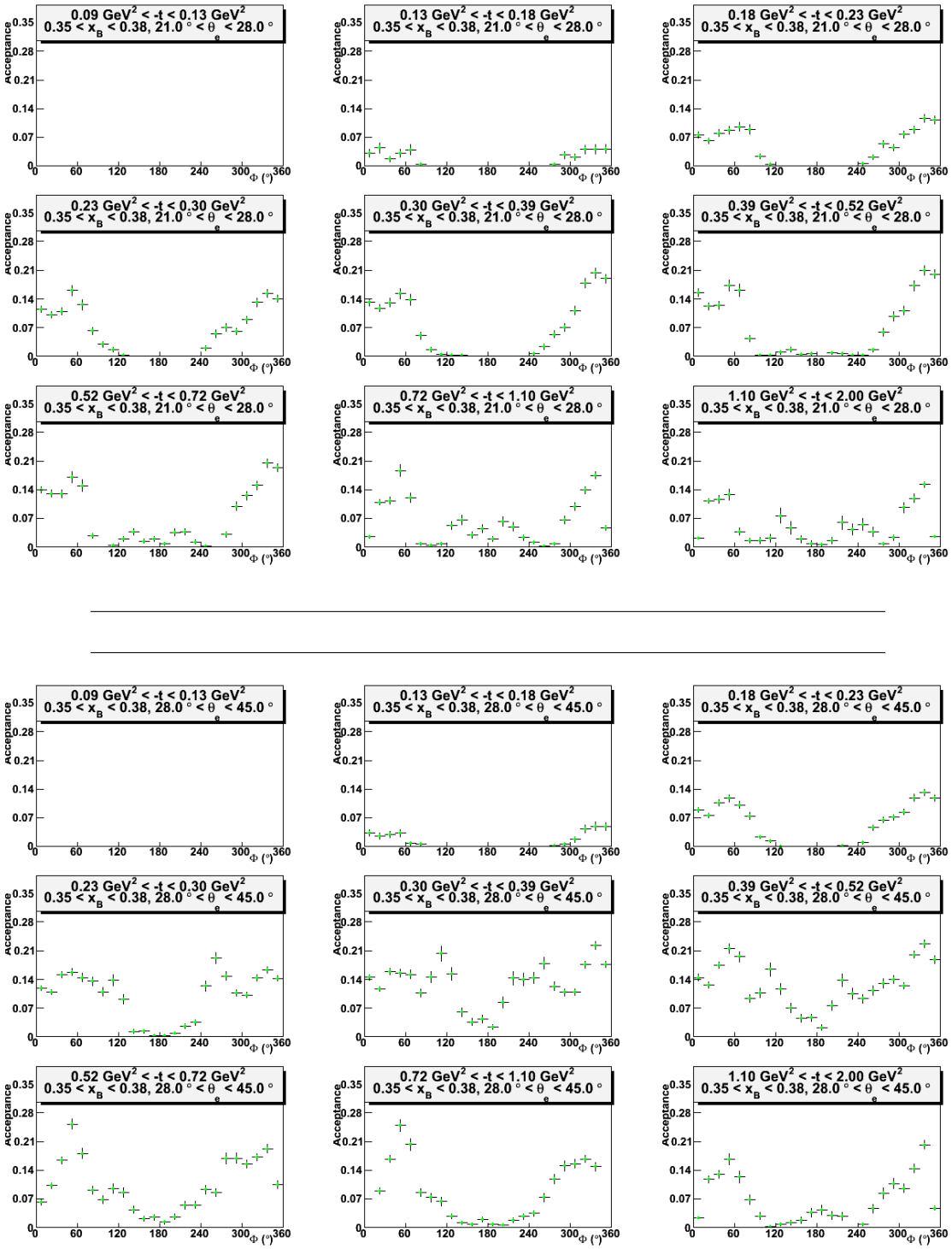

Figure A.9: On top, the acceptance as a function of ϕ for the sixteenth bin in x_B and θ_e, where $0.35 < x_B < 0.38$ and $21^\circ < \theta_e < 28^\circ$. On bottom, the acceptance as a function of ϕ for the seventeenth bin in x_B and θ_e, where $0.35 < x_B < 0.38$ and $28^\circ < \theta_e < 45^\circ$.

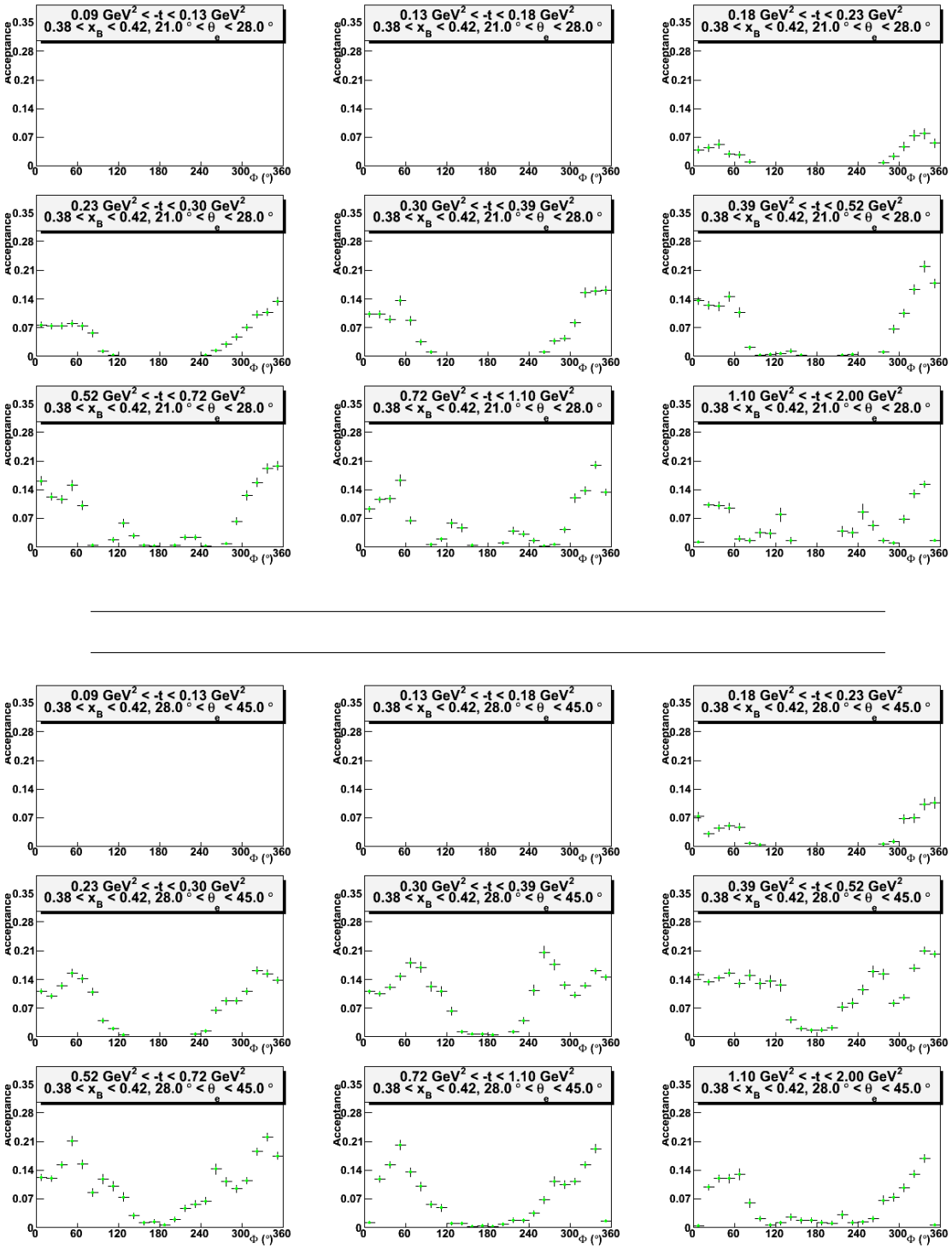

Figure A.10: On top, the acceptance as a function of ϕ for the eighteenth bin in x_B and θ_e, where $0.38 < x_B < 0.42$ and $21^\circ < \theta_e < 28^\circ$. On bottom, the acceptance as a function of ϕ for the nineteenth bin in x_B and θ_e, where $0.38 < x_B < 0.42$ and $28^\circ < \theta_e < 45^\circ$.

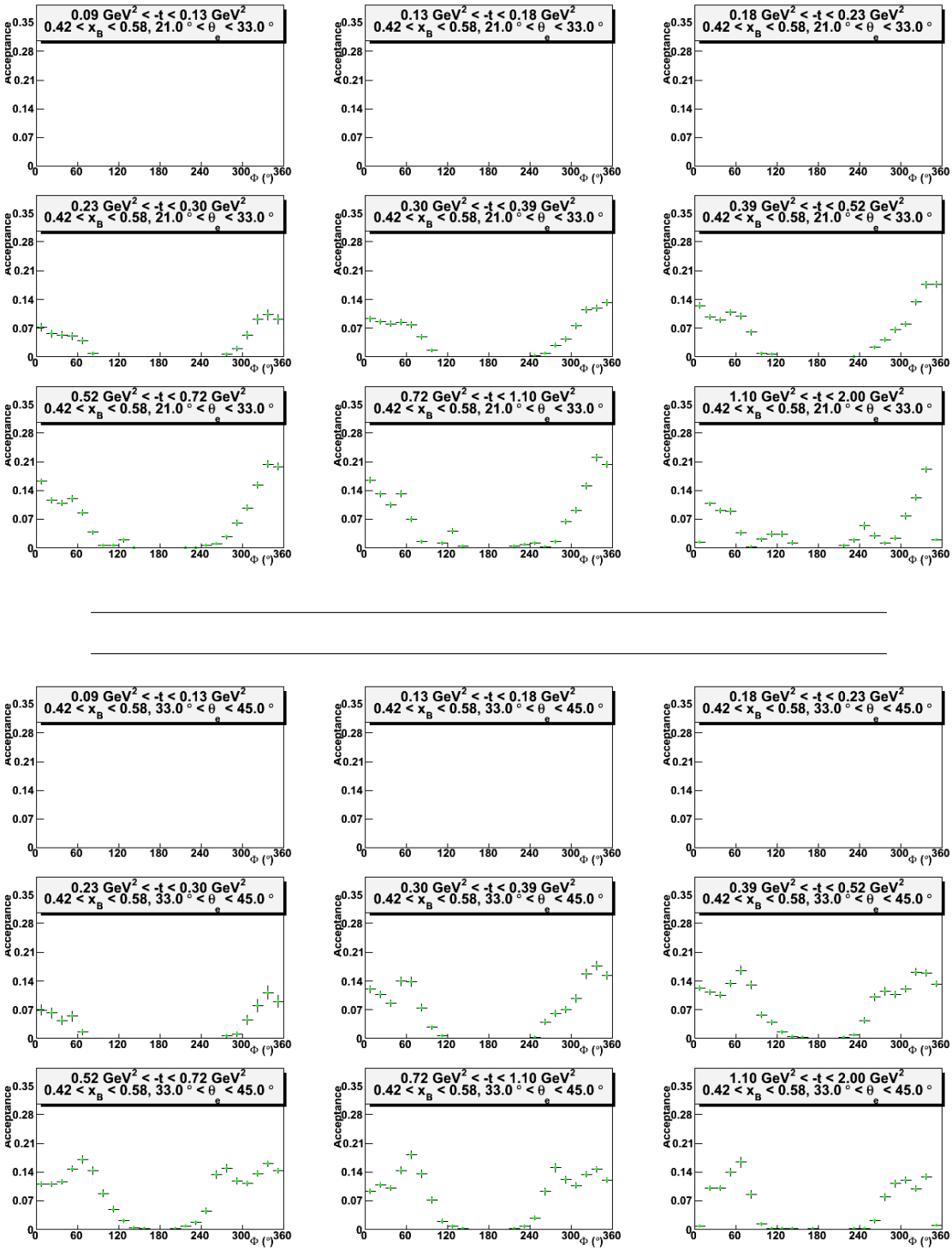

Figure A.11: On top, the acceptance as a function of ϕ for the twentieth bin in x_B and θ_e, where $0.42 < x_B < 0.58$ and $21^\circ < \theta_e < 33^\circ$. On bottom, the acceptance as a function of ϕ for the twenty-first bin in x_B and θ_e, where $0.42 < x_B < 0.58$ and $33^\circ < \theta_e < 45^\circ$.

B. Complete Results for Bin Volume Corrections

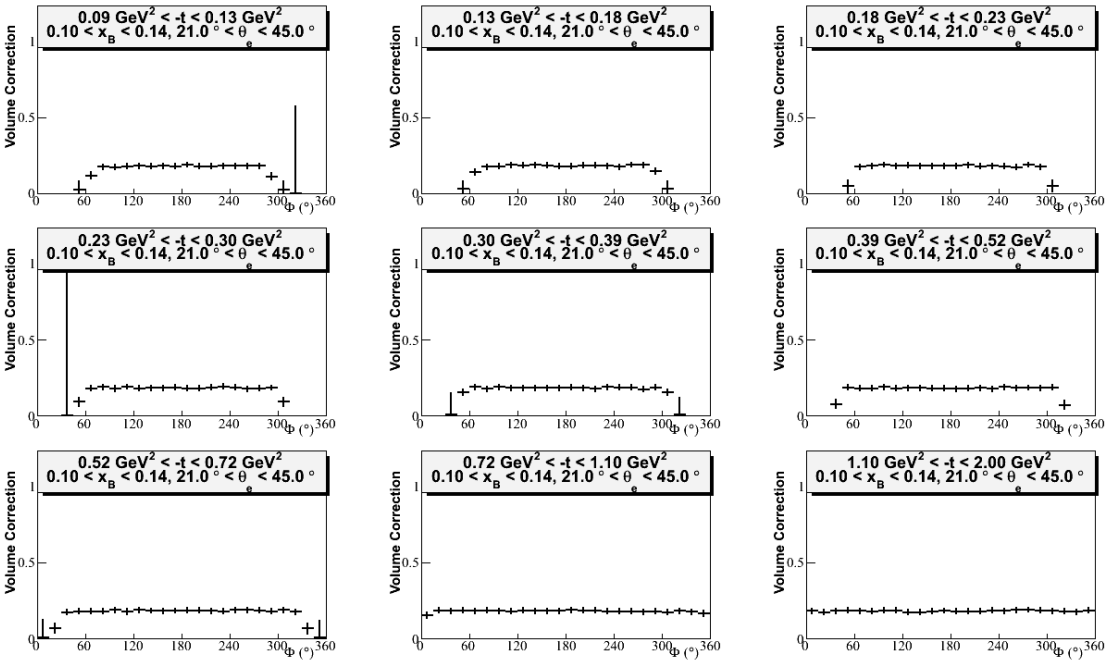

Figure B.1: The bin volume correction $\frac{N_{\text{bin}}}{N_{\text{super}}}$ as a function of Φ for the first bin in x_B and θ_e, where $0.1 < x_B < 0.14$ and $21^\circ < \theta_e < 45^\circ$.

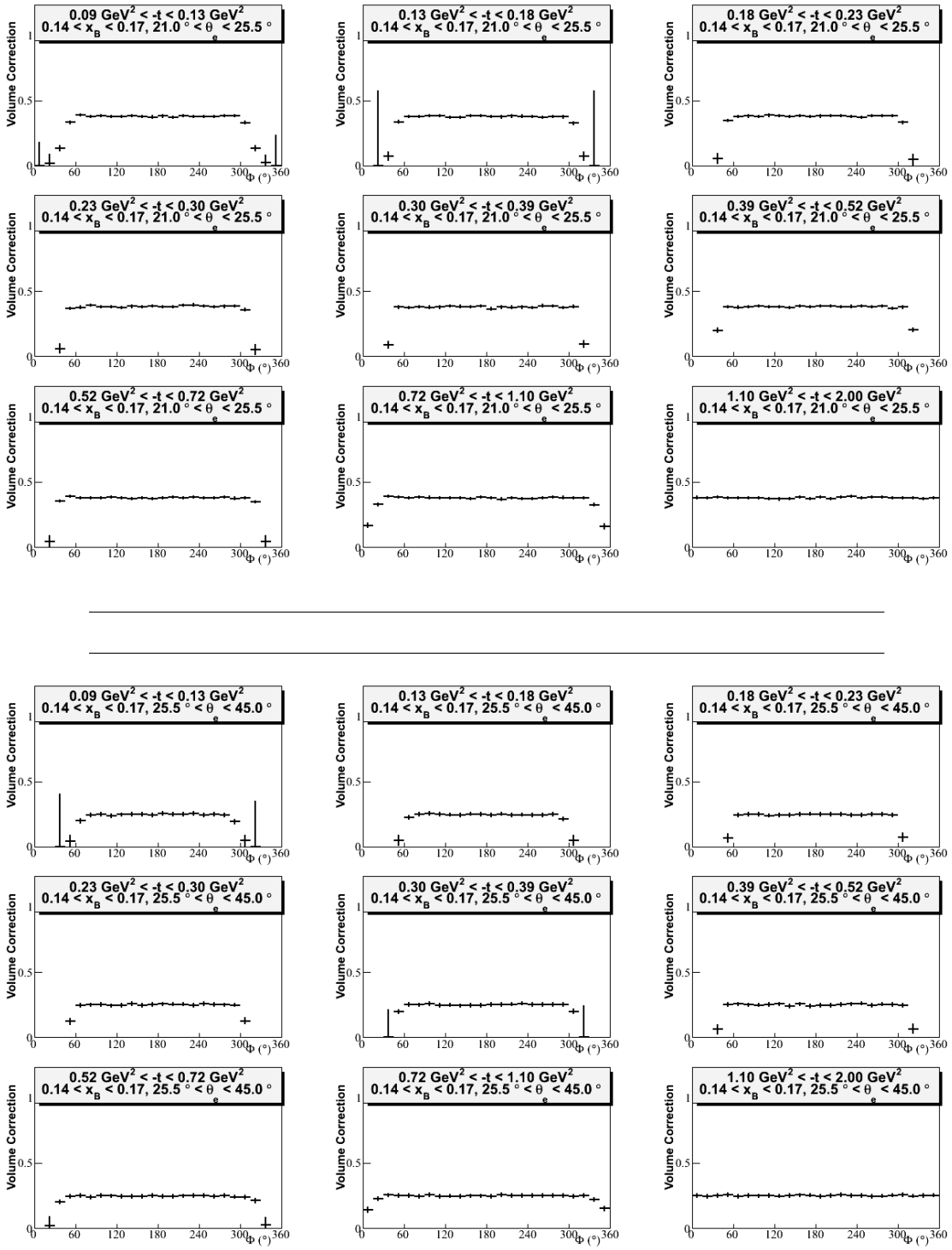

Figure B.2: On top, the bin volume correction $\frac{N_{\text{bin}}}{N_{\text{super}}}$ as a function of Φ for the second bin in x_B and θ_e, where $0.14 < x_B < 0.17$ and $21^\circ < \theta_e < 25.5^\circ$. On bottom, the bin volume correction $\frac{N_{\text{bin}}}{N_{\text{super}}}$ as a function of Φ for the third bin in x_B and θ_e, where $0.14 < x_B < 0.17$ and $25.5^\circ < \theta_e < 45^\circ$.

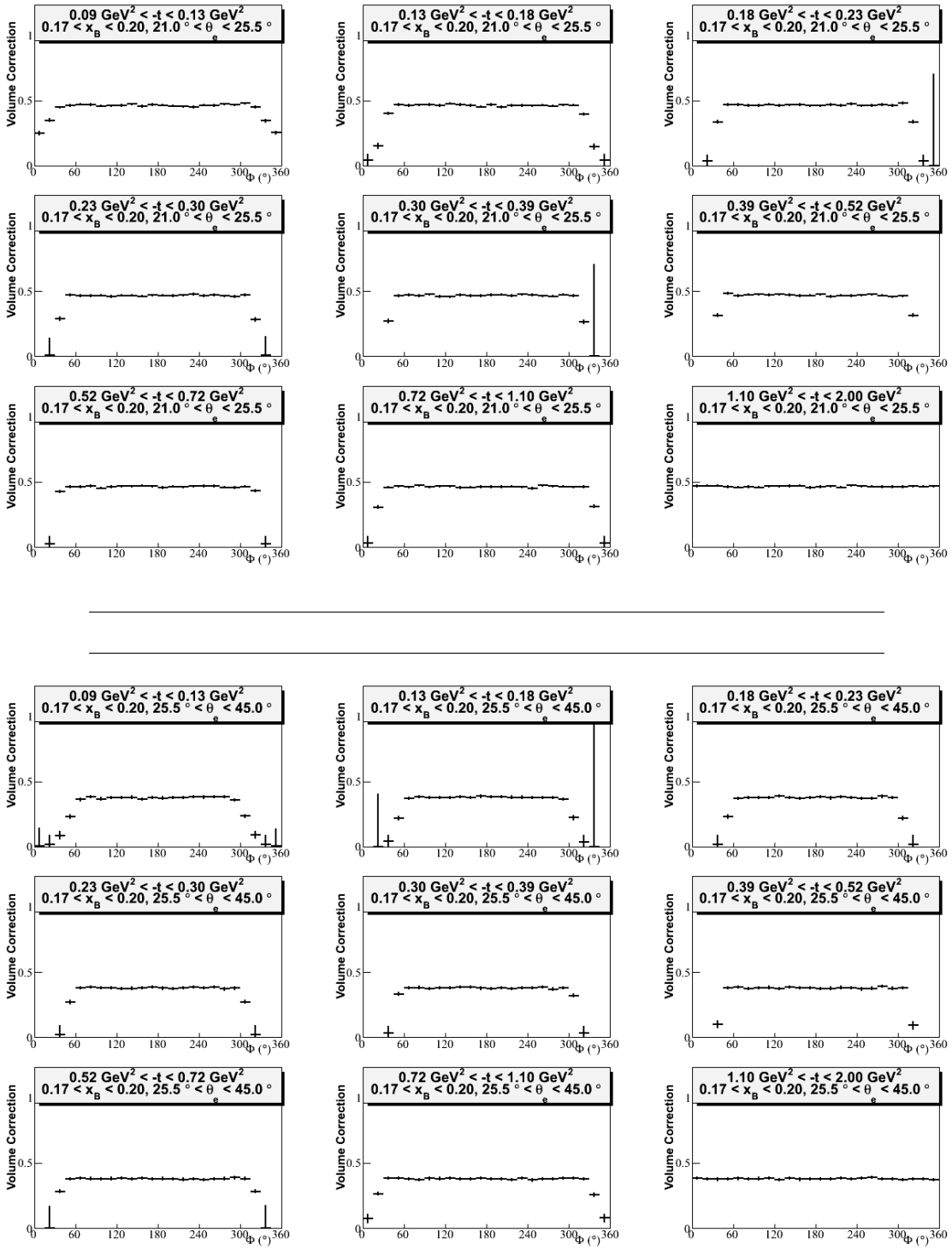

Figure B.3: On top, the bin volume correction $\frac{N_{\rm bin}}{N_{\rm super}}$ as a function of Φ for the fourth bin in x_B and θ_e, where $0.17 < x_B < 0.2$ and $21^\circ < \theta_e < 25.5^\circ$. On bottom, the bin volume correction $\frac{N_{\rm bin}}{N_{\rm super}}$ as a function of Φ for the fifth bin in x_B and θ_e, where $0.17 < x_B < 0.2$ and $25.5^\circ < \theta_e < 45^\circ$.

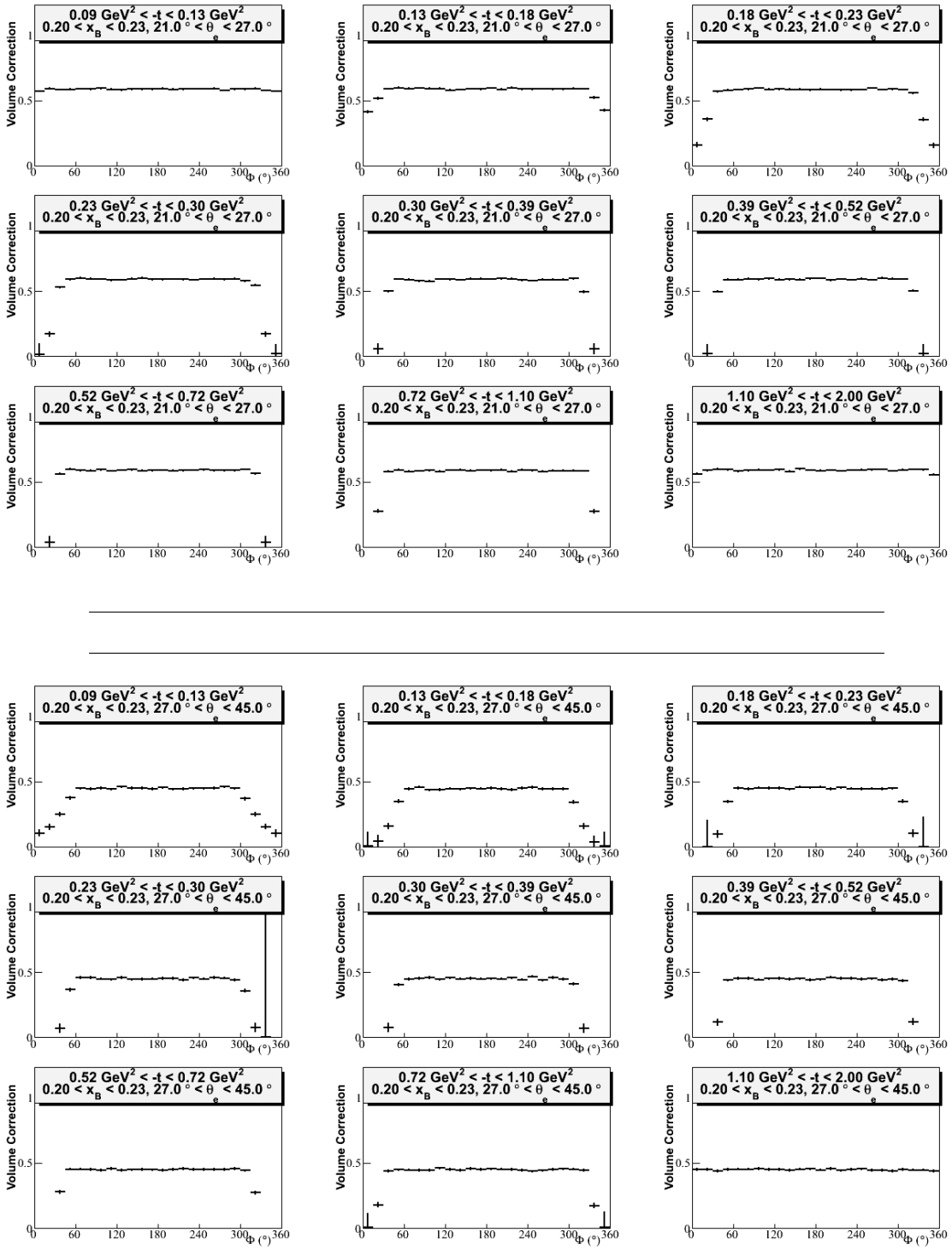

Figure B.4: On top, the bin volume correction $\frac{N_{\text{bin}}}{N_{\text{super}}}$ as a function of Φ for the sixth bin in x_B and θ_e, where $0.2 < x_B < 0.23$ and $21^\circ < \theta_e < 27^\circ$. On bottom, the bin volume correction $\frac{N_{\text{bin}}}{N_{\text{super}}}$ as a function of Φ for the seventh bin in x_B and θ_e, where $0.2 < x_B < 0.23$ and $27^\circ < \theta_e < 45^\circ$.

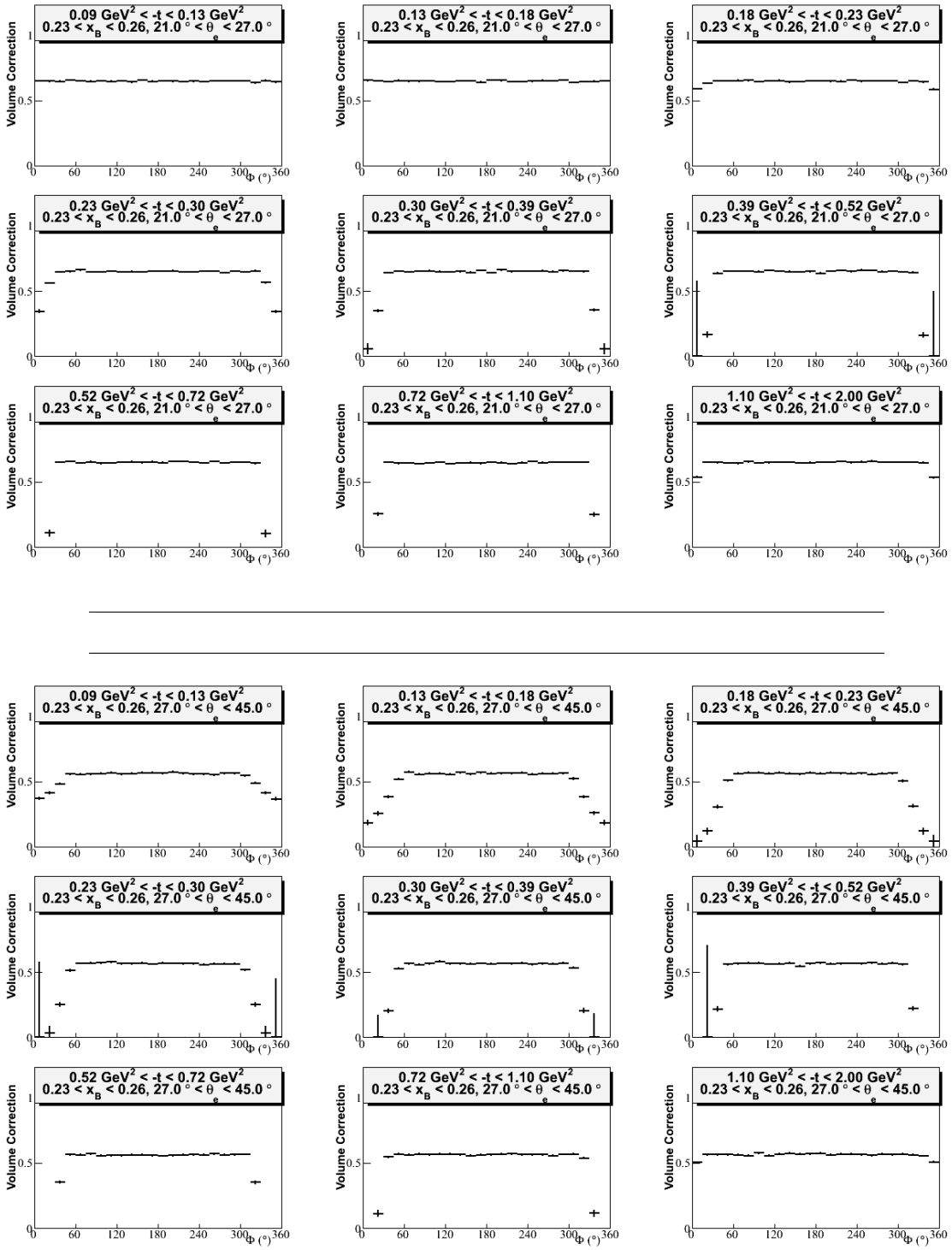

Figure B.5: On top, the bin volume correction $\frac{N_{\text{bin}}}{N_{\text{super}}}$ as a function of Φ for the eighth bin in x_B and θ_e, where $0.23 < x_B < 0.26$ and $21^\circ < \theta_e < 27^\circ$. On bottom, the bin volume correction $\frac{N_{\text{bin}}}{N_{\text{super}}}$ as a function of Φ for the ninth bin in x_B and θ_e, where $0.23 < x_B < 0.26$ and $27^\circ < \theta_e < 45^\circ$.

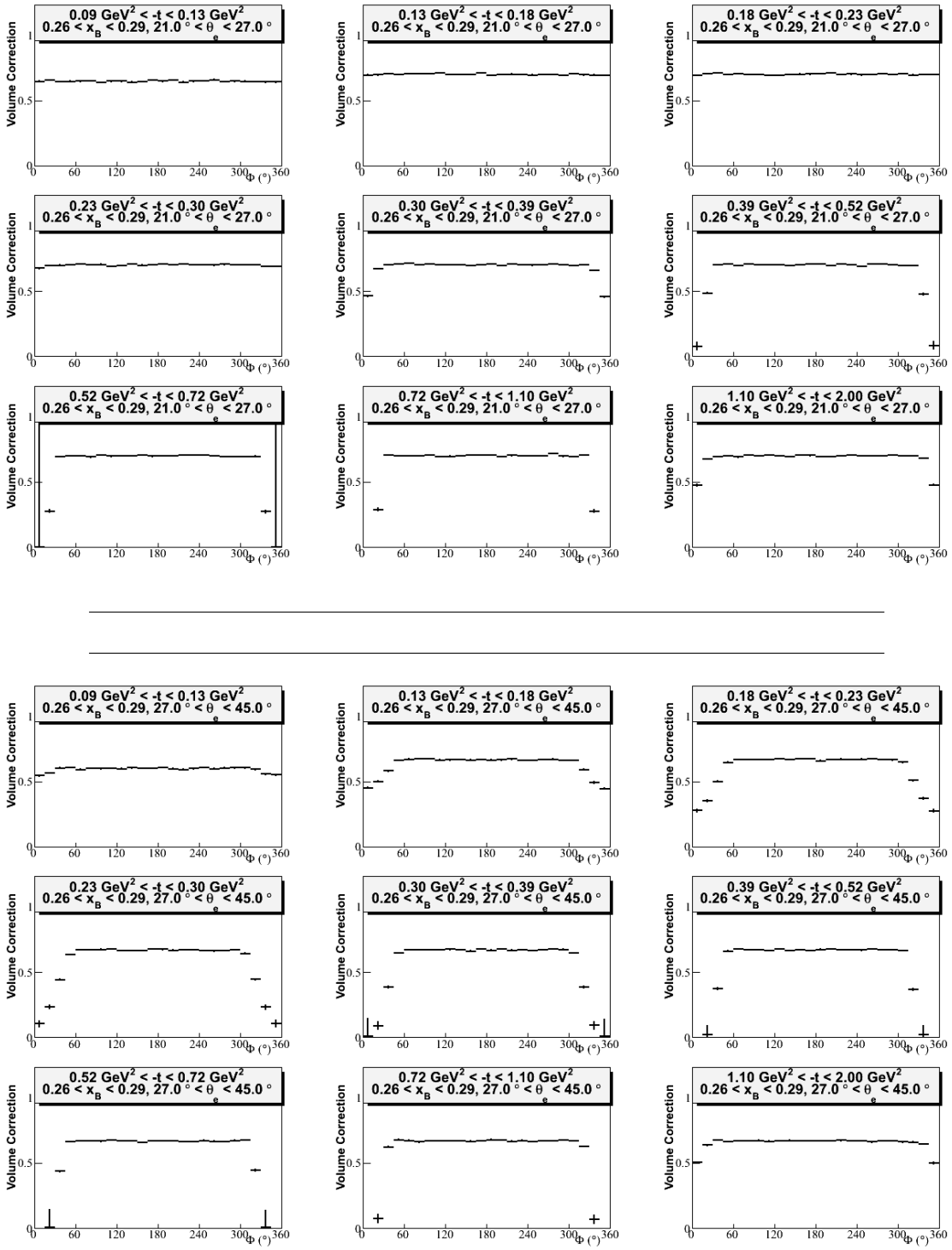

Figure B.6: On top, the bin volume correction $\frac{N_{\text{bin}}}{N_{\text{super}}}$ as a function of Φ for the tenth bin in x_B and θ_e, where $0.26 < x_B < 0.29$ and $21^\circ < \theta_e < 27^\circ$. On bottom, the bin volume correction $\frac{N_{\text{bin}}}{N_{\text{super}}}$ as a function of Φ for the eleventh bin in x_B and θ_e, where $0.26 < x_B < 0.29$ and $27^\circ < \theta_e < 45^\circ$.

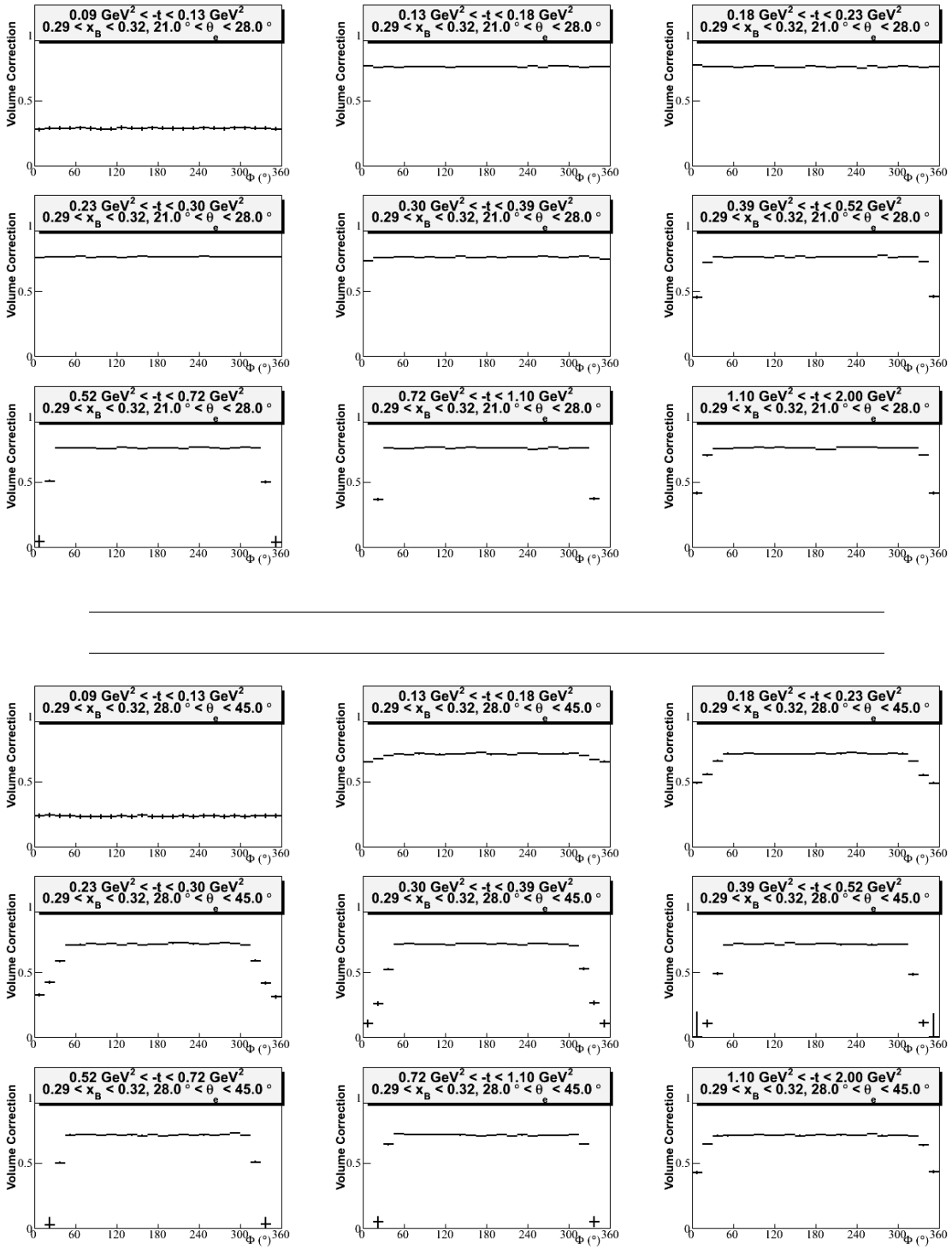

Figure B.7: On top, the bin volume correction $\frac{N_{\text{bin}}}{N_{\text{super}}}$ as a function of Φ for the twelfth bin in x_B and θ_e, where $0.29 < x_B < 0.32$ and $21^\circ < \theta_e < 28^\circ$. On bottom, the bin volume correction $\frac{N_{\text{bin}}}{N_{\text{super}}}$ as a function of Φ for the thirteenth bin in x_B and θ_e, where $0.29 < x_B < 0.32$ and $28^\circ < \theta_e < 45^\circ$.

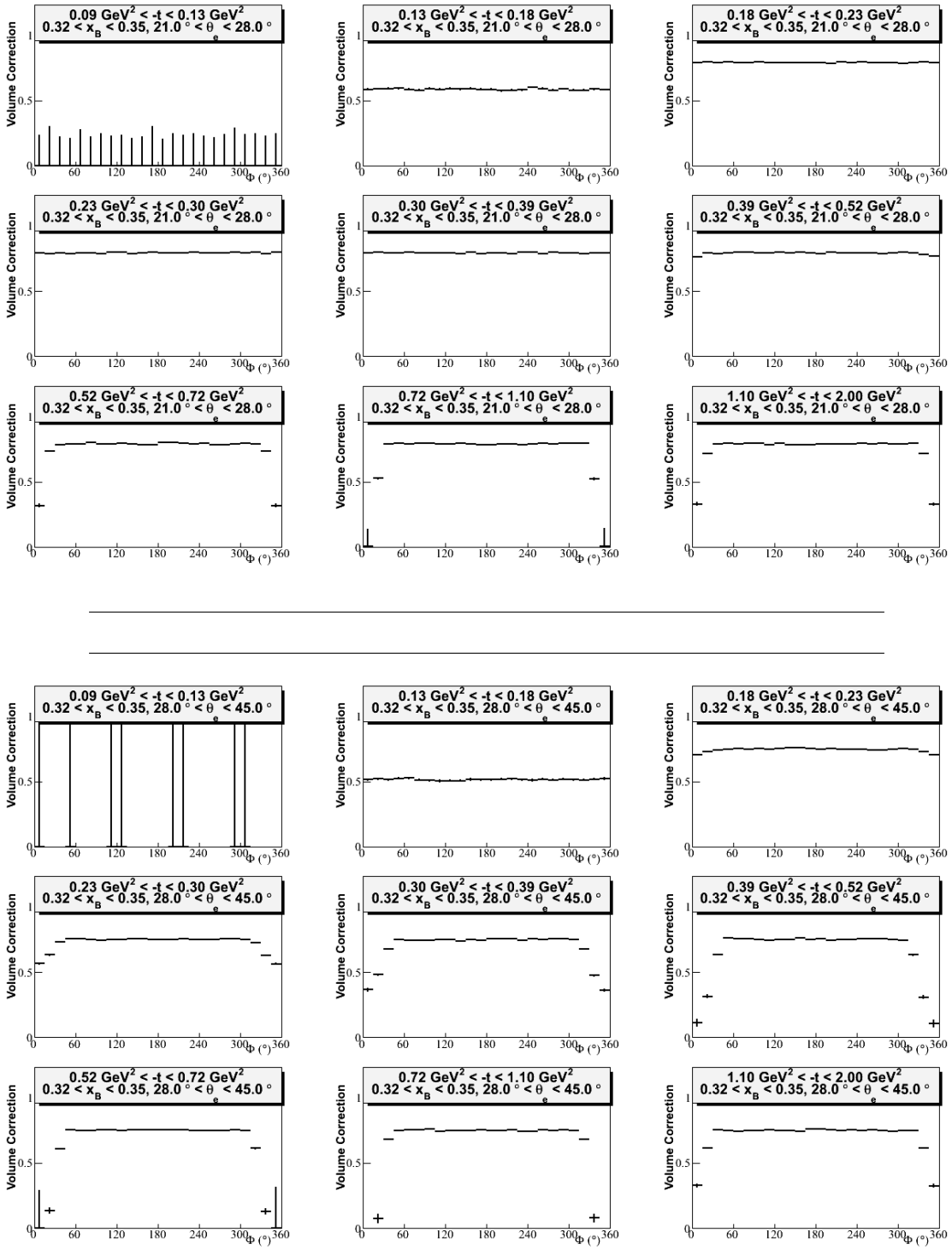

Figure B.8: On top, the bin volume correction $\frac{N_{\text{bin}}}{N_{\text{super}}}$ as a function of Φ for the fourteenth bin in x_B and θ_e, where $0.32 < x_B < 0.35$ and $21^\circ < \theta_e < 28^\circ$. On bottom, the bin volume correction $\frac{N_{\text{bin}}}{N_{\text{super}}}$ as a function of Φ for the fifteenth bin in x_B and θ_e, where $0.32 < x_B < 0.35$ and $28^\circ < \theta_e < 45^\circ$.

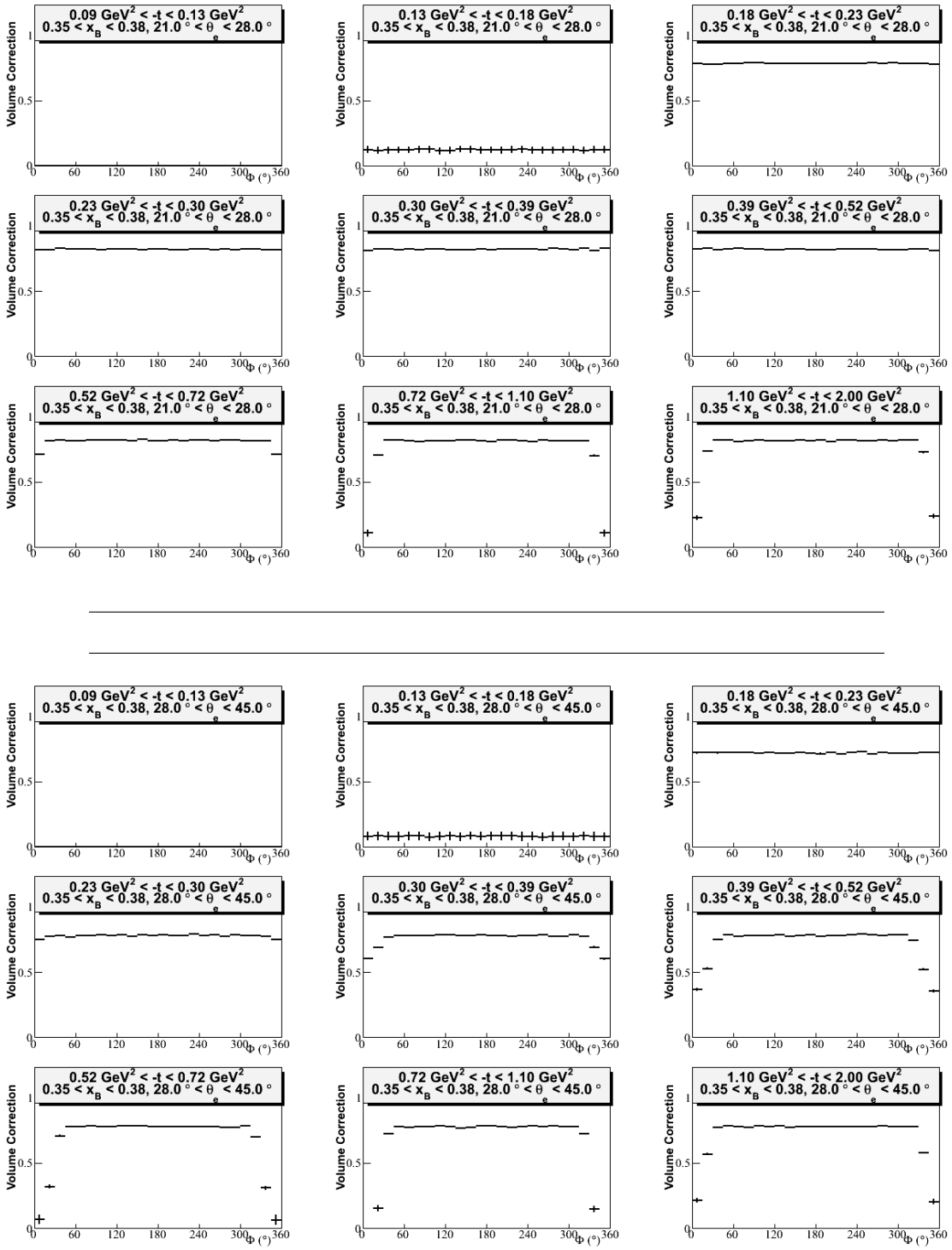

Figure B.9: On top, the bin volume correction $\frac{N_{\text{bin}}}{N_{\text{super}}}$ as a function of Φ for the sixteenth bin in x_B and θ_e, where $0.35 < x_B < 0.38$ and $21^\circ < \theta_e < 28^\circ$. On bottom, the bin volume correction $\frac{N_{\text{bin}}}{N_{\text{super}}}$ as a function of Φ for the seventeenth bin in x_B and θ_e, where $0.35 < x_B < 0.38$ and $28^\circ < \theta_e < 45^\circ$.

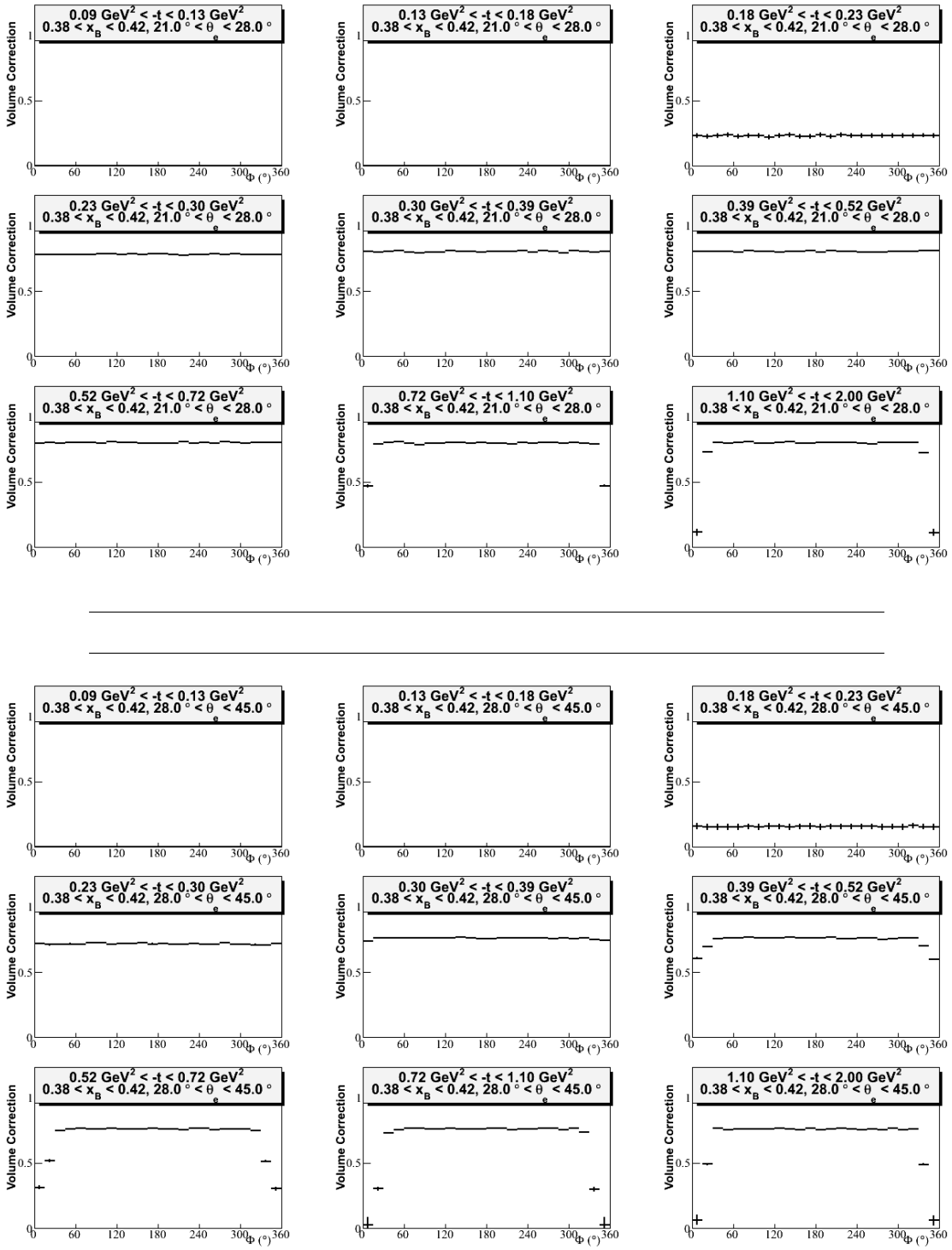

Figure B.10: On top, the bin volume correction $\frac{N_{\text{bin}}}{N_{\text{super}}}$ as a function of Φ for the eighteenth bin in x_B and θ_e, where $0.38 < x_B < 0.42$ and $21^\circ < \theta_e < 28^\circ$. On bottom, the bin volume correction $\frac{N_{\text{bin}}}{N_{\text{super}}}$ as a function of Φ for the nineteenth bin in x_B and θ_e, where $0.38 < x_B < 0.42$ and $28^\circ < \theta_e < 45^\circ$.

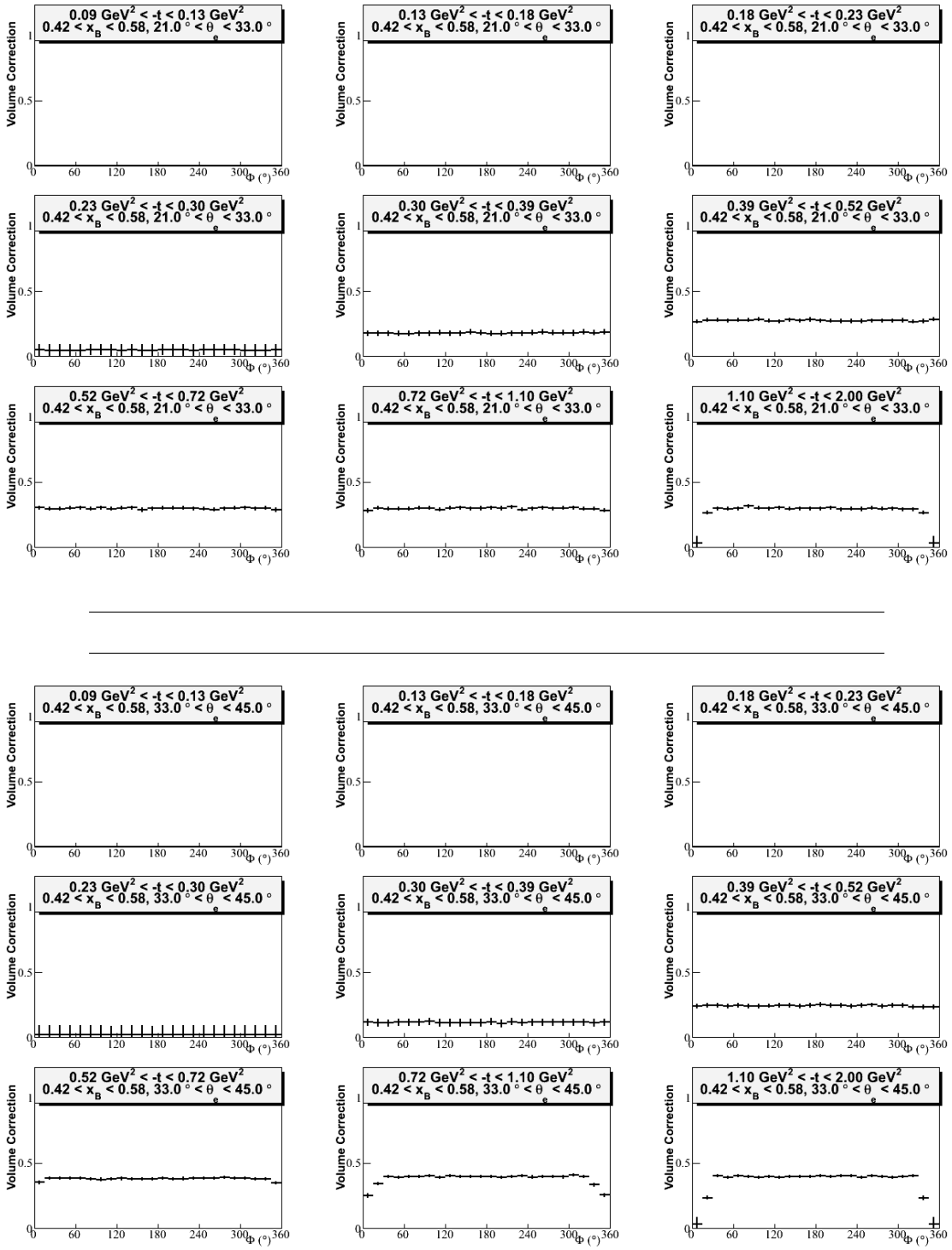

Figure B.11: On top, the bin volume correction $\frac{N_{\text{bin}}}{N_{\text{super}}}$ as a function of Φ for the twentieth bin in x_B and θ_e, where $0.42 < x_B < 0.58$ and $21^\circ < \theta_e < 33^\circ$. On bottom, the bin volume correction $\frac{N_{\text{bin}}}{N_{\text{super}}}$ as a function of Φ for the twenty-first bin in x_B and θ_e, where $0.42 < x_B < 0.58$ and $33^\circ < \theta_e < 45^\circ$.

C. Complete Results for Pion Subtraction Ratio

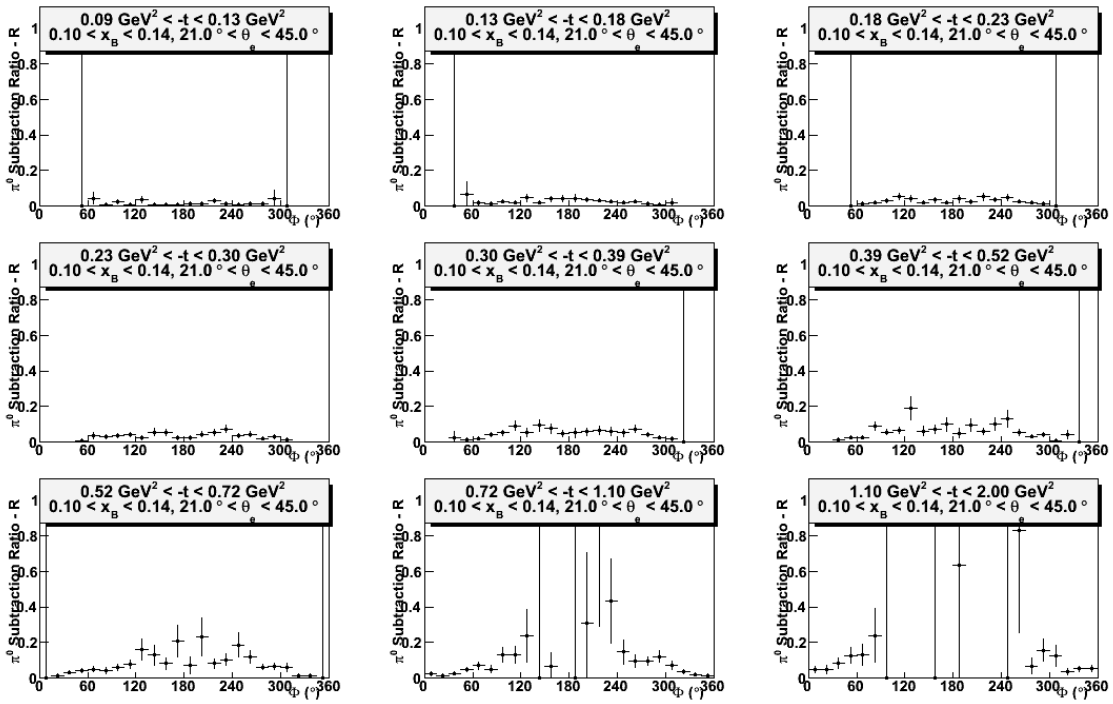

Figure C.1: the neutral pion subtraction ratio $R = \frac{N^{\gamma}_{\pi_0}}{N^{e+p+\gamma}}$ as a function of Φ for the first bin in x_B and θ_e, where $0.1 < x_B < 0.14$ and $21^\circ < \theta_e < 45^\circ$.

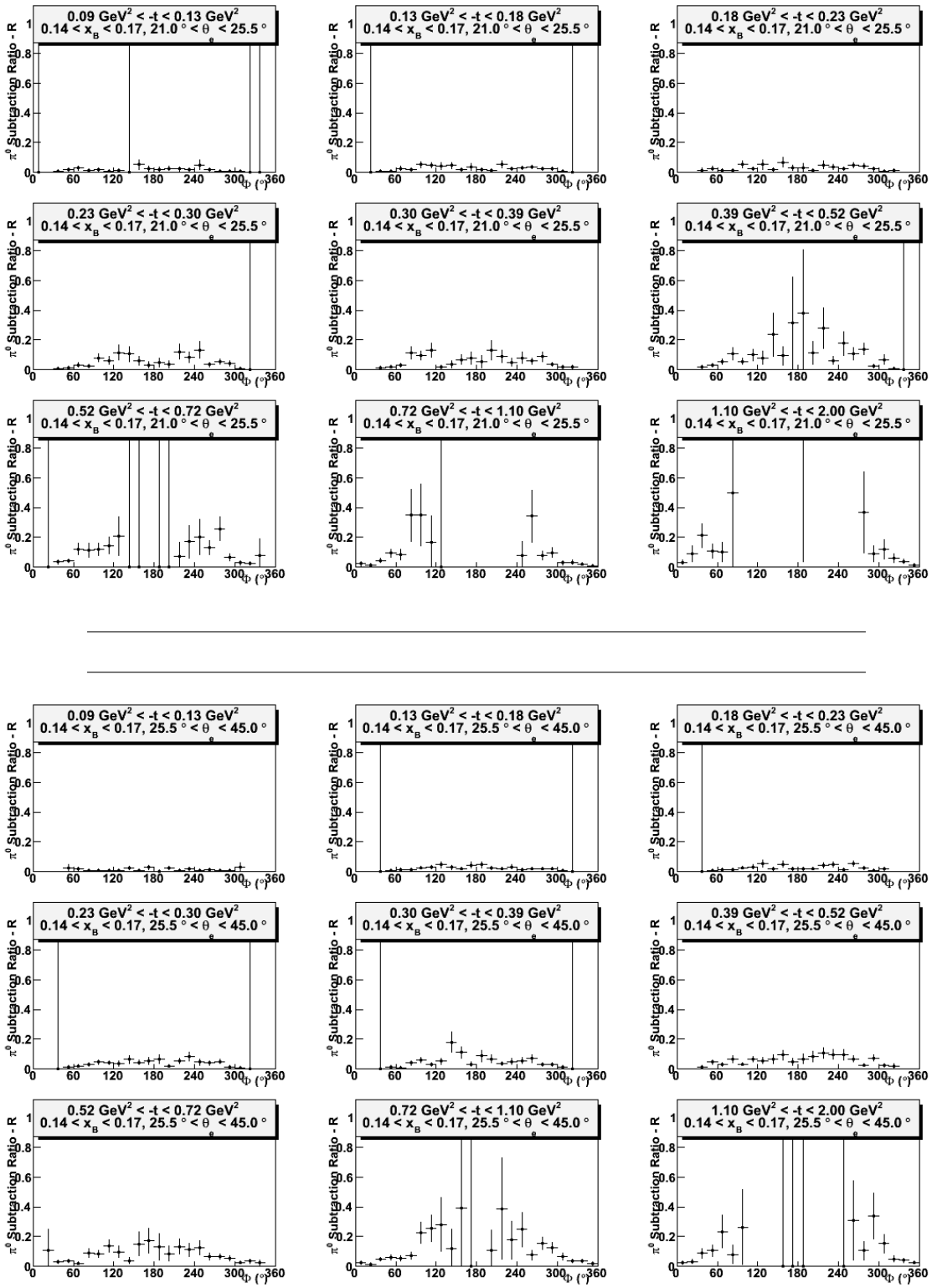

Figure C.2: On top, the neutral pion subtraction ratio $R = \frac{N^{\gamma}_{\pi 0}}{N^{e+p+\gamma}}$ as a function of Φ for the second bin in x_B and θ_e, where $0.14 < x_B < 0.17$ and $21^{\circ} < \theta_e < 25.5^{\circ}$. On bottom, the neutral pion subtraction ratio $R = \frac{N^{\gamma}_{\pi 0}}{N^{e+p+\gamma}}$ as a function of Φ for the third bin in x_B and θ_e, where $0.14 < x_B < 0.17$ and $25.5^{\circ} < \theta_e < 45^{\circ}$.

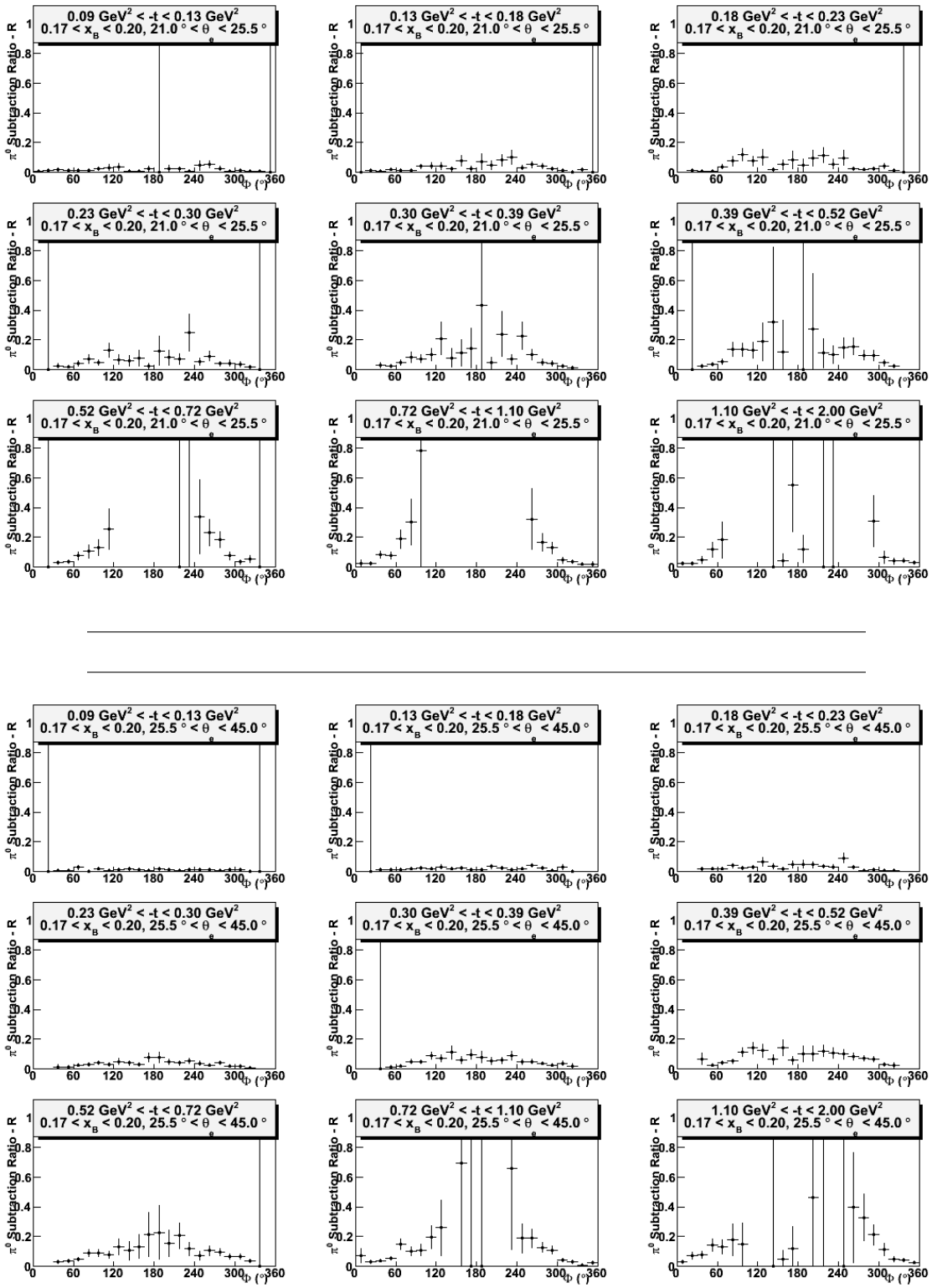

Figure C.3: On top, the neutral pion subtraction ratio $R = \frac{N^{\gamma}_{\pi 0}}{N^{e+p+\gamma}}$ as a function of Φ for the fourth bin in x_B and θ_e, where $0.17 < x_B < 0.2$ and $21^{\circ} < \theta_e < 25.5^{\circ}$. On bottom, the neutral pion subtraction ratio $R = \frac{N^{\gamma}_{\pi 0}}{N^{e+p+\gamma}}$ as a function of Φ for the fifth bin in x_B and θ_e, where $0.17 < x_B < 0.2$ and $25.5^{\circ} < \theta_e < 45^{\circ}$.

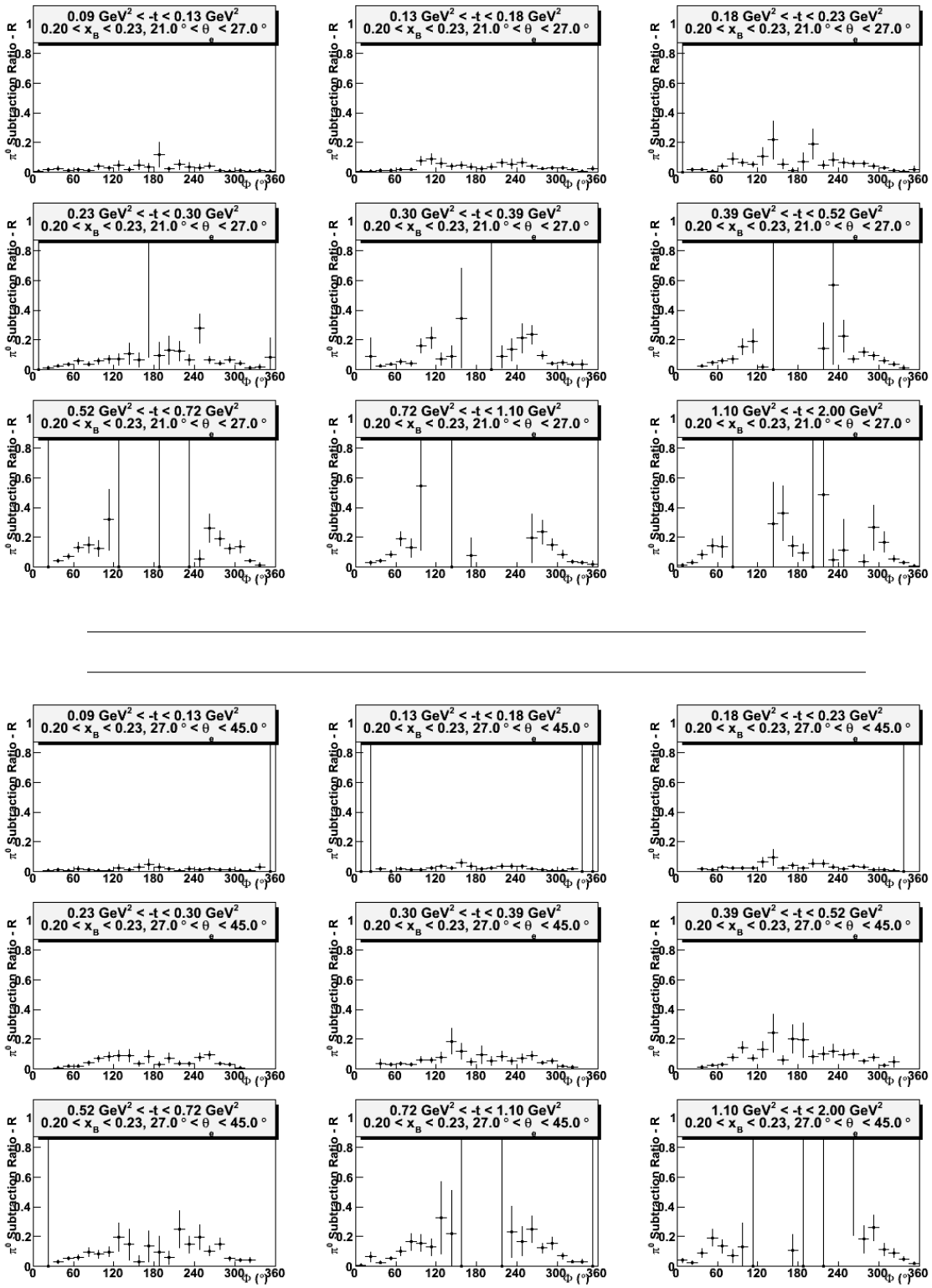

Figure C.4: On top, the neutral pion subtraction ratio $R = \frac{N^{\gamma}_{\pi_0}}{N^{e+p+\gamma}}$ as a function of Φ for the sixth bin in x_B and θ_e, where $0.2 < x_B < 0.23$ and $21^\circ < \theta_e < 27^\circ$. On bottom, the neutral pion subtraction ratio $R = \frac{N^{\gamma}_{\pi_0}}{N^{e+p+\gamma}}$ as a function of Φ for the seventh bin in x_B and θ_e, where $0.2 < x_B < 0.23$ and $27^\circ < \theta_e < 45^\circ$.

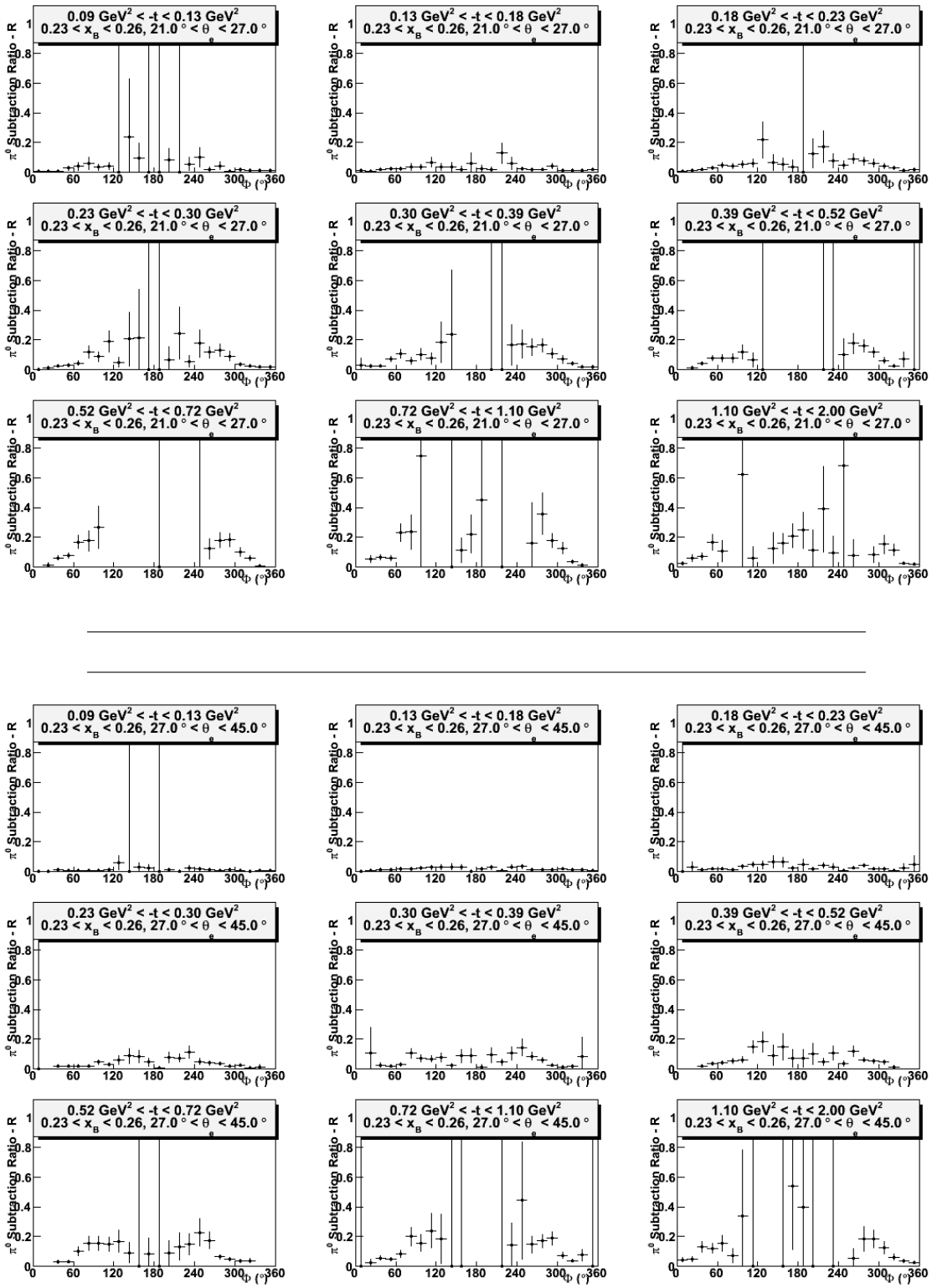

Figure C.5: On top, the neutral pion subtraction ratio $R = \frac{N^{\gamma}_{\pi 0}}{N^{e+p+\gamma}}$ as a function of Φ for the eighth bin in x_B and θ_e, where $0.23 < x_B < 0.26$ and $21^{\circ} < \theta_e < 27^{\circ}$. On bottom, the neutral pion subtraction ratio $R = \frac{N^{\gamma}_{\pi 0}}{N^{e+p+\gamma}}$ as a function of Φ for the ninth bin in x_B and θ_e, where $0.23 < x_B < 0.26$ and $27^{\circ} < \theta_e < 45^{\circ}$.

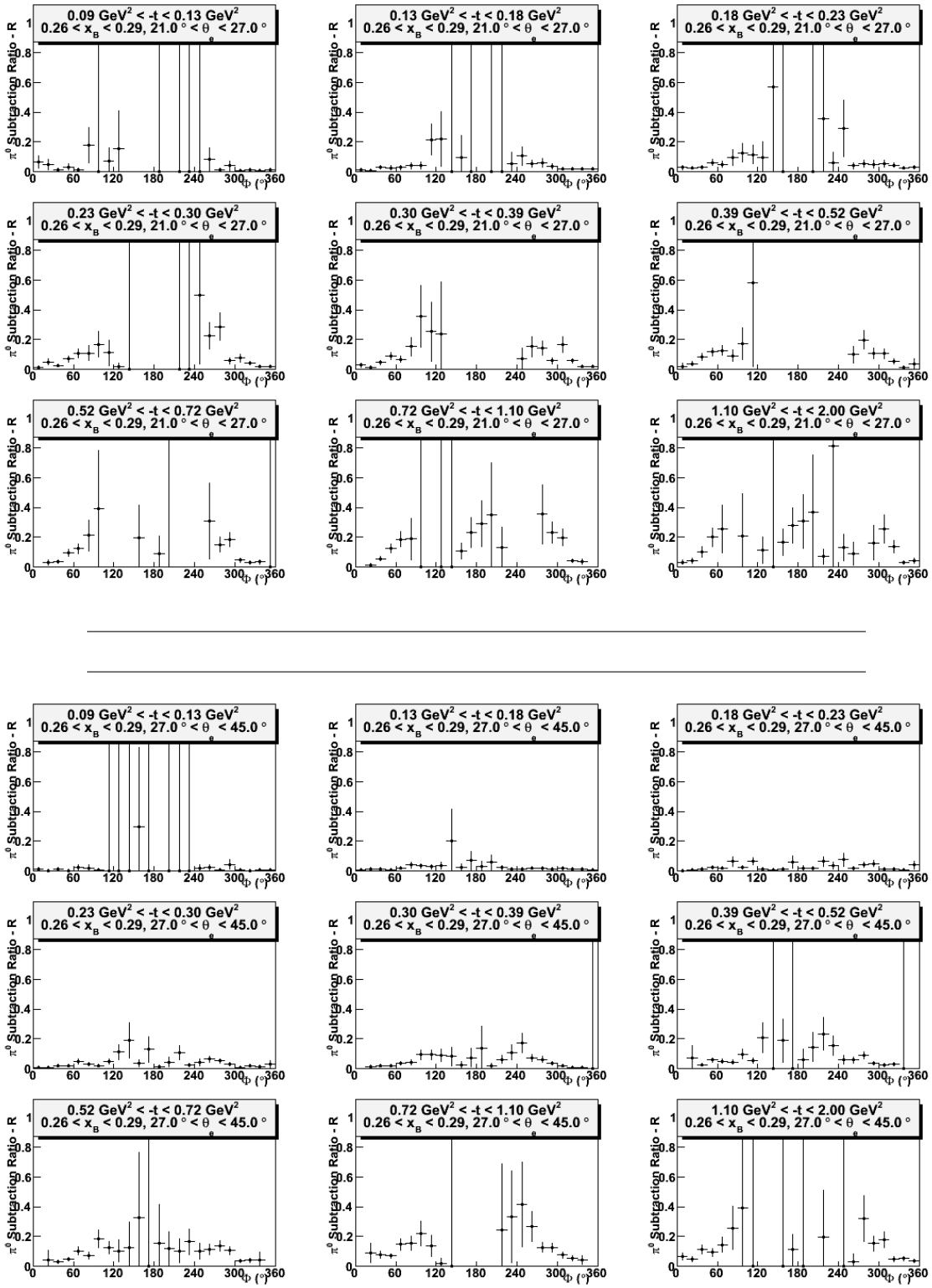

Figure C.6: On top, the neutral pion subtraction ratio $R = \frac{N^{\gamma}_{\pi_0}}{N^{e+p+\gamma}}$ as a function of Φ for the tenth bin in x_B and θ_e, where $0.26 < x_B < 0.29$ and $21^\circ < \theta_e < 27^\circ$. On bottom, the neutral pion subtraction ratio $R = \frac{N^{\gamma}_{\pi_0}}{N^{e+p+\gamma}}$ as a function of Φ for the eleventh bin in x_B and θ_e, where $0.26 < x_B < 0.29$ and $27^\circ < \theta_e < 45^\circ$.

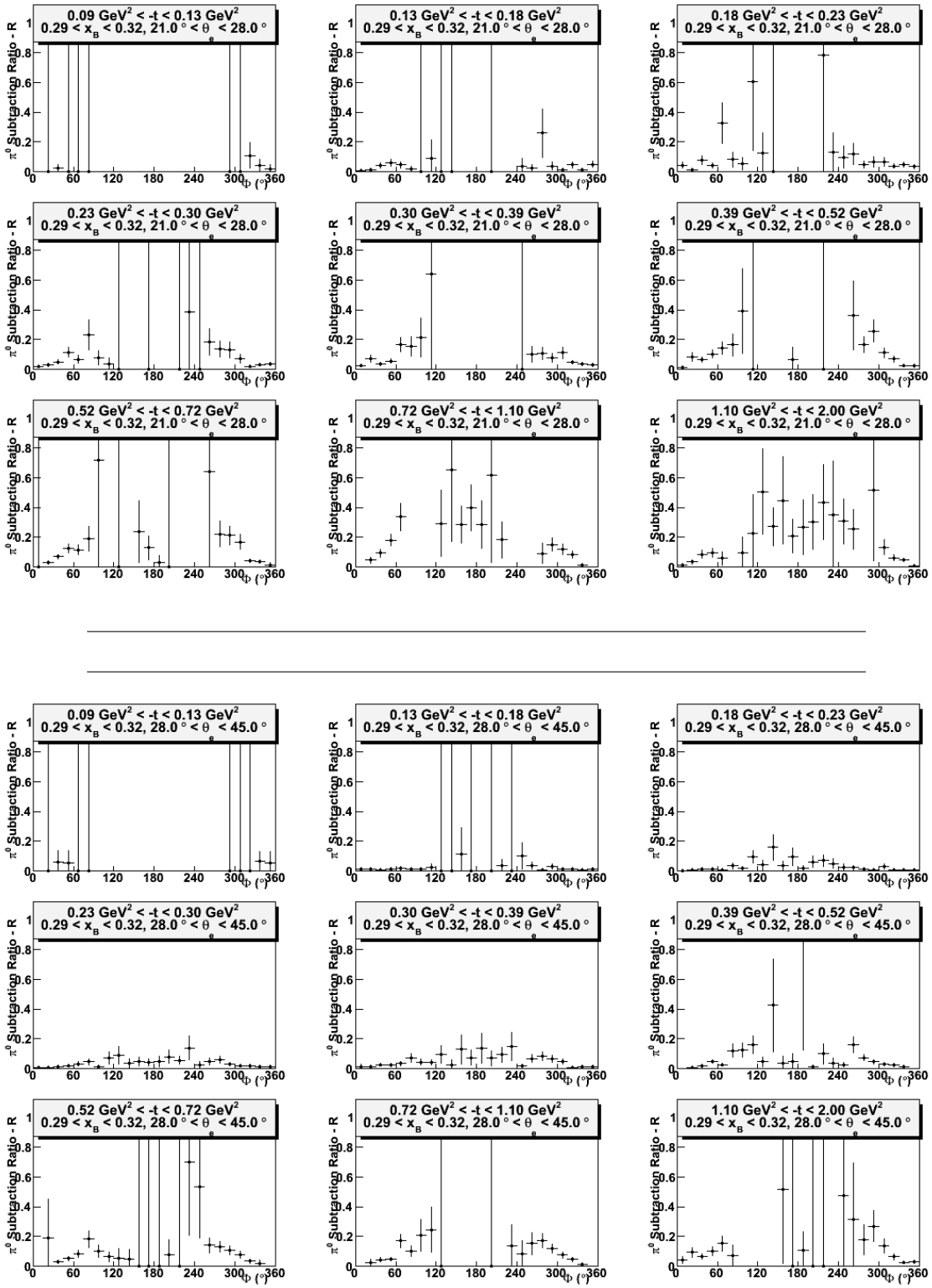

Figure C.7: On top, the neutral pion subtraction ratio $R = \frac{N^{\gamma}_{\pi_0}}{N^{e+p+\gamma}}$ as a function of Φ for the twelfth bin in x_B and θ_e, where $0.29 < x_B < 0.32$ and $21^\circ < \theta_e < 28^\circ$. On bottom, the neutral pion subtraction ratio $R = \frac{N^{\gamma}_{\pi_0}}{N^{e+p+\gamma}}$ as a function of Φ for the thirteenth bin in x_B and θ_e, where $0.29 < x_B < 0.32$ and $28^\circ < \theta_e < 45^\circ$.

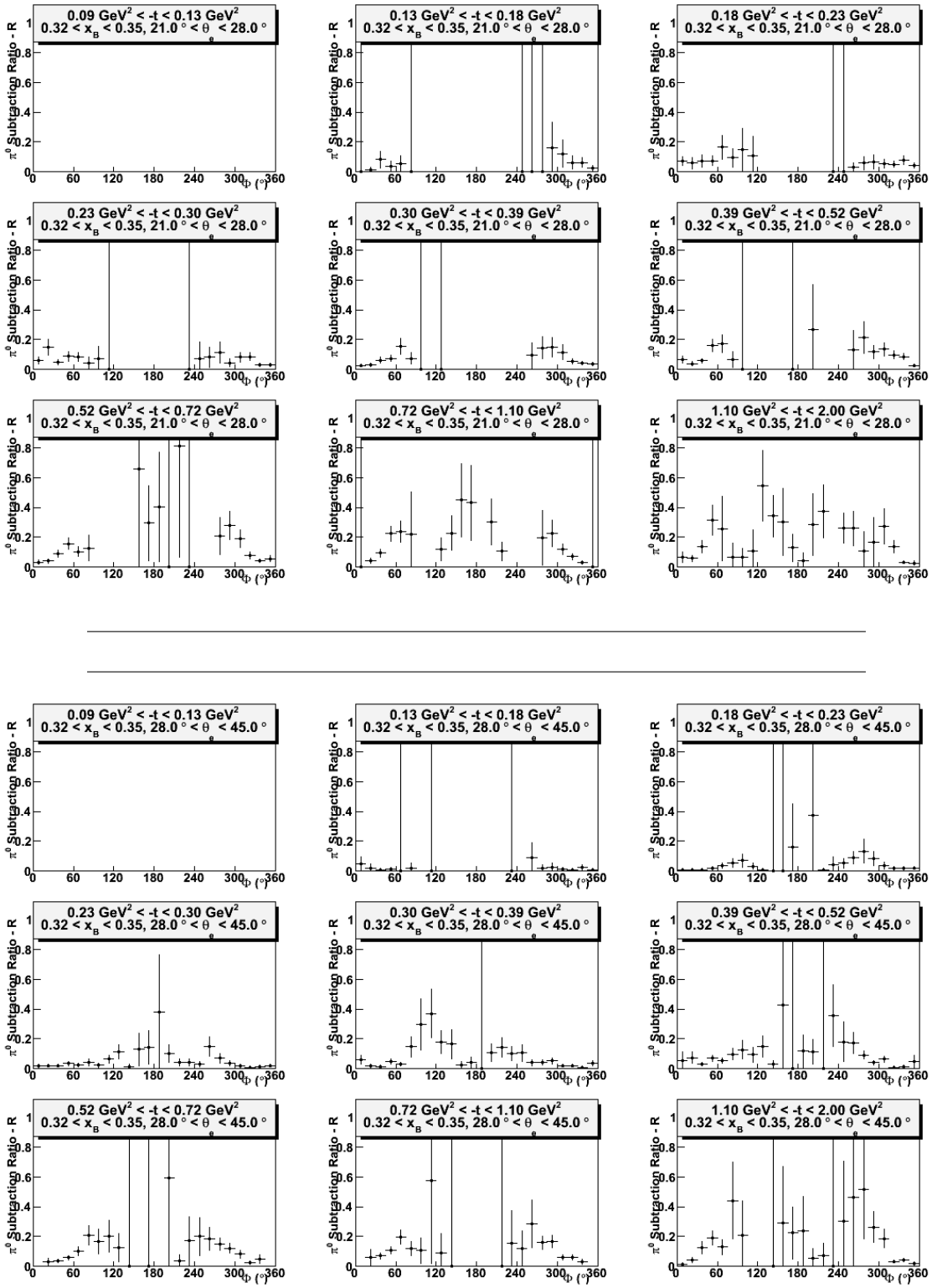

Figure C.8: On top, the neutral pion subtraction ratio $R = \frac{N^{\gamma}_{\pi 0}}{N^{e+p+\gamma}}$ as a function of Φ for the fourteenth bin in x_B and θ_e, where $0.32 < x_B < 0.35$ and $21^{\circ} < \theta_e < 28^{\circ}$. On bottom, the neutral pion subtraction ratio $R = \frac{N^{\gamma}_{\pi 0}}{N^{e+p+\gamma}}$ as a function of Φ for the fifteenth bin in x_B and θ_e, where $0.32 < x_B < 0.35$ and $28^{\circ} < \theta_e < 45^{\circ}$.

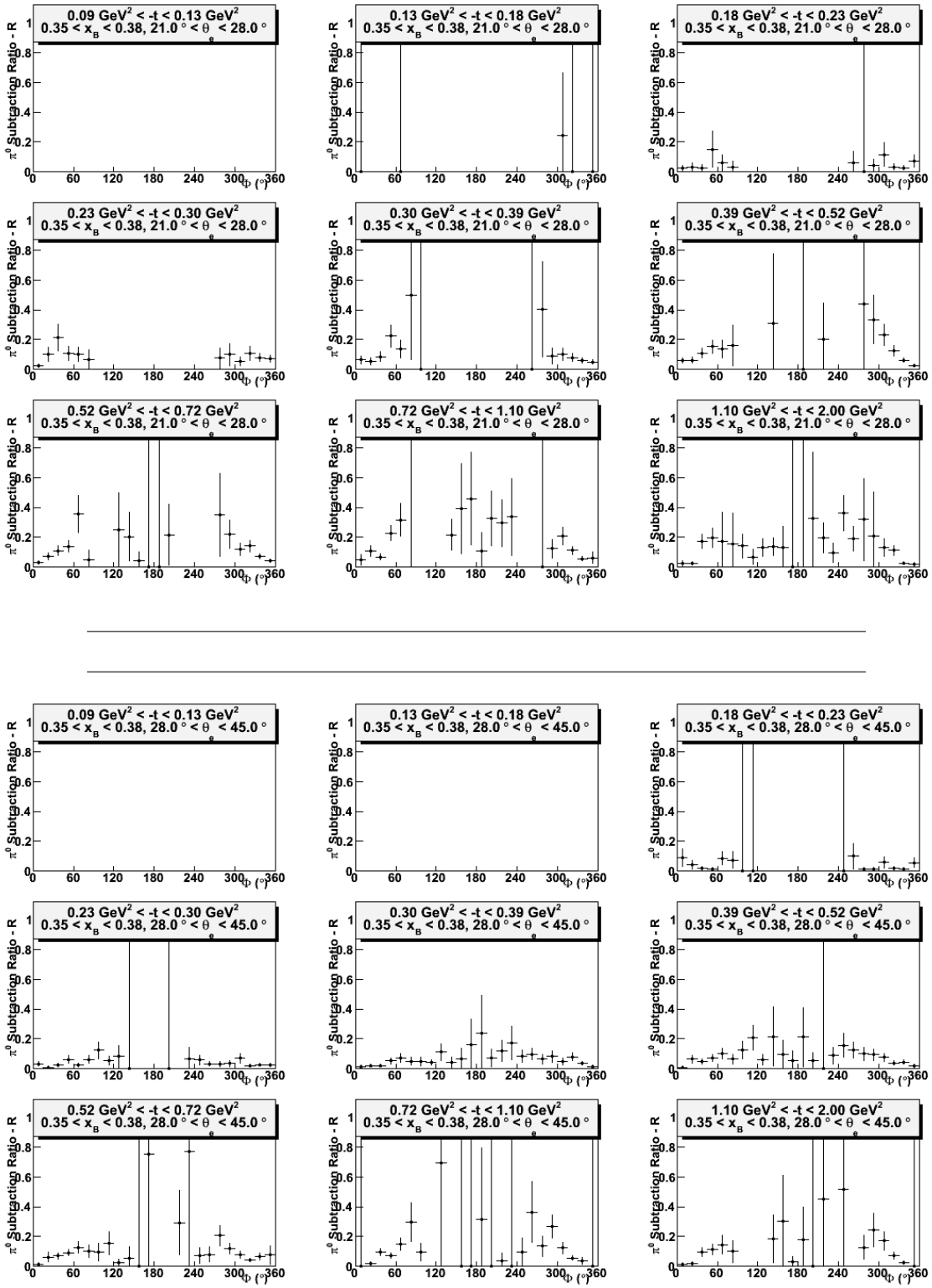

Figure C.9: On top, the neutral pion subtraction ratio $R = \frac{N^{\gamma}_{\pi_0}}{N^{e+p+\gamma}}$ as a function of Φ for the sixteenth bin in x_B and θ_e, where $0.35 < x_B < 0.38$ and $21^\circ < \theta_e < 28^\circ$. On bottom, the neutral pion subtraction ratio $R = \frac{N^{\gamma}_{\pi_0}}{N^{e+p+\gamma}}$ as a function of Φ for the seventeenth bin in x_B and θ_e, where $0.35 < x_B < 0.38$ and $28^\circ < \theta_e < 45^\circ$.

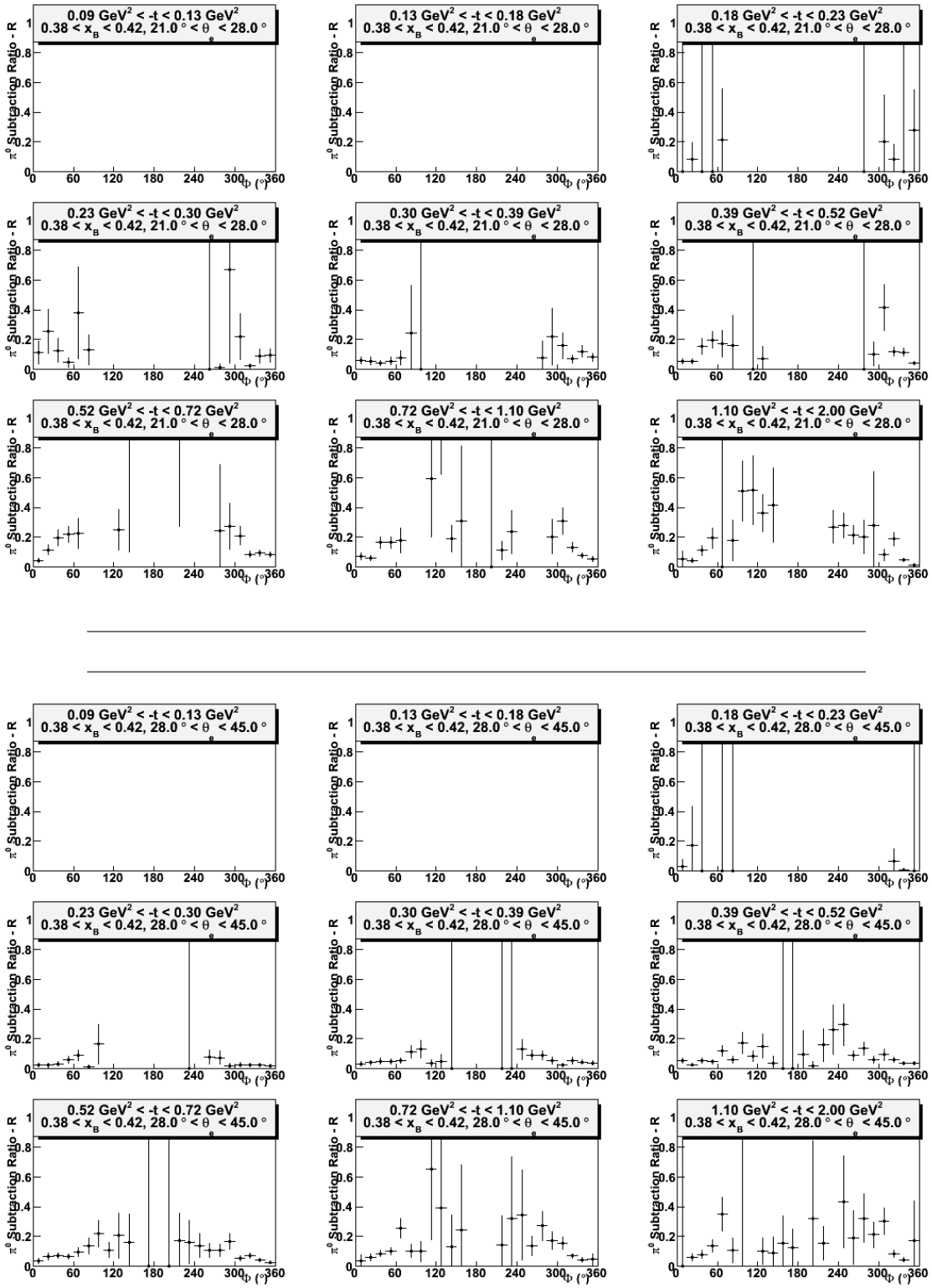

Figure C.10: On top, the neutral pion subtraction ratio $R = \frac{N^{\gamma}_{\pi_0}}{N^{e+p+\gamma}}$ as a function of Φ for the eighteenth bin in x_B and θ_e, where $0.38 < x_B < 0.42$ and $21^\circ < \theta_e < 28^\circ$. On bottom, the neutral pion subtraction ratio $R = \frac{N^{\gamma}_{\pi_0}}{N^{e+p+\gamma}}$ as a function of Φ for the nineteenth bin in x_B and θ_e, where $0.38 < x_B < 0.42$ and $28^\circ < \theta_e < 45^\circ$.

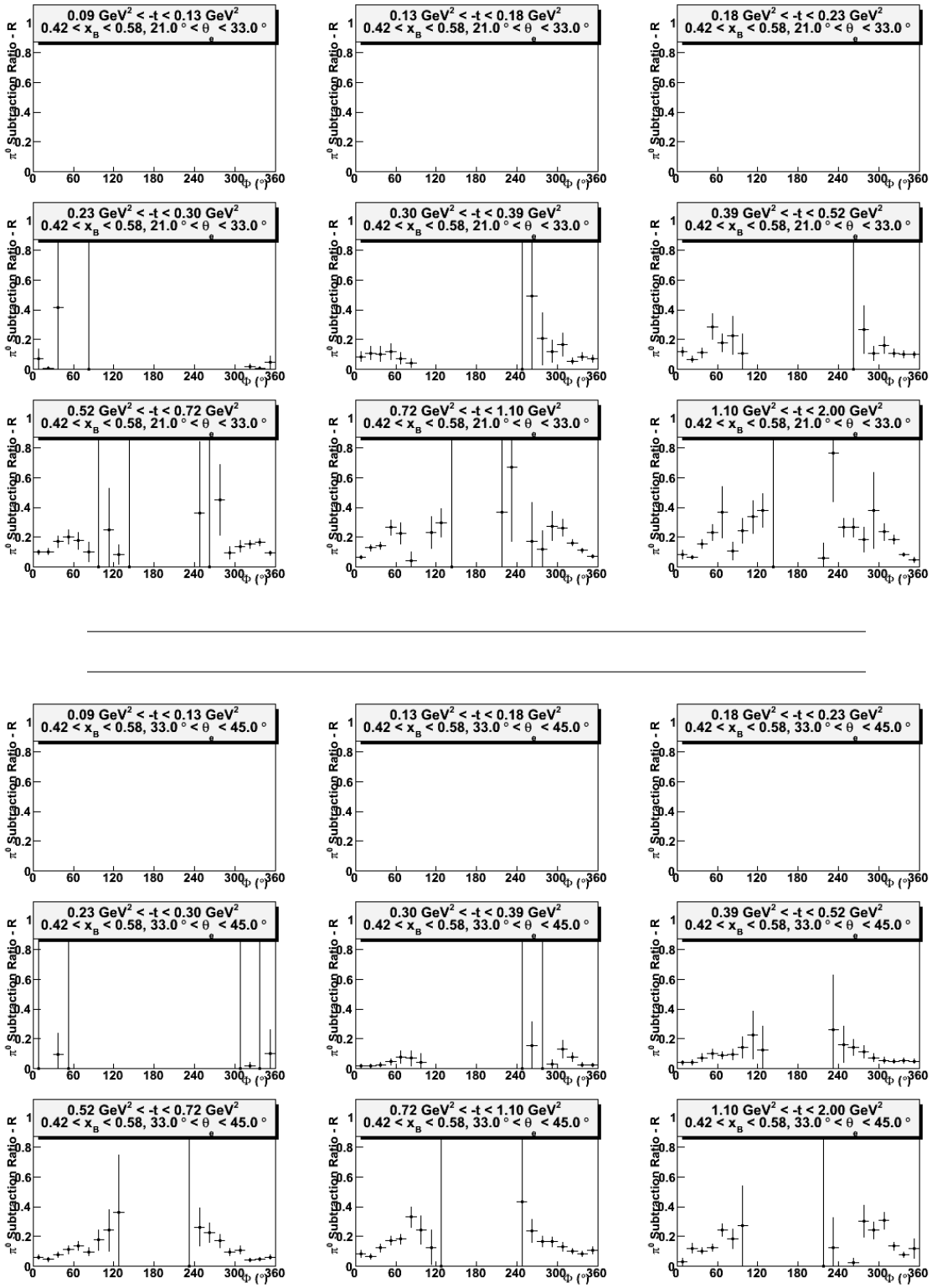

Figure C.11: On top, the neutral pion subtraction ratio $R = \frac{N^{\gamma}_{\pi_0}}{N^{e+p+\gamma}}$ as a function of Φ for the twentieth bin in x_B and θ_e, where $0.42 < x_B < 0.58$ and $21^\circ < \theta_e < 33^\circ$. On bottom, the neutral pion subtraction ratio $R = \frac{N^{\gamma}_{\pi_0}}{N^{e+p+\gamma}}$ as a function of Φ for the twenty-first bin in x_B and θ_e, where $0.42 < x_B < 0.58$ and $33^\circ < \theta_e < 45^\circ$.

D. Complete Results for Radiative Corrections

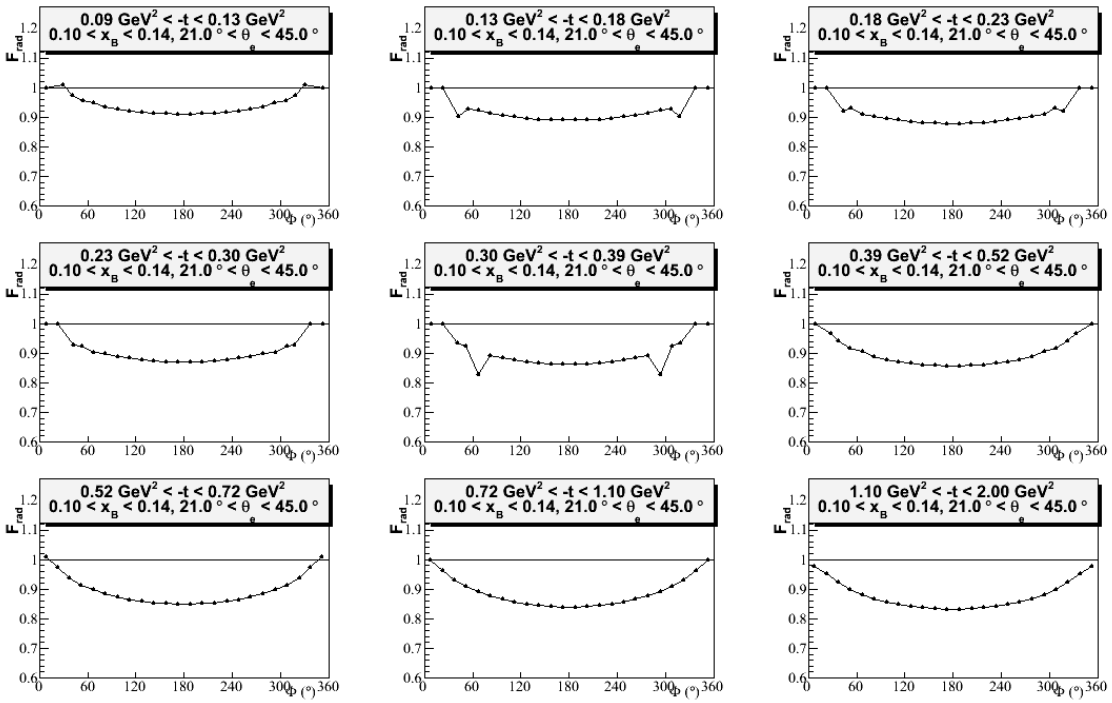

Figure D.1: The radiative corrections as a function of Φ for the first bin in x_B and θ_e, where $0.1 < x_B < 0.14$ and $21^\circ < \theta_e < 45^\circ$.

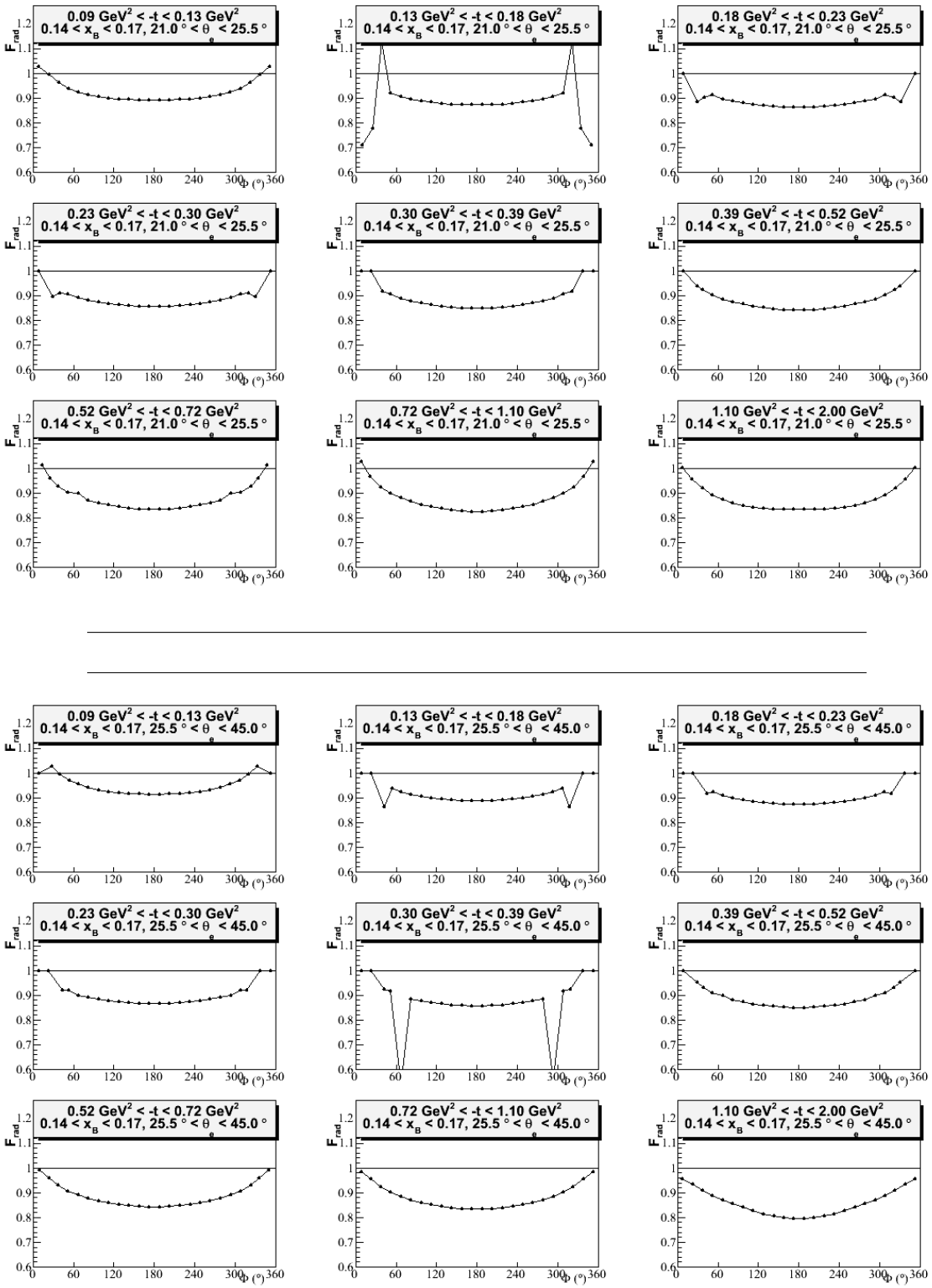

Figure D.2: On top, the radiative corrections as a function of Φ for the second bin in x_B and θ_e, where $0.14 < x_B < 0.17$ and $21^\circ < \theta_e < 25.5^\circ$. On bottom, the radiative corrections as a function of Φ for the third bin in x_B and θ_e, where $0.14 < x_B < 0.17$ and $25.5^\circ < \theta_e < 45^\circ$.

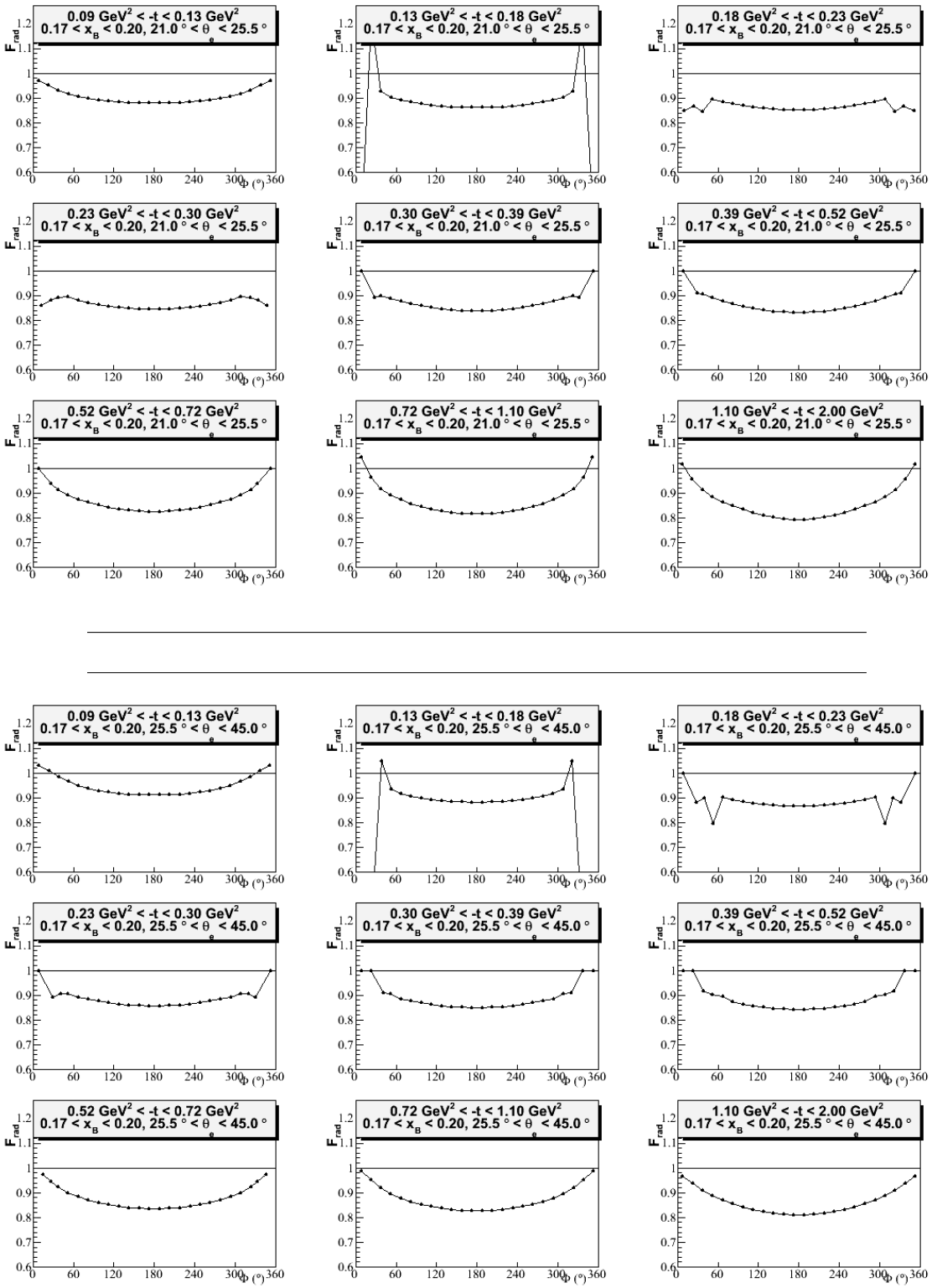

Figure D.3: On top, the radiative corrections as a function of Φ for the fourth bin in x_B and θ_e, where $0.17 < x_B < 0.2$ and $21^\circ < \theta_e < 25.5^\circ$. On bottom, the radiative corrections as a function of Φ for the fifth bin in x_B and θ_e, where $0.17 < x_B < 0.2$ and $25.5^\circ < \theta_e < 45^\circ$.

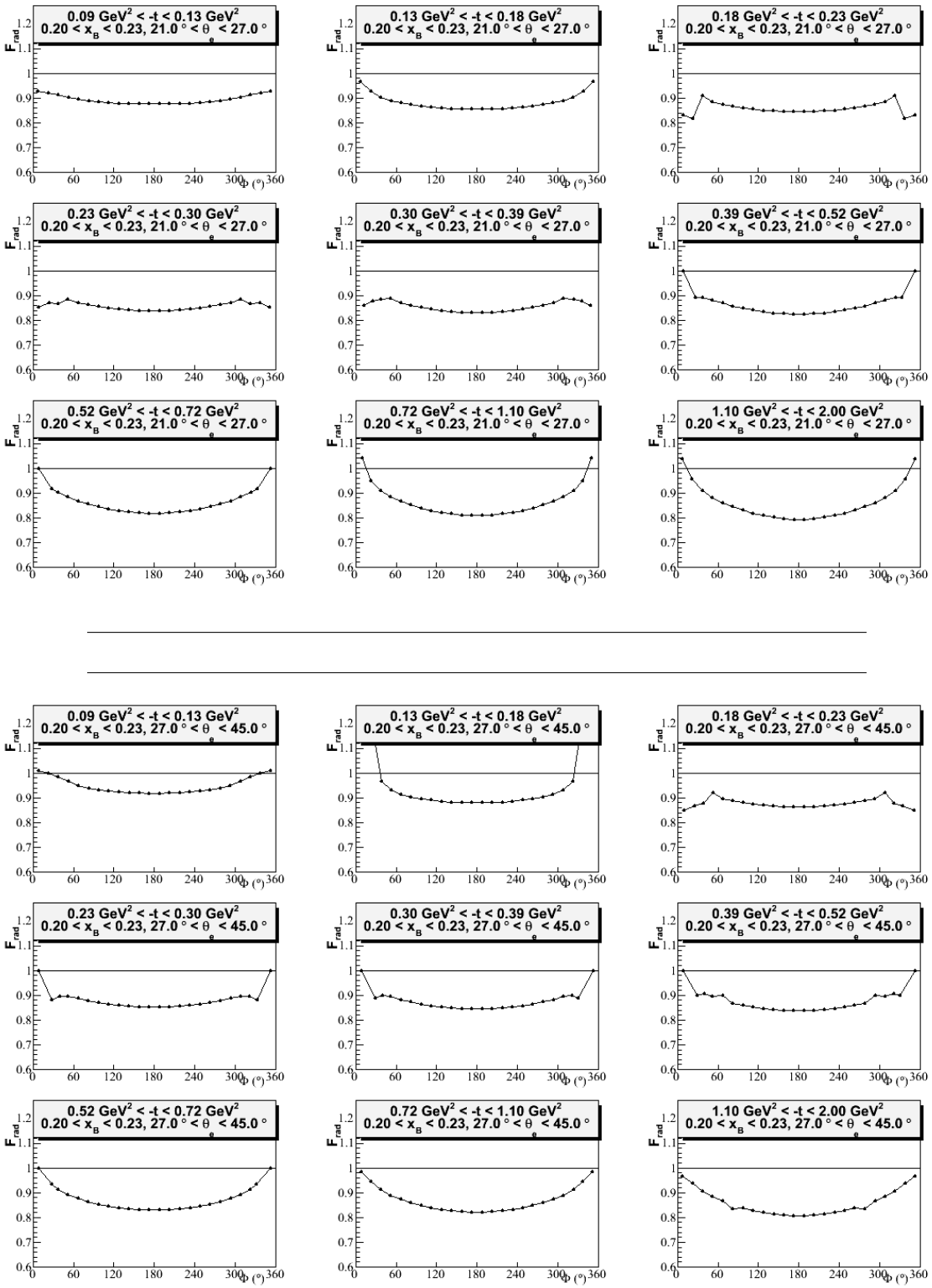

Figure D.4: On top, the radiative corrections as a function of Φ for the sixth bin in x_B and θ_e, where $0.2 < x_B < 0.23$ and $21^\circ < \theta_e < 27^\circ$. On bottom, the radiative corrections as a function of Φ for the seventh bin in x_B and θ_e, where $0.2 < x_B < 0.23$ and $27^\circ < \theta_e < 45^\circ$.

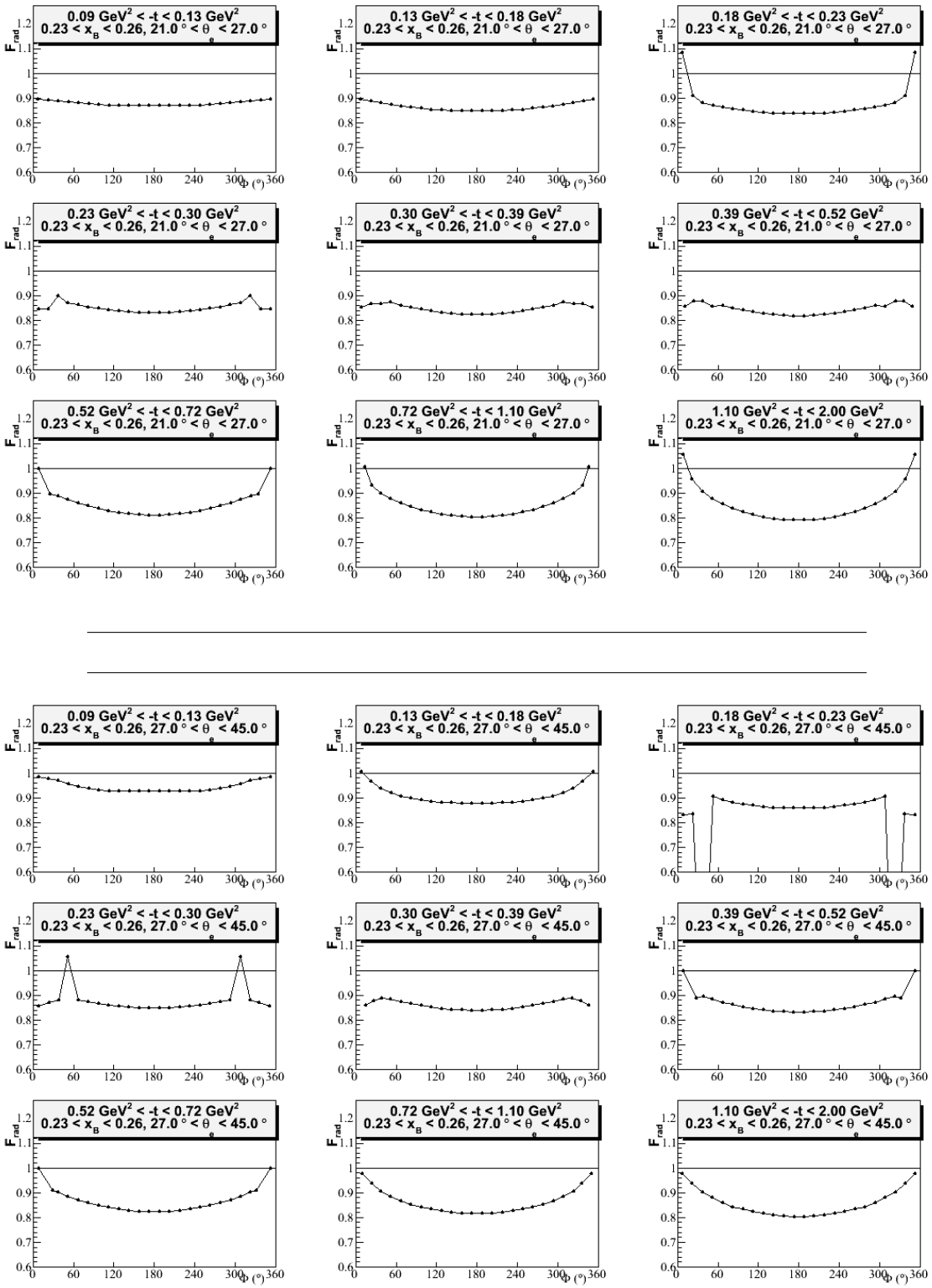

Figure D.5: On top, the radiative corrections as a function of Φ for the eighth bin in x_B and θ_e, where $0.23 < x_B < 0.26$ and $21^\circ < \theta_e < 27^\circ$. On bottom, the radiative corrections as a function of Φ for the ninth bin in x_B and θ_e, where $0.23 < x_B < 0.26$ and $27^\circ < \theta_e < 45^\circ$.

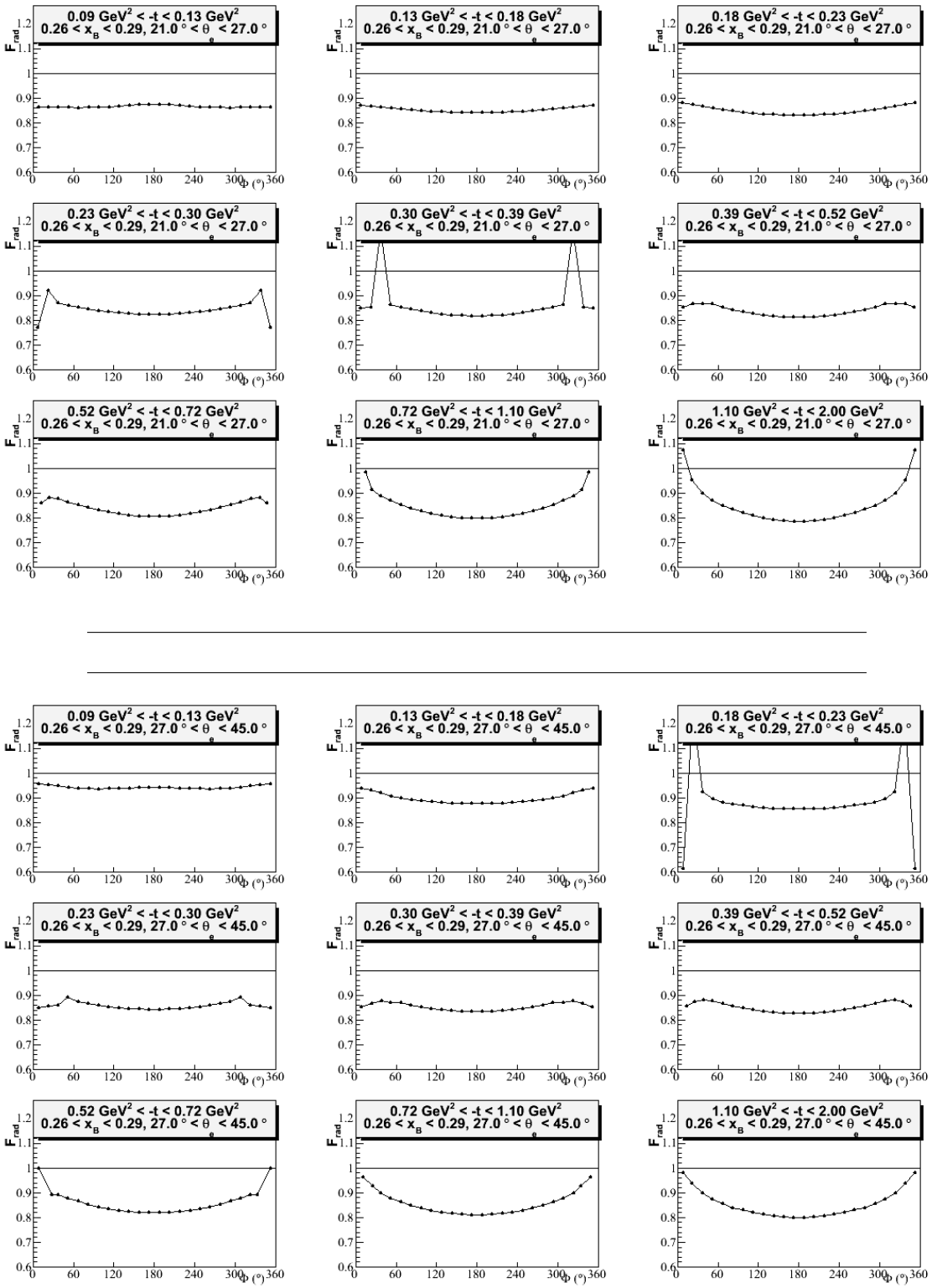

Figure D.6: On top, the radiative corrections as a function of Φ for the tenth bin in x_B and θ_e, where $0.26 < x_B < 0.29$ and $21^\circ < \theta_e < 27^\circ$. On bottom, the radiative corrections as a function of Φ for the eleventh bin in x_B and θ_e, where $0.26 < x_B < 0.29$ and $27^\circ < \theta_e < 45^\circ$.

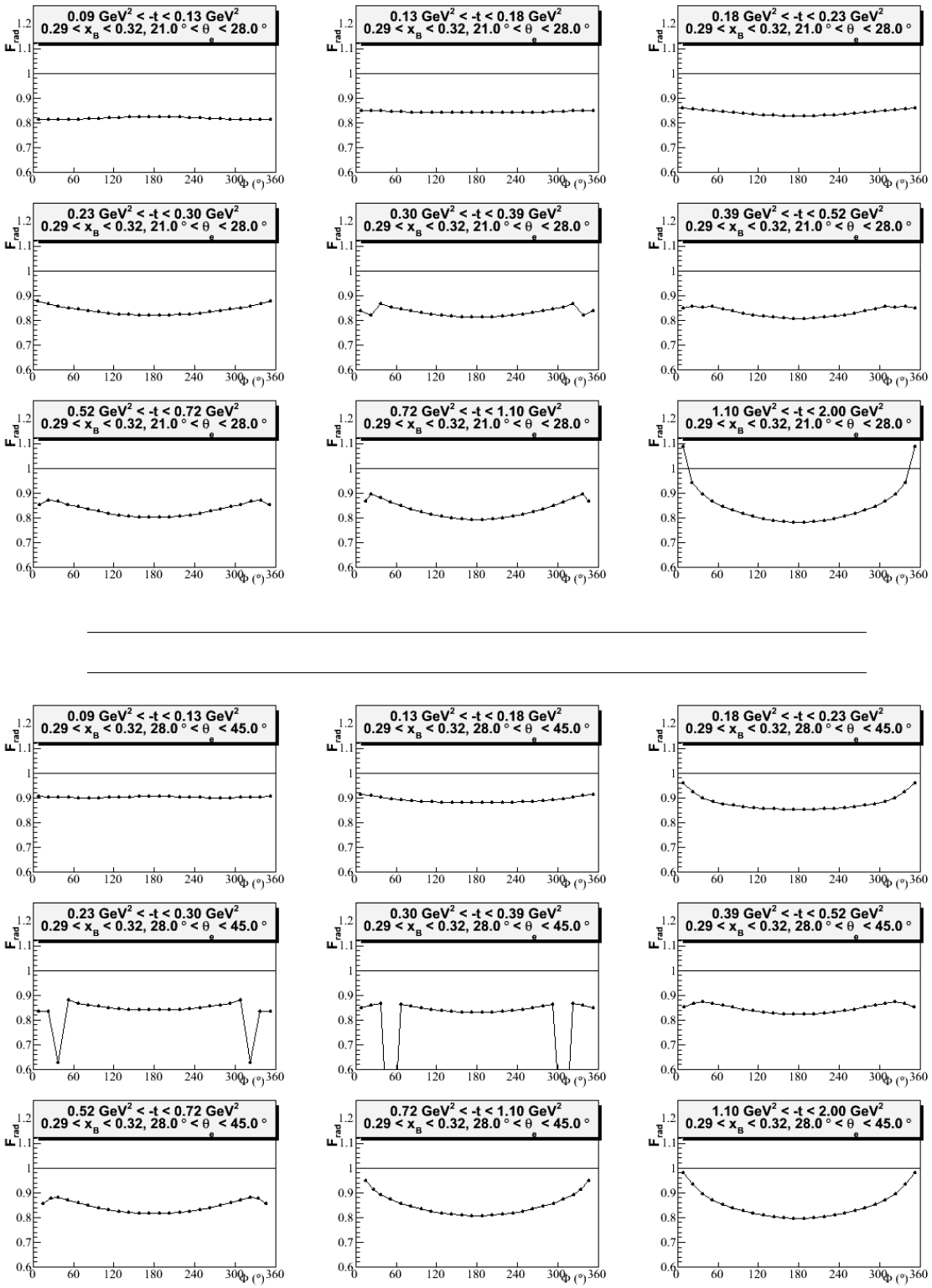

Figure D.7: On top, the radiative corrections as a function of Φ for the twelfth bin in x_B and θ_e, where $0.29 < x_B < 0.32$ and $21^\circ < \theta_e < 28^\circ$. On bottom, the radiative corrections as a function of Φ for the thirteenth bin in x_B and θ_e, where $0.29 < x_B < 0.32$ and $28^\circ < \theta_e < 45^\circ$.

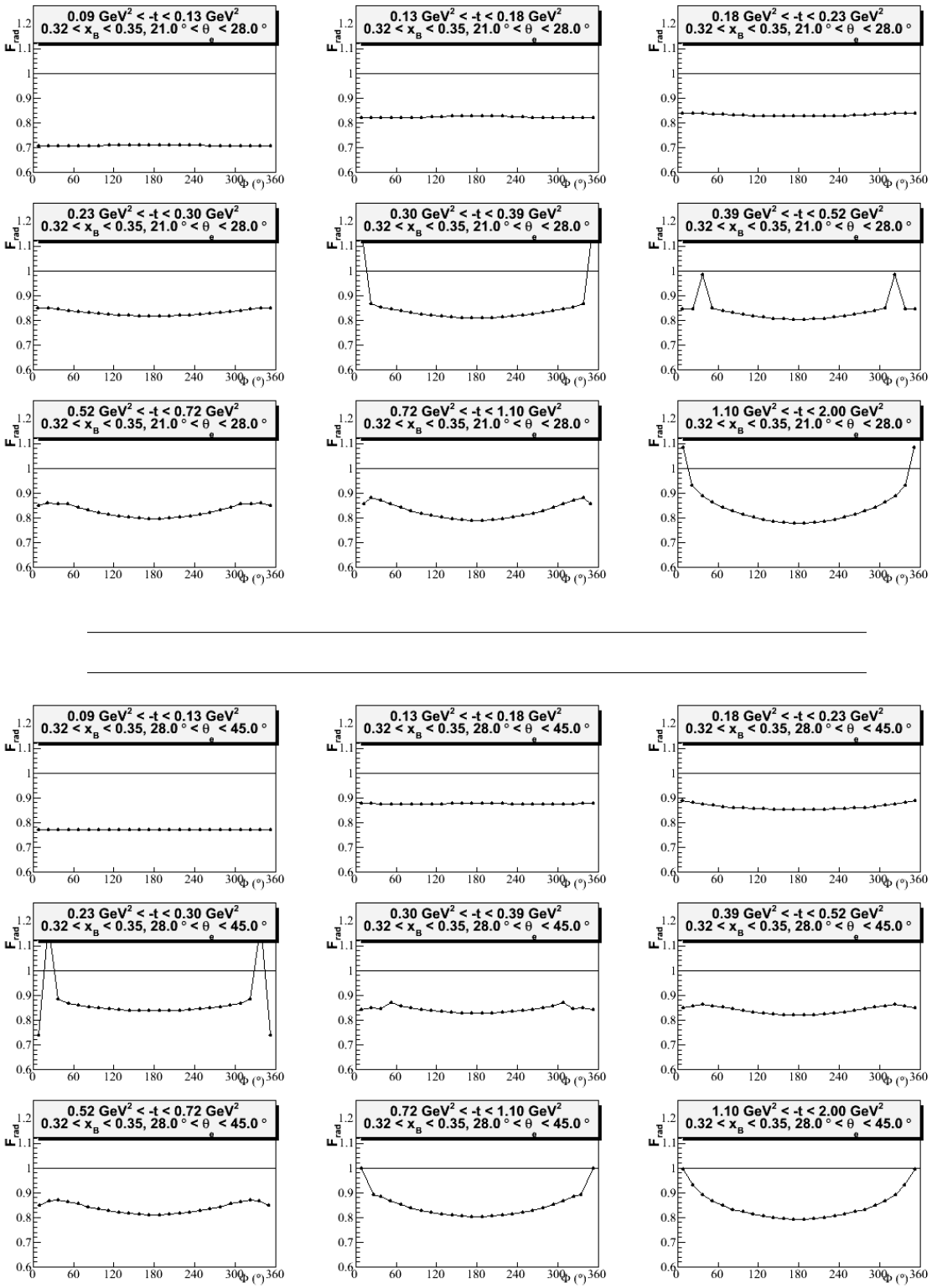

Figure D.8: On top, the radiative corrections as a function of Φ for the fourteenth bin in x_B and θ_e, where $0.32 < x_B < 0.35$ and $21^\circ < \theta_e < 28^\circ$. On bottom, the radiative corrections as a function of Φ for the fifteenth bin in x_B and θ_e, where $0.32 < x_B < 0.35$ and $28^\circ < \theta_e < 45^\circ$.

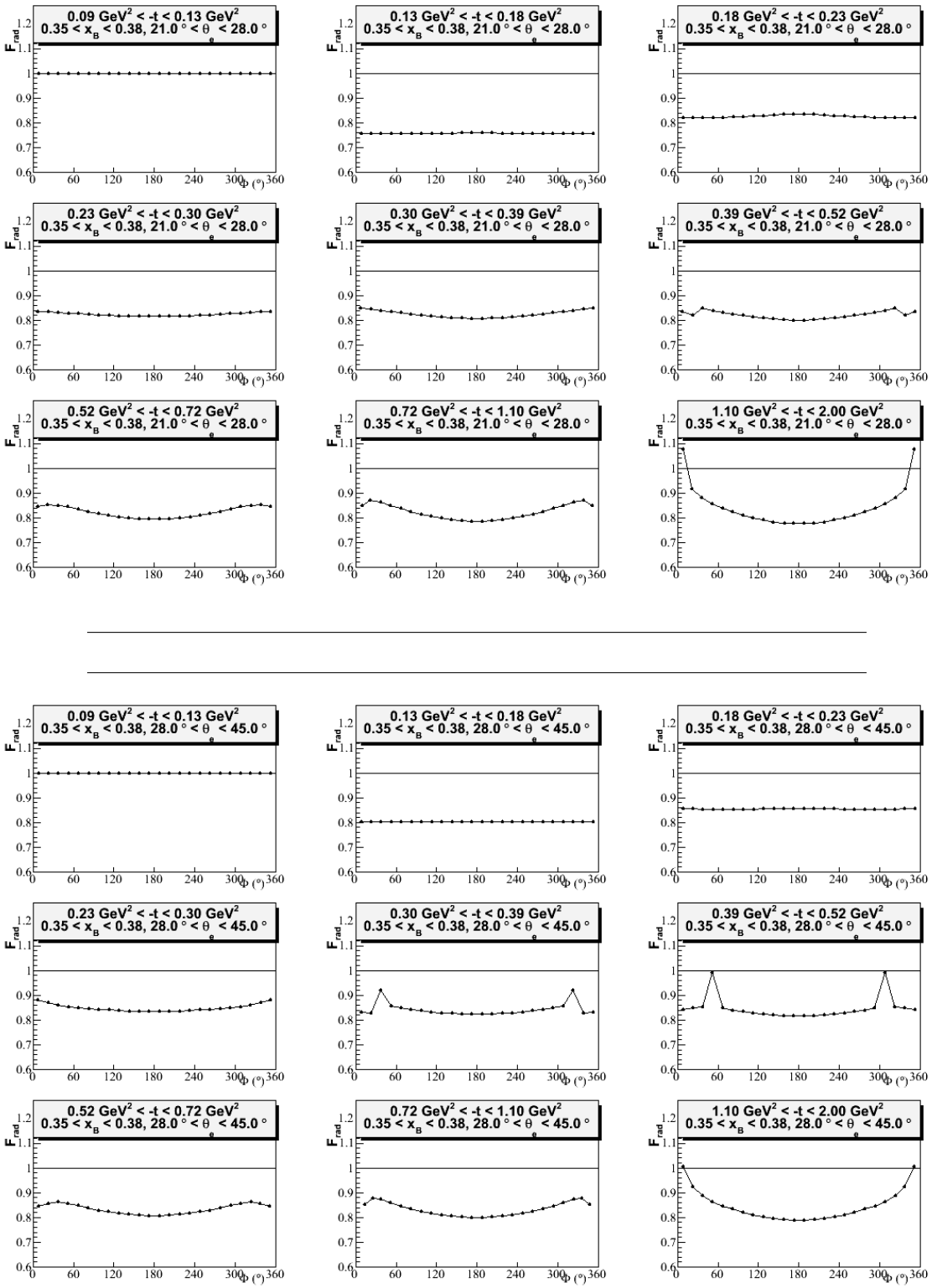

Figure D.9: On top, the radiative corrections as a function of Φ for the sixteenth bin in x_B and θ_e, where $0.35 < x_B < 0.38$ and $21^\circ < \theta_e < 28^\circ$. On bottom, the radiative corrections as a function of Φ for the seventeenth bin in x_B and θ_e, where $0.35 < x_B < 0.38$ and $28^\circ < \theta_e < 45^\circ$.

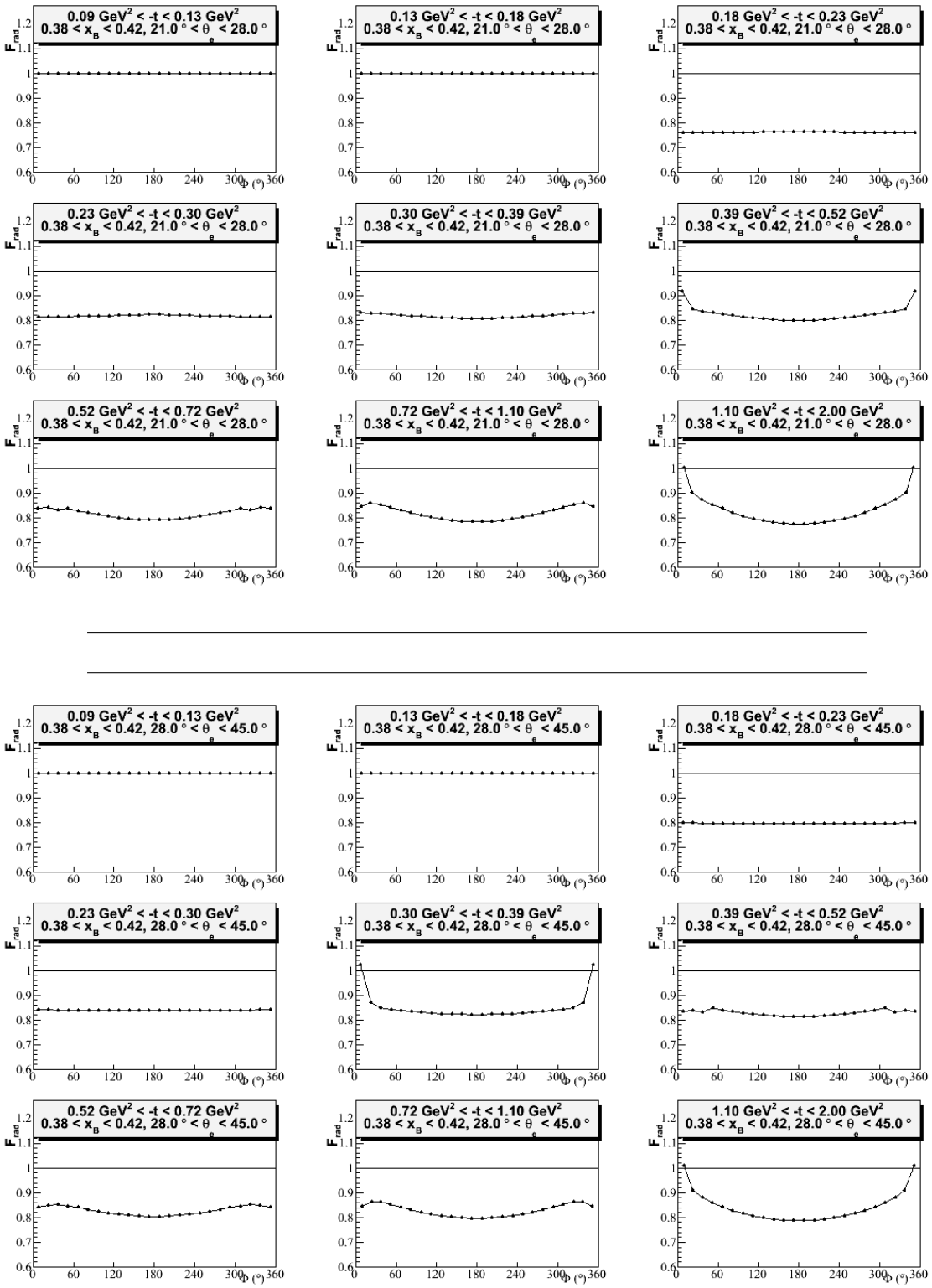

Figure D.10: On top, the radiative corrections as a function of Φ for the eighteenth bin in x_B and θ_e, where $0.38 < x_B < 0.42$ and $21^\circ < \theta_e < 28^\circ$. On bottom, the radiative corrections as a function of Φ for the nineteenth bin in x_B and θ_e, where $0.38 < x_B < 0.42$ and $28^\circ < \theta_e < 45^\circ$.

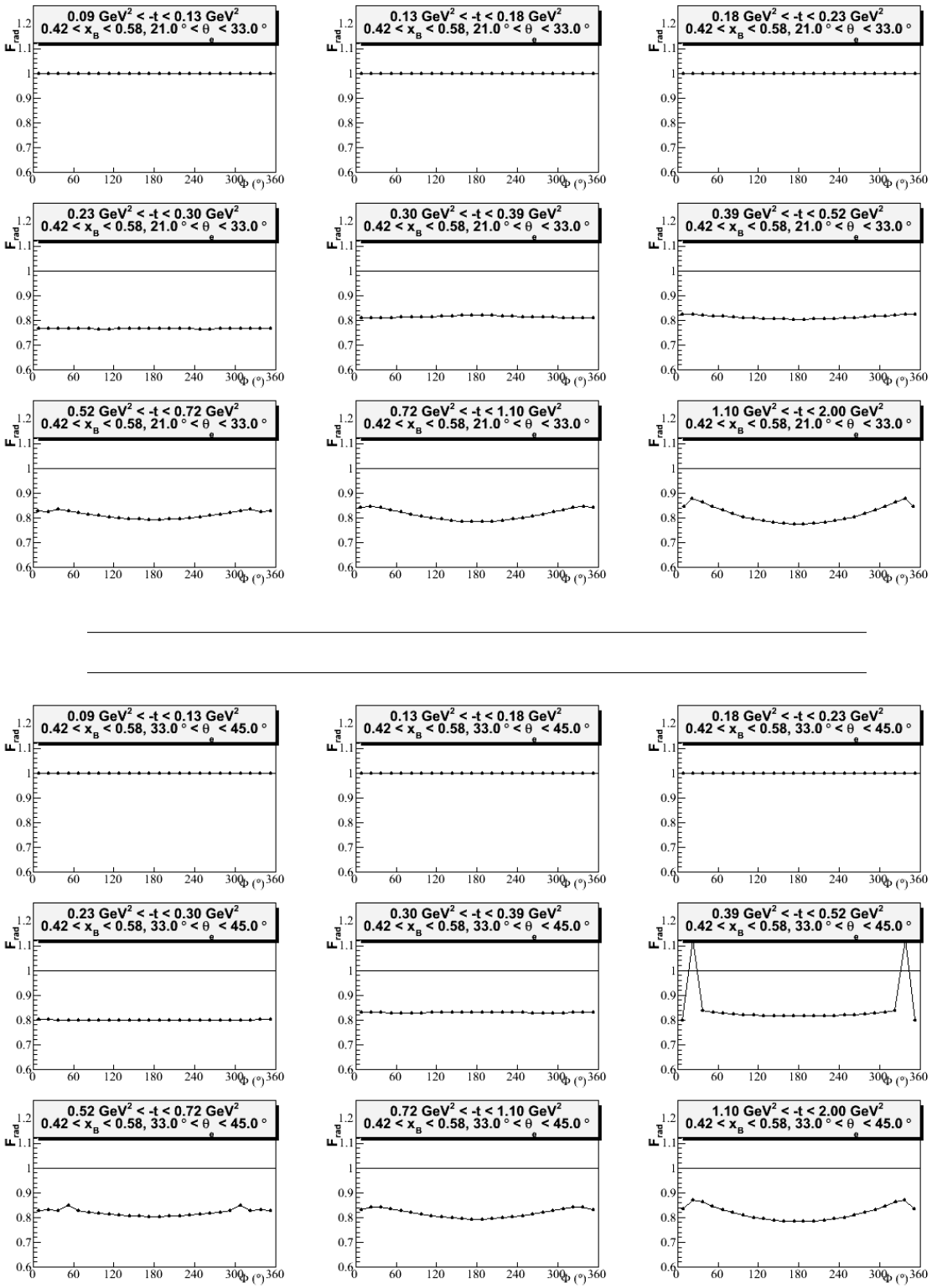

Figure D.11: On top, the radiative corrections as a function of Φ for the twentieth bin in x_B and θ_e, where $0.42 < x_B < 0.58$ and $21^\circ < \theta_e < 33^\circ$. On bottom, the radiative corrections as a function of Φ for the twenty-first bin in x_B and θ_e, where $0.42 < x_B < 0.58$ and $33^\circ < \theta_e < 45^\circ$.

E. Comparison with Parallel Analysis of e1-dvcs2, e1-dvcs1 - Full List of Plots

Comparison of Unpolarized Cross Sections:

Figure E.1 to Figure E.21 each contain the unpolarized cross section, and unpolarized cross section ratio as a function of Φ, for a given bin in x_B and θ_e. The comparison is between this analysis; e1-dvcs2 according to the parallel analysis by B. Guegan; and e1-dvcs1 according to the analysis by H.S. Jo. There are two sets of error bars for data points in this analysis only. The smaller error bar represents statistical errors only. The larger error bar represents the statistical error and estimated systematic error added together in quadrature. The systematic errors for analyses by B. Guegan and H.S. Jo are not yet available, therefore the errors associated with those points are statistical only.

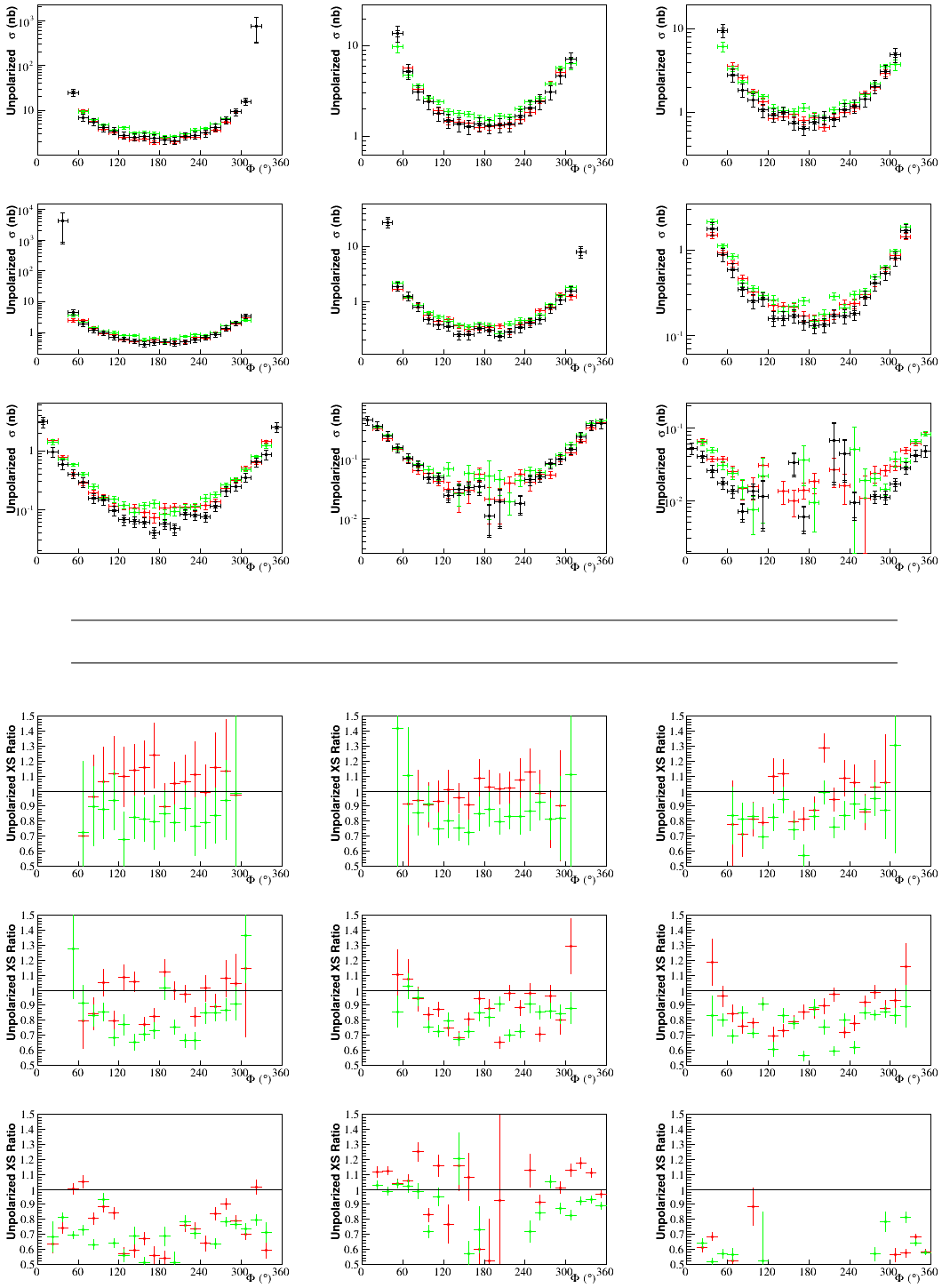

Figure E.1: On top, the unpolarized cross section as a function of Φ. Black represents this analysis. Green is e1-dvcs2 by B. Guegan. Red is e1-dvcs1 by H.S. Jo. On bottom, the unpolarized cross section ratios. Both are for the first bin in x_B and θ_e, where $0.1 < x_B < 0.14$ and $21^\circ < \theta_e < 45^\circ$. Each panel corresponds to a bin in $-t$ whose limits are: [0.09, 0.13, 0.18, 0.23, 0.30, 0.39, 0.52, 0.72, 1.10, 2.00] Green is $\frac{e1-dvcs2\ Saylor}{e1-dvcs2\ Guegan}$. Red is $\frac{e1-dvcs2\ Saylor}{e1-dvcs1\ Jo}$.

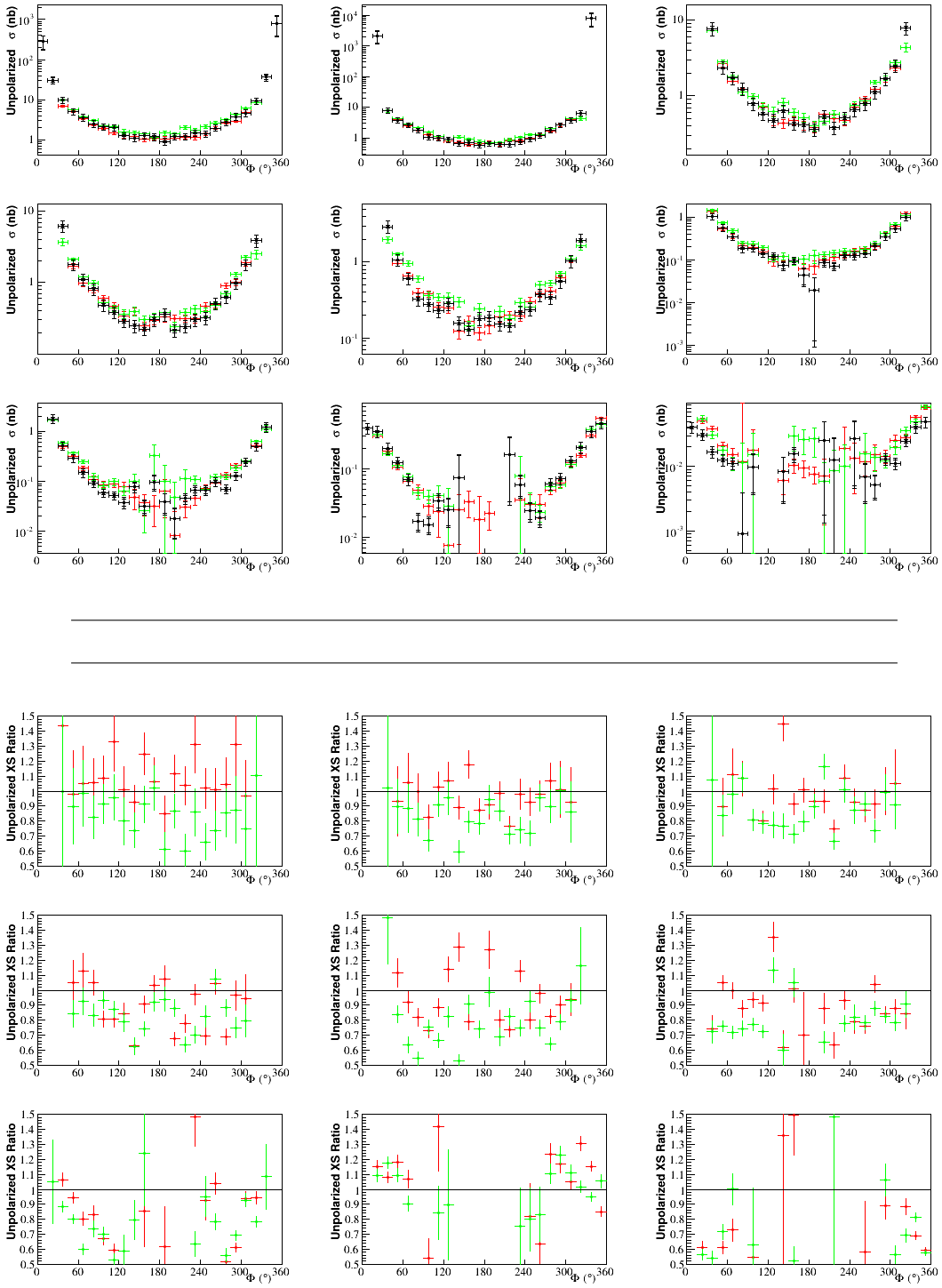

Figure E.2: On top, the unpolarized cross section as a function of Φ. Black represents this analysis. Green is e1-dvcs2 by B. Guegan. Red is e1-dvcs1 by H.S. Jo. On bottom, the unpolarized cross section ratios. Both are for the second bin in x_B and θ_e, where $0.14 < x_B < 0.17$ and $21^\circ < \theta_e < 25.5^\circ$. Each panel corresponds to a bin in $-t$ whose limits are: [0.09, 0.13, 0.18, 0.23, 0.30, 0.39, 0.52, 0.72, 1.10, 2.00] Green is $\frac{e1-dvcs2\ Saylor}{e1-dvcs2\ Guegan}$. Red is $\frac{e1-dvcs2\ Saylor}{e1-dvcs1\ Jo}$.

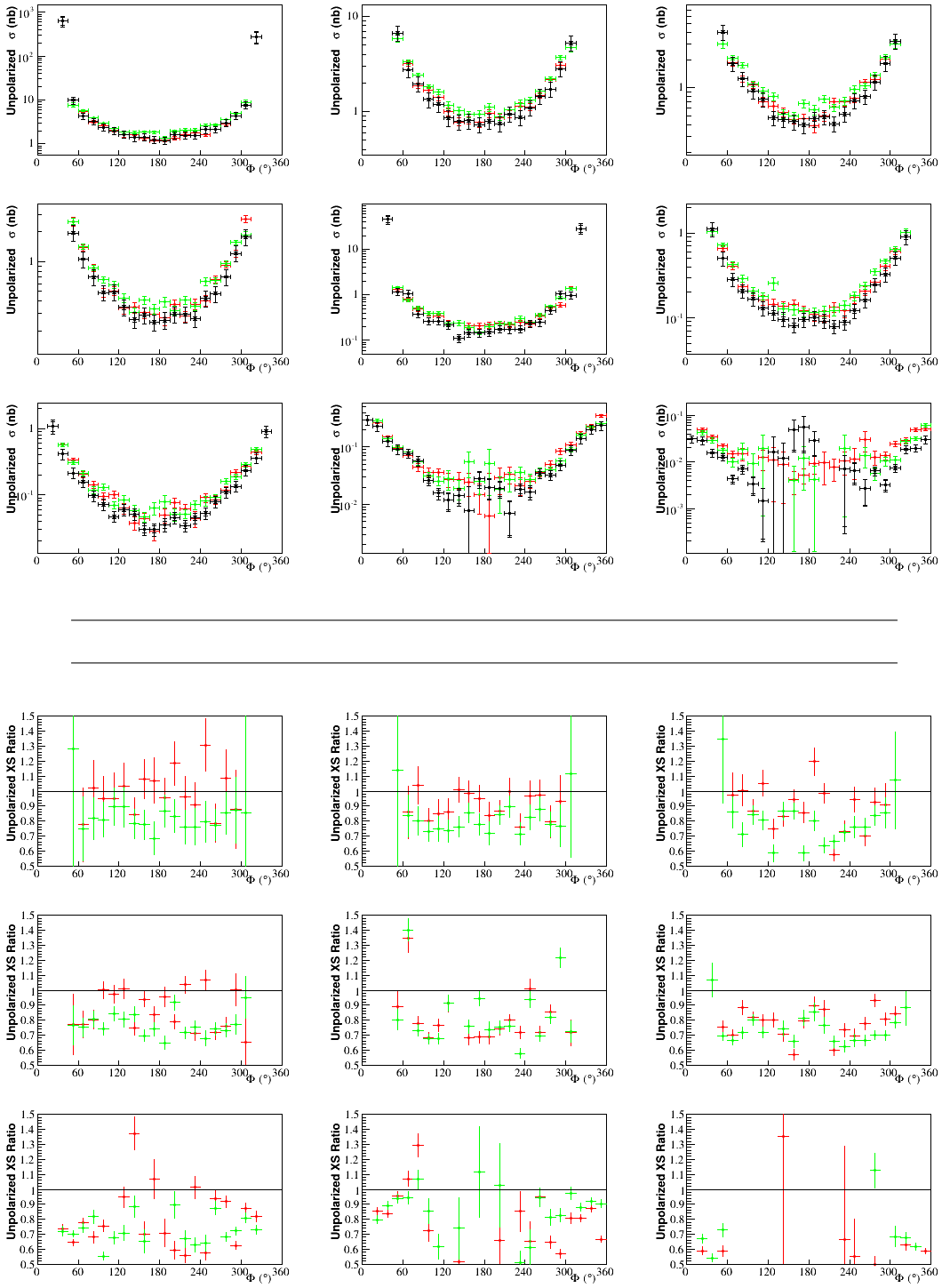

Figure E.3: On top, the unpolarized cross section as a function of Φ. Black represents this analysis. Green is e1-dvcs2 by B. Guegan. Red is e1-dvcs1 by H.S. Jo. On bottom, the unpolarized cross section ratios. Both are for the third bin in x_B and θ_e, where $0.14 < x_B < 0.17$ and $25.5^\circ < \theta_e < 45^\circ$. Each panel corresponds to a bin in $-t$ whose limits are: [0.09, 0.13, 0.18, 0.23, 0.30, 0.39, 0.52, 0.72, 1.10, 2.00] Green is $\frac{e1-dvcs2\ Saylor}{e1-dvcs2\ Guegan}$. Red is $\frac{e1-dvcs2\ Saylor}{e1-dvcs1\ Jo}$.

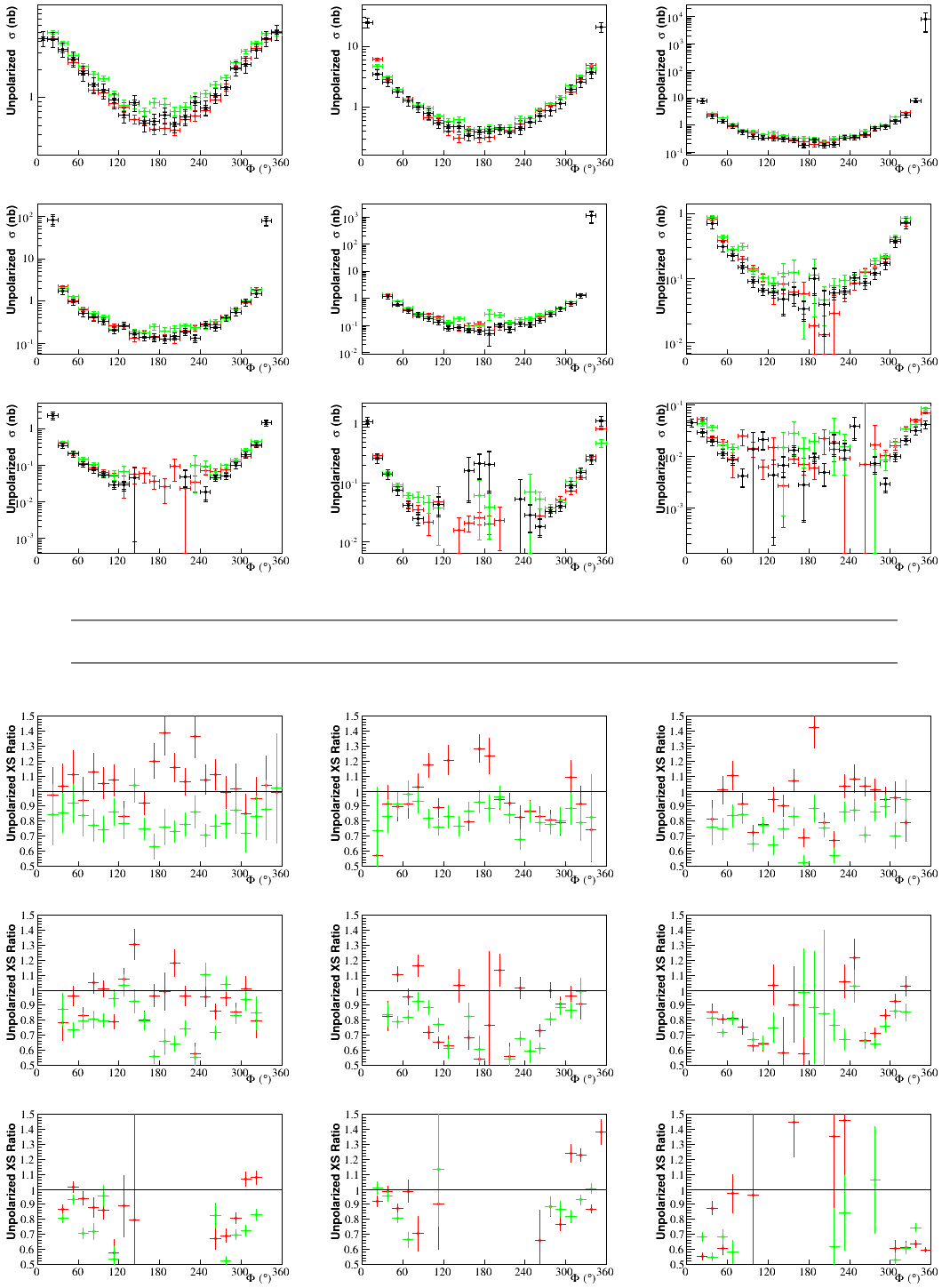

Figure E.4: On top, the unpolarized cross section as a function of Φ. Black represents this analysis. Green is e1-dvcs2 by B. Guegan. Red is e1-dvcs1 by H.S. Jo. On bottom, the unpolarized cross section ratios. Both are for the fourth bin in x_B and θ_e, where $0.17 < x_B < 0.2$ and $21^\circ < \theta_e < 25.5^\circ$. Each panel corresponds to a bin in $-t$ whose limits are: [0.09, 0.13, 0.18, 0.23, 0.30, 0.39, 0.52, 0.72, 1.10, 2.00] Green is $\frac{e1-dvcs2\ Saylor}{e1-dvcs2\ Guegan}$. Red is $\frac{e1-dvcs2\ Saylor}{e1-dvcs1\ Jo}$.

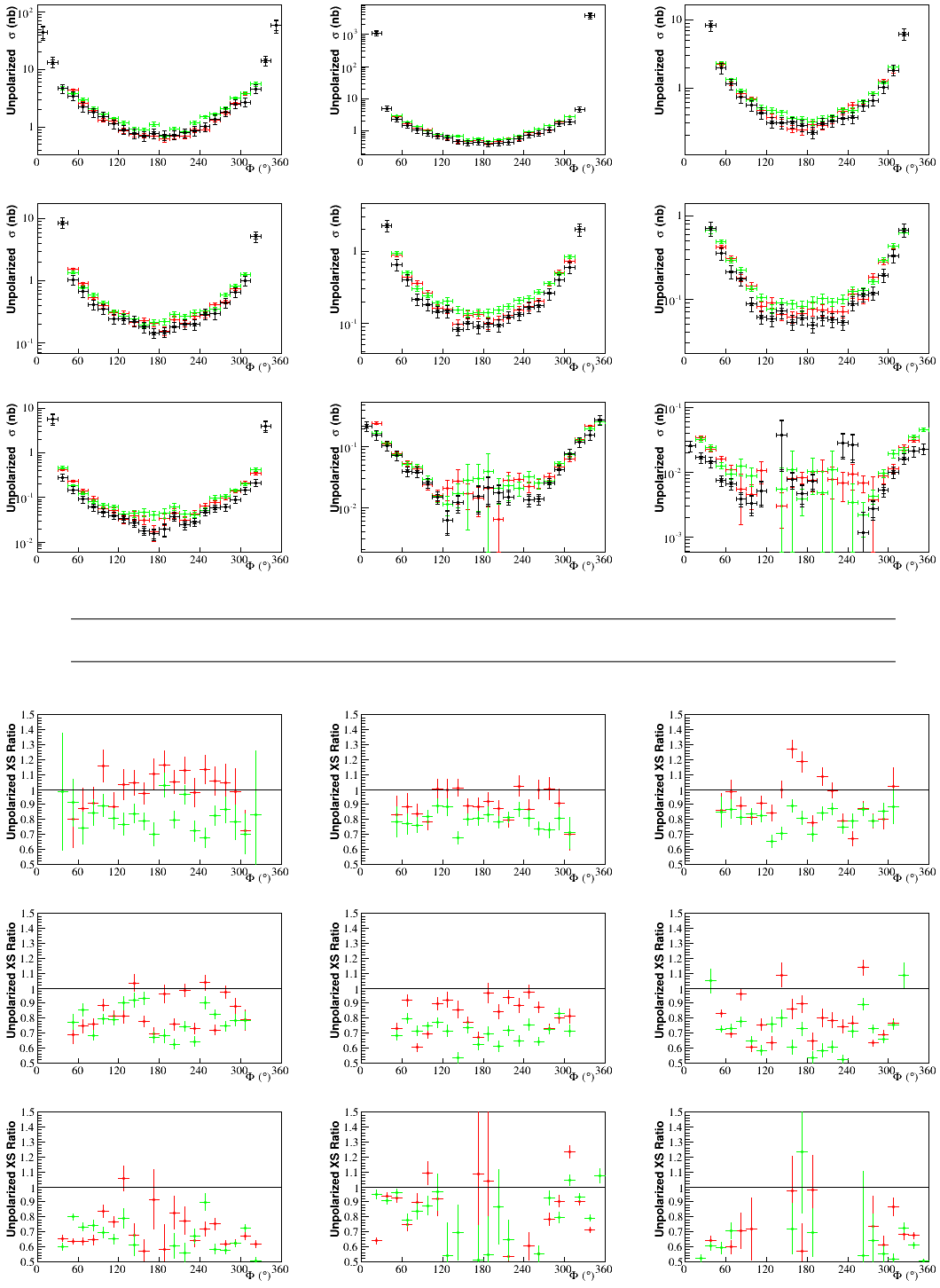

Figure E.5: On top, the unpolarized cross section as a function of Φ. Black represents this analysis. Green is e1-dvcs2 by B. Guegan. Red is e1-dvcs1 by H.S. Jo. On bottom, the unpolarized cross section ratios. Both are for the fifth bin in x_B and θ_e, where $0.17 < x_B < 0.2$ and $25.5^\circ < \theta_e < 45^\circ$. Each panel corresponds to a bin in $-t$ whose limits are: [0.09, 0.13, 0.18, 0.23, 0.30, 0.39, 0.52, 0.72, 1.10, 2.00] Green is $\frac{e1-dvcs2\ Saylor}{e1-dvcs2\ Guegan}$. Red is $\frac{e1-dvcs2\ Saylor}{e1-dvcs1\ Jo}$.

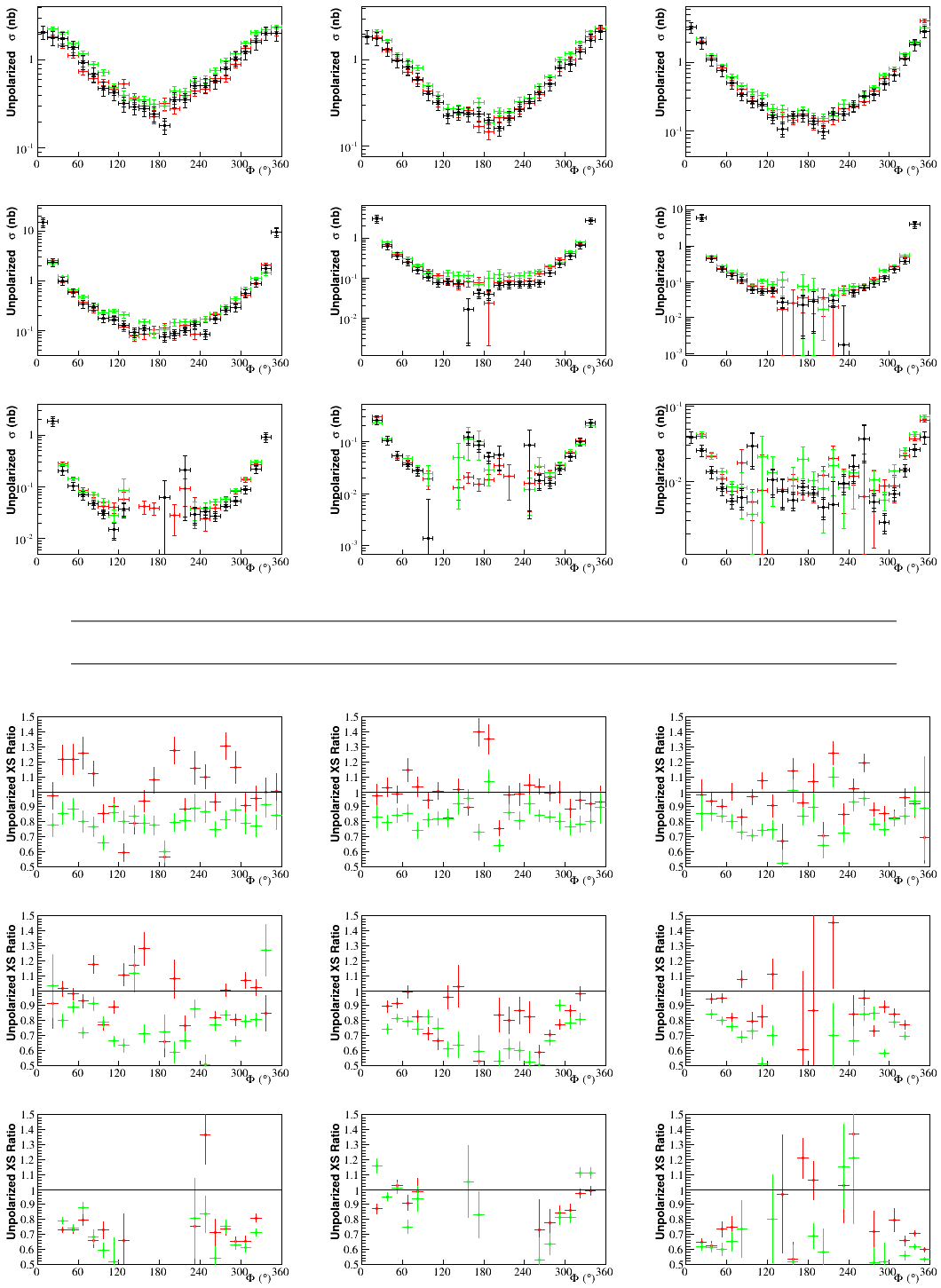

Figure E.6: On top, the unpolarized cross section as a function of Φ. Black represents this analysis. Green is e1-dvcs2 by B. Guegan. Red is e1-dvcs1 by H.S. Jo. On bottom, the unpolarized cross section ratios. Both are for the sixth bin in x_B and θ_e, where $0.2 < x_B < 0.23$ and $21^\circ < \theta_e < 27^\circ$. Each panel corresponds to a bin in $-t$ whose limits are: [0.09, 0.13, 0.18, 0.23, 0.30, 0.39, 0.52, 0.72, 1.10, 2.00] Green is $\frac{e1-dvcs2\ Saylor}{e1-dvcs2\ Guegan}$. Red is $\frac{e1-dvcs2\ Saylor}{e1-dvcs1\ Jo}$.

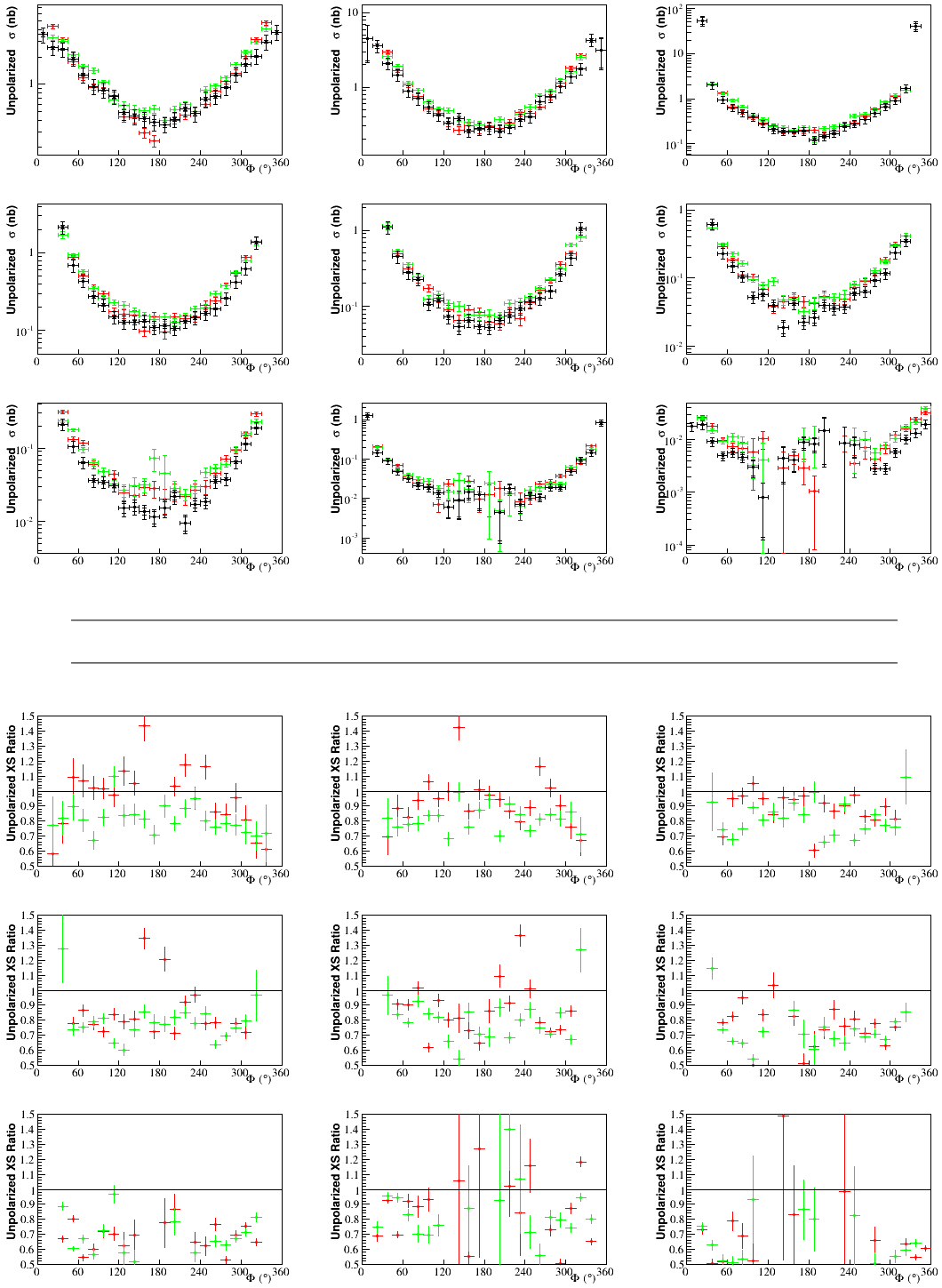

Figure E.7: On top, the unpolarized cross section as a function of Φ. Black represents this analysis. Green is e1-dvcs2 by B. Guegan. Red is e1-dvcs1 by H.S. Jo. On bottom, the unpolarized cross section ratios. Both are for the seventh bin in x_B and θ_e, where $0.2 < x_B < 0.23$ and $27^\circ < \theta_e < 45^\circ$. Each panel corresponds to a bin in $-t$ whose limits are: [0.09, 0.13, 0.18, 0.23, 0.30, 0.39, 0.52, 0.72, 1.10, 2.00] Green is $\frac{e1-dvcs2\ Saylor}{e1-dvcs2\ Guegan}$. Red is $\frac{e1-dvcs2\ Saylor}{e1-dvcs1\ Jo}$.

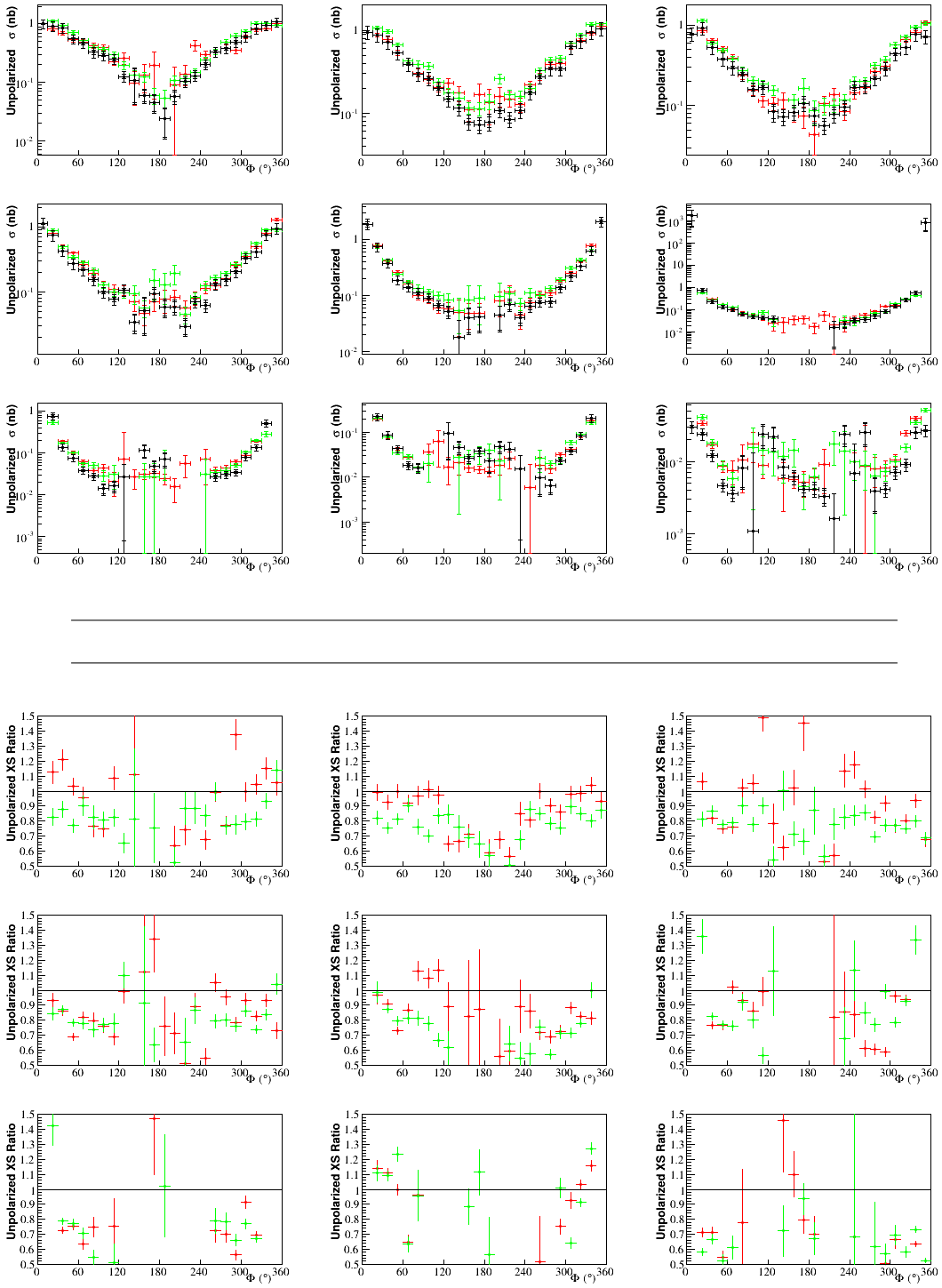

Figure E.8: On top, the unpolarized cross section as a function of Φ. Black represents this analysis. Green is e1-dvcs2 by B. Guegan. Red is e1-dvcs1 by H.S. Jo. On bottom, the unpolarized cross section ratios. Both are for the eighth bin in x_B and θ_e, where $0.23 < x_B < 0.26$ and $21^\circ < \theta_e < 27^\circ$. Each panel corresponds to a bin in $-t$ whose limits are: [0.09, 0.13, 0.18, 0.23, 0.30, 0.39, 0.52, 0.72, 1.10, 2.00] Green is $\frac{e1-dvcs2\ Saylor}{e1-dvcs2\ Guegan}$. Red is $\frac{e1-dvcs2\ Saylor}{e1-dvcs1\ Jo}$.

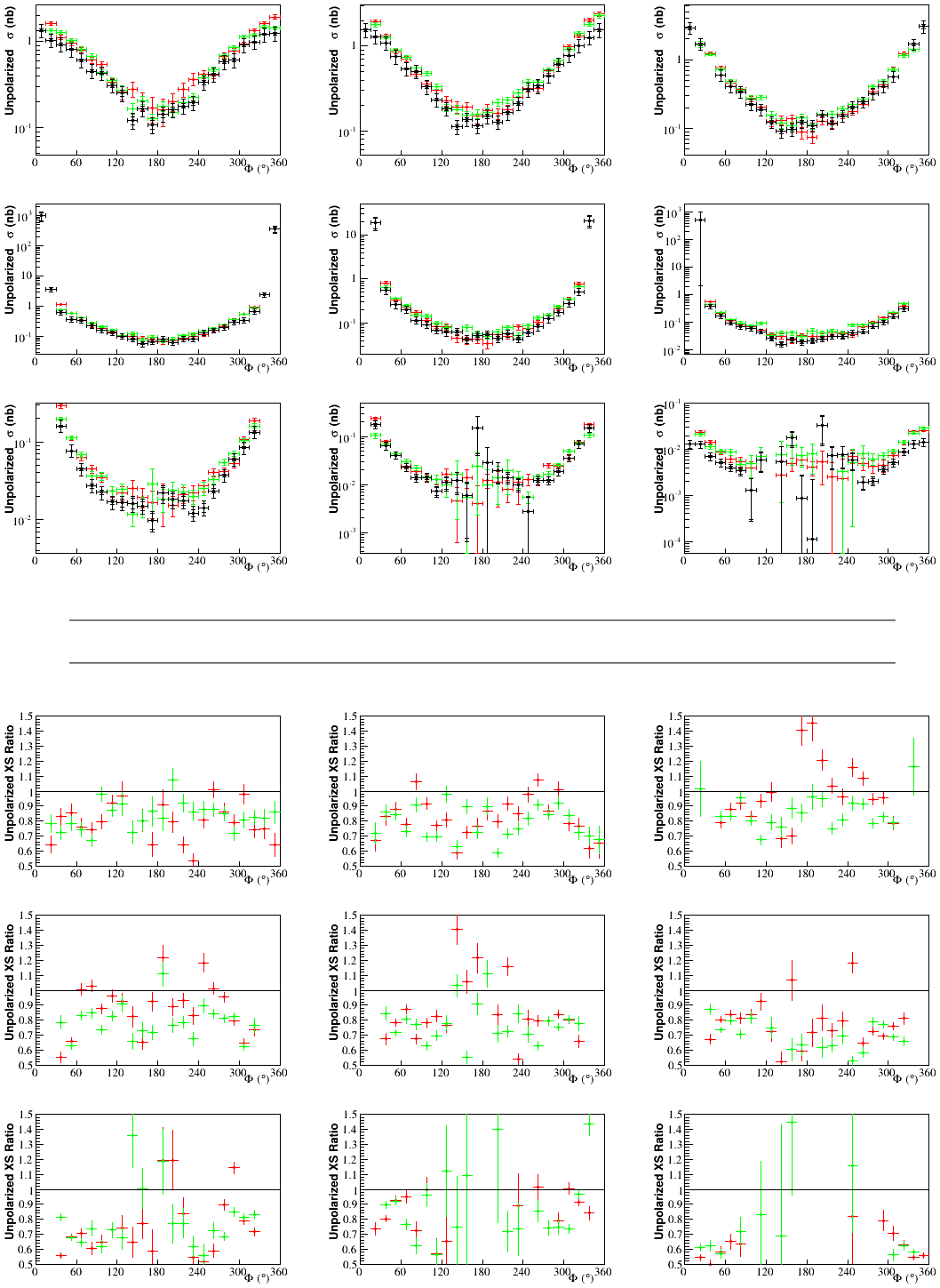

Figure E.9: On top, the unpolarized cross section as a function of Φ. Black represents this analysis. Green is e1-dvcs2 by B. Guegan. Red is e1-dvcs1 by H.S. Jo. On bottom, the unpolarized cross section ratios. Both are for the ninth bin in x_B and θ_e, where $0.23 < x_B < 0.26$ and $27^\circ < \theta_e < 45^\circ$. Each panel corresponds to a bin in $-t$ whose limits are: [0.09, 0.13, 0.18, 0.23, 0.30, 0.39, 0.52, 0.72, 1.10, 2.00] Green is $\frac{e1-dvcs2\ Saylor}{e1-dvcs2\ Guegan}$. Red is $\frac{e1-dvcs2\ Saylor}{e1-dvcs1\ Jo}$.

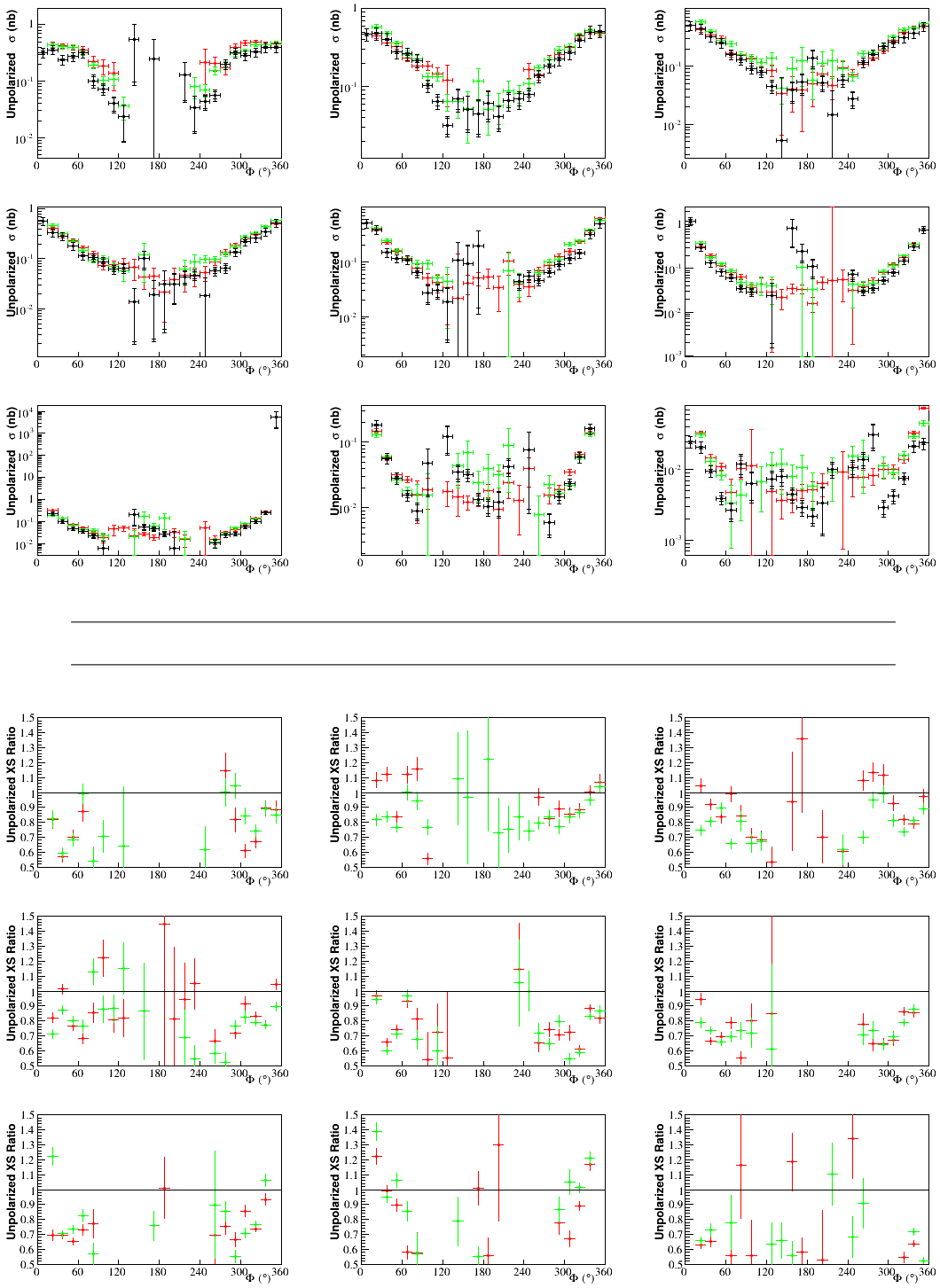

Figure E.10: On top, the unpolarized cross section as a function of Φ. Black represents this analysis. Green is e1-dvcs2 by B. Guegan. Red is e1-dvcs1 by H.S. Jo. On bottom, the unpolarized cross section ratios. Both are for the tenth bin in x_B and θ_e, where $0.26 < x_B < 0.29$ and $21^\circ < \theta_e < 27^\circ$. Each panel corresponds to a bin in $-t$ whose limits are: [0.09, 0.13, 0.18, 0.23, 0.30, 0.39, 0.52, 0.72, 1.10, 2.00] Green is $\frac{e1-dvcs2\ Saylor}{e1-dvcs2\ Guegan}$. Red is $\frac{e1-dvcs2\ Saylor}{e1-dvcs1\ Jo}$.

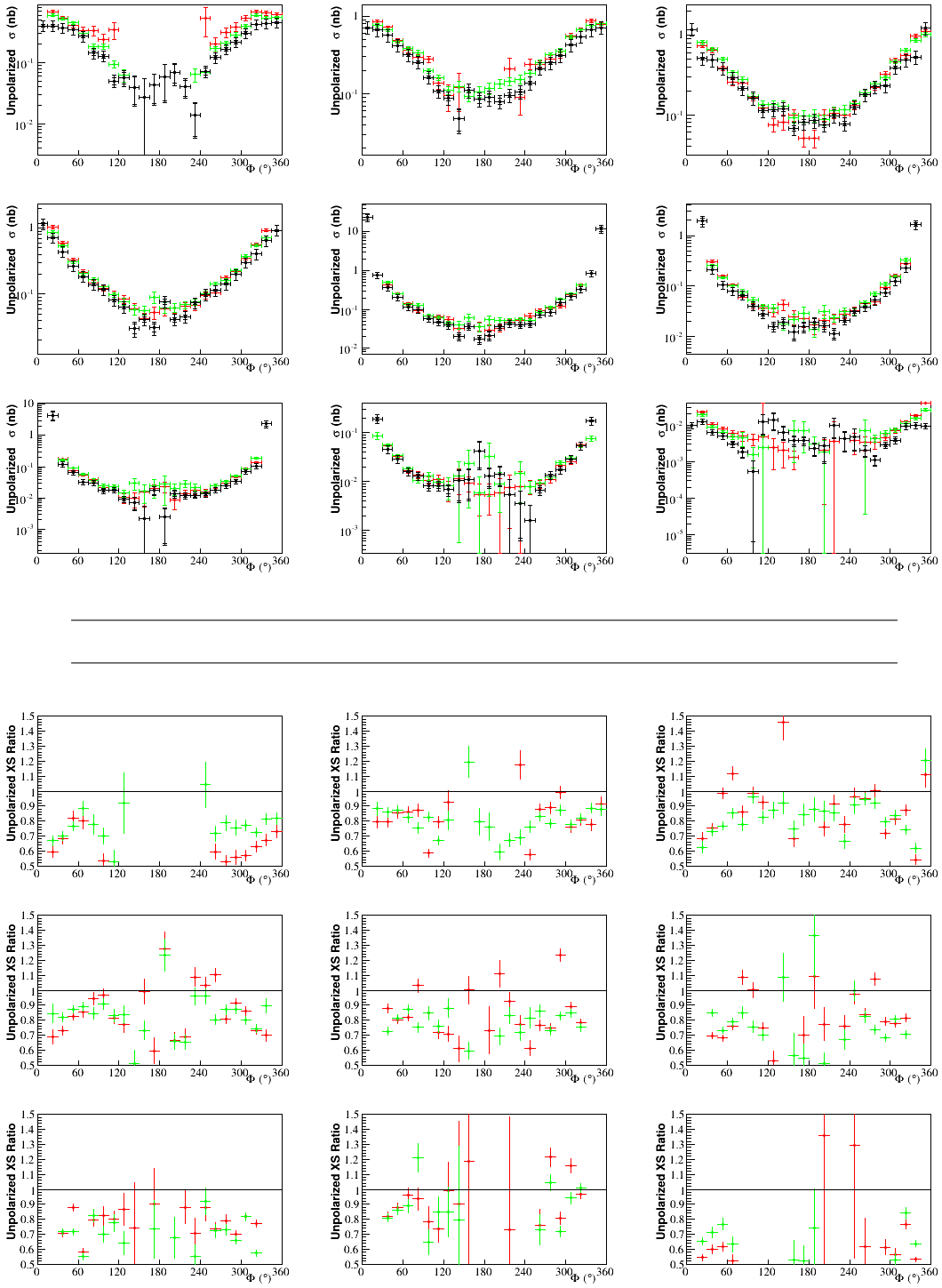

Figure E.11: On top, the unpolarized cross section as a function of Φ. Black represents this analysis. Green is e1-dvcs2 by B. Guegan. Red is e1-dvcs1 by H.S. Jo. On bottom, the unpolarized cross section ratios. Both are for the eleventh bin in x_B and θ_e, where $0.26 < x_B < 0.29$ and $27^\circ < \theta_e < 45^\circ$. Each panel corresponds to a bin in $-t$ whose limits are: [0.09, 0.13, 0.18, 0.23, 0.30, 0.39, 0.52, 0.72, 1.10, 2.00] Green is $\frac{e1-dvcs2\ Saylor}{e1-dvcs2\ Guegan}$. Red is $\frac{e1-dvcs2\ Saylor}{e1-dvcs1\ Jo}$.

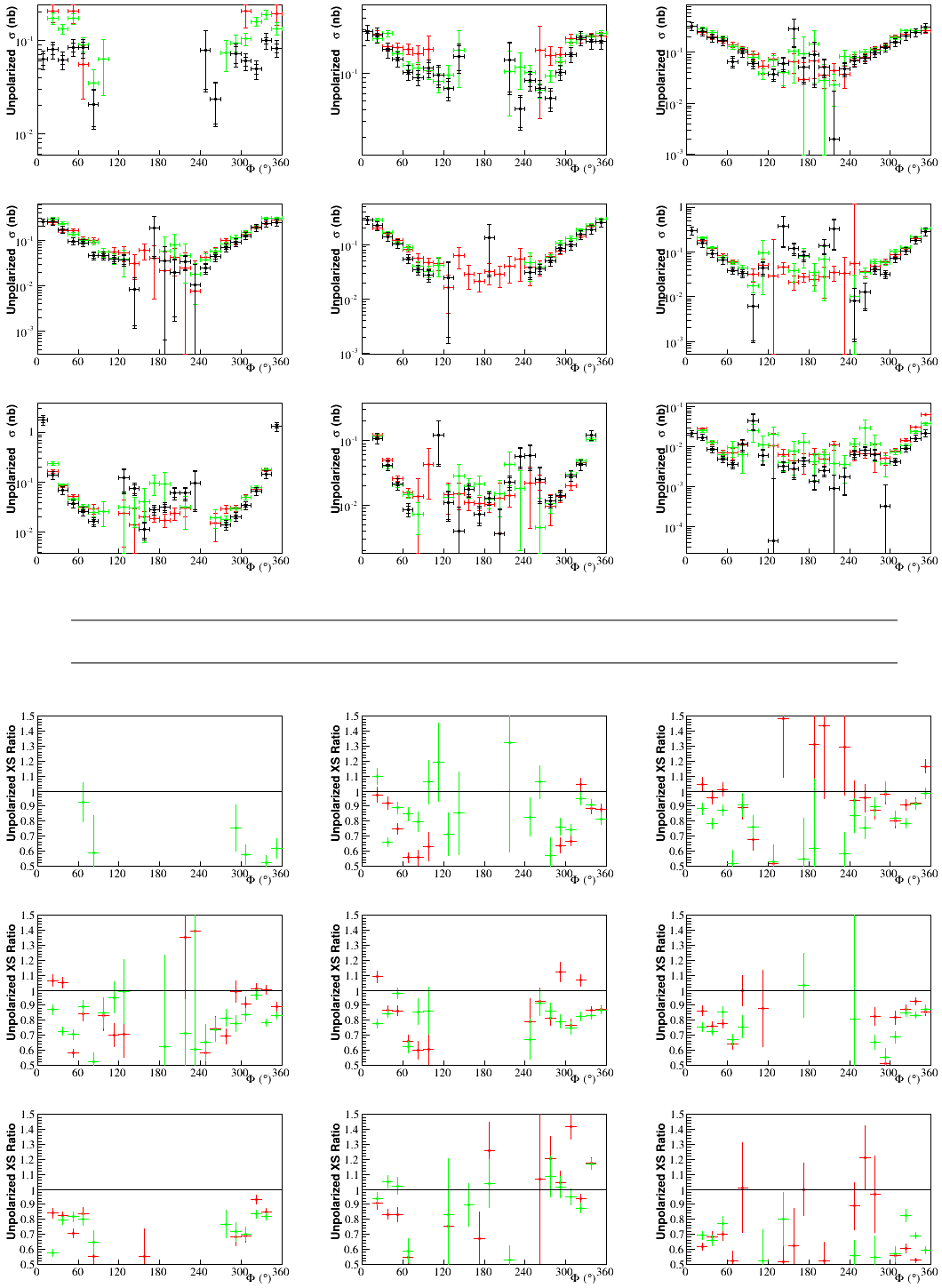

Figure E.12: On top, the unpolarized cross section as a function of Φ. Black represents this analysis. Green is e1-dvcs2 by B. Guegan. Red is e1-dvcs1 by H.S. Jo. On bottom, the unpolarized cross section ratios. Both are for the twelfth bin in x_B and θ_e, where $0.29 < x_B < 0.32$ and $21^\circ < \theta_e < 28^\circ$. Each panel corresponds to a bin in $-t$ whose limits are: [0.09, 0.13, 0.18, 0.23, 0.30, 0.39, 0.52, 0.72, 1.10, 2.00] Green is $\frac{e1-dvcs2\ Saylor}{e1-dvcs2\ Guegan}$. Red is $\frac{e1-dvcs2\ Saylor}{e1-dvcs1\ Jo}$.

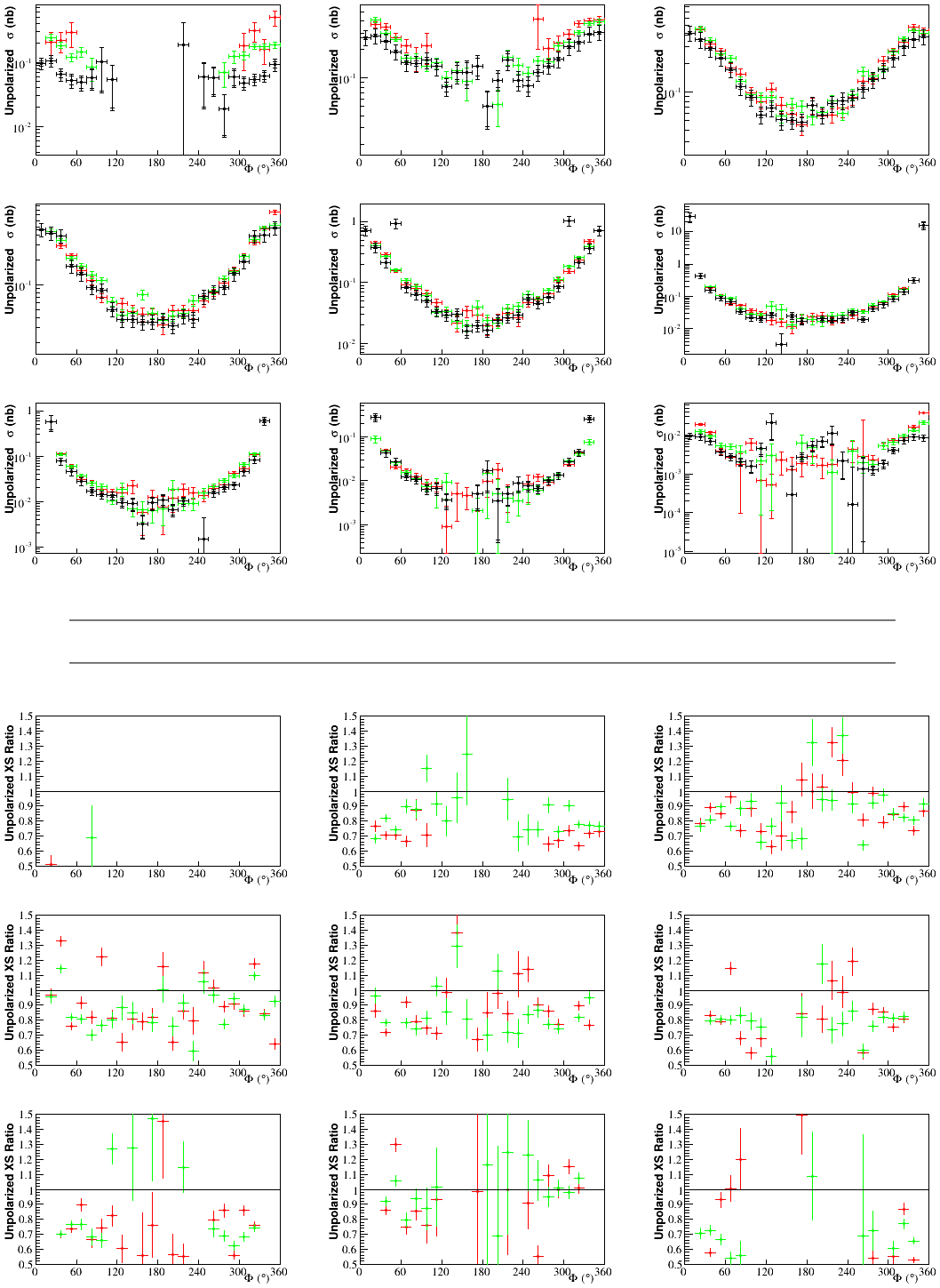

Figure E.13: On top, the unpolarized cross section as a function of Φ. Black represents this analysis. Green is e1-dvcs2 by B. Guegan. Red is e1-dvcs1 by H.S. Jo. On bottom, the unpolarized cross section ratios. Both are for the thirteenth bin in x_B and θ_e, where $0.29 < x_B < 0.32$ and $28^\circ < \theta_e < 45^\circ$. Each panel corresponds to a bin in $-t$ whose limits are: [0.09, 0.13, 0.18, 0.23, 0.30, 0.39, 0.52, 0.72, 1.10, 2.00] Green is $\frac{e1-dvcs2\ Saylor}{e1-dvcs2\ Guegan}$. Red is $\frac{e1-dvcs2\ Saylor}{e1-dvcs1\ Jo}$.

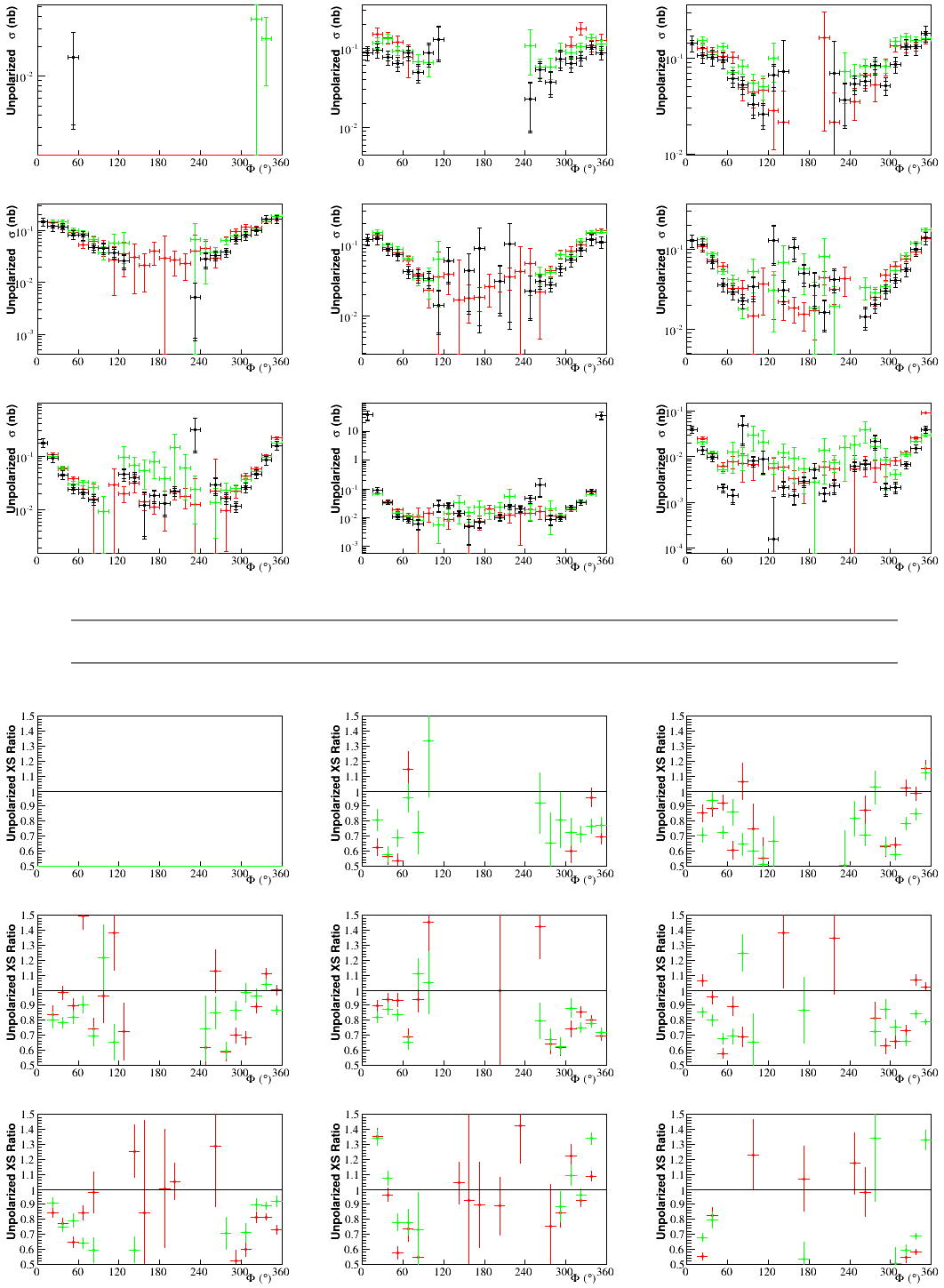

Figure E.14: On top, the unpolarized cross section as a function of Φ. Black represents this analysis. Green is e1-dvcs2 by B. Guegan. Red is e1-dvcs1 by H.S. Jo. On bottom, the unpolarized cross section ratios. Both are for the fourteenth bin in x_B and θ_e, where $0.32 < x_B < 0.35$ and $21^\circ < \theta_e < 28^\circ$. Each panel corresponds to a bin in $-t$ whose limits are: [0.09, 0.13, 0.18, 0.23, 0.30, 0.39, 0.52, 0.72, 1.10, 2.00] Green is $\frac{e1-dvcs2\ Saylor}{e1-dvcs2\ Guegan}$. Red is $\frac{e1-dvcs2\ Saylor}{e1-dvcs1\ Jo}$.

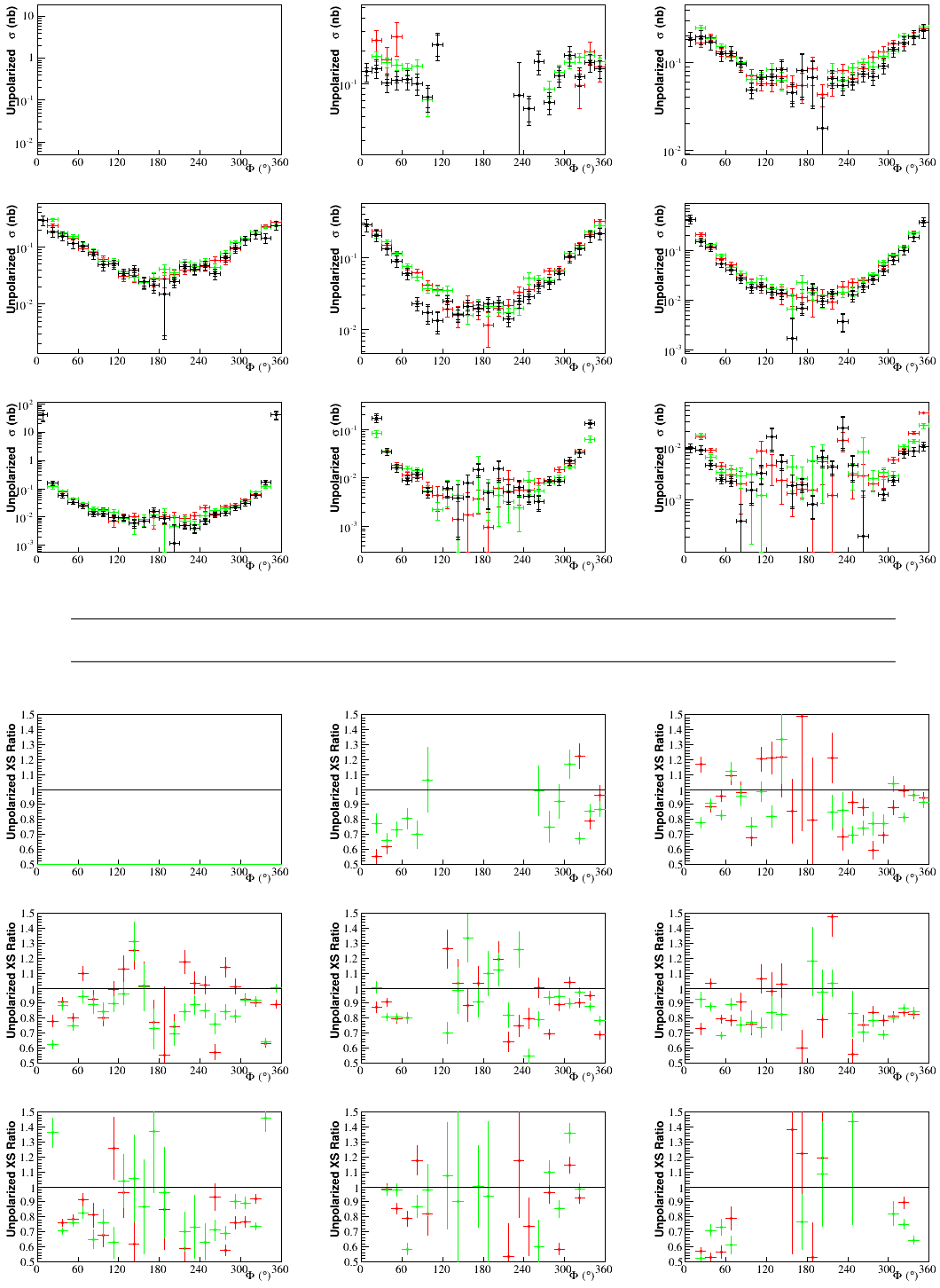

Figure E.15: On top, the unpolarized cross section as a function of Φ. Black represents this analysis. Green is e1-dvcs2 by B. Guegan. Red is e1-dvcs1 by H.S. Jo. On bottom, the unpolarized cross section ratios. Both are for the fifteenth bin in x_B and θ_e, where $0.32 < x_B < 0.35$ and $28^\circ < \theta_e < 45^\circ$. Each panel corresponds to a bin in $-t$ whose limits are: [0.09, 0.13, 0.18, 0.23, 0.30, 0.39, 0.52, 0.72, 1.10, 2.00] Green is $\frac{e1-dvcs2\ Saylor}{e1-dvcs2\ Guegan}$. Red is $\frac{e1-dvcs2\ Saylor}{e1-dvcs1\ Jo}$.

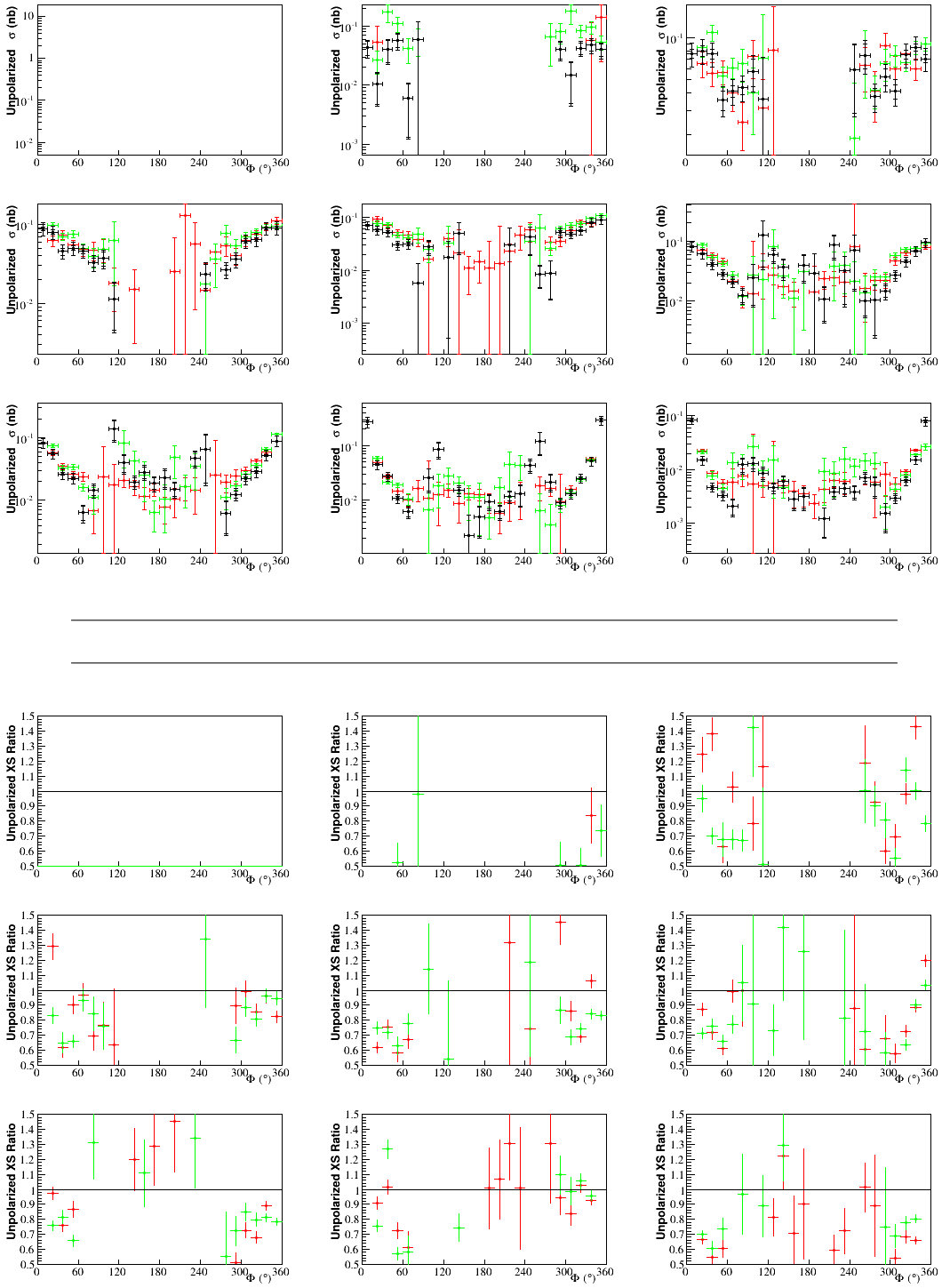

Figure E.16: On top, the unpolarized cross section as a function of Φ. Black represents this analysis. Green is e1-dvcs2 by B. Guegan. Red is e1-dvcs1 by H.S. Jo. On bottom, the unpolarized cross section ratios. Both are for the sixteenth bin in x_B and θ_e, where $0.35 < x_B < 0.38$ and $21^\circ < \theta_e < 28^\circ$. Each panel corresponds to a bin in $-t$ whose limits are: [0.09, 0.13, 0.18, 0.23, 0.30, 0.39, 0.52, 0.72, 1.10, 2.00] Green is $\frac{e1-dvcs2\ Saylor}{e1-dvcs2\ Guegan}$. Red is $\frac{e1-dvcs2\ Saylor}{e1-dvcs1\ Jo}$.

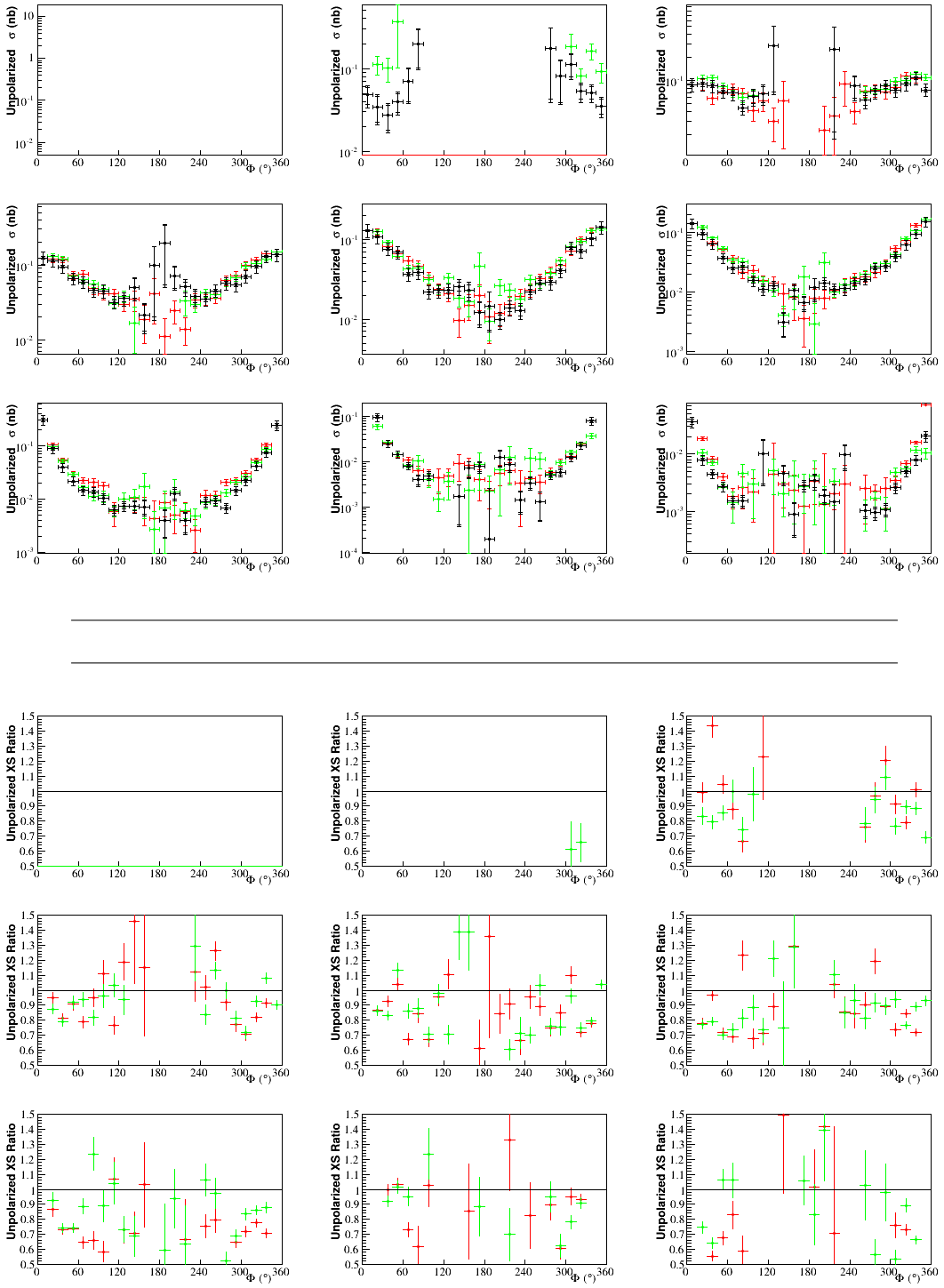

Figure E.17: On top, the unpolarized cross section as a function of Φ. Black represents this analysis. Green is e1-dvcs2 by B. Guegan. Red is e1-dvcs1 by H.S. Jo. On bottom, the unpolarized cross section ratios. Both are for the seventeenth bin in x_B and θ_e, where $0.35 < x_B < 0.38$ and $28^\circ < \theta_e < 45^\circ$. Each panel corresponds to a bin in $-t$ whose limits are: [0.09, 0.13, 0.18, 0.23, 0.30, 0.39, 0.52, 0.72, 1.10, 2.00] Green is $\frac{e1-dvcs2\ Saylor}{e1-dvcs2\ Guegan}$. Red is $\frac{e1-dvcs2\ Saylor}{e1-dvcs1\ Jo}$.

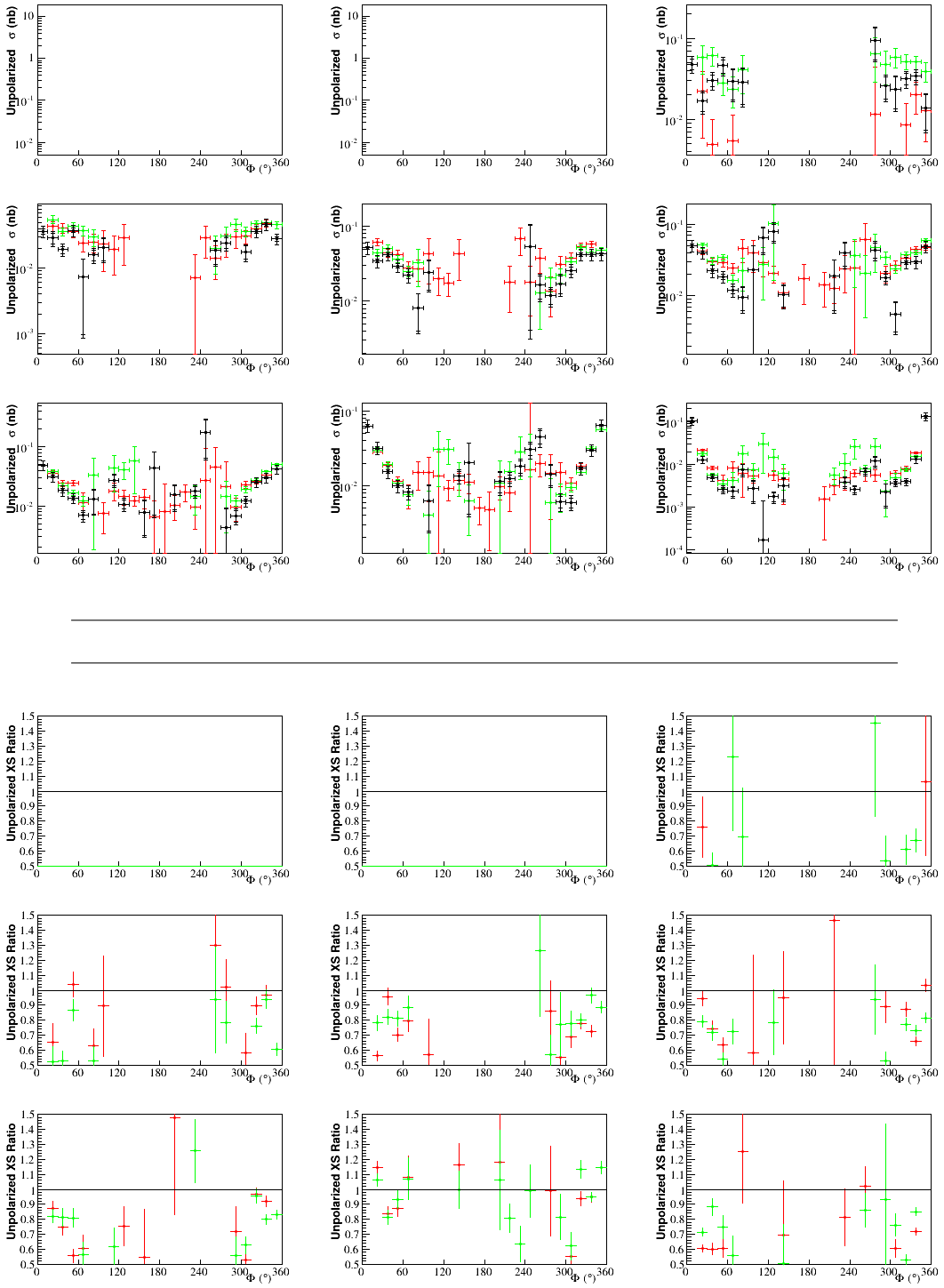

Figure E.18: On top, the unpolarized cross section as a function of Φ. Black represents this analysis. Green is e1-dvcs2 by B. Guegan. Red is e1-dvcs1 by H.S. Jo. On bottom, the unpolarized cross section ratios. Both are for the eighteenth bin in x_B and θ_e, where $0.38 < x_B < 0.42$ and $21^\circ < \theta_e < 28^\circ$. Each panel corresponds to a bin in $-t$ whose limits are: [0.09, 0.13, 0.18, 0.23, 0.30, 0.39, 0.52, 0.72, 1.10, 2.00] Green is $\frac{e1-dvcs2\ Saylor}{e1-dvcs2\ Guegan}$. Red is $\frac{e1-dvcs2\ Saylor}{e1-dvcs1\ Jo}$.

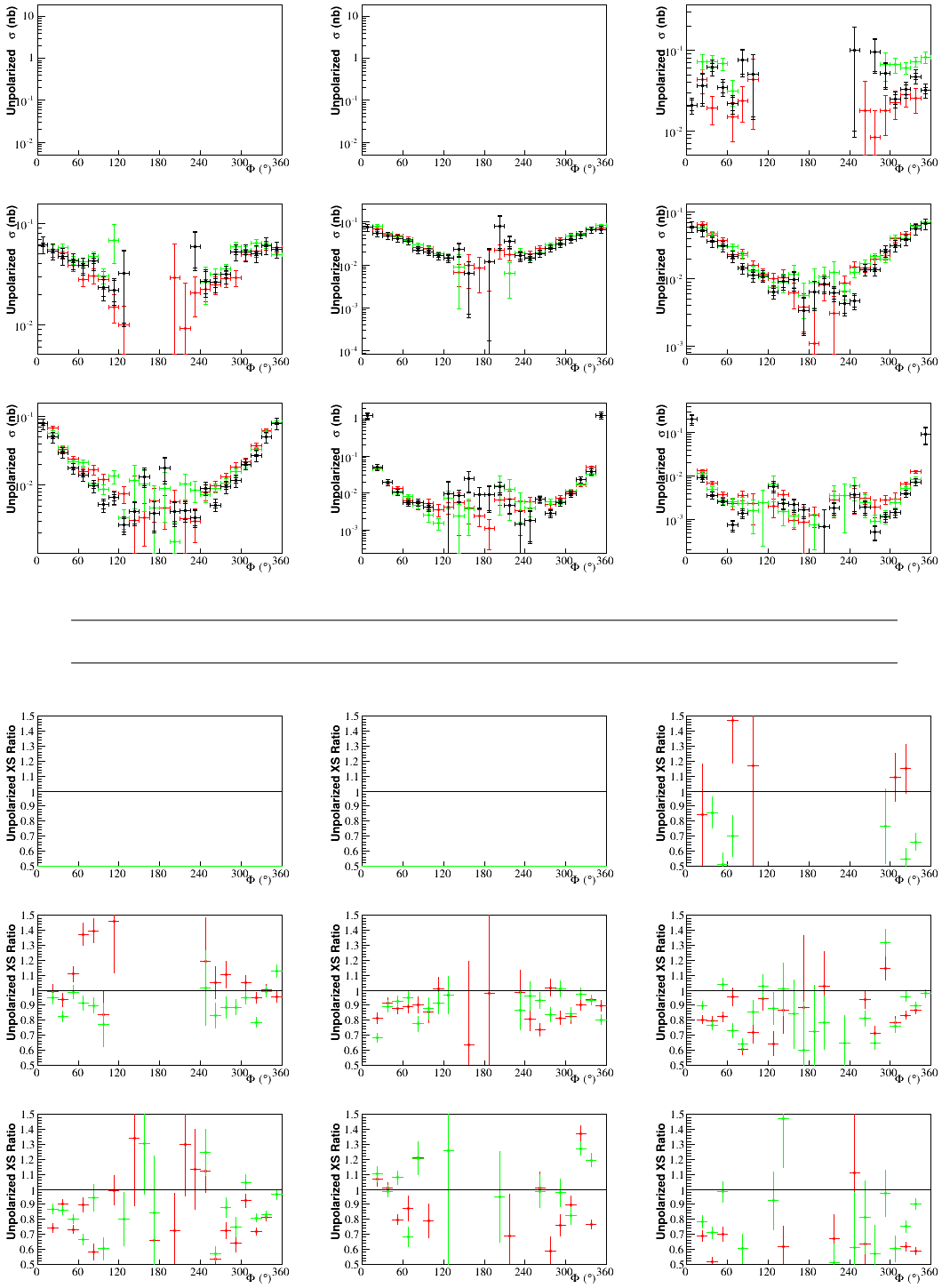

Figure E.19: On top, the unpolarized cross section as a function of Φ. Black represents this analysis. Green is e1-dvcs2 by B. Guegan. Red is e1-dvcs1 by H.S. Jo. On bottom, the unpolarized cross section ratios. Both are for the nineteenth bin in x_B and θ_e, where $0.38 < x_B < 0.42$ and $28^\circ < \theta_e < 45^\circ$. Each panel corresponds to a bin in $-t$ whose limits are: [0.09, 0.13, 0.18, 0.23, 0.30, 0.39, 0.52, 0.72, 1.10, 2.00] Green is $\frac{e1-dvcs2\ Saylor}{e1-dvcs2\ Guegan}$. Red is $\frac{e1-dvcs2\ Saylor}{e1-dvcs1\ Jo}$.

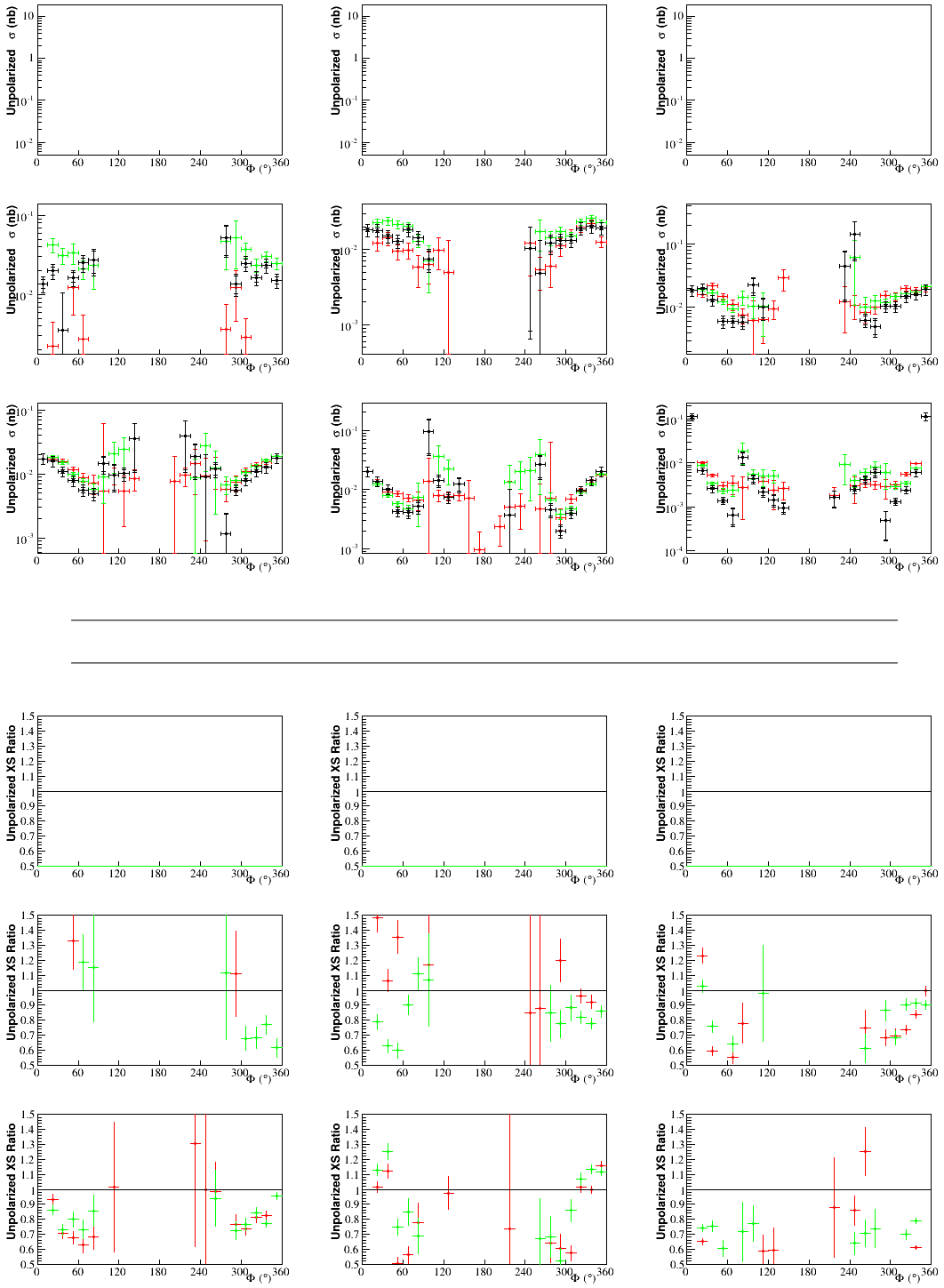

Figure E.20: On top, the unpolarized cross section as a function of Φ. Black represents this analysis. Green is e1-dvcs2 by B. Guegan. Red is e1-dvcs1 by H.S. Jo. On bottom, the unpolarized cross section ratios. Both are for the twentieth bin in x_B and θ_e, where $0.42 < x_B < 0.58$ and $21^\circ < \theta_e < 33^\circ$. Each panel corresponds to a bin in $-t$ whose limits are: [0.09, 0.13, 0.18, 0.23, 0.30, 0.39, 0.52, 0.72, 1.10, 2.00] Green is $\frac{e1-dvcs2\ Saylor}{e1-dvcs2\ Guegan}$. Red is $\frac{e1-dvcs2\ Saylor}{e1-dvcs1\ Jo}$.

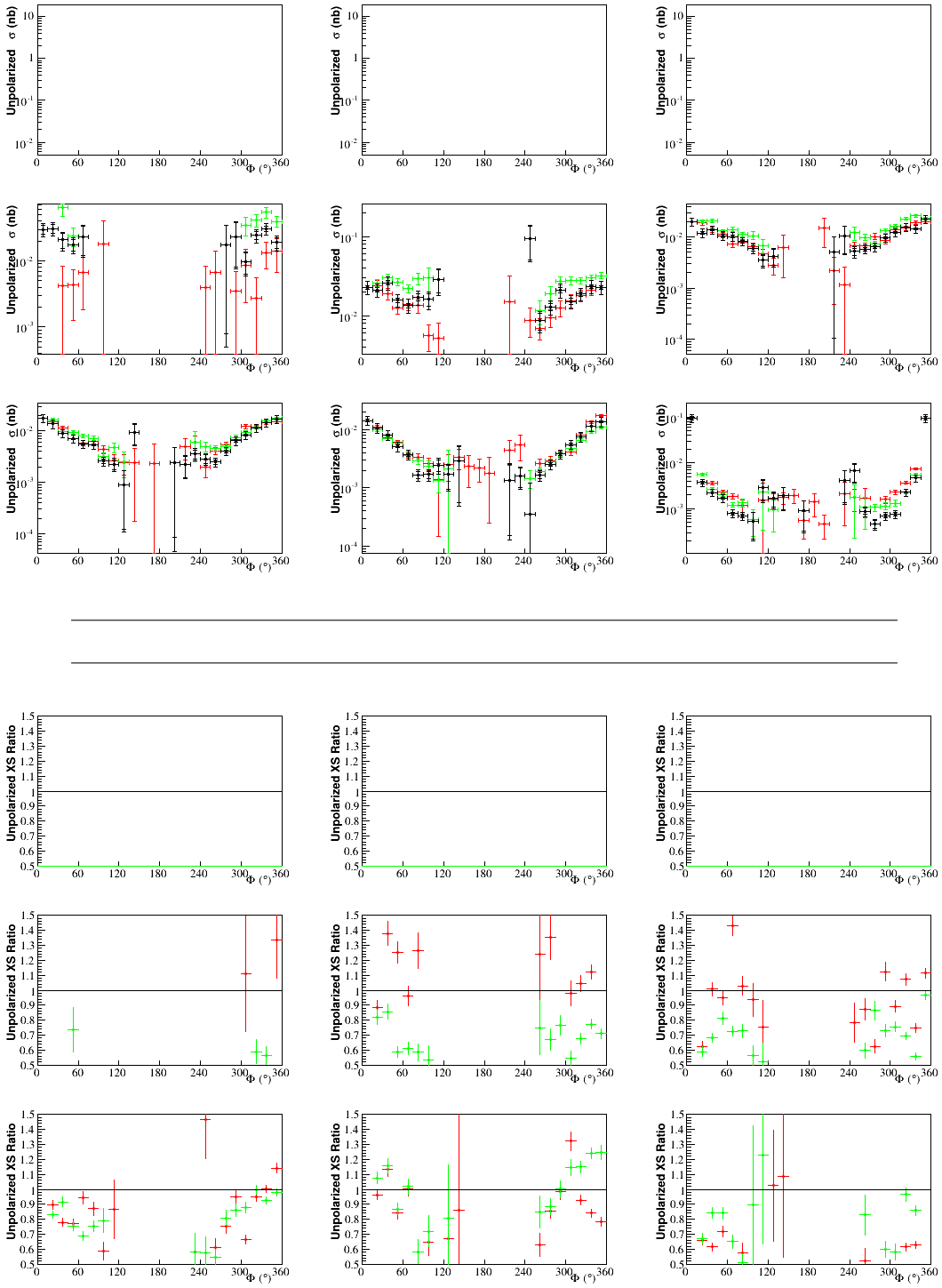

Figure E.21: On top, the unpolarized cross section as a function of Φ. Black represents this analysis. Green is e1-dvcs2 by B. Guegan. Red is e1-dvcs1 by H.S. Jo. On bottom, the unpolarized cross section ratios. Both are for the twenty-first bin in x_B and θ_e, where $0.42 < x_B < 0.58$ and $33^\circ < \theta_e < 45^\circ$. Each panel corresponds to a bin in $-t$ whose limits are: [0.09, 0.13, 0.18, 0.23, 0.30, 0.39, 0.52, 0.72, 1.10, 2.00] Green is $\frac{e1-dvcs2\ Saylor}{e1-dvcs2\ Guegan}$. Red is $\frac{e1-dvcs2\ Saylor}{e1-dvcs1\ Jo}$.

Comparison of Polarized Cross Section Differences:

Figure E.22 to Figure E.42 each contain the polarized cross section, and polarized cross section differences ratio as a function of Φ, for a given bin in x_B and θ_e. The comparison is between this analysis; e1-dvcs2 according to the parallel analysis by B. Guegan; and e1-dvcs1 according to the analysis by H.S. Jo.

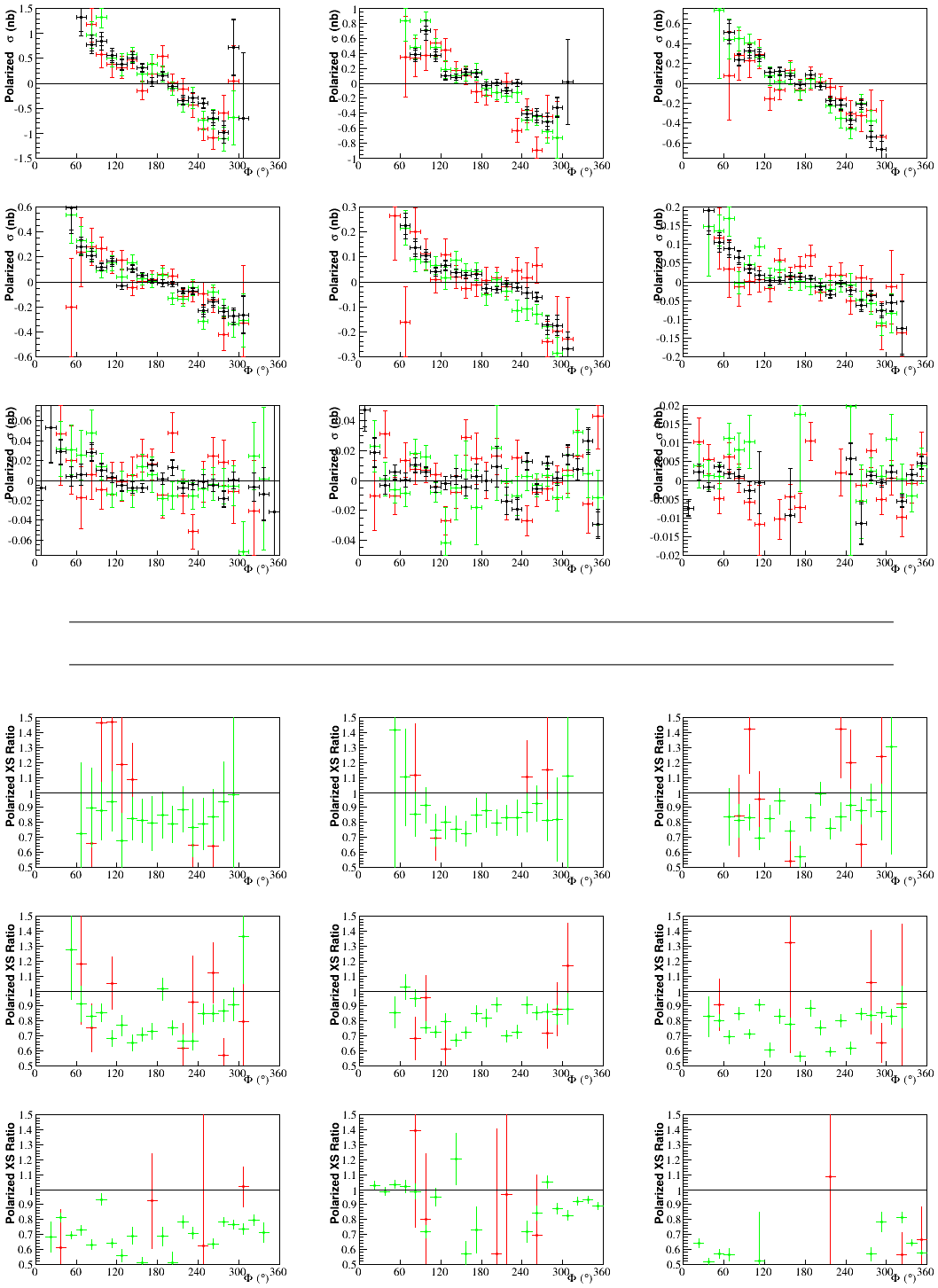

Figure E.22: On top, the polarized cross section differences as a function of Φ. Black represents this analysis. Green is e1-dvcs2 by B. Guegan. Red is e1-dvcs1 by H.S. Jo. On bottom, the polarized difference ratios. Both are for the first bin in x_B and θ_e, where $0.1 < x_B < 0.14$ and $21^\circ < \theta_e < 45^\circ$. Each panel corresponds to a bin in $-t$ whose limits are: [0.09, 0.13, 0.18, 0.23, 0.30, 0.39, 0.52, 0.72, 1.10, 2.00] Green is $\frac{e1-dvcs2\ Saylor}{e1-dvcs2\ Guegan}$. Red is $\frac{e1-dvcs2\ Saylor}{e1-dvcs1\ Jo}$.

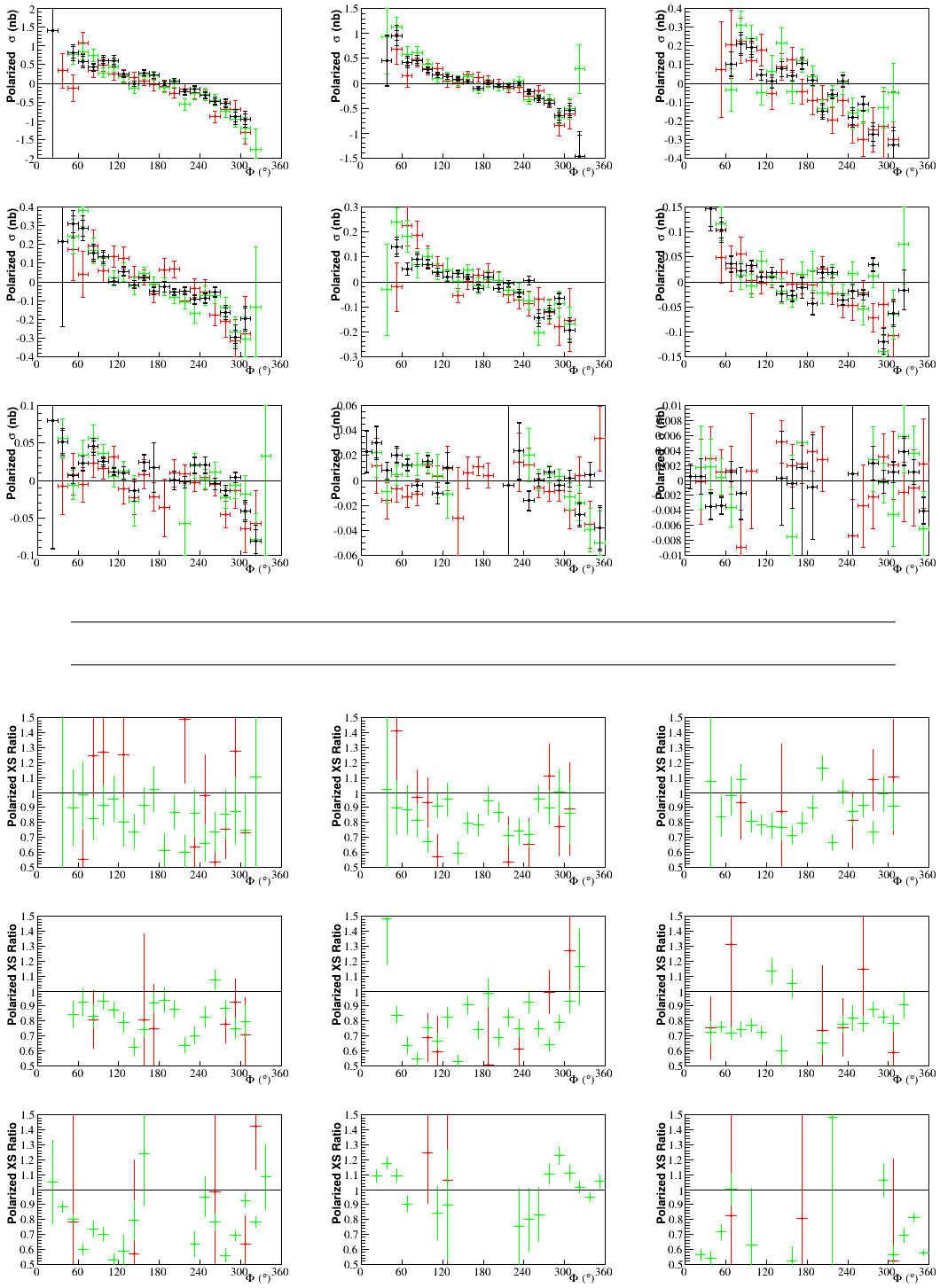

Figure E.23: On top, the polarized cross section differences as a function of Φ. Black represents this analysis. Green is e1-dvcs2 by B. Guegan. Red is e1-dvcs1 by H.S. Jo. On bottom, the polarized difference ratios. Both are for the second bin in x_B and θ_e, where $0.14 < x_B < 0.17$ and $21^\circ < \theta_e < 25.5^\circ$. Each panel corresponds to a bin in $-t$ whose limits are: [0.09, 0.13, 0.18, 0.23, 0.30, 0.39, 0.52, 0.72, 1.10, 2.00] Green is $\frac{e1-dvcs2\ Saylor}{e1-dvcs2\ Guegan}$. Red is $\frac{e1-dvcs2\ Saylor}{e1-dvcs1\ Jo}$.

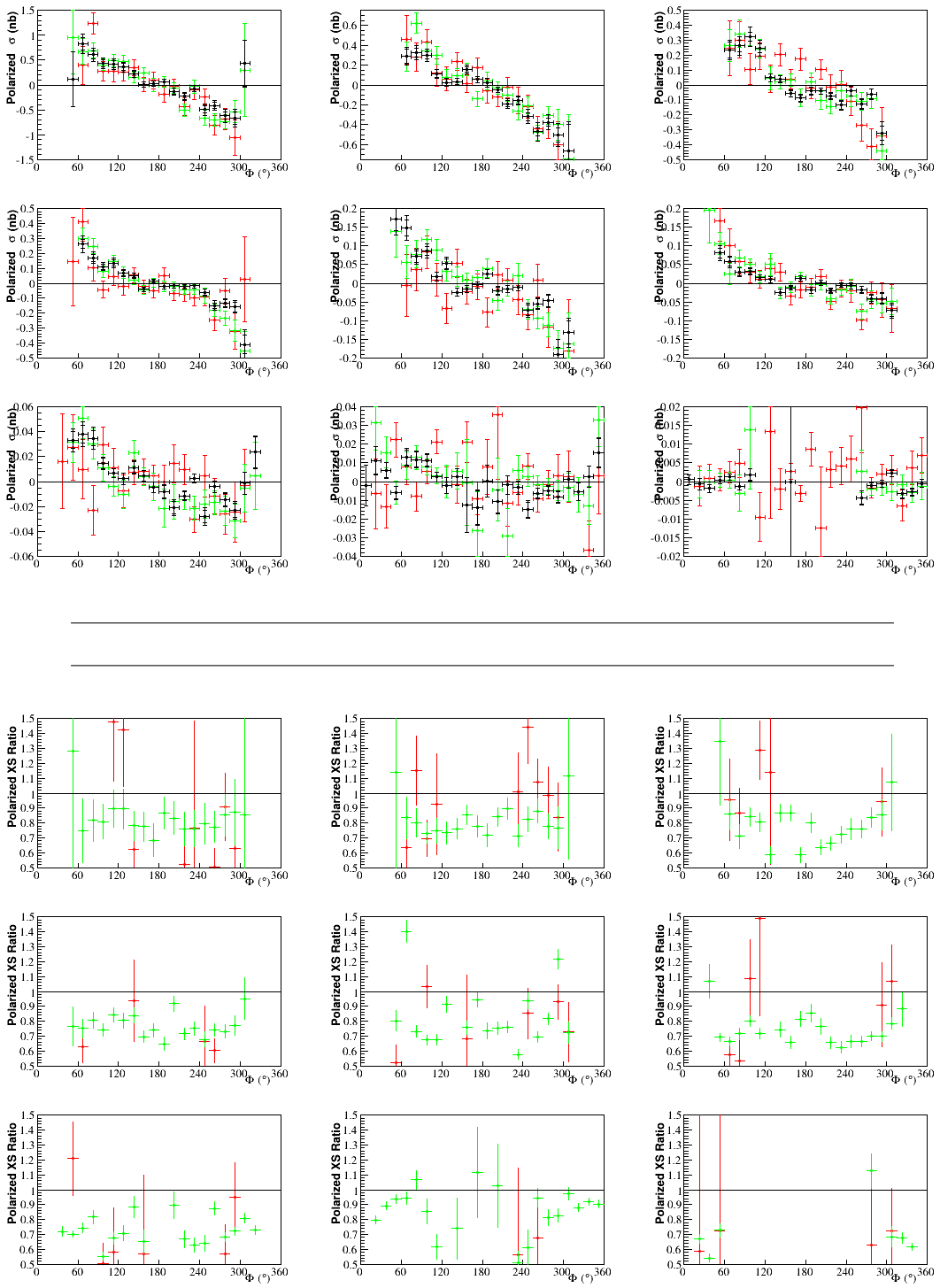

Figure E.24: On top, the polarized cross section differences as a function of Φ. Black represents this analysis. Green is e1-dvcs2 by B. Guegan. Red is e1-dvcs1 by H.S. Jo. On bottom, the polarized difference ratios. Both are for the third bin in x_B and θ_e, where $0.14 < x_B < 0.17$ and $25.5^\circ < \theta_e < 45^\circ$. Each panel corresponds to a bin in $-t$ whose limits are: [0.09, 0.13, 0.18, 0.23, 0.30, 0.39, 0.52, 0.72, 1.10, 2.00] Green is $\frac{e1-dvcs2\ Saylor}{e1-dvcs2\ Guegan}$. Red is $\frac{e1-dvcs2\ Saylor}{e1-dvcs1\ Jo}$.

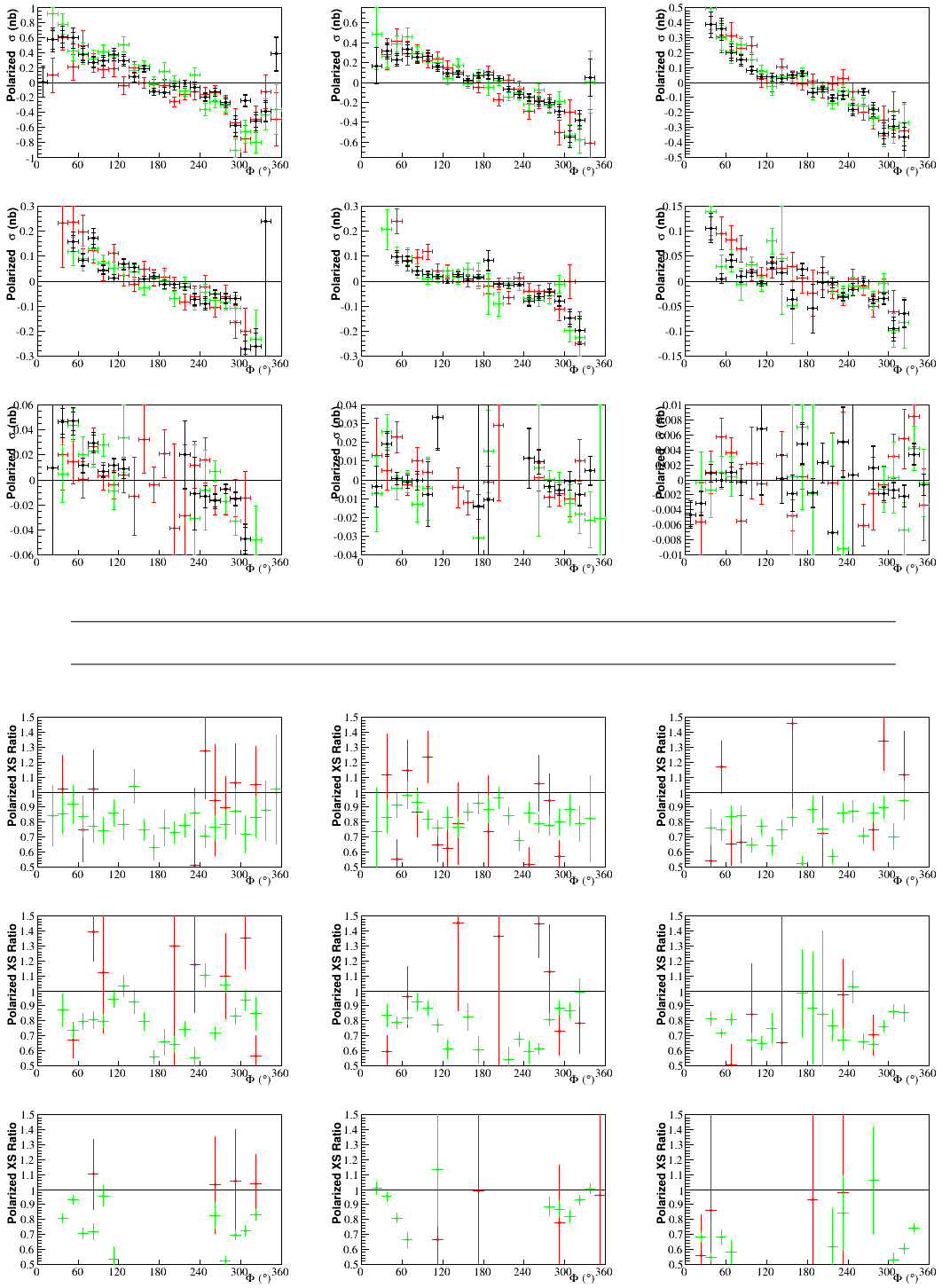

Figure E.25: On top, the polarized cross section differences as a function of Φ. Black represents this analysis. Green is e1-dvcs2 by B. Guegan. Red is e1-dvcs1 by H.S. Jo. On bottom, the polarized difference ratios. Both are for the fourth bin in x_B and θ_e, where $0.17 < x_B < 0.2$ and $21^\circ < \theta_e < 25.5^\circ$. Each panel corresponds to a bin in $-t$ whose limits are: [0.09, 0.13, 0.18, 0.23, 0.30, 0.39, 0.52, 0.72, 1.10, 2.00] Green is $\frac{e1-dvcs2\ Saylor}{e1-dvcs2\ Guegan}$. Red is $\frac{e1-dvcs2\ Saylor}{e1-dvcs1\ Jo}$.

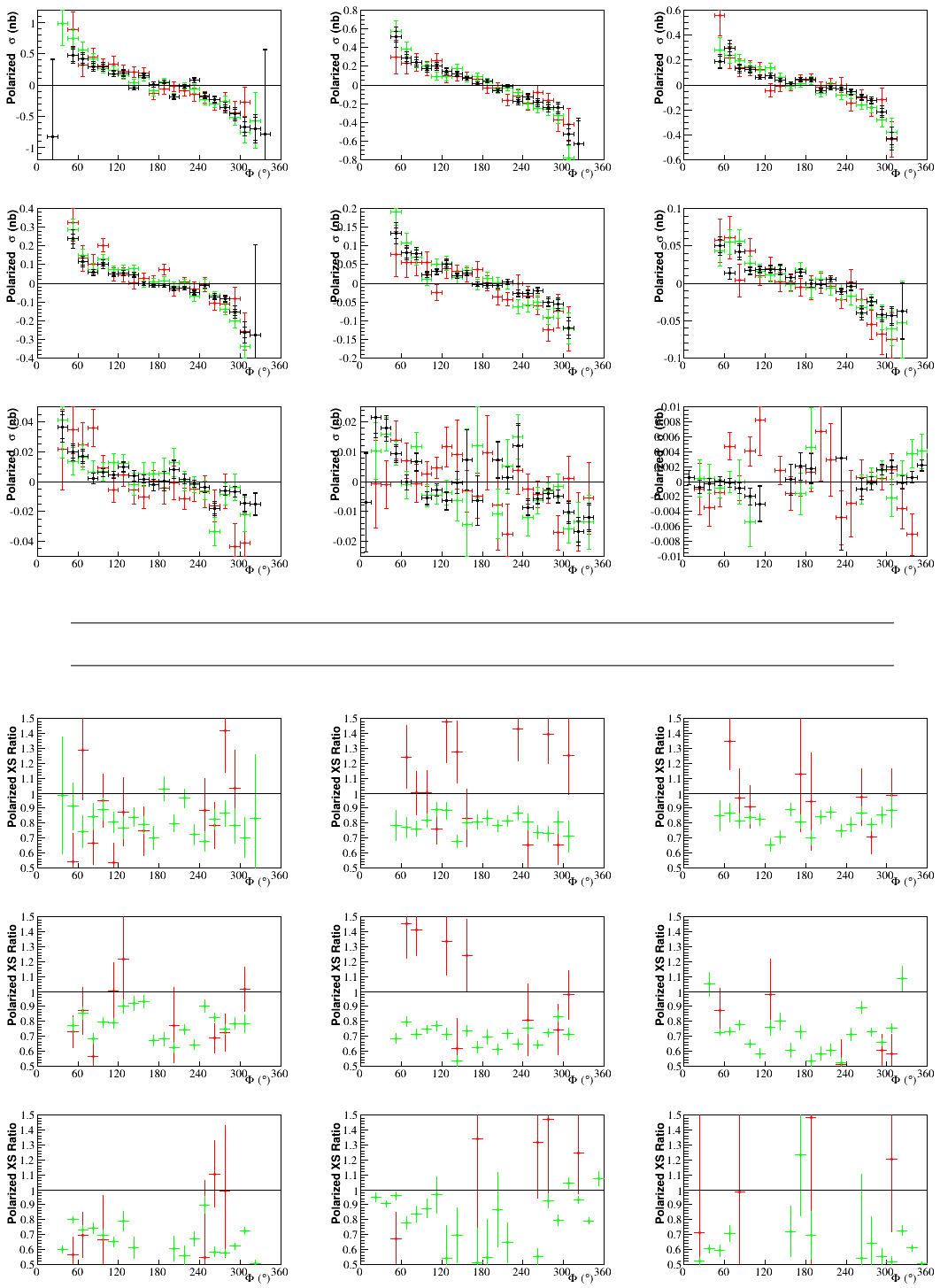

Figure E.26: On top, the polarized cross section differences as a function of Φ. Black represents this analysis. Green is e1-dvcs2 by B. Guegan. Red is e1-dvcs1 by H.S. Jo. On bottom, the polarized difference ratios. Both are for the fifth bin in x_B and θ_e, where $0.17 < x_B < 0.2$ and $25.5^\circ < \theta_e < 45^\circ$. Each panel corresponds to a bin in $-t$ whose limits are: [0.09, 0.13, 0.18, 0.23, 0.30, 0.39, 0.52, 0.72, 1.10, 2.00] Green is $\frac{e1-dvcs2\ Saylor}{e1-dvcs2\ Guegan}$. Red is $\frac{e1-dvcs2\ Saylor}{e1-dvcs1\ Jo}$.

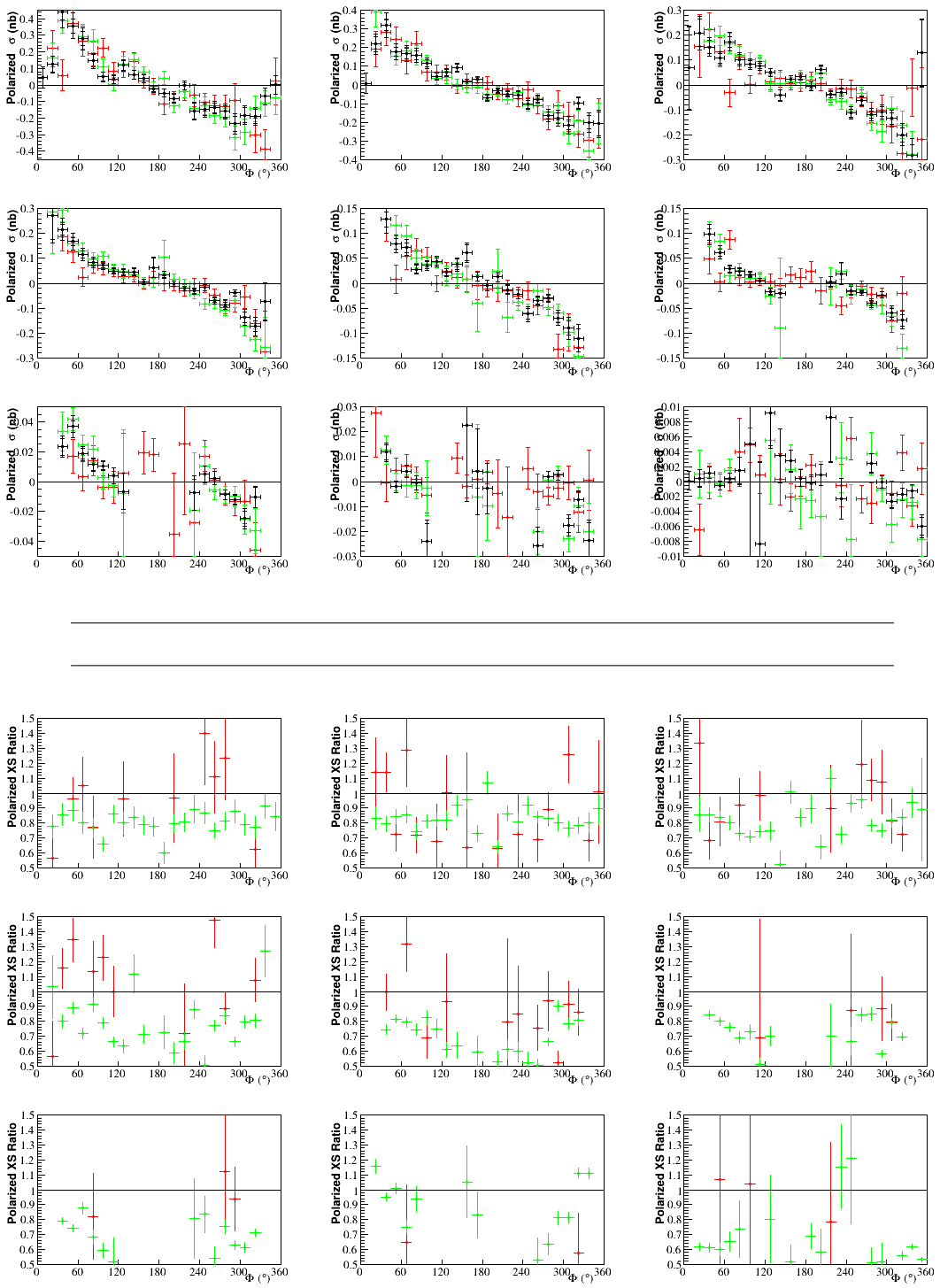

Figure E.27: On top, the polarized cross section differences as a function of Φ. Black represents this analysis. Green is e1-dvcs2 by B. Guegan. Red is e1-dvcs1 by H.S. Jo. On bottom, the polarized difference ratios. Both are for the sixth bin in x_B and θ_e, where $0.2 < x_B < 0.23$ and $21^\circ < \theta_e < 27^\circ$. Each panel corresponds to a bin in $-t$ whose limits are: [0.09, 0.13, 0.18, 0.23, 0.30, 0.39, 0.52, 0.72, 1.10, 2.00] Green is $\frac{e1-dvcs2\ Saylor}{e1-dvcs2\ Guegan}$. Red is $\frac{e1-dvcs2\ Saylor}{e1-dvcs1\ Jo}$.

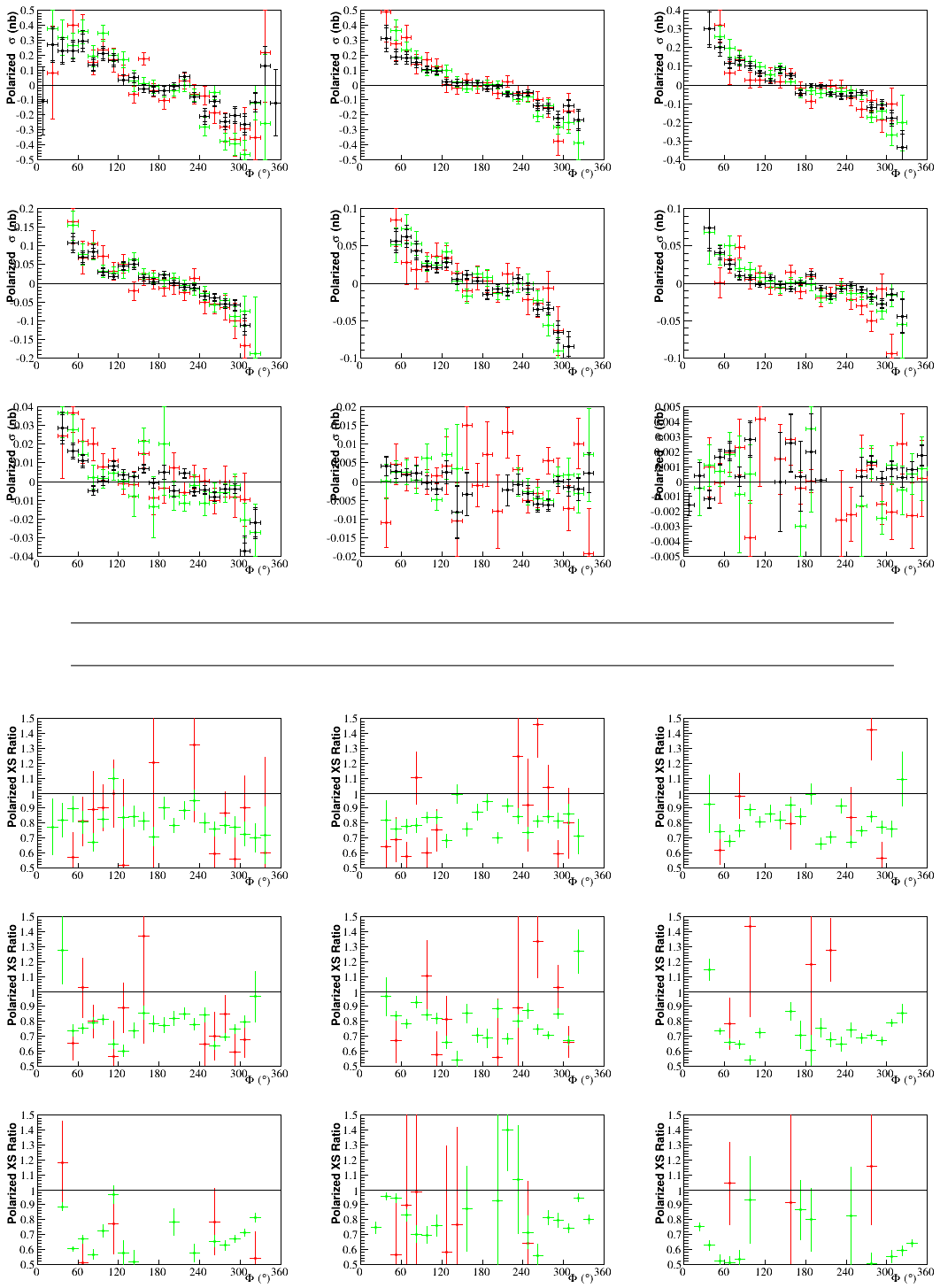

Figure E.28: On top, the polarized cross section differences as a function of Φ. Black represents this analysis. Green is e1-dvcs2 by B. Guegan. Red is e1-dvcs1 by H.S. Jo. On bottom, the polarized difference ratios. Both are for the seventh bin in x_B and θ_e, where $0.2 < x_B < 0.23$ and $27^\circ < \theta_e < 45^\circ$. Each panel corresponds to a bin in $-t$ whose limits are: [0.09, 0.13, 0.18, 0.23, 0.30, 0.39, 0.52, 0.72, 1.10, 2.00] Green is $\frac{e1-dvcs2\ Saylor}{e1-dvcs2\ Guegan}$. Red is $\frac{e1-dvcs2\ Saylor}{e1-dvcs1\ Jo}$.

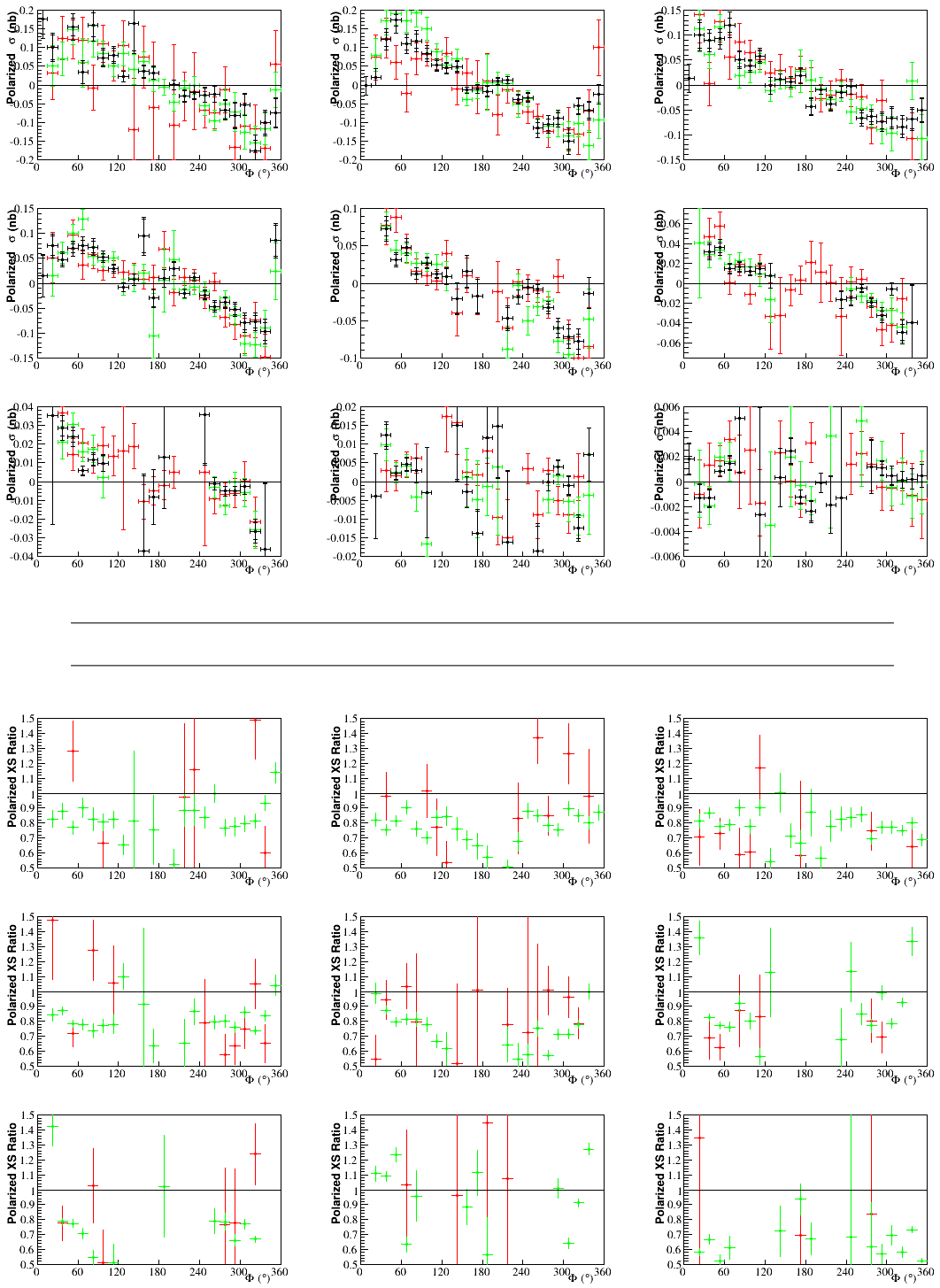

Figure E.29: On top, the polarized cross section differences as a function of Φ. Black represents this analysis. Green is e1-dvcs2 by B. Guegan. Red is e1-dvcs1 by H.S. Jo. On bottom, the polarized difference ratios. Both are for the eighth bin in x_B and θ_e, where $0.23 < x_B < 0.26$ and $21^\circ < \theta_e < 27^\circ$. Each panel corresponds to a bin in $-t$ whose limits are: [0.09, 0.13, 0.18, 0.23, 0.30, 0.39, 0.52, 0.72, 1.10, 2.00] Green is $\frac{e1-dvcs2\ Saylor}{e1-dvcs2\ Guegan}$. Red is $\frac{e1-dvcs2\ Saylor}{e1-dvcs1\ Jo}$.

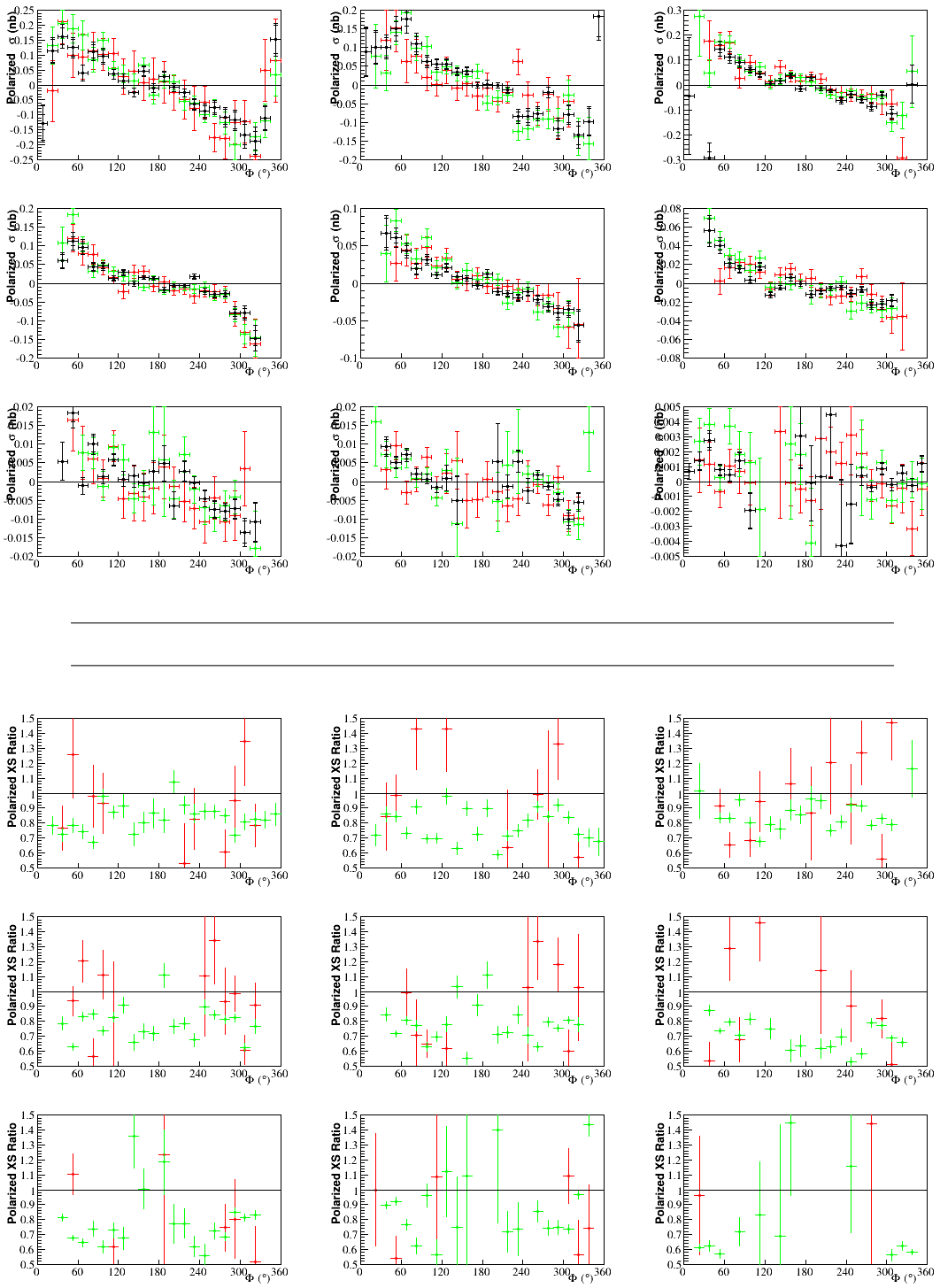

Figure E.30: On top, the polarized cross section differences as a function of Φ. Black represents this analysis. Green is e1-dvcs2 by B. Guegan. Red is e1-dvcs1 by H.S. Jo. On bottom, the polarized difference ratios. Both are for the ninth bin in x_B and θ_e, where $0.23 < x_B < 0.26$ and $27^\circ < \theta_e < 45^\circ$. Each panel corresponds to a bin in $-t$ whose limits are: [0.09, 0.13, 0.18, 0.23, 0.30, 0.39, 0.52, 0.72, 1.10, 2.00] Green is $\frac{e1-dvcs2\ Saylor}{e1-dvcs2\ Guegan}$. Red is $\frac{e1-dvcs2\ Saylor}{e1-dvcs1\ Jo}$.

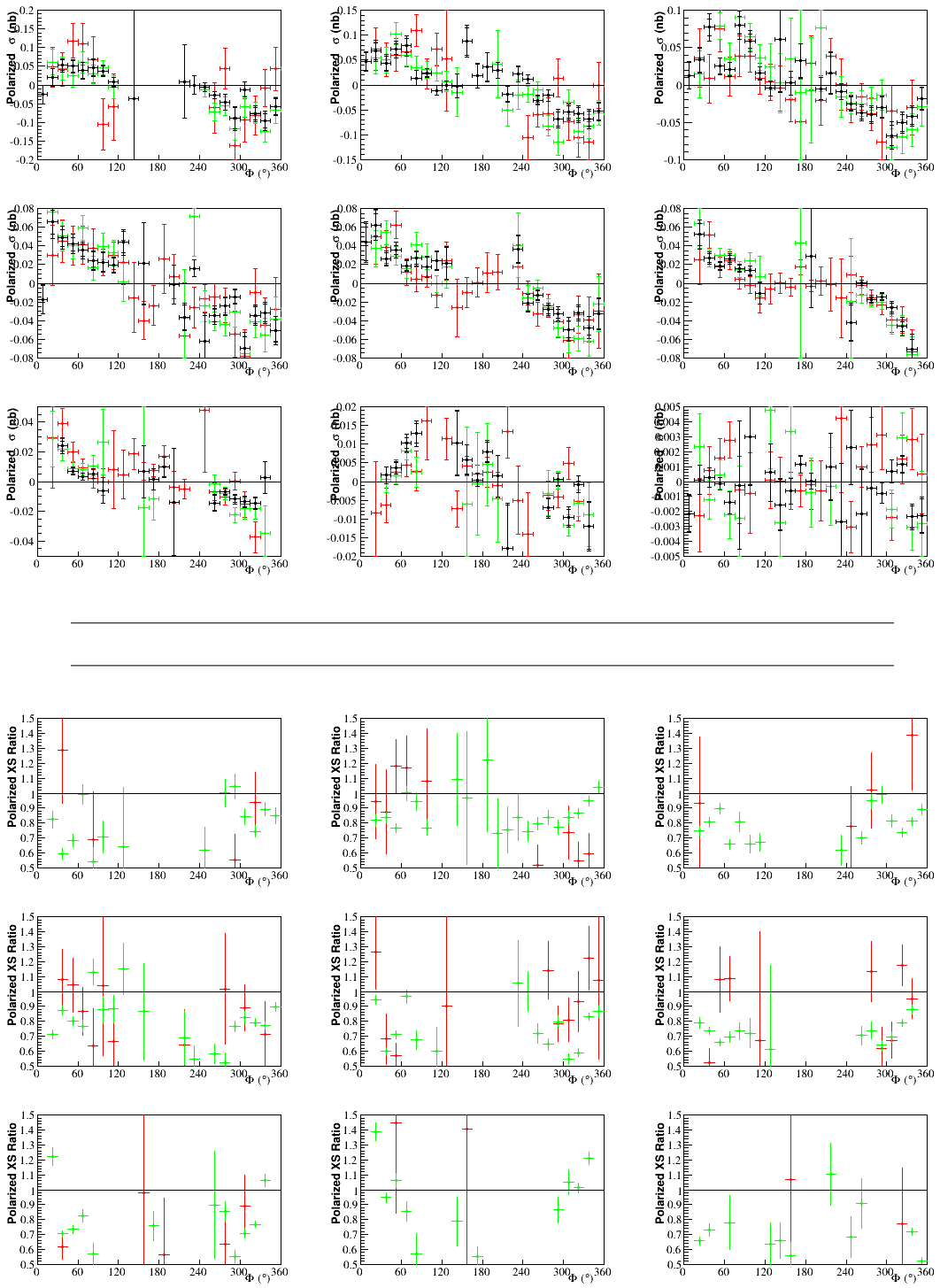

Figure E.31: On top, the polarized cross section differences as a function of Φ. Black represents this analysis. Green is e1-dvcs2 by B. Guegan. Red is e1-dvcs1 by H.S. Jo. On bottom, the polarized difference ratios. Both are for the tenth bin in x_B and θ_e, where $0.26 < x_B < 0.29$ and $21^\circ < \theta_e < 27^\circ$. Each panel corresponds to a bin in $-t$ whose limits are: [0.09, 0.13, 0.18, 0.23, 0.30, 0.39, 0.52, 0.72, 1.10, 2.00] Green is $\frac{e1-dvcs2\ Saylor}{e1-dvcs2\ Guegan}$. Red is $\frac{e1-dvcs2\ Saylor}{e1-dvcs1\ Jo}$.

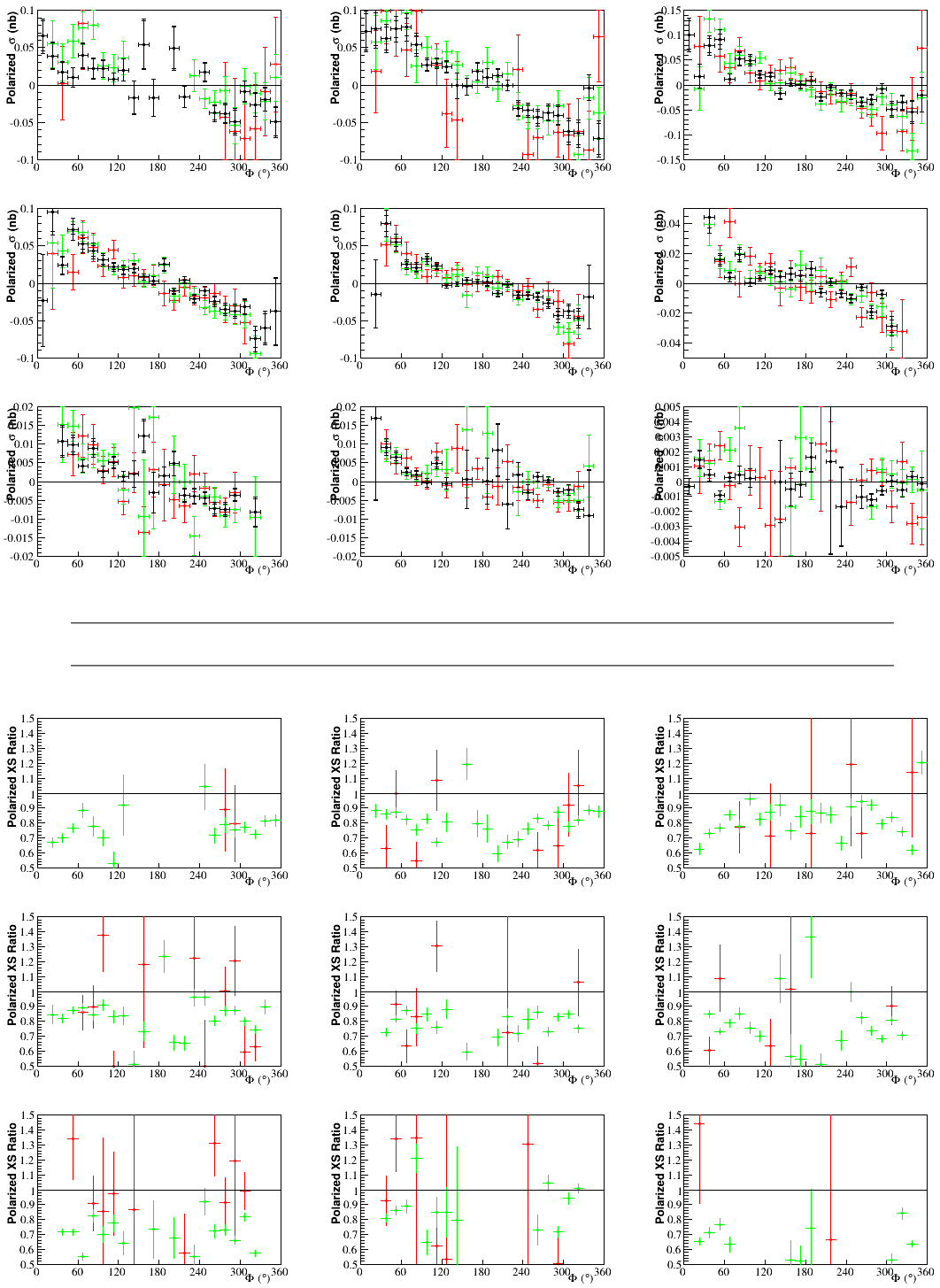

Figure E.32: On top, the polarized cross section differences as a function of Φ. Black represents this analysis. Green is e1-dvcs2 by B. Guegan. Red is e1-dvcs1 by H.S. Jo. On bottom, the polarized difference ratios. Both are for the eleventh bin in x_B and θ_e, where $0.26 < x_B < 0.29$ and $27^\circ < \theta_e < 45^\circ$. Each panel corresponds to a bin in $-t$ whose limits are: [0.09, 0.13, 0.18, 0.23, 0.30, 0.39, 0.52, 0.72, 1.10, 2.00] Green is $\frac{e1-dvcs2\ Saylor}{e1-dvcs2\ Guegan}$. Red is $\frac{e1-dvcs2\ Saylor}{e1-dvcs1\ Jo}$.

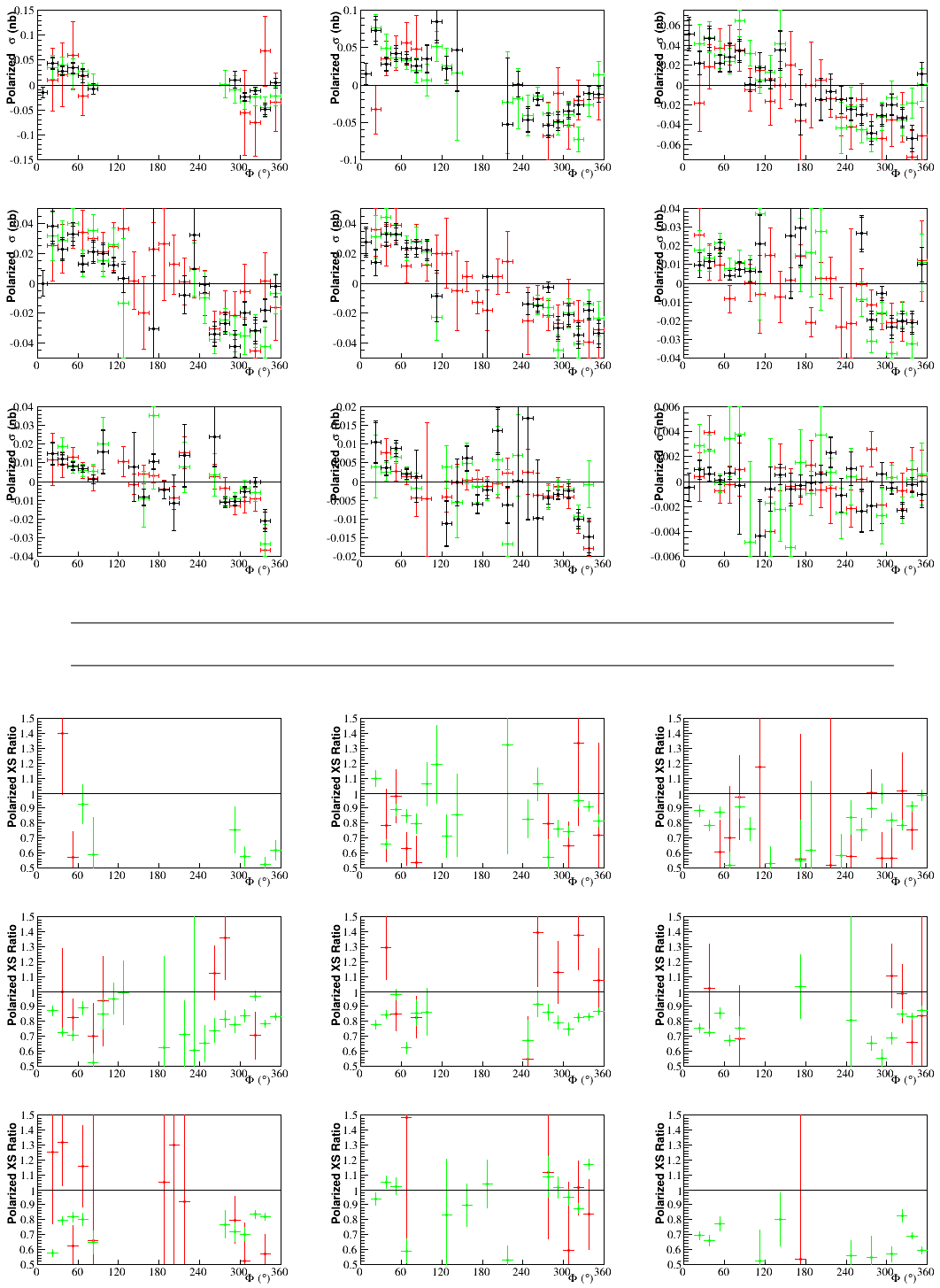

Figure E.33: On top, the polarized cross section differences as a function of Φ. Black represents this analysis. Green is e1-dvcs2 by B. Guegan. Red is e1-dvcs1 by H.S. Jo. On bottom, the polarized difference ratios. Both are for the twelfth bin in x_B and θ_e, where $0.29 < x_B < 0.32$ and $21^\circ < \theta_e < 28^\circ$. Each panel corresponds to a bin in $-t$ whose limits are: [0.09, 0.13, 0.18, 0.23, 0.30, 0.39, 0.52, 0.72, 1.10, 2.00] Green is $\frac{e1-dvcs2\ Saylor}{e1-dvcs2\ Guegan}$. Red is $\frac{e1-dvcs2\ Saylor}{e1-dvcs1\ Jo}$.

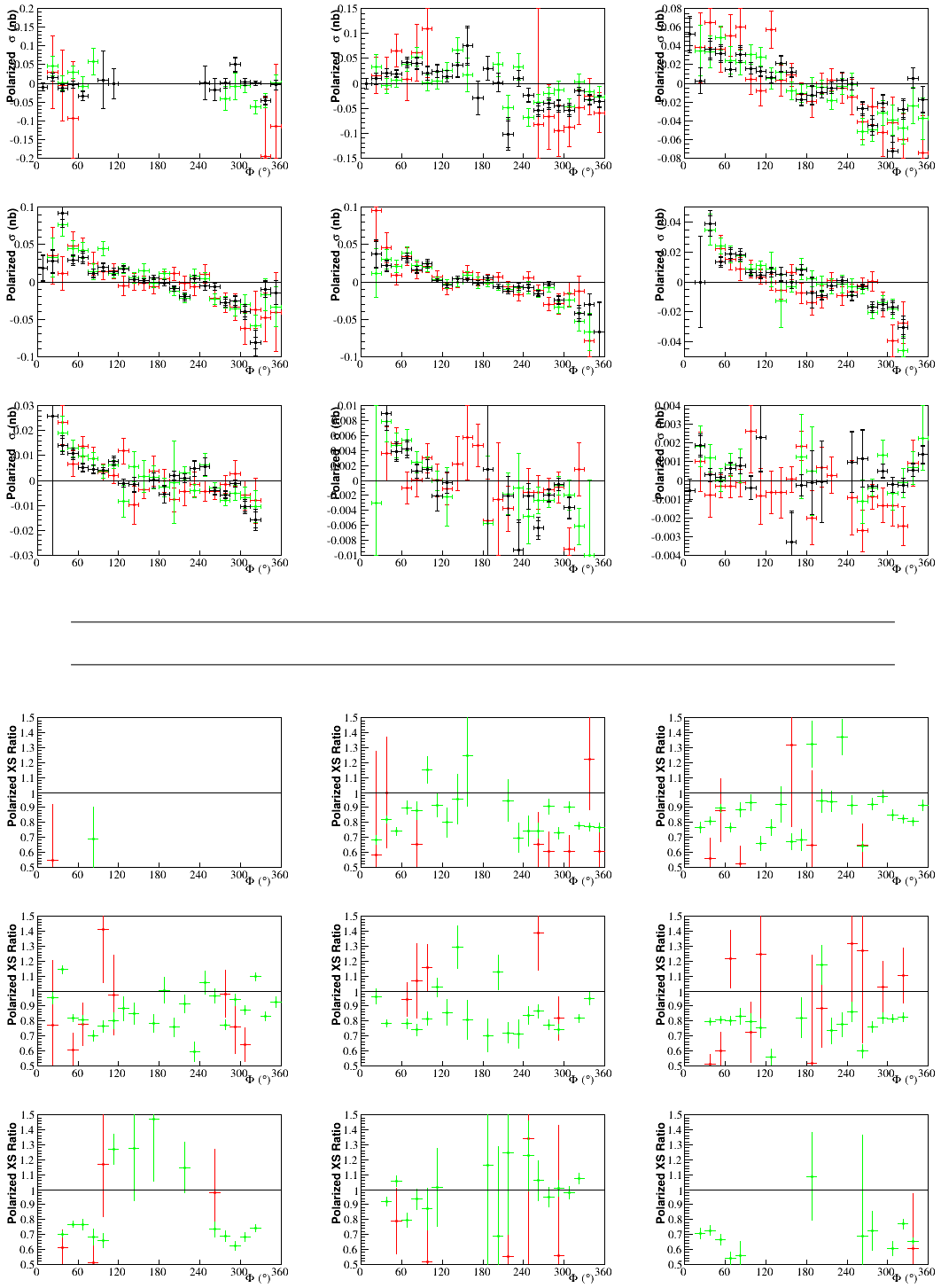

Figure E.34: On top, the polarized cross section differences as a function of Φ. Black represents this analysis. Green is e1-dvcs2 by B. Guegan. Red is e1-dvcs1 by H.S. Jo. On bottom, the polarized difference ratios. Both are for the thirteenth bin in x_B and θ_e, where $0.29 < x_B < 0.32$ and $28^\circ < \theta_e < 45^\circ$. Each panel corresponds to a bin in $-t$ whose limits are: [0.09, 0.13, 0.18, 0.23, 0.30, 0.39, 0.52, 0.72, 1.10, 2.00] Green is $\frac{e1-dvcs2\ Saylor}{e1-dvcs2\ Guegan}$. Red is $\frac{e1-dvcs2\ Saylor}{e1-dvcs1\ Jo}$.

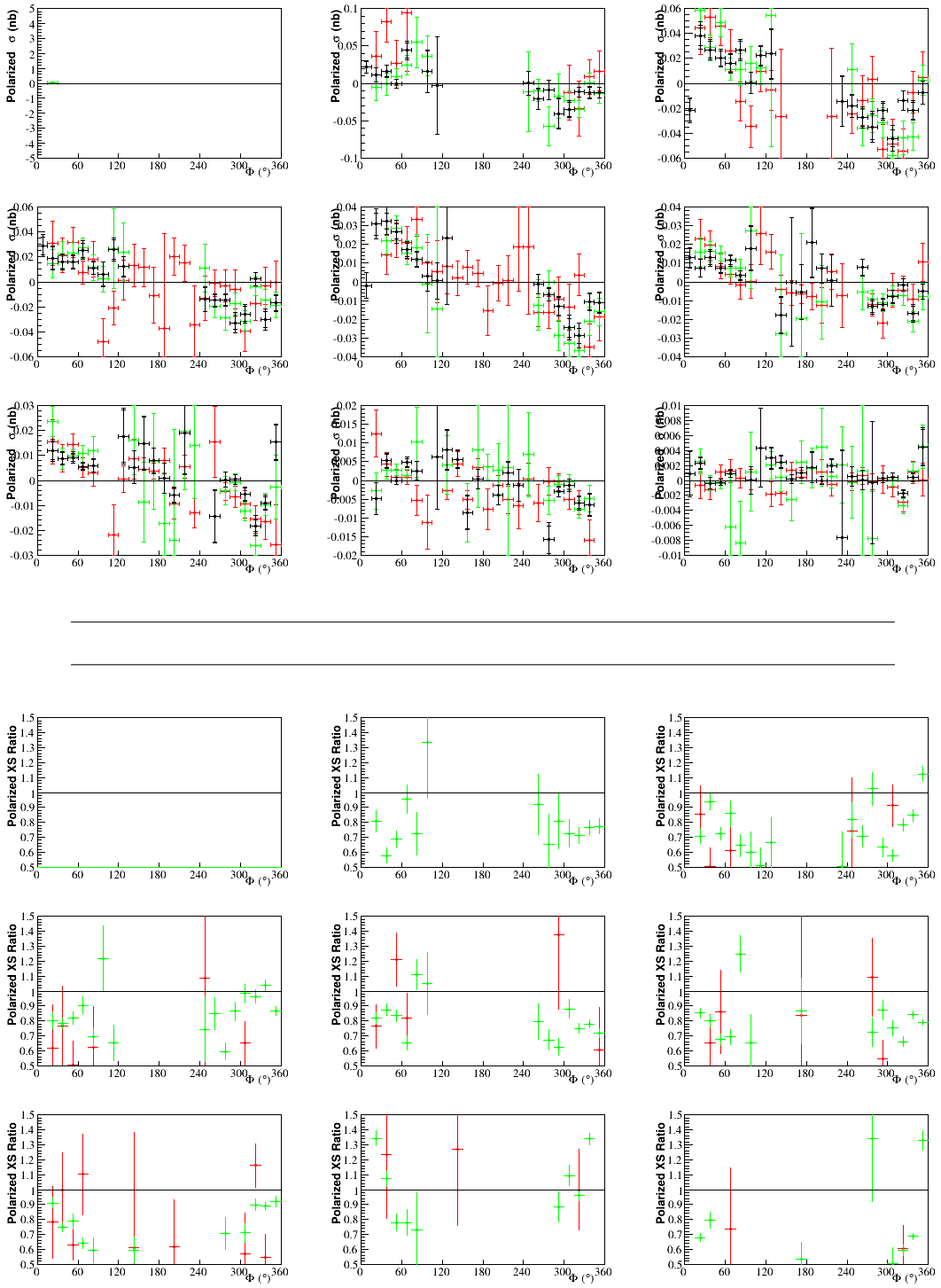

Figure E.35: On top, the polarized cross section differences as a function of Φ. Black represents this analysis. Green is e1-dvcs2 by B. Guegan. Red is e1-dvcs1 by H.S. Jo. On bottom, the polarized difference ratios. Both are for the fourteenth bin in x_B and θ_e, where $0.32 < x_B < 0.35$ and $21^\circ < \theta_e < 28^\circ$. Each panel corresponds to a bin in $-t$ whose limits are: [0.09, 0.13, 0.18, 0.23, 0.30, 0.39, 0.52, 0.72, 1.10, 2.00] Green is $\frac{e1-dvcs2\ Saylor}{e1-dvcs2\ Guegan}$. Red is $\frac{e1-dvcs2\ Saylor}{e1-dvcs1\ Jo}$.

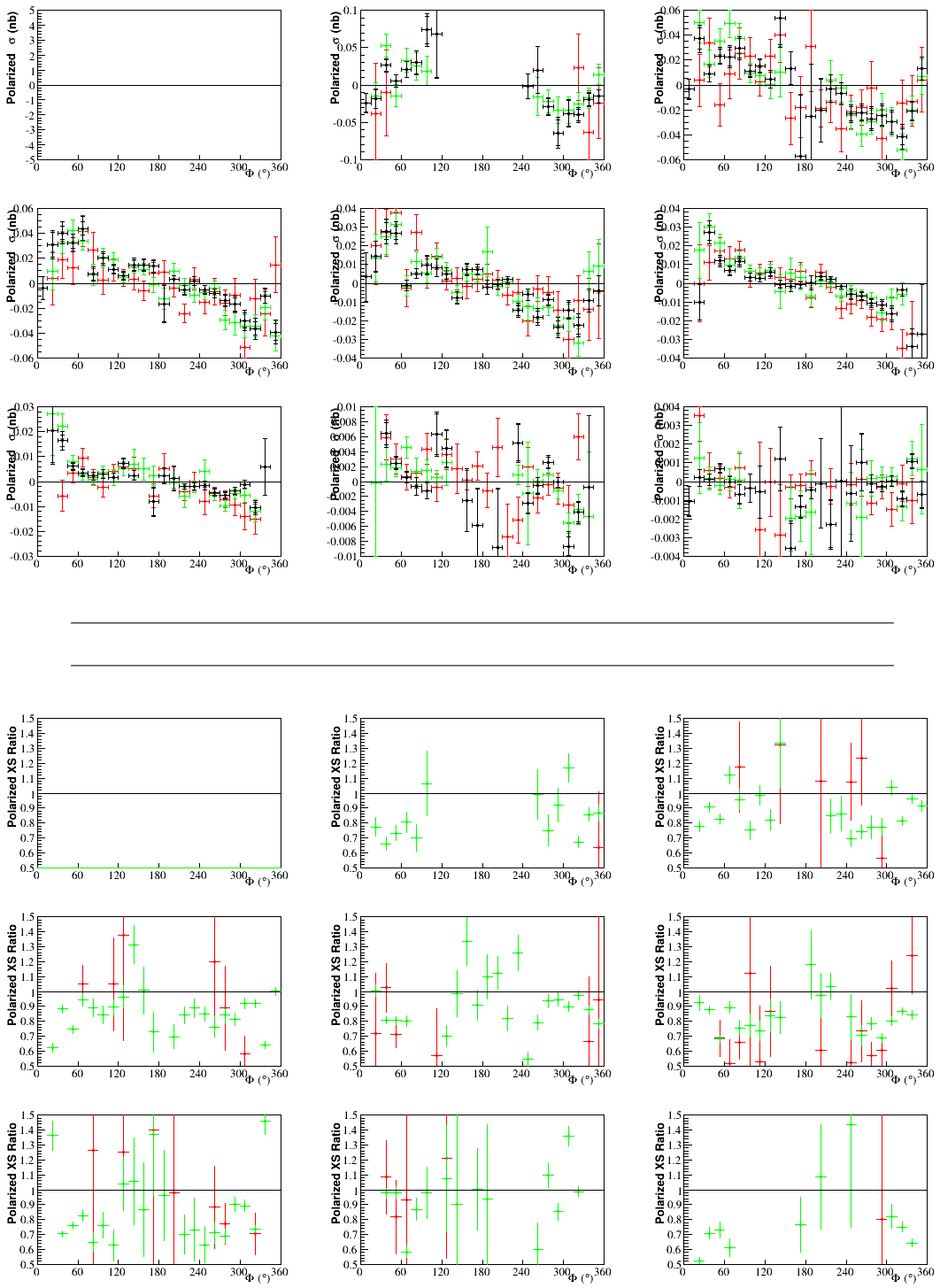

Figure E.36: On top, the polarized cross section differences as a function of Φ. Black represents this analysis. Green is e1-dvcs2 by B. Guegan. Red is e1-dvcs1 by H.S. Jo. On bottom, the polarized difference ratios. Both are for the fifteenth bin in x_B and θ_e, where $0.32 < x_B < 0.35$ and $28^\circ < \theta_e < 45^\circ$. Each panel corresponds to a bin in $-t$ whose limits are: [0.09, 0.13, 0.18, 0.23, 0.30, 0.39, 0.52, 0.72, 1.10, 2.00] Green is $\frac{e1-dvcs2\ Saylor}{e1-dvcs2\ Guegan}$. Red is $\frac{e1-dvcs2\ Saylor}{e1-dvcs1\ Jo}$.

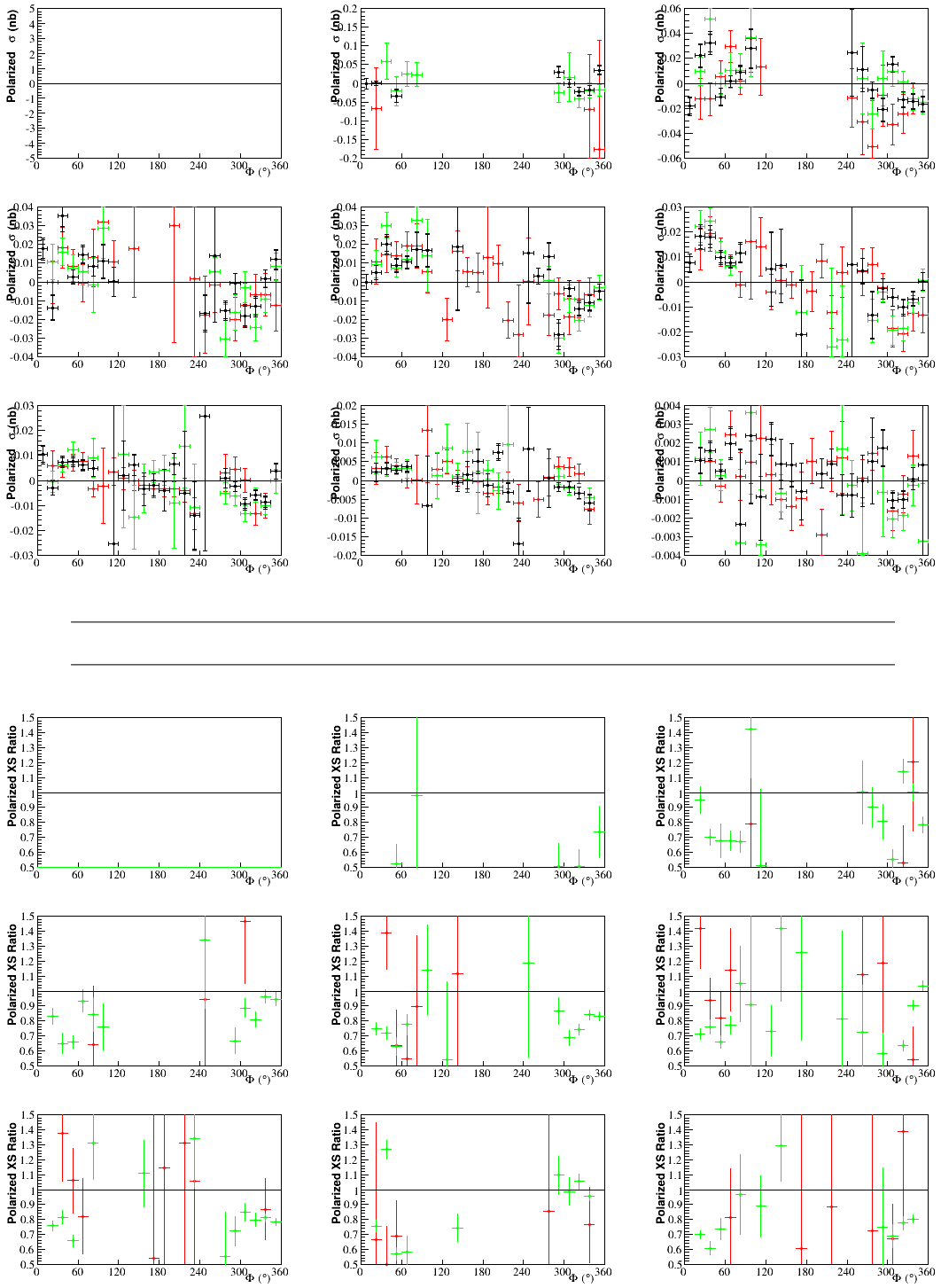

Figure E.37: On top, the polarized cross section differences as a function of Φ. Black represents this analysis. Green is e1-dvcs2 by B. Guegan. Red is e1-dvcs1 by H.S. Jo. On bottom, the polarized difference ratios. Both are for the sixteenth bin in x_B and θ_e, where $0.35 < x_B < 0.38$ and $21^\circ < \theta_e < 28^\circ$. Each panel corresponds to a bin in $-t$ whose limits are: [0.09, 0.13, 0.18, 0.23, 0.30, 0.39, 0.52, 0.72, 1.10, 2.00] Green is $\frac{e1-dvcs2\ Saylor}{e1-dvcs2\ Guegan}$. Red is $\frac{e1-dvcs2\ Saylor}{e1-dvcs1\ Jo}$.

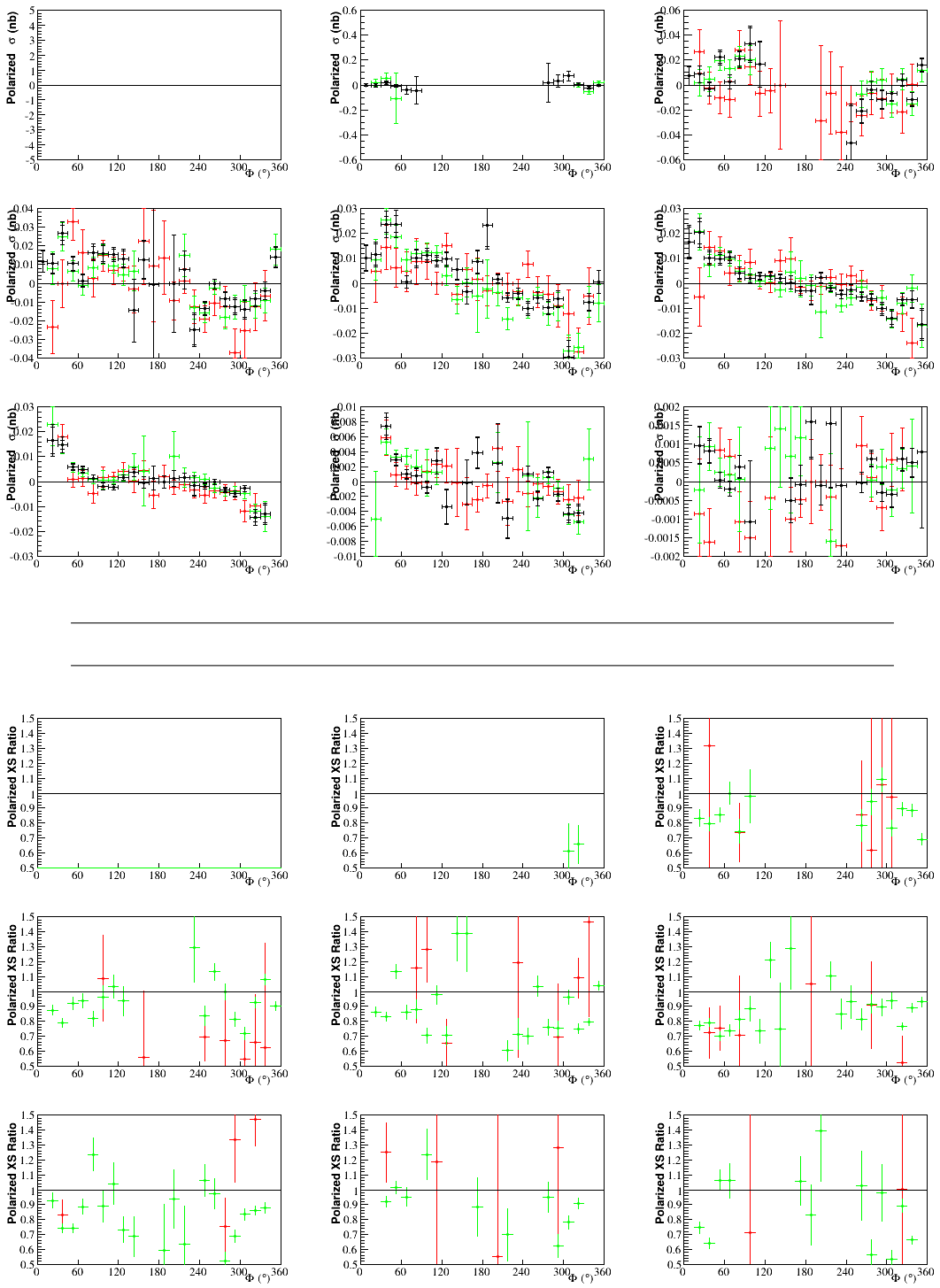

Figure E.38: On top, the polarized cross section differences as a function of Φ. Black represents this analysis. Green is e1-dvcs2 by B. Guegan. Red is e1-dvcs1 by H.S. Jo. On bottom, the polarized difference ratios. Both are for the seventeenth bin in x_B and θ_e, where $0.35 < x_B < 0.38$ and $28^\circ < \theta_e < 45^\circ$. Each panel corresponds to a bin in $-t$ whose limits are: [0.09, 0.13, 0.18, 0.23, 0.30, 0.39, 0.52, 0.72, 1.10, 2.00] Green is $\frac{e1-dvcs2\ Saylor}{e1-dvcs2\ Guegan}$. Red is $\frac{e1-dvcs2\ Saylor}{e1-dvcs1\ Jo}$.

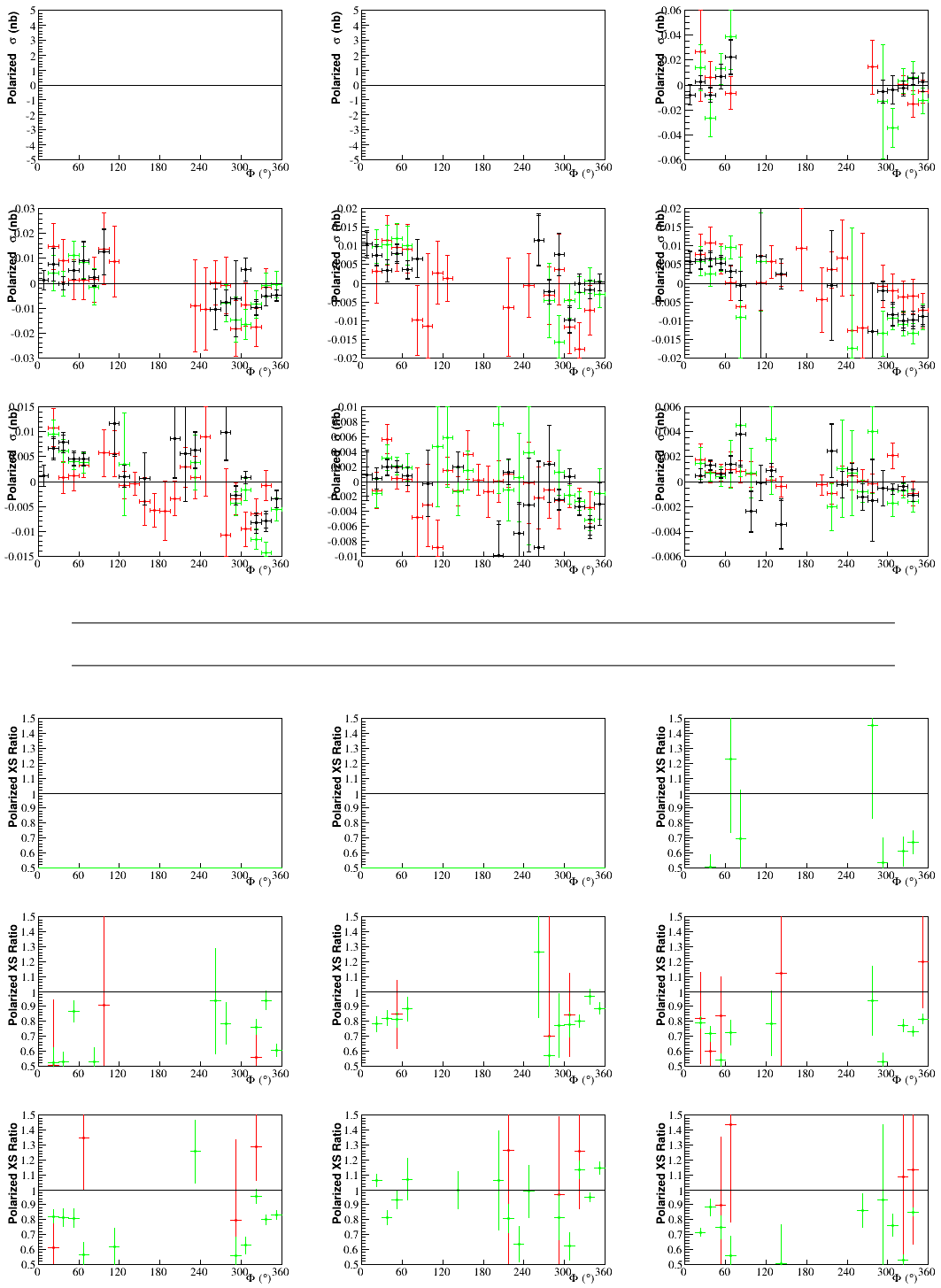

Figure E.39: On top, the polarized cross section differences as a function of Φ. Black represents this analysis. Green is e1-dvcs2 by B. Guegan. Red is e1-dvcs1 by H.S. Jo. On bottom, the polarized difference ratios. Both are for the eighteenth bin in x_B and θ_e, where $0.38 < x_B < 0.42$ and $21^\circ < \theta_e < 28^\circ$. Each panel corresponds to a bin in $-t$ whose limits are: [0.09, 0.13, 0.18, 0.23, 0.30, 0.39, 0.52, 0.72, 1.10, 2.00] Green is $\frac{e1-dvcs2\ Saylor}{e1-dvcs2\ Guegan}$. Red is $\frac{e1-dvcs2\ Saylor}{e1-dvcs1\ Jo}$.

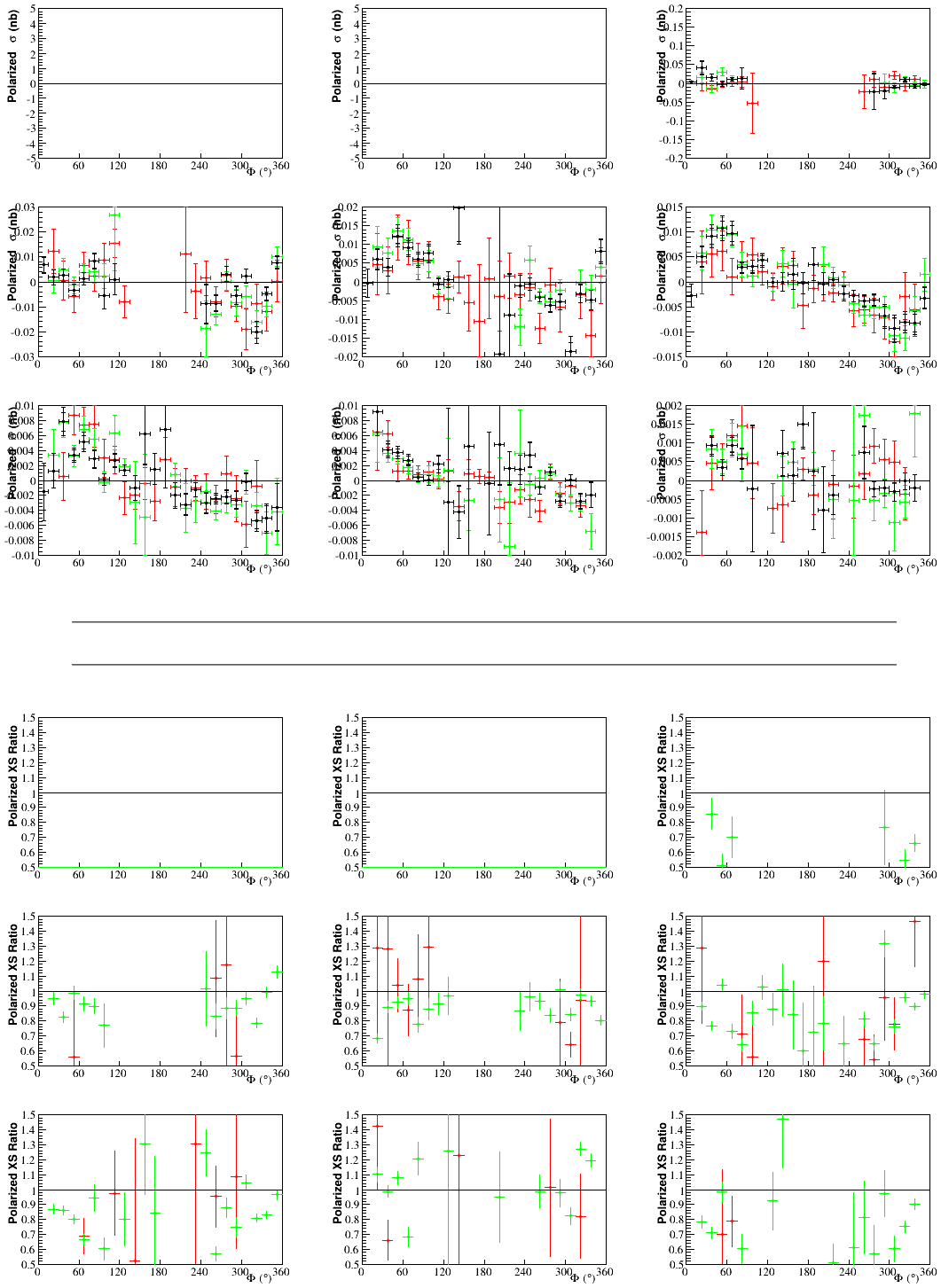

Figure E.40: On top, the polarized cross section differences as a function of Φ. Black represents this analysis. Green is e1-dvcs2 by B. Guegan. Red is e1-dvcs1 by H.S. Jo. On bottom, the polarized difference ratios. Both are for the nineteenth bin in x_B and θ_e, where $0.38 < x_B < 0.42$ and $28^\circ < \theta_e < 45^\circ$. Each panel corresponds to a bin in $-t$ whose limits are: [0.09, 0.13, 0.18, 0.23, 0.30, 0.39, 0.52, 0.72, 1.10, 2.00] Green is $\frac{e1-dvcs2\ Saylor}{e1-dvcs2\ Guegan}$. Red is $\frac{e1-dvcs2\ Saylor}{e1-dvcs1\ Jo}$.

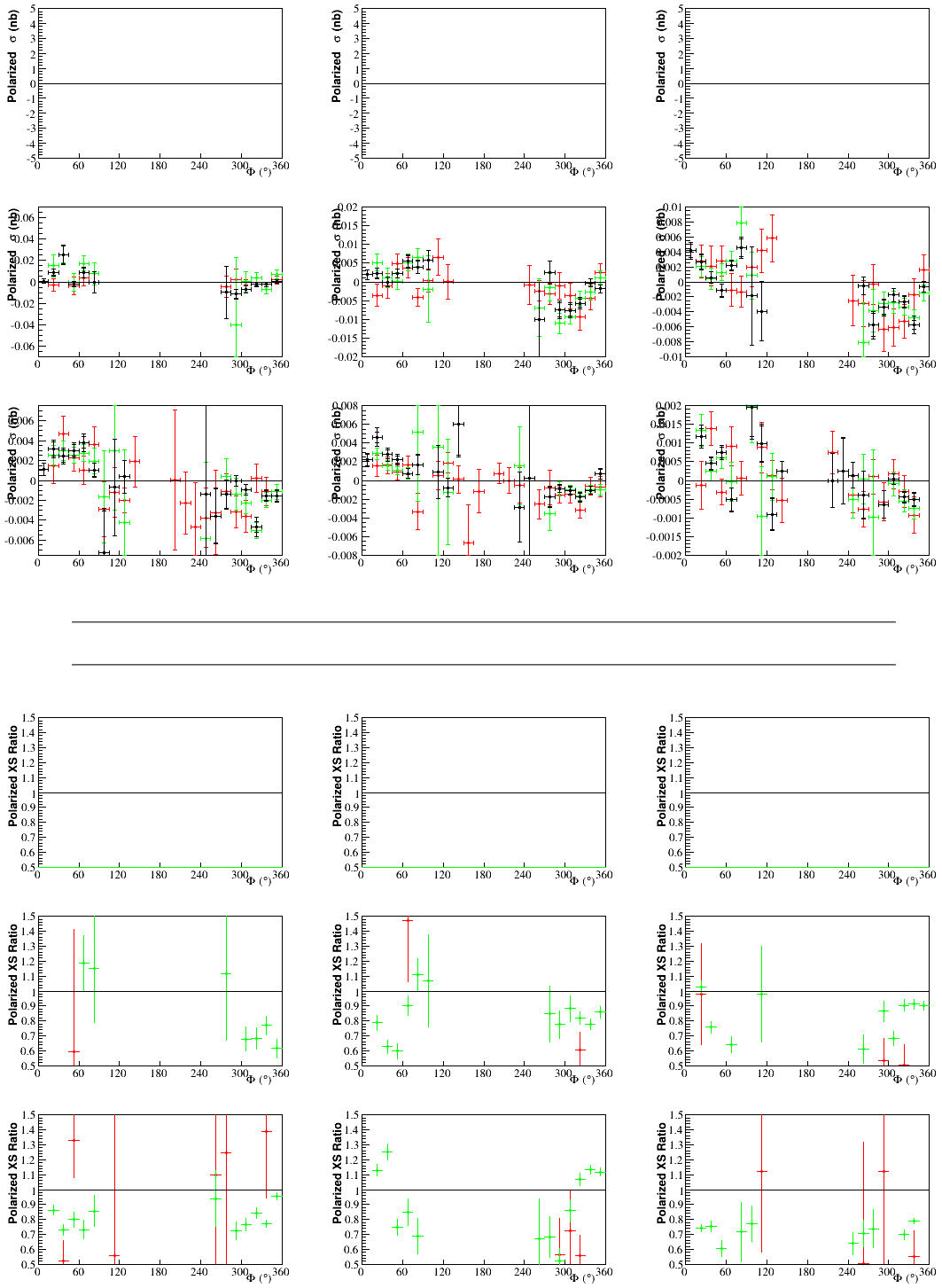

Figure E.41: On top, the polarized cross section differences as a function of Φ. Black represents this analysis. Green is e1-dvcs2 by B. Guegan. Red is e1-dvcs1 by H.S. Jo. On bottom, the polarized difference ratios. Both are for the twentieth bin in x_B and θ_e, where $0.42 < x_B < 0.58$ and $21^\circ < \theta_e < 33^\circ$. Each panel corresponds to a bin in $-t$ whose limits are: [0.09, 0.13, 0.18, 0.23, 0.30, 0.39, 0.52, 0.72, 1.10, 2.00] Green is $\frac{e1-dvcs2\ Saylor}{e1-dvcs2\ Guegan}$. Red is $\frac{e1-dvcs2\ Saylor}{e1-dvcs1\ Jo}$.

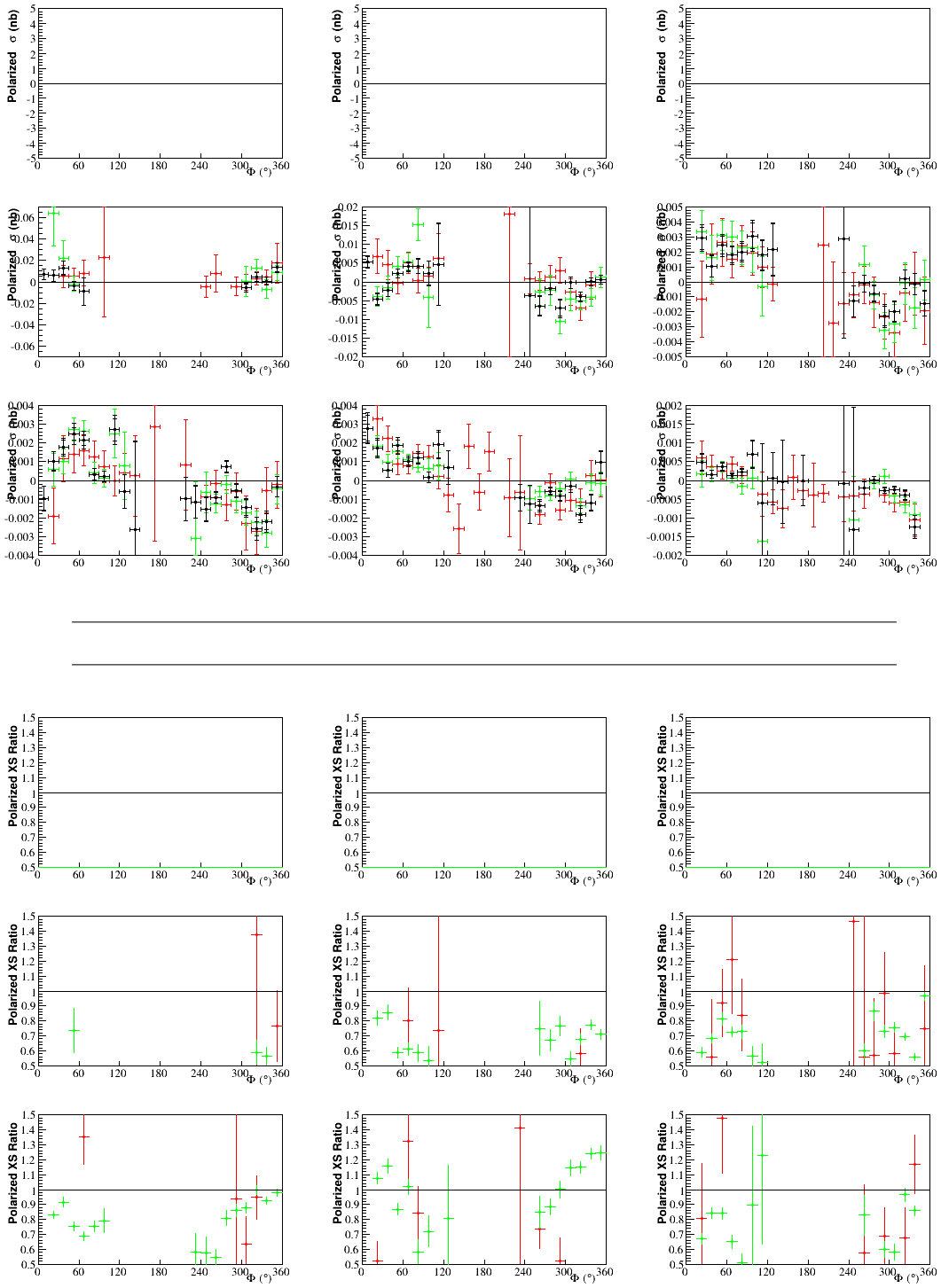

Figure E.42: On top, the polarized cross section differences as a function of Φ. Black represents this analysis. Green is e1-dvcs2 by B. Guegan. Red is e1-dvcs1 by H.S. Jo. On bottom, the polarized difference ratios. Both are for the twenty-first bin in x_B and θ_e, where $0.42 < x_B < 0.58$ and $33^\circ < \theta_e < 45^\circ$. Each panel corresponds to a bin in $-t$ whose limits are: [0.09, 0.13, 0.18, 0.23, 0.30, 0.39, 0.52, 0.72, 1.10, 2.00] Green is $\frac{e1-dvcs2\ Saylor}{e1-dvcs2\ Guegan}$. Red is $\frac{e1-dvcs2\ Saylor}{e1-dvcs1\ Jo}$.

Comparison of Beam Spin Asymmetries:

Figure E.43 to Figure E.63 each contain the beam spin asymmetry, and beam spin asymmetry ratio as a function of Φ, for a given bin in x_B and θ_e. The comparison is between this analysis; e1-dvcs2 according to the parallel analysis by B. Guegan; and e1-dvcs1 according to the analysis by H.S. Jo.

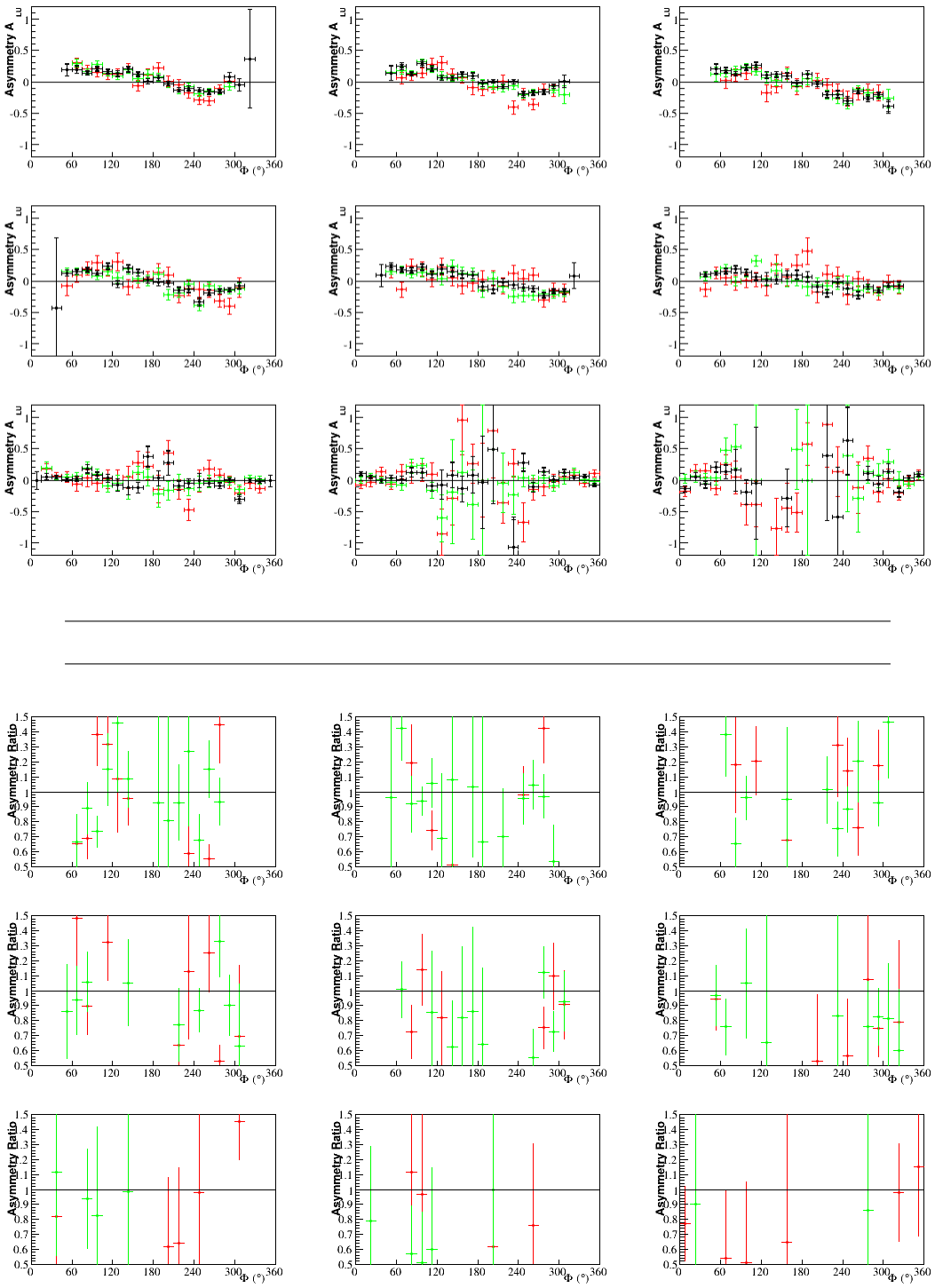

Figure E.43: On top, the asymmetry as a function of Φ. Black represents this analysis. Green is e1-dvcs2 by B. Guegan. Red is e1-dvcs1 by H.S. Jo. On bottom, the asymmetry ratios. Both are for the first bin in x_B and θ_e, where $0.1 < x_B < 0.14$ and $21^\circ < \theta_e < 45^\circ$. Each panel corresponds to a bin in $-t$ whose limits are: [0.09, 0.13, 0.18, 0.23, 0.30, 0.39, 0.52, 0.72, 1.10, 2.00] Green is $\frac{e1-dvcs2\ Saylor}{e1-dvcs2\ Guegan}$. Red is $\frac{e1-dvcs2\ Saylor}{e1-dvcs1\ Jo}$.

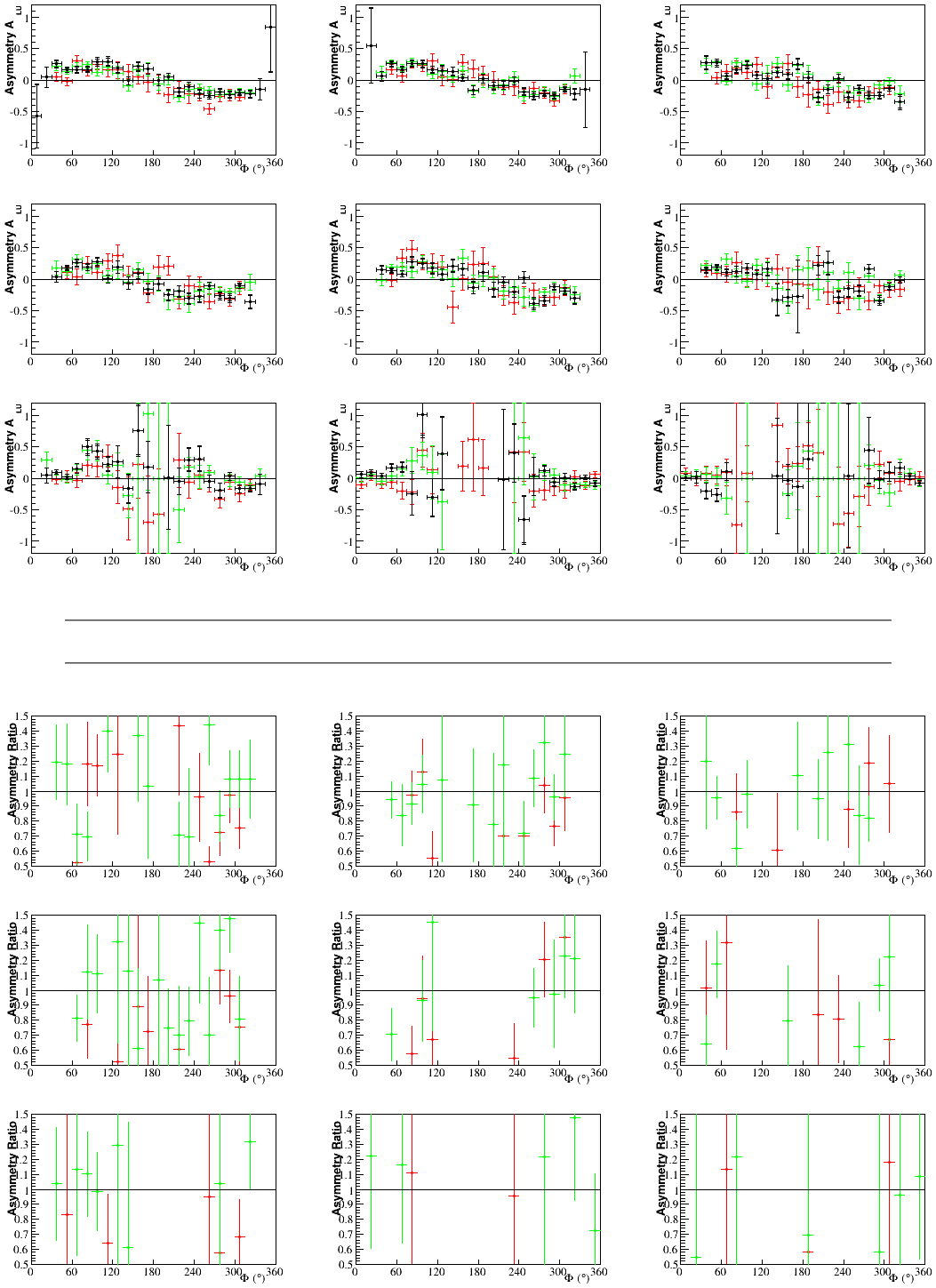

Figure E.44: On top, the asymmetry as a function of Φ. Black represents this analysis. Green is e1-dvcs2 by B. Guegan. Red is e1-dvcs1 by H.S. Jo. On bottom, the asymmetry ratios. Both are for the second bin in x_B and θ_e, where $0.14 < x_B < 0.17$ and $21^\circ < \theta_e < 25.5^\circ$. Each panel corresponds to a bin in $-t$ whose limits are: [0.09, 0.13, 0.18, 0.23, 0.30, 0.39, 0.52, 0.72, 1.10, 2.00] Green is $\frac{e1-dvcs2\ Saylor}{e1-dvcs2\ Guegan}$. Red is $\frac{e1-dvcs2\ Saylor}{e1-dvcs1\ Jo}$.

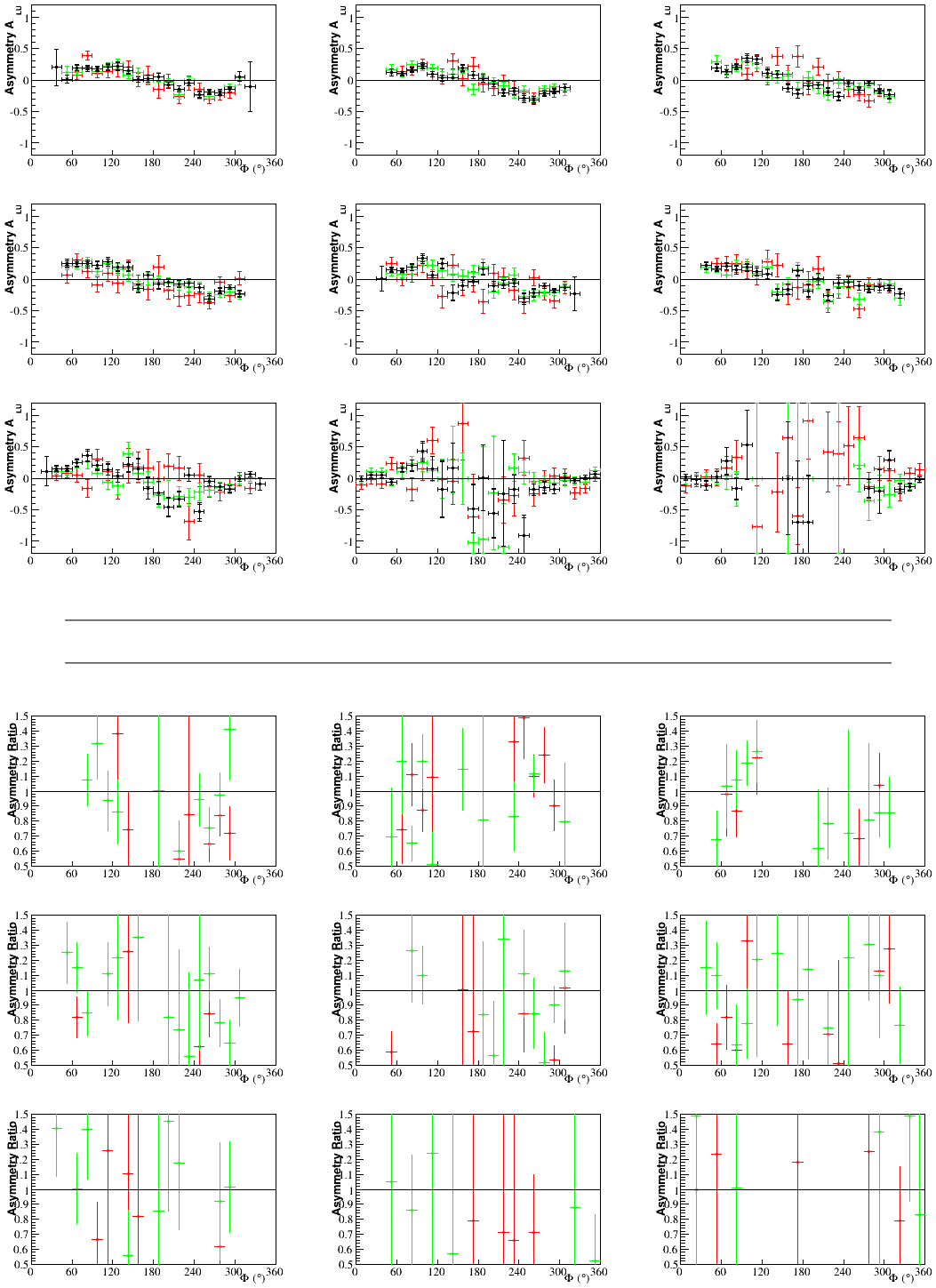

Figure E.45: On top, the asymmetry as a function of Φ. Black represents this analysis. Green is e1-dvcs2 by B. Guegan. Red is e1-dvcs1 by H.S. Jo. On bottom, the asymmetry ratios. Both are for the third bin in x_B and θ_e, where $0.14 < x_B < 0.17$ and $25.5^\circ < \theta_e < 45^\circ$. Each panel corresponds to a bin in $-t$ whose limits are: [0.09, 0.13, 0.18, 0.23, 0.30, 0.39, 0.52, 0.72, 1.10, 2.00] Green is $\frac{e1-dvcs2\ Saylor}{e1-dvcs2\ Guegan}$. Red is $\frac{e1-dvcs2\ Saylor}{e1-dvcs1\ Jo}$.

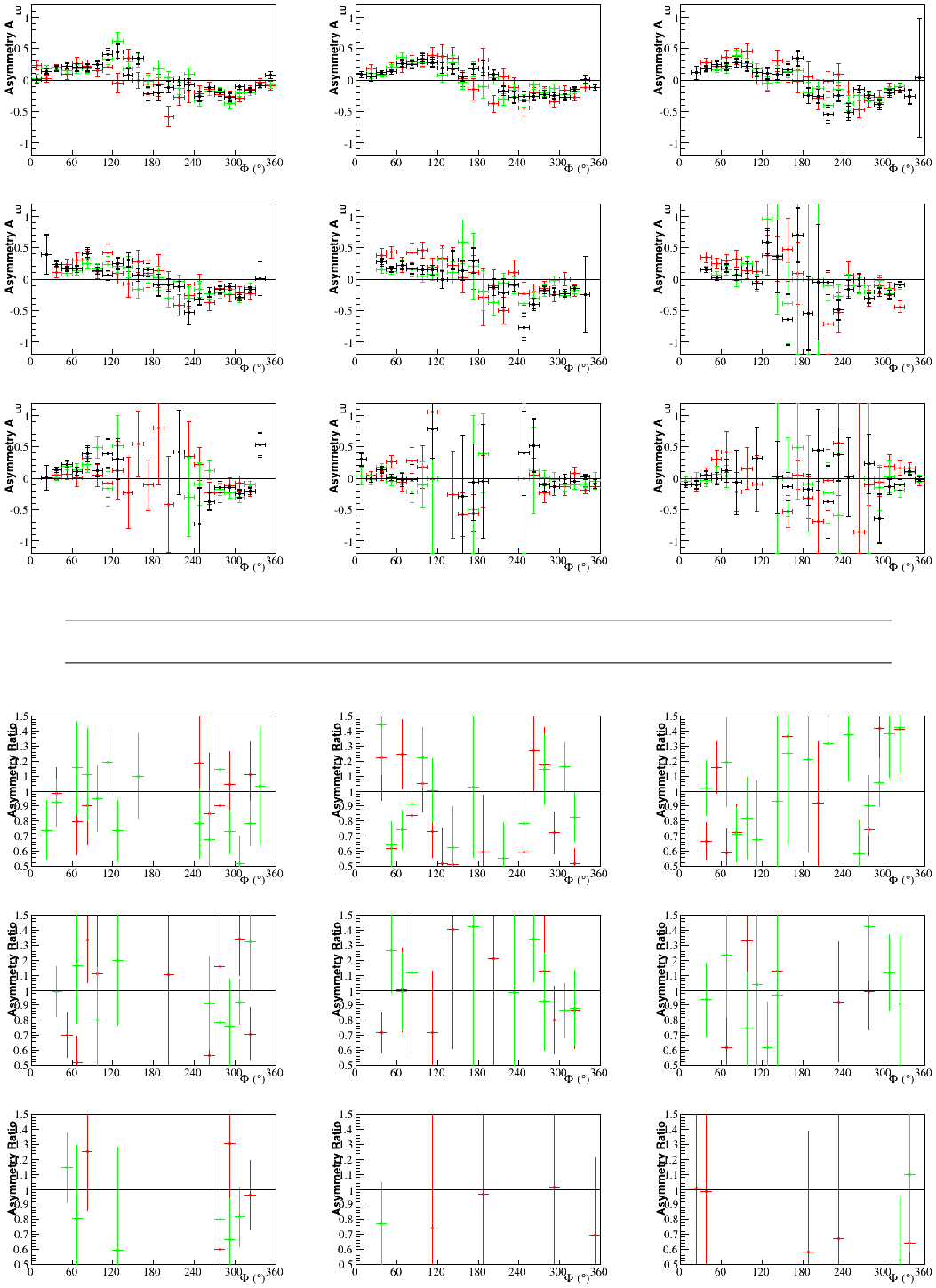

Figure E.46: On top, the asymmetry as a function of Φ. Black represents this analysis. Green is e1-dvcs2 by B. Guegan. Red is e1-dvcs1 by H.S. Jo. On bottom, the asymmetry ratios. Both are for the fourth bin in x_B and θ_e, where $0.17 < x_B < 0.2$ and $21^\circ < \theta_e < 25.5^\circ$. Each panel corresponds to a bin in $-t$ whose limits are: [0.09, 0.13, 0.18, 0.23, 0.30, 0.39, 0.52, 0.72, 1.10, 2.00] Green is $\frac{e1-dvcs2\ Saylor}{e1-dvcs2\ Guegan}$. Red is $\frac{e1-dvcs2\ Saylor}{e1-dvcs1\ Jo}$.

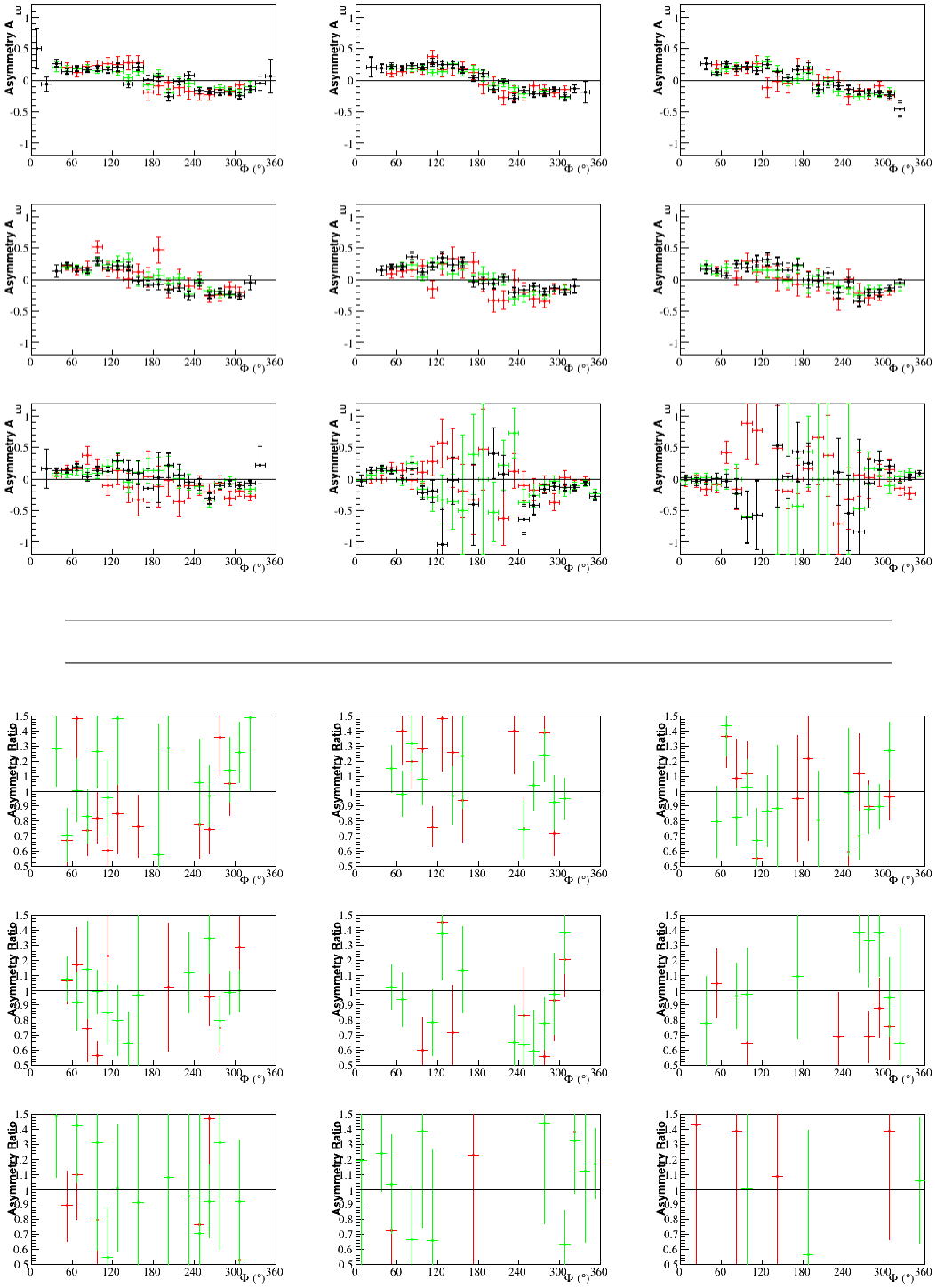

Figure E.47: On top, the asymmetry as a function of Φ. Black represents this analysis. Green is e1-dvcs2 by B. Guegan. Red is e1-dvcs1 by H.S. Jo. On bottom, the asymmetry ratios. Both are for the fifth bin in x_B and θ_e, where $0.17 < x_B < 0.2$ and $25.5^\circ < \theta_e < 45^\circ$. Each panel corresponds to a bin in $-t$ whose limits are: [0.09, 0.13, 0.18, 0.23, 0.30, 0.39, 0.52, 0.72, 1.10, 2.00] Green is $\frac{e1-dvcs2\ Saylor}{e1-dvcs2\ Guegan}$. Red is $\frac{e1-dvcs2\ Saylor}{e1-dvcs1\ Jo}$.

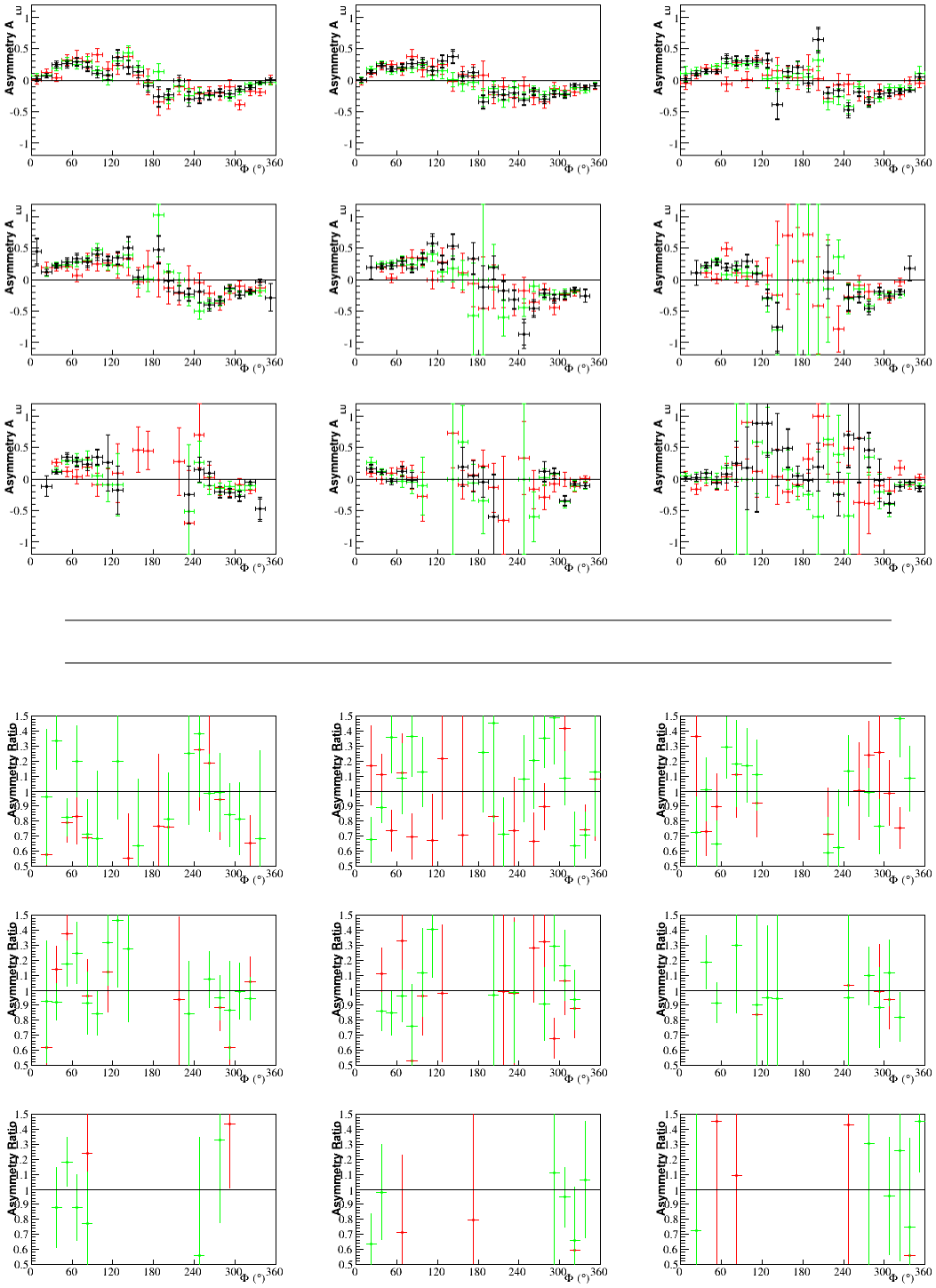

Figure E.48: On top, the asymmetry as a function of Φ. Black represents this analysis. Green is e1-dvcs2 by B. Guegan. Red is e1-dvcs1 by H.S. Jo. On bottom, the asymmetry ratios. Both are for the sixth bin in x_B and θ_e, where $0.2 < x_B < 0.23$ and $21^\circ < \theta_e < 27^\circ$. Each panel corresponds to a bin in $-t$ whose limits are: [0.09, 0.13, 0.18, 0.23, 0.30, 0.39, 0.52, 0.72, 1.10, 2.00] Green is $\frac{e1-dvcs2\ Saylor}{e1-dvcs2\ Guegan}$. Red is $\frac{e1-dvcs2\ Saylor}{e1-dvcs1\ Jo}$.

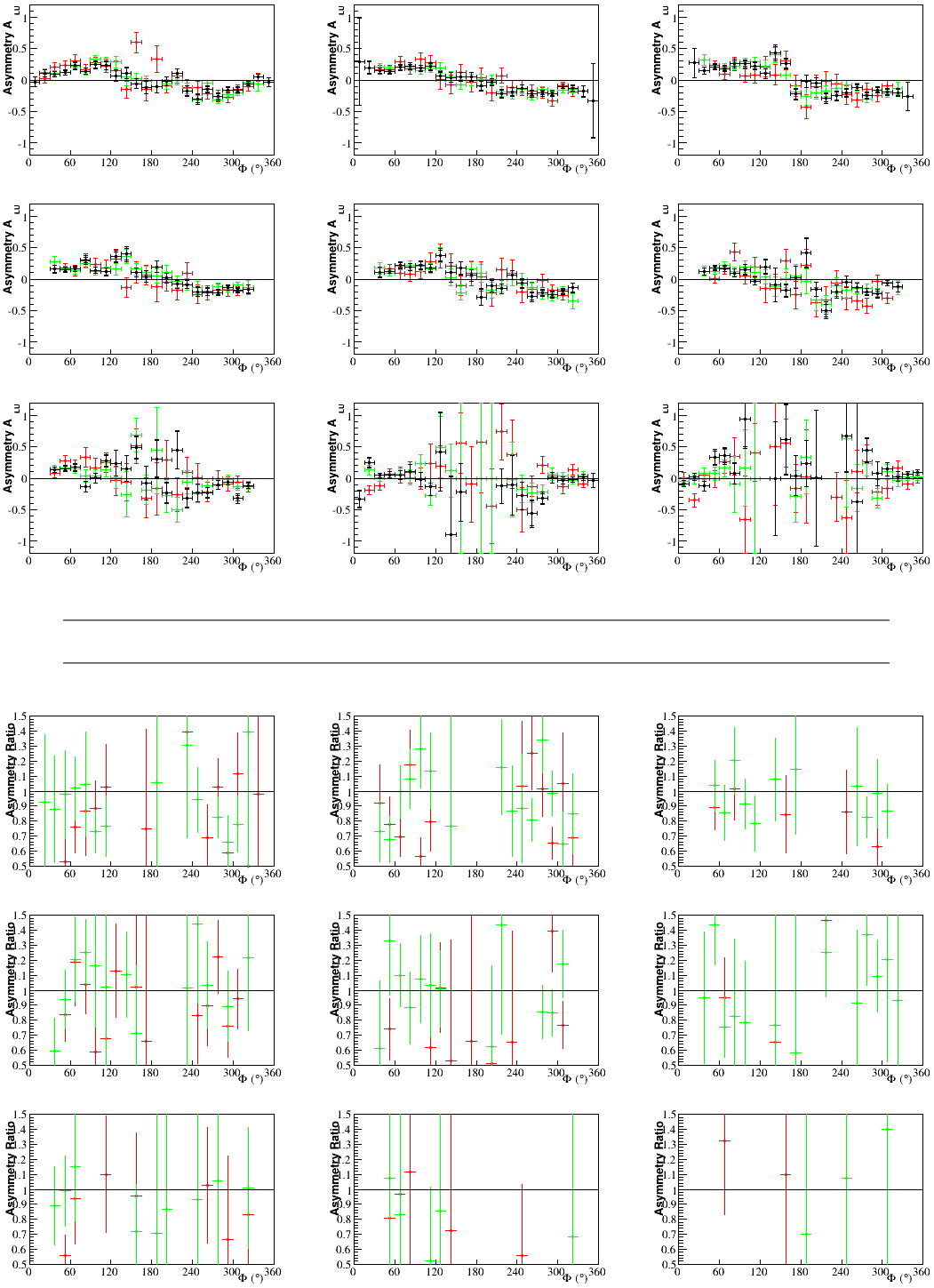

Figure E.49: On top, the asymmetry as a function of Φ. Black represents this analysis. Green is e1-dvcs2 by B. Guegan. Red is e1-dvcs1 by H.S. Jo. On bottom, the asymmetry ratios. Both are for the seventh bin in x_B and θ_e, where $0.2 < x_B < 0.23$ and $27^\circ < \theta_e < 45^\circ$. Each panel corresponds to a bin in $-t$ whose limits are: [0.09, 0.13, 0.18, 0.23, 0.30, 0.39, 0.52, 0.72, 1.10, 2.00] Green is $\frac{e1-dvcs2\ Saylor}{e1-dvcs2\ Guegan}$. Red is $\frac{e1-dvcs2\ Saylor}{e1-dvcs1\ Jo}$.

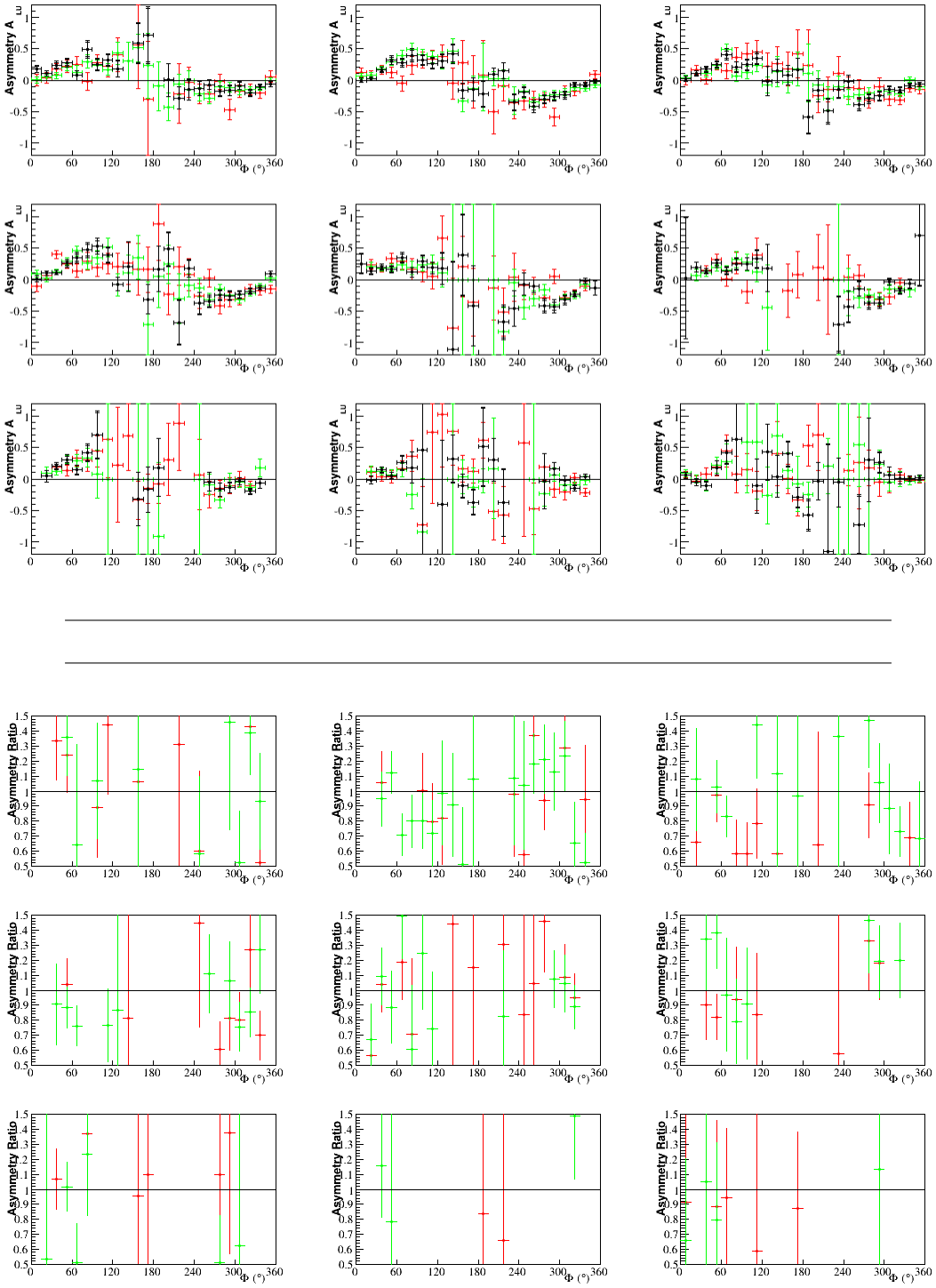

Figure E.50: On top, the asymmetry as a function of Φ. Black represents this analysis. Green is e1-dvcs2 by B. Guegan. Red is e1-dvcs1 by H.S. Jo. On bottom, the asymmetry ratios. Both are for the eighth bin in x_B and θ_e, where $0.23 < x_B < 0.26$ and $21^\circ < \theta_e < 27^\circ$. Each panel corresponds to a bin in $-t$ whose limits are: [0.09, 0.13, 0.18, 0.23, 0.30, 0.39, 0.52, 0.72, 1.10, 2.00] Green is $\frac{e1-dvcs2\ Saylor}{e1-dvcs2\ Guegan}$. Red is $\frac{e1-dvcs2\ Saylor}{e1-dvcs1\ Jo}$.

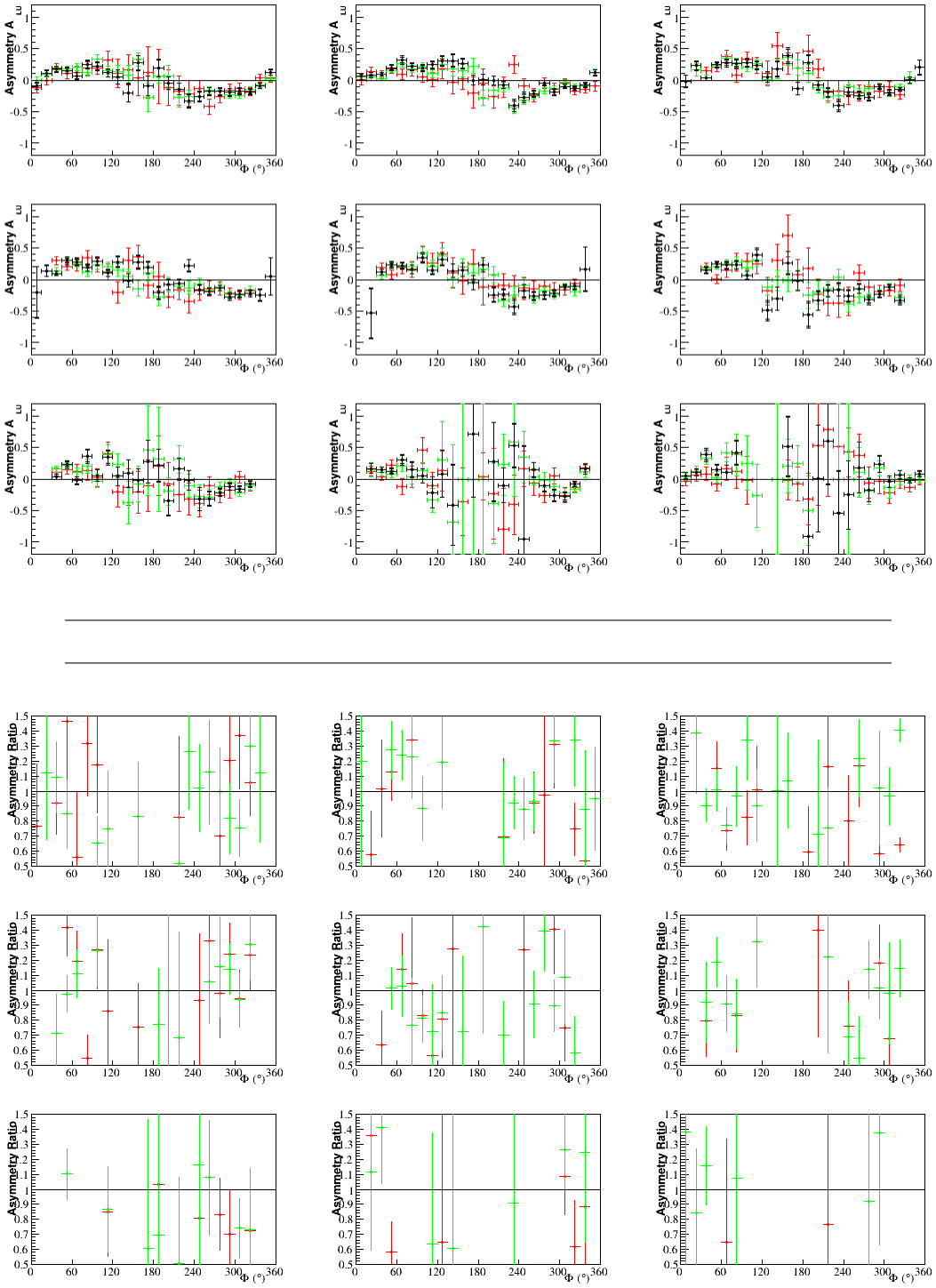

Figure E.51: On top, the asymmetry as a function of Φ. Black represents this analysis. Green is e1-dvcs2 by B. Guegan. Red is e1-dvcs1 by H.S. Jo. On bottom, the asymmetry ratios. Both are for the ninth bin in x_B and θ_e, where $0.23 < x_B < 0.26$ and $27^\circ < \theta_e < 45^\circ$. Each panel corresponds to a bin in $-t$ whose limits are: [0.09, 0.13, 0.18, 0.23, 0.30, 0.39, 0.52, 0.72, 1.10, 2.00] Green is $\frac{e1-dvcs2\ Saylor}{e1-dvcs2\ Guegan}$. Red is $\frac{e1-dvcs2\ Saylor}{e1-dvcs1\ Jo}$.

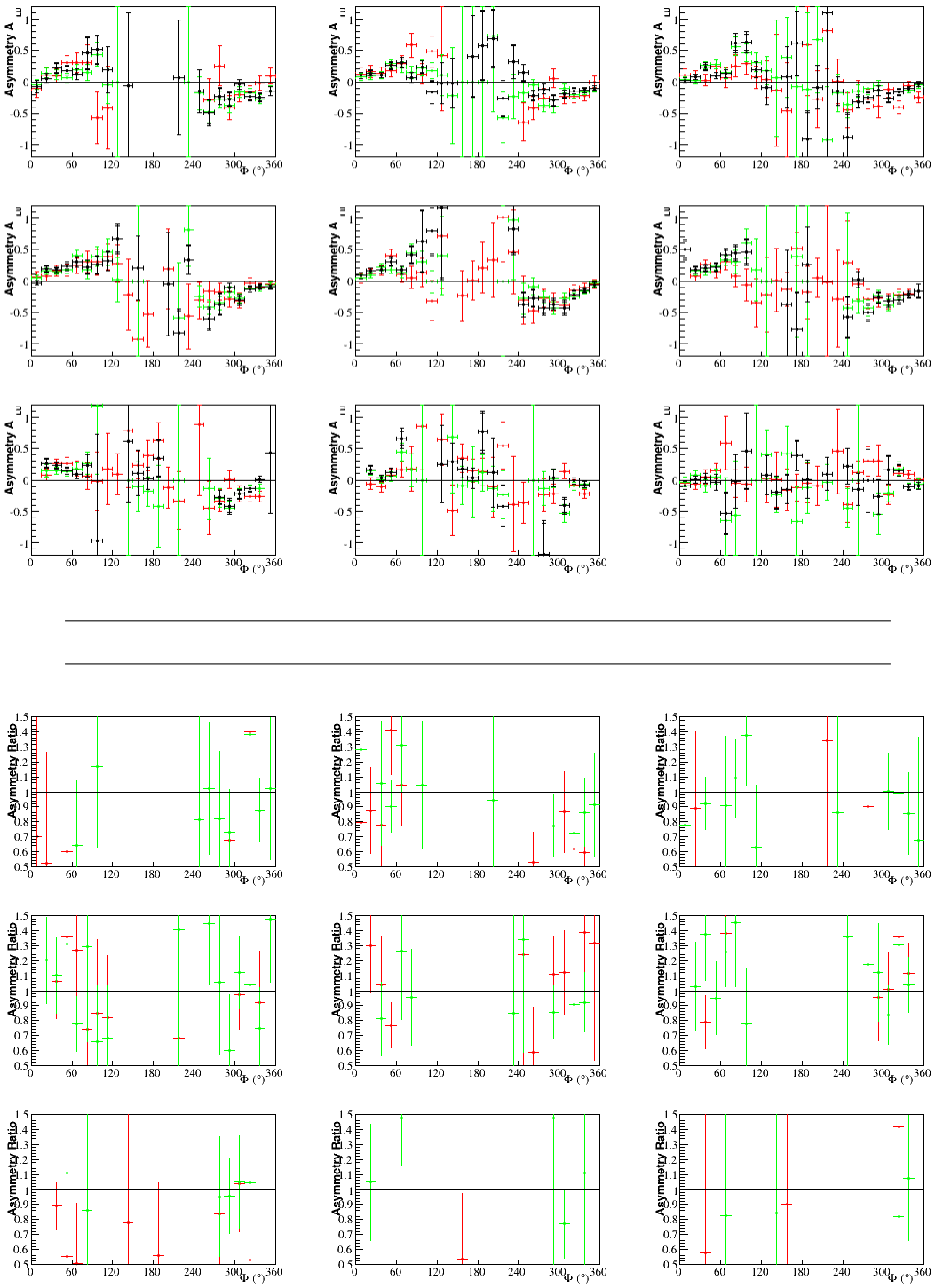

Figure E.52: On top, the asymmetry as a function of Φ. Black represents this analysis. Green is e1-dvcs2 by B. Guegan. Red is e1-dvcs1 by H.S. Jo. On bottom, the asymmetry ratios. Both are for the tenth bin in x_B and θ_e, where $0.26 < x_B < 0.29$ and $21^\circ < \theta_e < 27^\circ$. Each panel corresponds to a bin in $-t$ whose limits are: [0.09, 0.13, 0.18, 0.23, 0.30, 0.39, 0.52, 0.72, 1.10, 2.00] Green is $\frac{e1-dvcs2\ Saylor}{e1-dvcs2\ Guegan}$. Red is $\frac{e1-dvcs2\ Saylor}{e1-dvcs1\ Jo}$.

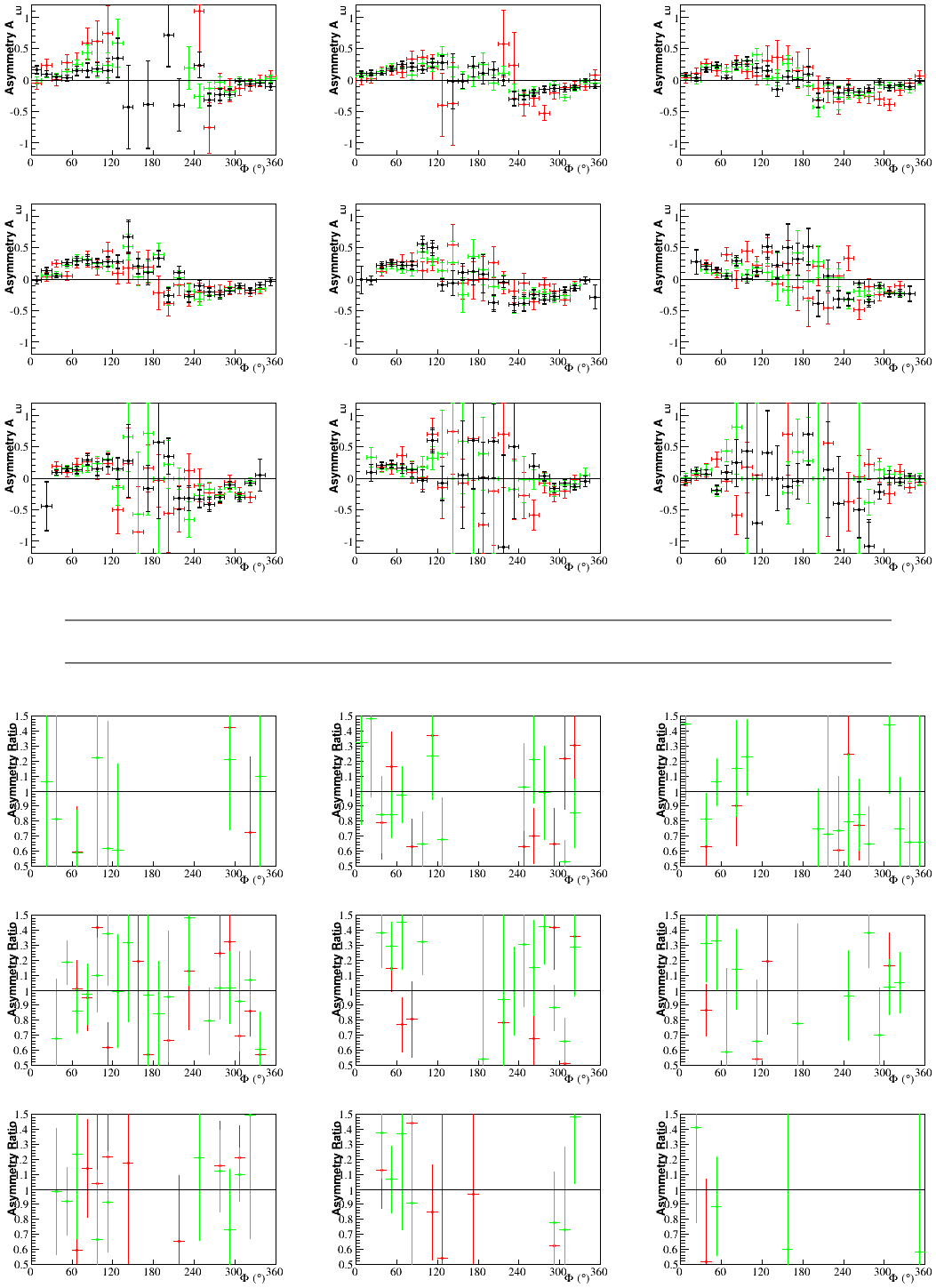

Figure E.53: On top, the asymmetry as a function of Φ. Black represents this analysis. Green is e1-dvcs2 by B. Guegan. Red is e1-dvcs1 by H.S. Jo. On bottom, the asymmetry ratios. Both are for the eleventh bin in x_B and θ_e, where $0.26 < x_B < 0.29$ and $27^\circ < \theta_e < 45^\circ$. Each panel corresponds to a bin in $-t$ whose limits are: [0.09, 0.13, 0.18, 0.23, 0.30, 0.39, 0.52, 0.72, 1.10, 2.00] Green is $\frac{e1-dvcs2\ Saylor}{e1-dvcs2\ Guegan}$. Red is $\frac{e1-dvcs2\ Saylor}{e1-dvcs1\ Jo}$.

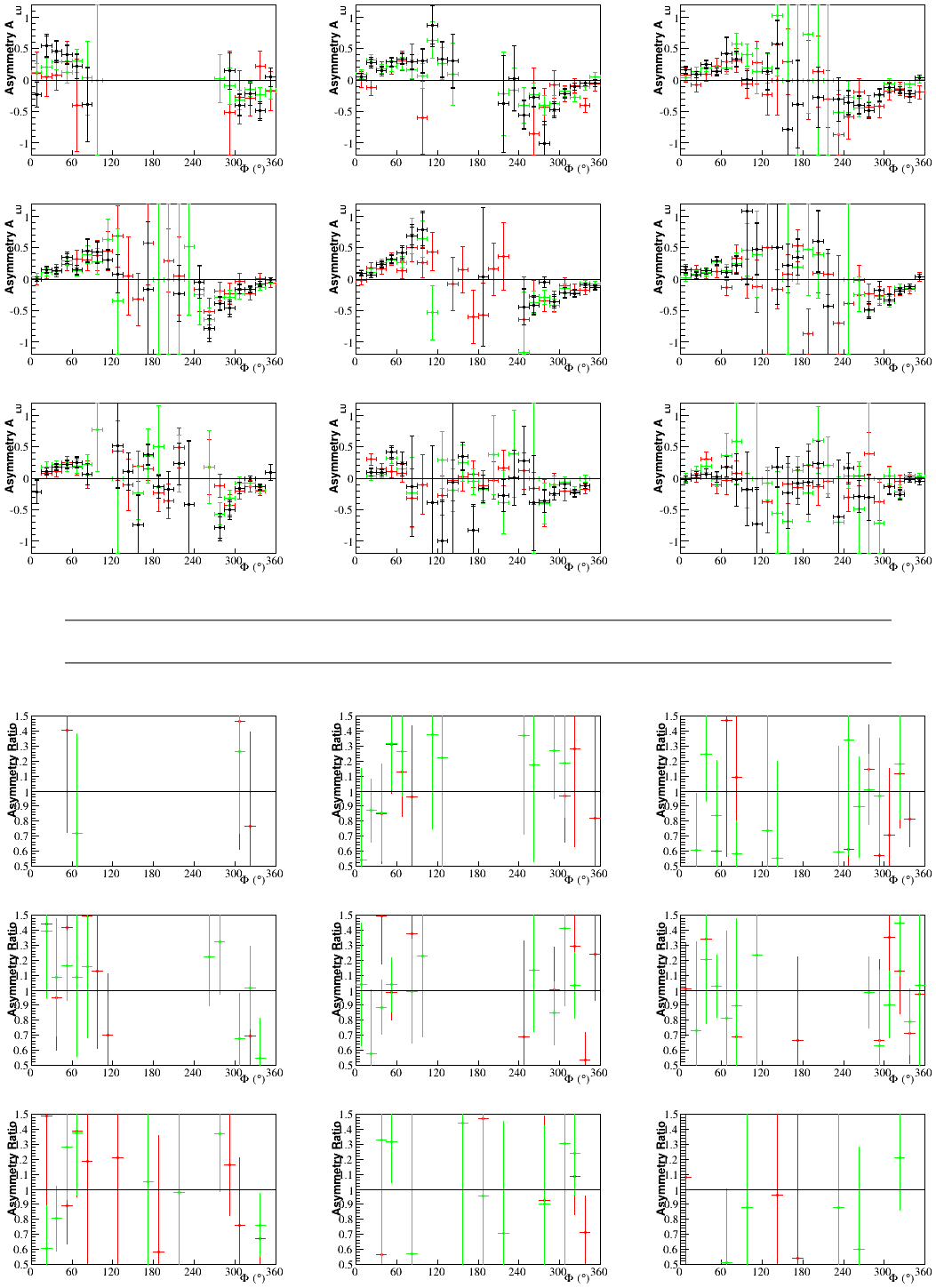

Figure E.54: On top, the asymmetry as a function of Φ. Black represents this analysis. Green is e1-dvcs2 by B. Guegan. Red is e1-dvcs1 by H.S. Jo. On bottom, the asymmetry ratios. Both are for the twelfth bin in x_B and θ_e, where $0.29 < x_B < 0.32$ and $21^\circ < \theta_e < 28^\circ$. Each panel corresponds to a bin in $-t$ whose limits are: [0.09, 0.13, 0.18, 0.23, 0.30, 0.39, 0.52, 0.72, 1.10, 2.00] Green is $\frac{e1-dvcs2\ Saylor}{e1-dvcs2\ Guegan}$. Red is $\frac{e1-dvcs2\ Saylor}{e1-dvcs1\ Jo}$.

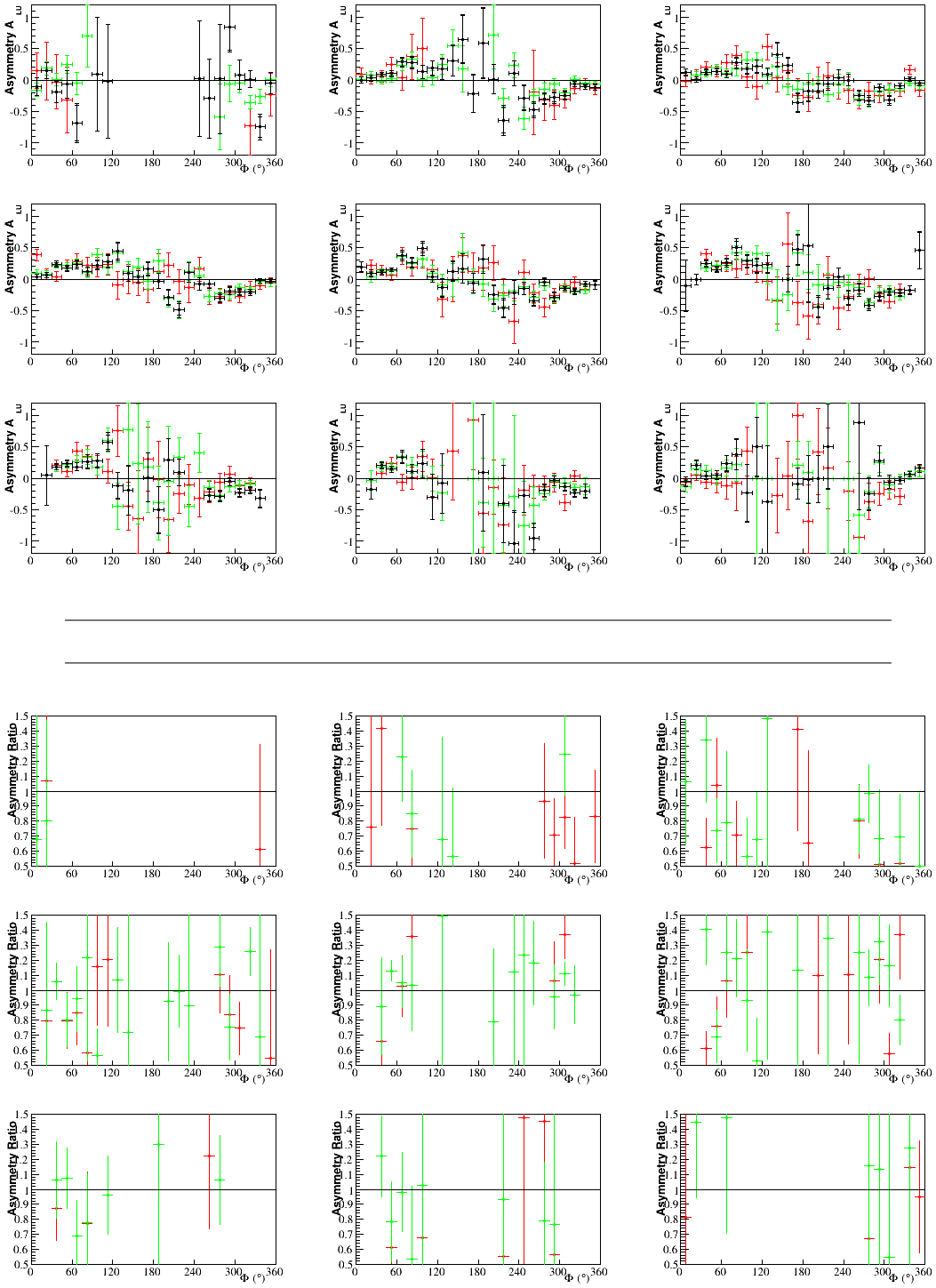

Figure E.55: On top, the asymmetry as a function of Φ. Black represents this analysis. Green is e1-dvcs2 by B. Guegan. Red is e1-dvcs1 by H.S. Jo. On bottom, the asymmetry ratios. Both are for the thirteenth bin in x_B and θ_e, where $0.29 < x_B < 0.32$ and $28^\circ < \theta_e < 45^\circ$. Each panel corresponds to a bin in $-t$ whose limits are: [0.09, 0.13, 0.18, 0.23, 0.30, 0.39, 0.52, 0.72, 1.10, 2.00] Green is $\frac{e1-dvcs2\ Saylor}{e1-dvcs2\ Guegan}$. Red is $\frac{e1-dvcs2\ Saylor}{e1-dvcs1\ Jo}$.

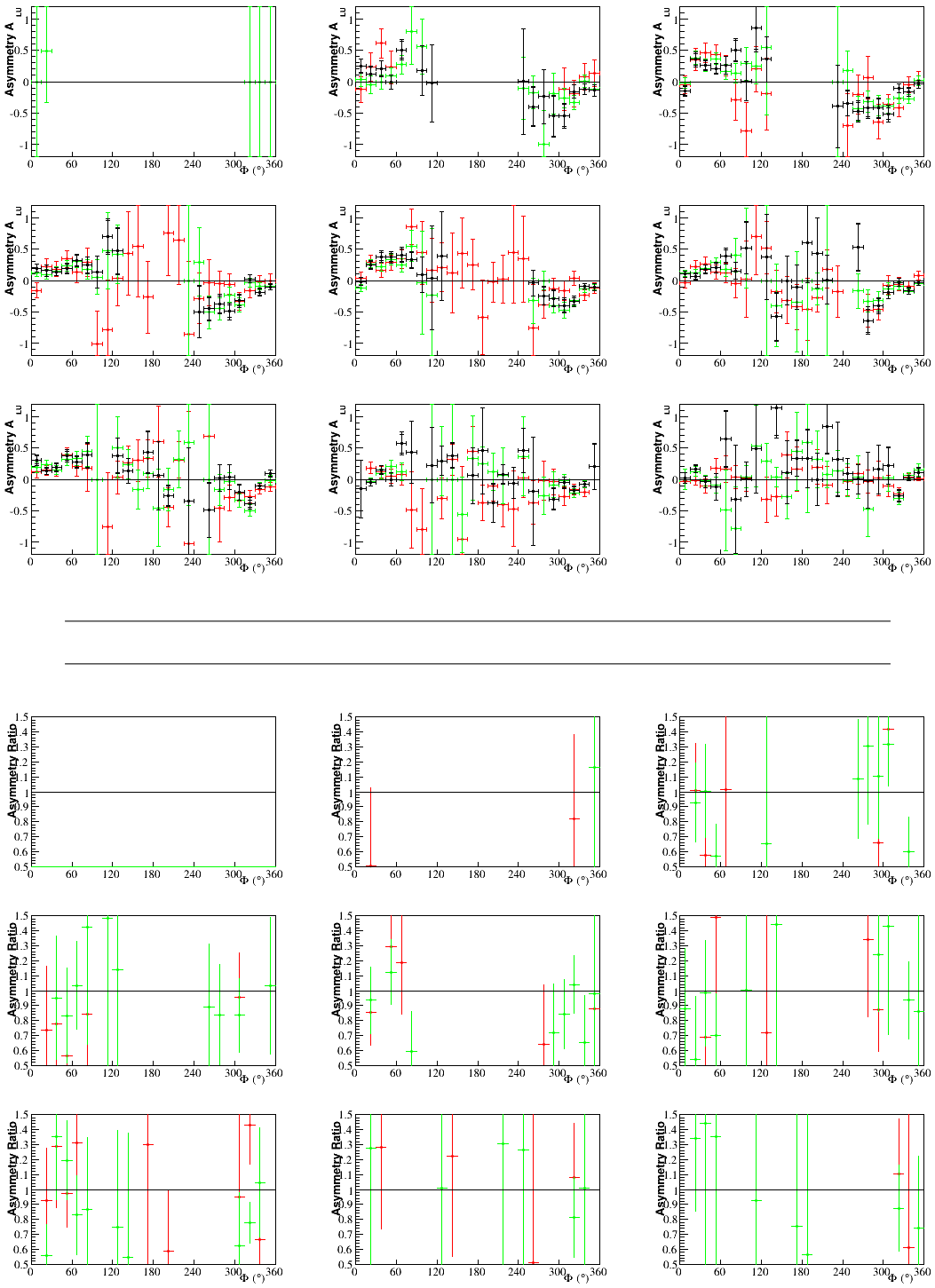

Figure E.56: On top, the asymmetry as a function of Φ. Black represents this analysis. Green is e1-dvcs2 by B. Guegan. Red is e1-dvcs1 by H.S. Jo. On bottom, the asymmetry ratios. Both are for the fourteenth bin in x_B and θ_e, where $0.32 < x_B < 0.35$ and $21^\circ < \theta_e < 28^\circ$. Each panel corresponds to a bin in $-t$ whose limits are: [0.09, 0.13, 0.18, 0.23, 0.30, 0.39, 0.52, 0.72, 1.10, 2.00] Green is $\frac{e1-dvcs2\ Saylor}{e1-dvcs2\ Guegan}$. Red is $\frac{e1-dvcs2\ Saylor}{e1-dvcs1\ Jo}$.

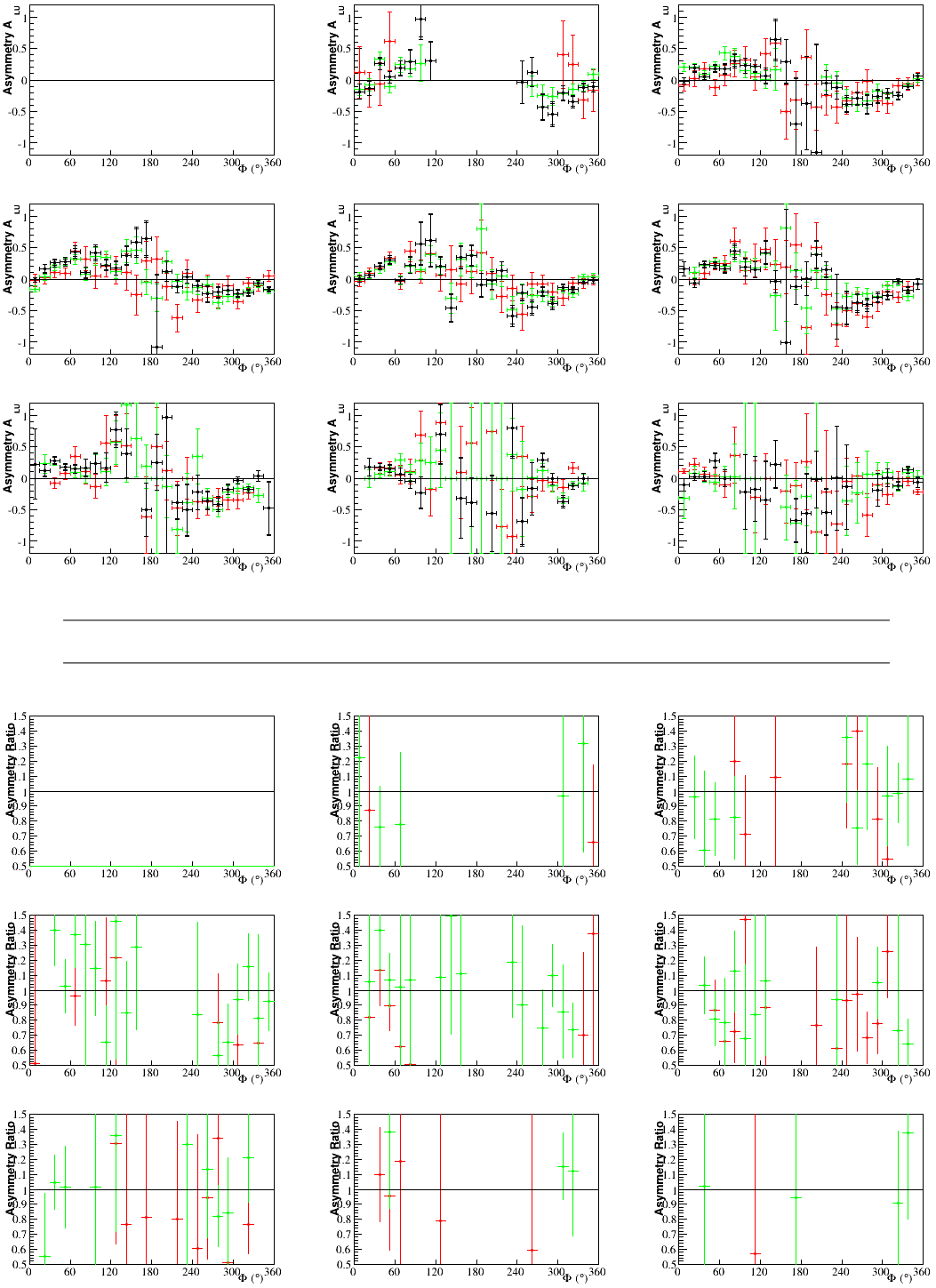

Figure E.57: On top, the asymmetry as a function of Φ. Black represents this analysis. Green is e1-dvcs2 by B. Guegan. Red is e1-dvcs1 by H.S. Jo. On bottom, the asymmetry ratios. Both are for the fifteenth bin in x_B and θ_e, where $0.32 < x_B < 0.35$ and $28^\circ < \theta_e < 45^\circ$. Each panel corresponds to a bin in $-t$ whose limits are: [0.09, 0.13, 0.18, 0.23, 0.30, 0.39, 0.52, 0.72, 1.10, 2.00] Green is $\frac{e1-dvcs2\ Saylor}{e1-dvcs2\ Guegan}$. Red is $\frac{e1-dvcs2\ Saylor}{e1-dvcs1\ Jo}$.

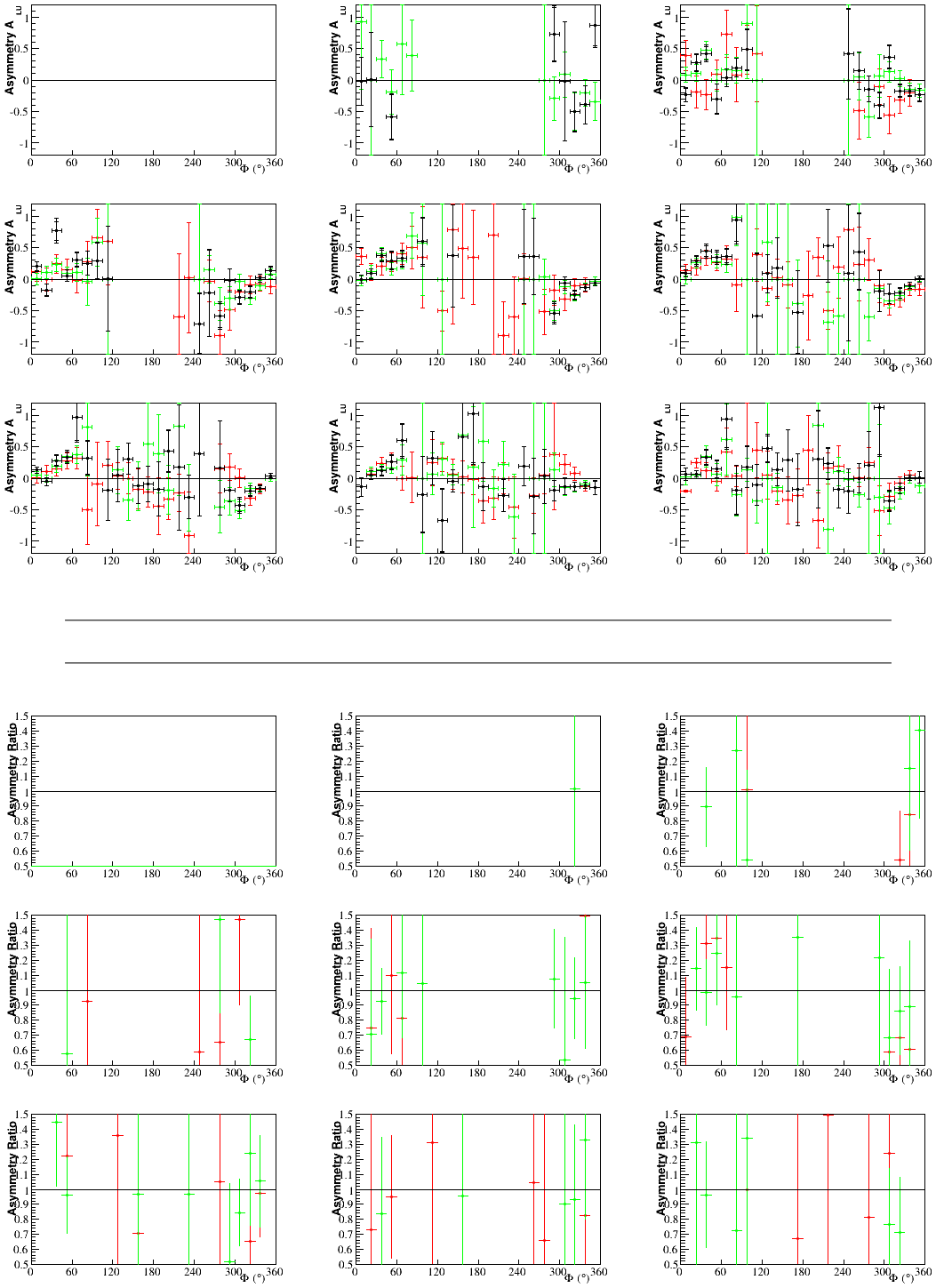

Figure E.58: On top, the asymmetry as a function of Φ. Black represents this analysis. Green is e1-dvcs2 by B. Guegan. Red is e1-dvcs1 by H.S. Jo. On bottom, the asymmetry ratios. Both are for the sixteenth bin in x_B and θ_e, where $0.35 < x_B < 0.38$ and $21^\circ < \theta_e < 28^\circ$. Each panel corresponds to a bin in $-t$ whose limits are: [0.09, 0.13, 0.18, 0.23, 0.30, 0.39, 0.52, 0.72, 1.10, 2.00] Green is $\frac{e1-dvcs2\ Saylor}{e1-dvcs2\ Guegan}$. Red is $\frac{e1-dvcs2\ Saylor}{e1-dvcs1\ Jo}$.

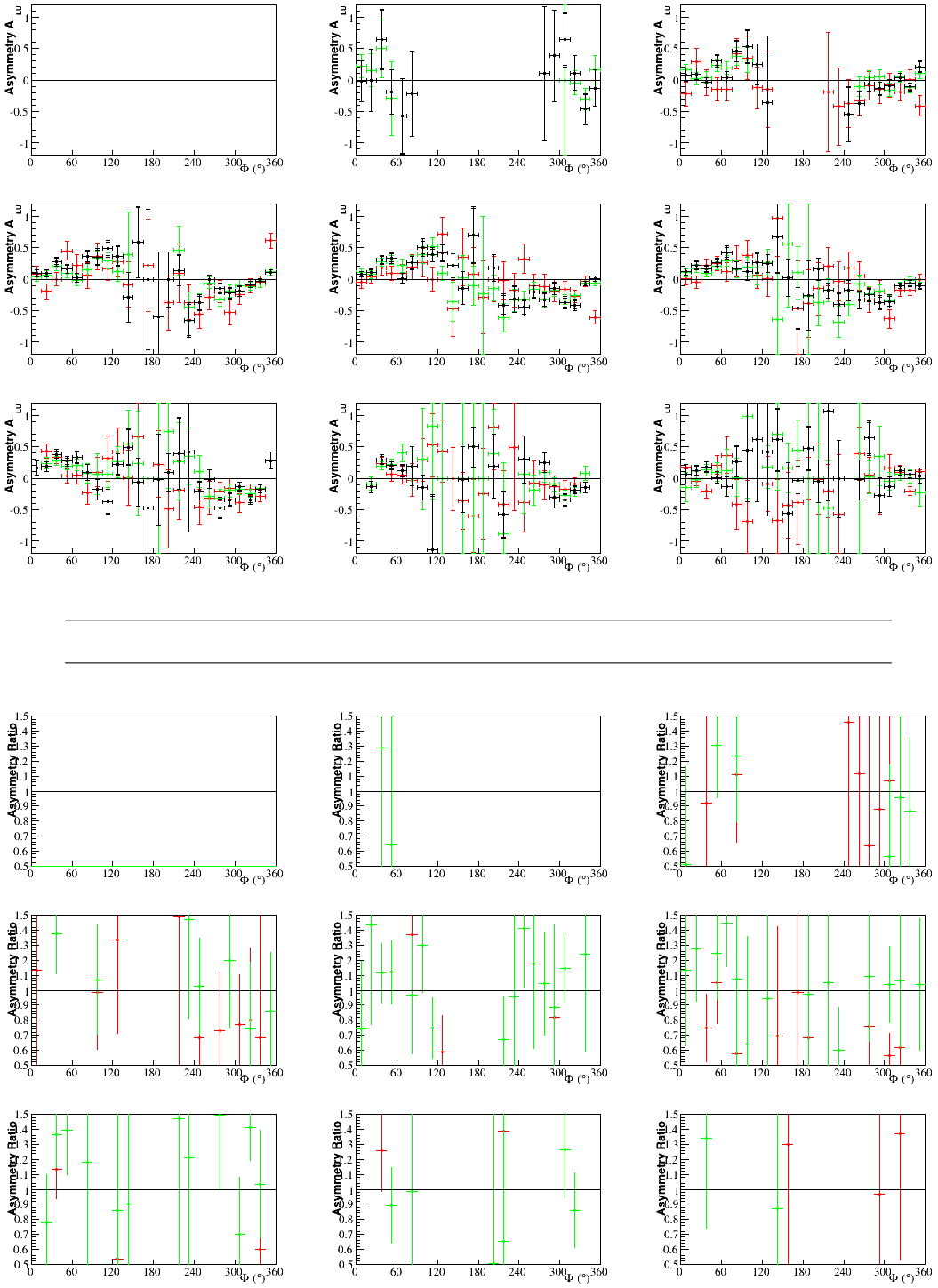

Figure E.59: On top, the asymmetry as a function of Φ. Black represents this analysis. Green is e1-dvcs2 by B. Guegan. Red is e1-dvcs1 by H.S. Jo. On bottom, the asymmetry ratios. Both are for the seventeenth bin in x_B and θ_e, where $0.35 < x_B < 0.38$ and $28^\circ < \theta_e < 45^\circ$. Each panel corresponds to a bin in $-t$ whose limits are: [0.09, 0.13, 0.18, 0.23, 0.30, 0.39, 0.52, 0.72, 1.10, 2.00] Green is $\frac{e1-dvcs2\ Saylor}{e1-dvcs2\ Guegan}$. Red is $\frac{e1-dvcs2\ Saylor}{e1-dvcs1\ Jo}$.

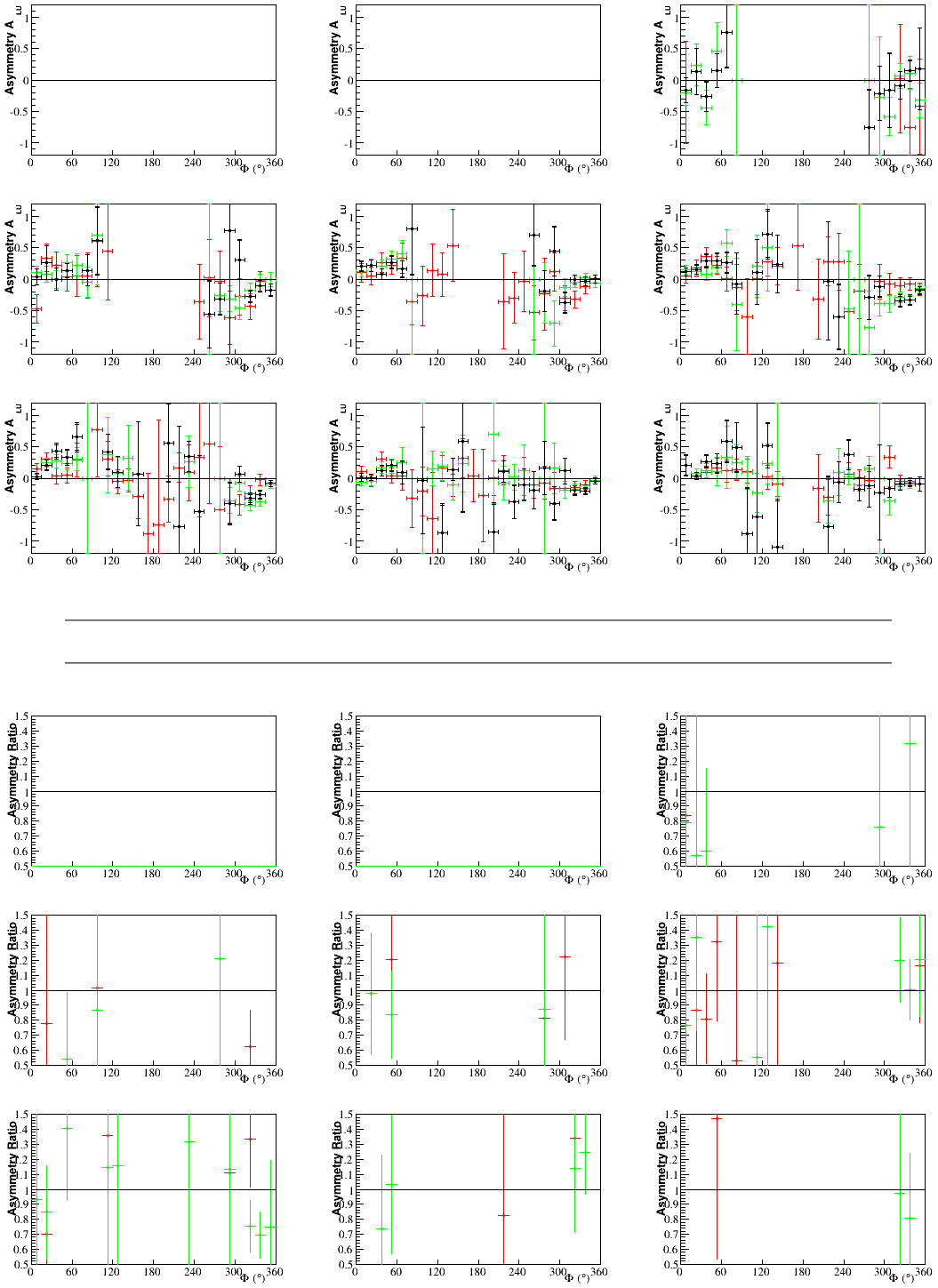

Figure E.60: On top, the asymmetry as a function of Φ. Black represents this analysis. Green is e1-dvcs2 by B. Guegan. Red is e1-dvcs1 by H.S. Jo. On bottom, the asymmetry ratios. Both are for the eighteenth bin in x_B and θ_e, where $0.38 < x_B < 0.42$ and $21^\circ < \theta_e < 28^\circ$. Each panel corresponds to a bin in $-t$ whose limits are: [0.09, 0.13, 0.18, 0.23, 0.30, 0.39, 0.52, 0.72, 1.10, 2.00] Green is $\frac{e1-dvcs2\ Saylor}{e1-dvcs2\ Guegan}$. Red is $\frac{e1-dvcs2\ Saylor}{e1-dvcs1\ Jo}$.

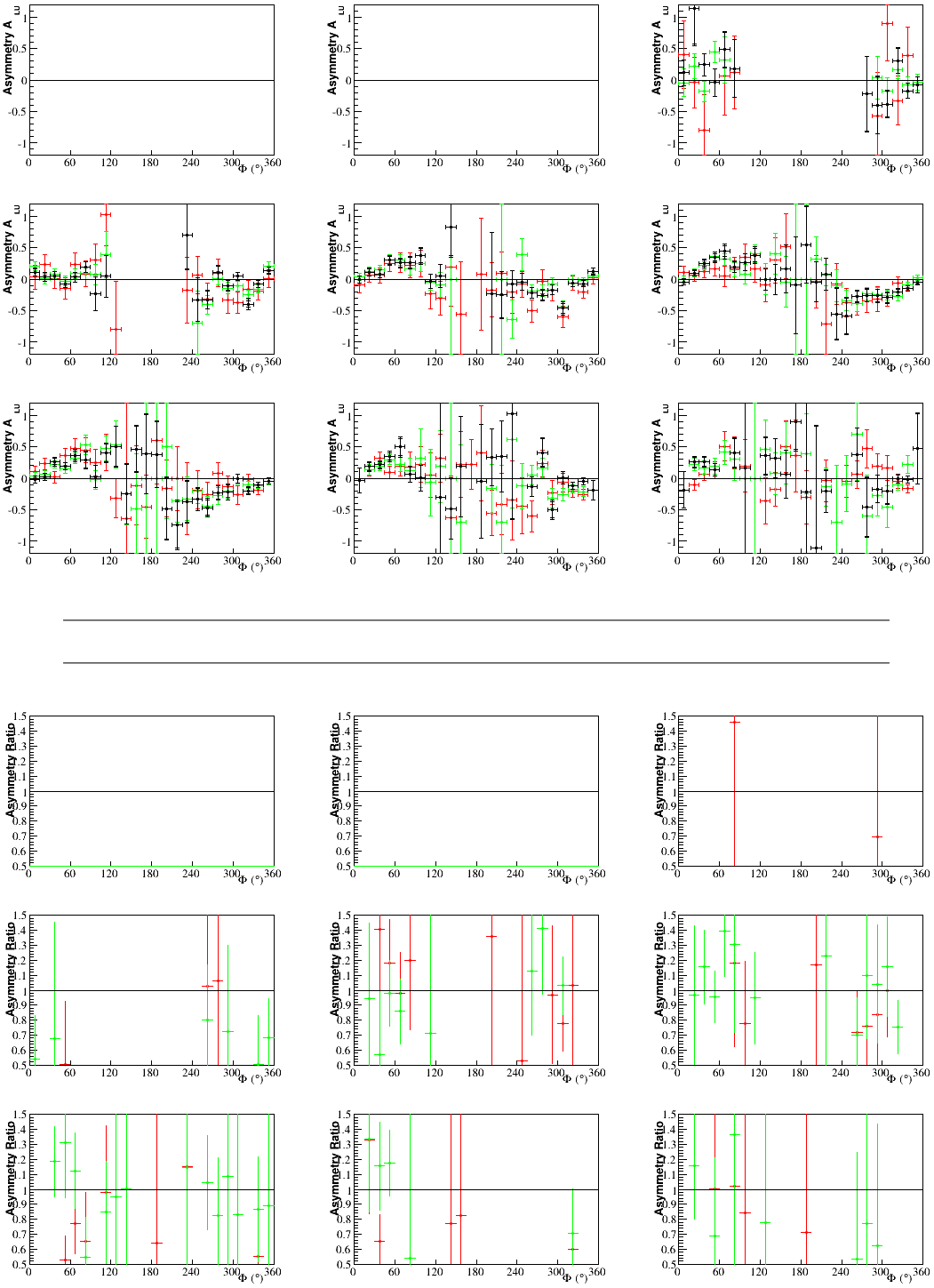

Figure E.61: On top, the asymmetry as a function of Φ. Black represents this analysis. Green is e1-dvcs2 by B. Guegan. Red is e1-dvcs1 by H.S. Jo. On bottom, the asymmetry ratios. Both are for the nineteenth bin in x_B and θ_e, where $0.38 < x_B < 0.42$ and $28^\circ < \theta_e < 45^\circ$. Each panel corresponds to a bin in $-t$ whose limits are: [0.09, 0.13, 0.18, 0.23, 0.30, 0.39, 0.52, 0.72, 1.10, 2.00] Green is $\frac{e1-dvcs2\ Saylor}{e1-dvcs2\ Guegan}$. Red is $\frac{e1-dvcs2\ Saylor}{e1-dvcs1\ Jo}$.

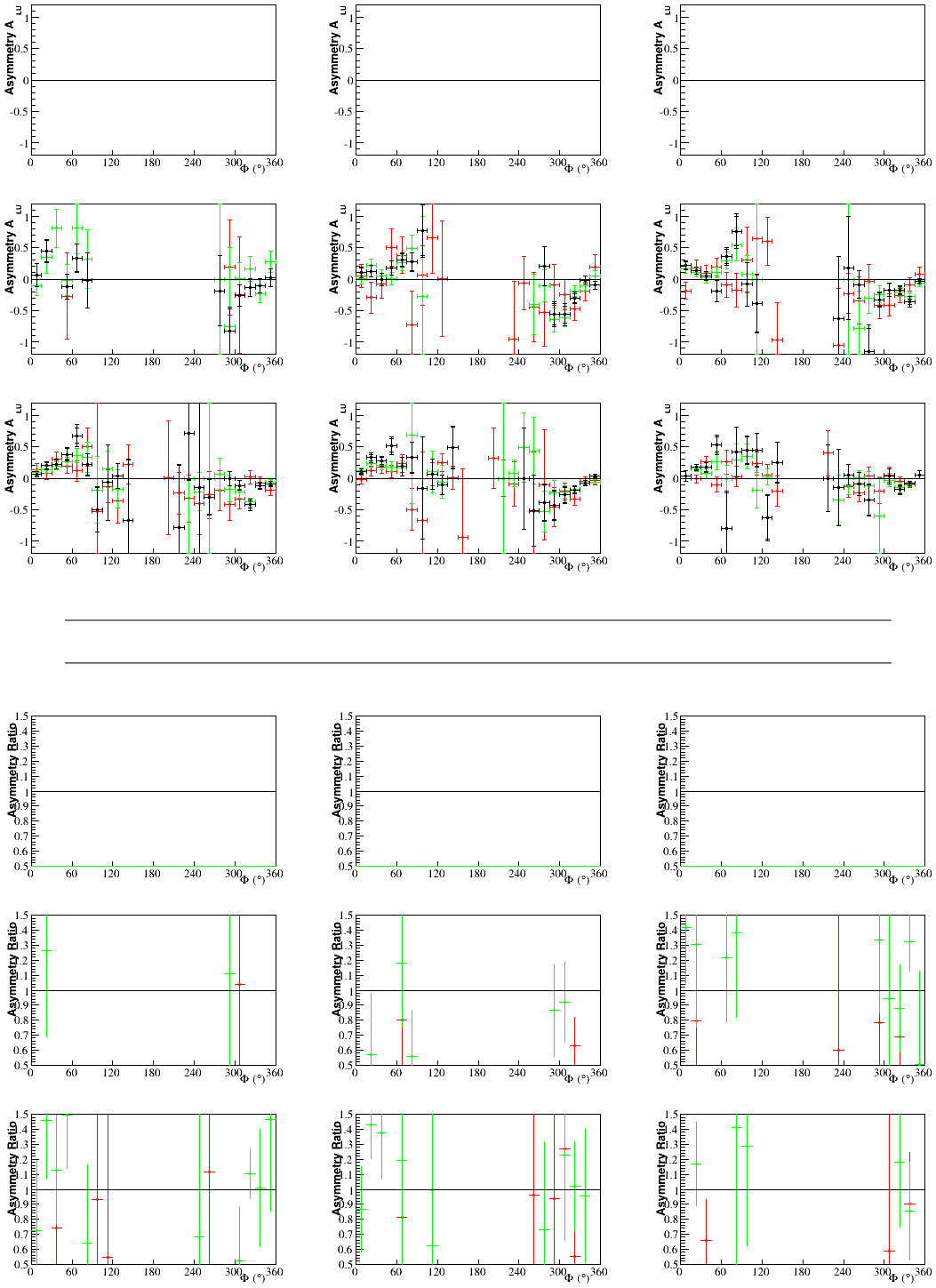

Figure E.62: On top, the asymmetry as a function of Φ. Black represents this analysis. Green is e1-dvcs2 by B. Guegan. Red is e1-dvcs1 by H.S. Jo. On bottom, the asymmetry ratios. Both are for the twentieth bin in x_B and θ_e, where $0.42 < x_B < 0.58$ and $21^\circ < \theta_e < 33^\circ$. Each panel corresponds to a bin in $-t$ whose limits are: [0.09, 0.13, 0.18, 0.23, 0.30, 0.39, 0.52, 0.72, 1.10, 2.00] Green is $\frac{e1-dvcs2\ Saylor}{e1-dvcs2\ Guegan}$. Red is $\frac{e1-dvcs2\ Saylor}{e1-dvcs1\ Jo}$.

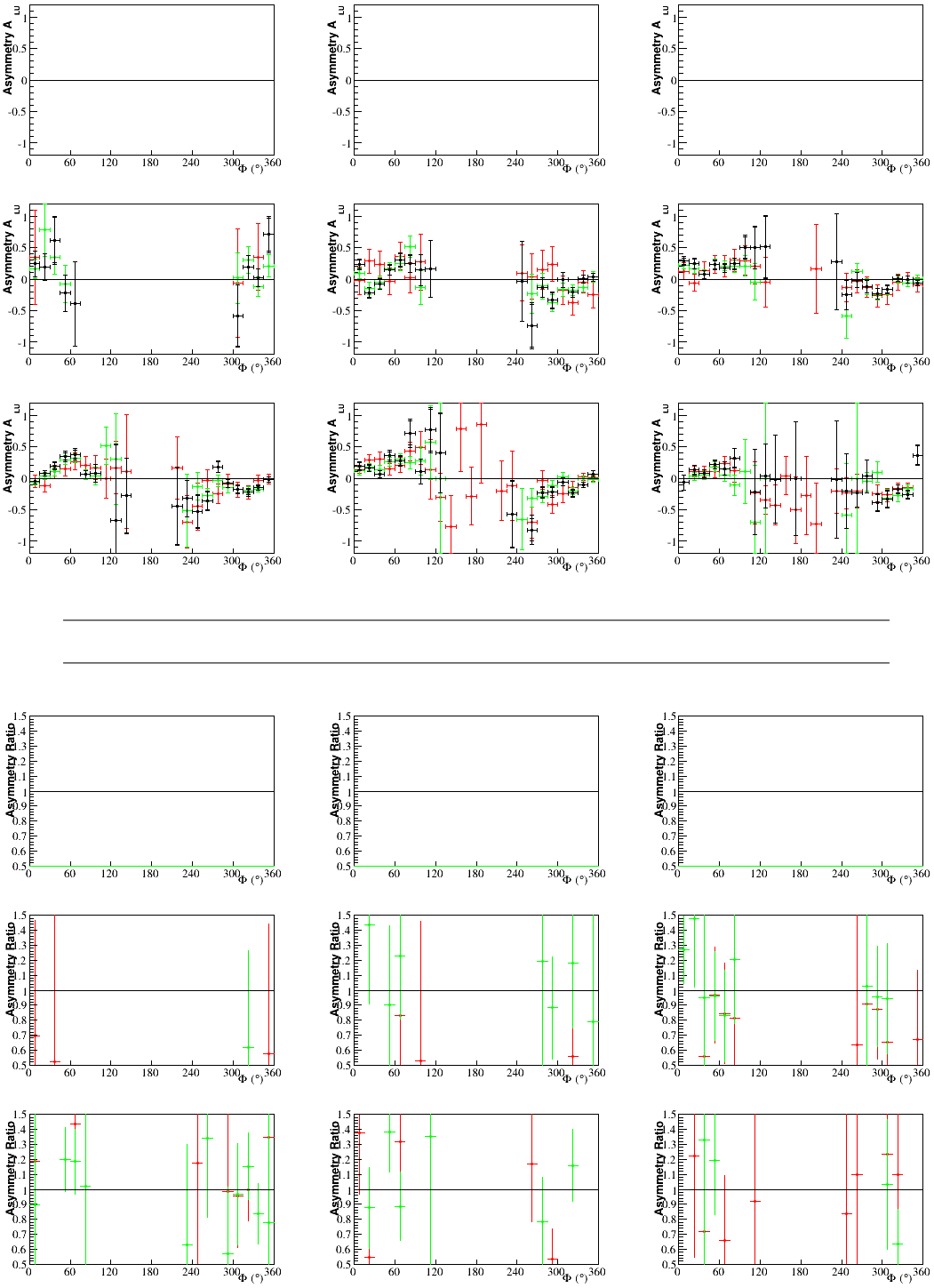

Figure E.63: On top, the asymmetry as a function of Φ. Black represents this analysis. Green is e1-dvcs2 by B. Guegan. Red is e1-dvcs1 by H.S. Jo. On bottom, the asymmetry ratios. Both are for the twenty-first bin in x_B and θ_e, where $0.42 < x_B < 0.58$ and $33^\circ < \theta_e < 45^\circ$. Each panel corresponds to a bin in $-t$ whose limits are: [0.09, 0.13, 0.18, 0.23, 0.30, 0.39, 0.52, 0.72, 1.10, 2.00] Green is $\frac{e1-dvcs2\ Saylor}{e1-dvcs2\ Guegan}$. Red is $\frac{e1-dvcs2\ Saylor}{e1-dvcs1\ Jo}$.

F. Complete Results for GPD Models

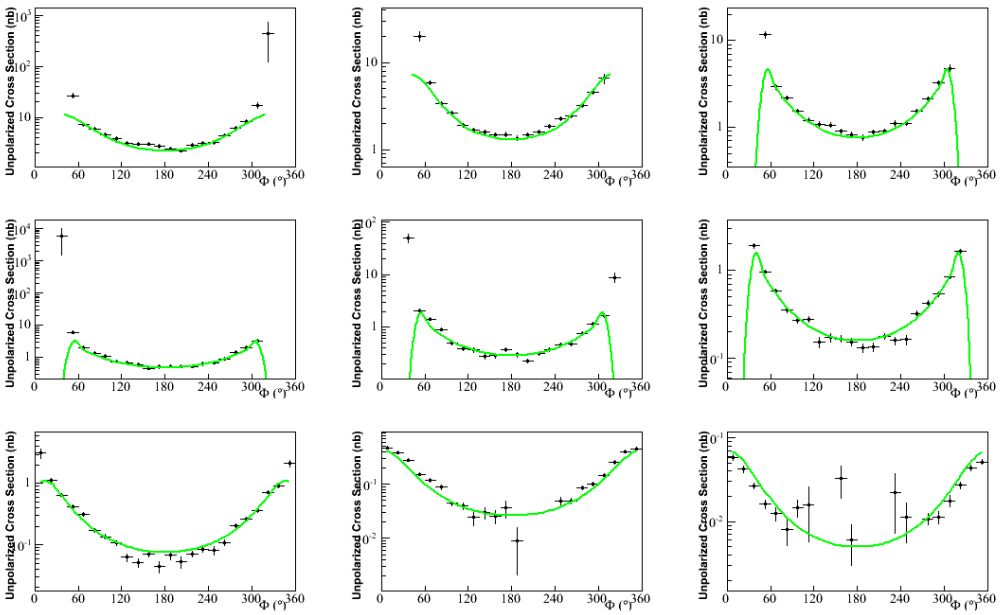

Figure F.1: The unpolarized cross section as a function of Φ for the first bin in x_B and θ_e, where $0.1 < x_B < 0.14$ and $21^\circ < \theta_e < 45^\circ$. Each panel corresponds to a bin in $-t$ whose limits are: [0.09, 0.13, 0.18, 0.23, 0.30, 0.39, 0.52, 0.72, 1.10, 2.00] For both, the green curve corresponds to VGG, the light magenta corresponds to KM10, and the dark magenta corresponds to KM10a.

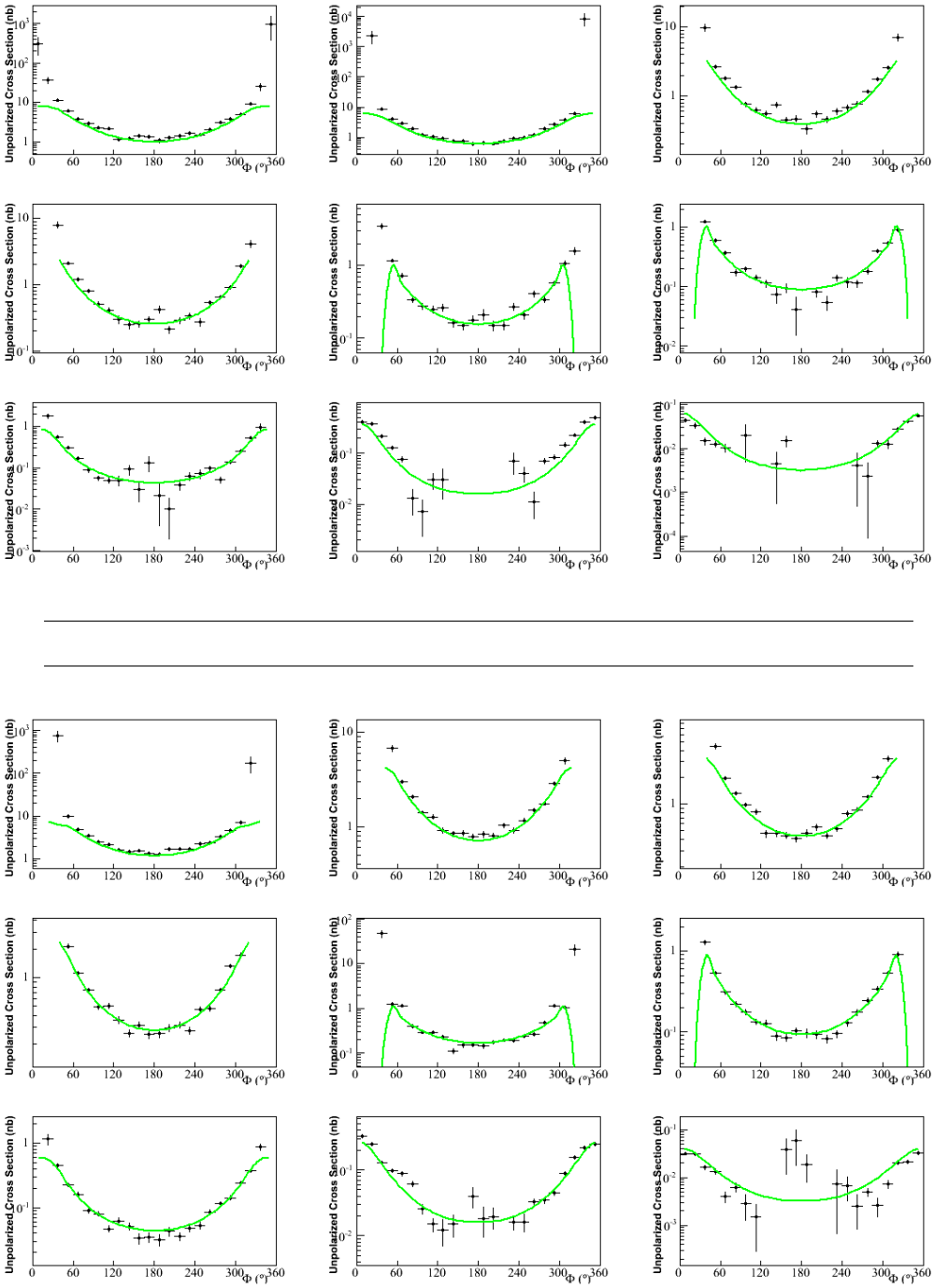

Figure F.2: On top, the unpolarized cross section as a function of Φ for the second bin in x_B and θ_e, where $0.14 < x_B < 0.17$ and $21^\circ < \theta_e < 25.5^\circ$. On bottom, the unpolarized cross section for the third bin in x_B and θ_e, where $0.14 < x_B < 0.17$ and $25.5^\circ < \theta_e < 45^\circ$. Each panel corresponds to a bin in $-t$ whose limits are: [0.09, 0.13, 0.18, 0.23, 0.30, 0.39, 0.52, 0.72, 1.10, 2.00] For both, the green curve corresponds to VGG, the light magenta corresponds to KM10, and the dark magenta corresponds to KM10a.

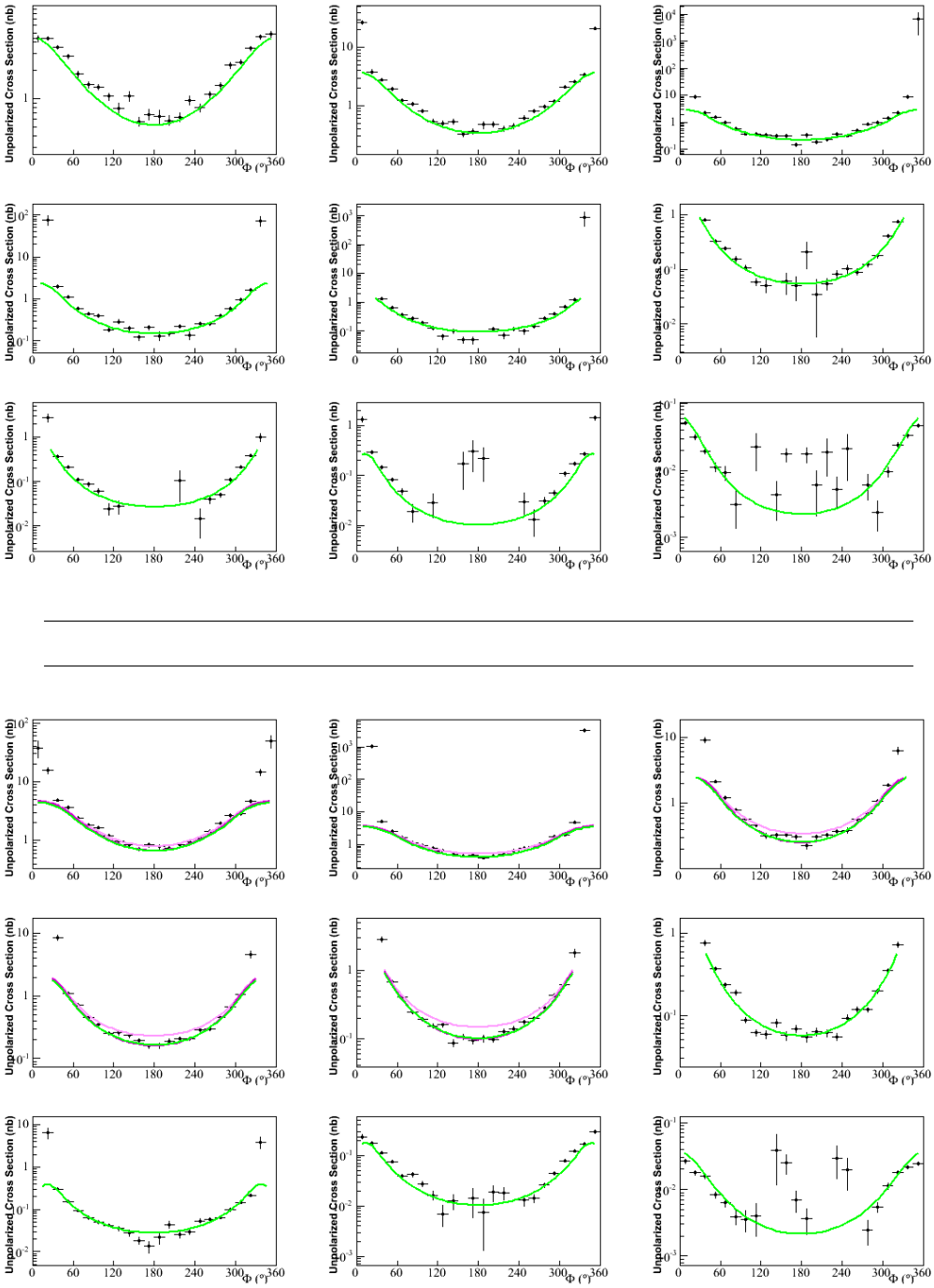

Figure F.3: On top, the unpolarized cross section as a function of Φ for the fourth bin in x_B and θ_e, where $0.17 < x_B < 0.2$ and $21^\circ < \theta_e < 25.5^\circ$. On bottom, the unpolarized cross section for the fifth bin in x_B and θ_e, where $0.17 < x_B < 0.2$ and $25.5^\circ < \theta_e < 45^\circ$. Each panel corresponds to a bin in $-t$ whose limits are: [0.09, 0.13, 0.18, 0.23, 0.30, 0.39, 0.52, 0.72, 1.10, 2.00] For both, the green curve corresponds to VGG, the light magenta corresponds to KM10, and the dark magenta corresponds to KM10a.

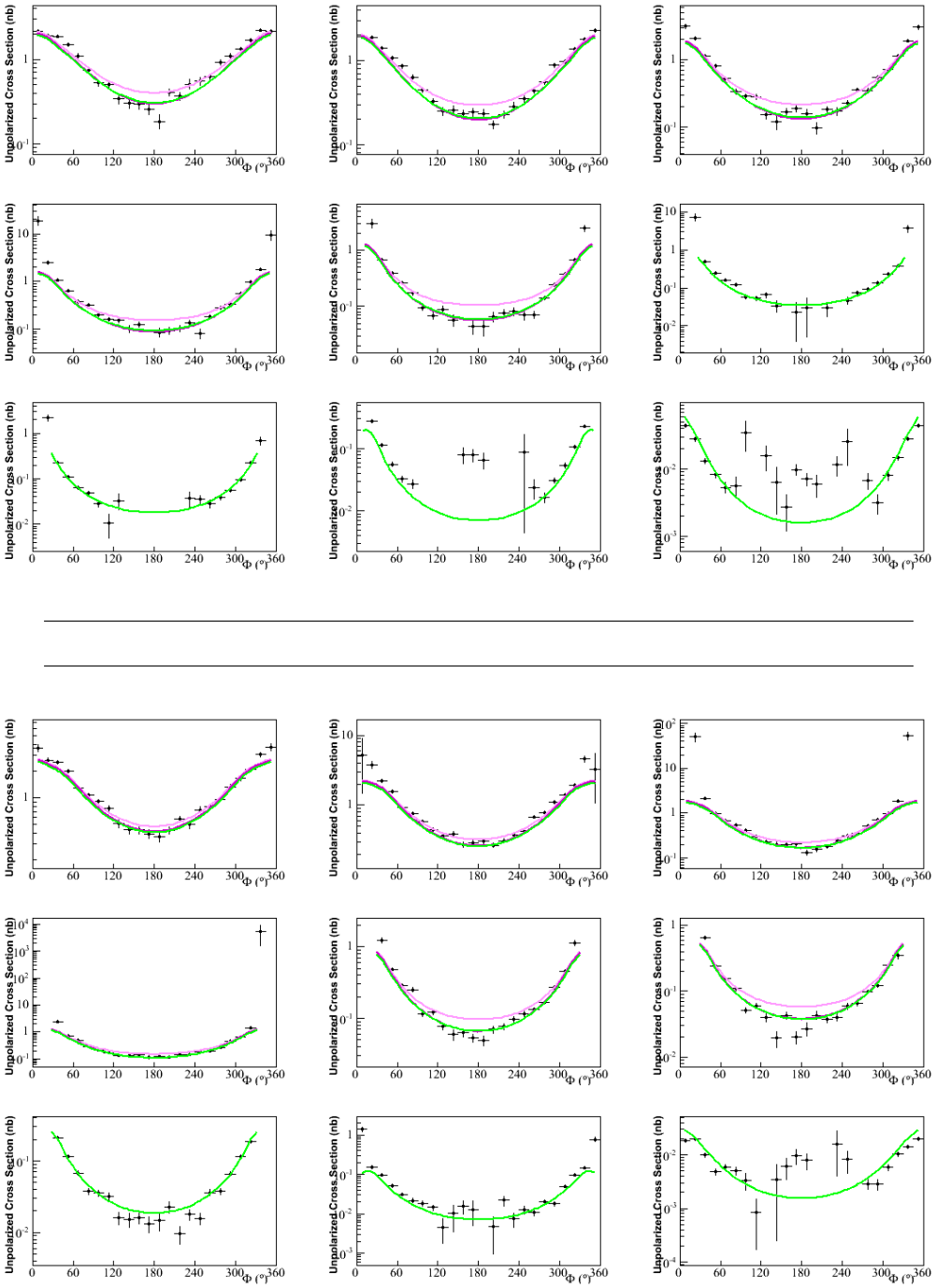

Figure F.4: On top, the unpolarized cross section as a function of Φ for the sixth bin in x_B and θ_e, where $0.2 < x_B < 0.23$ and $21^\circ < \theta_e < 27^\circ$. On bottom, the unpolarized cross section for the seventh bin in x_B and θ_e, where $0.2 < x_B < 0.23$ and $27^\circ < \theta_e < 45^\circ$. Each panel corresponds to a bin in $-t$ whose limits are: [0.09, 0.13, 0.18, 0.23, 0.30, 0.39, 0.52, 0.72, 1.10, 2.00] For both, the green curve corresponds to VGG, the light magenta corresponds to KM10, and the dark magenta corresponds to KM10a.

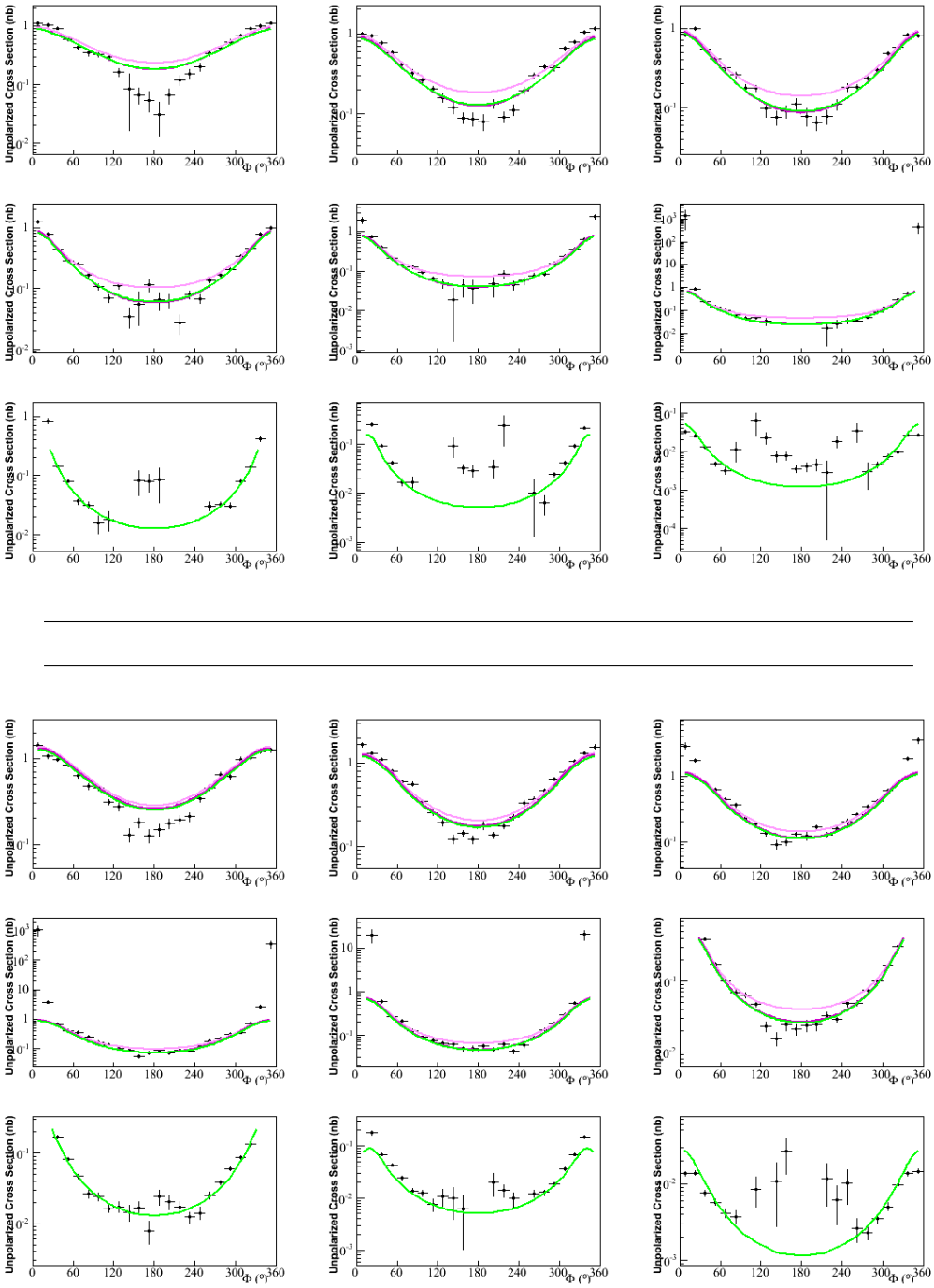

Figure F.5: On top, the unpolarized cross section as a function of Φ for the eighth bin in x_B and θ_e, where $0.23 < x_B < 0.26$ and $21^\circ < \theta_e < 27^\circ$. On bottom, the unpolarized cross section for the ninth bin in x_B and θ_e, where $0.23 < x_B < 0.26$ and $27^\circ < \theta_e < 45^\circ$. Each panel corresponds to a bin in $-t$ whose limits are: [0.09, 0.13, 0.18, 0.23, 0.30, 0.39, 0.52, 0.72, 1.10, 2.00] For both, the green curve corresponds to VGG, the light magenta corresponds to KM10, and the dark magenta corresponds to KM10a.

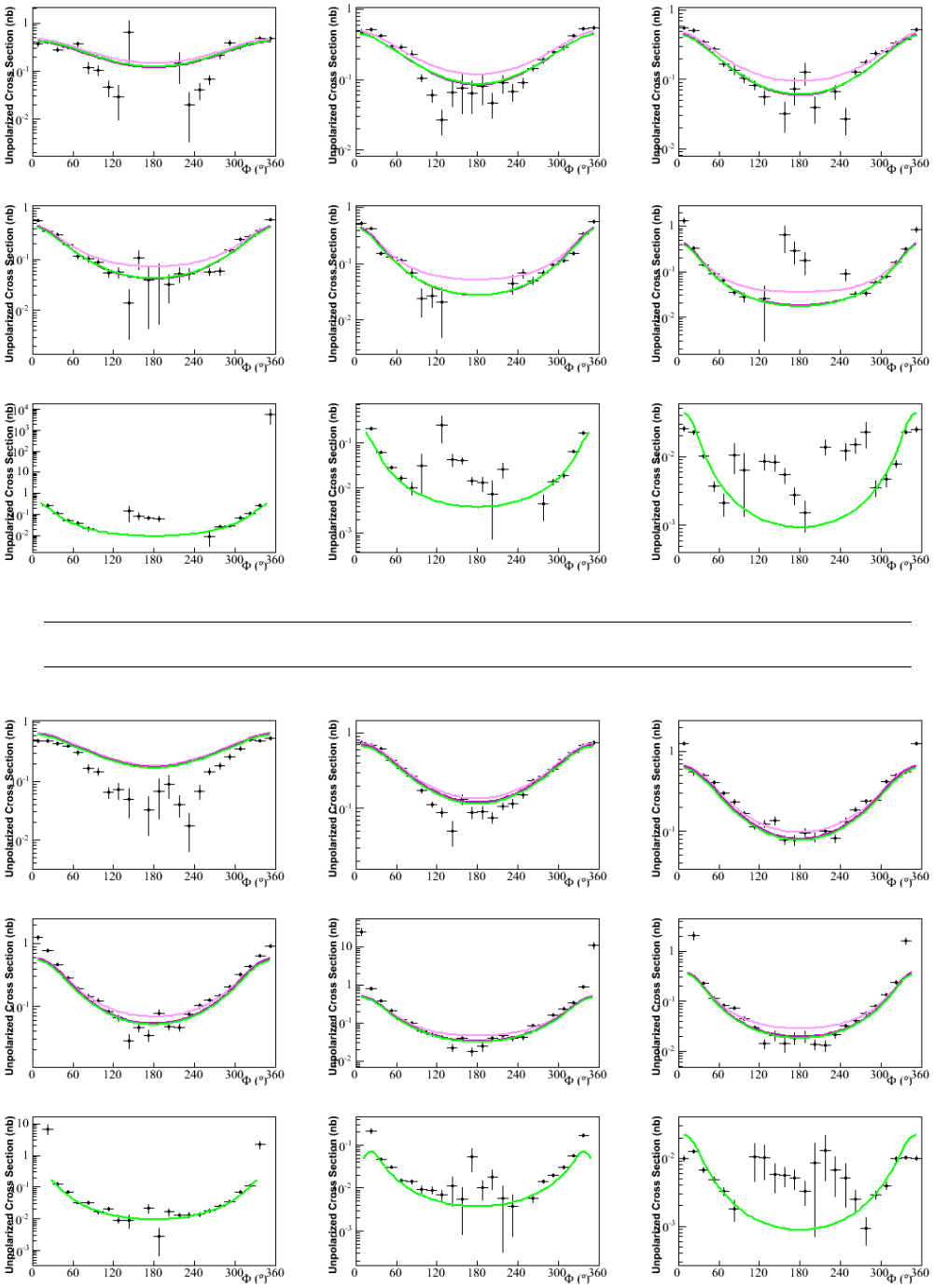

Figure F.6: On top, the unpolarized cross section as a function of Φ for the tenth bin in x_B and θ_e, where $0.26 < x_B < 0.29$ and $21^\circ < \theta_e < 27^\circ$. On bottom, the unpolarized cross section for the eleventh bin in x_B and θ_e, where $0.26 < x_B < 0.29$ and $27^\circ < \theta_e < 45^\circ$. Each panel corresponds to a bin in $-t$ whose limits are: [0.09, 0.13, 0.18, 0.23, 0.30, 0.39, 0.52, 0.72, 1.10, 2.00] For both, the green curve corresponds to VGG, the light magenta corresponds to KM10, and the dark magenta corresponds to KM10a.

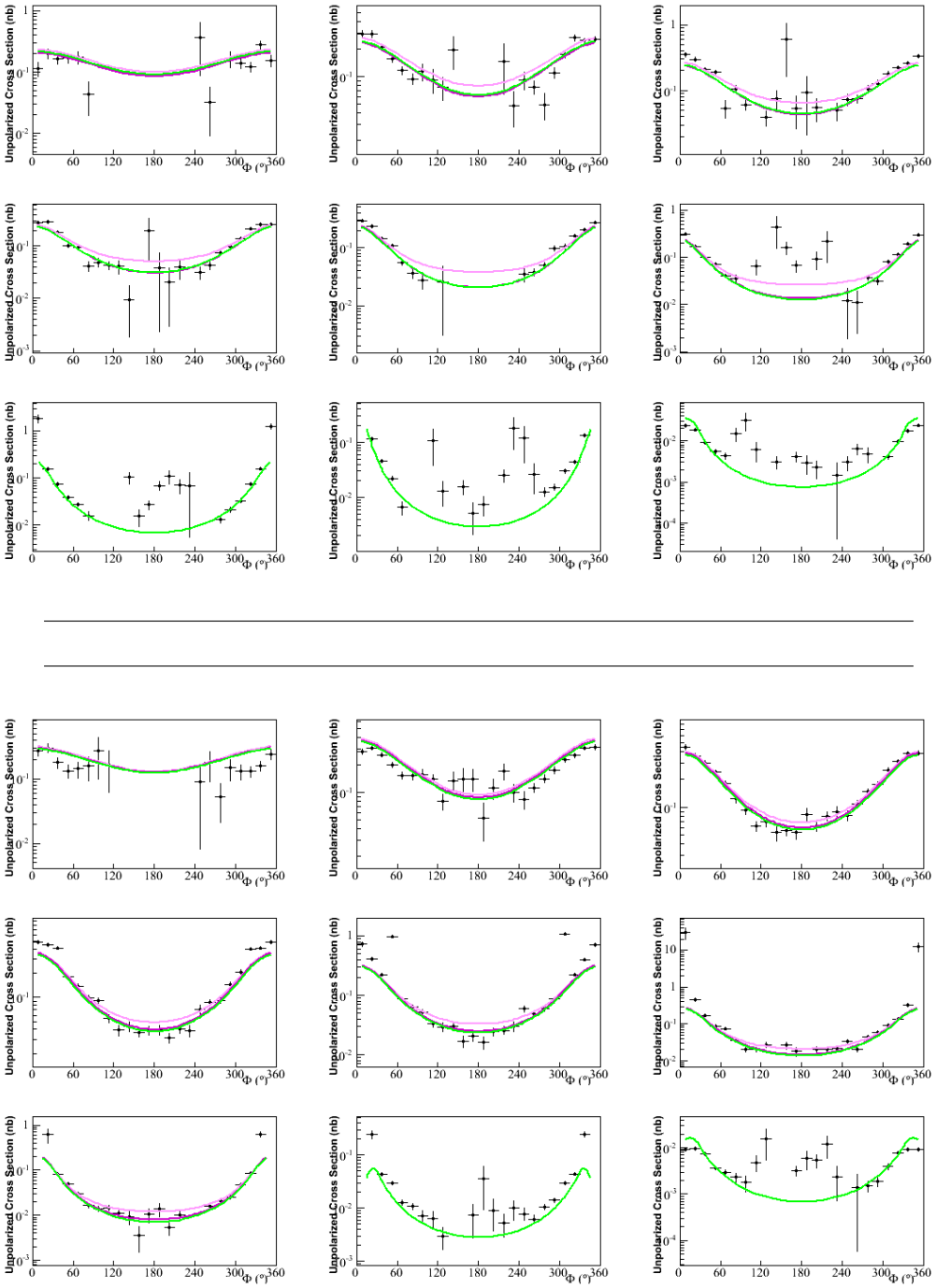

Figure F.7: On top, the unpolarized cross section as a function of Φ for the twelfth bin in x_B and θ_e, where $0.29 < x_B < 0.32$ and $21^\circ < \theta_e < 28^\circ$. On bottom, the unpolarized cross section for the thirteenth bin in x_B and θ_e, where $0.29 < x_B < 0.32$ and $28^\circ < \theta_e < 45^\circ$. Each panel corresponds to a bin in $-t$ whose limits are: [0.09, 0.13, 0.18, 0.23, 0.30, 0.39, 0.52, 0.72, 1.10, 2.00] For both, the green curve corresponds to VGG, the light magenta corresponds to KM10, and the dark magenta corresponds to KM10a.

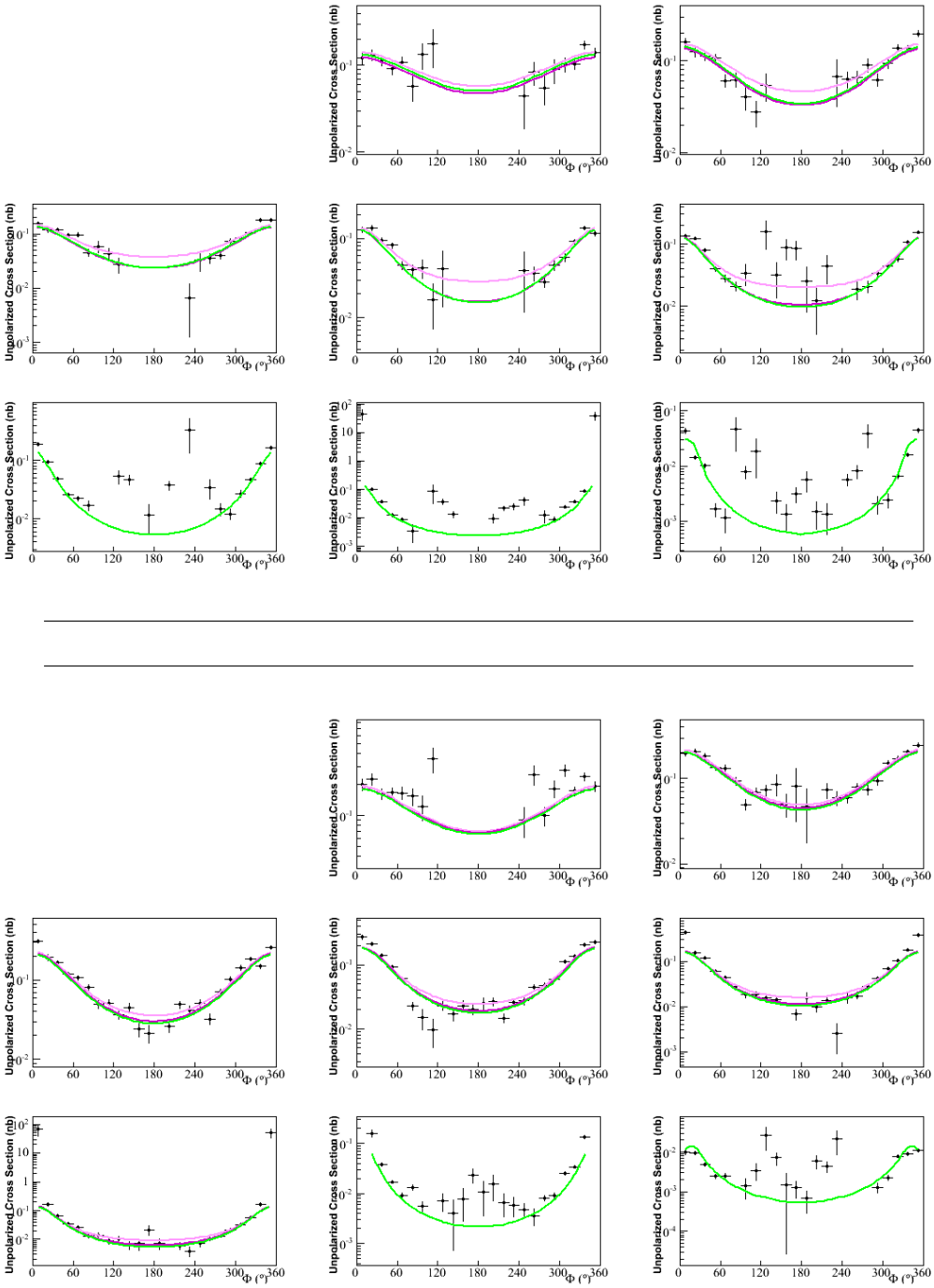

Figure F.8: On top, the unpolarized cross section as a function of Φ for the fourteenth bin in x_B and θ_e, where $0.32 < x_B < 0.35$ and $21^\circ < \theta_e < 28^\circ$. On bottom, the unpolarized cross section for the fifteenth bin in x_B and θ_e, where $0.32 < x_B < 0.35$ and $28^\circ < \theta_e < 45^\circ$. Each panel corresponds to a bin in $-t$ whose limits are: [0.09, 0.13, 0.18, 0.23, 0.30, 0.39, 0.52, 0.72, 1.10, 2.00] For both, the green curve corresponds to VGG, the light magenta corresponds to KM10, and the dark magenta corresponds to KM10a.

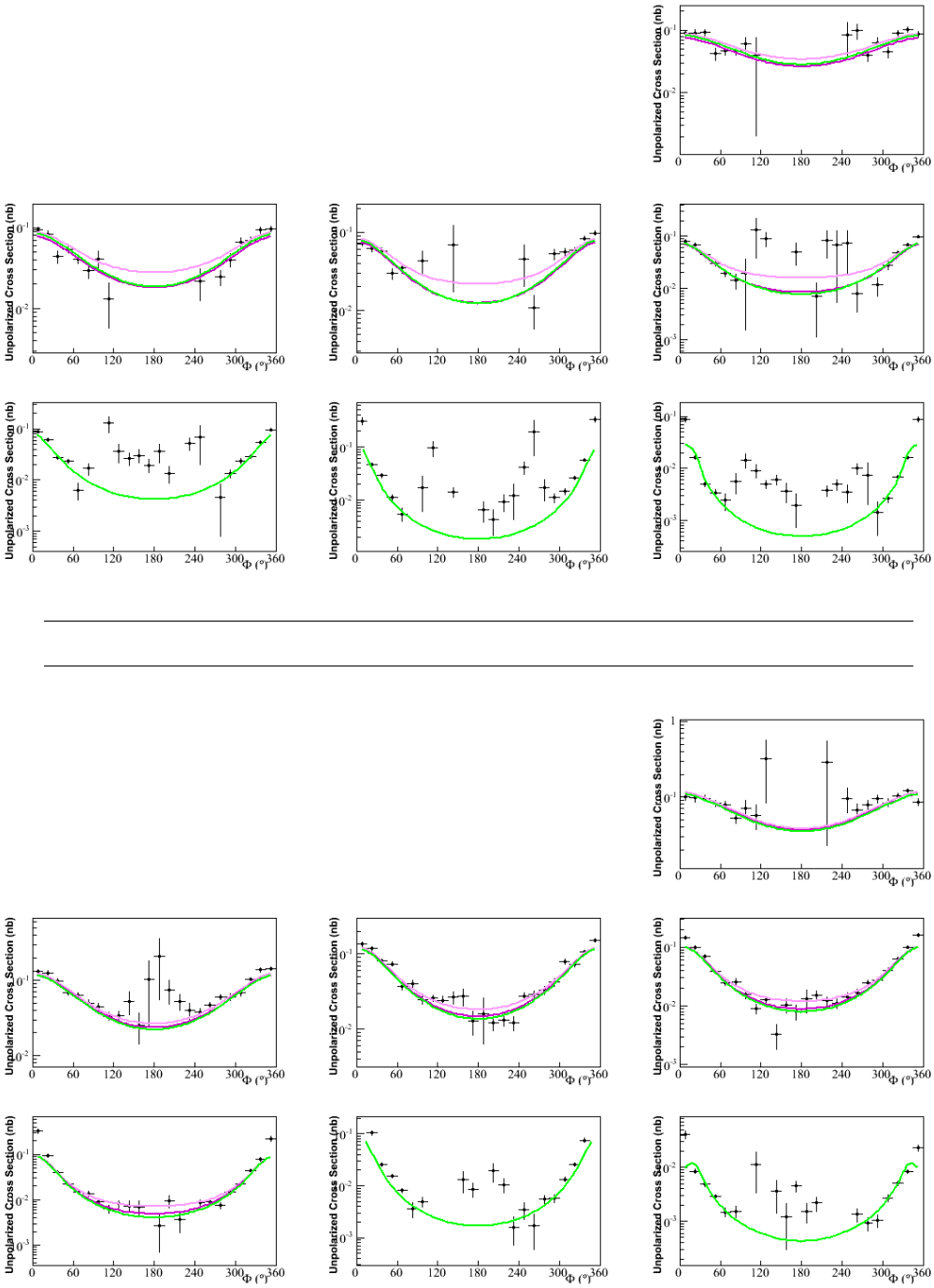

Figure F.9: On top, the unpolarized cross section as a function of Φ for the sixteenth bin in x_B and θ_e, where $0.35 < x_B < 0.38$ and $21^\circ < \theta_e < 28^\circ$. On bottom, the unpolarized cross section for the seventeenth bin in x_B and θ_e, where $0.35 < x_B < 0.38$ and $28^\circ < \theta_e < 45^\circ$. Each panel corresponds to a bin in $-t$ whose limits are: [0.09, 0.13, 0.18, 0.23, 0.30, 0.39, 0.52, 0.72, 1.10, 2.00] For both, the green curve corresponds to VGG, the light magenta corresponds to KM10, and the dark magenta corresponds to KM10a.

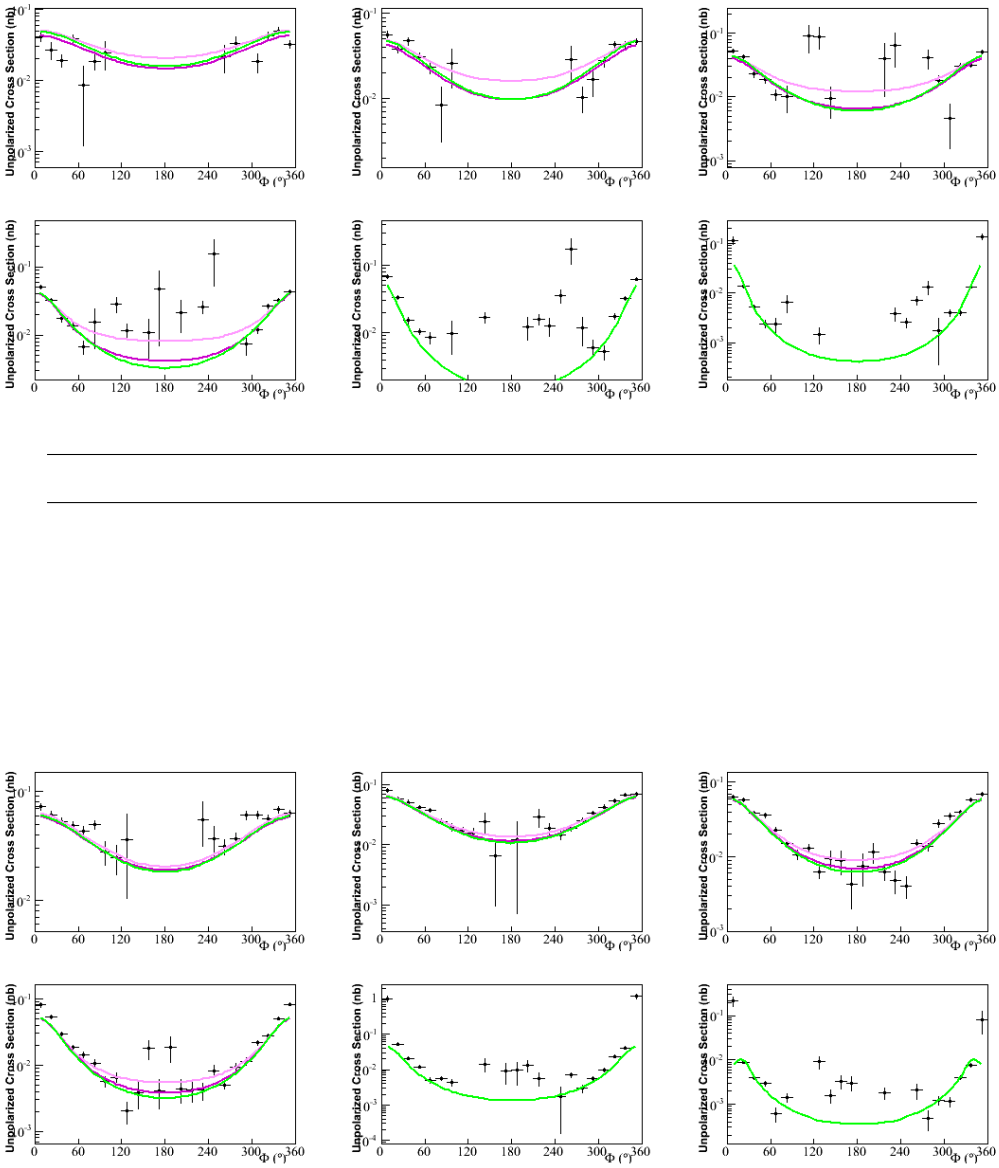

Figure F.10: On top, the unpolarized cross section as a function of Φ for the eighteenth bin in x_B and θ_e, where $0.38 < x_B < 0.42$ and $21^\circ < \theta_e < 28^\circ$. On bottom, the unpolarized cross section for the nineteenth bin in x_B and θ_e, where $0.38 < x_B < 0.42$ and $28^\circ < \theta_e < 45^\circ$. Each panel corresponds to a bin in $-t$ whose limits are: [0.09, 0.13, 0.18, 0.23, 0.30, 0.39, 0.52, 0.72, 1.10, 2.00] For both, the green curve corresponds to VGG, the light magenta corresponds to KM10, and the dark magenta corresponds to KM10a.

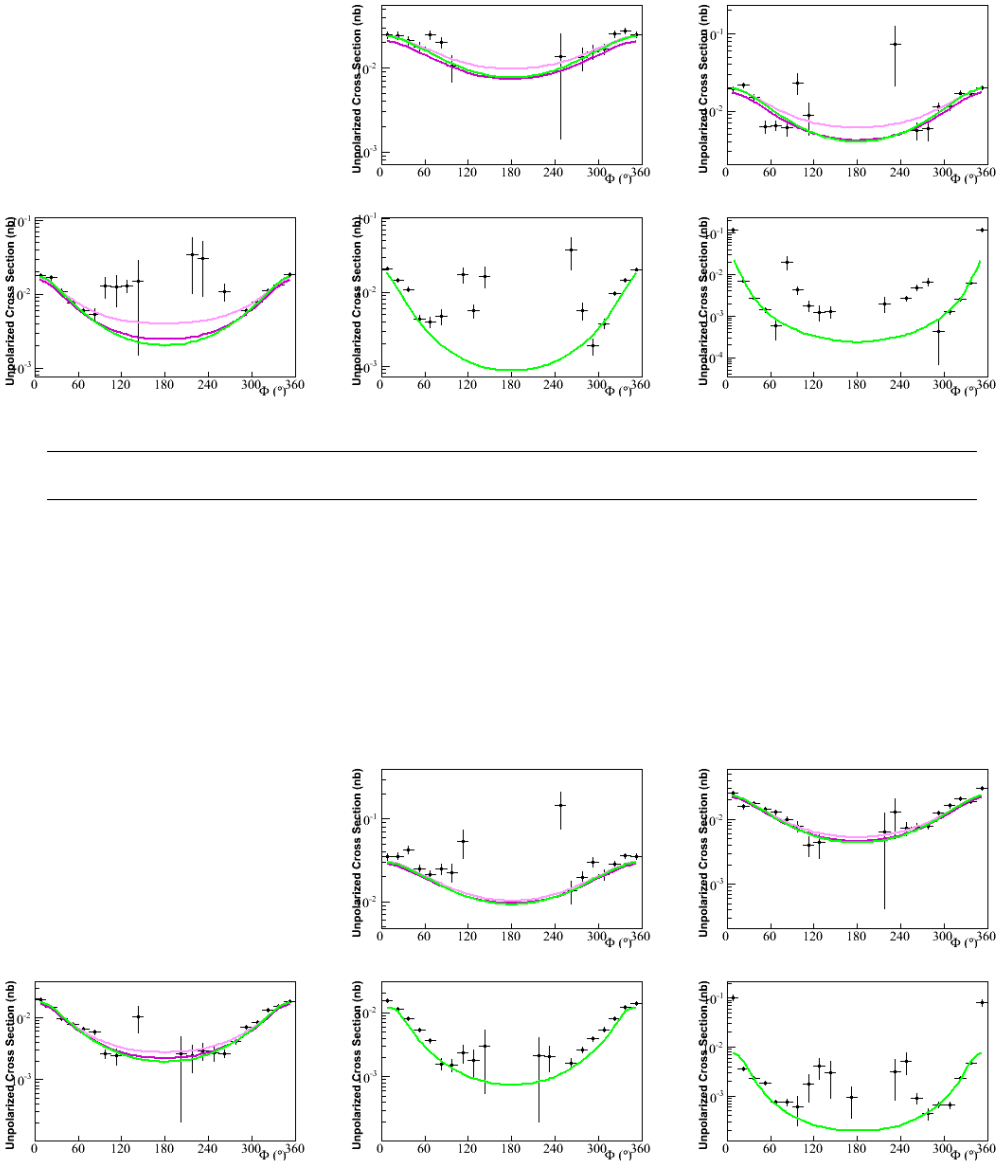

Figure F.11: On top, the unpolarized cross section as a function of Φ for the twentieth bin in x_B and θ_e, where $0.42 < x_B < 0.58$ and $21^\circ < \theta_e < 33^\circ$. On bottom, the unpolarized cross section for the twenty-first bin in x_B and θ_e, where $0.42 < x_B < 0.58$ and $33^\circ < \theta_e < 45^\circ$. Each panel corresponds to a bin in $-t$ whose limits are: [0.09, 0.13, 0.18, 0.23, 0.30, 0.39, 0.52, 0.72, 1.10, 2.00] For both, the green curve corresponds to VGG, the light magenta corresponds to KM10, and the dark magenta corresponds to KM10a.